Processus d'obduction : quelle ampleur, quelle durée, quelle (s) cause (s) ? Le cas de la branche nord de la Néotéthys en Anatolie et Petit Caucase (Turquie, Arménie)

Marc Hässig

▶ **To cite this version:**

Marc Hässig. Processus d'obduction : quelle ampleur, quelle durée, quelle (s) cause (s) ? Le cas de la branche nord de la Néotéthys en Anatolie et Petit Caucase (Turquie, Arménie). Sciences de la Terre. Université Nice Sophia Antipolis, 2014. Français. NNT : 2014NICE4033 . tel-01126862

HAL Id: tel-01126862

https://theses.hal.science/tel-01126862

Submitted on 6 Mar 2015

HAL is a multi-disciplinary open access archive for the deposit and dissemination of scientific research documents, whether they are published or not. The documents may come from teaching and research institutions in France or abroad, or from public or private research centers.

L'archive ouverte pluridisciplinaire **HAL**, est destinée au dépôt et à la diffusion de documents scientifiques de niveau recherche, publiés ou non, émanant des établissements d'enseignement et de recherche français ou étrangers, des laboratoires publics ou privés.

Université de Nice Sophia Antipolis – UFR Sciences
Ecole Doctorale des Sciences Fondamentales er Appliquées
Géoazur UMR 7329

THESE
pour obtenir le titre de
Docteur en Sciences
de l'UNIVERSITE de Nice Sophia Antipolis

Discipline : Sciences de la Terre

présentée et soutenue par
Marc HÄSSIG

Processus d'obduction : quelle ampleur, quelle durée, quelle(s) cause(s) ? Le cas de la branche nord de la Néotéthys en Anatolie et Petit Caucase (Turquie, Arménie)

Thèse dirigée par Marc SOSSON et Yann ROLLAND
soutenue le 24 juin 2014 devant le jury composé de

M. Yves LAGABRIELLE	DR, CNRS, Univ. Rennes	Rapporteur
M. Roland OBERHÄNSLI	Professeur, Univ. Potsdam	Rapporteur
Mme Carole PETIT	Professeur, Univ. Nice Sophia Antipolis	Examinateur
M. Andrea ZANCHI	Professeur, Univ. Milan-Bicocca	Examinateur
M. Stéphane GUILLOT	DR, CNRS, Univ. Joseph Fournier	Examinateur

Université de Nice Sophia Antipolis – UFR Sciences
Ecole Doctorale des Sciences Fondamentales er Appliquées
Géoazur, UMR 7329

THESE
pour obtenir le titre de
Docteur en Sciences
de l'UNIVERSITE de Nice-Sophia Antipolis

Discipline : Sciences de la Terre

présentée et soutenue par
Marc HÄSSIG

Processus d'obduction : quelle ampleur, quelle durée, quelle(s) cause(s) ? Le cas de la branche nord de la Néotéthys en Anatolie et Petit Caucase (Turquie, Arménie)

soutenue le 24 juin 2014 devant le jury composé de

M. Marc SOSSON	DR, CNRS, Univ. Nice Sophia Antipolis	Directeur
M. Yann ROLLAND	HDR, Univ. Nice Sophia Antipois	co-Directeur
M. Yves LAGABRIELLE	DR, CNRS, Univ. Rennes	Rapporteur
M. Roland OBERHÄNSLI	Professeur, Univ. Potsdam	Rapporteur
Mme Carole PETIT	Professeur, Univ. Nice Sophia Antipolis	Examinateur
M. Andrea ZANCHI	Professeur, Univ. Milan-Bicocca	Examinateur
M. Stéphane GUILLOT	DR, CNRS, Univ. Joseph Fournier	Examinateur

Université de Nice Sophia Antipolis – UFR Sciences
Ecole Doctorale des Sciences Fondamentales er Appliquées
Géoazur, UMR 7329

Université de Nice Sophia Antipolis – UFR Sciences
Ecole Doctorale des Sciences Fondamentales er Appliquées
Géoazur, UMR 7329

Thèse préparée au laboratoire Géoazur UMR 7329

Université de Nice Sophia Antipolis
Parc Valrose
28 avenue Valrose
06108 Nice Cedex 2
France

et

Campus CNRS, les Lucioles 1
250, rue Albert Einstein
Sophia Antipolis
06560 Valbonne
France

Cette thèse a fait l'objet d'un soutien financier du Ministère de la Recherche et de l'Enseignement Supérieur via l'attribution d'une bourse de recherche et a été réalisé dans le cadre du programme DARIUS.

Photo de couverture : *Panorama du sud au nord (de gauche à droite) de la zone de Vedi, 40 km au sud-est d'Erevan, Arménie.*

Université de Nice Sophia Antipolis – UFR Sciences
Ecole Doctorale des Sciences Fondamentales er Appliquées
Géoazur, UMR 7329

Université de Nice Sophia Antipolis – UFR Sciences
Ecole Doctorale des Sciences Fondamentales er Appliquées
Géoazur, UMR 7329

Remerciements

Si on m'avait dit lorsque je suis revenu en France à l'âge de seize ans, ne sachant ni lire ni écrire le français, que j'écrirai un manuscrit de thèse, je ne l'aurai pas cru. Bien entendu, plus d'une décennie après, la réalisation de ce projet n'a pas été sans difficultés mais l'aide et le soutien de nombreuses personnes que je tiens à remercier, m'ont permis de mener à bien mon projet dans d'excellentes conditions.

Il y a un peu moins de 6 ans, je débarquais à Nice pour m'inscrire dans le parcours recherche. Deux ans après et un Master 2 en poche, j'ai intègré l'équipe *Géochronologie-Géochimie-Pétrologie* (GGP), récemment incorporé avec d'autres pour former l'équipe *Dynamique Orogénique* dans le cadre d'une thèse. Depuis, ayant vécu des moments forts, aussi enthousiasmants que décourageants, et rencontré des personnalités aussi embrasées que rassurantes, j'aimerai remercier tous les gens qui m'ont aidé de quelconque manière et en particulier l'énumération suivante.

Je voudrais tout d'abord témoigner de ma gratitude envers ***Marc SOSSON*** et ***Yann ROLLAND*** qui ont été présents tout au long de ces 3 ans et demi (et plus en comptant la première et deuxième année de Master). Que ce soit sur le terrain, au laboratoire ou en salle de cours, d'un soutien permanent, vous avez su me prodiguer des conseils judicieux et de profiter de vos connaissances, de vos expériences et votre savoir-faire. A l'écoute, vous m'avez néanmoins laissé libre autant sur le plan scientifique que sur le plan organisationnel tout au long de ma thèse. Je vous remercie grandement.

Merci aux membres du jury qui m'ont fait l'honneur d'accepter, de s'intéresser et de juger ce travail. Je tiens donc à remercier ***Yves LAGABRIELLE***, ***Roland OBERHÄNSLI***, ***Andrea ZANCHI***, ***Séphane GUILLOT*** et ***Carole PETIT***.

Ma gratitude va également aux collègues arméniens ***Ara AVAGYAN***, ***Ghazar GALOYAN***, ***Mushegh MKRTCHYAN***, ***Lilit SAHAKYAN*** et ***Sargis VARDANYAN***. Je peux vous assurer qu'en arrivant dans un pays peu connu, un visage familier vaut bien tout l'or du monde. C'est pourquoi par la même occasion, je voudrais remercier ***Gültekin TOPUZ*** et ***Ömer Faruk ÇELIK***, des collègues turcs. Je remercie également ***Carla MÜLLER*** pour sa bonne humeur, ses sourires, sa manie de toujours garder un morceau de pain pour les animaux qu'on croiserait mais surtout pour sa manière de me motiver sur le terrain en fin de journée pour fournir un dernier effort

Je voudrais aussi témoigner de ma gratitude envers ***Thibault DURETZ*** pour sa connaissance en matière de modélisation numérique.

Je remercie ***Claude MERLET*** et ***Bernard BOYER*** de Géosciences Montpellier ainsi que ***Jean-Luc DEVIDAL*** l'Université Blaise Pascal, Clermont-Ferrand pour leur aide lors d'analyses à la microsonde.

Je remercie, à titre posthume, ***Michel MANETTI*** pour la découverte d'artistes, du travail de la pierre, l'aide technique,…et des longues discussions qui ont rendu les heures de divers broyage et de séparation minérale supportables. Je souhaite rajouter ***Sylvain GALLET***, sans qui une grande partie des analyses géochronologiques seraient du domaine du rêve.

Je tiens à remercier ***Gérard GIANNERINI*** et ***Jean-Marc LARDEAUX***. Formidables interlocuteurs, excellent géologues et pédagogues, j'ai apprécié votre volonté de transmettre

vos connaissances de la géologie, toujours dans la bonne humeur. Je n'oublierais jamais les très bons moments passés sur le terrain dans les Alpes, que ce soit lors de « Géotravers» ou en sortie avec les étudiants, ainsi que les innombrables discussions scientifiques et non scientifiques, un grand merci.

Je remercie l'ensemble des membres du laboratoire Géoazur avec qui j'ai pu avoir des discussions tout au long de ces années. Je voudrais remercier l'équipe de direction, en particulier ***Emmanuel TRIC*** et ***Jenny TREVISAN***, pour leur présence et assistance tout au long de ces quatre dernières années. Par la même occasion je tiens à exprimer ma gratitude à tous les gestionnaires que j'ai pu côtoyer (***Véronique LARGE***, ***Magali AUFEUVRE***, ***Reine SAIGHI***, ***Sandrine BERTETIC***, ***Frédéric SENECA*** et ***Valérie MERCIER-VALERO***) qui font réellement tourner Géoazur.

Il y a tout de même quelques personnes que j'aimerais remercier tout particulièrement pour les petits coups de pouce en plus: pour les sushis (***Julie SCHNEIDER***), les soirées (***Maurin VIDAL***), les discussions scientifiques et autres (***Christophe RENAC***), les cafés et les mots-croisés au soleil du matin (***Chrystele VERATI***). Sans oublier les membres de l'équipe enseignante de Valrose.

Merci aux amis thésards maintenant docteurs avec qui j'ai pu passer d'innombrable bons moments, toujours là pour partager (…les pétages de câble) : ***Benoit DERODE***, ***Flor BARAT***, ***Marianne MAROT*** et ***Clara CASTELLANOS LOPEZ*** merci pour ces moments de réconfort. Je crois qu'ils ont été autant bénéfiques pour vous que pour moi. Merci à ***Swann ZERATHE*** en particulier pour la pêche ainsi qu'à ***Auré SALA*** pour l'avoir laissé venir avec moi.

Je voudrais aussi remercier ceux pour qui la fin arrive ainsi qu'aux nouveaux qui sont arrivés alors que j'avais déjà commencé cette aventure. Merci ***Maëlle KELNER***, ***Cécile JOUBER***, ***Clément VITARD***, ***Chloé LOURY***, ***Flor MARY***, ***Virginie HASSOUN*** pour avoir partagé les pauses café, les prises de tête tout comme les fous rires et moments de décrochage. Je n'oublie pas ***Sadrac SAINT-FLEUR*** et ***Alain DUJARDIN*** et les aventures viennoises. Il y a aussi ***Clément PERRIN***, ***Quentin BLETERY*** et ***Nestor CERPA GILVONIO***, ***Julien BALESTRA***, ***Jérémy GIULIANO*** et ***Yevgeniya SHEREMET*** avec qui j'ai toujours apprécié discuté et rigoler sans oublier l'ami brésilien ***Edouardo FONTANA*** qui m'a appris qu'il y a toujours 2 choses…

Merci à ***J-C***, à ***Alex (Roger)***, à ***Lou***, au ***Lolo du Ghetto***, à ***Lou Scambi (le bienheureux)***, au ***Bastou'***, au ***Dodo (le dernier des dodos)***, à ***Wahib*** et tant d'autres amis de Nice qui ont fait de cette période une réelle aventure pleine de rebondissement et d'inattendus.

Maintenant voilà le tour des potes et la famille. ***Guillaume LEVACHER*** et ***Emma DECOUTRYE***, ***Marie-Carmen*** et ***Michel LEVACHER***, ***Stan LEDOCHOWSKI (Stashu)***, ***Olivier VAN DOOREN (alias Zitoon, alias Wone-2, alias Obi-wone, alias Le Belge, alias Vando)***, ***Antoine SERIS*** ainsi que son frère ***Pierre***, ***Jérôme PRAT*** et ***Gwén RIVIERE***, ***Maître Vince***, ***Adeline VOLLANT***, ***Julien CAILLON*** et sa femme ***Anne-Laure BILLAUD-CAILLON***, ***Magalie DEJOB*** et ***la X-Krew***, je vous dois à tous un grand merci pour le soutien que vous m'avez montré lorsque j'ai pris ma décision de partir de Lyon pour poursuivre ma

passion. Merci aussi pour l'accueil et l'hospitalité que vous m'avez offert à chaque fois que je remontais dans ma ville natale.

Je me sentirai mal si je ne prenais le temps de remercier les coloc' qui m'ont soutenu mais surtout supporté au cours ces deux dernières années, merci ***Bruno SCALABRINO***, ***Antony SARLIN*** et ***François LEVIEZ***.

Merci donc à tous les potes et d'innombrable autres (lyonnais, azuréens, valrosiens, villefranchois, sophipolitains parisiens, géorgiens, montpelliérains, sud-américains, turcs, italiens, espagnoles…) que je ne vois pas aussi souvent que j'aimerais, c'est toujours un plaisir de vous retrouver.

Enfin, je tenais à remercier mes 'co-bureau' que j'ai appris à connaitre aux cours de ces années de thèse ; ***Guillaume SANCHEZ***, ***Romain DARNAULT***, ***Adrien ROMAGNY*** et tout particulièrement l'ami ***Victorien BAUVE*** (*alias* ***Vickey Ryder***, *alias* ***Vickey sans cœur***,…) personnage extrêmement sympathique, serviable et toujours d'une vraie rock attitude rassurante, parfois déconcertante. Je pense que tu seras d'accord avec moi quand je dis que tout au long de ces 6 ans (Master 1, 2 et puis la Thèse), la cohabitation n'a certes pas été un exercice facile mais qu'il est bon d'avoir un ami à qui parler, contre qui faire rebondir des idées, envers et avec qui se lamenter, avec qui rigoler et pleurer, et même avec qui jouer en bourse. J'en garderais un très bon souvenir (les karaokés *« ...à base de popopopop »*, les soirées dans le vieux, les terrains, les innombrables discussions sur hydro-séismicité, le découplage socle/couverture, la géodynamique, l'héritage …la meilleur chartreuse-ito, qui gagnerait à la courte-paille et j'en passe…). Voilà, on a tous les deux réussi à la finir cette thèse. D'autres horizons et projets s'ouvrent à nous maintenant. Bon courage mon ami.

Pour finir, je tiens à exprimer ma profonde gratitude envers ***ma mère***, ***mes grands-parents*** ainsi qu'à ***mon frère, sa femme et leurs deux filles*** qui ont été une source de soutien et d'encouragement jusqu'au bout.

Université de Nice Sophia Antipolis – UFR Sciences
Ecole Doctorale des Sciences Fondamentales er Appliquées
Géoazur, UMR 7329

…à la mémoire de mon père.

Etudie, non pour savoir plus, mais pour savoir mieux.

Sénèque

Université de Nice Sophia Antipolis – UFR Sciences
Ecole Doctorale des Sciences Fondamentales er Appliquées
Géoazur, UMR 7329

Résumé

Dans de nombreuses chaînes de montagnes, on observe des témoins du processus d'obduction, correspondant au transport de la lithosphère océanique sur la croûte continentale. Le paradoxe intrinsèque de ce phénomène est celui-ci : des roches denses ($\rho>3$) se retrouvent au-dessus de roches moins denses ($\rho\approx2,7$). Les processus à l'origine de cette bizarrerie tectonique sont encore mal compris.

Les ophiolites du Petit Caucase et du NE de l'Anatolie correspondent à un exemple extrême de ce phénomène puisqu'on constate un transport de fragments de lithosphère océanique sur plusieurs centaines de kilomètres, à l'échelle de l'ensemble d'une bordure continentale (>1000 km) vers 90 Ma.

En adoptant une stratégie pluridisciplinaire lors de l'étude de ces ophiolites, nous avons pu préciser l'évolution des premiers stades de la fermeture néotéthysienne et en conséquence l'obduction de ces dernières, tels que :

- L'existence d'un domaine océanique continu d'est en ouest en subduction sous l'Eurasie, séparant l'Eurasie (au nord) de l'ensemble continental Sud-arménien-plateforme Taurides-Anatolides (au sud).
- La genèse d'un domaine océanique dans un contexte de supra-subduction à arrière-arc par ouverture lente, attribué à la formation de ces ophiolites, entre le Jurassique inférieur et Crétacé inférieur (c.180~150 Ma).
- L'obduction quasi simultanée de ces ensembles ophiolitiques, tout au long de la suture d'Izmir-Ankara-Erzincan et Sevan-Akera au Turonien-Coniacien-Santonien (c. 94~85 Ma).
- Un métamorphisme d'unités à la base de ces ophiolites (la semelle ophiolitique) permettant de contraindre leur dynamique de mise en place.
- Un volcanisme dans le bloc continental sud-arménien permettant de proposer une évolution des structures tectoniques inédites vers 160~130 Ma.

Ces données suggèrent fortement une mise en place commune de l'ensemble de ces corps ophiolitiques de la région d'étude sous la forme d'une nappe, dont l'épaisseur actuelle est très réduite (quelques kilomètres tout au plus). Ceci en fait l'une des plus grandes nappes ophiolitiques obduites du globe (à l'affleurement dans une chaîne de collision).

La modélisation numérique a validé l'hypothèse que la mise en place de cette nappe s'est faite grâce à des conditions thermiques particulières. Elle suggère que l'obduction d'ophiolites vieilles nécessite un état thermique de la lithosphère océanique proche de celui d'une lithosphère jeune (0-40 Ma). Un tel état thermique est suggéré pour les ophiolites du Caucase s.l. par la mise en place de laves alcalines sur l'ophiolite avant obduction sous forme de monts sous-marins et/ou de plateau océanique au Crétacé inférieur. Ceux-ci bloquant la subduction sous l'Eurasie expliquent également la quiescence du volcanisme sur cette marge, et le contexte de forçage tectonique de l'autre côté de l'océan, conduisant à l'obduction simultanée sur le bloc continental arménien-anatolien et sur l'Arabie.

Université de Nice Sophia Antipolis – UFR Sciences
Ecole Doctorale des Sciences Fondamentales er Appliquées
Géoazur, UMR 7329

Abstract

Within many mountain ranges slivers of preserved oceanic lithosphere evidence tectonic processes responsible for their emplacement on top of the continental crust. The first order anomaly inherent to this phenomenon is that dense rocks ($\rho>3$) end up on top of less dense rocks ($\rho\approx2.7$). The processes responsible for such a tectonic oddity remain uncertain.

The ophiolites of the Lesser Caucasus and NE Anatolia are prime examples of this phenomenon, tectonic transport of fragments of oceanic lithosphere is evidenced on the entire continental marge (>1000 km) around 90 Ma.

The multidisciplinary approach used throughout the study of the ophiolites of the Lesser Caucasus and NE Anatolian regions yielded clues specify the evolution of the Tethys and consequently the obduction of the ophiolites. These results include:

- The existence of a continuous oceanic domain, from East to West, separating Eurasia (to the North) from the South Armenian Block-Taurude-Anatolide Platform (to the South). This ocean was subducting towards the North under the Eurasian margin.
- The creation of oceanic crust in a supra-subduction to back-arc setting, through a slow ocean spreading process between Early Jurassic and Early Cretaceous times (c. 180~150 Ma).
- Nearly simultaneous obduction along the Izmir-Ankara-Erzinncan and Sevan-Akera suture zones of the ophiolites during Turonian-Coniacian-Santonian times (94~85 Ma).
- Directly under the ophiolites, metamorphic units (ophiolitic sole) allow us to constrain the emplacement of the ophiolites.
- Volcanism in the South Armenian Block allows us to propose an unprecedented evolution of the tectonic structures between c. 150~130 Ma.

This dataset strongly suggests common emplacement of the ophiolites of the study area, resembling a thrust sheet. This would be one of the biggest ophiolite nappe complexes in the world (outcropping in a mountain range).

Numerical modeling validates the hypothesis that emplacement of the ophiolitic nappe is due to particular thermal conditions. It suggests that in order to obduct old oceanic lithosphere obduction it needs to have a thermal state close to that of young oceanic lithosphere (0-40 km). Such a thermal rejuvenation is supposed for the ophiolites of the Caucasus s.l. evidenced by alkaline lavas emplaced on the ophiolite prior to the obduction event during the Late Cretaceous. Resulting seamounts and/or oceanic plateaus upon entery of the subduction zone under Eurasia would block it. This is compatible with the observed gap in the volcanism along the Eurasian margin as well as the obduction event on the South Armenian Block-Taurude-Anatolide Platform and Arabia.

Table des matières

Remerciements v

Résumé xi

Abstract xiii

Liste des Illustrations xix

Liste des Tableaux xxix

Introduction 1

Chapitre 1 – Ophiolite/Obduction : historique et problèmatique de la thèse 7

I.1 Concepts 9

1.1 Ophiolite 9

1.2 Obduction 13

I.2 Contexte général de la zone d'étude 16

I.3 Problèmatique avant thèse 18

Chapitre 2 - Méthodes analytiques 21

II.1 EMPA 23

1.1 Appareillage 23

1.2 Mode d'utilisation 24

1.3 Analyse qualitative 25

1.4 Analyse quantitative 25

1.5 Conditions opératoires 25

1.6 Préparation de l'échantillon 26

II.2 ICPMS 26

II.3 Géochronologie 28

3.1 Caractéristiques minérales 29

3.2 Protocole de séparation des minéraux 30

3.3 La méthode ^{39}Ar-^{40}Ar 32

3.4 La méthode U-Pb 34

II.4 Perple_X 38

Chapitre 3 - Etude géologique, pétrogéochimique et métamorphique des ophiolites nord-est anatoliennes et du Petit Caucase : implication géodynamique. 43

III.1 Article 1 – New structural and petrological data on the Amasia ophiolites (NW Sevan-Akera suture zone, Lesser Caucasus): Insights for a large-scale obduction in Armenia and NE Turkey) 45

Abstract 47

1.1 Introduction 48

1.2 Geological context 48

1.3 Field and sample observations 55

1.4 $^{40}Ar/^{39}Ar$ Dating 60

1.5 Geochemistry 64

1.6 Discussion 67

Acknowledgements 73

References 73

Tables 81

III.2 Article 2 – P-T-t history of the Amasia ophiolite "metamorphic sole" (Amasia, Lesser Caucasus): implications for the obduction process of an old oceanic lithosphère 85

Abstract 90

2.1 Introduction 91

2.2 Geological setting 92

2.3 Field Observations 96

2.4 Geochemistry 102

2.5 Petrography and mineral chemistry 104

2.6 Pressure-Temperature path of the Amasia amphibolites 107

2.7 $^{40}Ar/^{39}Ar$ Dating 111

2.8 Discussion 114

2.9 Conclusion 121

Acknowledgments 122

References 122

Tables 135

Chapitre 4 - Relations entre les ophiolites du N-E de l'Anatolie et du Petit Caucase : arguments pour une obduction de grande échelle de croute océanique. 149

IV.1 Article 3 – Linking the NE Anatolian and Lesser Caucasus ophiolites: evidence for large scale obduction of oceanic crust and implications for the formation of the Lesser Caucasus-Pontides Arc 151

Abstract 153

1.1 Introduction 155

1.2 Previous works across the NE Anatolia-Lesser Caucasus region 156
1.3 Structural Continuity 163
1.4 Discussion and Geodynamic implications 171
Acknowledgements 177
References 177
Table 189

Chapitre 5 - Métamorphisme du Bloc Sud Arménien (Jurassique Supérieur - Crétacé Inférieur) : subduction à vergence sud de la branche nord de la Néotéthys. 193

V.1 Article 4 – Multi-stage metamorphism in the South Armenian Block during the Late Jurassic to Early Cretaceous: tectonics over south-dipping subduction of Northern branch of Neotethys 195
Abstract 198
1.1 Introduction 199
1.2 Geological Setting 201
1.3 New Field Observations 206
1.4 Mineralogy and Pressure-Temperature path of metamorphic rocks 210
1.5 Geochronology and Geochemistry 212
1.6 Discussion 221
1.7 Conclusion 226
Acknowledgements 227
References 227
Tables 235

Chapitre 6 - Histoire de la branche nord de Néotéthys avant son obduction. ... 241

VI.1 Article 5 – From ocean crust geneis to obduction initiation: history of the northern branch of Neotethys prior to the Late Cretaceous obduction event in NE Anatolian and Lesser Caucasus regions 243
Abstract 248
1.1 Introduction 249
1.2 Main tectonic units 250
1.3 Discussion: what evolution of the geodynamic processes can explain the pre-obduction framework? 261
1.4 Conclusion 267
Acknowlegements 269
References 269

Chapitre 7 - Mise en place d'ophiolites préservées : une modélisation. 283

VII.1 Introduction 287
VII.2 Modélisation numérique 289
2.1 Configuration 289
2.2 Modèle 1 - rajeunissement thermique étendu à tout le domaine océanique 291
2.3 Modèle 2 - rajeunissement thermique du domaine océanique restreint à proximité de la marge continentale 294
2.4 Modèle 3 – sans rajeunissement thermique du domaine océanique 297
2.5 Modèle 4 – sans extension post-obduction 299
VII.3 Discussion de la modélisation 301
Conclusions Générale 303
Références 307
Annexes 331
Liste des Annexes 333

Liste des Illustrations

Figure 1 – Distribution des ophiolites Neoprotérozïque et Phanérozïque d'après Vaughan & Scarrow (2003), modifiée. 2

Figure 2 - Profils lithosphériques comparés HOT et LOT, et section définie par la sismique pour un fond océanique 'normal' composé d'une épaisse couche de produits d'origine magmatique (gabbros et basaltes), d'après Vissers & Nicolas (1995) et Nicolas (1997). .. 12

Figure 3 - Schéma d'une ophiolite de ride lente (LOT), d'après l'observation des ophiolites alpines (Lagabrielle, 1987; Lagabrielle *et al.*, 1989; Lagabrielle & Lemoine, 1997). 1, lherzolite serpentinisée (manteau) ; 2, gabbros ; 3, brèches (talus de debris) ; 4, volcans à laves en coussins. 12

Figure 4 - Schémas illustrant les quatre catégories d'obduction. 14

Figure 5 - Schéma des composants d'une microsonde éléctronique. 24

Figure 6 – Schéma conceptuel du spectromètre de masse ICP-MS. 28

Figure 7 - Etapes successives de séparation minérales. 30

Figure 8 - Séparateur magnétique Frantz. Figure 9 - Dispositif de séparation par liqueur dense. 32

Figure 10 - Schéma du dispositif d'analyse $^{40}Ar/^{39}Ar$. 34

Figure 11 - Graphique représentant la décroissance de la quantité d'uranium et l'augmentation de plomb au cours du temps. 35

Figure 12 – Diagramme illustrant le principe d'utilisation de la courbe concordia. 36

Figure 13 – Cristal de zircon presentant une inclusion. 36

Figure 14 - Tectonic map of the Middle East–Caucasus area, with main blocks and suture zones, after Avagyan et al. (2005), modified. Location of figure 2 indicated. 49

Figure 15 - Structural map of the Lesser Caucasus modified from Sosson et al. (2010). Location is indicated on figure 14. Plot of geological section figure 16 and location of figure 17 indicated. 52

Figure 16 - Interpretative crustal-scale sketch cross-section of the Armenian-Azerbaijan transect. Location is indicated on Figure 15. 53

Figure 17 - Structural map of the Amasia ophiolite window. Location is indicated on figure 16. Plot of geological sections of figure 18 along with dated samples by the Ar-Ar method and paleontological identification are shown. 54

Figure 18 - Synthetic lithostratigraphic log of the three main units of the Amasia ophiolite window. I, the upper unite corresponding to ophiolite. II, the metamorphic unit comprising of the tectonic melange and the lens of garnet bearing amphibolites. III, the lower unit. .. 55

Figure 19 - Sketch geological cross sections of Amasia ophiolite. Locations are indicated on figure 17. 56

Figure 20 - Representative field photographs of ophiolitic lithologies and structural relationships. A, Cretaceous volcanic tuff – lava flows with interlayered reef limestone on top of serpentinite to the north of the study area. B, Gabbro with important density of multi-centimeter dykes found along the northeastern bank of the eastern river valley. C, The northern contact thrusting gabbro, from the south, above Coniasian-Santonian flysch, to the north. D, Garnet-bearing amphibolite body thrusted to the south above Cretaceous limestone. The gabbro is also thrusted to the south onto the amphibolite body in lateral continuation of a tectonized melange. E, Folding approaching the contact with the flysch with north dipping stratification at the base of the amphibolite massif marking the major tectonic contact. F, North dipping thrust contact bringing the serpentinite onto the Coniasian-Santonian sediments. G, Cretaceous limestone with dissymmetrical folds, with axes aligned with the general strike of the thrust. H, Lower Eocene flysch deposits highly deformed by thrust faulting and related dissymmetrical folding. 59

Figure 21 - Representative field photographs of dated gabbro sample outcrops. Photos “A” are of AR-08-29 and photos “B” are of AR-09-20. 62

Figure 22 - $^{40}Ar/^{39}Ar$ age spectra Ca/K spectra and inverse isochrones of gabbro amphiboles. Locations of samples are shown on figure 17. 63

Figure 23 - Chemical composition of amphibole from the AR-08-21 and AR-08-22 gabbro samples, after Leake et al. (1997). Data concerning Sevan amphiboles from Galoyan et al. (2009). 64

Figure 24 - Diagrams for crustal rocks of the ophiolites. Data concerning Erzinncan-Erzurum region (Refahiye, Şahvelet and Karadağ) from Parlak et al. (2012) and concerning Stepanavan, Sevan and Vedi from Galoyan et al. (2007; 2009) and Rolland et al. (2009b; 2010). A, Ti/Y versus Nb/Y (after Pearce 1982). B, Zr/Ti versus Nb/Y (after Pearce 1996). 65

Figure 25 - Ta/Yb versus Th/Yb diagram (after Pearse 1982) for crustal rocks of the ophiolites. Data concerning Erzinncan-Erzurum region (Refahiye, Şahvelet and Karadağ) from Parlak et al. (2012) and concerning Stepanavan, Sevan and Vedi from Galoyan et al. (2007; 2009) and Rolland et al. (2009b; 2010). 65

Figure 26 - Chondrite normalized REE spider diagrams. Data concerning Erzinncan-Erzurum region (Refahiye, Şahvelet and Karadağ) from Parlak et al. (2012) and concerning Stepanavan, Sevan and Vedi from Galoyan et al. (2007; 2009) and Rolland et al. (2009b; 2010). Normalizing values are from Sun and McDonough (1989). 66

Figure 27 - N-MORB normalized multi-element spider diagrams. Data concerning Erzinncan-Erzurum region (Refahiye, Şahvelet and Karadağ) from Parlak et al. (2012) and concerning Stepanavan, Sevan and Vedi from Galoyan et al. (2007; 2009) and Rolland et al. (2009b; 2010). Normalizing values are from Sun and McDonough (1989). 66

Figure 28 - Middle Toarcian (c. 180 Ma), to Early Campanian (c. 83 Ma) palaeotectonic evolution of the Lesser Caucasus region and its neighboring areas, modified from Middle East Basins Evolution Programme palaeotectonic maps of the Middle East (Barrier and Vrielynck, 2008) to include our new data. 71

Figure 29 - Tectonic map of the Middle East–Caucasus area, with main blocks and suture zones, after Avagyan *et al*. (2005), modified. Location of Figure 30 indicated..... 93

Figure 30 - Structural map of the Lesser Caucasus modified from Sosson *et al*. (2010). Location is indicated on Figure 29. Plot of geological section Figure 31 and location of Figure 32 indicated. 95

Figure 31 - Interpretative crustal-scale sketch cross-section of the Armenia-Azerbaijan transect. Location is indicated on Figure 30. 96

Figure 32 - Structural map of the Amasia ophiolite window. Location is indicated on Figure 30. Plot of geological sections of Figure 33B along with the locations of photographs of Figure 34 as well as of samples investigated through ICP-MS, EPMA, and $^{40}Ar/^{39}Ar$ geochronology methods of Figures 36, 37 & 39, respectively. 97

Figure 33 - (A), synthetic litho-stratigraphic record of the three main units of the Amasia ophiolite window; I) upper unit corresponding to the un-metamorphosed ophiolite, II) metamorphic unit comprising of the tectonic mélange and the lens of garnet bearing amphibolites, III) the lower (Southern) unit. (B), sketch geological cross sections of Amasia ophiolite. Locations are indicated on Fig. 32. 98

Figure 34 - (A), landscape photography of greenschist facies tectonized mélange zone featuring marbleized limestone blocks. The W-E extension and scattering of the limestone is in accordance with North to South convergence and thrusting. (B), garnet-bearing amphibolite body thrusted to the south above Cretaceous limestone. The gabbro is also thrusted to the south onto the amphibolite body in lateral continuation of a tectonized mélange. (C), field photography of garnet amphibolites. The foliation and lineation are underlined by the red plan and black double arrow, respectively. (D), photography and sketch of garnet amphibolite outcrop. The garnets (red) are preferentially located in the levels rich in white minerals (light grey), and underline the foliation as well as mineral lineation. The yellow represents moss and lichen. (E) and (F), representative field photographies and sketches of greenschist facies rocks. Intense deformation is featured by C-S structures, scaling and molding of brecciated mélange elements. Locations of viewpoints are indicated on Fig. 32. 99

Figure 35 - (A1) and (A2), photographs of a thin section of garnet amphibolite sample AR-08-09c in plain and cross-polarized light, respectively. (A3), sketch of thin section photographs. Cross cutting relationships of amphiboles with micas (Phg) and chlorites (Chl) indicate the existence of amphiboles (Phg) prior to micas. This is also supported by the garnets (Grt) and amphiboles, which are molded by micas and chlorites. (B), back-scatter image of garnet amphibolite sample AR-09-08. Lineation is exhibited with the alignment of amphiboles (Am), white micas (Phg) and chlorites (Chl). (C), microscope photography of garnet amphibolite sample AR-09-09. The garnet is rolled in response to syn-kinematic growth during shearing. 101

Figure 36 - Diagrams of Amasia and Stepanavan ophiolitic rocks. (A), Ti/Y versus Nb/Y (after Pearce 1982). (B), Zr/Ti versus Nb/Y rock classification diagram (after Pearce, 1996). (C), Ta/Yb versus Th/Yb diagram (after Pearce, 1982) for source characteristics for ophiolitic and associated rocks of the Amasia and Stepanavan ophiolites. (D), N-MORB normalized multi-element spider diagrams. Normalizing values are from Sun and McDonough (1989). Locations of samples of the Amasia ophiolites are found on Fig. 32, as well as results of geochemical ICM-MS analyses in Table 10. 102

Figure 37 - Diagrams of analyzed of Amasia garnet amphibolite minerals. (A), triangular plots showing chemical compositions of Amasia amphibolite garnets. (B), compositional profiles of two garnets of the Amasia amphibolites. Note that the garnets are relatively homogenous in composition from core to rim. (C), Na/Ca+Na vs. Al/Al+Si ratios of amphiboles from amphibolite samples, abbreviations are according to Kretz (1983). (D), Si versus Al in white micas from amphibolite samples. (E), triangular plots showing chemical compositions of Amasia amphibolite chlorites. Locations of samples are indicated on Figure 32, as well as EPMA results in Tables 6, 7, 8 & 9. 106

Figure 38 - (A), pseudosection in the SiO2-Al2O3-FeO-MgO-CaO-Na2O-K2O-TiO2 system and calculated with Perple_X 6.6.6 (Connolly, 2009), using the internally consistent thermodynamic database of Holland and Powell (2003) and Connolly and Kerrick (2002) and whole rock and mineral geochemistry of sample AR-08-09c found in Fig. 36, Table 10 and Fig. 37, Table 7, respectively. The red shaded field corresponds to both mineral assemblage observed for relic garnet amphibolite paragenesis and the measured proportion of Al in amphiboles compared to predicted models. (B), Perchuk *et al*. (1985) garnet-amphibole thermometry based on Mg-Fe partitioning. Frequencies represent the number of combinations of garnet-amphibole pairs of EPMA analyses yielding a given temperature. (C), phengite-quartz-water P–T estimates for EPMA analyses of samples AR-08-09c, AR-08-25B and AR-09-08 using the method of Dubacq *et al*. (2010). (D), Si p.f.u. isopleths in phengite calculated and plotted on previous thermodynamic phengite-quartz-water calibration domains using the whole rock and phengite EPMA analyses of sample AR-08-09c (Table 9). The resulting domain corresponding to Si^{4+} content is shaded in yellow.. 111

Figure 39 - $^{40}Ar/^{39}Ar$ age, Ca/K spectra and inverse isochrones. (A), amphibole from sample AR-09-08. (B), amphibole from sample AR-09-15. (C), amphibole from sample AR-08-09c. (D), white mica from sample AR-08-09c. Locations of samples are shown on Fig. 32.

(E), compilation of ages which may also be found in Table 11, as well as detailed dating results in supplementary data files..... 113

Figure 40 - Compilation of determined PT-t paths for the Amasia-Sevan-Akera metamorphic rocks found in basal position of ophiolite bodies inferred through this study of the outcrops of Amasia garnet amphibolite in black and Stepanavan blueschist (Rolland *et al*., 2009a) in grey. 114

Figure 41 - Middle Toarcian (c. 180 Ma), to Early Campanian (c. 83 Ma) palaeotectonic evolution of the Lesser Caucasus region and its neighboring areas, modified from Middle East Basins Evolution Programme palaeotectonic maps of the Middle East (Barrier and Vrielynck, 2008) to include our new data with associated sketch cross-sections. 121

Figure 42 - Structural sketch map of the Tauride-Anatolides, Caucasus and Iranian belts (modified after Avagyan et al., 2005). Location of Figure 43 is indicated. 157

Figure 43 - Structural map of the Lesser Caucasus-Eastern Pontides-Northeast Anatolides regions. Turkish zone modified from the 1:1 250 000 geological map of Turkey (MTA 2011); the Georgian-Armenian zone of the Caucasus after Sosson et al. (2010); the Iranian zone from Mederer (2013)..... 161

Figure 44 - Geological map and cross-sections of the Refahiye ophiolite in the vicinity of Erzincan. A: Geological map featuring the position of the cross-sections (modified after Aktimur et al., 1995; Özen et al., 2006; Sarıfakıoğlu et al., 2009). B: Geological cross-section illustrating the positioning and structural relationships between the main units based on field observations..... 162

Figure 45 - Synthetic lithostratigraphic sections throughout the study area. 1, 3 and 4: modified after Gedik (2008); 2: modified after Moix et al. (2008); 5: modified after Bozkuş (1998); 6 and 7: modified after Sokolov (1977)..... 164

Figure 46 - Diagrams for crustal rocks of the ophiolites. Data concerning Erzincan–Erzurum region (Refahiye, Şahvelet and Karadağ) are from Parlak et al. (2013) and this study. Data concerning Amasia, Stepanavan, Sevan and Vedi are from Hässig et al. (2013), Galoyan et al. (2007, 2009) and Rolland et al. (2009, 2010). A1, B1, C1: Ti/Y vs. Nb/Y discrimination diagram (after Pearce, 1982). A2, B2, C2: Zr/Ti vs. Nb/Y classification diagram (after Pearce, 1996). A3, B3, C3: Ta/Yb vs. Th/Yb tectonic emplacement diagram (after Pearce, 1982)..... 166

Figure 47 - Chondrite normalized REE spider diagrams and N-MORB normalized multi-element spider diagrams. Data concerning Erzincan–Erzurum region (Refahiye, Şahvelet and Karadağ) from Parlak et al. (2013) and concerning Stepanavan, Sevan and Vedi from Galoyan et al. (2007, 2009) and Rolland et al. (2009b, 2010). Normalizing values are from Sun and McDonough (1989). 168

Figure 48 - Tectonic map of Mesozoic Ophiolites and ophiolitic mélanges from the Tethyan realm in Turkey and adjacent areas (modified after Stampfli, 2000) and representative geochronological data from rocks of the ophiolitic mélanges as well as from metamorphic soles (modified after Çelik et al., 2011). All data are from 40Ar/39Ar analyses except where stated otherwise: (1) Dilek et al. (1999); (2) Parlak and Delaloye (1999); (3) Çelik et al. (2006); (4) Chan et al. (2007); (5) Galoyan et al. (2009); (6) Önen (2003); (7) Harris et al. (1994); (8) Dimo-Lahitte et al. (2001); (9) Spray et al. (1984); (10) Roddick et al. (1979); (11) Koepke et al. (2002), K-Ar age data; (12) Hatzipanagiotou and Pe-Piper (1995), K-Ar age data; (13) Lanphere et al. (1975), K-Ar age data; (14) Rolland et al. (2010); (15) Çelik et al. (2011); (16) Hässig et al. (2013); (17) Topuz et al. (2013a), (18) Topuz et al. (2013b). Abbreviations, AO: Antalya Ophiolite; BHO: Beyşehir-Hoyran Ophiolite; EO: Eldivan ophiolite; KO: Kınık Ophiolite; LO: Lesvos Ophiolite; MO: Mersin Ophiolite; ORO: Orhaneli Ophiolite; PKO: Pozantı-Karsantı Ophiolite; SO: Sevan Ophiolite; mu: muscovite; hb: hornblende. (*) age data from gabbro. 171

Figure 49 - Middle Toarcian (c. 180 Ma) to present day palaeotectonic evolution of the NE Anatolian-Lesser Caucasus region. Maps modified from Middle East Basins Evolution Programme palaeotctonic maps of the Middle East (Barrier and Vrielynck, 2008) illustrating our new interpretation. 177

Figure 50 - A, tectonic map of the Middle East–Caucasus area, with main blocks and suture zones, after Avagyan et al. (2005), modified. Location of Figure 1B is indicated. B, structural map of the Lesser Caucasus, modified from Sosson et al. (2010). Location of figure 51A is indicated. 200

Figure 51 - A, structural map of the Tsaghkuniats massif, modified from Aghamalyan (1983). Location of this map is indicated on figure 1B. Plot of geological sections of Figure B and C along with localization of dated samples by the U-Pb and $^{40}Ar/^{39}Ar$ methods and paleontological identification. Location of field photographs of Figure 52 indicated as well. B and C, sketch geological cross sections of the Tsaghkuniats massif. 202

Figure 52 - Representative field photographs of the lithologies of the Tsaghkuniats massif and interpreted structural relationships. A, a view to the west of the unconformity of Upper Cretaceous to Paleocene sedimentary series on top of crystalline basement made of metasedimentary rocks, north of the town of Bjni below. B, outcrop of the granodiorite massif north-east of the town of Aghveran. C, normal fault contact of metasedimentary rocks on top of gneiss. D, normal fault contact of metasedimentary rocks on top of gneiss seen in another valley just west of C. E, gneiss outcrop with C-S deformation indicated. F, well deformed mica-schist with cross-cutting andalusite. G, intense deformation with coinciding C and S planes and synthetic C' planes concordant to general shearing. H, folds re-deforming in mica-schist. I, deformed pyrite indicating shear movement. 206

Figure 53 - Representative microphotographs of fin sections of rock samples of the Tsaghkuniats massif showing mineral relationships of $^{40}Ar/^{39}Ar$ dated mineral phases. A1 and A2, plane and cross-polarized images, respectively, centered on amphibole of

granodiorite sample AR-03-64. B1 and B2, plane and cross-polarized images, respectively, centered on amphibole of granodiorite sample AR-03-64. C, cross-polarized images centered on white mica of micaschist sample AR-03-62M. D, cross-polarized image centered on white mica of micaschist sample AR-03-62M. The white mica molds the garnet and biotite. E, cross-polarized images centered on white mica of leucogranite sample AR-03-64. F, cross-polarized images centered on white mica of leucogranite sample AR-03-64. G, H and I, electron back-scatter (EBS) images of metaschist sample AR-03-64B. J, K1 and K2, optical microscope photography of sample AR-03-62M showing relics of garnet, kyanite and staurolite included in andalusite. 207

Figure 54 - Mineral deformations and associations found in sampled outcrops. A, zoom of Figure 52I of deformed pyrite indicating shear movement in well-foliated metamorphic rock. B, C1, C2, D1 and D2, microphotographs taken with a stereo microscope of shear bands found in micaschist thin sections. B, C1 and D1, are taken in LPNA whereas C2 and D2 are in LPA. E, cross polarized microphotograph of andalusite cross-cutting preexisting white micas. The andalusite features relic kyanite mineral fragments at its core and is molded by biotite. F1 and F2, plane and cross-polarized micrographs, respectively, zoom on andalusite cross-cutting white mica lineation. 209

Figure 55 - A, profile of a garnet from sample AR-03-62M, (see Figures 55C4 and 55D1). B, Garnet-Biotite-Plagioclase thermobarometry using representative rim biotite and garnet compositions with associated plagioclase within sample AR-03-62M. Calibrations from: 1, Ganguly and Saxena (1984) ; 2, Hodges and Spear (1982) ; 3, Hodges and Crowley (1985) ; 4, Perchuk and Lavrent'eva (1983) ; 5, Ferry and Spear (1978); 6, Hoisch (1990); 7, Hodges and Crowley (1985); 8, Ghent and Stout (1981). C, PT path mineralogical evolution within the same sample (AR-03-62M), using the grid established by Holland and Powell (1998) for the system KFASH. Mineral abbreviations after Kretz (1983). 212

Figure 56 - U-Pb laser ICP-MS ablation concordia, A, and Tera-Wasserburg age diagrams, B, for the samples ARL10-33. C1, C2, C3 and C4 scanning electron microscope photography of dated granodiorite zirons corresponding to numbered analyses of table 15, respectfully. Location of the sample is shown on Figure 52. 215

Figure 57 - Chondrite normalized REE and N-MORB and primitive mantle normalized multi-element spider diagrams of the granodiorite sample ARL-10-33. Normalizing values are from Sun and McDonough (1989). 217

Figure 58 - $^{40}Ar/^{39}Ar$ age spectra, normal isochrones and Ca/K spectra of dated samples. Locations of samples are shown on Figure 52. 220

Figure 59 - Cooling model for $^{40}Ar/^{39}Ar$ and U-Pb dating results with error margins. 223

Figure 60 - PT-t path including metamorphic (Figure 55C), $^{40}Ar/^{39}Ar$ and U-Pb age data. . 224

Figure 61 - Sketch geodynamic model proposed for the SAB (Lesser Caucasus) from Middle Jurassic to Upper Cretaceous-Paleocene times. 226

Figure 62 - Tectonic map of the Middle East–Caucasus area, with main blocks and suture zones, after Avagyan et al. (2005), modified. Location of Figure 63 is indicated. 251

Figure 63 - Structural map of the Lesser Caucasus-Eastern Pontides-Northeast Anatolides regions. Turkish zone modified from the 1:1 250 000 geological map of Turkey (MTA 2011); the Georgian-Armenian zone of the Caucasus after Sosson et al. (2010); the Iranian zone from Mederer (2013). The green shading represents proposed extent of the ophiolitic nappe..... 252

Figure 64 - Tectonic map of Mesozoic Ophiolites and ophiolitic mélanges from the Tethyan realm in Turkey and adjacent areas (modified after Stampfli, 2000) and representative geochronological data from rocks of the ophiolitic mélanges as well as from metamorphic soles (modified after Çelik et al., 2011). All data are from 40Ar/39Ar analyses except where stated otherwise: (1) Dilek *et al.* (1999); (2) Parlak and Delaloye (1999); (3) Çelik *et al.* (2006); (4) Chan *et al.* (2007); (5) Galoyan *et al.* (2009); (6) Önen (2003); (7) Harris *et al.* (1994); (8) Dimo-Lahitte *et al.* (2001); (9) Spray *et al.* (1984); (10) Roddick *et al.* (1979); (11) Koepke *et al.* (2002), K-Ar age data; (12) Hatzipanagiotou and Pe-Piper (1995), K-Ar age data; (13) Lamphere *et al.* (1975), K-Ar age data; (14) Rolland *et al.* (2010); (15) Çelik *et al.* (2011); (16) Hässig *et al.* (2013); (17) Topuz *et al.* (2013a); (18) Topuz *et al.* (2013b). Abbreviations, AO: Antalya Ophiolite; BHO: Beyşehir-Hoyran Ophiolite; EO: Eldivan ophiolite; KO: Kınık Ophiolite; LO: Lesvos Ophiolite; MO: Mersin Ophiolite; ORO: Orhaneli Ophiolite; PKO: Pozantı-Karsantı Ophiolite; SO: Sevan Ophiolite; mu: muscovite; hb: hornblende. (*) age data from gabbro. The bold numbers indicate positioning of radiolarian biostratigraphy reported in Figure 65. The red frame indicates the position of Figure 63. 254

Figure 65 - Compilation of chronological data including extension of the radiolarian fauna, magmatic series of the ophiolite bodies outcropping emplaced prior to the obduction event and metamorphic lithologies marking the limit between the ophiolites and the Eurasian margin as well as between the ophiolites and the underthrusted EAP-SAB margin from the İzmir-Ankara-Erzincan and Sevan-Akera sutures including the Bornova Zone and the Karaburun Peninsula, modified after Moix & Goričan (2013). The evolution of the various geological contexts between the Eurasian margin and the EAP-SAB is further argued by both biostratigrapghic and radiochronologic data. The red lines underline the emplacement of OIB type volcanism on the oceanic crust to be obducted. Locations are numbered and plotted on Figure 64: (1) Çakmakoğlu & Bilgin (2006); (2) Tekin & Göncüoğlu (2009); (3) Tekin *et al.* (2006) in Göncüoğlu *et al.* (2006a); (5) Tekin & Göncüoğlu (2007) and Tekin & Göncüoğlu (2008); (4) Tekin *et al.* (2012a); (10) Göncüoğlu *et al.* (2000); (7) Göncüoğlu *et al.* (2006b); (8) Göncüoğlu *et al.* (2006b); (9) Tekin *et al.* (2002) and Göncüoğlu *et al.* (2006a, 2010); (6) Servais (1982); (11) Bragin & Tekin (1996); (12) Rojay *et al.* (2004); (13) Çelik (2010) and Üner (2010) in Tekin *et al.* (2012b); (14) Tüysüz & Tekin (2007); (15) Boccaletti *et al.* (1966); (16) Bozkurt *et al.* (1997); (17) Hässig *et al.* (2013, 2014) and Danelian *et al.* (2014); (18) Danelian *et al.* (2008, 2012) and Rolland *et al.* (2010); (19) Galoyan *et al.* (2009) and Asatryan *et al.* (2010, 2012). Plots for magmatic

rocks between (16) and (17) are for the Refahiye ophiolite from Topuz *et al.* (2013a, b) as for metamorphic rocks along with Aslan *et al.* (2011). Plots for metamorphic rocks between (17) and (18) are for the Stepanavan ophiolite from Rolland *et al.* (2009a)..... 258

Figure 66 - Sketch geodynamic model proposed for the oceanic domain between the northern margin of the EAP-SAB and the southern margin of Eurasia from Early Jurassic to Late Cretaceous times, from ophiolite genesis to just prior to emplacement over the EAP-SAB. 262

Figure 67 - Reconstitution du bloc TAP-SAB et des bassins océaniques environnants au Santonien, suite à l'obduction, d'après les données paléomagnétiques (Meijers et al., en révision). Les étoiles et marges d'erreur associées indiquent les paléo-latitudes des roches calcaires en discordance sur l'ophiolite obduite, mises en place juste après l'obduction). La position 1 décrit la position la plus méridionale et 2 la plus septentrionale du bloc TAP-SAB. L'obliquité du bloc est déduite d'une déclinaison de 40° impliquant une rotation de même valeur au moment de la fermeture de la branche nord de l'océan Téthys. La position 3 décrit la possibilité d'une zone de subduction très oblique, par rapport à la marge eurasienne, en bordure occidentale du bloc de Kirshehir (ou Central Anatolian Crystalline Complex, CACC, Lefebvre, 2011). 288

Figure 68 – Représentation schématique de la configuration pré-obduction (en haut) et la distribution des champs de composition de référence utilisée au cours des modélisations (en bas). 290

Figure 69 – Evolution temporelle du modèle 1 caractérisé par une lithosphère océanique vieille mais d'un âge thermique de 5 Ma sur la totalité de son étendu..... 292

Figure 70 - Evolution temporelle du modèle 2 caractérisé par une lithosphère océanique vieille mais d'un âge thermique de 5 Ma sur restreint à un domaine proche de la marge continentale..... 296

Figure 71 - Evolution temporelle du modèle 3 caractérisé par une lithosphère océanique vieille n'ayant pas subi de rajeunissement thermique. 298

Figure 72 - Evolution temporelle du modèle 2 caractérisé par une lithosphère océanique vieille mais d'un âge thermique de 5 Ma sur restreint à un domaine proche de la marge continentale. Ce modèle ce distingue du modèle 2 par l'absence de la pas d'extension post-obduction. 300

Liste des Tableaux

Tableau 1 – Récapitulatif des minéraux utilisés pour datation avec les méthodes $^{40}Ar/^{39}Ar$ et U-Pb. 29

Table 2 - Electron microprobe analyses of the representative minerals of gabbro samples of the Amasia ophiolite. 81

Table 3 - Representative whole-rock analyses of samples from ophiolitic complex of Amasia. 83

Table 4 - Amphibole $^{40}Ar/^{39}Ar$ dating results from the ophiolite gabbro samples AR-08-29 and AR-09-20. 84

Table 5 - Nannofossils dating with (WGS84) GPS locations. 84

Table 6 - Representative whole-rock analyses of samples from ophiolitic complex of Amasia. 135

Table 7 - Electron microprobe analyses of representative garnets from metamorphic rocks of the Amasia ophiolite complex. Oxydes and end-member proportions are given in percentages. 137

Table 8 - Electron microprobe analyses of representative amphiboles from metamorphic rocks of the Amasia ophiolite complex. 140

Table 9 - Electron microprobe analyses of representative chlorites from metamorphic rocks of the Amasia ophiolite complex. 144

Table 10 - Electron microprobe analyses of representative micas from metamorphic rocks of the Amasia ophiolite complex. 146

Table 11 - $^{40}Ar/^{39}Ar$ dating results. 148

Table 12 - Representative whole-rock analyses of samples from ophiolitic complexes of NE Anatolia and Lesser Caucasus. "< L.D.": under detection level. 189

Table 13 - Nannofossil dating with (WGS84) GPS locations. 235

Table 14 - Electron microprobe analyses of the representative minerals of micaschist sample AR-03-62M. 236

Table 15 - Detailed U-Pb results for dated zircons. 236

Table 16 - Detailed $^{40}Ar/^{39}Ar$ results for dated amphibole, muscovites and biotite. 237

Table 17 - Summary of $^{40}Ar/^{39}Ar$ and U-Pb dating results with (WGS84) GPS locations. 239

Table 18 - Major, trace and rare earth element contents of granodiorite pluton sample ARL10-33. 240

Tableau 19 – Paramètres thermiques et rhéologique des lithologies utilisé lors des modélisations. 290

Introduction

Dans de nombreuses chaînes de montagnes de collision, des assemblages de roches ultrabasiques (pour la première fois décrites par Brongniart dans les Apennins en 1821 comme des ophiolites) et basiques ont été identifiés, en général associées avec des sédiments pélagiques. Depuis les années 1970 (Penrose field conference, 1972), il est classiquement admis que ces assemblages représentent des lambeaux de lithosphère océanique transportés sur la croûte continentale. Dans Coleman (1971) le paradoxe intrinsèque de ce phénomène fut mis en avant : des roches denses (>3) se retrouvent au-dessus de roches moins denses (~2,7). Pour expliquer ceci Coleman évoque l'obduction comme le processus qui conduit à la formation d'un complexe ophiolitique, fonctionnant au premier ordre avant la collision dans le cycle de Wilson. Mais la question mérite d'être posée : l'obduction est-elle un mécanisme intrinsèque ou correspond-elle à un 'simple' mécanisme de subduction continentale ? Par ailleurs plusieurs questions découlent de la première : Quelles sont les forces à l'origine d'un tel transport ? Dans quels contextes géodynamiques particuliers peut-on envisager des obductions ? Existe-t-il différents types d'obductions ?

A travers le globe, il y a environ 150 ophiolites identifiées dans des chaînes de montagnes. L'âge de ces ensembles ainsi que celui de leur mise en place sur une lithosphère continentale s'étale de 3.8 Ga, au Groenland (Ophiolites d'Isua), à 2~3 Ma, au Chili (Ophiolites de Taitao) (**Figure 1**). La gamme de distribution temporelle de ces objets suppose qu'il s'agit d'un processus ayant couramment accompagné la tectonique des plaques dès son origine avec la formation de plaques suffisamment rigides et différenciées. Cependant, l'ambiguïté du terme « ophiolite » nécessite une clarification. En effet, deux genres ayant des caractéristiques propres sont regroupés sous cette dénomination.

Le premier genre correspond à des ophiolites non-métamorphisées, dites aussi préservées. Un exemple bien connu en Europe est le massif ophiolitique du Chenaillet qui se trouve tout proche de la ville de Briançon dans les Alpes occidentales françaises. Cette ophiolite est principalement constituée de péridotites serpentinisées traversées par des gabbros. L'ensemble est recouvert par des édifices volcaniques ayant produit des basaltes en coussins (Cady, 1995; Chalot-Prat & Manatschal, 2202a; 2002b; Manatschal *et al.*, 2002; Chalot-Prat, 2005). Il s'agit d'une section extrêmement bien préservée d'une ancienne lithosphère océanique obduite sur un prisme d'accrétion métamorphique et une lithosphère continentale sous-charriée lors de la collision alpine. Le deuxième genre d'ophiolite est connu

comme ophiolites métamorphisées ou subduites. Le complexe ophiolitique du Mont Viso est de ce genre, situé dans la région du Piémont il constitue l'un des plus hauts sommets des Alpes occidentales italiennes. Les métagabbros présentent des transformations minéralogiques dans un contexte de haute pression. En effet, ils ont été métamorphisés dans les conditions des faciès schiste bleu (marqué par la présence de glaucophane) et éclogitique (éclogites à grenat, phengite et jadéite) (Lombardo *et al.*, 1978; Tricart & Lemoine, 1986; Philippot, 1988; Lagabrielle & Polino, 1988; Schwartz, 2000; Agard *et al.*, 2002; Lardeaux *et al.*, 2006; Tricart & Schwartz., 2006; Yamato *et al.*, 2007; Guillot *et al.*, 2009; Schwartz *et al.*, 2009). Il s'agit ici de roches de haute à ultra-haute pression exhumées, témoins d'une ancienne subduction en partie responsable de la fermeture de l'océan alpin.

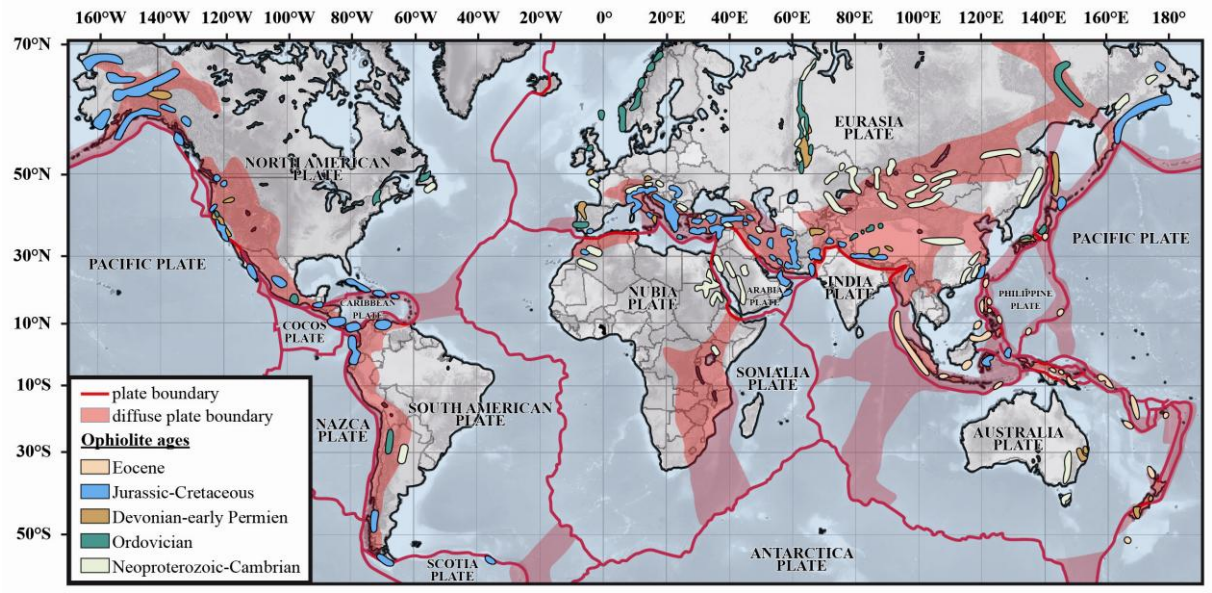

Figure 1 – Distribution des ophiolites Neoprotérozïque et Phanérozïque d'après Vaughan & Scarrow (2003), modifiée.

Ainsi, l'on constate que le terme d'ophiolite ne distingue pas les fragments de lithosphère océanique entraînés en subduction de ceux ayant échappé à celle-ci (et pour lesquels seuls le terme d'obduction peut être considéré pertinent).

Concernant désormais le mécanisme d'obduction. Différents modèles sont proposés.

(1) La première catégorie de modèles suppose qu'il s'agit d'une variante de subduction continentale, un modèle initialement proposé par Davies (1977). Dans ce contexte, une lithosphère continentale fortement couplée au slab dense éclogitisé est tiré dans une subduction intra-océanique sous une lithosphère océanique comme cela est proposé pour le Chenaillet (e.g., Lardeaux, 2013, *et les références qui y figurent*), les ophiolites himalayennes de Tso Morari (Mascle & Guillot, 2012), ou l'ophiolite d'Oman (Agard *et al.*, 2007, Yamato *et al.*, 2007; Chemenda, 1994, *et les références qui y figurent*), entre autres.

(2) D'autres auteurs considèrent que l'obduction est initiée au sein du domaine océanique en réponse à un phénomène global anormal : augmentation de la vitesse de plaques, (Agard *et al.*, 2007); point chaud (Vaughan & Scarrow, 2003)…

Par ailleurs, concernant le lieu de l'initiation de l'obduction, différents modèles sont envisagés, proposant (i) l'initiation de l'obduction soit au niveau d'une dorsale médio-océanique (Coleman, 1971; Moores & Vine, 1971; Cann, 2003, *et les références qui y figurent*) soit (ii) dans un bassin marginal (Saunders & Tardey, 1984; Rautenschlien *et al.*, 1985; Hébert & Laurent, 1990; Thy & Xenophontos, 1991; Beccaluva *et al.*, 1994; Bédard *et al.*, 1998; Dilek *et al.*, 1999; Shervais, 2000; Dilek & Flower, 2003), ou bien encore dans la lithosphère océanique indifférenciée, dû au flambage de celle-ci (Agard *et al.*, 2007)

Dans le cas où la lithosphère océanique s'est formée au-dessus d'une zone de subduction (ophiolites de type supra-subduction, SSZ, Pearce *et al.*, 1984; 2003), l'obduction est possible lorsque l'arrivée d'une marge continentale entre dans la subduction et bloque son fonctionnement. La zone de subduction sert alors de zone de charriage. Dans cette hypothèse, une semelle métamorphique se forme dans cette zone par transformation des sédiments et laves de la plaque plongeante (Searle & Cox, 1999).

Si les ophiolites se forment au niveau d'une dorsale médio-océanique, dans un premier temps un écaillage intra-océanique se fait au niveau de la dorsale. Lors de cet écaillage, les laves et sédiments chevauchés par la lithosphère océanique chaude sont rabotés et métamorphisés. Ils constituent alors la '***semelle métamorphique***' de l'ophiolite.

Lors de la fin de l'obduction proprement dite, l'ensemble « ophiolite et semelle métamorphique » peuvent continuer leur progression sur la marge continentale par glissement gravitaire dans un bassin d'avant pays formé sur la marge continentale par flexure et/ou subsidence (Goguel, 1948; Merle, 1998; Rawling & Lister, 2002; Lagabrielle *et al.*, 2005; Chardon & Chevillotte, 2006; Lagabrielle & Chauvet, 2008; Ulrich, 2010; Lagabrielle *et al.*, 2013), ou bien par un sous-charriage prolongé de la lithosphère continentale (ex : Himalaya).

Le travail de recherche présenté dans ce mémoire concerne les ophiolites du nord-est de l'Anatolie en Turquie et du Petit Caucase en Arménie. Le choix porté sur ces ophiolites, qui ont été depuis une dizaine d'années étudiés en détails répond à deux constatations essentielles concernant l'âge et la dimension des objets obduits.

(i) La lithosphère océanique est âgée d'environ 80 à 50 Ma au moment de son obduction (qui dure 10 millions d'années au maximum), elle est donc dans ce cas déjà très refroidie et dense et ne semble pas compatible avec un modèle ou l'obduction pourrait être initiée au

niveau d'une ride océanique. Ainsi, l'écart d'âge entre la formation et la mise en place des objets rendent possible l'identification de différents processus géodynamiques pouvant être responsables de cette obduction (variation des vitesses d'accrétion océanique, de subduction, mise en place d'autres zones de subduction, apparition de point chaud…). La collision intervenant plus tard (10 millions d'années après dans l'exemple du Petit Caucase) n'a par conséquent pas d'influence sur la structure et le mode de l'obduction.

(ii) Les ophiolites font apparemment partie d'un même ensemble qui a été transporté sur des distances importantes (> 100 km de large sur plusieurs centaines de kilomètre de long). Ce paramètre est essentiel pour définir le mécanisme responsable de l'obduction. En effet, on peut par exemple penser que ces dimensions sont trop importantes pour pouvoir être uniquement causées par une obduction initiée par un processus de subduction continentale.

Beaucoup de travaux se rapportant à l'Arménie ont été rédigés en arménien ou en russe. Ils constituent avec les récents travaux effectuées par les équipes françaises sur ce domaine, une base d'études ayant comme objectif d'étudier l'origine de ophiolites (genèse, géométrie, dynamique,…). Les travaux à propos des ophiolites turques et iraniennes, axés sur leur origine et mise en place, se sont portés depuis peu plus particulièrement sur leurs continuités latérales. Dû à des différends politiques la coordination scientifique entre ces pays est difficile. Pour ces raisons il est nécessaire de reprendre ces données, de les comparer, de les synthétiser. Nous avons ainsi extrait les données et résultats antérieurs afin d'exposer un inventaire des ophiolites nord téthysiennes de la zone d'étude. Ainsi, nous avons pu révéler les points obscurs sur leur genèse, sur leur structure, sur les processus responsables de leurs mise en place. Ces données viennent en complément de nouvelles investigations menées en collaboration avec des équipes locales (arménienne et turque).

Notre étude concerne plus précisément l'analyse des processus magmatiques, métamorphiques et tectoniques mis en jeu lors de la mise en place d'une nappe de lithosphère océanique préservée (non-métamorphique) sur un domaine continental. La fermeture de l'espace océanique nord téthysien a conduit à des subductions et à l'obduction de segments de lithosphère océanique (métamorphisée ou préservée). Plus précisément, nous avons étudié les ophiolites situées au sud de la suture nord téthysienne (Izmir-Ankara-Erzincan-Amasia-Sevan-Akera) entre Refahiye (Turquie) et Khoy (Iran). Ces ophiolites chevauchent un domaine constitué de plusieurs microcontinents (Tauride, Anatolide et Sud Arménien). La fermeture océanique est suivie d'une collision continentale (à partir du Crétacé terminal-

Paléocène). Cette dernière phase a découpé et décalé les corps ophiolitiques et recouvert ceux-ci par une épaisse couverture volcano-sédimentaire.

Du fait de la grande homogénéité des âges des ophiolites et des structures le long de l'Anatolie (e.g., Çelik *et al.*, 2011), l'exemple étudié est l'un des plus remarquables à l'échelle globale. Nous expliquerons qu'il est envisageable que l'enchaînement des processus proposés dans cette zone étude puissent également s'appliquer aux ophiolites et leurs mise en place plus à l'est ainsi qu'à l'ouest, à l'échelle de toute l'Anatolie. La fraîcheur et les bonnes conditions d'affleurement étant propices à en faire un cas d'école concernant le processus d'obduction.

Afin d'exposer tous les arguments et illustrer le modèle d'obduction dans la zone d'étude, ce mémoire s'articule en sept parties (chapitres, intégrant cinq publications en tant que 1er auteur dont deux publiées et trois soumises à révision) :

1- Le premier chapitre reprendra les travaux antérieurs depuis les années soixante ainsi que les débats en cours concernant les questions de composition, d'âge de formation et de mise en place des ophiolites.

2- Le second chapitre exposera les méthodes et outils utilisés au cours de cette étude.

3- Le troisième chapitre développera en deux sous-chapitres l'étude géologique, pétro-géochimique et métamorphique, ainsi que ses implications, de la région frontière entre les domaines ophiolitiques arméniens et turcs (Amasia, Arménie):

   - Le premier sous chapitre analyse et traîte les caractéristiques structurales et pétro-géochimiques des ophiolites d'Amasia (Arménie). Cette zone ophiolitique comprend une série complète de différenciation avec des gabbros et des basaltes montrant des affinités de type MORB et une deuxième série de laves alcalines avec des affinités de type OIB. Les nouvelles données de datations obtenues sur les hornblendes des gabbros suggèrent la formation d'une croûte océanique au Jurassique moyen. Cette partie fait l'objet d'un article publié dans *Tectonophysics*.
   - Le second analyse et traite les caractéristiques structurales et pétro-géochimiques des roches métamorphiques de la semelle des ophiolites d'Amasia. Cette zone ophiolitique comprend une écaille d'amphibolite à grenat étiré dans un mélange tectonique de faciès schiste vert en position basale du corps ophiolitique. Les nouvelles données de datations obtenues sur amphibole et mica blanc de l'écaille d'amphibolite à grenat permettent

de mettre en évidence un chemin PT-t antihoraire. Cette partie fait l'objet d'un article soumis à *Journal of the Geological Society*.

4- Le quatrième chapitre analyse l'ensemble des données (structurales, pétro-géochimiques et géochronologiques) de toute la zone d'étude concernant la mise en place de ces différentes ophiolites concluant sur leur appartenance à une seule nappe ophiolitique. Cette partie apporte pour la première fois une synthèse des données récentes sur les roches magmatiques, métamorphiques ainsi que sur les contraintes stratigraphiques entre les territoires arménien et turc. Elle fait l'objet d'un article publié dans *Geodinamica Acta*.

5- Le cinquième chapitre explore l'histoire métamorphique du socle cristallin du microcontinent sud arménien dans la seule localité où il affleure, la région de Tsaghkuniats près de Bjni (juste au Nord de Erevan). Cette partie apporte pour la première fois des données géochronologiques sur les événements thermiques affectant la lithosphère continentale arménienne avant l'obduction par les ophiolites étudiées, mais propose aussi un scénario géodynamique inédit intégrant une subduction vers le sud, sous les blocs continentaux chevauchés par la nappe ophiolitique. Elle fait l'objet d'un article soumis à *Journal of Asian Earth Sciences*.

6- Le sixième chapitre analyse les processus géodynamiques anté-obduction impliqués dans la zone d'étude. Il en ressort un modèle conceptuel élaboré à partir des données géologiques de surface. Ce chapitre se caractérise principalement par une discussion concernant la configuration de base du modèle d'obduction proposé par la suite, en conclusion de cette thèse. Elle fait l'objet d'un article soumis à *Geological Society of London, Special Publication*.

7- Le septième chapitre sert de conclusion. Les nouvelles données et nouveaux résultats présentés dans les chapitres précédents sont résumés afin de répondre aux questions scientifiques que nous nous étions fixées au début de cette étude. Dans cette partie nous présentons une modélisation intégrant les caractéristiques générales du domaine océanique maintenant disparu dont les ophiolites sont les seules reliques, sur la base de la reconstitution des événements géodynamiques successifs proposée pour les ophiolites du Petit Caucase-NE Anatolie. En conséquence, une discussion des processus à l'origine de l'obduction est proposée pour expliquer le cas d'étude et plus généralement le mécanisme d'obduction.

<u>Chapitre 1</u> – Ophiolite/Obduction : historique et problèmatique de la thèse

« Ce qu'on dit être nouveau en ce monde, c'est l'histoire qu'on ignore. »

Harry S. Truman

Ce travail de recherche concerne le processus de mise en place des ophiolites du Petit Caucase (Arménie) ainsi que celles de NE Anatolie (NE Turquie). Avant de présenter les nouvelles données, analyses et interprétations, nous décrirons les données antérieures, qui sont aussi nombreuses que de nature différente. Afin de mieux argumenter les reconstructions proposées par la suite nous passerons tout d'abord en revue les ensembles majeurs d'ophiolites recensés dans le monde pour en dégager les modèles de formation et de mise en place (obduction) principaux. Cela permettra également de mieux développer les particularités des ophiolites de la zone d'étude par la suite.

La zone d'étude s'étend sur plus de 700 km d'est en ouest et plus de 150 km du nord au sud. Les articles portant sur la partie arménienne sont pour la plupart publiés avant les années 1990, écrits en russe ou en arménien (et synthétisés dans la thèse de Galoyan, 2008). Certaines sources bibliographiques portant sur la région de NE Anatolie, résumés de conférences et communiqués, n'ont été publiées qu'en turc. Cela justifie le besoin d'une synthèse de ces différents travaux, afin de bien introduire cette thèse. Une synthèse des résultats antérieurs est présentée pour en extraire les points obscurs, tant sur le plan des structures que sur le plan de l'évolution géodynamique, depuis la genèse des ophiolites jusqu'à leur obduction.

I.1 Concepts

1.1 Ophiolite

Le mot « ophiolite », du grecque '*ophi*' (serpent), fut utilisé pour la première fois par le géologue français Alexandre Brongniart en 1813 (Brongniart, 1813) pour caractériser la texture et la minéralogie de roches majoritairement composées de serpentine. En 1821, une corrélation a été décrite entre ces serpentinites et d'autres roches telles que des gabbros, roches volcaniques et des chailles (roches siliceuses) (Brongniart, 1821). Remarquons toutefois que dans Brongniart (1827) le terme « ophiolite » est utilisé exclusivement pour désigner une minéralogie serpentineuse. Fouqué & Lévy (1879) introduisirent le terme dérivé « ophite » pour désigner les gabbros et basaltes associés.

Dans Suess (1909), l'auteur décrit la disposition de niveaux riches en serpentinites en nappes incorporées dans les chaînes de montagnes. C'est en 1926 que ce type d'association de roches ou « Alpine Type Peridotites », affleurant dans des chaînes de montagnes ont été désignées comme des ophiolites (Benson, 1926).

Le sens moderne du terme « ophiolite » est en grand partie à attribuer à Gustav Steinmann. Steinmann (1905, 1927) décrivit les relations existant sur le terrain entre des serpentinites, des gabbros, des basaltes et des radiolarites. Steinmann (1927) propose alors d'utiliser le terme ophiolite pour désigner cette association de roches. L'origine de l'ophiolite à de grands fonds océaniques est alors établie tout comme la relation pétrogénétique entre roches ultramafiques et mafiques. L'association de serpentinites, roches magmatiques, et radiolarites a conduit à l'expression « la trinité de Steinmann ».

Dès la fin des années 1950s, le développement des concepts aboutissant à la tectoniques des plaques a donné lieu à des études concernant l'origine des ophiolites (i.e. Oliver *et al.*, 1969; Coleman, 1971; Dewey & Bird, 1971; Moores & Vigne, 1971). Les travaux menés par Hess (1955, 1962, 1965), Wilson (1959), Gass (1963), Ricou (1968), Vuagnat (1968), Moores (1969) et Thayer (1969) ont grandement participé à l'évolution du terme « ophiolite ». Les données géophysiques suggèrent que la stratification de la croûte océanique est semblable la succession de roche dans les complexes ophiolitiques (Salisbury & Christensen, 1978).

Deux grandes écoles de pensée sont alors apparues : (1) la première suivait les travaux de Steinmann (1927), Brunn (1959), et Aubouin (1965) tandis que (2) l'autre suivait Hess (1955) et Dietz (1963). Concernant les premiers (e.g. Aubouin, 1965) les ophiolites sont générées par la différenciation d'extrusions profondes gigantesques sur le fond marin. Les seconds (e.g., Hess, 1955) proposent que ophiolites représentent le fond de l'océan ; et sont mises en place lors d'une phase orogénique. Ce modèle sera également élaboré plus tard par Miyashiro (1973) sur la base d'analyses géochimiques. Les modèles de Hess et Dietz ont formé la base du modèle de la tectonique des plaques proposé par Le Pichon *et al.* (1976).

Wilson (1959) a été parmi les premiers à cartographier avec précision et à fournir d'excellentes illustrations des caractéristiques macroscopiques et microscopiques des ophiolites de Chypre. Les études suivantes (i.e. Gass, 1963; Moores & Vine, 1971; Miyashiro, 1973; Panayiotou, 1980; Robinson *et al.*, 1987; Malpas *et al.*, 1990) ont fait du complexe ophiolitique de Troodos l'une des ophiolites les plus connues du monde. Parmi les nombreuses découvertes effectuées à Chypre, figurait celle du complexe filonien, qui a eu un impact profond sur les modèles de chambre magmatique et a conduit à l'hypothèse que les ophiolites se forment au niveau d'une dorsale océanique.

En septembre 1972, lors de la conférence de Penrose, une première définition internationalement reconnue par les spécialistes de l'époque a été proposée pour les ophiolites (Penrose field conference, 1972). Les ophiolites ont été assimilées à des fragments de

lithosphère océanique créée au niveau d'une dorsale médio-océanique. Un volume conséquent de données sismiques du fond de l'océan rendait tentant de faire la comparaison entre la série ophiolitique préservée observée sur le terrain, plus tard appelé « Penrose ophiolite », et la stratigraphie de la lithosphère océanique obtenue par les méthodes géophysiques.

Au cours des années, suivant l'élaboration de cette définition, de nombreuses études intégrant des outils de discrimination géochimique ont conduit à la reconnaissance d'une grande diversité d'ophiolites. Il devenait évident que des ophiolites pouvaient être générées dans une grande variété d'environnements géodynamiques, non seulement au niveau d'une dorsale médio-océanique, mais aussi dans un contexte d'arc insulaire (Miyashiro, 1973). Le lien entre les ophiolites et les zones de subduction fut discuté par Sun & Nesbitt (1978) afin d'expliquer l'origine des basaltes appauvris en Ti (boninites; Cameron *et al.*, 1979). Cela a conduit à l'idée que certaines ophiolites pourraient avoir été formées dans des zones au-dessus des zones de subduction. Ceci déboucha sur le modèle de formation de croûte océanique en zone de supra-subduction (Allègre *et al.*, 1982). Ce modèle est soutenu par Pearce *et al.* (1984) qui met en avant l'hypothèse de Miyashiro (1973). Ainsi Dilek & Furnes (2011) ont défini deux catégories d'ophiolites : (1) les ophiolites formées en relation avec le fonctionnement d'une zone de subduction, et (2) les ophiolites formées sans lien direct avec une zone de subduction. L'identification de contextes d'avant- et d'arrière-arc comme analogues actuels d'environnements de formation d'ophiolites (Moores *et al.*, 1984) a marqué un tournant dans la compréhension de l'origine des ophiolites et leur utilité pour reconstruire les contextes tectoniques passés.

Les détails structuraux des ophiolites fournissent des perspectives sur la dynamique de la lithosphère océanique. Nicolas (1989) résume globalement les immenses progrès réalisés dans la compréhension de la pétrogenèse, de l'évolution structurale, de l'obduction et du remaniement des ophiolites et de la lithosphère océanique. Il introduit les notions d'ophiolite de type harzburgite (HOT) et de type lherzolite (LOT) (**Figure 2**). La comparaison des données de forages et des ophiolites à l'affleurement premettra par la suite de relier les ophiolites de type HOT à une dynamique océanique rapide (exemple : la dorsale pacifique), marquée par de forts taux de fusion, et les LOT à une dynamique d'océan lent à ultra-lent (type Atlantique ou Océan Indien), (Lagabrielle & Cannat, 1990; Lagabrielle & Lemoine, 1997; **Figure 3**).

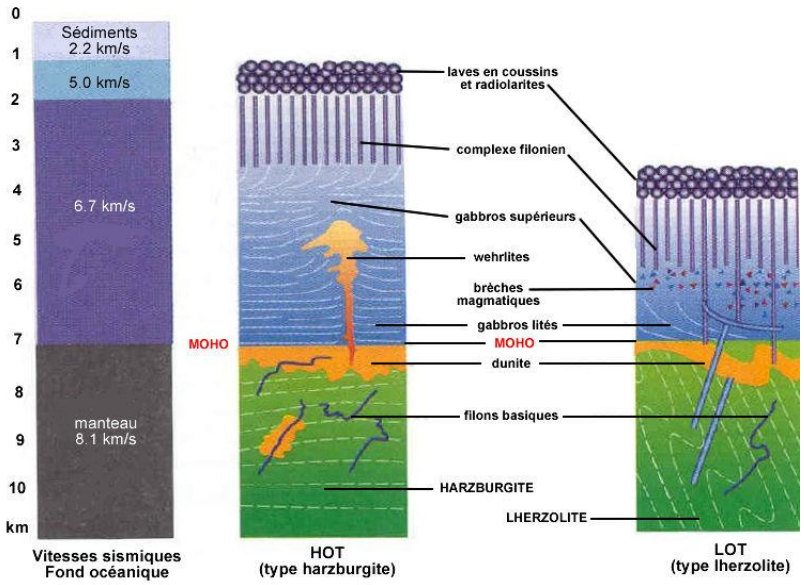

Figure 2 - Profils lithosphériques comparés HOT et LOT, et section définie par la sismique pour un fond océanique 'normal' composé d'une épaisse couche de produits d'origine magmatique (gabbros et basaltes), d'après Vissers & Nicolas (1995) et Nicolas (1997).

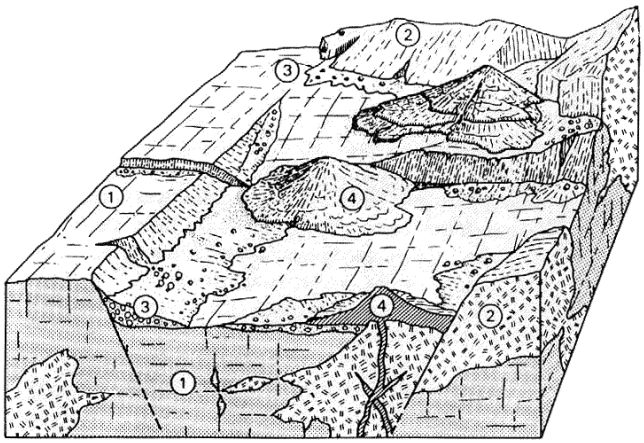

Figure 3 - Schéma d'une ophiolite de ride lente (LOT), d'après l'observation des ophiolites alpines (Lagabrielle, 1987; Lagabrielle *et al.*, 1989; Lagabrielle & Lemoine, 1997). 1, lherzolite serpentinisée (manteau) ; 2, gabbros ; 3, brèches (talus de debris) ; 4, volcans à laves en coussins.

A ces deux types principaux d'ophiolites, il convient également d'ajouter les marges étirées, puisqu'elles comprennent une section de péridotites mises à l'affleurement souvent sur plusieurs centaines de km, appelés 'fonds du 3e type' par Juteau & Maury (1997). Cette mise à l'affleurement survient dans un stade de rifting avancé juste avant l'ouverture océanique proprement dite. Il peut donc exister une continuité entre un fond serpentineux exhumé au cours de mécanismes extensifs (e.g., Lagabrielle, 2009) et une ride lente, puis plus rapide. Ce domaine de transition entre une marge continentale et un domaine océanique 'normal' est communément appelé OCT (Ocean-Continent Transition, e.g., Florineth &

Froitzheim, 1994; Hermann *et al.*, 1997; Manatschal & Nievergelt, 1997; Molli, 1996; Marroni *et al.*, 1998).

Remarquons que ces différents fonds océaniques peuvent conduire à la mise en place d' « ophiolites » sur les marges continentales par des processus d'obduction qui peuvent être fort différents et propres à chaque contexte. La présence d'une grande zone serpentineuse par exemple dans le domaine de l'OCT peut être un des facteurs favorisant l'obduction, tandis que des fonds océaniques plus rapides et ne présentant pas d'OCT pourraient présenter des domaines de faiblesse rhéologique au niveau de la ride (e.g., Coleman, 1981).

Ainsi il devient évident qu'afin de mieux comprendre l'obduction des ophiolites du Petite Caucase et NE Anatolie, nous devons essayer de bien caractériser leur contexte de formation.

1.2 Obduction

Coleman (1971) introduit le terme « obduction » pour décrire le processus de mise en place des ophiolites, ainsi marquant la distinction avec l'habituel sort de la lithosphère océanique, la subduction. Malgré plus de 40 années études, les étapes successives du processus d'obduction sont encore sources de débat (Cluzel *et al.*, 2001; Crawford *et al.*, 2003; Schellart *et al.*, 2006; Wattham *et al.*, 2008; Ulrich *et al.*, 2010; Titus *et al.*, 2011; Cluzel *et al.*, 2012). Différents modèles ont été proposés depuis l'identification des ophiolites comme reliques de domaines océaniques maintenant disparus. L'obduction serait liée aux processus se produisant au niveau des frontières de plaques convergentes (Dewey, 1976). Les relations tectoniques et stratigraphiques résultant de ce processus peuvent présenter une grande variabilité. Par conséquent, il est évident que cette variation du style de mise en place tectonique des ophiolites est à attribuer en partie à la variabilité du contexte tectonique de formation du planché océanique.

Le processus d'obduction peut néanmoins être classé selon quatre catégories (**Figure 4**);

(1) subduction continentale/accretion-collision (Dewey & Bird, 1970; 1971; Church & Stevens, 1971; Dewey, 1976; Smith & Woodcock, 1976; Gealey, 1977; Malpas & Stevens, 1977; Welland & Mitchell, 1977; Searle & Malpas, 1980),

(2) glissement gravitaire/obduction passive (i.e. Williams & Smyth, 1973; Glennie *et al.*, 1973; Stoneley, 1975; Coleman, 1977; Lagabrielle *et al.*, 2013),

(3) propagation gravitaire (i.e. Elliott, 1976; Searle & Malpas, 1980),

(4) jeu de failles transformantes (i.e. Brookfield, 1977; Karson & Dewey, 1978).

Remarquons que ces concepts peuvent être complémentaires ou non selon le contexte de formation du planché océanique considéré. La propagation d'une obduction n'est pas significativement différent de la mise en place de nappes de charriages (Elliott, 1976; Rod, 1982), le matériel déplacé est différent mais les processus physiques sont similaires.

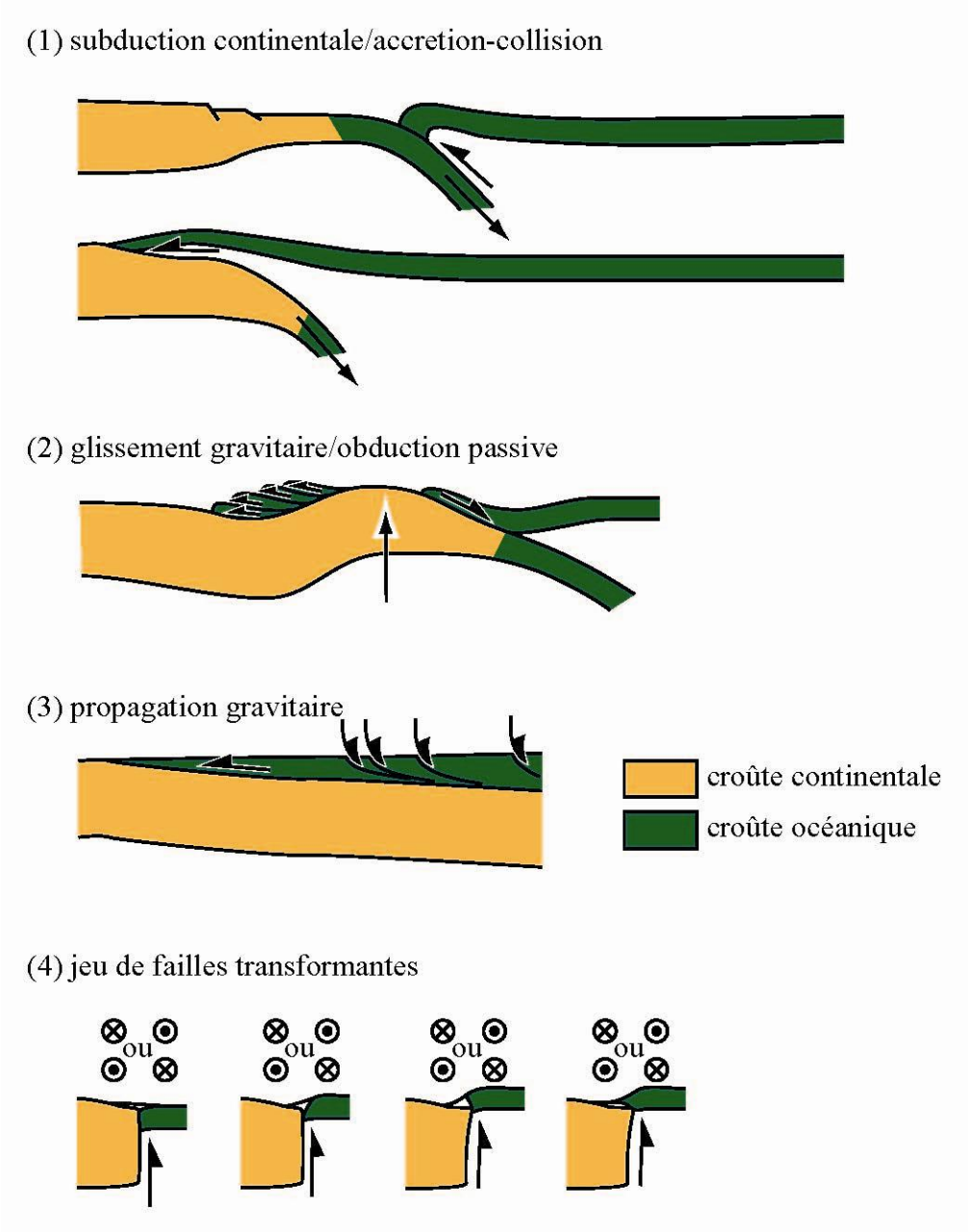

Figure 4 - Schémas illustrant les quatre catégories d'obduction.

Le modèle d'obduction actuellement admis (Coleman, 1981) propose que le transport tectonique des ophiolites sur une marge continentale résulte de l'évolution d'une zone de subduction intra-océanique ou s'initiant à proximité d'une marge. Le domaine océanique entre la marge continentale et la zone de subduction disparait progressivement jusqu'à l'arrivé

de la marge continentale dans la zone de subduction. La subduction évolue de manière à entrainer le continent en profondeur (subduction continentale). McKenzie (1969) argumente que la flottabilité relativement élevé de la croûte continentale est susceptible d'empêcher la subduction continentale. Au cours de cette étape une tranche géante, « une nappe », de lithosphère océanique est poussée sur la marge continentale. Lors des premiers stades de subduction continentale des flyschs, des mélanges tectoniques et des olistostromes contenant des éléments ophiolitiques sont amenées progressivement dans la fosse, alimentant la formation de niveaux transgressifs sur la marge continentale (Dewey, 1976). Les sédiments alimentant ainsi la fosse sont entrainés dans le contact inter-plaque et ainsi métamorphisé (Coleman, 1981). C'est le couplage des contraintes structurales et métamorphiques issues de l'étude des ophiolites elles-mêmes ainsi que celle de toutes les roches métamorphiques sous l'ophiolite (la semelle ophiolitique) qui fournissent les éléments nécessaires pour la reconstruction de scénarios de mise en place. Les chemins PT-t à la fois horaire et antihoraires enregistrés par ces roches métamorphique sont ainsi interprétés comme témoignant d'un sous-charriage (subduction) du domaine continental et le charriage (obduction) du domaine océanique (Searle & Cox, 1999), respectivement. Les reconstructions de l'obduction pour les régions Alpes orientales (Manatschal & Muntener, 2009), Macédonie (Bozovic *et al.*, 2013), Oman (Yamato *et al.*, 2007), Nouvelle Calédonie (Lagabrielle *et al.*, 2013), Californie (Harper *et al.*, 1996), Terre-Neuve (Cawood & Suhr, 1992) et Urals (Brown *et al.*, 2006) limite à 5 Ma l'écart entre la genèse des ophiolites et la subduction continentale, et 20 Ma pour le cycle total entre genèse et emplacement final du corps ophiolitique sur la marge continentale.

Cependant, les causes de ce contexte particulier restent à être précisées. La détermination des conditions permettant à la mise en place de ces objets denses constitués de manteau et la croûte océanique sur un domaine moins dense de croûte continentale peuvent fournir des indices concernant la cause (ou les causes) de telles « bizarreries » géologiques (Agard *et al.*, 2007).

Deux causes de l'obduction sont actuellement discutées. La première est exposée et argumentée par Vaughan & Scarrow (2003) et découle de l'observation que les événements de l'obduction semblent postérieurs au début de la mise en place d'un volcanisme attribué à des panaches mantelliques (Ishiwatari, 1994; Stein & Hoffmann, 1994; Yakubchuk *et al.*, 1994). Ces panaches seraient à l'origine du soulèvement et de l'accélération du mouvement des plaques tectoniques. La modification de divers facteurs, modifiant le couplage au niveau

des zones de subduction, tels que le taux de convergence, la rugosité (ou présence d'aspérités), la flottabilité du panneau plongeant et la dynamique du manteau (Vaughan, 1995). Seules les aspérités majeures, tels que plateaux basaltiques sous-marins, entrant en subduction sont susceptibles d'augmenter de manière significative le couplage interplaque. Aujourd'hui on peut voir cet effet de verrouillage d'une zone de subduction au nord de la Papouasie-Nouvelle-Guinée où le plateau basaltique d'Ontong-Java entre en subduction (Hill & Raza, 1999). Les panaches mantelliques seraient également responsables du rajeunissement thermique de la lithosphère océanique.

Ainsi Vaughan & Scarrow (2003) propose que l'ensemble des perturbations causé par les panaches mantelliques (baisse de la densité et rajeunissement thermique de la lithosphère océanique, augmentation des vitesses des mouvements horizontaux dans la tectonique des plaques, mise en place de reliefs pouvant perturber le fonctionnement 'habituel' des zones de subduction,…) sont à l'origine de l'obduction de vastes domaines océaniques.

Agard *et al.* (2007) considère que l'obduction sert d'accommodation inertielle à la convergence continentale. Suite à des observations et reconstructions géodynamiques concernant la genèse et la mise en place des ophiolites d'Oman, les auteurs analyses les variations des vitesses de convergence entre l'Arabie et l'Eurasie (Scholz & Campos, 1995; Conrad *et al.*, 2004; Heuret & Lallemand, 2005) et celle de la subduction du domaine océanique sous l'Eurasie (Platt, 2000). Ces modèles ainsi que les déductions qui en découlent ont permis de corréler l'initiation et propagation de l'obduction d'Oman à une augmentation de la convergence entre l'Arabie et l'Eurasie et de proposer que la subduction sous l'Eurasie était incapable d'accommoder cette accélération de convergence. Ainsi, l'accélération du mouvement de plaques, le ralentissement de la subduction et/ou l'augmentation de la production à la ride sont des facteurs (causes) avancés pour l'initiation de l'obduction.

La cause de l'obduction proposée par Agard *et al.* (2007) n'est pas incompatible avec celle de Vaughan & Scarrow (2003). Les auteurs sont en accord avec un modèle dans lequel l'obduction se fait en réponse à la perturbation d'une subduction préexistante bordant le domaine océanique. Ainsi l'obduction serait un processus tectonique compensant une subduction incapable d'accommoder la convergence continentale.

I.2 Contexte général de la zone d'étude

Suite à de récentes études concernant ces ophiolites du Petit Caucase (Galoyan, 2008; Rolland *et al.*, 2009a; 2009b; Danelian *et al.*, 2010; Sosson *et al.*, 2010; Rolland *et al.*, 2010;

2011; 2012) les auteurs sont en accord pour dire qu'elles ont une origine commune. C'est-à-dire que ces lambeaux de croûte océanique préservés (non-métamorphisés) ont appartenu à un même domaine océanique. Celui-ci s'est formé dans un contexte de supra-subduction à arrière arc. Ces interprétations valident l'appartenance de l'ensemble de ces corps à une seule structure, dont la limite nord marque une seule suture (Knipper & Khain, 1980; Adamia *et al.*, 1981; Aghamalyan, 1996; Knipper *et al.*, 1997). L'hypothèse alternative était qu'elle marquait trois structures indépendantes s'appuyant sur leurs orientation, leurs localisation et sur le fait qu'elles n'avaient jamais été chariées (Aslanyan & Satian, 1977; Satian, 2005; Satian *et al.*, 2005).

Les reconstitutions tectonique et géodynamique du Petit Caucase ne sont pas encore précisément déterminées car elles dépendent en grande partie de l'évolution de ces corps ophiolitiques. Ces reconstitutions doivent prendre en compte l'héritage géologique du domaine océanique obducté, acquit depuis le début de son accrétion au milieu du Mésozoïque (Jurassique moyen) jusqu'à son obduction à la fin du Mésozoïque (Crétacé supérieur), qui n'est que peu souvent préservé de la déformation lié au développement de la zone de suture en contexte de collision.

Tout comme dans le Petit Caucase, dans le nord-est de l'Anatolie des affleurements d'ophiolites ainsi que de mélange ophiolitique marquent la zone de suture Izmir-Ankara-Erzincan (Şengör & Yılmaz, 1981; Robertson & Dixon, 1984; Yılmaz *et al.*, 1997; Okay & Şahintürk 1997; Rice *et al.*, 2006, 2009; Özen *et al.*, 2008; Çolakoğlu, 2009; Sarıfakıoğlu *et al.*, 2009). Elles témoignent de la position de cette suture téthysienne par leur allongement presque E-W. Plus au sud, il existe aussi des affleurements en position distale comparable à la zone de Vedi dans le Petit Caucase. Cependant, concernant le calendrier tectonique aucun scénario ne fait l'unanimité contrairement aux ophiolites du Petit Caucase. Par exemple, l'âge de la subduction de la partie nord de ce domaine océanique sous la marge eurasienne est supposé être Jurassique (Adamia *et al.*, 1981; Hess *et al.*, 1995; Nikishin *et al.*, 2003), Cenomanien-Turonien (Yılmaz *et al.*, 1997; Okay & Şahintürk, 1997) ou Albien (Okay *et al.*, 2006). Ceci est également valable pour la fin de cette subduction et par conséquent l'âge de collision continentale qui a successivement été avancé fin Eocène (Peccerillio et Taylor, 1976; Şengör & Yılmaz, 1981; Robinson *et al.*, 1995), Eocène moyen (Yılmaz *et al.*, 1997) ou Paleocène (Okay & Şahintürk, 1997). Des modèles tectonique alternatif ont été proposés afin d'allier anciennes et nouvelles observations (Okay & Şahintürk, 1997; Rice *et al.*, 2006; 2009; Rolland *et al.*, 2009a; Robertson & Ustaömer, 2012).

I.3 Problèmatique avant thèse

L'objet de cette thèse est de contraindre le processus d'obduction pour les ophiolites provenant de la branche nord de la Néotéthys. Les données étant éparses dans cette région du monde (NE Turquie et Arménie) il convient de trouver les liens entre ces zones. Par conséquent afin de mieux localiser dans l'espace les zones d'obduction et leur continuité, cette thèse s'appuie sur un travail de cartographie, d'analyse structurale, de pétrologie et de datation sur des zones mal étudiées ou en cours d'étude (NE Anatolie et SE de la suture Sevan-Akera).

Ainsi nous cherchons à répondre à trois questions :

- ***Qu'elle est l'ampleur de la nappe obductée au front de la zone de suture ?***

En Arménie la nappe atteint au moins 100 km de portée (Sosson *et al.*, 2010). Mais si les ophiolites de l'Anatolie sont de la même nature géochimique et d'un âge en rapport avec celles du Petit Caucase alors la nappe ophiolitique serait bien plus importante. Elle atteindrait ainsi au moins 200 km de portée. Ce qui en ferait l'une des plus grandes nappes ophiolitiques obductées du globe (à l'affleurement dans une chaîne).

- ***Quelle est la durée de l'obduction ?***

La partie frontale de l'obduction des ophiolites du Petit Caucase est datée entre 90 et 83 Ma (Coniacien-Santonien). Mais on ne sait pas à quel moment s'est initiée l'obduction. Il existe des traces de métamorphisme HT-BP dans la zone de suture près d'Amasia (Arménie) (Aghamalian, 1978), mais ces roches ne nous ont pas encore donné de renseignement précis sur l'âge exact du métamorphisme qui pourrait correspondre à celui d'une semelle d'unité obductée.

- ***Quelle est la (les) cause(s) de l'obduction ?***

Cette question a été soulevée à maintes reprises pour d'autres cas, et l'on admet aujourd'hui que la principale cause est l'accélération de la convergence et /ou l'apparition de panaches mantelliques intra-océaniques ayant pour effet d'augmenter la flottabilité la lithosphère océanique et de conduire à son écaillage pendant la fermeture du domaine océanique. Une autre explication serait l'entrée d'une lithosphère continentale dans une subduction intra-océanique comme l'ont proposé Hafkenschied *et al.* (2006) pour la Téthys au niveau du Zagros-Oman. Ce processus aurait-il provoqué l'obduction dans le Petit Caucase et en Anatolie ? Ceci est vraisemblable et la nature des ophiolites (tendance géochimique de bassin-arrière arc : Galoyan *et al.*, 2007 ; Rolland *et al.*, 2009 ; Galoyan *et al.*, 2009) et la présence par endroit de roches métamorphiques HP-BT sous ces ophiolites (Rolland et al.,

2007) suggère qu'en effet une subduction intra-océanique de type SSZ devait être présente dans l'océan téthysien.

Ensuite pour tester les hypothèses découlant de nos observations, pour vérifier la vraisemblance des réponses que nous fournissons à ces questions et pour de les replacer dans un cadre plus régional, un travail de modélisation numérique sera conduit. Ceci permettra de comprendre les causes du processus d'obduction et plus précisément dans cette région du monde.

Chapitre 2* - *Méthodes analytiques

« Il n'y a pas une méthode unique pour étudier les choses. »

Aristote, extrait de *Traité de l'Ame*

II.1 EMPA

L'analyse d'un échantillon par Sonde Electronique (Electron Probe Micro Analysis) permet de déterminer sa composition. Elle s'appuie sur la mesure de l'intensité du rayonnement X caractéristique émis par un élément donné, dans des conditions particulières d'excitation.

Raymond Castaing a été le premier à établir les bases physiques de l'analyse quantitative en démontrant l'existence d'une relation entre cette intensité et la concentration de l'élément correspondant (Castaing, 1951). Au cours des 40 dernières années, la microanalyse a largement évolué. Si les bases physiques posées par Castaing sont sensiblement les mêmes, nous avons maintenant à notre disposition des moyens de calcul performants grâce au développement des calculateurs. Les différents modèles développés depuis ont permis d'affiner les effets de ralentissement et de rétrodiffusion des électrons, l'absorption et la fluorescence.

Les modèles les plus récents s'appliquent à des situations de plus en plus complexes et il est désormais possible de quantifier des éléments difficiles à mesurer tels que les éléments légers, des structures complexes telles les couches minces et les échantillons stratifiés. L'augmentation de la puissance des calculateurs associée à l'amélioration des algorithmes de calcul, permet, entre autres, le traitement des images quantitatives en temps réel et l'optimisation de la mesure par simulation analytique.

1.1 Appareillage

Une microsonde électronique (**Figure 5**), comme un microscope électronique à balayage, est constituée d'un canon à électrons, d'une colonne électronique destinée à réduire le diamètre de la sonde électronique au niveau de l'échantillon, d'un dispositif interne de balayage du faisceau électronique, de détecteurs pour le rayonnement X, éventuellement d'autres détecteurs (électrons, photons visibles), et aussi d'un microscope optique.

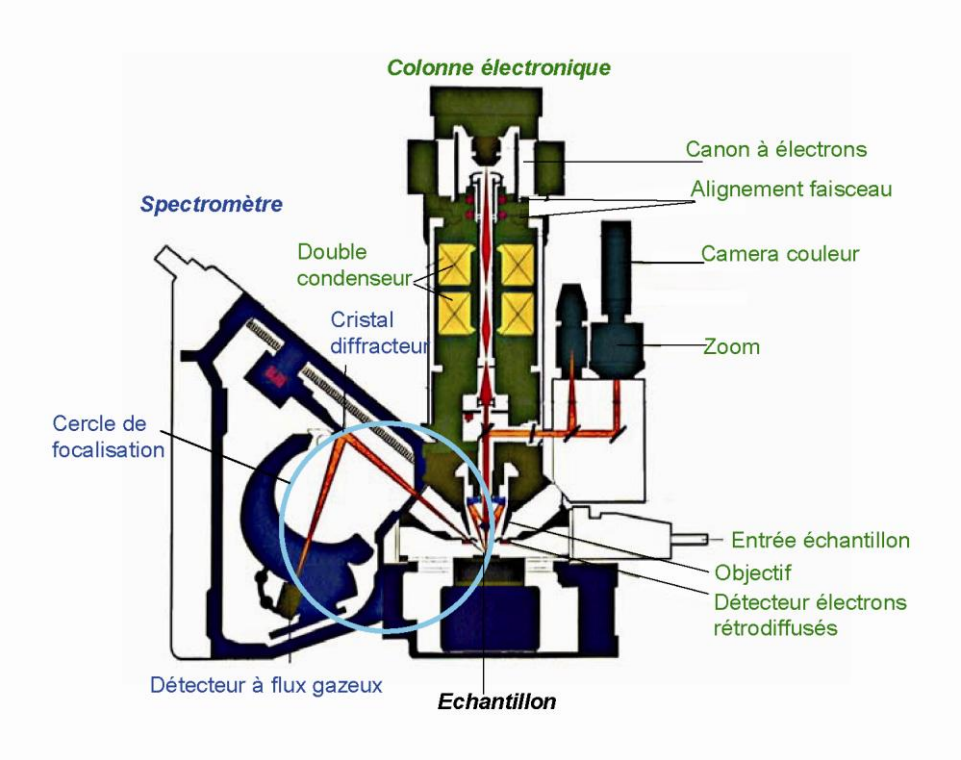

Figure 5 - Schéma des composants d'une microsonde éléctronique.

Le canon à électrons utilise le plus souvent l'effet thermoélectronique, ce qui correspond tout simplement à un fil de tungstène en pointe (le filament) qui est chauffé par effet Joule à une température de 2700 K. Les électrons émis par le filament sont accélérés par le champ électrique qui règne entre le filament (polarisé négativement) et l'anode reliée à la masse. Ce champ électrique correspond à la tension d'accélération des électrons.

La colonne électronique est constituée de plusieurs lentilles électromagnétiques, dont le but est à la fois d'obtenir sur l'échantillon un faisceau focalisé de faible diamètre et d'ajuster l'intensité du faisceau primaire en fonction des besoins.

1.2 Mode d'utilisation

Si à l'origine, la microanalyse a été développée dans le but essentiel de fournir une information quantitative ponctuelle, l'aspect « imagerie » a pris une importance de plus en plus grande.

-mode ponctuel. En positionnant à l'aide du microscope électronique à balayage ou du microscope optique la sonde sur la phase à analyser, on peut obtenir la composition élémentaire dans un volume de l'ordre du micron cube.

-mode " traversée " ou " profil ". En déplaçant linéairement le faisceau électronique, ou l'échantillon, et en mesurant la variation de l'émission X d'un élément donné, on obtient un profil de concentration correspondant. Ce mode d'utilisation est en général qualitatif. Ce mode peut être quantitatif, mais nécessite un échantillon parfaitement poli sur tout le trajet du déplacement.

-mode image. C'est le mode habituel du microscope électronique à balayage. On peut ainsi obtenir l'image de la distribution des éléments de l'échantillon. Ce mode peut être qualitatif, ou quantitatif et visualisé en pseudo couleurs.

1.3 Analyse qualitative

La mesure d'un spectre permet de préciser la nature des éléments. L'intensité des raies donne une estimation de la concentration.

1.4 Analyse quantitative

Nécessite des conditions de préparation d'échantillon et des conditions opératoires draconiennes.

-échantillon massifs. La microanalyse par sonde électronique est capable de quantifier avec une incertitude de l'ordre du % ou mieux les échantillons massifs.

-échantillon stratifiés. Il est possible également de quantifier les différentes couches d'un échantillon composé de matériaux différents. La profondeur maximale analysée sera de l'ordre d'une dizaine de microns. Des couches d'une épaisseur monoatomique peuvent être quantifiées en concentration et en épaisseur.

1.5 Conditions opératoires

-Choix de la tension d'accélération. Cette tension d'accélération (HT) devra être choisie de manière à exciter tous les éléments de l'échantillon. Le volume analysé est proportionnel à la tension d'accélération, et en première approximation le volume excité double tous les 5 keV. L'intensité émise sera également proportionnelle à cette tension. Très grossièrement si le volume double, l'intensité mesurée double. On augmente la sensibilité en augmentant la HT, mais on perd en résolution spatiale.

-Choix de l'intensité du faisceau électronique. L'intensité du faisceau électronique doit être suffisante pour que le signal X soit statistiquement significatif. Quand on augmente

l'intensité électronique, le diamètre de la sonde augmente, on a donc une perte de résolution (faible comparée à la HT). On ne peut augmenter indéfiniment l'intensité du faisceau électronique, car il y aura destruction de l'échantillon.

1.6 Préparation de l'échantillon

Pour l'analyse quantitative il est nécessaire d'avoir un échantillon poli optiquement. Une surface rugueuse au sens microscopique (c'est-à-dire des défauts de planéité de l'ordre du micron) entraîne des modifications importantes de l'émission X primaire et donc des concentrations calculées. Pour les échantillons isolants il est nécessaire d'effectuer une faible métallisation de surface, afin d'établir la continuité électrique entre l'échantillon et la masse de l'appareil (le faisceau électronique étant un courant électrique).

Il est nécessaire de respecter les conditions suivantes de préparations d'échantillons afin d'avoir des échantillons uniformes et de bonnes qualités. Le premier critère de qualité sur les résultats est la préparation de l'échantillon (90% des incertitudes sur les résultats proviennent de l'état de surface de l'échantillon). Les surfaces doivent être planes, polies optiquement (0.1micron) et parfaitement propres. Pour les matériaux non conducteurs, une métallisation avec une couche de carbone (250 ± 20 Å d'épaisseur) est effectuée (la qualité de la couche déposée est dépendante de la propreté des surfaces).

Il est important de noter que les problèmes liés à la préparation des échantillons et à leur contamination sont une des sources majeures d'incertitude de l'analyse par sonde électronique.

Il est nécessaire de faire une étude optique préliminaire et poussée de son échantillon utilisant une lumière réfléchie et transmise sur les mêmes sections polies et lames mince que celles prévues pour analyses. Cette étude permet outre l'étude structurale des échantillons, de choisir dans un premier temps les échantillons les mieux adaptés au problème.

II.2 ICPMS

La spectrométrie de masse est une technique instrumentale d'analyse reposant sur la séparation, la qualification mais surtout la quantification des éléments chimiques qui constituent un échantillon en fonction de leur masse. Elle est basée sur le couplage d'une torche à plasma générant des ions et d'un spectromètre de masse quadripolaire qui sépare ces ions en masse. Cette technique permet de déterminer la composition chimique d'un échantillon ainsi que mesurer des concentrations d'éléments très faible.

Suite au broyage de l'échantillon (broyeur agate), l'analyse des échantillons par ICP-MS se divise en quatre parties : introduction-nébulisation, ionisation, séparation en masse, détection.

L'échantillon est mis en solution. Un passeur automatique d'échantillons couplé à une pompe péristaltique introduit la solution dans une chambre de vaporisation où le nébuliseur la transforme en un aérosol liquide composé de micro-gouttelettes de quelques micromètres à l'aide d'argon gazeux. L'aérosol ainsi formé est envoyé dans une torche à plasma d'argon à très haute température (entre 6.000 et 10.000 °C) pour vaporiser, dissocier, atomiser et ioniser la plupart des éléments.

Une partie de ce plasma (10%) est échantillonnée par un premier orifice de 1 mm de diamètre environ au sommet d'un cône en nickel ou en platine appelé « le sampler ». Sous l'effet du vide modéré (1~2 mbar) qui règne dans une chambre de pompage différentiel, qui permet de passer de la pression atmosphérique au vide secondaire du spectromètre de masse, le plasma se détend et passe ensuite dans un deuxième orifice, « le skimmer ». Un système de vide différentiel accélère les ions du plasma vers un ensemble de lentilles électrostatiques qui extrait les ions chargés positivement et les transporte vers un filtre de masse quadripôlaire. Cet ensemble de lentilles est aussi appelé lentille ionique.

Ce filtre de masse permets la transmission de seulement les ions présentant un rapport masse sur charge particulier, déterminé en fonction de la fréquence appliquée au quadripôle. Le principe du spectromètre est basé sur la séparation des éléments en fonction de leur charge et de leur masse. Le spectromètre est composé de quatre barres cylindriques qui sont séparées en deux paires opposées, soumises à un courant continu (DC) et alternatif (RF). Les deux paires de cylindres ont des tensions continues opposées et alternatives de même amplitude mais de signe opposé. Dans le plan formé par la paire de barres positive les ions légers sont trop déviés et heurtent les barres. L'ion à analyser et ceux ayant une masse supérieure restent entre les deux barres. Dans ce plan le quadripôle joue le rôle de filtre passe-haut. Dans le plan de la paire de barres négative, ce sont les ions lourds qui sont déviés, ce qui équivaut à un filtre passe-bas. En combinant ces deux filtres, seuls les ions ayant le rapport masse/charge désiré seront transmis au détecteur (**Figure 6**).

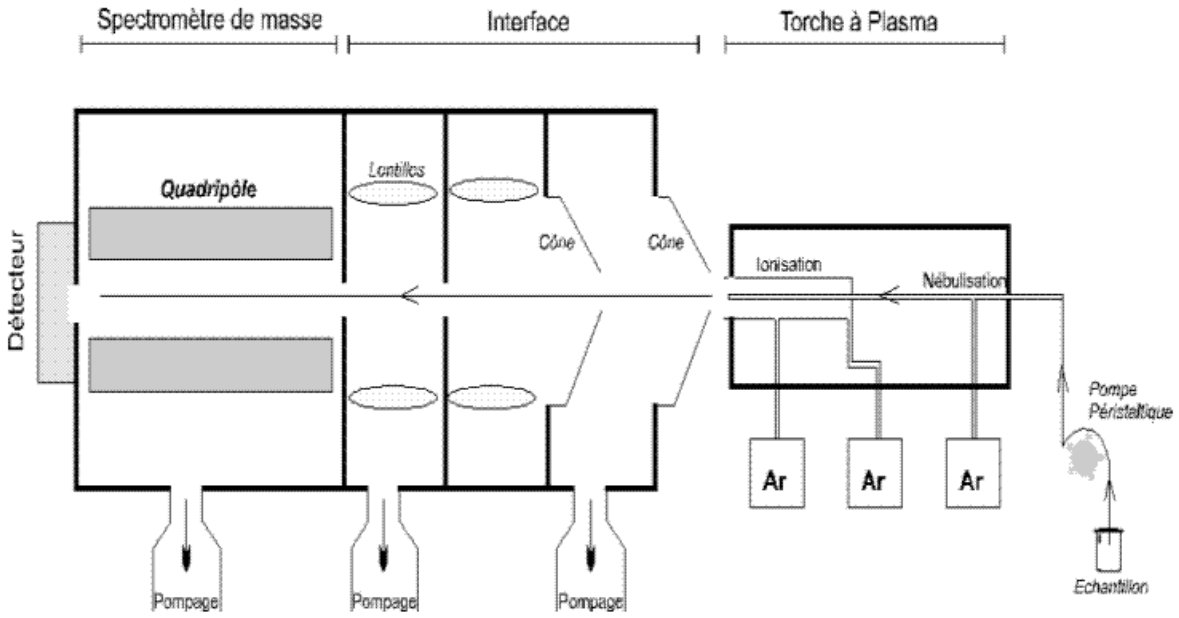

Figure 6 – Schéma conceptuel du spectromètre de masse ICP-MS.

La détection s'effectue grâce à un multiplicateur d'électrons. Pour un isotope donné, le nombre d'ions mesuré permet de calculer directement la concentration de l'élément analysé grâce à un logiciel de traitement quantitatif et qualitatif de l'enregistrement. Les nombres d'électrons sont convertis en concentrations grâce à l'utilisation de deux types de calibrations : externe (solutions étalon) et interne (spikes). Pour les roches, les matrices sont complexes et un traitement supplémentaire des données est nécessaire.

L'ICP-MS est utilisé pour l'analyse simultanée des éléments en trace et « ultra-traces » (teneur est inférieure à 10^{-6} g/g) et pour la détermination des rapports isotopiques dans les roches. Cette technique est d'une excellente sensibilité permettant de détecter des éléments présents au niveau du ppt dans une solution de roche. Sans aucune séparation chimique, il permet l'analyse de nombreux éléments en trace au niveau du ppb (10^{-9} g/g). La précision varie d'un élément à l'autre en fonction du potentiel d'ionisation et des matrices étudiées, l'incertitude moyenne étant inférieure à 3 %.

II.3 Géochronologie

Les méthodes de datation utilisées, afin d'obtenir des contraintes géochronologique dans le cadre de ce travail, ont nécessité avant tout une phase d'observation microscopique afin de caractériser les phases minérales présentes. Cette étape d'identification a été suivie d'analyses chimiques afin de déterminer les particularités ainsi que l'adéquation de ces

minéraux pour les méthodes envisagées. Ces phases de caractérisation ont été réalisées sur des lames minces polis.

S'en est suivie des opérations de séparation minéralogique afin d'extraire et isoler des monocristaux d'amphibole, mica blanc, biotite et zircon pour datation utilisant les méthodes $^{40}Ar/^{39}Ar$ et U-Pb.

3.1 Caractéristiques minérales

Les minéraux qui sont datable par les deux méthodes ont des caractéristiques particulières permettant de les isolées (**Tableau 1**).

Nom	Formule	Classe	Densité	Susceptibilité magnétique
Hornblende	$Ca_2(Mg,Fe,Al)_5(AlSi)_8O_{22}(OH)_2$	Silicate	$2,9 < \rho < 3,4$	$0,1A < \chi_m < 0.8A$
Muscovite	$KAl_2(AlSi_3O_{10})(F,OH)_2$	Silicate	$\rho \sim 2,8$	Non magnétique
Biotite	$K(Fe,Mg)_3AlSiO_{10}(F,OH)_2$	Silicate	$2,9 < \rho < 3,4$	$0,3A < \chi_m < 0,5A$
Zircon	$ZiSiO_2$	Silicate	$4,6 < \rho < 4,7$	Non magnétique

Tableau 1 – Récapitulatif des minéraux utilisés pour datation avec les méthodes $^{40}Ar/^{39}Ar$ et U-Pb.

3.2 Protocole de séparation des minéraux

Il existe une série d'étapes afin de correctement isoler les minéraux pouvant être datés pour chaque méthode (**Figure 7**).

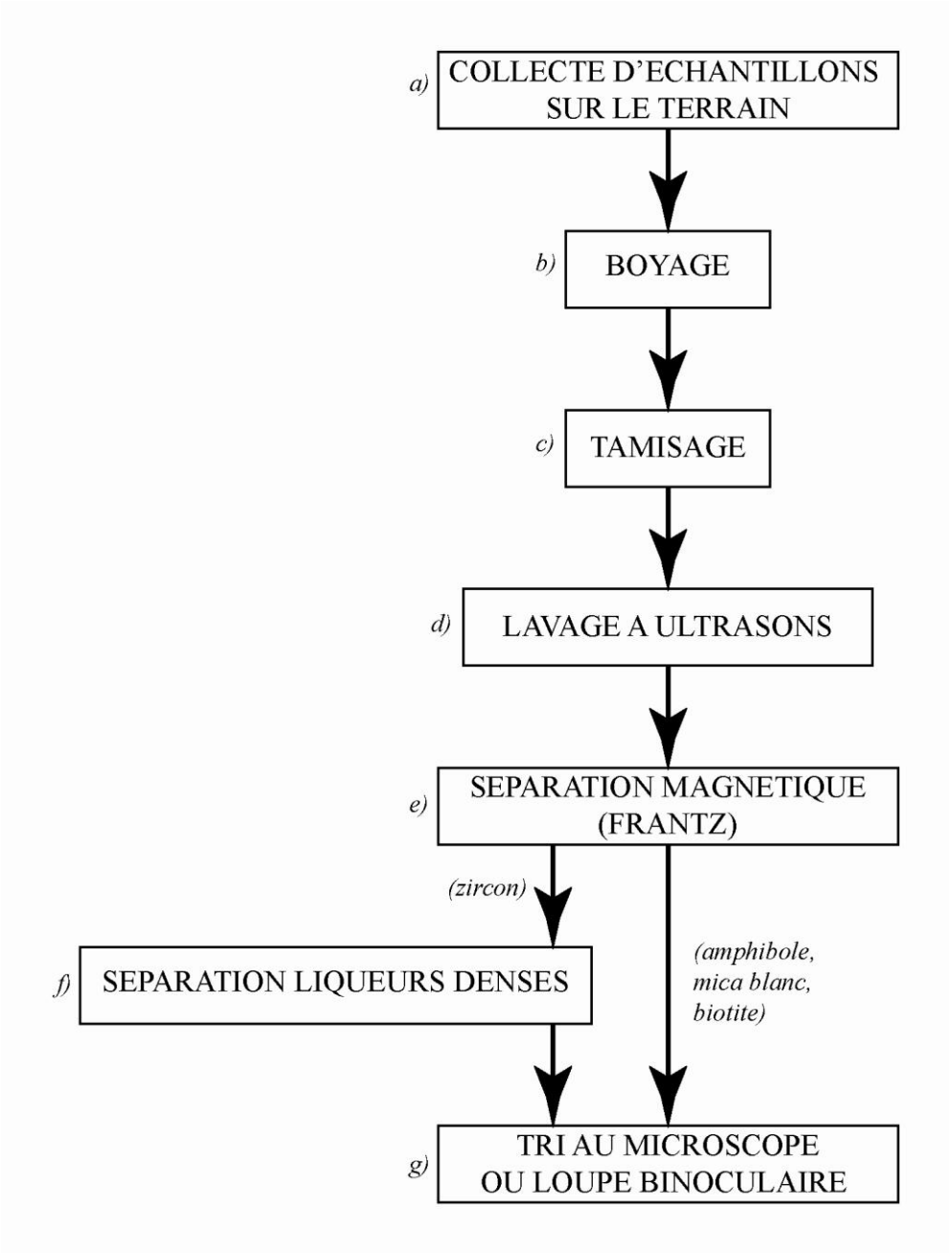

Figure 7 - Etapes successives de séparation minérales.

- Commentaires :
  a) Les échantillons sont prélevés à partir d'affleurements sains et préservés afin d'assurer la qualité des minéraux datés. Ceci est particulièrement important pour la datation $^{40}Ar/^{39}Ar$ car des minéraux altérés, tel que la biotite chloritisé, sont susceptible de présenter des pertes en argon.
  b) Le broyage s'effectue avec un broyeur à mâchoires (larges puis plus petites) pour réduire la taille des morceaux de l'échantillon avant l'utilisation d'un broyeur à disques rotatif. Le but de cette étape est de réduire l'échantillon en poudre.
  c) Le tamisage est réalisé dans le but de récupérer différentes fractions granulométrique des échantillons réduits en poudre. Il se fait une tamiseuse à vibration utilisant des tamis de 200mm de diamètre ayant des mailles de 300µm, 200µm et 100µm.
  d) Les fractions obtenues sont lavées avec de l'eau. Elles sont également agités par ultrasons pour nettoyer les grains de poussières fines et de particules jugées trop petites.
  e) Les trois fractions ainsi lavées sont ensuite passé dans un dispositif à séparation magnétique de type Frantz (**Figure 8**). Pour la datation $^{40}Ar/^{39}Ar$, ceci ne sert qu'à réduire la fraction à trier en séparant les minéraux magnétiques (fraction contenant les hornblendes et biotites) des minéraux non-magnétiques (contenant les micas blancs). Pour la datation U-Pb, trois passages sont effectués. Le premier sert à éliminer les minéraux les plus magnétiques avec des régales de champ de 0.5A, de pente de 8° et de contrepente de 6°. Les minéraux les moins magnétiques sont récupérés pour le deuxième passage avec des réglages de champ de 1.5A, de même pente 8° et de contrepente de 3°. Les minéraux les moins magnétiques sont encore une fois récupérés pour le troisième passage avec des réglages de champ de 1.5A, de pente 8° et de contrepente de 2°. Les meilleurs minéraux pour datation U-Pb seront les derniers non magnétiques (contenant les zircons).
  f) Pour datation U-Pb, les fractions non-magnétiques obtenues sont passés dans une solution de liqueur dense (**Figure 9**). Les minéraux plus denses que la solution (dont les zircons) la traversent alors que les minéraux moins denses sont retenus.
  g) Pour les deux méthodes de datation une étape de tri à la main au microscope ou loupe binoculaire s'en suit afin de sélectionner les plus beau grains (grains uniques, sans inclusions visible et de forme le moins arrondis).

Figure 8 - Séparateur magnétique Frantz.

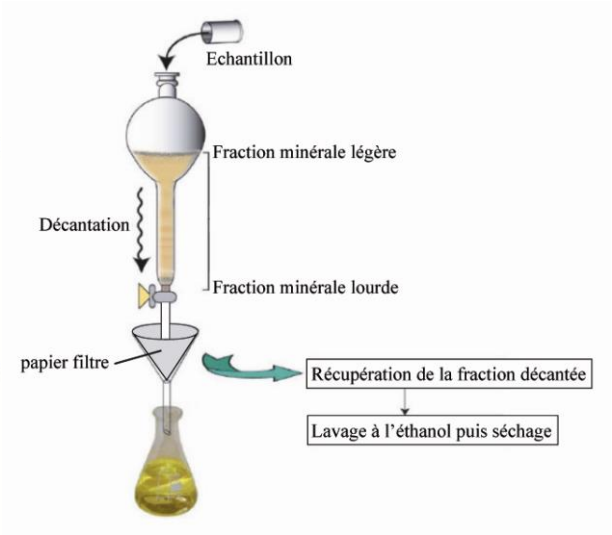

Figure 9 - Dispositif de séparation par liqueur dense.

3.3 La méthode ^{39}Ar-^{40}Ar

Afin de replacer dans un calendrier tectonique la formation ainsi que les variations de conditions en termes de pression et température des roches étudiées, la méthode 40Ar/39Ar sur des amphiboles, micas blancs et biotites a été utilisée. Ces minéraux ont été extraient de roches magmatiques plutoniques (i.e. gabbros) ainsi que roches métamorphiques (schistes, amphibolites et gneiss) provenant du socle cristallin du Bloc Sud Arménien (SAB), des roches ophiolitique chevauchant le SAB ainsi que des ophiolites de nord-est Anatolie et des roches se trouvant directement sous les ophiolites composant leurs semelle.

3.3.1 Introduction à la technique ^{40}Ar/^{39}Ar

La technique de datation ^{40}Ar/^{39}Ar est la variante la plus communément utilisé de la méthode conventionnelle K-Ar. Elle est basée sur la décomposition naturelle du ^{40}K en ^{40}Ar. La technique repose sur l'idée que l'abondance relative des isotopes du potassium est constante dans les minéraux analysés.

Pour la méthode ^{40}Ar/^{39}Ar l'échantillon à daté est tout d'abord irradié dans un réacteur nucléaire afin de transformer une proportion des atomes ^{39}K en ^{39}Ar suite à l'interaction avec des neutrons rapides. Suite à l'irradiation, l'échantillon est placé dans un système pourvu d'un vide poussé. L'argon est alors extrait par étapes successif de chauffe jusqu'à fusion totale. Après chaque étape de chauffe l'argon extrait est purifié et analysé par un spectromètre de masse isotopique. L'avantage de la méthode est que le rapport entre isotope père (^{40}K) et fils

($^{40}Ar^*$) est mesuré lors de la même analyse, rendant inutile le besoin d'une analyse séparé pour le potassium. Ceci permet de surmonter les problèmes d'inhomogénéité au sain d'un même échantillon et permet, en principe, de dater des échantillons de plus petite taille. En prime, cela permet de mesurer des rapports isotopiques de manière plus précise, réduisant les erreurs analytiques en comparaison à la méthode K-Ar conventionnelle ;

L'avantage majeur de cette technique est quelle s'effectue par étape de chauffe successive à des températures croissantes. L'argon alors extrait à chaque étape peut être analysée isotopiquement donnant une série d'âges apparents pour un échantillon (minéral) donnée. Cette méthode de chauffage, connue comme « chauffage par paliers » ou « chauffage incrémentale » (Merrihue & Turner, 1966), permet d'obtenir un aperçu de la distribution de $^{40}Ar^*$ dans l'échantillon analysé. Cette méthode repose sur le principe de libération d'argon par diffusion thermique au fur et à mesure que l'échantillon est porté à des températures de plus en plus élevé. Au cours des étapes de chauffe, $^{40}Ar^*$ et ^{39}Ar seront libéré en proportion égale dû à leurs coefficient de diffusion proche, donnant un rapport $^{40}Ar^*/^{39}Ar_k$ plus ou moins constant pour chaque fraction de gaz extraite pour chaque palier de chauffe. Un graphique représentant l'âge apparent $^{40}Ar^*/^{39}Ar_k$ pour chaque palier en fonction de la proportion totale d'argon libéré (par convention ^{39}Ar) donnera alors un motif plat, dont on fait référence par le terme de « plateau ». Un spectre d'âge plat, ainsi obtenu, est couramment considérer comme une indication que l'échantillon représente un système fermé. Néanmoins, un échantillon peut perdre une partie de son $^{40}Ar^*$ après cristallisation initiale, suite à un événement métamorphique impliquant un fort réchauffement ou au cours d'exhumation/refroidissement prolongé. Un tel échantillon aura une structure cristalline contenant des sites ayant un rapport $^{40}Ar^*/^{40}K$ différent qui se révéleront lors du chauffage par palier et donneront ainsi un spectre d'âge qui ne sera pas plat.

Idéalement, la méthode $^{40}Ar/^{39}Ar$ permet de définir un âge de refroidissement en relation avec l'exhumation de la roche échantillonné ou l'âge du dernier événement thermique ayant rouvert le système.

Puisque les spectromètres de mass utilisé lors de datations $^{40}Ar/^{39}Ar$ ne mesurent pas habituellement les abondances absolues, des procédures de standardisation ont été adopté afin de calibrer les machines. Un standard couramment utilisé est l'argon atmosphérique. La composition isotopique atmosphérique en argon a été mesurée par Nier (1950) et a permis d'obtenir une valeur de 295.5 pour le rapport $^{40}Ar/^{39}Ar$ tel que stipule Steiger & Jäger (1977). La prise en compte de cette valeur est essentielle afin de mesurer avec succès un âge

$^{40}Ar/^{39}Ar$, des corrections doivent être effectuées pour toute contamination atmosphérique contenue dans l'échantillon ou dans le vide de la ligne d'extraction menant au spectromètre de masse.

Plus de précisions concernant la théorie ainsi que la technique de datation $^{40}Ar/^{39}Ar$, le lecteur est dirigé vers McDougall & Harrison (1988).

3.3.2 Dispositif de datation $^{40}Ar/^{39}Ar$ utilisé

Les datations $^{40}Ar/^{39}Ar$ ont été réalisées par paliers de température croissant en utilisant un laser CO2 de 50W Synrad©; les isotopes ont été mesurés en mode statique sur un spectromètre VG3600 équipé d'un système de détection Daly au laboratoire de Géochimie, Géochronologie et Pétrologie de l'UMR7329 Géoazur (**Figure 10**).

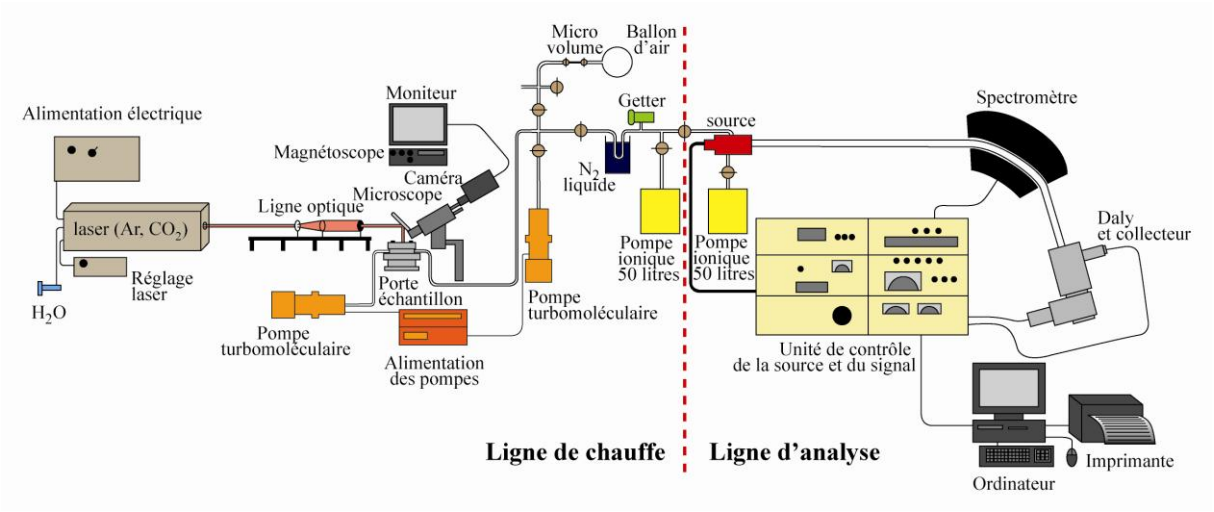

Figure 10 - Schéma du dispositif d'analyse $^{40}Ar/^{39}Ar$.

3.4 La méthode U-Pb

Parmi les différents couples radiométriques utilisés en géologie, le système U-Pb est probablement l'un des plus employé. Un des principaux avantages de ce système réside dans le fait qu'il associe deux isotopes pères d'un même élément (^{235}U et ^{238}U) qui se désintègrent suivant des constantes de désintégration différentes pour donner deux isotopes fils d'un autre élément (le ^{207}Pb et le ^{206}Pb respectivement). Ainsi, au cours du temps, la quantité d'uranium décroît régulièrement alors que les quantités de plomb, issues de la désintégration radioactive, augmentent proportionnellement (**Figure 11**). En parallèle et en liaison directe avec le

processus de désintégration radioactive de l'uranium, la composition isotopique du plomb se modifie également, donnant une autre mesure du temps écoulé.

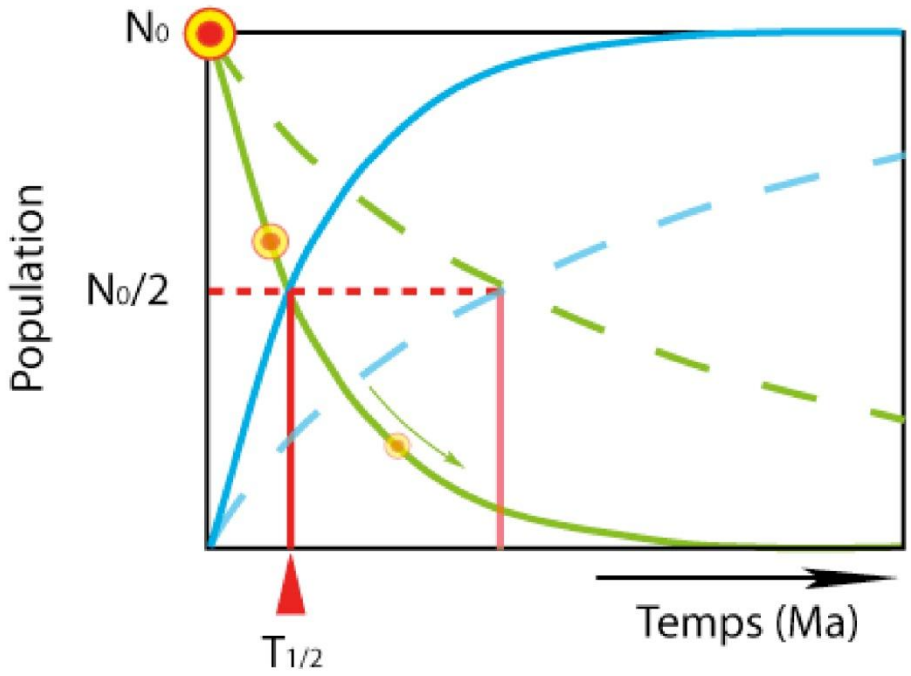

Figure 11 - Graphique représentant la décroissance de la quantité d'uranium et l'augmentation de plomb au cours du temps.

Pour le système U/Pb, cette propriété permet de calculer trois âges à partir de trois rapports isotopiques distincts : deux rapports Pb/U ($^{206}Pb/^{238}U$ et $^{207}Pb/^{235}U$) et un rapport de composition isotopique du plomb ($^{207}Pb/^{206}Pb$). La comparaison entre ces trois âges permet de préciser de façon remarquable si le système U-Pb du minéral considéré est resté clos ou s'il a évolué en système ouvert. Au contraire des autres méthodes utilisées en géochronologie, la méthode U-Pb offre l'avantage, même si le radiochronomètre a évolué en système ouvert, de pouvoir donner une bonne indication de l'âge. Ainsi, il est parfois possible de retrouver non seulement l'âge initial du système mais également celui de son ouverture. Cette combinaison unique de deux chronomètres naturels a été très tôt exploitée par Wetherill (1956) dans le diagramme "concordia" (**Figure 12**).

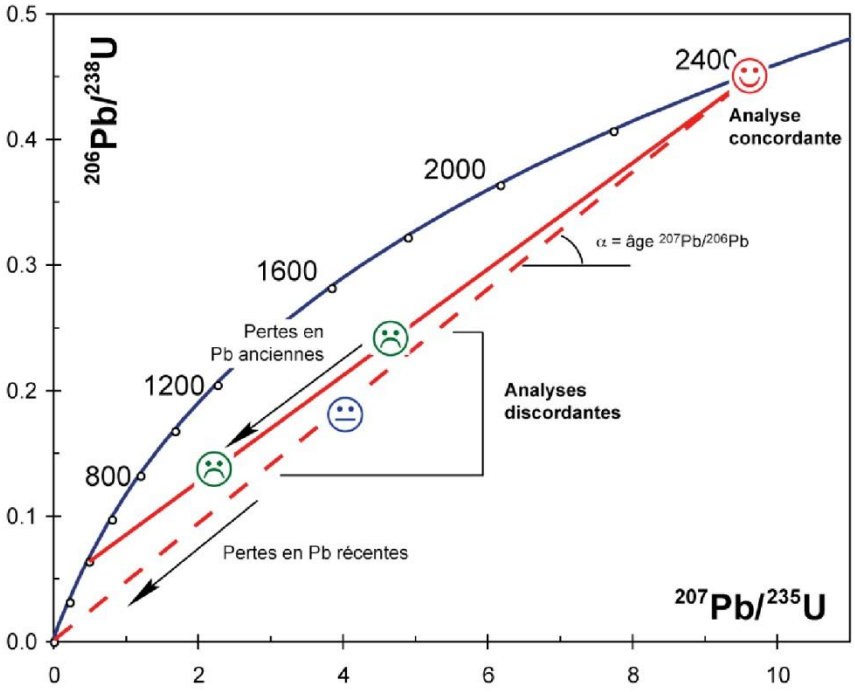

Figure 12 – Diagramme illustrant le principe d'utilisation de la courbe concordia.

Certains minéraux peuvent intégrer des éléments radioactifs dans leur réseau cristallin soit directement car ils entrent dans la formule chimique du minéral en tant que constituant principal, soit par substitution à un élément principal en raison de similarité de taille et de charge dans la majorité des cas (exp. substitution de l'U^{4+} au Zr^{4+} dans le réseau cristallin du zircon; **Figure 13**). Les minéraux les plus intéressants en géochronologique U-Pb sont ceux qui, lors de leur cristallisation, intègrent dans leur réseau cristallin une quantité notable d'éléments radioactifs pères (U), tout en excluant l'intégration de Pb commun.

Figure 13 – Cristal de zircon presentant une inclusion.

Ainsi, la totalité des éléments fils présents dans ces minéraux à un instant t est d'origine radiogénique. Ceci est à opposer à d'autres minéraux qui, en plus des isotopes pères, intègrent dans leur réseau, au moment de leur cristallisation, des quantités non négligeables d'élément correspondant à l'isotope fils (substitution de Ca^{2+} par Pb^{2+} par exemple dans le cas de l'apatite). La présence de ces isotopes fils, non radiogéniques, dans le système dès la cristallisation du minéral nécessite une correction, qui dans le cas du système U-Pb pourra être réalisée grâce à l'analyse de phases minérales à rapport U/Pb très faible (feldspath, galène…) ou par estimation grâce à des modèles d'évolution de la composition isotopique en Pb en milieu crustal (Stacey & Kramers, 1975; Cumming & Richards 1975).

3.4.1 Introduction à la technique U-Pb

L'analyse U-Pb par voie ponctuelle permet d'étudier des portions de grains, sans manipulation chimique préalable, et ce, en utilisant un faisceau ionique capable d'éroder progressivement la surface de l'échantillon puis d'analyser la composition isotopique du nuage d'ions ainsi produits. Bien que, dans un premier temps limitée à l'analyse des rapports $^{207}Pb/^{206}Pb$ (e.g. Andersen 1973), cette technique a rapidement évolué afin de permettre la mesure fiable des rapports Pb/U (Hinthorne *et al.*, 1979). Les progrès analytiques constants, et en particulier l'utilisation de la haute résolution (e.g. Hinton & Long, 1979) pour résoudre les interférences moléculaires observées sur les isotopes du Pb, ont depuis permis d'appliquer avec succès cette technique à la datation d'échantillons d'âges très variés (Froude *et al.*, 1983; Compston & Pidgeon, 1986; Deloule *et al.*, 2001) ou à des phases minérales ayant préservées au niveau de leur structure interne une grande complexité (Black *et al.*, 1986; Williams & Claesson, 1987; Compston & Kröner, 1988; Kinny *et al.*, 1988). Cette technique ne permet pas de distinguer une séquence d'évènements se produisant dans un intervalle de temps limité (< 15 Ma). La méthode est cependant rapide, quasiment non destructrice, et présente une résolution spatiale de quelques dizaines de microns ce qui permet l'analyse individuelle de différentes parties d'un même cristal pouvant correspondre à une croissance polyphasée.

Les sondes ioniques sont donc des appareils de choix pour déterminer l'âge d'échantillons ou de minéraux très complexes. C'est le cas par exemple, de roches polymétamorphiques ou bien pour les études visant à déconvoluer le spectre d'âge des populations de zircons détritiques ou encore celles visant à déterminer, dans les granitoïdes, l'âge des matériaux sources ayant subi le processus de fusion partielle.

II.4 Perple_X

I.1.2. La modélisation de l'espace P-T : les pseudosections (PERPLEX)

Traditionnellement, les grilles pétrogénétiques montrent les relations de phases pour toutes les compositions possibles d'un système en fonction de variables environnementales (P,T…). Les champs divariants de stabilité des phases minérales sont ainsi représentés sans tenir compte de la composition de la roche totale. Par conséquent, il devient nécessaire de recalculer des diagrammes de phases représentant fidèlement la composition du système étudié. Ainsi, les sections de diagrammes de phases (ou pseudosections) calculées à partir d'une composition de roche totale définie et une minéralogie observée et chimiquement quantifiée (comme avec le logiciel Perplex) ont offert une alternative aux méthodes classiques de projections de phases.

I.1.2.1. Théorie et principes

Le principe d'une pseudosection est de modéliser les assemblages minéralogiques à l'équilibre dans l'espace P-T à partir d'une composition chimique d'un volume de roche et des données thermodynamiques disponibles. Les pseudosections calculées pour un système chimique défini préalablement correspondent donc à des portions ou sections de l'espace P-T pour lesquels les paragenèses sont prédites. Les informations thermobarométriques sont extraites grâce à la position dans l'espace P-T des champs de stabilité des minéraux ainsi que par les proportions et les compositions minéralogiques dans ces mêmes champs. Une comparaison avec les paragenèses et les compositions chimiques observées dans les échantillons permet donc une estimation des conditions thermobarométriques de formation de l'association minéralogique (e.g. Vance & Mahar, 1998). L'avantage de cette méthode, hormis l'estimation des conditions P-T, est qu'elle permet la modélisation d'une portion du chemin P-T à partir de l'analyse de l'évolution minéralogique et chimique lors de transformations texturales de la roche. Les pseudosections permettent ainsi de comparer les paragenèses observées avec celles prédites, même celles qui ont pu disparaitre. Pour ces raisons et du fait d'être indépendante de la chimie de la roche, cette méthode se révèle être très avantageuse dans les zones texturellement compliquées, comme c'est le cas ici, où le métamorphisme se localise essentiellement dans des zones de cisaillement.

I.1.2.2. Construction d'une pseudosection avec Perplex (P-T et T-X ou P-X)

Plusieurs approches dont les modes de calcul d'équilibre diffèrent, ont été développées et largement utilisées par les géologues. Le logiciel utilisé dans la présente étude est le logiciel PERPLEX crée par Connolly & Kerrick (1987). Basé sur le principe de calcul des surfaces d'équilibre où l'énergie libre du système chimique représenté par un assemblage de minéraux est minimale, cette technique permet d'estimer l'équilibre le plus stable pour une composition donnée et ce en tout point de l'espace défini préalablement. Autrement dit, le logiciel calcule, pour tout couple (P-T) les phases minérales stables en minimisant l'énergie libre du système.

I.1.2.2.1. Minimisation linéaire de l'énergie libre : simplicité et rapidité

Le problème de la minimisation est de trouver la quantité et la composition des phases qui minimisent l'énergie libre de Gibbs (G) du système chimique à pression et température constante (White *et al.*, 1958 ; De Capitani & Brown, 1987). La fonction d'énergie libre est une fonction non linéaire de la composition ; par conséquent la solution numérique des calculs d'équilibre de phases est compliquée, incertaine et nécessite souvent un temps de calcul important. Connolly et Kerrick en 1987 ont développé une méthode d'approximation par laquelle les variations continues de composition de phases minérales sont représentées par une série de valeurs discrètes de composition telles que chaque composition ont les propriétés thermodynamiques de la solution solide à une composition choisie. L'énergie libre devient donc une fonction linéaire de la composition définie par chaque segment entre les pseudocompositions. La précision de l'approximation est dépendante de l'espacement entre les pseudocompositions; étant donnée les ressources numériques actuelles et l'exactitude des modèles thermodynamiques des phases minérales, ceci ne constitue pas une importante limitation de la méthode.

I.1.2.2.2. Stabilité des assemblages de minéraux : une détermination automatisée

Le principe de base de la thermobarométrique est que les assemblages minéralogiques utilisés sont à l'équilibre. Le plus souvent il est nécessaire de connaitre préalablement les différentes phases stables (Powell & Holland, 1988). Le logiciel Perplex présente l'avantage de déterminer et tester de manière automatique la stabilité des associations minérales obtenues lors du calcul d'équilibre sans qu'aucune des phases supposées à l'équilibre ne lui soient spécifiées (Connolly & Petrini, 2002). Ceci présente un certain avantage en ce qu'il évite une

connaissance préalable des minéraux à l'équilibre, notamment, dans le cas où certains minéraux présentent un équilibre métastable.

I.1.2.2.3. Stratégie numérique : une résolution à plusieurs niveaux de la grille P-T-X

La technique de minimisation linéaire fournit une carte des équilibres minéralogiques d'un système thermodynamique pour une section de l'espace P-T-X. Les champs de stabilité dans lesquels la composition chimique et les proportions des phases stables varient en continu sont définis en tout point de l'espace. Une stratégie est proposée par Connolly & Kerrick (2002) et Connolly (2005) afin de déterminer directement les relations de phases en fonction de variables environnementales (P, T…). Les auteurs proposent ainsi un protocole de calcul d'équilibre de phase en tout point d'une grille, dont la résolution est définie préalablement par l'utilisateur et présente plusieurs niveaux de définition. Plus simplement, les pseudocompositions stables sont déterminées après 1,2 et 3 passages successifs à chaque nœud du maillage de la grille par minimisation linéaire de la surface d'énergie libre. Au premier passage, si le même assemblage est stable aux sommets d'une cellule alors l'assemblage est considéré comme stable à chaque niveau de résolution de la grille ; si la cellule est hétérogène, un calcul avec une résolution plus fine sera automatiquement effectué lors du deuxième passage.

La conséquence des pseudocompositions est que les variations continues des compositions de phases stables deviennent discontinues ; chaque champ de stabilité de phases d'une section caractérise alors des champs dits « pseudodivariants » dont chacun est défini par une pseudocomposition. Les limites entre les champs « pseudodivariants » représentent ainsi soit une vraie transformation de phase soit une variation de la composition d'une solution solide. Dans le but de représenter uniquement les vraies limites de phases, les pseudocompositions qui représentent les mêmes phases sont considérées comme identiques.

Au final, une carte des relations de phases ou champ de stabilité dont les limites représentent les transformations minérales peut être ainsi construite. Les propriétés telles que la composition chimique et les proportions des phases minérales mémorisées lors de chaque minimisation peuvent être déterminées. Étant donné que ces propriétés varient de manière continue en fonction des variables environnementales, elles sont estimées par interpolation ou extrapolation triangulaires. Cette stratégie de grille à plusieurs niveaux de résolution présente donc l'avantage d'être simple, rapide puisqu'elle réduit considérablement le nombre de minimisation à calculer et avec un niveau d'efficacité comparable à d'autres techniques.

Il faut néanmoins garder à l'esprit qu'il s'agit d'une solution exacte à un problème qui a été simplifié. Toutefois, la confrontation avec les autres méthodes basées sur le calcul d'équation non linéaire montre que la méthode approximative utilisée par le logiciel PERPLEX est comparable. L'approximation occasionnée par la linéarisation de la fonction d'énergie libre est identique à l'incertitude des modèles thermodynamiques des phases.

<u>Chapitre 3</u> - Etude géologique, pétrogéochimique et métamorphique des ophiolites nord-est anatoliennes et du Petit Caucase : implication géodynamique.

« La pierre n'a point d'espoir d'être autre chose que pierre. Mais de collaborer, elle s'assemble et devient temple. »

Antoine de Saint-Exupéry, extrait de *Citadelle*

III.1 Article 1 – New structural and petrological data on the Amasia ophiolites (NW Sevan-Akera suture zone, Lesser Caucasus): Insights for a large-scale obduction in Armenia and NE Turkey)

Les ophiolites du Petit Caucase appartiennent à la ceinture ophiolitique nord-téthysienne. Celles-ci représentent la prolongation orientale de la ceinture ophiolitique anatolienne (suture d'Izmir-Ankara-Erzincan) (Knipper, 1975; Knipper & Khain, 1980; Adamia *et al.*, 1981; Şengör & Yılmaz, 1981; Dercourt *et al.*, 1986; Adamia *et al.*, 1987; Ricou, 1994; Yılmaz *et al.*, 2000; Galoyan 2008). Au nord de l'Arménie, cette suture se prolonge par la celle de Sevan-Akera, orientée globalement NW-SE. Elle marque la frontière entre le SAB, au sud, et la marge active de l'Eurasie, au nord. La mise en place d'une marge active de type andin (Somkheto-Karabakh) durant une grande partie du Mésozoïque (Bajocien à Campanien) et de l'Eocène moyen et supérieur témoignerait en faveur d'une subduction plongeant vers le nord sous l'Eurasie (Knipper, 1975; Adamia *et al.*, 1977; Adamia *et al.*, 1981; Maghakyan *et al.*, 1985; Adamia *et al.*, 1987).

Les travaux précédents sur les ophiolites de cette région dans le cadre de la thèse de Galoyan (2008) montrent que les ophiolites arméniennes des zones de Stepanavan, Sevan et Vedi sont toutes de type LOT avec des caractéristiques litho-structurales et pétro-géochimiques identiques (Galoyan *et al.*, 2007; Galoyan, 2008; Rolland *et al.*, 2010; Sosson *et al.*, 2010). De plus, les âges de formation du plancher océanique sont tous compris entre le Jurassique inférieur et moyen. Les datations ont été obtenus par la méthode $^{40}Ar/^{39}Ar$ sur amphiboles de gabbro de Sevan et de diorite de Vedi, donnant respectivement 165,3 ± 1,7 Ma et de 178,7 ± 2,6 Ma (Galoyan *et al.*, 2009; Rolland *et al.*, 2010). Ces datations radiochronologiques sont confirmées par les assemblages de radiolaires reconnues dans ces zones (Danelian *et al.*, 2000; 2008; 2012; Asatryan *et al.*, 2009; 2010)

Le massif ophiolitique d'Amasia est situé à 5 km NW de la ville Amasia dans le prolongement ouest de la zone de Sevan-Akera. Sur une surface de ~30 km^2 affleurent des peridotites et pyroxénites serpentinisées, des gabbros et plagiogranites (en filons d'une épaisseur de 1cm à 1m), des radiolarites, des basaltes ainsi que des roches métamorphiques (amphibolites à grenat : Sokolov, 1974; Aghamalyan, 1998). Tatevosyan (1950) décrit des

gabbros au nord et des roches volcaniques Turoniennes au sud. Toujours d'après Tatevosyan (1950), ces roches volcaniques recouvrent en discordance des schistes et sont surmontées par des calcaires du Crétacé supérieur. Les roches ultrabasiques et gabbroïques du massif ophiolitique d'Amasia ont déjà fait l'objet d'études montrant que les péridotites sont parfois fortement serpentinisées. Toutefois, malgré cette serpentinisation il est toutefois possible de reconnaître qu'il s'agit de lherzolites (Tatevosyan, 1950).

Sur la base de directions structurales différentes, certains auteurs ont proposé que les ophiolites Sevan-Akera et Stepanavan-Amasia proviendraient de différents segments de croûte océanique (Melikyan, 2004). Afin de valider l'hypothèse de Galoyan (2008) concernant la présence d'une seule et même nappe ophiolitique obduite à l'échelle du SAB, et donc afin de lever l'ambigüité concernant l'appartenance, et donc la continuité, du massif ophiolitique d'Amasia à la suture Sevan-Akera, nous avons effectué une étude pétro-structurale incluant des datations $^{40}Ar/^{39}Ar$ de ce massif.

Notre cartographie a mis en évidence une série comprenant (1) de la croûte océanique gabbroïque non métamorphisée, (2) des serpentinites, (3)mélange tectonique de faciès schiste vert composé basaltes en coussins déformés avec des radiolarites intercalées, et (4) une écaille basale d'amphibolites à grenat. Cette semelle métamorphique montre des caractéristiques géochimiques similaires à celles de l'ophiolite. Ces unités sont découpées par des failles inverses et déformés par des phases post-Eocène de compression de la zone de suture au cours de, et après, la collision du SAB avec l'Eurasie. Les datations $^{40}Ar/^{39}Ar$ sur les amphiboles des gabbros ont donné des âges de 169,0 ± 4,6 à 175,8 ± 3,9 Ma.

L'ensemble de ces âges ainsi que les compositions des roches ophiolitiques sont similaires à ceux des autres ophiolites arméniennes et de celles de Turquie du NE. Aussi, toutes ces données sont donc bien en accord avec la mise en place d'une seule nappe ophiolitique à l'échelle de l'Anatolie du NE et de l'Arménie au début du Crétacé supérieur (c. 90 Ma). Ces résultats suggèrent également que l'ensemble du domaine obduit provient d'un domaine où la croûte océanique formée est contaminée par la subduction. Il pourrait s'agir d'un bassin arrière-arc, ou d'une zone surplombant la subduction. Ce bassin se serait ouvert au Jurassique, puis obduit par la suite sur le SAB-TAP.

Cette étude a fait l'objet d'une publication parue dans *Tectonophysics*.

Tectonophysics 588 (2013) 135–153

Contents lists available at SciVerse ScienceDirect

Tectonophysics

journal homepage: www.elsevier.com/locate/tecto

New structural and petrological data on the Amasia ophiolites (NW Sevan–Akera suture zone, Lesser Caucasus): Insights for a large-scale obduction in Armenia and NE Turkey

M. Hässig [a,*], Y. Rolland [a], M. Sosson [a], G. Galoyan [b], C. Müller [c], A. Avagyan [b], L. Sahakyan [b]

[a] *Géoazur, Université de Nice Sophia-Antipolis, Centre National de la Recherche Scientifique (UMR 7329), Observatoire de la Côte d'Azur, Bât. 1, 250 rue A. Einstein, 06560 Valbonne, France*
[b] *Institute of Geological Sciences, National Academy of Sciences of Armenia, 24a Baghramian Avenue, 375019 Yerevan, Armenia*
[c] *6 bis rue Haute, 92500 Rueil Malmaison, France*

Abstract

The ophiolites of Amasia in the northwestern part of the Sevan-Akera suture zone (Lesser Caucasus, NW Armenia) correspond to a well-preserved example of a major obduction of oceanic lithosphere over the South Armenian continental block. Our mapping evidenced a series of (1) un-metamorphosed gabbroic oceanic crust, (2) serpentinites and a greenschist grade tectonic melange composed of deformed pillow-basalts, radiolarites and cherts, and (3) a basal slice of garnet amphibolites bearing similar compositional features as the ophiolite. These units are sliced and deformed by post-Eocene thrusting related to the shortening of the suture zone after the collision of the South Armenian Block with Eurasia. $^{40}Ar/^{39}Ar$ dating on gabbro amphiboles yielded ages of 169.0 ± 4.6 to 175.8 ± 3.9 Ma. This age and geochemical composition of ophiolite rocks are similar to those of other ophiolite outcrops in Armenia and NE Turkey. Structural and geochemical analyses undertaken on the garnet amphibolites suggest it to represent the obducted ophiolite metamorphic sole. All these data are in agreement with the presence of a unique ophiolite nappe at the scale of NE Turkey-Armenia originating from a Jurassic intra-oceanic back-arc basin, obducted onto the Armenian-Taurides-Anatolides microblocks in the early Late Cretaceous (c. 90 Ma).

Keywords : Ophiolites; $^{40}Ar/^{39}Ar$; Lesser Caucasus; Armenia; Amasia; Izmir-Ankara-Erzincan-Sevan suture

1.1 Introduction

In order to better understand the different phases linked with the opening and closing of the Tethyan Ocean leading to the current structure of the Lesser Caucasus, it is important to identify the different units involved in the Tethyan paleosuture *s.l.* and their corresponding geodynamic context. The evolution of central and northern Neotethys can be deduced from both the geochemical and geochronological study of preserved oceanic crust domains obducted (ophiolites) in the Lesser Caucasus and the metamorphic rocks beneath ophiolites. These studies yield key time and palaeogeographic data from the East Mediterranean area to the NW Himalayan belt (Sengör and Yılmaz, 1981; Ricou et al., 1985; Dercourt et al., 1986; Ricou, 1994; Okay and Tüysüz, 1999; Stampfli et al., 2001; Robertson et al., 2004; Barrier and Vrielynck, 2008; Galoyan et al., 2009; Rolland et al., 2010; Sosson et al., 2010). Ophiolites provide constraints on oceanic opening by the dating of related magmatic rocks and of its closure by the dating of metamorphic rocks and post-accretionary sedimentary complexes unconformably overlying the suture zone. Datings undertaken along the Ankara-Erzincan-Sevan suture zone suggest a similar Lower-Middle Jurassic age of the oceanic crust (Çelik et al., 2011; Galoyan, 2008; Galoyan et al., 2009; Rolland et al., 2009b; 2010). A major difficulty in the Lesser Caucasus Mesozoic geodynamic reconstruction lies in the paucity of outcrops due to thick post-obduction (Eocene to Quaternary) deposit of sediments and volcanites over the ophiolitic nappe (Sosson et al., 2010). Therefore, to link the NE Turkey and Armenia ophiolitic domains, one of the main questions posed in this study is the origin of the ophiolite: "are all the NE Turkey-Armenia ophiolites remnants of the same oceanic lithosphere, obducted over the Armenian-Tauride-Anatolide Block?"

In this paper is reported new geological, petrologic and $^{40}Ar/^{39}Ar$ chronological data obtained on the Amasia ophiolite (NW Armenia) which strongly suggests a common origin with the other Armenian ophiolites (Sevan, Stepanavan and Vedi ophiolites) and NE Turkey (Refahiye, Şahvelet, Karadağ and Kırdağ).

1.2 Geological context

During the Mesozoic, the Southern margin of the Eurasian continent was involved in the closure of the Paleotethys and opening Neotethys Ocean (Adamia et al., 1981). Later, from the Jurassic to the Eocene, subductions, obductions, micro-plate accretions, and finally

continent–continent collision occurred between Eurasia and Arabia, and resulted in the closure of Neotethys (Sosson et al., 2010; **Figure 14**).

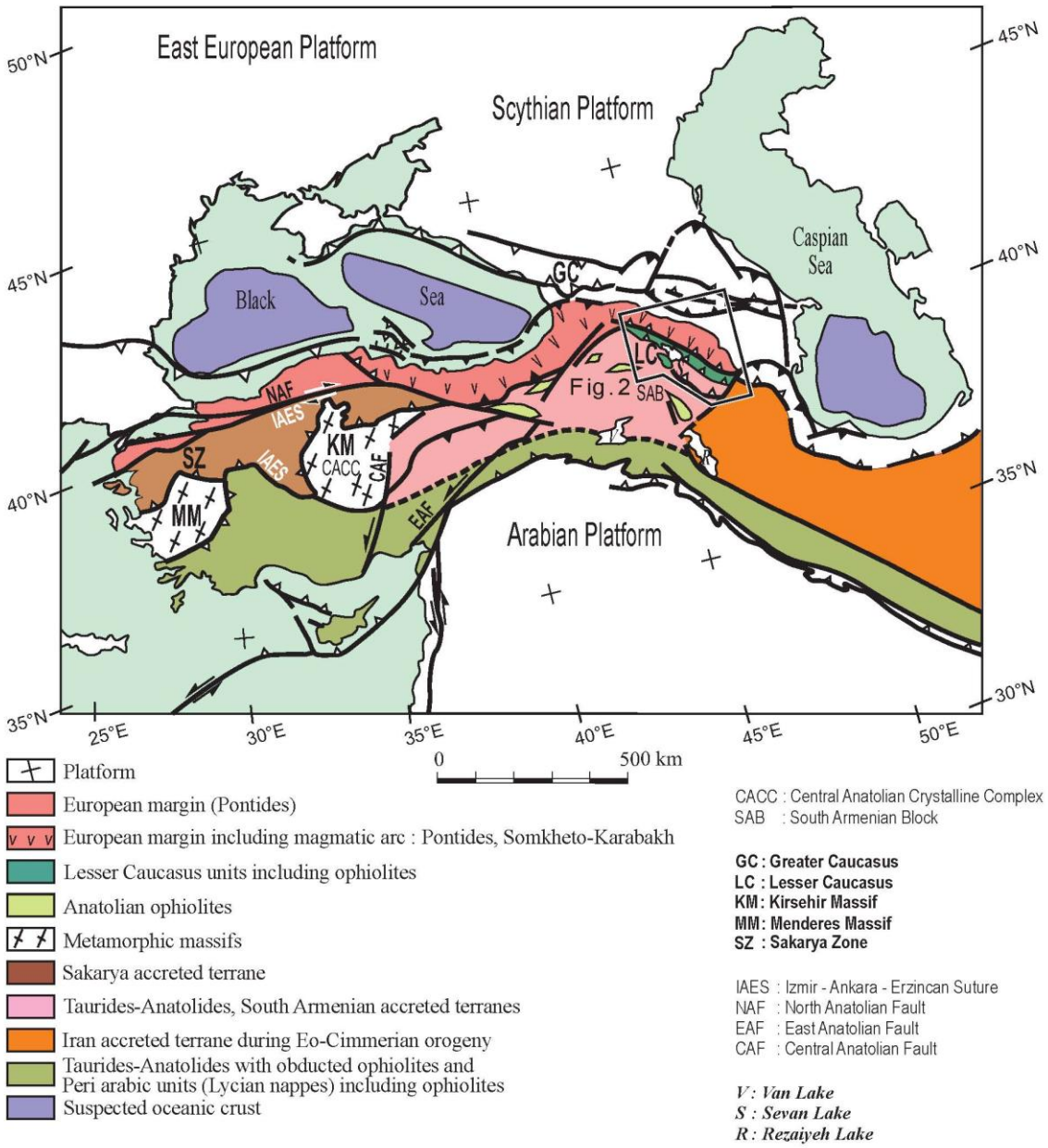

Figure 14 - Tectonic map of the Middle East–Caucasus area, with main blocks and suture zones, after Avagyan et al. (2005), modified. Location of figure 2 indicated.

The study of Armenian ophiolites allows reconstructing part of this complex history. Previous geological, petrological and geochemical works on these ophiolites were carried out mostly during the 1970's and 1980's (Knipper, 1975; Sokolov, 1977; Knipper and Sokolov, 1977; Knipper and Khain, 1980; Adamia et al., 1981; Zakariadze et al., 1983, 1990; Knipper et al., 1986; Knipper et al., 1997; Satian, 2005; Zakariadze et al., 2005). These works showed a

mainly Jurassic age for the ophiolite bodies, with varied geochemistry (from tholeiitic to calc-alkaline and alkaline), which was interpreted as a complex oceanic context with varied magmatic sources closed by subduction in the Late Cretaceous. More recent works (Hacker, 1991; Yilmaz et al., 1993; Hacker et al., 1996; Harper et al., 1996; Searle and Cox, 1999; Okay et al., 2001; Stampfli et al., 2001; de Sigoyer et al., 2004; Ding et al., 2005; Galoyan et al., 2009; Rice et al., 2009; Rolland et al., 2009a-b; 2011a-b; Agard et al., 2010; Sosson et al., 2010) evidence processes which include Neotethyan oceanic crust obduction and the collision–accretion of microplates to the Eurasian margin before the final Arabia–Asia collision.

North of the obduction zone, in the Eurasian part of the Lesser Caucasus the subduction of the Tethys is evidenced by a thick and mainly calcalkaline volcanogenic and volcanoclastic series dated as Bajocian to Santonian (e.g. Adamia et al., 1981 for a review). At this period of time the northern Lesser Caucasus was characterized by an island arc domain called the Somkheto-Karabakh Island Arc (Knipper, 1975; Adamia et al., 1977; 1987; Ricou et al., 1986; Sosson et al., 2010). During the Early Cretaceous an active erosion event took place, which resulted in the unroofing of plutons of the magmatic arc. This erosion event is the result of significant uplift and denudation during the Early Cretaceous. The reasons for such a change in the Eurasian active margin strain field could be the subduction of the spreading ridge of the back-arc basin. The basement formations are quite similar to those known all along the Eurasian margin (Sosson et al., 2010 for a review).

The Eastern Pontides are interpreted as a part of the Sakarya Zone (Okay and Şahintürk, 1997) They represent an active continental margin of Eurasia, which was formed as result of northward subduction of Neotethys during Late Cretaceous (Şengör and Yılmaz, 1981; Akıncı, 1984; Okay and Şahintürk, 1997; Parlak et al., 2012). There is no consensus concerning onset of subduction since Jurassic (Adamia et al., 1981; Hess et al., 1995; Nikishin et al., 2003), Cenomanian-Turonian (Yılmaz et al., 1997; Okay and Şahintürk, 1997) or Albian (Okay et al., 2006) ages have been proposed. The lack of consensus equally stands when considering the end subduction and continental collision; end of Eocene (Peccerillio and Taylor, 1976; Şengör and Yılmaz, 1981; Robinson et al., 1995), Middle Eocene (Yılmaz et al., 1997) or Paleocene (Okay and Şahintürk, 1997) have been proposed.

South of the obduction zone, the South Armenian Block (SAB) (Knipper, 1975; Knipper and Khain, 1980) is a microplate also corresponds to the Turkish and Iranian platform (Sengör and Yılmaz, 1981; **Figure 14**). In Armenia the SAB is represented by a

Proterozoic metamorphic basement well exposed north of Yerevan, an incomplete Palaeozoic sedimentary succession (mainly represented by Upper Devonian to Upper Permian carbonates and shales) in the SW (north of the Araks Valley), Triassic limestones and sandstones and some Jurassic sedimentary and volcanogenic formations, Cenomanian to Turonian limestone and flysch (Nalivkin, 1976; Sosson et al., 2010) (**Figures 15** and **16**).

The East Anatolian Platform (EAP) represents a continental platform between the northern and southern branches of Neotethys (Bozkurt and Mittwede, 2001). As the SAB, the EAP represents a sliver of continental crust having rifted off northern Gondwana and drifted north to collide with Eurasia (Stocklin, 1974; 1977; Adamia et al., 1977; Biju-Duval et al., 1977; Dercourt et al., 1986; Şengün, 2006).

Upper Cretaceous obduction on the SAB is deduced from Upper Coniacian to Santonian flysch (reworking the ophiolites), which conformably covers Cenomanian-Turonian reef limestones and flysch of the SAB (Sokolov, 1977; Sosson et al., 2010; **Figure 16**). Obduction took place while a magmatic arc occurred along the southern edge of Eurasia (Somkheto-Karabagh island arc, Lesser Caucasus; Eastern Pontides arc, Anatolia; **Figure 14**), which implies that at least two subduction zones were active at the same time (Rolland et al., 2011a). The onset of collision or the continental subduction of the SAB below the Eurasian margin is dated as Late Cretaceous-Paleocene. This process occurred around 20 Ma later than the obduction (Late Coniacian–Santonian, 88–83 Ma) of the marginal basin over the SAB (Sosson et al., 2010). Oceanic closure is indicated by the late-Middle Eocene unconformity on the SAB, the suture zone and the Eurasia margin. Ending of subduction and subsequent accretion of the SAB to the Eurasian margin results in subduction jump to the south of the SAB and related Tauride-Anatolide Block(s) (TAB) in the same period of time. Evidence for this southward jump in subduction can be found between the Bitlis-Pütürge massifs and SAB. A HP metamorphic evolution bracketed between 74-71 Ma (Göncüoğlu and Turhan, 1984; Hempton, 1985; Oberhänsli et al., 2010). The metamorphic age is in agreement with a continental subduction event that occurred before final closure of the southern Neotethys and Arabian-Eurasian collision. $^{40}Ar/^{39}Ar$ dates agree for initial subduction of the Eastern Bitlis massif at 74 Ma followed by underthrusting of the Pütürge massif under blueschists conditions at 71 Ma (Rolland et al., 2012).

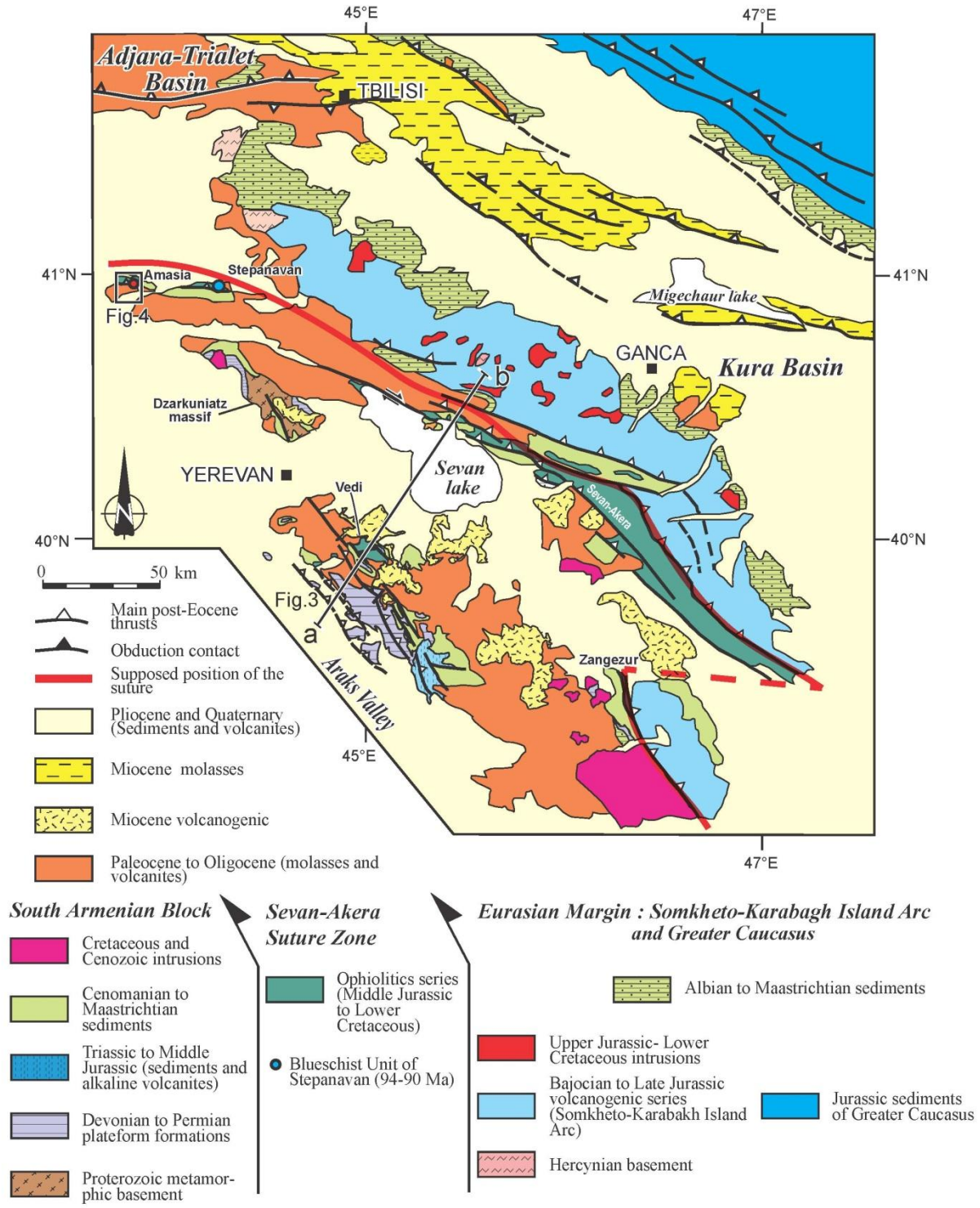

Figure 15 - Structural map of the Lesser Caucasus modified from Sosson et al. (2010). Location is indicated on figure 14. Plot of geological section figure 16 and location of figure 17 indicated.

For a compilation of works about the ophiolites of the Lesser Caucasus, the reader is referred to Galoyan et al. (2007, 2009) and Rolland et al. (2009b). These authors have shown the following geochemical tendencies in the ophiolite-related nappes: (1) the basalts and gabbros mainly bear an enriched tholeiitic composition, contaminated by subduction

components, (2) above these series, a layer of alkaline basalt lava flows with large pillows is supposed to represent Ocean Island Basalts (OIB) erupted in seamounts or oceanic plateau(s), (3) locally some arc-related basalts have been described. In Armenia, the oceanic gabbros of the tholeiitic series are dated to 170-150 Ma similar to radiolarian ages (Danelian et al., 2010), while the alkaline series were dated at c. 117 Ma (Rolland et al., 2009b).

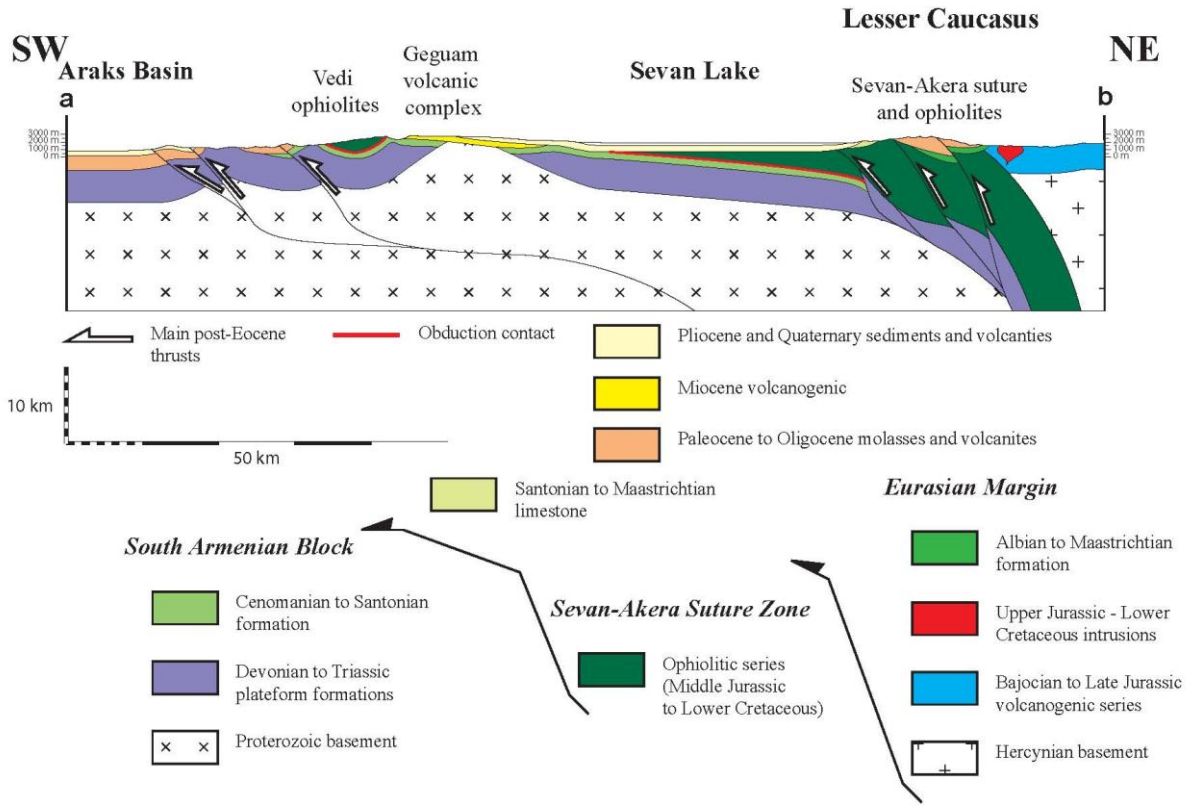

Figure 16 - Interpretative crustal-scale sketch cross-section of the Armenian-Azerbaijan transect. Location is indicated on Figure 15.

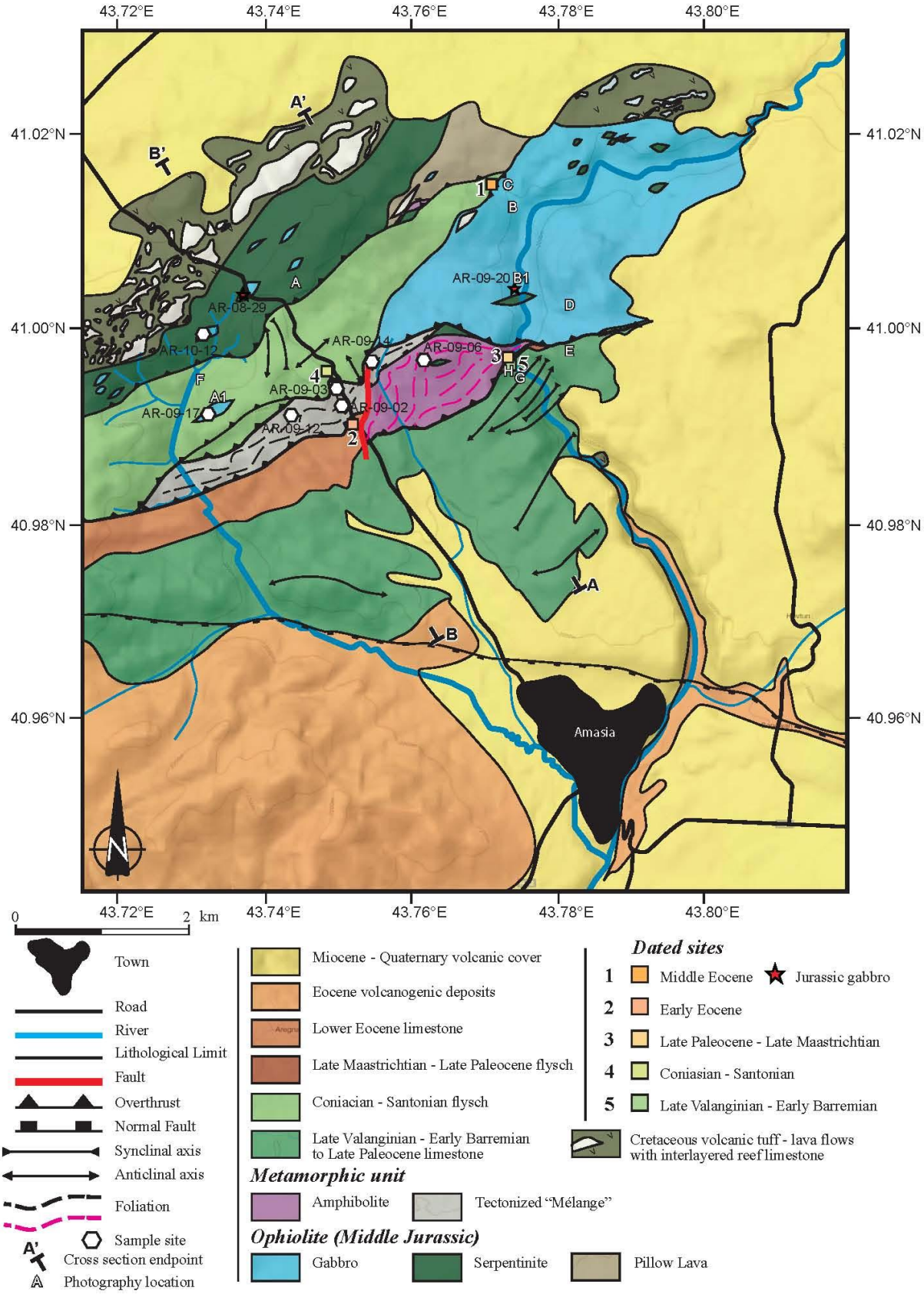

Figure 17 - Structural map of the Amasia ophiolite window. Location is indicated on figure 16. Plot of geological sections of figure 18 along with dated samples by the Ar-Ar method and paleontological identification are shown.

The Amasia ophiolite is aligned within the Lesser Caucasus ophiolite belt (Amasia-Sevan-Akera ophiolites), striking SE–NW in northern Armenia (**Figure 16**), generally interpreted as representing the suture zone (e.g., Zakariadze et al., 2007) between Eurasia and the SAB. In Stepanavan, East of Amasia, ophiolites have been described in association with blueschists and amphibolite facies metamorphic rocks dated at 94-91 Ma (Pressure peak) to 73-71 Ma (High temperature retrogression; Rolland et al., 2009a). These metamorphic rocks evidence the presence of a subduction zone active at least in the Middle Cretaceous and closing in the Late Cretaceous at 80-75 Ma (Rolland et al., 2011a).

1.3 Field and sample observations

According to the field observations and the new geological map with cross sections we have made (**Figure 17** and **19**), 3 main lithotectonic units have been identified (from top to bottom) (**Figure 18**);

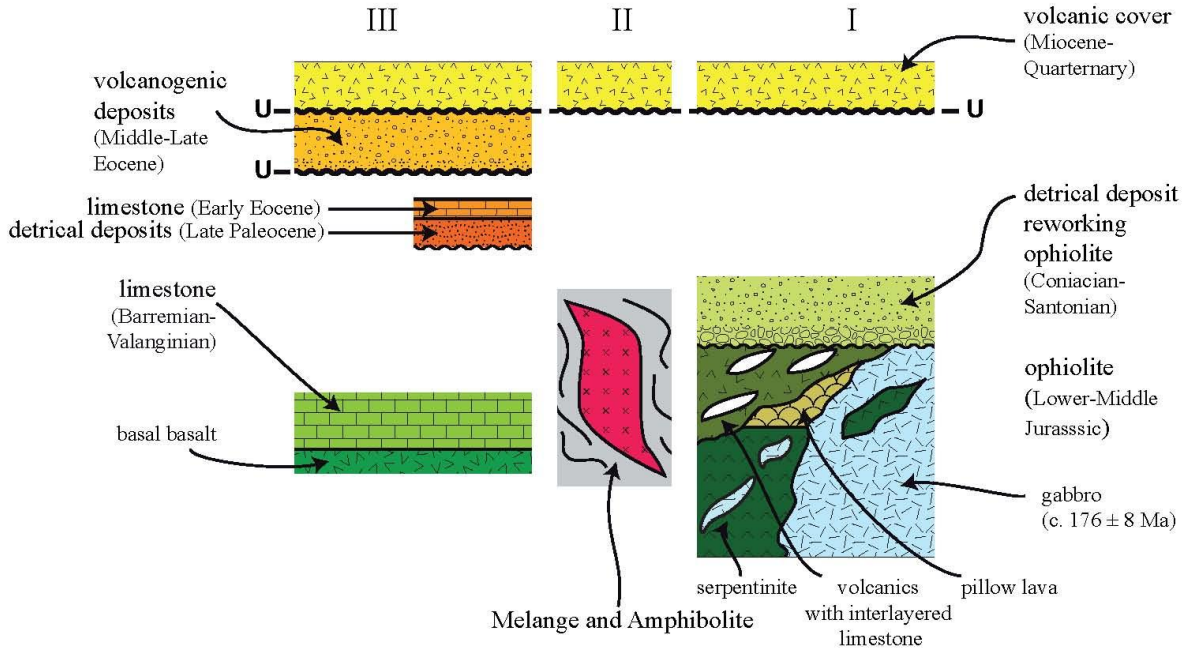

Figure 18 - Synthetic lithostratigraphic log of the three main units of the Amasia ophiolite window. I, the upper unite corresponding to ophiolite. II, the metamorphic unit comprising of the tectonic melange and the lens of garnet bearing amphibolites. III, the lower unit.

1 - An upper unit (ophiolites) with serpentinite, gabbro, pillow lava and volcanic rocks with interlayered reef limestone. Included in this unit a Coniacian-Santonian detrical deposit, reworking elements from the entire ophiolitic unit.

2 - A tectonic melange of low grade (greenschist facies) meta-basalt, meta-chert and metamorphosed serpentinite which includes lenses of ophiolite and a major garnet bearing amphibolites unit,

3 - A lower unit of basal basalts, overlain by Valanginian-Barremian limestones, which are in turn unconformably covered by late Paleocene flysch to Lower Eocene limestone as well as Mid- to Upper Eocene volcanogenic deposits (as in all of the Lesser Caucasus) (Sosson et al., 2010).

All of these units are unconformably overlain by a Miocene to Quaternary volcanic cover.

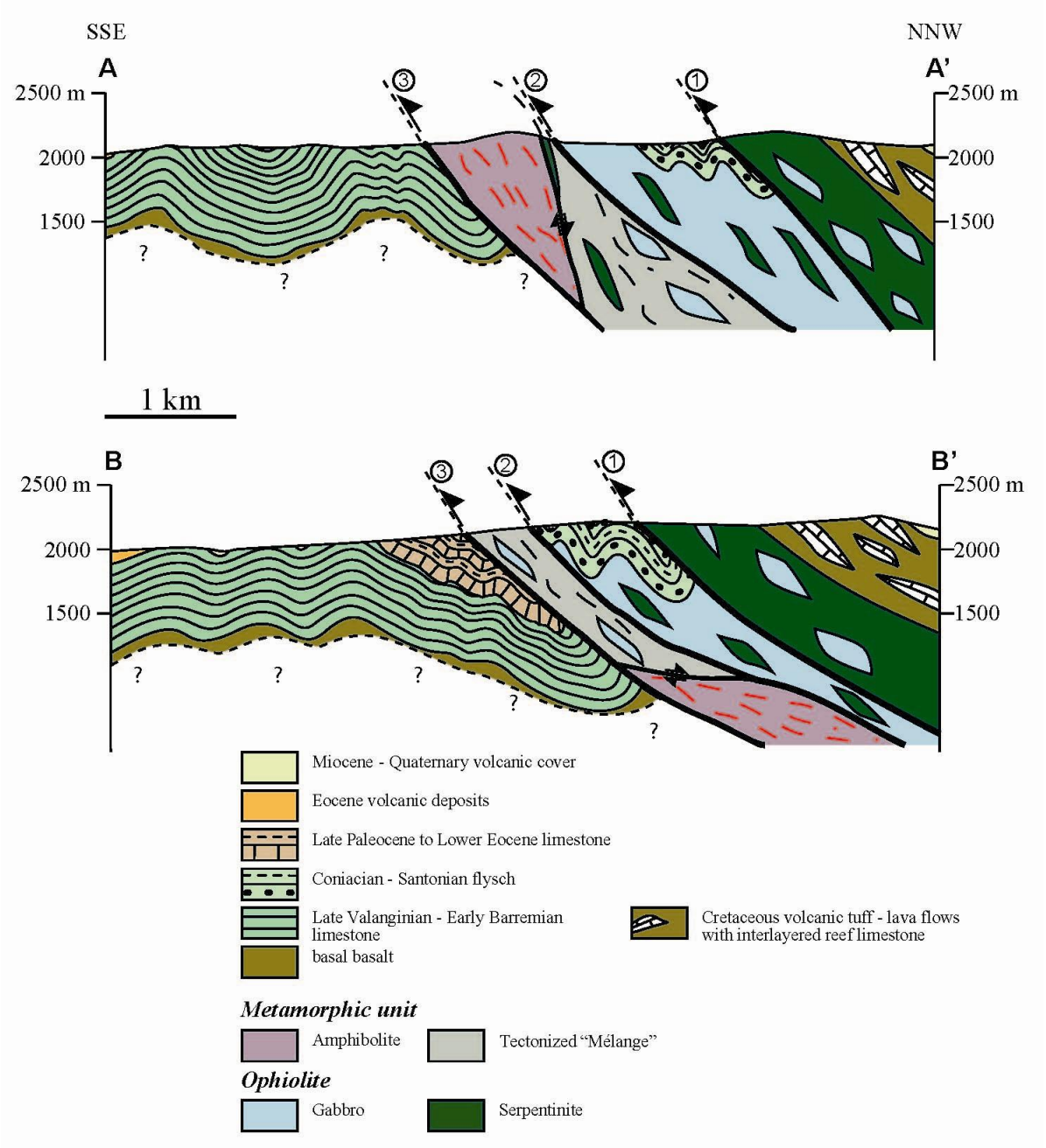

Figure 19 - Sketch geological cross sections of Amasia ophiolite. Locations are indicated on figure 17.

1.3.1 The upper unit (ophiolite)

The northern part of the map corresponds to an ophiolitic series (upper unit) generally dipping towards NNW. Sampling for dating of formation and characterization was undergone in this unit (**Figure 17**). It is composed, from top to bottom, of interbedded reef limestones embedded in volcanic tuffs and lava flows of supposed Cretaceous times, serpentinites comprising lenses of gabbros, scattered outcrops of volcanic rocks, and gabbros with punctual lenses of serpentinites (**Figure 20A**). These volcanics are linked to arc related volcanism and erosion, including possible OIB volcanism deposited on the seafloor prior to obduction. The lenses of gabbros in the serpentinites are generally well preserved and show a WSW-ENE stretching direction. These lenses are also penetrated by dikes of acidic composition (plagiogranite) and quartz veins. The outcrops of serpentinite in the gabbro do not have neatly defined contacts but appear in patches suggesting a gradational transition from the gabbro, in agreement with a cumulative origin. The northern contact of the gabbro with the serpentinites is deduced by a greater number of outcrops of serpentinites, multi-centimetric amphiboles and an increase in dike thickness and density approaching the contact zone. It is masked by Coniacian-Santonian flysch. Thus, the tectonic intercalation nucleates on previous ocean-floor faults, which illustrates the role of previous anisotropies in the obduction tectonics (**Figure 20B** and **20C**).

A syn-tectonic detrital deposits reworking elements of the ophiolite rests unconformably on top. Along the northern limit of the outcrop it is overthrusted by serpentinite (upper ophiolitic unit) towards the south (**Figure 20F**). Its southern limit is characterized by deformation by thrusting and scaling onto the metamorphic unit. Its nannofossil age (**Table 5**) is bracketed to the Coniacian-Santonian (89.3-83.5 Ma). The deformation consequent to this thrust is marked by dissymmetrical folds, with axes aligned with the general strike of the thrust. This fault, characterized by a NNW dip, was subsequently active during or after the deposit of this detrital material, i.e. syn-post Coniacian (89 Ma). Laterally to the east, this formation is unconformably lying along on gabbro. At its extreme NE limit with the gabbro, the detrital deposits are overthrusted by the gabbros along a fault contact with a SE dip.

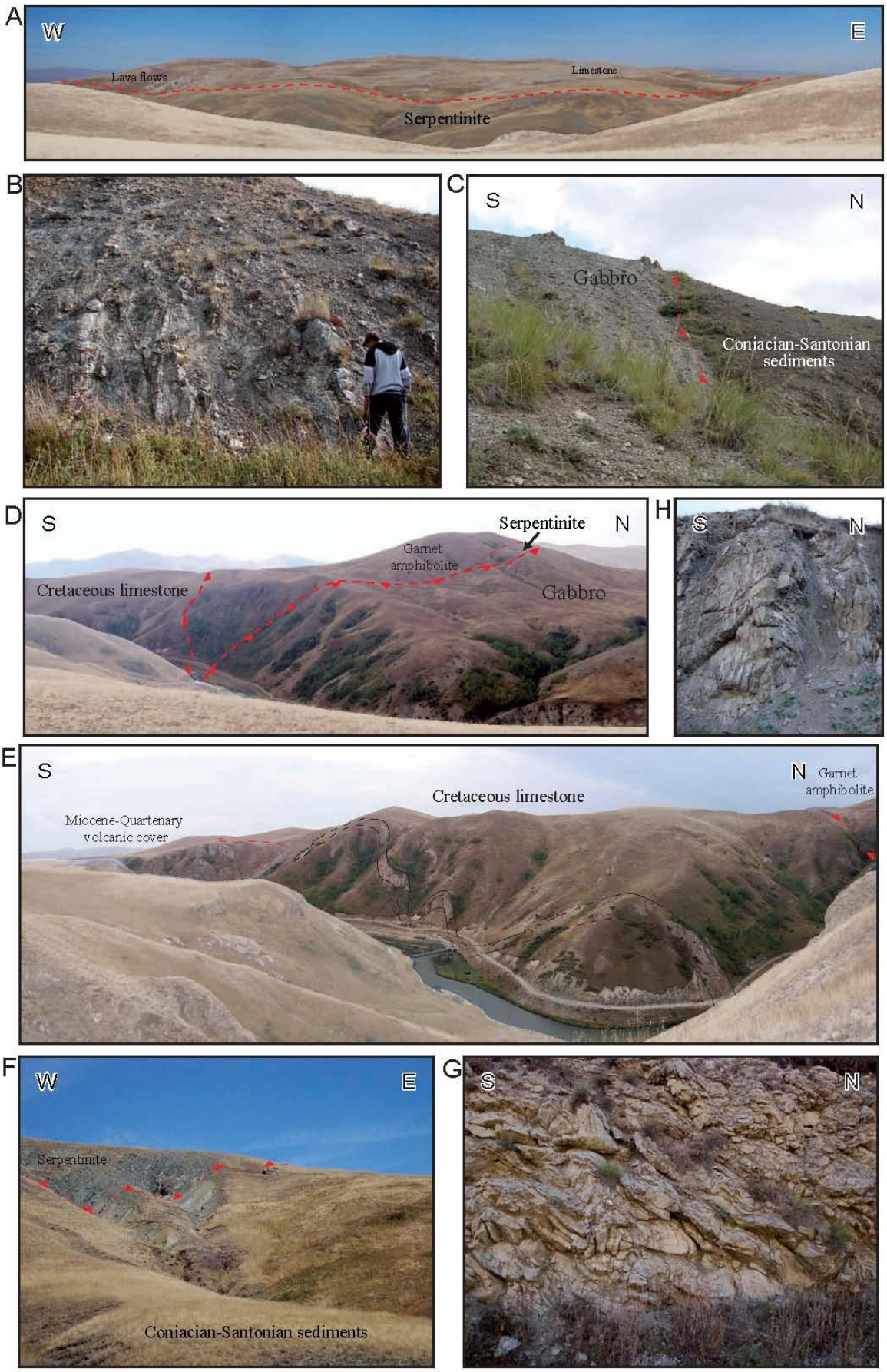
A
W
E
Lava flows
Limestone
Serpentinite
B
C
S
N
Gabbro
Coniacian-Santonian sediments
D
S
Serpentinite
N
Garnet amphibolite
Cretaceous limestone
Gabbro
H
S
N
E
S
N
Garnet amphibolite
Cretaceous limestone
Miocene-Quartenary volcanic cover
F
W
E
Serpentinite
Coniacian-Santonian sediments
G
S
N

Figure 20 - Representative field photographs of ophiolitic lithologies and structural relationships. A, Cretaceous volcanic tuff – lava flows with interlayered reef limestone on top of serpentinite to the north of the study area. B, Gabbro with important density of multi-centimeter dykes found along the northeastern bank of the eastern river valley. C, The northern contact thrusting gabbro, from the south, above Coniasian-Santonian flysch, to the north. D, Garnet-bearing amphibolite body thrusted to the south above Cretaceous limestone. The gabbro is also thrusted to the south onto the amphibolite body in lateral continuation of a tectonized melange. E, Folding approaching the contact with the flysch with north dipping stratification at the base of the amphibolite massif marking the major tectonic contact. F, North dipping thrust contact bringing the serpentinite onto the Coniasian-Santonian sediments. G, Cretaceous limestone with dissymmetrical folds, with axes aligned with the general strike of the thrust. H, Lower Eocene flysch deposits highly deformed by thrust faulting and related dissymmetrical folding.

1.3.2 The tectonic melange

Underneath this ophiolitic series, there is a tectonic melange made of serpentinites, gabbros, basaltic lavas and metasediments. Most of the sampling was undergone in this unit (**Figure 17**). This melange represents relics of the oceanic domain underthrusted throughout obduction initiation and the intraoceanic part of the obduction process (Gaggero et al., 2009). The limestone blocks which are incorporated in this level are morphologically arranged in discontinuous lenses stretched out with the surrounding rock, which locally present boudinage. This deformation is in agreement with NNE-SSW shortening and with general top to the south sense of shear. Tectonically below this low-grade tectonic unit, to the East, there is a large (≈ 2 km²) outcrop of garnet-bearing amphibolite (**Figure 20D**).

The outcrop of amphibolites also has a lens shape and is also elongated in an ENE-WSW direction. A penetrative foliation is marked by an alternation of amphibole rich dark levels and mica-, garnet- and quartz-rich, red or white levels. The alignment of the amphiboles, chlorites and phengites, along with the presence of rolled garnets evidence**s** that the amphibolite massif was tectonized with top to the south sense of shear. Locally within this unit some highly strained lens shaped serpentinite inclusions are observed, which present an ENE-WSW stretching direction.

Two stages of metamorphism have been identified in the amphibolites, comprising (1) a High Temperature (HT) paragenesis in the amphibolites facies (hornblende-plagioclase-garnet), and (2) a retrogressive Greenschist facies paragenesis (chlorite-epidote-albite).

1.3.3 The lower unit

The third unit of the studied area is characterized by Cretaceous limestone unconformably overlying basalts.

The limestone outcrops are very weathered and present important folding and fracturing. The stratification is well marked and depicts various folds with axes generally

oriented NE-SW. The folding of the limestone increases as it dips north under the tectonic melange, approaching the contact with the flysch and the major tectonic contact at the base of the amphibolites. The stratification of the limestone dips to the north, under the amphibolite massif (**Figure 20E**).

Extremely deformed detrital deposits are found in stratigraphic contact unconformably on top of the Valanginian-Barremian limestone (**Table 5**). This unit shows a sedimentary contact with the limestone further to the south. This sedimentary basin locates, with its northern limit, a major thrust. This north-dipping fault throws the tectonized melange and the ophiolite on top of the flysch. Paleontological datings (**Table 5** and **Figure 17**) show Maastrichtian-Campanian (83.5-65.5 Ma) ages in the flysch series evolving to Lower-Eocene (< 40.4 Ma) ages in the limestones to the West. The flysch deposits are highly deformed by thrust faulting and related dissymmetrical folding (**Figure 20G**). The Lower Eocene series is better preserved, the stratification is slightly deformed, showing little faulting and folding. Its northern contact features sub-vertical dipping below the major thrust (**Figue 20H**).

1.4 $^{40}Ar/^{39}Ar$ Dating

1.4.1 Analytical procedures

1.4.1.1 Electron microprobe analysis

Mineral compositions were determined by electron probe microanalysis (EPMA). The analyses are presented in **Table 2**. They were carried out using a Cameca Camebax SX100 electron microprobe at 15 kV and 10 nA beam current, at the Blaise Pascal University (Clermont-Ferrand, France). Natural samples were used as standards.

1.4.1.2 $^{40}Ar/^{39}Ar$ analysis

Geochronology was undertaken by laser $^{40}Ar/^{39}Ar$ dating of amphiboles. Results are presented in **Table 4** (detailed results may be found in **Annexes 1** and **2**). The amphiboles were analyzed by EPMA prior to dating in order to check mineral composition homogeneity. Grains between 800 µm and 500 µm were separated by careful selection by hand-picking under a binocular microscope to prevent the presence of altered grains. The samples were then irradiated in the nuclear reactor at McMaster University in Hamilton (Canada), in position 5c, along with Hb3gr hornblende neutron fluence monitor, for which an age of 1072 Ma is adopted (Turner et al., 1971). The total neutron flux density during irradiation was 9.0×10^{18}

neutron cm^{-2}. The estimated error bar on the corresponding $^{40}Ar^*/^{39}Ar_K$ ratio is ± 0.2% (1r) in the volume where the samples were set. All $^{40}Ar/^{39}Ar$ measurements were undergone in the University of Nice-Sophia Antipolis (UMR 7329 Géoazur). Analyses of amphibole grains were undertaken by step heating with a 50 W CO2 Synrad 48-5 continuous laser beam. Measurement of isotopic ratios was done with a VG3600 mass spectrometer equipped with a Daly detector system. Detailed procedures are described in Jourdan et al. (2004). The typical blank values for extraction and purification of the laser system are in the range 4.2–8.75, 1.2–3.9, and 2–6 cc STP for masses 40, 39 and 36, respectively. Mass discrimination was monitored by regularly analyzing air pipette volumes. Decay constants are those given by Steiger and Jäger (1977). Uncertainties on apparent ages are given at the 2σ level and do not include the error on the $^{40}Ar^*/^{39}Ar_K$ ratio of the monitor. The criteria generally used in the laboratory for defining a ‘‘plateau’’ age are the following: (1) it should contain at least 70% of total ^{39}Ar released; (2) there should be at least three successive step-heating fractions in the plateau; (3) the integrated age of the plateau (weighted average of apparent ages of individual fractions comprising the plateau) should agree with each apparent age of the plateau with a 1σ error.

1.4.2 Results

The gabbro samples, AR-09-20 (**Figures 21 1A** and **21 1B**) and AR-08-29 (**Figures 21 2A** and **21 2B**), were sampled from massif and well preserved outcrops. Plateau ages (**Table 5**; **Figures 22 1a** and **22 2a**) were obtained after analysis of a single amphibole grain for each sample. Considering the homogeneous distribution of Ca/K values during the experiments (**Figures 22 1b** and **22 2b**) and EPMA analysis (**Figure 23**), only one mineral phase has contributed to the Ar-Ar signal in each sample.

The amphibole from the sample AR-09-20 gave a plateau age of 169.0 ± 4.9 Ma with a good MSWD of 1.46. This age was calculated using the last six heating steps representing 97.3 % of the total ^{39}Ar gas freed during the whole analysis. The inverse isochron age acquired is 171.7 ± 3.9 Ma with a good MSWD of 0.85, in accordance with the plateau age. Furthermore, this representation allows the validation of this age as the $(^{36}Ar/^{40}Ar)_0$ value is of 262 ± 30.2), which is close to the air value (295).

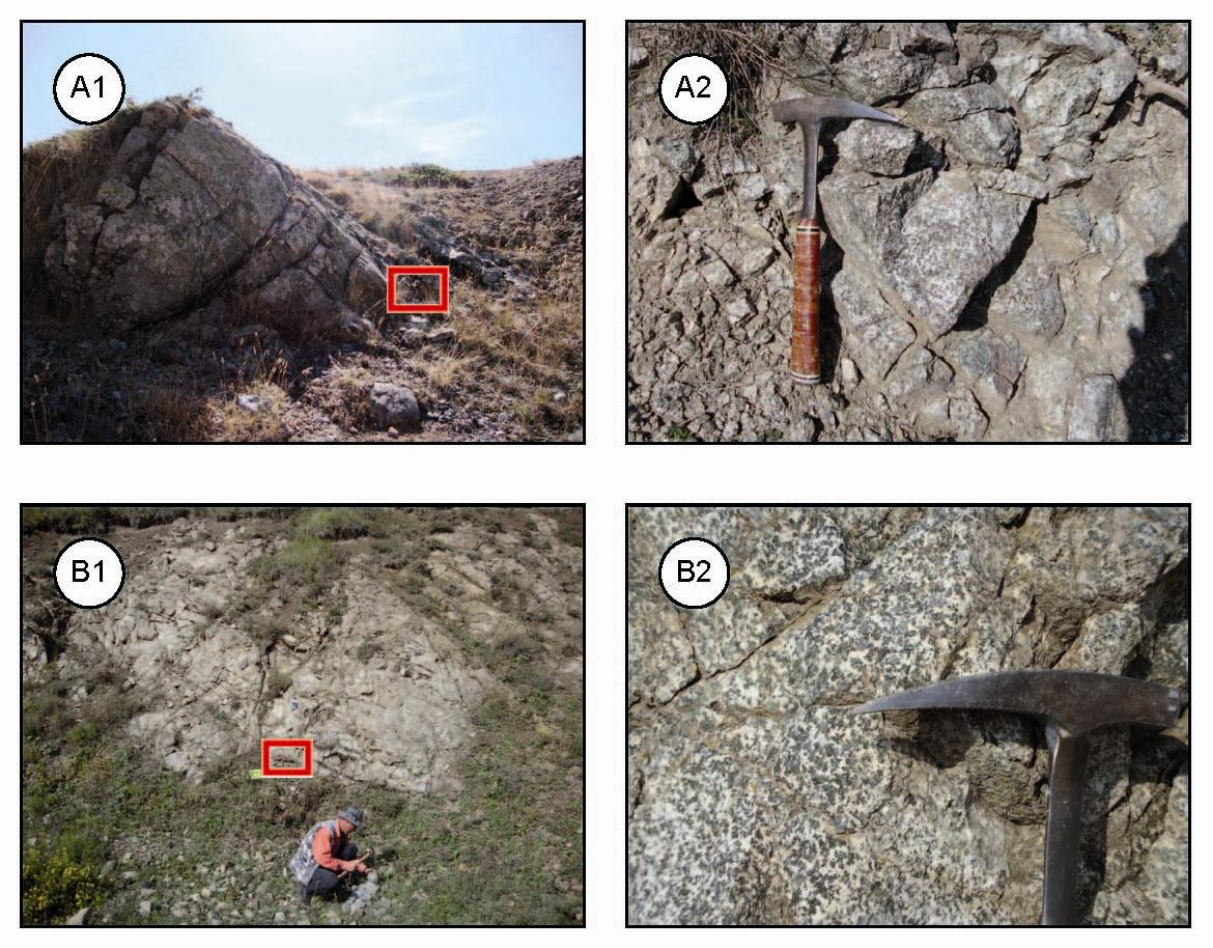

Figure 21 - Representative field photographs of dated gabbro sample outcrops. Photos "A" are of AR-08-29 and photos "B" are of AR-09-20.

The amphibole from the sample AR-08-29 gave a plateau age of 175.8 ± 3.9 Ma with a good MSWD of 0.98. This age was calculated using the last five heating steps representing 98.1 % of the total ^{39}Ar gas freed during the whole routine. The inverse isochron age acquired is 178.6 ± 5.4 Ma with a similar MSWD of 0.98, in accordance with the plateau age. The $(^{36}Ar/^{40}Ar)_0$ is also close to the present air value.

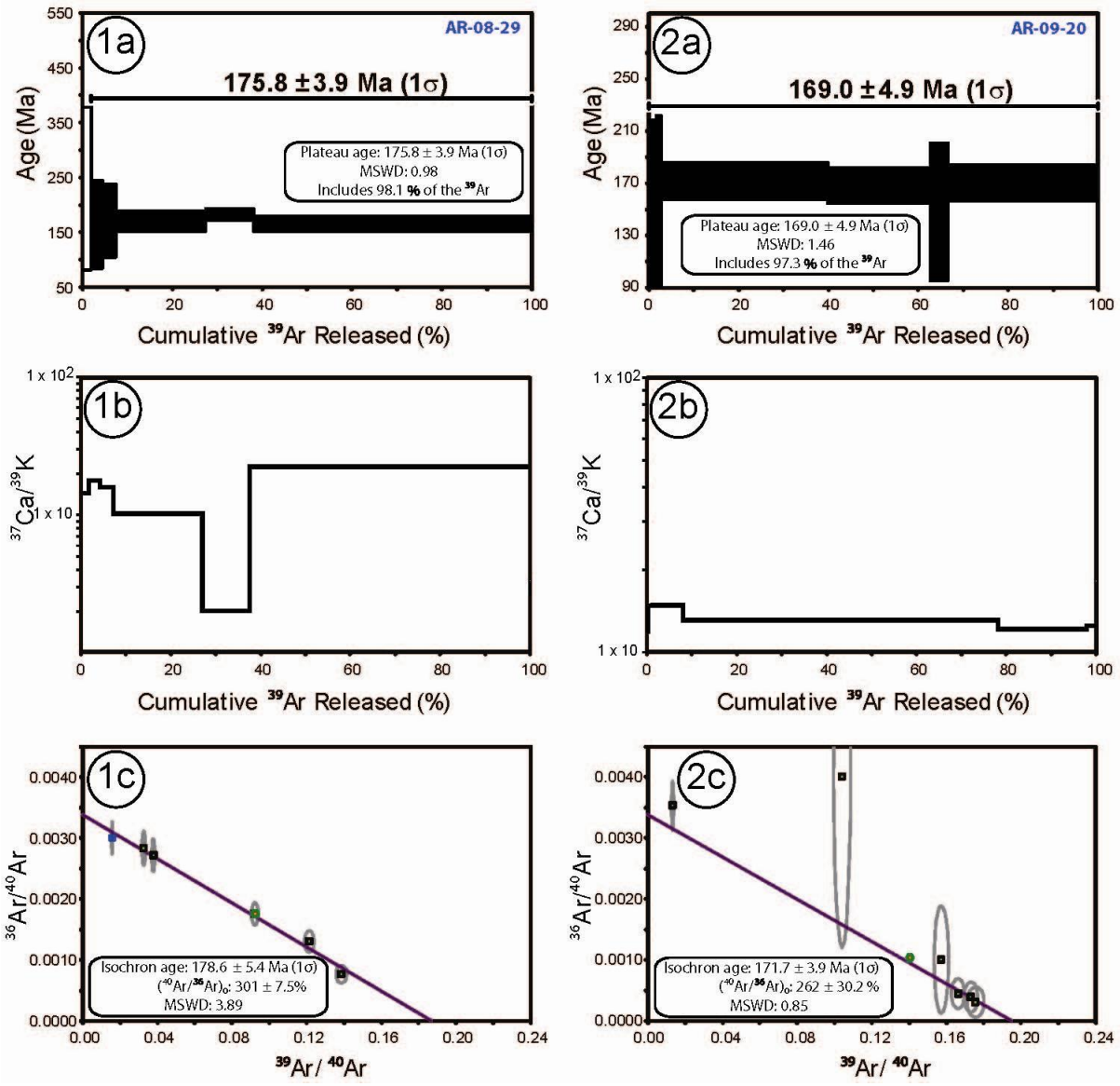

Figure 22 - $^{40}Ar/^{39}Ar$ age spectra Ca/K spectra and inverse isochrones of gabbro amphiboles. Locations of samples are shown on figure 17.

In conclusion, the two gabbro amphibole Ar-Ar ages agree with a crystallization age during oceanic crust formation at about 169-176 Ma, at the end of the Lower Jurassic (Toarcian), in agreement with other datings obtained in Armenian ophiolites (Galoyan et al., 2009; Rolland et al., 2009b).

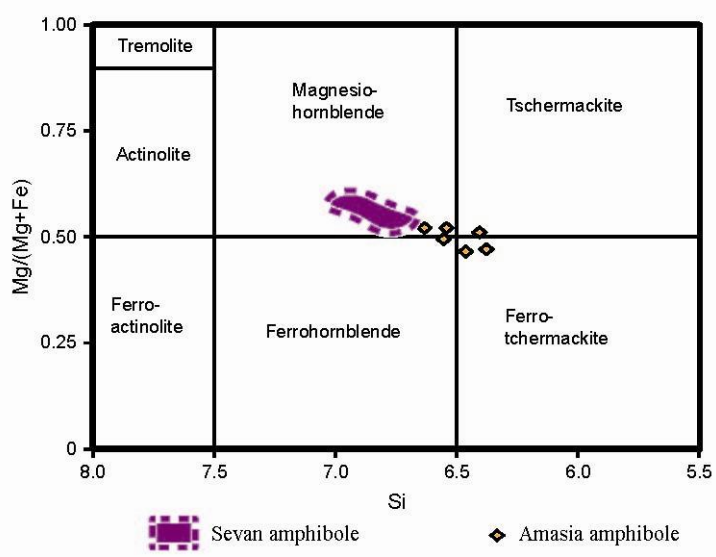

Figure 23 - Chemical composition of amphibole from the AR-08-21 and AR-08-22 gabbro samples, after Leake et al. (1997). Data concerning Sevan amphiboles from Galoyan et al. (2009).

1.5 Geochemistry

1.5.1 Analytical procedures

Samples from the Amasia ophiolite and related metamorphics were analyzed for elements major, trace and Rare Earth Elements (REE; **Table 3**). Samples were analyzed at the C.R.P.G. (Nancy, France). Analytical procedures and analyses of standards can be found on the following website (http://www.crpg.cnrs-nancy.fr/SARM).

The sampling was undertaken during three field work campaigns in 2008, 2009 and 2010. Additional data pertaining to the other Armenian ophiolites along with the Turkish ophiolites are published in Galoyan (2008) and Parlak et al. (2012), respectively. In order to designate rock groups, trends and tectonic environments (Pearce and Cann, 1973; Floyd and Winchester, 1975; 1978; Pearce and Norry, 1979; Pearce, 1982; 1983; 1996) the option to study the relatively immobile elements, such as Ti, Zr, Y, Nb, Ta, Th, V and REEs, was chosen since the immobility of these elements during low grade submarine alteration is constrained in a number of studies (e.g. Hart et al., 1974; Humphris and Thompson, 1978) (**Figures 24** and **25**). Chondrite normalized REE plots and Normal Mid Oceanic Ridge Basalt (N-MORB) normalized spidergrams for the Turkish and Armenian ophiolites are presented in **Figures 26** and **27**, respectively. We analyzed two types of rocks: (1) magmatic rocks (basalt, gabbro and plagiogranite) from the ophiolite unit and (2) metamorphic rocks (amphibolites)

from the metamorphic sole. In Amasia, considering the geochemical data obtained from samples of the ophiolites and related metamorphic rocks, two tendencies are well observed.

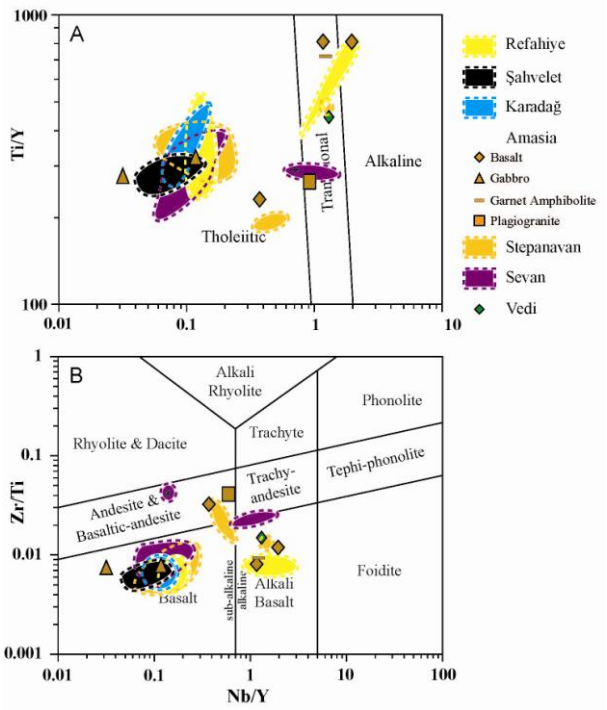

Figure 24 - Diagrams for crustal rocks of the ophiolites. Data concerning Erzinncan-Erzurum region (Refahiye, Şahvelet and Karadağ) from Parlak et al. (2012) and concerning Stepanavan, Sevan and Vedi from Galoyan et al. (2007; 2009) and Rolland et al. (2009b; 2010). A, Ti/Y versus Nb/Y (after Pearce 1982). B, Zr/Ti versus Nb/Y (after Pearce 1996).

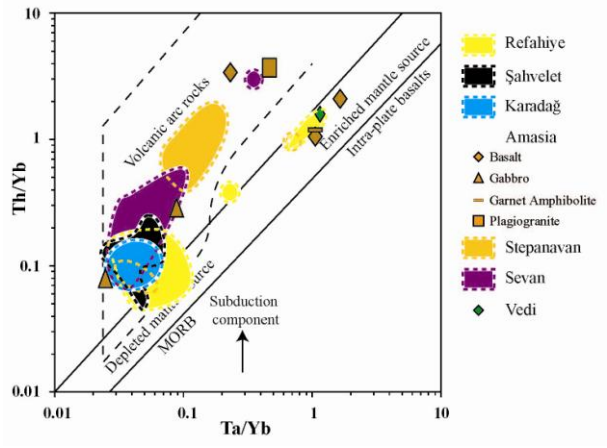

Figure 25 - Ta/Yb versus Th/Yb diagram (after Pearse 1982) for crustal rocks of the ophiolites. Data concerning Erzinncan-Erzurum region (Refahiye, Şahvelet and Karadağ) from Parlak et al. (2012) and concerning Stepanavan, Sevan and Vedi from Galoyan et al. (2007; 2009) and Rolland et al. (2009b; 2010).

1.5.2 Supra-subduction tholeiitic signature

A tholeiitic (MORB-type) affiliation is found for the gabbro samples with some fertile contamination. Ti/Y vs. Nb/Y and Zr/Ti vs. Nb/Y diagrams plot these samples as basaltic tholeiitic composition (**Figure 24**). The trace element patterns show generally marked negative anomalies in Ta-Nb and enrichment in Large Ion Lithophile Elements (LILE) (**Figures 26** and **27**). This variable enrichment can be explained by different degrees of fractional crystallization, as exemplified by increasing enrichments in all trace elements in the plagiogranite, with respect to gabbros., except for the negative Eu and Ti anomalies exhibited in this most differentiated rock, which is ascribed to plagioclase and amphibole/titanite fractionation, respectively. Indeed, the gabbros have rather flat spectra while the plagiogranite along with one of the basalt samples are more enriched in all elements and especially LILE. In

the Pearce (1996) diagram (**Figure 25**), this enrichment is interpreted as a contamination of a depleted mantle source by a subduction component. The association of serpentinites, gabbros, plagiogranites and basalts is part of a typical ophiolite assemblage, suggestive of an oceanic crust. Therefore, this ophiolite probably represents a supra-subduction back- or fore-arc basin.

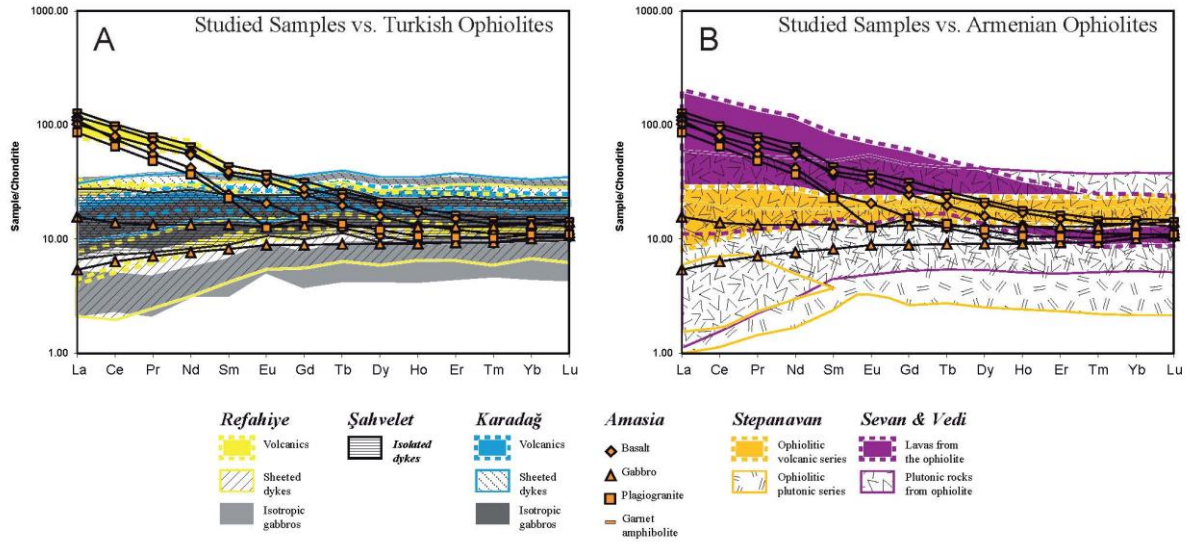

Figure 26 - Chondrite normalized REE spider diagrams. Data concerning Erzinncan-Erzurum region (Refahiye, Şahvelet and Karadağ) from Parlak et al. (2012) and concerning Stepanavan, Sevan and Vedi from Galoyan et al. (2007; 2009) and Rolland et al. (2009b; 2010). Normalizing values are from Sun and McDonough (1989).

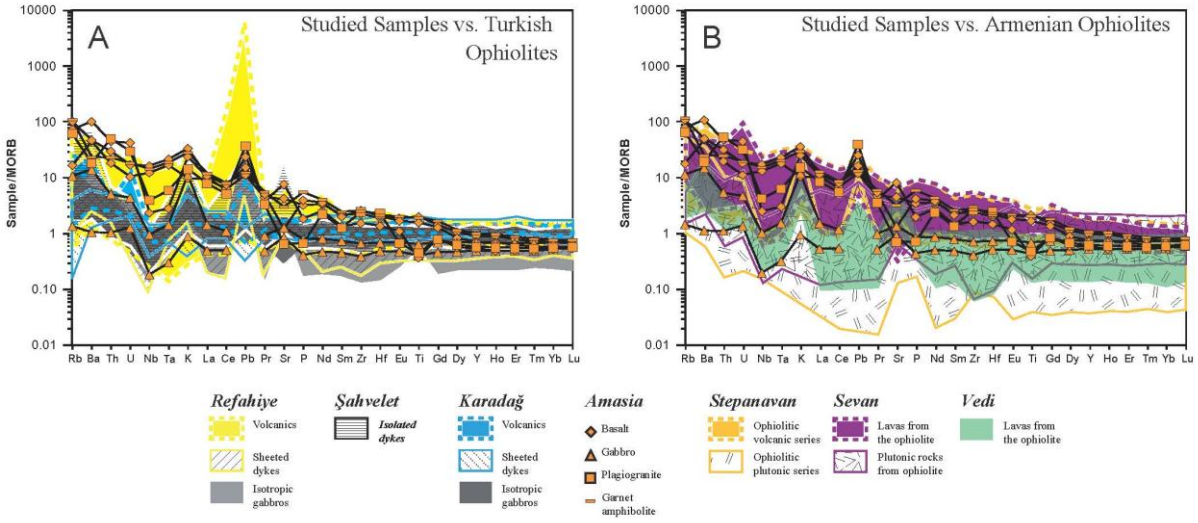

Figure 27 - N-MORB normalized multi-element spider diagrams. Data concerning Erzinncan-Erzurum region (Refahiye, Şahvelet and Karadağ) from Parlak et al. (2012) and concerning Stepanavan, Sevan and Vedi from Galoyan et al. (2007; 2009) and Rolland et al. (2009b; 2010). Normalizing values are from Sun and McDonough (1989).

1.5.3 Alkaline signature

The second tendency that is observed is formed by rocks with an alkaline basalt composition. Spidergrams show neat enrichments in LILE, LREE, Ti and Pb for these samples, with no Nb-Ta negative anomalies in respect to LREE enrichment (**Figures 26** and **27**). The garnet bearing amphibolite has a very similar composition to that of alkaline basalts either plotting in Ti/Y vs. Nb/Y and Zr/Ti vs. Nb/Y diagrams as alkaline or transitional rocks (**Figure 24**). The amphibolite also displays similar patterns as alkaline basalts in spider diagrams. The basalt MORB-normalized spider-diagrams and plot in the Pearce (1996) diagram are consistent with an Ocean Island Basalt (OIB) signature, characterized by lack of Nb and Ta negative anomalies and general enrichment in incompatible elements. Particularly, the samples show depletion in HREE which may be explained by a different source containing garnets. As quoted by Galoyan (2008), we interpret these features as representing an OIB signature.

1.6 Discussion

The similarities between the analyses obtained in Amasia with the different study areas in Armenia and NE Turkey reinforce the model proposed in several former publications, in which a single oceanic crustal domain was obducted at the scale of the Lesser Caucasus (Galoyan, 2008; Galoyan et al., 2009; Rolland et al., 2009b; 2010; 2011a-b; Sosson et al., 2010), proposed at the scale of Armenia and for NE Turkey (Parlak et al., 2012). In the following discussion we propose the first comparison of geochemical data from both sides putting some light on this large-scale ophiolite obduction, and related processes: formation of the metamorphic rocks beneath the ophiolite and post-ophiolite OIB event.

1.6.1 Comparison of Amasia ophiolite Ar-Ar ages with other ophiolites along Turkey (to the W) and Armenia (to the E) Izmir-Ankara-Erzincan-Sevan suture

The petrochemical characteristics and Ar-Ar age of the Amasia ophiolite are similar to those of the Stepanavan and Sevan ophiolites (Galoyan et al., 2007; 2009; Rolland et al., 2009b; 2010) to the East, with an overall tholeiitic tendency influenced by a subduction component. These similar results tend to infer that the ophiolites correspond to the formation

of oceanic crust in the same setting, thus suggesting the lateral continuation of these structures. $^{40}Ar/^{39}Ar$ hornblende ages obtained by Galoyan et al. (2009) in the Sevan ophiolite are of 170.5 ± 4.4 Ma and 165.3 ± 1.7 Ma, while $^{40}Ar/^{39}Ar$ dating experiments by Rolland et al. (2010) in the Vedi one provided a magmatic crystallization age of hornblende at 178.7 ± 2.6 Ma, and further evidence of greenschist facies crystallization during hydrothermal alteration until *c*. 155 Ma. Therefore, the ages obtained in the Amasia ophiolite by the same method at 169.0 ± 4.6 Ma and 175.8 ± 7.7 Ma confirm the Middle Jurassic age of the ophiolite. Based on the ages of the three locations it can be suggested that the Armenian ophiolites are part of the same obducted oceanic crust section of c. 170-175 Ma age that underwent hydrothermal alteration for about 10 Ma after oceanic crust crystallization, which is the case in slow-spreading ophiolite types (see discussions in Galoyan et al., 2009 and Rolland et al., 2009b, 2010). Similar ages of gabbro amphiboles are found in northern Turkey along the İzmir-Ankara-Erzincan suture with $^{40}Ar/^{39}Ar$ plateau ages between 167 and 177 Ma, suggesting a similar age for oceanic crust formation (Çelik et al., 2011).

1.6.2 Comparison of Amasia geochemistry with other ophiolites, Turkey (to the W) and Armenia (to the E), along Izmir-Ankara-Erzincan-Sevan suture

Considering their geochemical composition the Amasia gabbros bear similar characteristics as for other Armenian ophiolites, marked by a supra-subduction contamination with depletions in Nb-Ta, and general LILE enrichment. This evidences their emplacement in a context with a high contamination of slab-derived fluids. As a full ophiolitic lithological assemblage has been found in Armenian ophiolites (comprising radiolarites, pillow basalts, gabbros, plagiogranites and serpentinites), these rocks likely feature the formation of oceanic crust in a marginal basin environment (fore- or back-arc). The main problem for the interpretation of this marginal basin in terms of fore- or back-arc is the position of the former volcanic arc that should have been formed at this time. In Armenia, the presence of meta-volcanites in the blueschist units found below the obduction in Stepanavan (Rolland et al., 2009b) suggests that the arc was subducted and thus the basin was a back-arc one. However, the question is still posed. The most likely polarity for the former subduction zone is north dipping from the south of the marginal basin. This is suggested by the overall south verging tectonic pile, comprising the Eurasian margin, the ophiolite and the SAB (**Figure 16**).

Further, an alkaline (OIB) tendency is also observed for some of the metamorphic rocks, and basalts topping the ophiolite section. Similar OIB compositions are also found in Turkey associated to the ophiolite (Refahiye and Karadağ volcanites, Parlak et al., 2012). This alkaline composition is compatible with the presence of a series of rocks formed from a mantle plume emplaced on top of the ophiolite. Its emplacement in Armenia has been dated at c. 117 Ma by Ar-Ar on amphibole (Rolland et al., 2009b), prior to the obduction of the oceanic domain in the Coniacian-Santonian (**Table 5**).

In contrast to the tholeiitic suite, the alkaline suite shows no sign of slab derived components, and is more likely related to an enriched mantle source, such as that in hot spot settings, and is thought to be unrelated to the subduction. But some lateral influence of the subduction zone with the mantle plume is not impossible.

1.6.3 Emplacement of the ophiolite by obduction onto the South Armenian Block

This ophiolite, now linked to the others to the East (Stepanavan), already linked to the other Armenian ophiolites (Sevan and Vedi), requires at least 60 km tectonic transport from the Sevan-Akera suture to Vedi for its emplacement in its current position. The geochemical composition of the metamorphic unit beneath the ophiolite, comprised of a tectonized melange including garnet amphibolites, shows a distinct alkaline tendency similar to the alkaline suite described on top of the ophiolite in other Armenian locations (see previous section). Observations undertaken in the Amasia area are thus compatible with a model of obduction of a back-arc domain with oceanic crust slicing after OIB emplacement, which explains why we find alkaline rocks both underneath and on top of the ophiolite. The alkaline outcrops would have been under-thrusted as the ophiolite underwent an intra-oceanic scaling process.

However, considering the intra-oceanic subduction, the volcanic arc is missing. The only evidence of any remains of such a volcanic structure can be found in the ophiolitic sole by geochemical signatures. Two hypotheses on the disappearance of this arc are (1) the alteration and erosion of the volcanic arc during the obduction or (2) the subduction of the fore-arc block dragging the volcanic arc with it, as proposed by Shemenda (1994), and as suggested by some volcanic blocks in the Stepanavan blueschists. More to the west, in eastern

Turkey, remnants for such intra-oceanic subduction have been found (Parlak et al., 2012; Topüz et al., 2012).

1.6.4 Reconstruction of the 'ophiolite' history

From all the available geological data, we propose the following model for the evolution of the Amasia Ophiolite (**Figure 28**):

1- The magmatic and metamorphic rocks of the Amasia ophiolite have similar geochemical compositions to those of the other Armenian ophiolites (Sevan, Stepanavan and Vedi) as well as the Turkish ophiolites (Refahiye, Şahvelet and Karadağ). The ophiolitic rocks of Amasia are of similar age to those of the other Armenian ophiolites (around 170 Ma) (Galoyan et al., 2009; Rolland et al. 2009a; 2009b; Sosson et al., 2010).

2- The two magmatic suites were emplaced one on top of the other: a gabbroic basement of supposedly back-arc oceanic crust topped by thick basaltic flows with an alkaline tendency. This confirms the hypothesis of a single ophiolitic nappe (Galoyan, 2008) over the SAB topped by a volcanic series of hot-spot type, dated c. 117 Ma in Rolland et al. (2009b).

3- The ages of the syn-tectonic sedimentary deposits limit the beginning of obduction of this oceanic domain to Coniacian-Santonian times. Dating undergone on the flysch at Sevan and Vedi indicate similar dates. This is compatible with the context of the closing of Neotethys.

4- This new contribution in the comprehension of the geodynamic evolution of the Lesser Caucasus supports the presence of two north dipping subductions zones: (1) a subduction under the Eurasian margin and to the south by (2) an intra-oceanic subduction allowing the continental domain to subduct under the oceanic lithosphere, thus leading to ophiolite emplacement. This confirms recent geodynamic models (Rolland et al., 2010; Sosson et al., 2010).

5- The missing of the volcanic arc formed above the intra-plate subduction may be explained by its dragging under the obducting ophiolite with scaling by faulting and tectonic erosion. It is hypothesized that the generation of blueschists of Stepanavan corresponds to this missing volcanic arc (Galoyan et al., 2007; Rolland et al., 2009a). In the Erzincan region geochemical traces (Parlak et al., 2012) and field observations lead to the confirmation of this hypothesis because of low-grade metamorphic rocks of

volcanic origin that may be found under ophiolitic rocks overthrusted from north to south along the northern edge of the Erzincan basin.

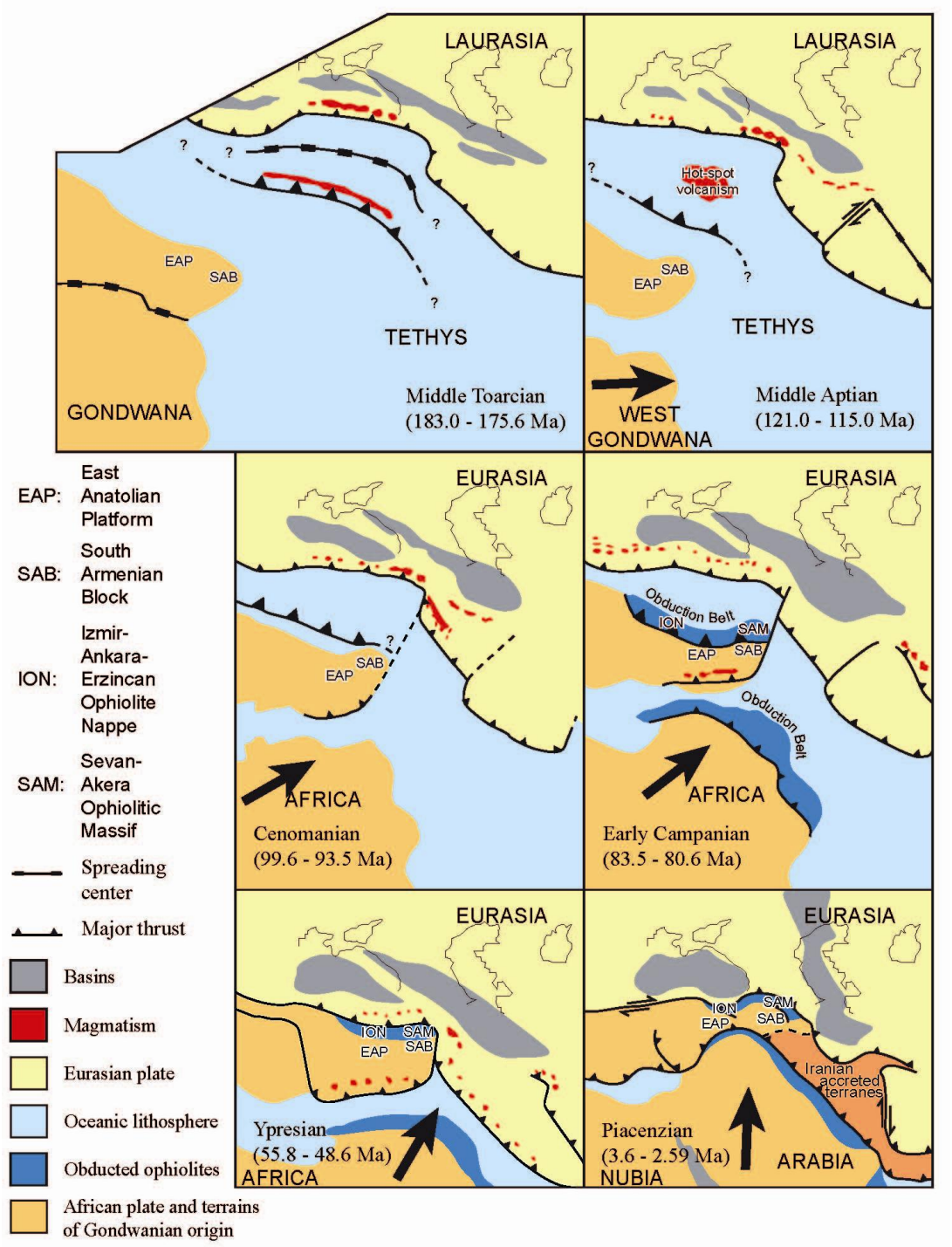

Figure 28 - Middle Toarcian (c. 180 Ma), to Early Campanian (c. 83 Ma) palaeotectonic evolution of the Lesser Caucasus region and its neighboring areas, modified from Middle East Basins Evolution Programme palaeotectonic maps of the Middle East (Barrier and Vrielynck, 2008) to include our new data.

1.6.5 Conclusive remarks and perspective of work

The petro-geochemical features and age of the Amasia ophiolite are in part similar to those of the Armenian ophiolites to the east (Galoyan, 2008) and the Turkish ophiolites to the west (Parlak et al., 2012), particularly the Jurassic part of the ophiolite, which may have been formed in a similar context. In the Jurassic times, the same processes might be responsible for the formation of the Amasia ophiolite and the other Armenian and Turkish ophiolites, including a back-arc setting environment. Several hypotheses might be drawn at this stage of the study. (1) The Armenian ophiolites might represent the continuation of the Turkish ophiolites along the Ankara-Erzincan suture zone further east. This hypothesis is supported by the fact that the Armenian ophiolite nappe is shown to be transported on a metamorphic sole, and is shown to be obducted onto the SAB (Knipper and Khain, 1980). We propose that this obduction connects to the basal contact of the NE Turkish ophiolite, but still few ages were obtained on the ophiolites there to validate this hypothesis. However, lateral continuation from Armenia to NE Turkey is apparent from the geometry and position of ophiolites on geological maps. Such correlation suggests an obducted ophiolitic nappe of at least 700 km in length along the Ankara-Erzurum-Sevan-Akera suture zone on top of the Tauride block continuing laterally to the SAB. In view of the information brought to light within this paper, the Izmir-Ankara-Erzincan-Sevan-Akera ophiolite obduction is amongst the most exceptional case of obduction on earth.

As for the correspondence with the peri-Arabic ophiolites (for example the Oman ophiolite), the oceanic domains were obducted onto Arabia within the same time span as those obducted onto the SAB and Tauride block (Okay et al., 2001; Agard et al., 2010; Sosson et al., 2010). However, preliminary paleomagnetic analyses to determine the movements of the continental fragments indicate that the SAB and the Tauride block were much closer to the Eurasian margin than the Arabian margin (Meijers et al., 2012). From this work it also would seem that an ocean domain separates the SAB and Tauride block from the Arabian margin until Upper Cretaceous times. This ocean domain corresponding to southern Neotethys closes completely during Eocene times (Rolland et al., 2012).

The preservation of initial obduction contacts and ophiolite structure makes it a potential target for understanding the obduction processes leading to such important tectonic transport of oceanic crust remnants onto continental lithospheres.

Acknowledgements

This work was supported by the MEBE (Middle East Basin Evolution) and DARIUS programs jointly supported by a consortium including oil companies, the University Pierre and Marie Curie and the INSU/CNRS. Fieldwork was facilitated by the support of the Armenian Academy of Science (Institute of Geological Sciences). The technical help of M. Manetti in the preparation and mineral analysis is also acknowledged along with G. Delanoy for thin sections. We wish to thank J.L. Devidal in Clermont-Ferrand, P. Capiez in Lyon and S. Gallet in Nice for their involvement during data acquisition. This publication is a contribution of "GEOAZUR", University of Nice–Sophia Antipolis, CNRS, France.

References

Adamia, S.A., Lordkipanidze, M.B., Zakariadze, G.S., 1977. Evolution of an active continental margin as exemplified by the Alpine history of the Caucasus. Tectonophysics, 40, pp. 183-189.

Adamia, Sh.A., Chkhotua, T., Kekelia, M., Lordkipanidze, M., Shavishvili, I., Zakariadze, G., 1981. Tectonics of Caucasus and adjoining regions: implications for the evolution of the Tethys ocean. Journal of Structural Geology 3, pp. 437-447.

Adamia, S., Belov, A., Kekelia, M., Shavishvili, I., 1987. Paleozoic tectonic development of the Caucasus and Turkey (Geotraverse C). *In:* Flugel, H.W., Sassi, F.P., Grecula, P., (eds) Pre-Variscan and Variscan Events in the Alpin-Mediterranean Mountain Belts. Mineralia Slovaca, Alfa Bratislava, pp. 22-50.

Agard, P., Searle, M.P., Alsop, G.I., Dubacq, B., 2010. Crustal stacking and expulsion tectonics during continental subduction: P-T deformation constraints from Oman. Tectonics 29, pp. 1-19.

Akıncı, Ö.T. 1984. The eastern Pontide volcanosedimentary belt and associated massive sulphide deposits. In: Dixon, J.E., Robertson, A.H.F., (eds) The Geological Evolution of the Eastern Mediterranean. Geological Society, London, Special Publication, 17, pp. 415-428.

Avagyan, A., Sosson, M., Philip, M.H., Karakhanian, A., Rolland, Y., Melkonyan, R., Rebai, S., Davtyan, V., 2005. Neogene to quaternary stress field evolution in Lesser Caucasus and adjacent regions using fault kinematics analysis and volcanic cluster data. Geodinamica Acta 18, pp. 401-416.

Avagyan, A., Sosson, M., Karakhanian, A., Philip, H., Rebai, S., Rolland, Y., Melkonyan, R., Davtyan, V., 2010. Recent Ectonic Stress Evolution in the Lesser Caucasus and Adjacent Regions. Geological Society London Special Publications, vol. 340, pp. 393-408.

Barrier, E., Vrielynck, B., 2008. Palaeotectonic map of the Middle East, Atlas of 14 maps, Tectonosedimentary-Palinspastic maps from Late Norian to Pliocene. Commission for the Geologic Map of the World (CCMW, CCGM), Paris, France.

Biju-Duval, B., Dercourt, J., Le Pichon, X., 1977. From the Tethys Ocean to the Mediterranean Seas: A Plate Tectonic Model of the Evolution of the Western Alpine System. In: Biju-Duval and L. Montadert (Eds). Structural History of the Mediterranean basins. Editions Technip, Paris, pp. 143-164.

Bozkurt, E., Mittwede, S.K., 2001. Introduction to the Geology of Turkey – A Synthesis. Inernational Geology Review, vol. 43, pp. 578-594.

Çelik, Ö.F., Marzoli, A., Marschik,R., Chiaradia, M., Neubauer,F., Öz, I., 2011. Early–Middle Jurassic intra-oceanic subduction in the İzmir-Ankara-Erzincan Ocean, Northern Turkey. Tectonophysics 509, pp. 120-134.

Danelian, T., Asatryan, G., Sahakyan, L., Galoyan, G., Sosson, M., Avagyan, A., 2010. New and revised radiolarian biochronology for the sedimentary cover of ophiolites in the Lesser Caucasus (Armenia). Geological Society, London, Special Publications 340, pp. 383-391.

De Sigoyer, J., Guillot, S., Dick, P., 2004. Exhumation of the ultrahigh-pressure Tso Morari unit in eastern Ladakh (NW Himalaya): A case study. Tectonics 23, pp. 1-18.

Dercourt, J., Zonenshain, L.P., Ricou, L.-E., Kazmin, V.G., Le Pichon, X., Knipper, A.L., Grandjacquet, C., Sbortshikov, I.M., Geyssant, J., Lepvrier, C., Pechersky, D.H., Boulin, J., Sibuet, J.-C., Savostin, L.A., Sorokhtin, O., Westphal, M., Bazhenov, Lauer, J.P., Biju-Duval, B., 1986. Geological evolution of the Tethys belt from the for the Atlantic to the Pamirs since the Lias. Tectonophysics 123, pp. 241-315.

Ding, L., Kapp, P., Wan, X., 2005. Paleocene–Eocene record of ophiolite obduction and initial India-Asia collision, south central Tibet. Tectonics 24, pp. 1-9.

Floyd, P.A., Winchester, J.A., 1975. Magma type and tectonic setting discrimination using immobile elements. Earth Planetary Science Letters 27, pp. 211-218.

Floyd, P.A., Winchester, J.A., 1978. Identification and discrimination of altered and metamorphosed volcanic rocks using immobile elements. Chemical Geology 21, pp. 291-306.

Galoyan, G., 2008. Etude Pétrologiques, Géochimiques et Géochronologiques des Ophiolites du Petit Caucase (Arménie). PhD thesis, University of Nice–Sophia Antipolis.

Galoyan, G., Rolland, Y., Sosson, M., Corsini, M., Melkonyan, R., 2007. Evidence for superposed MORB, oceanic plateau and volcanic arc series in the Lesser Caucasus (Stepanavan, Armenia). Comptes Rendus Geosciences 339, pp. 482-492.

Galoyan, G., Rolland, Y., Sosson, M., Corsini, M., Billo, S., Verati, C., Melkonyan, R., 2009. Geology, geochemistry and $^{40}Ar/^{39}Ar$ dating of Sevan ophiolites (Lesser Caucasus,

Armenia): Evidence for Jurassic Back-arc opening and hot spot event between the South Armenian Block and Eurasia. Journal of Asian Earth Sciences 34, pp. 135-153.

Gaggero, L., Marroni, M., Pandolfi, L., Buzzi, L., 2009. Modeling the oceanic lithosphere obduction: Constraints from the metamorphic sole of Mirdita ophiolites (Northern Albania). Ofioliti 34, pp. 17-42.

Göncüoğlu, M.C., Turhan, N., 1984. Geology of the Bitlis Metamorphic Belt. In: Tekeli, O., Göncüoglu, M.C. (eds.), International Symposium on the Geology of the Taurus Belt, Proceedings, pp. 237-244.

Hacker, B.R., 1991. The role of deformation in the formation of metamorphic field gradients: Ridge subduction beneath the Oman ophiolite, Tectonics, 10, pp. 455-473.

Hacker, B.R., Mosenfelder, J.L., Gnos, E., 1996. Rapid emplacement of the Oman ophiolite: Thermal and geochronologic constraints. Tectonics 15, pp. 1230-1247.

Harper, G.D., Grady, K., Coulton, A.J., 1996. Origin of the amphibolite "sole" of the Josephine ophiolite: Emplacement of a cold ophiolite over a hot arc. Tectonics 15, pp. 296-313.

Hart, S.R., Erlank, A.J., Kable, E.J.D., 1974. Sea floor basalt alteration: some chemical and Sr isotopic effects. Contributions to Mineralogy and Petrology 44, pp. 219-230.

Hempton, M.R., 1985. Structure and deformation history of the Bitlis Suture near Lake Hazar, SE Turkey. Geological Society of America Bulletin 96, pp. 223-243.

Hess, J.C., Aretz, J., Gurbanov, A.G., Emmermann, R., Lippolt, H.J., 1995. Subduction related Jurassic andesites in the northern Great Caucasus. Geologische Rundschau, 84, pp. 319-333.

Humpris, S.E., Thompson, G., 1978. Trace element mobility during hydothermal alteration of ocean basalts. Geochimica and Cosmochimica Acta 42, pp. 127-136.

Jourdan, F., Feraud, G., Bertrand, H., Kampunzu, A.B., Tshoso, G., Le Gall, B., Tiercelin, J.J., Capiez, P., 2004. The Karoo triple junction questioned: evidence fromJurassic and Proterozoic $^{40}Ar/^{39}Ar$ ages and geochemistry of the giant Okavango dyke swarm (Botswana). Earth and Planetary Science Letters 222, pp. 989-1006.

Knipper, A.L., 1975. The oceanic crust in the structure of the Alpine Folded Belt (South Europe, western part of Asia and Cuba). Transactions 267, Moscow 'Nauka' (in Russian).

Knipper, A.L., Khain, E.V., 1980. Structural position of ophiolites of the Caucasus. Ofioliti, Special Issue 2, pp. 297–314.

Knipper, A.L., Sokolov, S.D., 1977. Vedi ophiolites (Armenia) autochton or allochton? Geotektonica 10, pp. 55-66 (in Russian).

Knipper, A.L., Ricou, L.E., Dercourt, J., 1986. Ophiolites as indicators of the geodynamic evolution of the Tethyan ocean. Tectonophysics 123, pp. 213–240.

Knipper, A.L., Bragin, N.Y., Satian M.A., 1997. Upper Triassic-Lower Jurassic volcanogenic and sedimentary deposits of the Old Zod Pass (Transcaucasia). Stratigraphy Geol. Correlation 5, pp. 58–65 (in Russian).

Leake, B.E., Woolley, A.R., Arps, C.E.S., Birch, W.D., Gilbert, M.C., Grice, J.D., Hawthorne, F.C., Kato, A., Kisch, H.J., Krivovichev, V.G., Linthout, K., Laird, J., Mandarino, J.A., Maresch, W.V., Nickel, E.H., Rock, N.M.S., Schumacher, J.C., Smith, D.C., Stephenson, N.C.N., Ungaretti, L., Whittaker, E.J.W., Youzhi, G., 1997. Nomenclature of amphiboles: report of the subcommittee on amphiboles of the international mineralogical association, Commission on new minerals and mineral names. American Mineralogist 82, pp. 1019-1037.

Meijers, M., Sosson, M., Rolland, Y., Smith, B., Mensink, M., Grigoryan, A., Avagyan, A., Sahakyan, L., Sadradze, N., Adamia, S., Müller, C., 2012. Paleomagnetism of the Armenian block and its foreland: Constraints on the Tethyan Plate reconstructions and oroclinal bending during the Phanerozoic. 65th Geological Congress of Turkey.

Nalivkin, P.V., (ed.) 1976. Geological Map of Caucasus at 1/500000 scale. Ministry of Geology, USSR, Cief.

Nikishin, A.M., Korotaev, M.V., Ershov, A.V., Brunet, M.F., 2003. The Black Sea Basin: tectonic history and Neogene-Quaternary rapid subsidence modelling. Sedimentary Geology, 156, pp. 149-168.

Oberhänsli, R., Candan, O., Bousquet, R., Rimmele, G., Okay, A., Goff, J., 2010. Alpine HP evolution of the eastern Bitlis complex, SE Turkey. In: Sosson, M., Kaymakci, N., Stephanson, R., Bergarat, F., Storatchenoko, V., (eds.), Sedimentary Basin Tectonics from the Black Sea and Caucasus to the Arabian Platform, vol. 340. Geological Society of London Special Publication, pp. 461-483.

Okay, A.İ., Şahintürk, Ö., 1997. Geology of the Eastern Pontides. In: Robinson, A.G., (ed.) Regional and Petroleum Geology of the Black Sea and Surrounding Region. American Association of Petroleum Geologists Memoir, 68, Tulsa, Oklahoma, pp. 291-311.

Okay, A.I., Tüysüz, O., 1999. Tethyan sutures of northern Turkey. In "The Mediterranean Basins: Tertiary extension within the Alpine orogen" (eds. B. Durand, L. Jolivet, F. Horváth and M. Séranne), Geological Society, London, Special Publication 156, pp. 475-515.

Okay, A.I., Tansel, I., Tüysüz, O., 2001. Obduction, subduction and collision as reflected in the Upper Cretaceous–Lower Eocene sedimentary record of western Turkey. Geological Magazine 138, pp. 117-142.

Parlak, O., Çolakoğlu, A., Dönmez, C., Sayak, H., Yildirim, N., Türkel, A., Odabaşi, İ., 2012. Geochemistry and tectonic significance of ophiolites along the Ankara-Erzincan suture zone in northeastern Anatolia. Geological Society of London in press.

Pearce, J.A., 1982. Trace element characteristics of lava from destructive plate boundaries. In: Thorpe, R.S. (eds.) Andesites. Wiley, New York, pp. 525-548.

Pearce, J.A., 1983. Role of the sub-continental lithosphere in magma genesis at active continental margins. In: Hawkesworth, C.J., Norry, M.J. (eds.) Continental basalts and mantle xenoliths. Shiva, Nantwich, pp. 30-249.

Pearce, J.A., 1996. A users guide to basalt discrimination diagrams. In: Wyman, D.A. (eds.) Trace element geochemistry of volcanic rocks: applications for massive sulphide exploration. Geochemistry short course notes. Geological Association of Canada 12, pp. 79-113.

Peace, J.A., Cann, J.R., 1973. Tectonic setting of basaltic volcanic rocks determined using trace element analysis. Earth Planetary Science Letters 19, pp. 290-300.

Pearce, J.A., Norry, M.J., 1979. Petrogenetic implications of Ti, Zr, Y and Nb variations in volcanic rocks. Contributions to Mineralogy and Petrology 69, pp. 33-47.

Peccerillio, A., Taylor, S.R., 1976. Geochemistry of Eocene calc-alkaline volcanic rocks from the Kastamonu area, northern Turkey. Contributions to Mineralogy and Petrology, 58, pp. 63-81.

Rice, S.P., Robertson, A.H.F., Ustaömer, T., Inan, N., Tasli, K., 2009. Late Cretaceous–Early Eocene tectonic development of the Tethyan suture zone in the Erzincan area, Eastern Pontides, Turkey. Geological Magazine, 146, pp. 567-590.

Ricou, L.E., 1994. Tethys reconstructed: plates, continental fragments and their bounderies since 260 Ma from Central America to South-estern Asia. Gedinamica Act 7, pp. 169-218.

Ricou, L.E., Dercourt, J., Geyssant, J., Grand-Jaquet, C., Lepcrier, C., Biju-Duval, B., 1986. Geological constraints on the Alpine evolution of the Mediterranean Tethys. Tectonophysics, 123, pp. 83-122.

Ricou, L.E., Zonenshain, L.P., Dercourt, J., Kazmin, V.G., Le Pichon, X., Knipper, A.L., Grandjacquet, C., Sborshchikov, I.M., Geyssant, J., Lepvrier, C., Pechersky, D.M., Boulin, J., Sibuet, J.C., Savostin, L.A., Sorokhtin, O., Westphal, M., Bazhenov, M.L., Lauer, J.P., Biju-Duval, B., 1985. Méthodes pour l'établissement de neuf cartes paléogéographiques de l'Atlantique au Pamir depuis le Lias. Bulletin de la Société Géologique de France 8, pp. 625-635.

Robertson, A., 2004. Development of concepts concerning the genesis and emplacement of Tethysan ophiolites in the Eastern Mediterranean and Oman regions. Earth-Science Reviews 66, pp. 331-387.

Robinson, A., Spadini, G., Cloetinhg, S., Rudat, J., 1995. Stratigraphic evolution of the Black Sea: inferences from basin modelling. Marine and Petroleum Geology, 12, pp. 821-835.

Rolland, Y., Billo, S., Corsini, M., Sosson, M., Galoyan, G., 2009a. Blueschists of the Amasia-Stepanavan Suture Zone (Armenia): linking Tethys subduction history from E-

Turkey to W-Iran. International Journal Earth Sciences (Geologische Rundschau) 98, pp. 533-550.

Rolland, Y., Galoyan, Gh., Bosch, D., Sosson, M., Corsini, M., Fornari, M., Vérati, C., 2009b. Jurassic Back-arc and hot-spot related series in the Armenian ophiolites - Implications for the obduction process. Lithos 112, pp. 163-187.

Rolland Y., Galoyan G., Sosson, M., Melkonian R., Avagyan A., 2010. The Armenian ophiolites : insights for Jurassic Back-arc formation, Lower Cretaceous hot-spot magmatism, and Upper Cretaceous obduction over the South Armenian Block. In: M.Sosson, N. Kaymakci, R. Stephanson, F. Bergarat, and V. Storatchenoko (eds.) Sedimentary basin tectonics from the Black Sea and Caucasus to the Arabian Platform. Geological Society of London, Special Publication 340, pp. 353–382.

Rolland, Y., Sosson, M., Adamia, Sh., Sadradze, N., 2011a. Prolonged Variscan to Alpine history of an active Eurasian margin (Georgia, Armenia) revealed by $^{40}Ar/^{39}Ar$ dating. Gondwana Research 20, pp. 798-815.

Rolland, Y., Perincek, D., Kaymakci, N., Sosson, M., Barrier, E., Avagyan, A., 2012. Evidence for ~80-75 Ma subduction jump during Anatolide-Tauride-Armenian block accretion and ~48 Ma Arabia-Eurasia collision in Lesser Caucasus-East Anatolia. Journal of Geodynamics, 56-57, pp. 76-85.

Satian, M. A., 2005. Mesozoic ophiolite basins of the Transcaucasian geotraverse. Izvestia of National Academy of Science of Armenia, Nauki o Zemle 1, pp. 3-8 (in Russian).

Searle, M., Cox, J., 1999. Tectonic setting, origin, and obduction of the Oman ophiolite. Geological Society of America Bulletin 111, pp. 104-122.

Sengör, A.M.C., Yilmaz, Y., 1981. Tethyan evolution of Turkey: A plate tectonic approach. Tectonophysics 75, pp. 181-241.

Şengün, M., 2006. A critical review of the Anatolian geology: A dialectic to sutures and evolution of the Anatolian Tethys and Neotethys. Mineral Research Exploration Bulletin 133, pp. 1-29.

Shemenda, A.I., 1994. Subduction: Insights from physical modeling. Kluwer Academic Publishers, 215.

Sokolov, 1977. The Olistostromes and Ophiolitic Nappes of the Lesser Caucasus. Izdatelstvo 'Nauka', Moscow (in Russian).

Sosson, M., Rolland, Y., Danelian, T., Muller, C., Melkonyan, R., Adamia, S., Kangarli, T., Avagyan, A., Galoyan, G., 2010. Subductions, obduction and collision in the Lesser Caucasus (Armenia, Azerbaijan, Georgia), new insights. Geological Society, London, Special Publications 340, pp. 329-352.

Stampfli et al., 2001. Palaeotectonic and palaeogeographic evolution of the western Tethys and PeriTethyan domain (IGCP Project 369). Episodes 24, pp. 222-228.

Steiger, R. H., Jäger, E., 1977. Subcommission on geochronology: convention on the use of decay constants in geo- and cosmochronology. Earth and Planetary Science Letters 36, pp. 359-362.

Stöcklin, J., 1974. Possible ancient continental margins in Iran. *In:* Burk, C.A. & Drake, C.L., (eds) The Geology of Continental Margins. Springer, New York, pp. 873-887.

Stöcklin, J., 1977. Structural correlation of the Alpine ranges between Iran and Central Asia. Les Mémoires de la Société géologique de France, 8, pp. 333-353.

Sun, S.S., McDonough, W.F., 1989. Chemical and isotopic systematic of oceanic basalts: implications for mantle composition and processes. In: Saudners A.D., Norry, M.J. (Eds.), Magmatism in Ocean Basins, Geological Society, London, Special Publications 42, pp. 313-345.

Topüz, G., Göçmengil, G., Rolland, Y., Çelik, Ö.F., 2012. Coexistance of the Paleo-and Neo-Tethys Accretionary Complexes and Problem of the Cimmerian Continent in the Eastern Mediterranean: Insights from the Refahiye Area (NE Turkey). 65th Geological Congress of Turkey. Ankara.

Turner, G., Huneke, J.C., Podose, F.A., Wasserburg, G.J., 1971. $^{40}Ar/^{39}Ar$ ages and cosmic ray exposure ages of Apollo 14 samples. Earth and Planetary Science Letters 12, pp. 15-19.

Yılmaz, Y., Yiğitbaş, E., Can Genç, S., 1993. Ophiolitic and metamorphic assemblages of Southeast Anatolia and their significance in the geological evolution of the orogenic belt. Tectonics 10, pp. 1280-1297.

Yılmaz, Y., Tüysüz, O., Yığıtbaş, E., Genç, S.C., ŞENGÖR, A.M.C., 1997. Geology and tectonic evolution of the Pontides. *In*: Robinson, A.G., (ed) *Regional and Petroleum Geology of the Black Sea and Surrounding Regions*. American Association of Petroleum Geologists Memoir, 68, Tulsa, Oklahoma, 183-226.

Zakariadze, G.S., Knipper, A.L., Sobolev A.V., Tsamerian, O.P., Dmitriev, L.V., Vishnevskaya, V.S., Kolesov, G.M., 1983. The ophiolite volcanic series of the Lesser Caucasus. Ofioliti 8, pp. 439-466.

Zakariadze G.S., Knipper A.L., Bibikova E.V., Silantiev S.A., Zlobin S.K., Gracheva T.V., Makarov S.A., Kolesov T.M., 1990. The setting and age of the plutonic part of the NE Sevan ophiolite complex. Izvestia NAS USSR, Geological series 3, 17-30, (in Russian).

Zakariadze, G.S., Dilek, Y., Bogdanovsky, O.G., Karpenko, S.F., Vishnevskaya, V.S., Solov'eva, N.V., 2005. Age limits of the Lesser Caucasus paleooceanic allochthon. Abstracts of the International Symposium on the Geodynamics of Eastern Mediterranean: Active Tectonics of the Aegean Region, 15–18 June 2005, Kadir Has University, Istanbul, Turkey, p. 229.

Tables

Sample	AR-08-21								
DataSet/Point	57 / 1 .	58 / 1 .	59 / 1 .	60 / 1 .	61 / 1 .	62 / 1 .	63 / 1 .	64 / 1 .	67 / 1 .
Mineral phase	Amphibole	Amphibole	Plagioclase	Amphibole	Plagioclase	Amphibole	Rutile	Plagioclase	Ilmenite
Oxide %									
SiO2	44.63	44.81	65.89	44.96	66.04	43.57	0.05	65.56	0.01
K2O	0.13	0.13	0.00	0.12	0.06	0.24	0.03	0.07	-
CaO	8.69	8.59	2.11	9.95	2.48	9.05	0.16	2.46	0.04
Na2O	2.90	2.75	10.68	2.12	10.33	2.92	0.04	10.10	0.05
Al2O3	13.50	13.93	21.50	12.01	21.55	14.76	0.03	21.70	0.03
MgO	10.10	10.65	-	10.90	0.01	10.04	-	0.01	0.19
FeO	16.61	15.66	0.22	16.17	0.09	15.55	0.79	0.03	47.40
MnO	0.13	0.12	0.01	0.17	0.04	0.11	0.04	0.04	0.88
TiO2	0.44	0.55	0.01	0.39	-	0.67	100.63	-	50.95
Cr2O3	-	-	0.01	-	0.03	-	0.00	0.02	0.02
Total	97.13	97.19	100.44	96.78	100.62	96.90	101.76	99.98	99.56
Weight %									
Si	20.86	20.94	30.80	21.01	30.87	20.36	0.02	30.65	0.00
K	0.11	0.11	0.00	0.10	0.05	0.20	0.03	0.06	-
Ca	6.21	6.14	1.51	7.11	1.77	6.47	0.11	1.76	0.03
Na	2.15	2.04	7.92	1.57	7.66	2.16	0.03	7.49	0.03
Al	7.15	7.37	11.38	6.36	11.40	7.81	0.01	11.48	0.02
Mg	6.09	6.42	-	6.57	0.00	6.06	-	0.00	0.12
Fe	12.91	12.17	0.17	12.57	0.07	12.08	0.61	0.03	36.85
Mn	0.10	0.09	0.00	0.13	0.03	0.09	0.03	0.03	0.68
Ti	0.27	0.33	0.00	0.23	-	0.40	60.32	-	30.54
Cr	-	-	0.01	-	0.02	-	0.00	0.01	0.02
O	41.27	41.56	48.63	41.11	48.74	41.26	40.58	48.45	31.28
Total	97.11	97.18	100.43	96.77	100.62	96.90	101.76	99.96	99.56
StdDev wt%									
Si	0.39	0.39	0.54	0.40	0.54	0.39	0.03	0.53	0.03
K	0.06	0.06	0.04	0.06	0.05	0.06	0.04	0.05	0.05
Ca	0.25	0.25	0.13	0.27	0.14	0.26	0.05	0.14	0.04
Na	0.16	0.16	0.33	0.14	0.32	0.16	0.05	0.32	0.06
Al	0.17	0.17	0.21	0.16	0.21	0.18	0.03	0.21	0.03
Mg	0.18	0.18	0.02	0.18	0.02	0.18	0.03	0.02	0.04
Fe	0.43	0.42	0.07	0.42	0.06	0.41	0.11	0.07	0.77
Mn	0.07	0.07	0.06	0.07	0.06	0.07	0.07	0.06	0.12
Ti	0.07	0.08	0.05	0.07	0.06	0.08	0.83	0.05	0.55
Cr	0.06	0.06	0.06	0.06	0.06	0.06	0.06	0.05	0.06
Atomic %									
Si	17.17	17.14	22.19	17.38	22.21	16.75	0.02	22.19	0.00
K	0.07	0.06	0.00	0.06	0.03	0.12	0.02	0.03	-
Ca	3.58	3.52	0.76	4.12	0.89	3.73	0.07	0.89	0.02
Na	2.16	2.04	6.97	1.59	6.74	2.17	0.04	6.63	0.05
Al	6.12	6.28	8.53	5.47	8.54	6.69	0.01	8.66	0.02
Mg	5.79	6.07	-	6.29	0.00	5.76	-	0.00	0.15
Fe	5.34	5.01	0.06	5.23	0.03	5.00	0.29	0.01	20.16
Mn	0.04	0.04	0.00	0.05	0.01	0.04	0.01	0.01	0.38
Ti	0.13	0.16	0.00	0.11	-	0.19	33.02	-	19.48
Cr	-	-	0.00	-	0.01	-	0.00	0.00	0.01
O	59.62	59.69	61.48	59.70	61.55	59.57	66.51	61.59	59.74
Total	100.02	100.00	100.01	100.01	100.00	100.00	100.00	100.01	100.00

Table 2 - Electron microprobe analyses of the representative minerals of gabbro samples of the Amasia ophiolite.

Sample	AR-08-22				
DataSet/Point	68 / 1 .	69 / 1 .	71 / 1 .	72 / 1 .	73 / 1 .
Mineral phase	Amphibole	Plagioclase	Quartz	Amphibole	Plagioclase
Oxide %					
SiO2	42.98	66.77	99.86	43.14	65.41
K2O	0.49	0.07	0.03	0.22	0.09
CaO	8.88	1.90	-	8.61	2.08
Na2O	2.96	10.63	-	2.78	10.49
Al2O3	14.79	21.25	-	13.93	21.63
MgO	9.12	-	-	9.25	0.00
FeO	16.53	0.08	0.04	17.14	0.03
MnO	0.29	-	-	0.29	0.01
TiO2	0.68	0.03	-	0.39	-
Cr2O3	0.02	-	0.02	0.01	-
Total	96.75	100.73	99.95	95.75	99.75
Weight %					
Si	20.09	31.21	46.68	20.16	30.57
K	0.41	0.06	0.03	0.19	0.08
Ca	6.34	1.36	-	6.16	1.49
Na	2.19	7.89	-	2.06	7.78
Al	7.83	11.25	-	7.37	11.45
Mg	5.50	-	-	5.58	0.00
Fe	12.85	0.07	0.03	13.32	0.02
Mn	0.22	-	-	0.22	0.01
Ti	0.41	0.02	-	0.23	-
Cr	0.01	-	0.02	0.01	-
O	40.88	48.86	53.19	40.45	48.34
Total	96.75	100.70	99.94	95.75	99.74
StdDev wt%					
Si	0.38	0.54	0.76	0.38	0.53
K	0.08	0.05	0.04	0.06	0.05
Ca	0.26	0.12	0.04	0.25	0.13
Na	0.17	0.33	0.03	0.16	0.33
Al	0.18	0.21	0.02	0.17	0.21
Mg	0.17	0.02	0.02	0.17	0.02
Fe	0.43	0.07	0.07	0.44	0.06
Mn	0.08	0.06	0.06	0.09	0.06
Ti	0.08	0.05	0.05	0.07	0.05
Cr	0.06	0.06	0.05	0.06	0.06
Atomic %					
Si	16.66	22.40	33.32	16.91	22.16
K	0.24	0.03	0.01	0.11	0.04
Ca	3.69	0.68	-	3.62	0.75
Na	2.22	6.91	-	2.11	6.89
Al	6.76	8.40	-	6.44	8.64
Mg	5.27	-	-	5.41	0.00
Fe	5.36	0.02	0.01	5.62	0.01
Mn	0.10	-	-	0.10	0.00
Ti	0.20	0.01	-	0.11	-
Cr	0.01	-	0.01	0.00	-
O	59.50	61.57	66.66	59.57	61.51
Total	100.00	100.03	100.02	100.00	100.01

Table 2 - Electron microprobe analyses of the representative minerals of gabbro samples of the Amasia ophiolite (continued).

N° Lab	AR-09-02	AR-09-03	AR-09-06	AR-09-12	AR-09-14	AR-09-17	AR-10-12
Formation	Plagiogranite	Basalte	Garnet Amphibolite	Gabbro	Basalt	Gabbro	Basalt
SiO2	67.09	44.65	40.20	53.43	46.18	45.43	56.85
Al2O3	9.40	13.66	12.26	14.69	12.76	14.68	17.84
Fe2O3	4.87	11.55	10.93	10.46	10.42	8.37	6.38
MnO	0.10	0.17	0.07	0.16	0.19	0.15	0.16
MgO	2.05	3.23	2.08	4.80	3.66	7.59	2.43
CaO	5.48	8.25	13.15	4.65	10.38	18.45	7.03
Na2O	1.93	3.26	3.96	4.73	2.28	0.40	3.88
K2O	1.11	2.59	2.18	0.88	0.76	0.07	1.84
TiO2	0.60	2.12	2.61	0.88	2.70	0.54	0.50
P2O5	0.08	0.49	0.69	0.10	0.40	0.05	0.23
LOI	6.79	8.59	11.19	4.34	9.45	3.03	2.87
Total	99.49	98.56	99.34	99.11	99.20	98.77	100.01
Mg #	43.5	33.9	25.8	45.6	39.1	62.4	41.1
Rb	36.88	61.18	66.02	6.43	9.98	0.81	44.23
Sr	62.92	115.50	287.50	122.70	407.20	82.16	732.60
Y	17.05	21.23	29.86	20.76	27.02	14.68	16.04
Zr	194.30	204.70	201.40	52.50	176.80	30.50	120.90
Nb	9.89	40.52	35.66	2.38	30.76	0.45	5.82
Ba	122.40	315.90	157.00	93.91	304.90	7.12	683.40
Hf	5.01	4.55	4.67	1.51	4.17	1.07	2.99
Ta	0.83	3.03	2.66	0.20	2.38	0.04	0.40
Pb	11.91	4.89	3.96	u.b.l	3.59	u.b.l	7.62
Th	6.46	3.83	2.95	0.65	2.36	0.13	5.77
U	1.51	0.86	0.91	0.22	0.52	0.06	2.13
V	75.58	187.40	294.40	286.80	244.10	240.10	110.60
Cr	169.50	83.64	u.b.l	13.24	44.39	77.09	6.34
Co	8.97	19.96	32.74	30.39	31.08	35.43	13.83
Ni	50.63	62.66	25.47	23.62	50.84	65.31	5.07
Cu	13.48	8.10	41.51	37.35	61.91	10.59	31.48
Zn	57.65	79.63	154.90	42.99	87.58	63.26	70.12
La	21.08	28.78	32.08	3.83	24.98	1.32	27.03
Ce	41.27	60.41	64.86	8.89	50.84	4.06	47.78
Pr	4.69	7.15	7.85	1.29	6.24	0.68	5.36
Nd	17.45	27.76	31.64	6.33	26.07	3.65	19.88
Sm	3.53	5.62	6.87	2.07	6.00	1.26	3.80
Eu	0.73	1.83	2.22	0.74	2.05	0.51	1.19
Gd	3.11	5.03	6.62	2.70	5.68	1.82	3.15
Tb	0.51	0.74	0.97	0.48	0.89	0.34	0.47
Dy	3.06	4.04	5.57	3.31	5.17	2.31	2.71
Ho	0.60	0.75	1.04	0.73	0.97	0.52	0.53
Er	1.73	2.01	2.78	2.14	2.50	1.55	1.55
Tm	0.26	0.29	0.39	0.33	0.35	0.24	0.24
Yb	1.81	1.83	2.48	2.25	2.24	1.67	1.70
Lu	0.28	0.28	0.37	0.36	0.33	0.27	0.26
Eu/Eu*	1.16	0.99	1.03	1.03	0.96	0.99	0.96
$(La/Sm)_N$	6.87	3.72	3.43	1.22	2.89	0.61	5.37
$(La/Yb)_N$	7.84	10.63	8.93	1.10	7.91	0.50	10.67

Table 3 - Representative whole-rock analyses of samples from ophiolitic complex of Amasia.

Step	Laser power (mW)	Atmospheric cont (%)	$^{37}Ar_{Ca}/^{39}Ar_K$	$^{40}Ar^*/^{39}Ar_K$	Age (Ma±1σ)
Amphibole AR-08-29, J = 0.02, plateau age: 175.8 ± 7.7 Ma (98.1 % ^{39}Ar), isochron age: 178.6 ± 10.8 Ma (MSWD: 3.89)					
1	500	89.95	14.38	6.42	207.66 ± 37.88
2	550	82.87	17.80	5.34	174.58 ± 21.25
3	600	79.45	15.96	5.43	177.13 ± 22.26
4	620	50.92	10.22	5.33	174.20 ± 5.66
5	655	23.29	2.02	5.52	180.02 ± 4.66
6	1111	40.39	22.41	4.92	161.29 ± 3.26
Amphibole AR-09-20, J = 0.02 , plateau age: 169.0 ± 9.7 Ma (97.3 % ^{39}Ar), isochron age: 171.7 ± 7.7 Ma (MSWD: 0.85)					
1	400	94.23	249.87	4.41	145.46 ± 64.99
2	480	36.18	62.65	6.29	204.14 ± 57.74
3	553	12.18	31.99	5.59	182.60 ± 3.43
4	600	10.90	30.49	5.45	178.12 ± 3.29
5	640	19.30	33.62	5.40	176.55 ± 21.48
6	999	11.73	34.69	5.33	174.31 ± 3.54

Table 4 - Amphibole $^{40}Ar/^{39}Ar$ dating results from the ophiolite gabbro samples AR-08-29 and AR-09-20.

Sample	Latitude	Longitude	Elevation m	Age	Nannofossil assemblage	Zonation
AR-08-38	N 40°99631	E 43°77476	1970	Late Paleocene		NP5
AR-08-40	N 40°99631	E 43°77476	1970			NP9
AR-08-41	N 40°99631	E 43°77476	1970	Late Maastrichian		
AR-08-42	N 40°99461	E 43°77882	1970	Late Valanginian - Early Barremian		
AR-08-56	N 40°99581	E 43°75018	2197			
AR-08-57	N 40°99581	E 43°75018	2197			
AR-08-58	N 40°99581	E 43°75018	2197			
AR-08-59	N 40°99581	E 43°75018	2197	Coniacian - Santonian		
AR-08-60	N 40°99581	E 43°75018	2197			
AR-08-61	N 40°99581	E 43°75018	2197			
AR-08-62	N 40°99581	E 43°75018	2197			
AR-08-65	N 40°99051	E 43°75325	2158	Early Eocene		NP12-13 NP16
ARC 01	N 41°01577	E 43°77178	2030	Middle Eocene		
ARC 02	N 41°01577	E 43°77178	2030			

Table 5 - Nannofossils dating with (WGS84) GPS locations.

III.2 Article 2 – P-T-t history of the Amasia ophiolite "metamorphic sole" (Amasia, Lesser Caucasus): implications for the obduction process of an old oceanic lithosphère

Notre cartographie du massif ophiolitique d'Amasia a mis en évidence (1) de la croûte océanique gabbroïque non métamorphisée, (2) des serpentinites ainsi qu'un mélange tectonique de faciès schiste vert et (3) une tranche basale d'amphibolites à grenat incorporée dans ce mélange. Le contact d'obduction initial étant préservé en fait une cible potentielle pour la compréhension des processus correspondant à la propagation d'une nappe ophiolitique en obduction, en particulier concernant les étapes de transport tectonique d'un segment de croûte océanique sur une lithosphère continentale. D'après Meliksetyan *et al.* (1984), les amphibolites à grenat d'Amasia témoignent d'un métamorphisme polyphasé. Ces amphibolites donnent un âge Carbonifère moyen (330 Ma) par la méthode Rb-Sr pour le faciès éclogite, et Santonien-Campanien (80 ± 5 Ma), par la méthode K/Ar attribué au faciès schiste vert par ces auteurs. Cependant, il semble totalement improbable que les amphibolites à grenat se soient formés il y a 330 Ma puisque l'âge de la croûte océanique dont semblent elles dériver est Jurassique ! De plus, l'application de méthodes géochronologiques telles que Rb-Sr et K/Ar sur roche totale sur ces lithologies ayant fortement subi de l'hydrothermalisme, n'est pas appropriée. Nous verrons cependant que le dernier âge de 80 Ma se rapproche fortement de celui que nous avons obtenu par la méthode Ar-Ar.

Dans la section précédente nous avons pu asseoir le fait que toutes les ophiolites arméniennes font partie du même ensemble. 50 km à l'est d'Amasia, le massif ophiolitique de Stepanavan présente aussi des roches métamorphiques, en position basale de l'unité ophiolitique, mais de faciès schiste bleu, localement réchauffé dans le faciès amphibolites (amphibolites à glaucophane-zoïsite avec ou sans grenat) (Galoyan *et al.*, 2007; Rolland *et al.*, 2009a). Les travaux de Morkovkina *et al.* (1982) ont montré en utilisant la méthode K/Ar que ces amphibolites à grenat ont un âge de 164 ± 16 Ma et les amphibolites à glaucophane ont un âge de 90 ± 10 Ma (sur glaucophane). Ce deuxième âge confirme les âges obtenus avec la même méthode sur les mêmes amphibolites à glaucophane de 83-85 Ma (sur glaucophane) par Baghdasaryan & Ghukasyan (1962). Par ailleurs, le glaucophane ne contenant pas de K, il semblerait plutôt que ces auteurs aient pu dater des inclusions de mica blanc. Plus récemment

Rolland *et al.* (2009a), en utilisant la méthode $^{40}Ar/^{39}Ar$ sur phengites, ont montré que les amphibolites à glaucophane de Stepanavan ont subi un métamorphisme polyphasé. L'âge de 95-91 Ma obtenu sur les phengites de haute pression est interprété comme marqueur d'un métamorphisme HP au cours d'une phase de subduction au Cénomanien-Turonien. L'âge de 73,5-71 Ma donné par des phengites associées à un cisaillement de plus basse pression indique que cette première phase de subduction est suivie d'une phase de déformation au cours de l'exhumation dans le faciès schiste vert (épidote-amphibolite) pendant le Campanien supérieur-Maastrichtien. Les auteurs proposent que ceci marque l'entrée dans la subduction sous l'Eurasie du SAB.

En vue de ces nouveaux résultats et interprétations, utilisant la méthode $^{40}Ar/^{39}Ar$ moins sujette à des perturbations dus à des processus géologiques postérieurs, nous avons entrepris une nouvelle étude petro-chronologique des amphibolites à grenat du massif d'ophiolitique d'Amasia. Les roches métamorphiques montrent deux paragenèses : (1) un assemblage grenat-amphibole, entouré par (2) un deuxième assemblage chlorite-phengite. La thermobarométrie révèle un chemin de sens antihoraire défini par (1) un pic HT-LP de $6 < P < 7$ kbar , $T > 630$ ° C et (2) un pic MT-MP à $8 < P < 10$ kbar , $580 < T < 620$ ° C. Nous proposons que cette semelle métamorphique a été amphibolitisée le long d'un gradient très élevé pour ensuite être incorporée dans un mélange de MP-MT. L'incorporation d'écailles de petite dimension dans ce mélange conduit à son refroidissement au cours d'un enfouissement/épaississement, et peut-être à une augmentation légère des conditions de pression.

Les nouvelles datations $^{40}Ar/^{39}Ar$ ont été réalisées sur les amphiboles (hornblende) et micas blanc (phengite) afin de contraindre temporellement les conditions pic des paragenèses HT et MP. Les âges obtenus sont similaires, dans les marges d'erreurs, donnant 90,8 ± 3,0 Ma et 90,8 ± 1,2 Ma pour les amphiboles et les phengites, respectivement. Nous interprétons ces nouvelles données comme un témoin d'une évolution tectonique très rapide. Nous avançons alors un scénario intégrant (1) l'écaillage d'une partie de la croûte océanique et son sous-charriage à l'avant de l'obduction à c. 91 Ma, la croûte océanique chevauchante étant relativement chaude. Ensuite, le système évoluerait jusqu'à (2) l'incorporation de ces écailles dans la partie basale de l'obduction (la semelle) à c. 90-88 Ma.

Ce modèle est soutenu par la subsistance d'un gradient géothermique relativement chaud suite à la mise en place d'OIB à 117 Ma (à Stepanavan; Rolland *et al.*, 2009b) ainsi que

des datations biostratigraphiques (radiolaires; Danelian *et al.*, 2014) témoignant de la mise en place de laves sur la future ophiolite au Cénomanien.

Remarquons que les deux chemins PTt, proposés par Rolland *et al.* (2009a) pour les roches métamorphiques de Stepanavan et celui que nous proposons pour celles d'Amasia, convergent dans des conditions MP-MT (5,5 kbar, 500 ° C). Cela suggère leur couplage dans le prisme d'accrétion de la subduction sous l'Eurasie et donc une exhumation commune au cours de l'Eocène.

Cette étude a fait l'objet d'une publication en qui sera prochainement soumise dans *Journal of the Geological Society*.

P-T-t history of the Amasia ophiolite 'metamorphic sole' (Armenia, Lesser Caucasus): implications for the obduction process of an old oceanic lithosphere

M. Hässig[1,*], Y. Rolland[1], M. Sosson[1], G. Galoyan[2], A. Avagyan[2]

[1] Géoazur, Université Nice-Sophia Antipolis, Centre National de la Recherche Scientifique (UMR 7329), Observatoire de la Côte d'Azur, 250 av Einstein 06560 Valbonne, France.

[2] Institute of Geological Sciences, National Academy of Sciences of Armenia, 24a Baghramian Avenue, Yerevan, 375019 Armenia.

Abstract

The Sevan-Akera suture zone ophiolites form part of a major obduction, up to 300 km of horizontal transport, of the northern branch of Neotethys oceanic crust over the South Armenian/Taurides continental block. The emplacement of these ophiolites occurred throughout Coniacian to Santonian times (91-83 Ma), prior to continent-continent collision. Near the locality of Amasia (NW Armenia), garnet-bearing amphibolites are embedded within a greenschist facies tectonic mélange unit found below the base of the non-metamorphic obducted oceanic unit. The metamorphic rocks show two parageneses: (1) a HT-LP assemblage of garnet-amphibole, surrounded by (2) MP-MT retrogression by chlorite-phengite. Thermobarometry reveals a counterclockwise path defined by (1) a HT-LP peak of $6 < P < 7$ kbar, $T > 630$°C and (2) a MT-MP peak at $8 < P < 10$ kbar, $580 < T < 620$°C. $^{40}Ar/^{39}Ar$ dating on amphiboles (hornblende) and white micas (phengite) yields for both HT and MP peaks similar within-error ages of 90.8 ± 3.0 Ma and 90.8 ± 1.2 Ma, respectively. The PTt history of the metamorphic sole argues for a rapid tectonic process, including the slicing of oceanic crust and its incorporation within an accretionary prism below a relatively hot oceanic crust at c. 91-90 Ma. This metamorphic sole was first amphibolitized along a HT-MP gradient, due to a relatively hot geotherm following the emplacement of OIB at 117 Ma. Secondly, the thickening of the overriding compartment of this subduction zone at c. 90-88 Ma caused these conditions to change to MT-MP, as the South Armenian Block entered the subduction zone. Blueschist facies rocks at Stepanavan (N Armenia) occur in a similar tectonic position along the Sevan-Akera suture farther East. The blueschists show a slightly older HP-LT peak (95-91 Ma) followed by a younger (73-71 Ma) MT-MP peak as compared to the Amasia amphibolites. Both PTt paths converge at MP-MT conditions (5.5 kbar, 500°C) suggesting their coupling in the accretionary prism, and thus inferring common exhumation in the Eocene. The obduction process ended within 1-5 Ma of its onset, at 89-83 Ma, as indicated by paleontological ages in both under-thrusted (sub-ophiolitic) and uncomformably overlying (supra-ophiolitic) sediments.

Key Words: obduction, ophiolite, metamorphic sole, counter-clockwise PT path, Lesser Caucasus

2.1 Introduction

There is still much controversy concerning the explanation of oceanic crust obduction initiation and subsequent transport onto the continental crust. Obducted ophiolite sequences generally include thick slices of undeformed oceanic lithosphere originating from a supra-subduction zone setting, detached from its mantle basement and obducted over a continental margin (Spray, 1983). Models for obduction initiation include an early stage of buckling (Agard *et al*., 2007) or ridge subduction (Hacker, 1991), leading to intra-oceanic thrusting, which may result in the development of a metamorphic sole (e.g., Michard *et al*., 1991). Later, the intra-oceanic subduction process continues to a 'marginal' stage where the oceanic lithosphere is thrusted over the passive continental margin (Dilek and Whitney, 1997; Gray and Gregory, 2000; Engi *et al*., 2001; Bortolotti *et al*., 2005), or under-plated by the latter, known as obduction. The relative position of the initiation of intra-oceanic thrusting, the particular physical and/or geochemical properties of the lithologies forming the involved oceanic lithospheres (e.g., the role played by plume events) and geodynamic settings recorded throughout the metamorphic processes are still subject to debate (e.g., Agard *et al*., 2007).

The reconstruction of the geodynamic evolution of oceanic basins that were formed in the Neo-Tethyan domain allows better identification and understanding of the role of the dominant factors involved in oceanic closure, including obduction processes. Key examples of obducted ophiolite sequences are found throughout the Tethyan collisional belts (Adamia *et al*., 1981; Göncüoğlu and Turhan, 1984; Hempton, 1985; Zakariadze *et al*., 1990; Yılmaz, 1993; Lytwyn and Casey, 1995; Carosi *et al*., 1996; Hacker *et al*., 1996; Searle and Cox, 1999; Okay *et al*., 2001; Ding *et al*., 2005; Barrier and Vrielynck, 2008; Galoyan, 2008; Gaggero *et al*., 2009; Agard *et al*., 2010; Oberhänsli *et al*., 2010; Parlak *et al*., 2012; Rolland *et al*., 2012). Part of the history of central and northern Neotethys can be deduced from both the study of the oceanic crust obducted in the Armenian Lesser Caucasus and of the metamorphic rocks found directly underneath the ophiolite bodies, whose formation is linked to ophiolite emplacement (e.g., Sengör and Yılmaz, 1981; Ricou *et al*., 1985; Dercourt *et al*., 1986; Ricou, 1994; Harper *et al*., 1996; Dilek and Whitney, 1997; Okay and Tüysüz, 1999; Zakariadze *et al*., 2005; Elitok and Drüppel, 2008; Festa *et al*., 2010). Such 'suture zone' lithologies provide key timing and palaeogeographic data for geodynamic reconstructions of the still puzzling region stretching from the Mediterranean area to SE Asia (Stampfli and Borel, 2002; Robertson, 2004; Barrier and Vrielynck, 2008; Galoyan *et al*., 2009; Rolland *et*

al., 2010; Sosson *et al*., 2010). Furthermore, their geometry and geochemistry provide key information in order to reconstruct the nature of the oceanic domain which has now disappeared (Cloos and Shreve, 1988; Ellis *et al*., 1999; Engi *et al*., 2001; Stampfli *et al*., 2001; Federico *et al*., 2007; Galoyan, 2008; Gaggero *et al*., 2009; Guilmette *et al*., 2009; Rolland *et al*., 2009a) and thus the setting prior to metamorphism of subducted rocks. The Armenian part of the Lesser Caucasus region features intact and unmetamorphosed sections of obducted oceanic crust. These unique and remarkable objects were only slightly affected by the later collisional history, featuring both its metamorphic sole and its sedimentary front (Sosson *et al*., 2010; Rolland *et al*., 2012; Hässig *et al*., 2013), which enables to further reconstruct part of the obducted ophiolite nappe geometry and history.

In this paper we report new structural, petrologic, geochemical and $^{40}Ar/^{39}Ar$ chronological data obtained on the garnet amphibolite outcrop from the basal tectonic contact of the Amasia ophiolite (NW Armenia). The results obtained concerning these metamorphic rocks are coherent with a counterclockwise Pressure-Temperature-time (P-T-t) path for this unit. This path complements previous P-T-t estimates of the metamorphic rocks outcropping above the South Armenian Block (SAB) and below the obducted ophiolites in the area of Stepanavan (Rolland *et al*., 2009a). Based on the metamorphic data we propose a geodynamic reconstruction for the obduction of the Lesser Caucasus ophiolites in Armenia.

2.2 Geological setting

The study of Armenian ophiolites and associated lithologies allows the reconstruction of the northern part of the Neotethyan domain and thus identifies the processes undergone throughout the formation of this region, which the first step is progressive terrane accretion (Pourteau *et al*., 2013).

Previous works on these ophiolites along the Sevan-Akera Suture Zone in the 1970's and 1980's show a Jurassic age and multiple geochemical tendencies, interpreted as formed in a supra-subduction domain (e.g., Palandjyan, 1971; Knipper, 1975; Sokolov, 1977; Knipper and Sokolov, 1977; Knipper and Khain, 1980; Abovyan, 1981; Adamia *et al*., 1981; Zakariadze *et al*., 1983; Knipper *et al*., 1986). More recently, several authors propose models including include Neotethyan oceanic crust obduction in the Coniacian times and collision–accretion of microplates to the Eurasian margin in the Upper Cretaceous-Paleogene, before the final Arabia–Eurasia collision (Yilmaz *et al*., 1993; Knipper *et al*., 1997; Okay *et al*.,

2001; Galoyan *et al*., 2007; 2009; Rice *et al*., 2009; Rolland *et al*., 2009a; 2009b; 2011; 2012; Agard *et al*., 2010; Sosson *et al*., 2010; Pourteau *et al*., 2013).

North of the Sevan-Akera Suture zone, in the Georgian part of the Lesser Caucasus, a thick magmatic arc formed above north-dipping subduction is dated to the Upper Jurassic Lower Cretaceous times (e.g. Adamia *et al*., 1981 for a review).

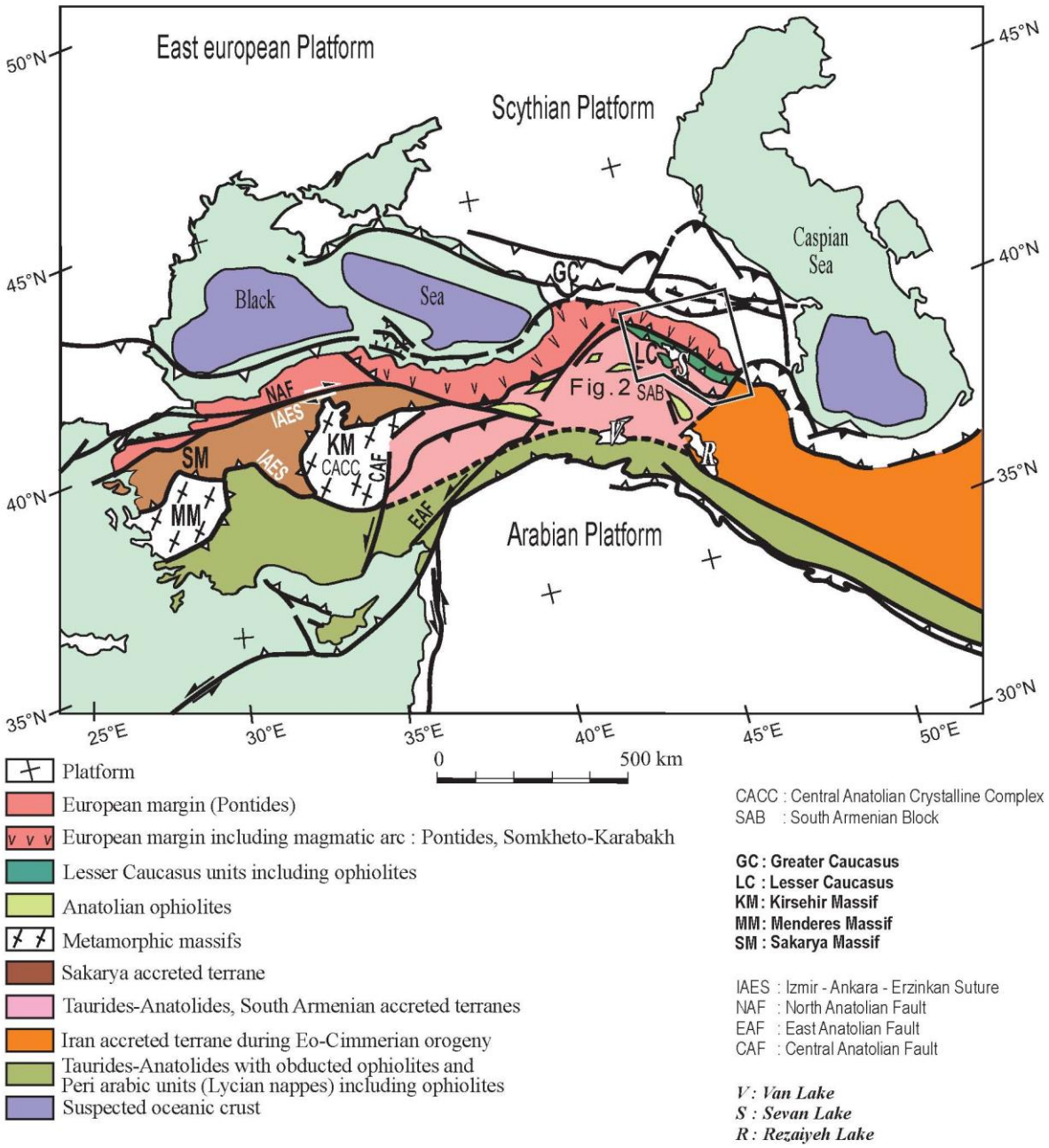

Figure 29 - Tectonic map of the Middle East–Caucasus area, with main blocks and suture zones, after Avagyan *et al*. (2005), modified. Location of Figure 30 indicated.

South of the obducted ophuiolite, the South Armenian Block (SAB) (Knipper, 1975; Knipper and Khain, 1980) is a Gondwanian originating microplate corresponding to the

Taurides-Anatolides (Sengör and Yılmaz, 1981; **Figure 29**). Coniacian to Santonian (90-83 Ma) obduction onto the SAB is marked by flysch series reworking the ophiolites at the obduction front and reef series of identical age sealing the obduction nappe in the southern part of the SAB (Vedi area: Sokolov, 1977; Sosson *et al*., 2010; **Figures 30** & **31**). These geological observations imply that two subduction zones were active at the same time: North of the SAB and south of the Georgia Eurasian margin (Rolland *et al*., 2011). Collision of the SAB with the Eurasian margin is dated as Late Cretaceous-Paleocene (Rolland *et al*., 2012). This collision/accretion results in a subduction jump to the south of the Taurides-Anatolides. This process occurred around 10 Ma after the obduction (Late Coniacian–Santonian, 88–83 Ma). In the Bitlis-Pütürge massifs of SE Turkey High Pressure (HP) metamorphic evolution is bracketed between 82-79 Ma in the Bitlis and 74-71 Ma in the Pütürge massif (Hempton, 1985; Oberhänsli *et al*., 2010; 2014; Rolland *et al*., 2012).

For a synthesis concerning the Lesser Caucasus ophiolites, we refer toGaloyan *et al*. (2007, 2009), Rolland *et al*. (2009b, 2010) and Hässig *et al*. (2013). These works evidence the following relations within the ophiolite nappe structure: (1) serpentinites cross-cut by gabbros dated at c. 175-165 Ma and overlain by basalts and radiolarites of similar age (Danelian *et al*., 2010). These rocks have tholeiitic compositions contaminated by subduction components. (2) Above these series, alkaline Ocean Island Basalt (OIB) pillow lavas emplaced in the Lower Cretaceous times.

The Amasia ophiolite is part of the ophiolite belt in northern Armenia (**Figure 30**). In Stepanavan, East of Amasia, ophiolites have been described in association with blueschist and amphibolite facies metamorphic rocks dated at 94-91 Ma, High Pressure (HP) peak, to 73-71 Ma, High Temperature (HT) retrogression (Rolland *et al*., 2009a). These metamorphic rocks evidence the presence of a subduction zone active in the Middle Cretaceous and stopping in the Late Cretaceous at 80-75 Ma (Rolland *et al*., 2011).

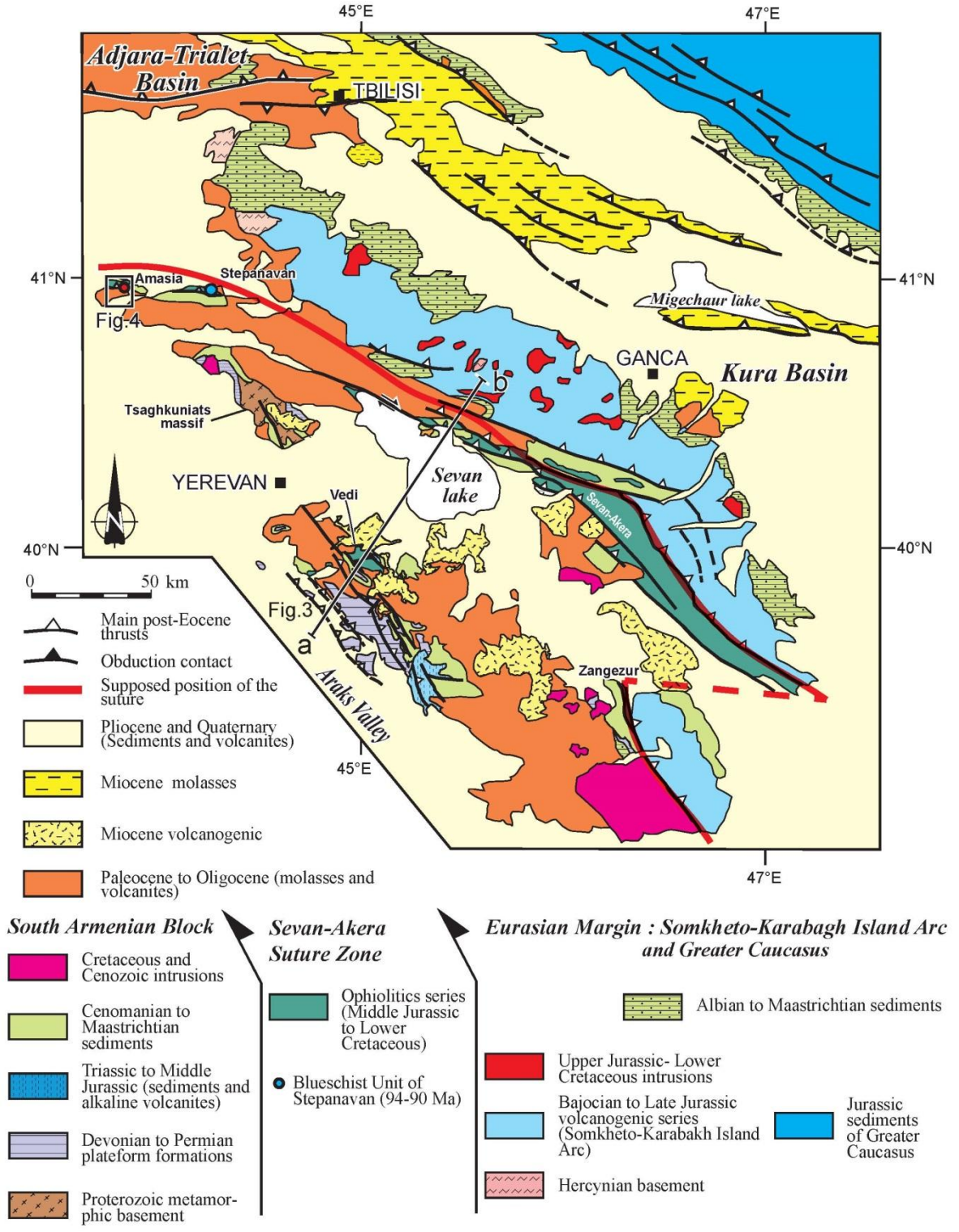

Figure 30 - Structural map of the Lesser Caucasus modified from Sosson *et al*. (2010). Location is indicated on Figure 29. Plot of geological section Figure 31 and location of Figure 32 indicated.

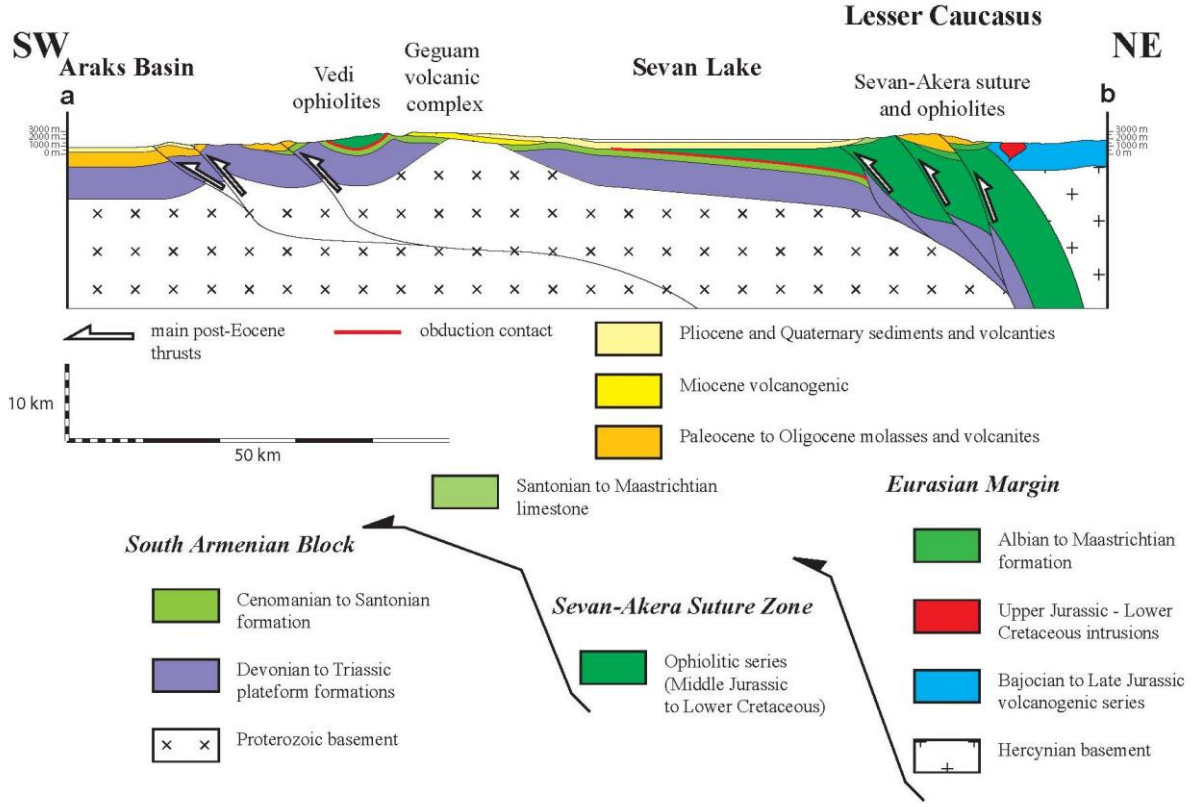

Figure 31 - Interpretative crustal-scale sketch cross-section of the Armenia-Azerbaijan transect. Location is indicated on Figure 30.

2.3 Field Observations

A full description of the geology of the Amasia ophiolite is provided in Hässig *et al.* (2013), which is summarized below. According to the field observations, the geological map and cross-sections (**Figures 32**, **33A** & **33B**), three main lithotectonic units have been identified (from top to bottom):

1 - An upper ophiolitic unit constituted by serpentinites, gabbros, basaltic pillow lavas and volcanic rocks with interlayered reef limestones. This unit, as in other localities in Armenia, is interpreted as representing un-metamorphosed obducted oceanic crust formed during mid-Jurassic times (dated at 169.0±4.6 to 175.8±3.9 Ma by $^{40}Ar/^{39}Ar$ on gabbro amphibole; Hässig *et al.*, 2013). Ending of obduction is constrained by a Coniacian-Santonian (88-83 Ma) detrital deposit reworks elements from the entire ophiolite, deposited on top of this unit.

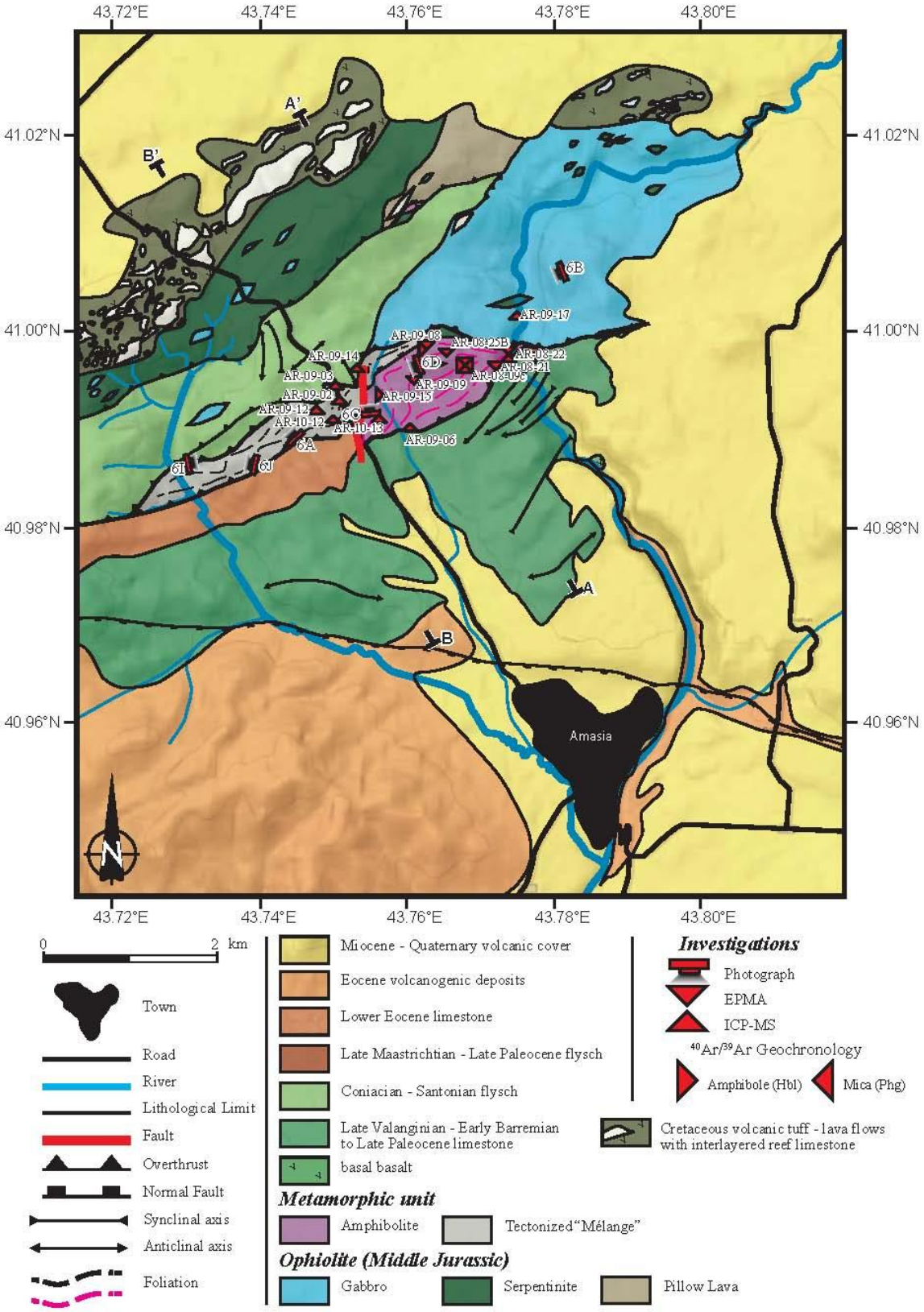

Figure 32 - Structural map of the Amasia ophiolite window. Location is indicated on Figure 30. Plot of geological sections of Figure 33B along with the locations of photographs of Figure 34 as well as of samples investigated through ICP-MS, EPMA, and $^{40}Ar/^{39}Ar$ geochronology methods of Figures 36, 37 & 39, respectively.

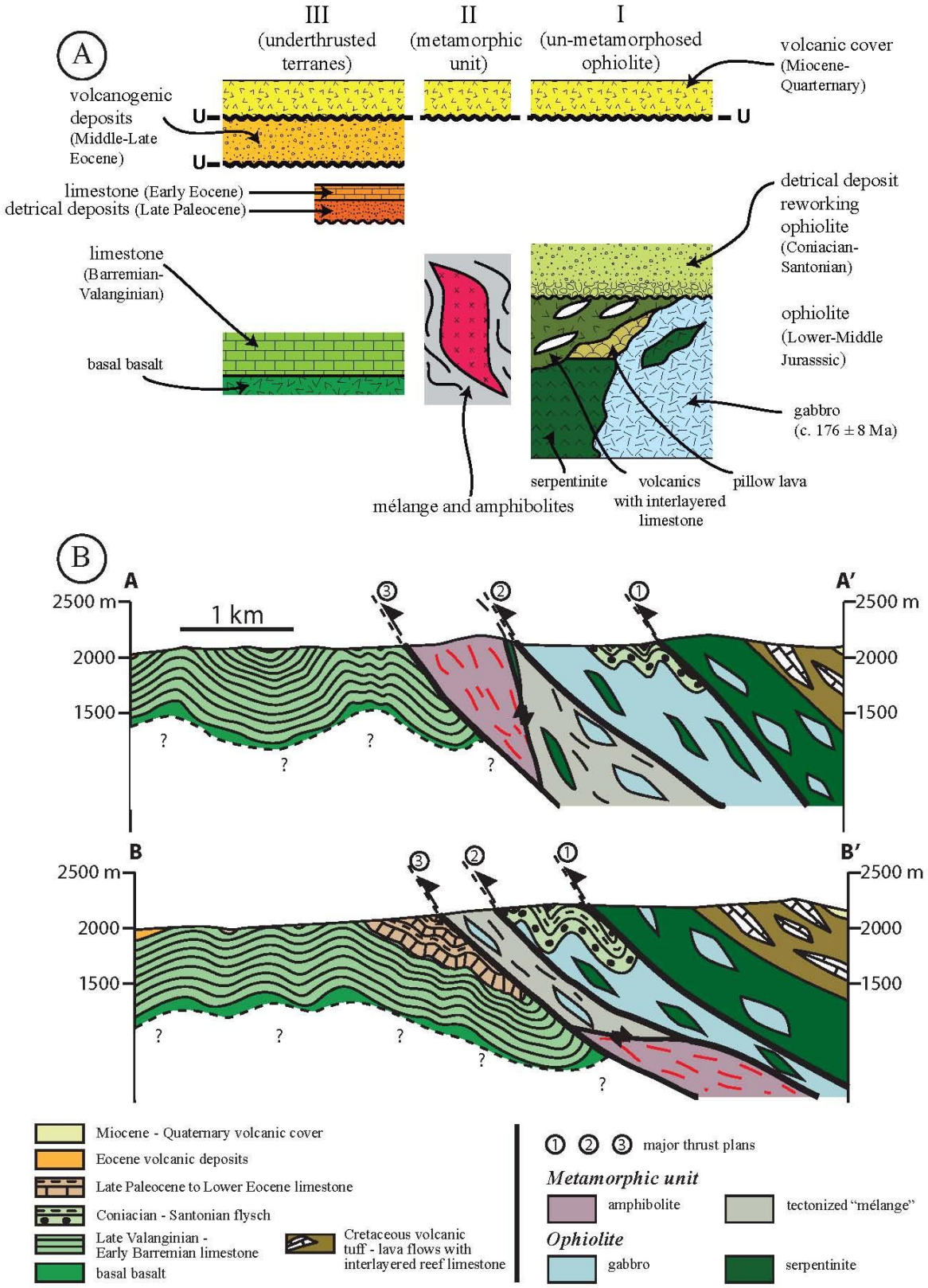

Figure 33 - (A), synthetic litho-stratigraphic record of the three main units of the Amasia ophiolite window; I) upper unit corresponding to the un-metamorphosed ophiolite, II) metamorphic unit comprising of the tectonic mélange and the lens of garnet bearing amphibolites, III) the lower (Southern) unit. (B), sketch geological cross sections of Amasia ophiolite. Locations are indicated on Fig. 32.

2 - Thrusted by the ophiolitic unit, a tectonic mélange of low grade (greenschist facies) meta-basalts, meta-cherts and metamorphosed serpentinites (**Figures 34A**, **E** & **F**) is exposed, which includes lenses of ophiolites and metasediments (**Figures 33B** & **34B**). The limestone blocks incorporated in this mélange are marbleized and arranged in elongated boudins along with serpentinites and basalts (**Figure 34A**). Kinematics indicate top-to-the-south sense of shear. Within this tectonic mélange a kilometric-size (≈ 2 km²) boudin of garnet bearing amphibolites has been mapped (**Figure 34B**). The garnet-bearing amphibolite body also has an elongated shape in the ENE-WSW direction. Amphibolites show a penetrative foliation marked by alternations of amphibole and garnet-rich dark levels alternating plagioclase and quartz-rich lighter colored levels (**Figures 34C** & **34D**). The lineation of the chlorites and phengites along with that of amphiboles and the presence of rolled garnets evidences that this unit was tectonized, with a southward sense of shear (**Figure 35**).

3 - These two units are thrusted on top of a southern (third) unit comprising brecciated basalts overlain by Lower Cretaceous limestones, unconformably covered by late Paleocene flysch grading up into Lower Eocene limestone and Mid- to Upper Eocene volcanogenic deposit. This structure features timing for final collision of SAB and Eurasia as in all of the Lesser Caucasus (see Sosson *et al*., 2010). Ongoing post-collisional magmatism is represented by a Miocene to Quaternary volcanic cover sealing the nappe-stack.

Figure 34 - (A), landscape photography of greenschist facies tectonized mélange zone featuring marbleized limestone blocks. The W-E extension and scattering of the limestone is in accordance with North to South convergence and thrusting. (B), garnet-bearing amphibolite body thrusted to the south above Cretaceous limestone. The gabbro is also thrusted to the south onto the amphibolite body in lateral continuation of a tectonized mélange. (C), field photography of garnet amphibolites. The foliation and lineation are underlined by the red plan and black double arrow, respectively. (D), photography and sketch of garnet amphibolite outcrop. The garnets (red) are preferentially located in the levels rich in white minerals (light grey), and underline the foliation as well as mineral lineation. The yellow represents moss and lichen. (E) and (F), representative field photographies and sketches of greenschist facies rocks. Intense deformation is featured by C-S structures, scaling and molding of brecciated mélange elements. Locations of viewpoints are indicated on Fig. 32.

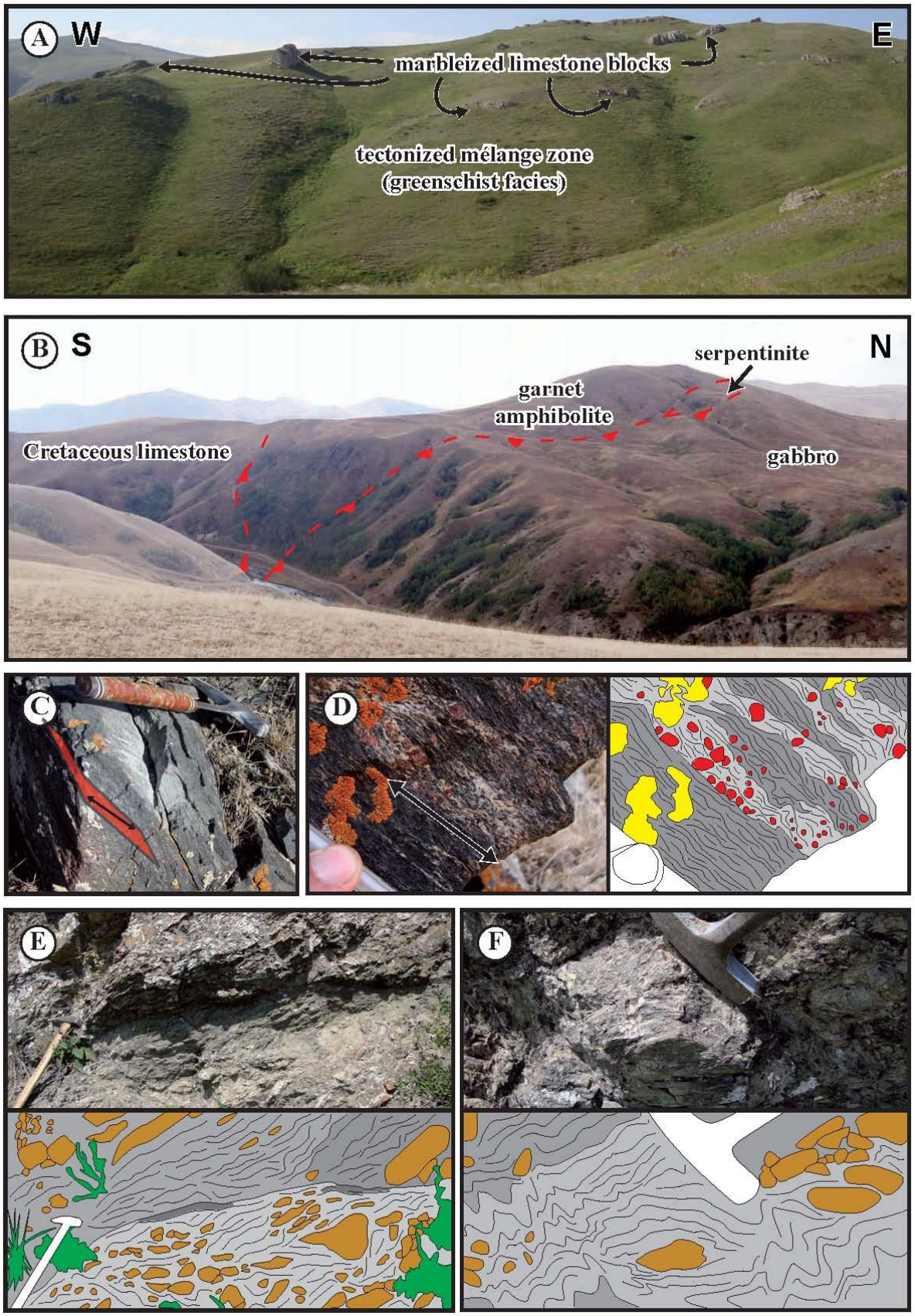
A
W
E
marbleized limestone blocks
tectonized mélange zone
(greenschist facies)
B
S
N
serpentinite
garnet
amphibolite
Cretaceous limestone
gabbro
C
D
E
F

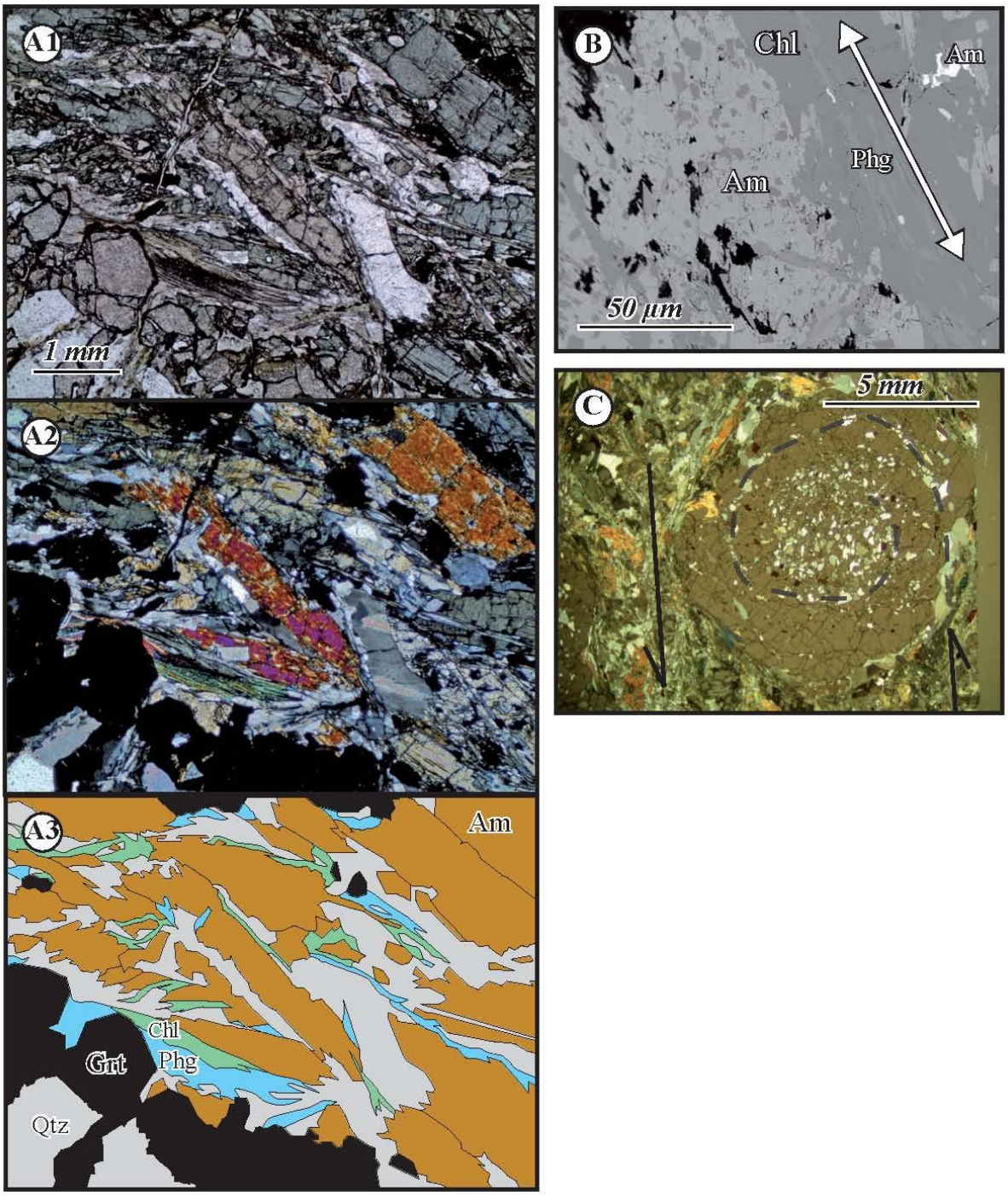

Figure 35 - (A1) and (A2), photographs of a thin section of garnet amphibolite sample AR-08-09c in plain and cross-polarized light, respectively. (A3), sketch of thin section photographs. Cross cutting relationships of amphiboles with micas (Phg) and chlorites (Chl) indicate the existence of amphiboles (Phg) prior to micas. This is also supported by the garnets (Grt) and amphiboles, which are molded by micas and chlorites. (B), back-scatter image of garnet amphibolite sample AR-09-08. Lineation is exhibited with the alignment of amphiboles (Am), white micas (Phg) and chlorites (Chl). (C), microscope photography of garnet amphibolite sample AR-09-09. The garnet is rolled in response to syn-kinematic growth during shearing.

2.4 Geochemistry

The ophiolite lithologies have already been linked to the other Lesser Caucasus ophiolites, namely the Stepanavan, Sevan and Vedi ones, and NE Anatolian ophiolites (Refahiye, Şahvelet and Karadağ) (Hässig *et al*., 2013; 2014). The different ophiolites may represent one major obduction (Galoyan *et al*., 2009; Rolland *et al*., 2009b; 2010; Yılmaz *et al*., 2013).

Two rock groups were analyzed: (1) magmatic rocks (basalt, gabbro and plagiogranite) from the preserved ophiolite unit and (2) metamorphic rocks (garnet-amphibolites) from the tectonic mélange, which leads to the identification of two distinct geochemical tendencies (**Figure 36**; **Table 6**). Analytical procedures may be found in Appendix S1.

2.4.1 Supra-subduction tholeiitic signature

As already evidenced in previous works (Hässig *et al*., 2014 and references therein) tholeiitic (MORB-type) affinity is found for the gabbro samples with, to a lesser extent, some fertile contamination as for some basalt samples, with slight trace element variations indicative of a supra-subduction environment (**Figures 36A**, **B**, **C** & **D**). Negative Eu and Ti anomalies with relative Nb-Ta depletion, is interpreted as resulting from the melting of mantle source contaminated by subduction fluids. The ophiolite assemblage is suggestive of an oceanic crust in a back- or fore-arc basin position.

Similarly to those unmetamorphosed ophiolitic rocks, the analyzed Stepanavan amphibolite from the sub-ophiolitic metamorphic rocks has a tholeiitic affinity, mainly characterized by enrichments in LILEs (e.g., Ba, Th, U) and negative Nb, Zr, and Sr anomalies which also resemble those of subduction-related arc volcanics (Perfit *et al*., 1980; Pearce *et al*., 1984). It is possible that these amphibolites share a common origin as ophiolite.

Figure 36 - Diagrams of Amasia and Stepanavan ophiolitic rocks. (A), Ti/Y versus Nb/Y (after Pearce 1982). (B), Zr/Ti versus Nb/Y rock classification diagram (after Pearce, 1996). (C), Ta/Yb versus Th/Yb diagram (after Pearce, 1982) for source characteristics for ophiolitic and associated rocks of the Amasia and Stepanavan ophiolites. (D), N-MORB normalized multi-element spider diagrams. Normalizing values are from Sun and McDonough (1989). Locations of samples of the Amasia ophiolites are found on Fig. 32, as well as results of geochemical ICM-MS analyses in Table 10.

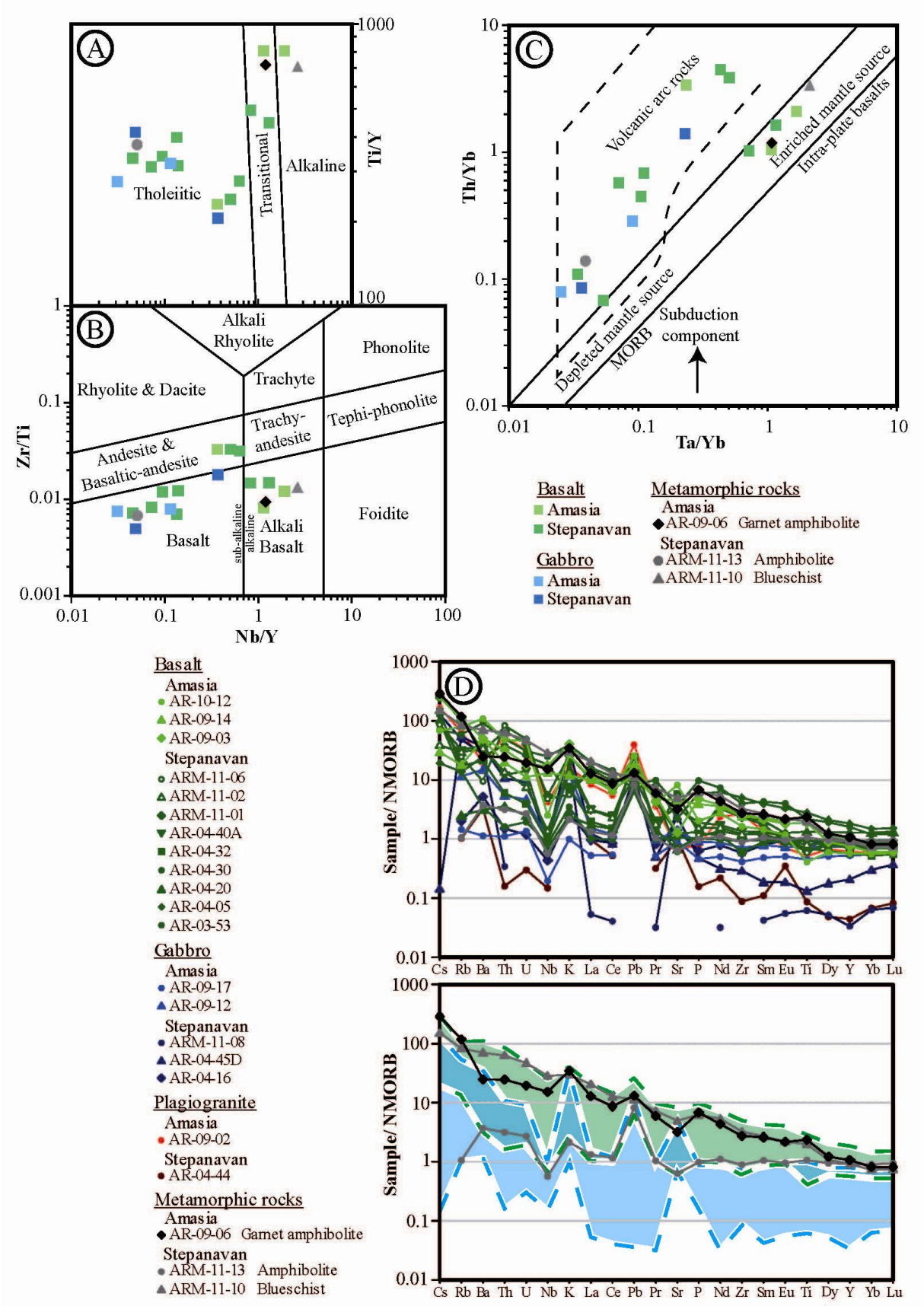
A
Tholeiitic
Transitional
Alkaline
Ti/Y
1000
100
1
B
Alkali Rhyolite
Phonolite
Rhyolite & Dacite
Trachyte
Tephi-phonolite
Trachy-andesite
Andesite & Basaltic-andesite
Basalt
sub-alkaline
alkaline
Alkali Basalt
Foidite
Zr/Ti
Nb/Y
0.001
0.01
0.1
1
10
100
C
Volcanic arc rocks
Enriched mantle source
Intra-plate basalts
Depleted mantle source
MORB
Subduction component
Th/Yb
Ta/Yb
0.01
0.1
1
10
Basalt
Amasia
Stepanavan
Gabbro
Amasia
Stepanavan
Metamorphic rocks
Amasia
AR-09-06 Garnet amphibolite
Stepanavan
ARM-11-13 Amphibolite
ARM-11-10 Blueschist
Basalt
Amasia
AR-10-12
AR-09-14
AR-09-03
Stepanavan
ARM-11-06
ARM-11-02
ARM-11-01
AR-04-40A
AR-04-32
AR-04-30
AR-04-20
AR-04-05
AR-03-53
Gabbro
Amasia
AR-09-17
AR-09-12
Stepanavan
ARM-11-08
AR-04-45D
AR-04-16
Plagiogranite
Amasia
AR-09-02
Stepanavan
AR-04-44
Metamorphic rocks
Amasia
AR-09-06 Garnet amphibolite
Stepanavan
ARM-11-13 Amphibolite
ARM-11-10 Blueschist
D
Sample/ NMORB
1000
100
10
1
0.1
0.01
Cs Rb Ba Th U Nb K La Ce Pb Pr Sr P Nd Zr Sm Eu Ti Dy Y Yb Lu

2.4.2 Alkaline signature

The second affinity is represented by rocks with an alkaline basalt composition (i.e. Hässig *et al*., 2014) (**Figure 36A**, **B**, **C** & **D**). The garnet bearing amphibolites of Amasia Stepanavan blueschists have a similar composition to alkaline basalts, which may suggest a similar origin. For all these rocks, the diagrams are consistent with an OIB signature. In particular, the samples show neat depletions in HREE, which is ascribed to a source containing garnets (e.g., Rollinson, 1993).

The geochemical characteristics and age of the Amasia ophiolite suggest a formation in a marginal basin at Jurassic times in a supra-subduction zone setting (fore- or back-arc). Further, the similar ages and compositions concerning the obducted ophiolites onto the SAB strongly suggest that these are scattered relics of a major obduction event.

In N-MORB normalized multi-element spidergrams (**Figure 36D**) the alkaline amphibolite and blueschist samples display patterns with enrichments in incompatible elements and slightly negative Nb and Sr anomalies. These patterns are consistent with those of typical ocean island basalts (Sun and McDonough, 1989). Such a setting has already been documented by Galoyan *et al*. (2007, 2009) and dated at 117 Ma for alkali pillow lavas in the Vedi area (Rolland *et al*., 2009b).

2.5 Petrography and mineral chemistry

Two parageneses have been identified in the garnet bearing amphibolites after optical microscope observations (**Figure 35**), comprising of (1) an amphibolite facies paragenesis (amphibole-plagioclase-garnet), and (2) a retrogressive greenschist facies paragenesis (white mica-chlorite). In the following, mineral name abbreviations are following Kretz (1983). Analytical procedures may be found in Appendix S1.

2.5.1 Amphibolites

The amphibolites paragenesis found in the rocks of the kilometer-scale garnet-amphibolite lens included in the mélange, underlaying the obducted ophiolite, are characterized by garnet, amphibole, rutile and plagioclase (**Figure 35**).

The *garnets* are polyhedral, globular, millimetric to centimetric in size with numerous quartz inclusions. The inclusions found in some garnets are arranged along a ‘snow-ball’ spiral pattern (**Figure 35C**), evidencing growth during simple shear deformation. Garnets are

intensely fractured and corroded. Fractures and rims are infilled and molded by phengites and chlorites. Microprobe analyses (**Table 7**; **Figure 37A**) show that garnets are solutions of almandine (57.8 to 68.6 %), pyrope (8.1 to 32.9 %), grossular (7.3 to 27.6 %) and spessartite (0.05 to 5.1 %) end members. Two tendencies have been identified: low pyrope (AR-08-09c and AR-09-09) and low grossular compositions (AR-09-08). Transects do not evidence any significant zoning in the garnets (**Figure 37B**). These observations imply that the garnets have grown syn-kinematically under relatively homogenous pressure and thermal conditions throughout their crystallization.

The *amphiboles* of the Amasia amphibolites underline the foliation (**Figure 34C**, **34D**, **35A**). These minerals are fractured. The amphiboles are molded as well as cross-cut by phengite and chlorite. They have fairly homogenous compositions (**Table 8**; **Figure 37C**). A slight increase of Fe and Ca to the detriment of Mg is observed form core to the mineral edges. These only minor variations indicate that the amphibole crystallization occurred in almost constant pressure and temperature conditions. The amphiboles observed are all of high temperature type, and are of intermediate compositions between barroisite, pargasite, tschermakite and edenite poles (Leake *et al*., 1997). The amphiboles being in textural equilibrium with the garnets, we argue for their common formation in a high temperature context.

Rutiles are found in all the amphibolites. They are associated with the different mineral phases. Many of them have a dark aureole of ilmenite, formed during a stage of retromorphosis. The scarce plagioclases are of intermediate composition (between oligoclase and andesine). Both rutiles and plagioclases are in textural equilibrium with amphiboles and garnets.

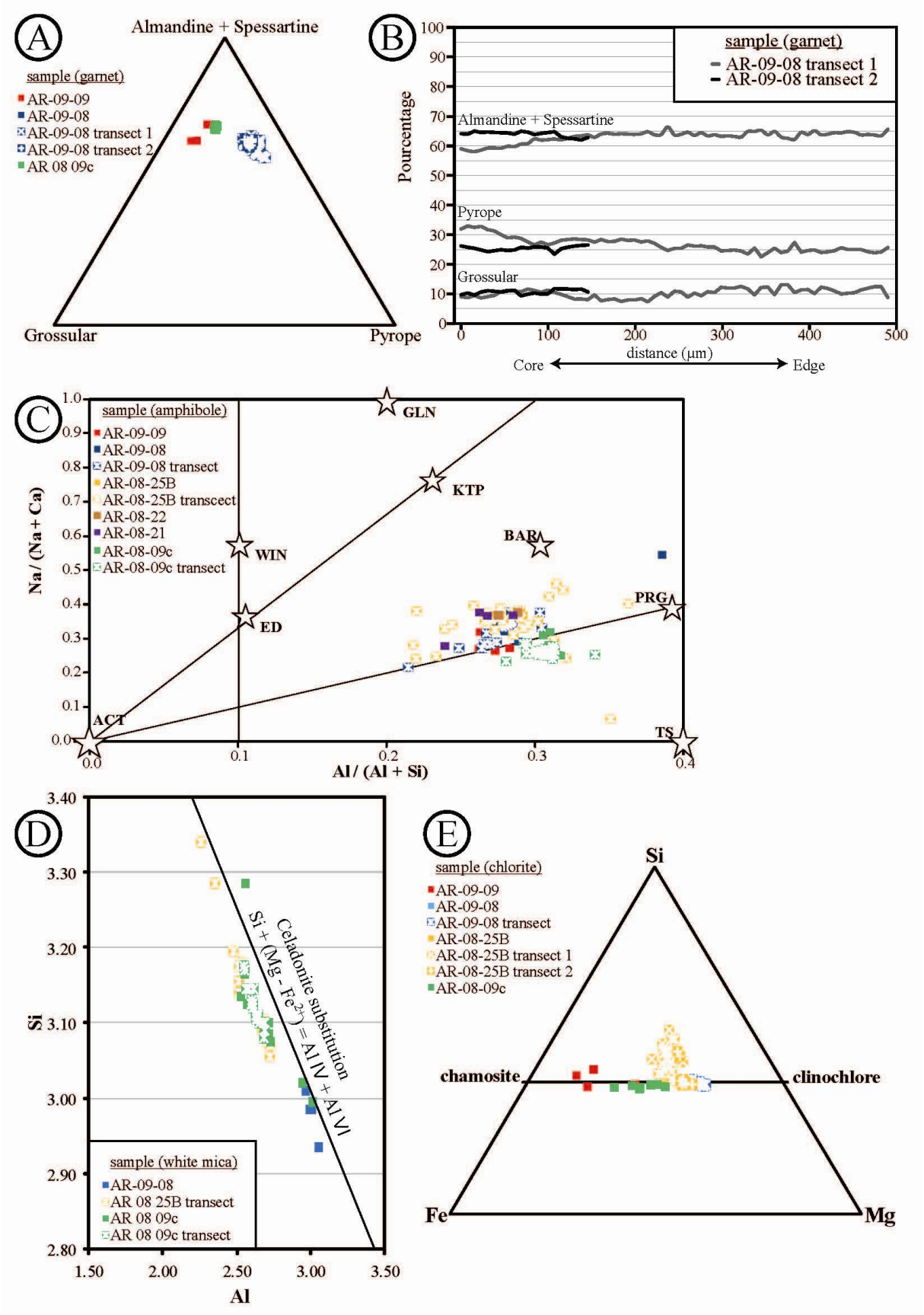

Figure 37 - Diagrams of analyzed of Amasia garnet amphibolite minerals. (A), triangular plots showing chemical compositions of Amasia amphibolite garnets. (B), compositional profiles of two garnets of the Amasia amphibolites.

Note that the garnets are relatively homogenous in composition from core to rim. (C), Na/Ca+Na vs. Al/Al+Si ratios of amphiboles from amphibolite samples, abbreviations are according to Kretz (1983). (D), Si versus Al in white micas from amphibolite samples. (E), triangular plots showing chemical compositions of Amasia amphibolite chlorites. Locations of samples are indicated on Figure 32, as well as EPMA results in Tables 6, 7, 8 & 9.

2.5.2 Greenschists

The greenschist facies paragenesis is evidenced by the presence of chlorites, epidotes and white micas. The chlorites, epidotes and phengites most often wrap and mold the amphiboles and garnets, while chlorites and epidotes consume the amphiboles throughout their growth (**Figures 35A** & **B**), which suggests the following reaction:

$$Amph + Grt + Pl + H_2O \rightarrow Ep + Chl + Phe + Qtz \quad (1)$$

The analyzed chlorites (**Table 9**) mostly range at intermediate X_{Fe} [Fe/(Fe+Mg)] contents ($0.57 < X_{Fe} < 0.78$) (**Figure 37E**).

The white micas are phengitic. They are intermediate solid solutions of muscovite and celadonite with a level of Si^{4+} substitution varying between 2.94 and 3.34 p. f. u. and a mean value of 3.12 ± 0.07 (**Figure 37D**; **Table 10**). In laboratory experiments, the Si content of phengite increases progressively with increase in pressure (Velde, 1965; Massonne and Schreyer, 1987; Domanik and Holloway, 1996; 2000). These compositions agree with crystallization of the phengites during a relatively short stage of the PT evolution as evidenced by low standard deviation for analyses of Si substitution. Locally, paragonites are interlayered within the phengites.

2.6 Pressure-Temperature path of the Amasia amphibolites

The Pressure (P) - Temperature (T) history is investigated using pseudosection modeling as well as thermo-barometric calibrations using mineralogical and whole-rock composition of the sample AR-08-09c, which has been dated by $^{40}Ar/^{39}Ar$ on amphibole and phengite (see section $^{40}Ar/^{39}Ar$ Dating). Supplementary samples (AR-08-25B, AR-09-08 and AR-09-09) have been selected to investigate the degree chemical and PT variability within the amphibolite unit.

2.6.1 Perpl_X pseudosection modeling

The pressure and temperature conditions of amphibolite facies paragenesis were investigated using pseudosection modeling performed in SiO_2-Al_2O_3-FeO-MgO-CaO-Na_2O-K_2O-TiO_2 system and calculated with Perple_X 6.6.6 (Connolly, 2009), using the internally consistent thermodynamic database of Holland and Powell (2003) and Connolly and Kerrick (2002). Solution models used are chlorite [Chl(HP)], phengite [Pheng(HP)], garnet [Gt(HP)], plagioclase [Pl(h)], amphibole [GlTrTsPg] and orthopyroxene [Opx(HP)] (solution model references available at http://www.perplex.ethz.ch/PerpleX_solution_model_glossary.html). Average bulk compositions used as model input are given in **Table 6**. NaCaKFMASH P-T pseudosection for this sample of garnet amphibolites is presented for this bulk composition in **Figure 38A**. Mineral abbreviations used are those of Kretz (1983).

In order to better constrain P-T conditions of the garnet-amphibole paragenesis, Al p.f.u. isopleths in amphiboles were calculated using EPMA amphiboles analyses (**Table 8**). In view of fairly homogenous EPMA compositions of amphiboles, constraints were brought to the model. The resulting domain corresponds to Al content ranging from 1.55 to 1.65 p.f.u., which corresponds to HT-LP metamorphic conditions ($T>625°C$ and $5.5<P<6.8$ kbar) for the first garnet- amphibole paragenesis.

2.6.2 Thermobarometric calibrations

Two parageneses are texturally identified: the first HT one is featured by the stability of amphibole and garnet, while the second lower temperature one is featured by chlorite and phengite overgrowths. For the first paragenesis garnet–amphibole geothermometry (Perchuk *et al*., 1985) was used to constrain the thermal conditions of the HT-LP assemblage. An advantage of using partitioning of Fe and Mg between garnet and coexisting ferromagnesian minerals in metamorphic rocks lies in their significant variation with temperature (Råheim and Green, 1974; Ferry and Spear, 1978; Krogh and Råheim, 1978; O'Neill and Wood, 1979; Ellis and Green, 1979; Green and Hellman, 1982; Graham and Powell, 1984) and the independence of these calculated temperatures with the fugacities of volatile species throughout metamorphism. Representative EPMA analyses of garnet and amphibole mineral phases were used. Amphibole and garnet oxide percentages were acquired from a polished thin section of samples AR-08-09c, AR-09-08 and AR-09-09 (**Tables 7** & **8**). The results are plotted as frequencies of temperatures obtained for combinations of amphibole-garnet pairs on

Figure 38B. The resulting calculated temperatures of 625~675°C validate and precise the thermal conditions calculated using Perpl_X thermodynamic modeling.

2.6.3 Phengite-Quartz-H_2O thermometry

The second paragenesis, formed in the greenschist facies, overprints the amphibolite facies (garnet+amphibole) paragenesis. In order to evaluate the P-T conditions of this greenschist facies retrogression the phengite–quartz–water method documented by Dubacq *et al*. (2010) was applied to each phengite EPMA analysis acquired in samples AR-08-09c, AR-08-25B and AR-09-08. Dubacq *et al*. (2010) showed that the mica–quartz–water equilibrium could be used as a barometer at given temperature conditions. For each phengite analysis a divariant P–T line, along which the interlayer water content varies, was calculated; the results are plotted in **Figure 38C**. The P-T lines depict geothermal gradients ranging from 10 to 45 °C/km with bulk spread along 20 ± 5°C/km.

In order to better constrain P-T conditions of the greenschist paragenesis, Si p.f.u. isopleths in phengite were calculated and plotted with the phengite EPMA analyses of dated sample AR-08-09c (**Table 10**) using Perpl_X thermodynamic modeling. In view of fairly homogenous EPMA compositions of phengites, constraints were brought to the model. The resulting domain (**Figure 38D**) corresponds to Si^{4+} content equal to or inferior to 3.14 p.f.u., in agreement with the mica-quartz-water calibrations. Resulting values (T = 580~620°C and P = 8~10 kbar) are in agreement with MT-MP metamorphic conditions featuring a thermal retrogression at slightly higher pressure of the former amphibolite-facies minerals.

In conclusion, the two metamorphic steps are relatively close in the P-T space. They suggest an anticlockwise PT path (**Figure 40**) at slightly higher temperature and lower pressure conditions than neighboring Stepanavan blueschists (Rolland *et al*., 2009a).

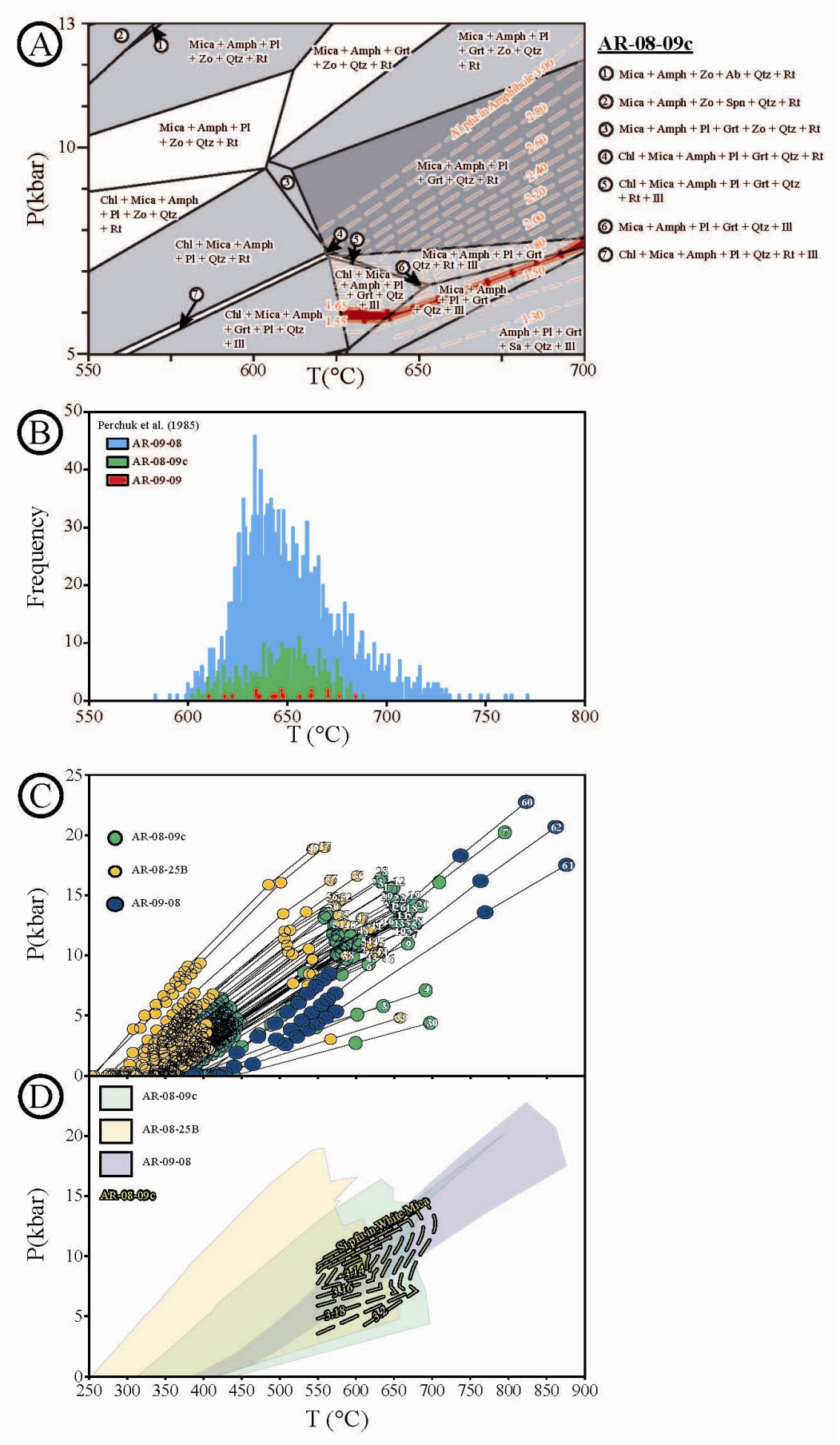
A
AR-08-09c
1 Mica + Amph + Zo + Ab + Qtz + Rt
2 Mica + Amph + Zo + Spn + Qtz + Rt
3 Mica + Amph + Pl + Grt + Zo + Qtz + Rt
4 Chl + Mica + Amph + Pl + Grt + Qtz + Rt
5 Chl + Mica + Amph + Pl + Grt + Qtz + Rt + Ill
6 Mica + Amph + Pl + Grt + Qtz + Ill
7 Chl + Mica + Amph + Pl + Qtz + Rt + Ill
Mica + Amph + Pl + Zo + Qtz + Rt
Mica + Amph + Grt + Zo + Qtz + Rt
Mica + Amph + Pl + Grt + Zo + Qtz + Rt
Mica + Amph + Pl + Grt + Qtz + Rt
Chl + Mica + Amph + Pl + Zo + Qtz + Rt
Chl + Mica + Amph + Pl + Qtz + Rt
Chl + Mica + Amph + Pl + Grt + Qtz + Ill
Chl + Mica + Amph + Grt + Pl + Qtz + Ill
Mica + Amph + Pl + Grt + Qtz + Rt + Ill
Mica + Amph + Pl + Grt + Qtz + Ill
Amph + Pl + Grt + Sa + Qtz + Ill
P(kbar)
T(°C)
B
Perchuk et al. (1985)
AR-09-08
AR-08-09c
AR-09-09
Frequency
T (°C)
C
AR-08-09c
AR-08-25B
AR-09-08
P(kbar)
D
AR-08-09c
AR-08-25B
AR-09-08
AR-08-09c
Sk-pl-in-White-Mica
P(kbar)
T (°C)

Figure 38 - (A), pseudosection in the SiO2-Al2O3-FeO-MgO-CaO-Na2O-K2O-TiO2 system and calculated with Perple_X 6.6.6 (Connolly, 2009), using the internally consistent thermodynamic database of Holland and Powell (2003) and Connolly and Kerrick (2002) and whole rock and mineral geochemistry of sample AR-08-09c found in Fig. 36, Table 10 and Fig. 37, Table 7, respectively. The red shaded field corresponds to both mineral assemblage observed for relic garnet amphibolite paragenesis and the measured proportion of Al in amphiboles compared to predicted models. (B), Perchuk *et al*. (1985) garnet-amphibole thermometry based on Mg-Fe partitioning. Frequencies represent the number of combinations of garnet-amphibole pairs of EPMA analyses yielding a given temperature. (C), phengite-quartz-water P–T estimates for EPMA analyses of samples AR-08-09c, AR-08-25B and AR-09-08 using the method of Dubacq *et al*. (2010). (D), Si p.f.u. isopleths in phengite calculated and plotted on previous thermodynamic phengite-quartz-water calibration domains using the whole rock and phengite EPMA analyses of sample AR-08-09c (Table 9). The resulting domain corresponding to Si^{4+} content is shaded in yellow.

2.7 $^{40}Ar/^{39}Ar$ Dating

Geochronology was undertaken by single-grain laser $^{40}Ar/^{39}Ar$ dating on different mineral phases, amphiboles and white micas for amphibolites and green-schists parageneses, respectively. Detailed results may be found in **Annexes 3**, **4**, **5** and **6**.

2.7.1 Dating of amphiboles

The amphibole from the sample AR-09-08 (K390) yielded a plateau age of 87.7 ± 2.8 Ma with a MSWD of 0.06 (**Figure 39A**),computed with the last three heating steps (94.7 % of released ^{39}Ar) The inverse isochron age is 86.0 ± 7.0 Ma with a MSWD of 0.02, in agreement with the plateau age.

The amphibole from the sample AR-09-15 (K402) yielded a plateau age of 91.2 ± 1.6 Ma with a MSWD of 0.59 (**Figure 39B**) computed with six out of seven heating steps pertaining 98.0 % of total released ^{39}Ar. The inverse isochron age is 89.3 ± 3.8 Ma (1σ) with a MSWD of 0.74, in agreement with the plateau age.

The amphibole from the sample AR-08-09c (K427) yielded a plateau age of 90.3 ± 1.5 Ma with a MSWD of 0.01 (**Figure 39C**) computed with the last five heating steps representing 92.8 % of total released ^{39}Ar. The inverse isochron age is 90.2 ± 1.9 Ma with a MSWD of 0.01, in agreement with the plateau age.

In conclusion, the three amphibole $^{40}Ar/^{39}Ar$ ages agree with a common crystallization age during the amphibolite HT peak at about 90 ± 0.5 Ma.

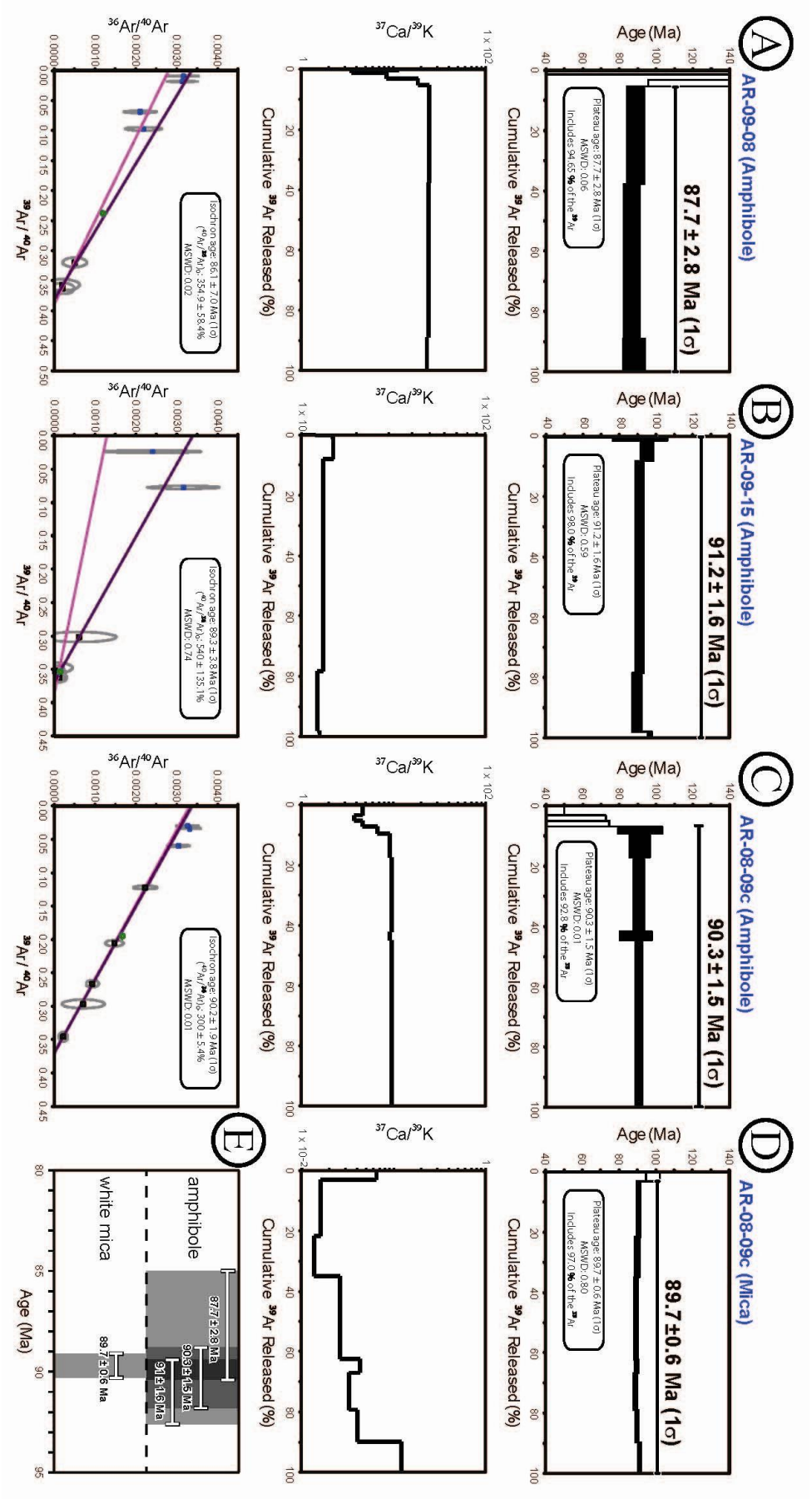
A
AR-09-08 (Amphibole)
87.7 ± 2.8 Ma (1σ)
B
AR-09-15 (Amphibole)
91.2 ± 1.6 Ma (1σ)
C
AR-08-09c (Amphibole)
90.3 ± 1.5 Ma (1σ)
D
AR-08-09c (Mica)
89.7±0.6 Ma (1σ)
E
amphibole
white mica
87.7 ± 2.8 Ma
90.3 ± 1.5 Ma
91 ± 1.6 Ma
89.7 ± 0.6 Ma
Age (Ma)
Cumulative 39Ar Released (%)
37Ca/39K
36Ar/40Ar
39Ar/40Ar

Figure 39 - $^{40}Ar/^{39}Ar$ age, Ca/K spectra and inverse isochrones. (A), amphibole from sample AR-09-08. (B), amphibole from sample AR-09-15. (C), amphibole from sample AR-08-09c. (D), white mica from sample AR-08-09c. Locations of samples are shown on Fig. 32. (E), compilation of ages which may also be found in Table 11, as well as detailed dating results in supplementary data files.

2.7.2 Dating of phengites

The phengite from the sample AR-08-09c (K428) yielded a plateau age of 89.7 ± 0.7 Ma with a good MSWD of 0.80 (**Figure 39D**) computed with the last seven heating steps representing 97.0 % of the total ^{39}Ar gas freed during the whole analysis. The inverse isochron overlaps within 1σ error the plateau age.

This age indicates that the MP-MT chlorite-phengite paragenesis age is similar within error to the amphibolite HT peak age obtained above, and likely occurred between 89 and 90 Ma.

In conclusion of the $^{40}Ar/^{39}Ar$ dating section, the amphibole and phengite $^{40}Ar/^{39}Ar$ ages obtained on Amasia amphibolites are similar within error. They agree with a crystallization during a rapid metamorphic cycle related to oceanic crust obduction at about 89-90 Ma (**Figures 39E** & **40**), at the beginning of the Late Cretaceous (Turonian), just prior to paleontological dating obtained at the front of Armenian ophiolites obduction (89-83 Ma; Sosson *et al*., 2010).

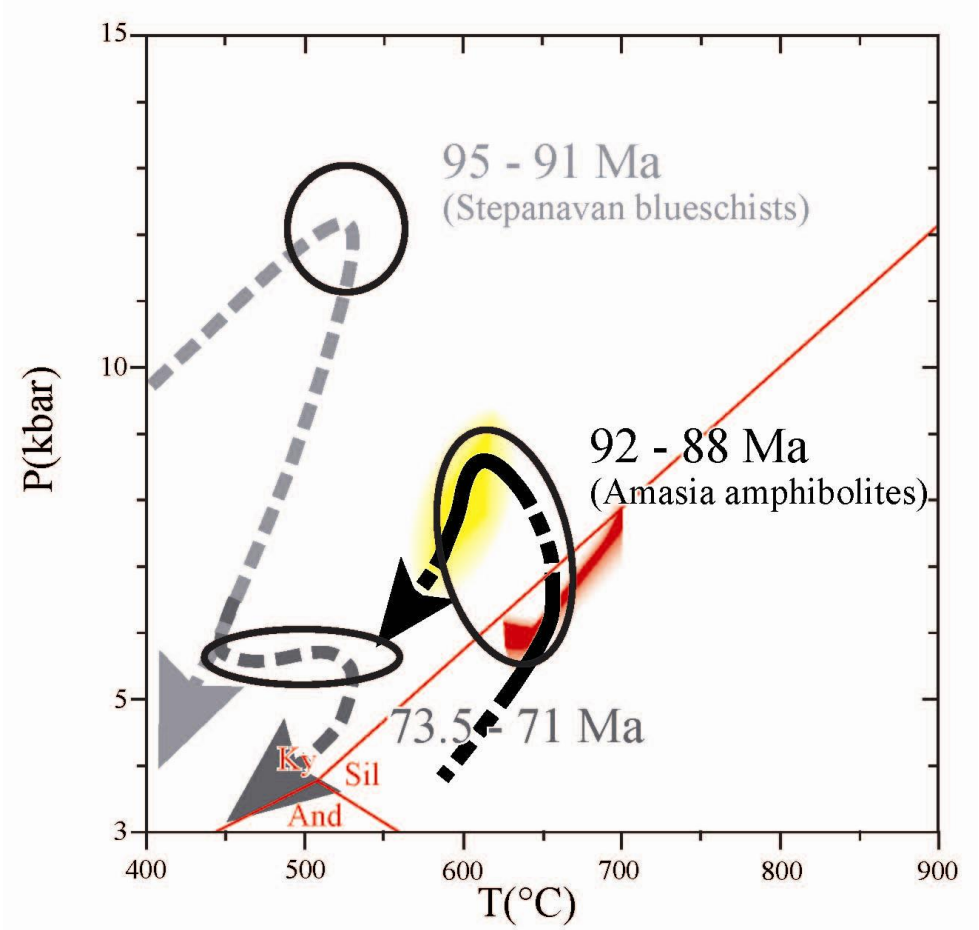

Figure 40 - Compilation of determined PT-t paths for the Amasia-Sevan-Akera metamorphic rocks found in basal position of ophiolite bodies inferred through this study of the outcrops of Amasia garnet amphibolite in black and Stepanavan blueschist (Rolland *et al.*, 2009a) in grey.

2.8 Discussion

The study of the metamorphic rocks found under ophiolites provides key data for the understanding of obduction processes (e.g., Wakabayashi and Dilek, 2000; Gaggero *et al.*, 2009). The so-called 'metamorphic sole' of obducted ocean lithosphere recorded variations in temperature and pressure throughout processes ranging from intra-oceanic subduction to obduction due to the progression of a relatively cold sinking slab and hot overriding plate and yields insights into the obduction dynamics (e.g., Coleman, 1981; Agard *et al.*, 2010). Such examples are widespread in Anatolia (Whitechurch *et al.*, 1984; Collaku *et al.*, 1991; Robertson and Karamata, 1994; Abd El-Naby *et al.*, 2000; Al-Riyami *et al.*, 2002; Çelik and Delaloye, 2003; 2004; 2006; Beccaletto and Jenny, 2004; Çelik *et al.*, 2006; Çelik, 2007). In the following discussion we argue for the presence of a single and major ophiolite nappe in the Lesser Caucasus region, based on a comparison of geochemical, mineral and geochronological data of the various ophiolite outcrops. Further, based on the PTt history of

underlying 'metamorphic sole' rocks, we propose a reconstruction of the obduction history in this region.

2.8.1 Evidence for one large ophiolite nappe obducted in the Lesser Caucasus

The similarity of the Amasia ophiolite petrology with the other Armenian and NE Turkey ophiolites reinforces the model of a single ophiolitic nappe obducted over the Taurides-Anatolides (Yılmaz *et al*., 2013; Hässig *et al*., 2014 and references therein). The geochemical and geochronological features are the following (**Figure 36**):

Sample geochemistry is marked by depletions in Nb–Ta, and LILE enrichments, which is in agreement with a formation context involving contamination of slab-derived fluids due to supra-subduction contamination (Hässig *et al*., 2013). Since a full ophiolitic lithological assemblage was described in Armenian ophiolites (comprising radiolarites, pillow basalts, gabbros, plagiogranites and serpentinites), in the corresponding geodynamic context is a marginal basin environment (fore- or back-arc). The main problem in the determination of the relative position of this marginal basin in terms of fore- or back-arc is the unknown position of the former volcanic arc that ought to be formed. In Armenia, the presence of meta-volcanites in the blueschist units found below the obduction contact in Stepanavan (Rolland *et al*., 2009b) suggests that the arc was accreted to, and subducted with, the sinking slab. Thus, the basin would have been in a back-arc position. However, the question still remains. The most likely polarity for the former intra-oceanic subduction zone is north dipping, south of the marginal basin. This is suggested by the overall north verging tectonic pile, comprising in the SAB, the ophiolite and the Eurasian margin (**Figures 31** & **33B**). Such a geometry is also observed in the other ophiolite outcrops in both Armenia and NE Anatolia (e.g. Hässig *et al*., 2014 and references therein).

Field investigations systematically evidence alkaline OIB type basalts topping the ophiolite sections in the Lesser Caucasus (Galoyan *et al*., 2007; 2009; Rolland *et al*., 2009b). In Turkey, alkaline rocks are also associated to the ophiolites (Refahiye and Karadağ volcanites; Parlak *et al*., 2012). These alkaline rocks have been dated at c. 117 Ma by the $^{40}Ar/^{39}Ar$ method on amphibole (Rolland *et al*., 2009b). Thus, OIB formation occurred prior to the obduction of the oceanic crust. An alkaline (OIB) tendency is 0observed for some of the metamorphic rocks found directly under the ophiolites as well. The geochemical composition

of the Amasia garnet amphibolites from the metamorphic unit beneath the ophiolite shows a similar alkaline tendency as the alkaline suite described on top of the Armenian ophiolite. Subophiolitic amphibolites and blueschists from elsewhere along the northern Neotethys suture have compositions indicative of different volcanic suites protoliths (MORB, WPB, and IAT) which were stacked together during intra-oceanic subduction in a Neotethyan basin (Lytwyn and Casey, 1995; Parlak *et al*., 1995; Çelik and Delaloye, 2003; Vergili and Parlak, 2005; Çelik and Delaloye, 2006; Parlak *et al*., 2006; Elitok and Drüppel, 2008). The alkaline tendencies found in the metamorphic rocks may be interpreted as being relics of seamounts and/or oceanic plateaus emplaced on the subducting oceanic plate, later overthrusted by the ophiolite. Another interpretation is that these tendencies represent pieces of the ophiolite from the upper plate, which itself comprises of different geochemical tendencies. Following this hypothesis, the upper plate oceanic lithosphere was dismembered and incorporated to the sole lithologies as the ophiolite progressed throughout subduction and obduction processes (e.g. Whitechurch *et al*., 1984; Jaillard *et al*., 1997; Wakabayashi and Dilek, 2003; Huene *et al*., 2004; Sage *et al*., 2006; Yamamoto *et al*., 2009).

The Izmir–Ankara–Erzincan–Sevan–Akera ophiolite obduction appears to be amongst most exceptional cases of obductions. Due to similar tectonic settings, emplacement ages, and to the presence of similar geochemical compositions and similar Jurassic ages (e.g. Çelik *et al*., 2011; Topuz *et al*., 2013a; 2013b; Uysal *et al*., 2013) for the ophiolite belt into NE Anatolia, along the Ankara–Erzincan suture zone further west, we propose that this obduction connects to the basal contact of the NE Turkish ophiolite (following Hässig *et al*., 2014 and Yılmaz *et al*., 2013). Such correlation suggests an obducted ophiolitic nappe of at least 700 km in length and up to 300 km in width along the Ankara–Erzurum–Sevan–Akera suture zone on top of the Tauride Block continuing laterally to the SAB.

2.8.2 Model for the initiation and propagation of the Lesser Caucasus obduction

From all the available geological data, particularly with new PT-t data from the amphibolites of the Amasia ophiolite metamorphic sole, we propose the following model for the evolution of the northern branch of Neotethys (**Figure 41**):

1- The magmatic rocks of the Amasia ophiolites, along with correlated Lesser Caucasus and NE Anatolia region share similar geochemical signatures influenced by a subduction

component in an oceanic basin environment (Hässig *et al*., 2014). These data argue for simultaneous crust formation in a supra-subduction setting in the Middle to Upper Jurassic times.

2- Two north dipping subduction zones are evidenced by simultaneous magmatism on the Eurasian active margin and in the intra-oceanic setting, responsible for the formation of the Supra Subduction Zone type ophiolite bodies (e.g., Rolland *et al*., 2010; Sosson *et al*., 2010). The later intra-oceanic subduction is argued to likely evolve into an obduction contact accountable for ophiolite emplacement at the arrival of the SAB in the subduction zone.

3- Two magmatic suites were emplaced one on top of the other: (1) a gabbroic basement of thinned back-arc oceanic crust, (2) topped by thick basaltic flows with an alkaline tendency. The presence of identical alkali basalts in similar stratigraphic positions strongly favors the formation of several oceanic islands or one large plateau related to hot spot magmatism (e.g., Galoyan, 2008). Observations undertaken in the Amasia area are thus compatible with a model of obduction of a Supra Subduction Zone ophiolitic domain through intra-oceanic subduction and active oceanic margin slicing after OIB emplacement (**Figure 41**). This model explains the position of alkaline rocks both underneath, as sheared lenses occur in the mélange, and also above ophiolite as pillow lavas. The alkaline outcrops would have been under-thrusted during intra-oceanic subduction or during emplacement of the overriding ophiolite bodies.

4- The flysch deposits give an upper temporal limit to the obduction of this oceanic crust in Santonian times (84-83 Ma). Paleontological dating undertaken on the flysch in Amasia, Sevan and Vedi indicates similar dates (Sosson *et al*., 2010, Hässig *et al*., 2013), which agrees for a fast obduction process dragging the deep metamorphic sole on top superficial rocks within 6 to 7 Ma.

5- Considering the hypothesis of ophiolite formation during intra-oceanic subduction, a problem is posed by the absence of the volcanic arc in Armenia. There, theonly evidence of such an island arc can be found in the ophiolitic sole through the geochemical composition of metamorphic rocks. Two hypotheses on the disappearance of this arc may be proposed: (1) the alteration and erosion of the volcanic arc by uplift during the obduction or (2) the accretion and subduction of the fore-arc block and dragging of the volcanic arc with it, as proposed by Shemenda (1994) in his analogical model of subduction. This latter model is preferred based on (1) the presence of some volcanic blocks in the Stepanavan blueschists in Armenia. There, it is hypothesized that the Stepanavan blueschists correspond to the missing

volcanic arc dragged into the subduction zone (Galoyan *et al*., 2007; Rolland *et al*., 2009a) (**Figure 41**). (2) More to the west, in northeastern Turkey, remnants for such intra-oceanic subduction, including eclogites, have been found (Topüz *et al*., 2013a; 2013b, Uysal *et al*., 2013). In the Erzincan region bibliographic data as well as field observations (Hässig *et al*., 2014) lead to further argue this hypothesis by the presence of low-grade metamorphic rocks of volcanic origin. This outcrop reveals metamorphic rocks with calc-alkali tendencies overthrusted by ophiolitic rocks from North to South along the northern edge of the Erzincan basin (Gücer *et al*., 2007; Aslan *et al*., 2011). Therefore, the absence of the volcanic arc formed above the intra-oceanic subduction may be explained by its accretion to the subducting slab and its dragging under the obducting ophiolite through scaling by faulting and tectonic erosion into the subduction channel, gradually evolving into an "obduction channel" due to variations in sinking slab dip.

2.8.3 Significance of the counterclockwise PTt path

The counterclockwise PTt path that is obtained for the Amasia amphibolites coincides with clockwise the PTt path of neighboring Stepanavan blueschists. This, together with the model of obduction initiation proposed above, suggest that:

(1) HT-LP conditions in Amasia and formation of garnet amphibolites, is due to obduction initiation in the back-arc domain within the thinned oceanic crust, significantly heated by the emplacement of hot-spot series at c. 117 Ma.

(2) MP-LT conditions during the chlorite-phengite retrogression of garnet amphibolites are ascribed to intercalation in the subduction channel with the blueschists.

(3) Common exhumation process after the MP-LT conditions of the blueschists and amphibolites explain their similar tectonic position. In this scenario, the slices of metamorphic rocks represent relics of subducted oceanic and volcanic arc lithosphere (Stepanavan blueschists). The Amasia garnet amphibolites recorded a more complex history starting from alkaline volcanic rocks originally emplaced on the seafloor, (i) underthrusted down to ~20 km below hot oceanic crust during obduction initiation in the back-arc, followed by (ii) their incorporation into the subducting slab until a depth of about 30 km in the accretionary prism (where they merge with blueschists), (iii) their exhumation within this prism (or tectonic mélange). (iv) Finally, the amphibolites and blueschists were transported into the tectonic mélange at the obduction interplate contact onto the SAB.

2.8.4 Comparisons with other obductions in the Caucasus-Arabic domain

When considering the timing of obductions in the Middle East region it appears thatthe Lesser Caucasus and Oman ophiolites were obducted within the same time span (~90 Ma) (e.g. Agard *et al*., 2010). However, preliminary paleomagnetic analyses that both ophiolites were in distinct geographical locations distant of about 1200 km; (Meijers *et al*., 2012). Further, these authors propose that a >1500 km large ocean domain till separated the SAB and TAB from the Arabian margin until Upper Cretaceous times. This ocean domain corresponds to the southern Neotethys, which likely closed during the Late Eocene times (Rolland *et al*., 2012). Thus, synchronous obductions occurred on both the northern and southern Neotethyan edges, significantly before the stages of continental subduction. Linking the history of metamorphic rocks to that of syn- to post-obduction sediments from the southerly Vedi area and paleomagnetism, gives strong arguments to infer that at the end of the obduction event (Santonian, 83-84 Ma) a residual oceanic domain (less than 1200 km) still remained to be closed north of the obduction zone before final SAB-TAP collision with the Eurasian margin (Meijers *et al*., 2013). This, in turn implies that the obduction process of preserved oceanic lithosphere is not linked to its subduction further north under Eurasia, but solely to the dynamics of the intra-oceanic subduction.

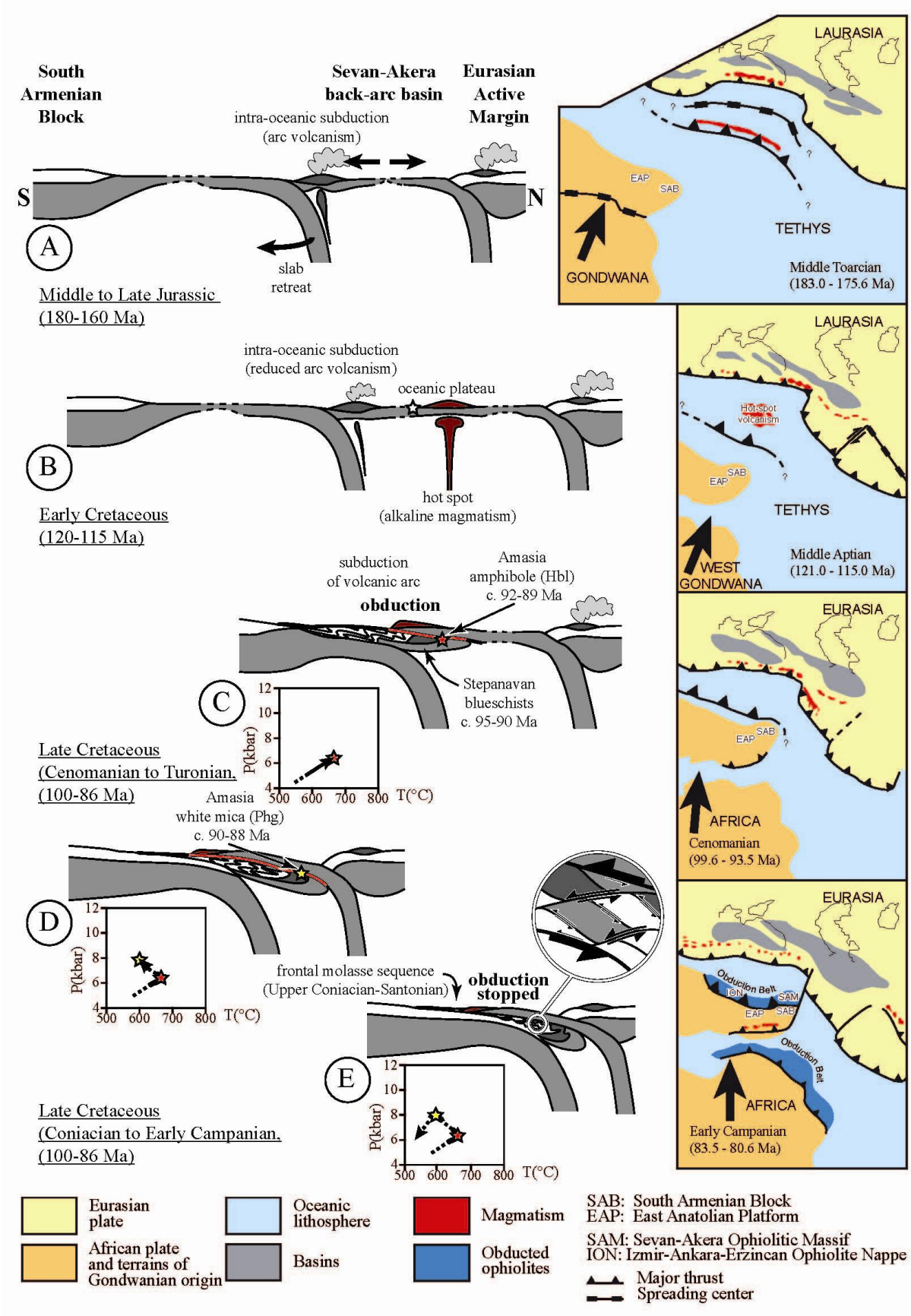
South Armenian Block
Sevan-Akera back-arc basin
Eurasian Active Margin
intra-oceanic subduction (arc volcanism)
S
N
A
slab retreat
Middle to Late Jurassic (180-160 Ma)
LAURASIA
EAP
SAB
TETHYS
GONDWANA
Middle Toarcian (183.0 - 175.6 Ma)
intra-oceanic subduction (reduced arc volcanism)
oceanic plateau
B
hot spot (alkaline magmatism)
Early Cretaceous (120-115 Ma)
Hot-spot volcanism
WEST GONDWANA
Middle Aptian (121.0 - 115.0 Ma)
subduction of volcanic arc
obduction
Amasia amphibole (Hbl) c. 92-89 Ma
Stepanavan blueschists c. 95-90 Ma
C
P(kbar)
T(°C)
Late Cretaceous (Cenomanian to Turonian, (100-86 Ma)
Amasia white mica (Phg) c. 90-88 Ma
EURASIA
AFRICA
Cenomanian (99.6 - 93.5 Ma)
D
frontal molasse sequence (Upper Coniacian-Santonian)
obduction stopped
Obduction Belt
ION
SAM
E
Late Cretaceous (Coniacian to Early Campanian, (100-86 Ma)
Early Campanian (83.5 - 80.6 Ma)
Eurasian plate
African plate and terrains of Gondwanian origin
Oceanic lithosphere
Basins
Magmatism
Obducted ophiolites
SAB: South Armenian Block
EAP: East Anatolian Platform
SAM: Sevan-Akera Ophiolitic Massif
ION: Izmir-Ankara-Erzincan Ophiolite Nappe
Major thrust
Spreading center

Figure 41 - Middle Toarcian (c. 180 Ma), to Early Campanian (c. 83 Ma) palaeotectonic evolution of the Lesser Caucasus region and its neighboring areas, modified from Middle East Basins Evolution Programme palaeotectonic maps of the Middle East (Barrier and Vrielynck, 2008) to include our new data with associated sketch cross-sections.

2.9 Conclusion

The petrologic study of Amasia ophiolites argues for the presence of one large obduction in the Lesser Caucasus, which occurred at Middle Cretaceous times at c. 90 Ma. The history of metamorphic rocks preserved in ophiolite 'soles', below the un-metamorphosed oceanic units, highlights an example of syn-obduction metamorphism featured by a counter-clockwise PTt path. The metamorphic rocks preserve two successive parageneses featured by (1) amphibole-garnet-plagioclase at the HT-LP peak (at P = 5.8~7.0 kbar, T = 625~675°C) and (2) a chlorite-phengite retrogression at MT-MP conditions (P = 7.8~9.8 kbar, T = 620~660°C). The increase in P is ascribed to thickening of the overriding compartment of the subduction zone at c. 90-89 Ma, as well as subsequent underthrusting of amphibolites under the future ophiolite, as the South Armenian Block enters the subduction zone. In this paper, the obduction is dated for the first time by direct $^{40}Ar/^{39}Ar$ dating on amphiboles (hornblende) and white micas (phengite) yielding for both HT and MP peaks similar within-error ages of 90 ± 0.5 Ma and 89-90 Ma, respectively. This dating accounts for a very rapid tectonic evolution featured by (1) the slicing of oceanic crust and its dragging under the obduction front below a relatively hot oceanic crust at c. 91 Ma and (2) the incorporation of the basal obduction slices within the subduction zone deep prism at 91-90 Ma. Following tectonic evolution is featured by (3) a common exhumation of blueschists + garnet amphibolites within the subduction zone (accretionary prism), and their incorporation in a greenschist facies tectonic mélange. (4) The latter is transported at the base of the obduction. Ending of obduction occurred within 1-5 Ma at c. 89-83 Ma, as shown by paleontological ages in both thrusted (sub-ophiolitic) and uncomformably overlying (supra-ophiolitic) sediments, in the Armenian foreland. Final exhumation of Amasia and Stepanavan metamorphic rocks occurred in the Eocene, during the final Arabia-Eurasia collision, as shown y Eocene unconformity on top of these rocks.

Acknowledgments

This work was supported by the MEBE and DARIUS programs coordinated by E. Barrier and M.F. Brunet from the University Pierre and Marie Curie and the INSU/CNRS. Fieldwork was facilitated by the support of the Armenian National Academy of Science (Institute of Geological Sciences). The technical help of M. Manetti in the preparation and mineral analysis is also acknowledged along with G. Delanoy for thin sections. We wish to thank J.L. Devidal in Clermont-Ferrand, P. Capiez in Lyon and S. Gallet in Nice for their involvement during data acquisition. This publication is a contribution of "GEOAZUR", University of Nice-Sophia Antipolis, and CNRS, France.

References

Abd El-Naby, H., Frisch, W., Hegner, E., 2000. Evolution of the Pan-African Wadi Haimur metamorphic sole, Eastern Desert, Egypt. Journal of Metamorphic Geology, 18, pp. 639-651.

Abovyan, S.B., 1981. The mafic-ultramafic complexes of the ophiolite zones of Armenian SSR. Izdatelstvo NAS Arm.SSR, Yerevan, 306 p. (in Russian).

Adamia, Sh.A., Chkhotua, T., Kekelia, M., Lordkipanidze, M., Shavishvili, I., Zakariadze, G., 1981. Tectonics of Caucasus and adjoining regions: implications for the evolution of the Tethys ocean. Journal of Structural Geology, 3, pp. 437-447.

Agard, P., Searle, M.P., Alsop, G.I., Dubacq, B., 2010. Crustal stacking and expulsion tectonics during continental subduction: P-T deformation constraints from Oman. Tectonics, 29, pp. 1-19.

Agard, P., Jolivet, L., Vrielynck, B., Burov, E., Monié, P., 2007. Plate acceleration: The obduction trigger? Earth and Planetary Science Letters, 258, pp. 428-441.

Al-Riyami, K., Robertson, A., Dixon, J., Xenophontos, C., 2002. Origin and emplacement of the Late Cretaceous Baer–Bassit ophiolite and its metamorphic sole in NW Syria. Lithos, 65, pp. 225-260.

Aslan, Z., Gücer, M.A., Arslan, M., 2011. 39Ar-40Ar dating on plagioclases of metabasic metagranitic rocks in the Yoncayolu metamorphic, NE Turkey. Goldschmidt Conference Abstracts, p. 460.

Barrier, E., Vrielynck, B., 2008. Palaeotectonic map of the Middle East, Atlas of 14 maps, Tectonosedimentary-Palinspastic maps from Late Norian to Pliocene. Commission for the Geologic Map of the World (CCMW, CCGM), Paris, France.

Beccaletto, L., Jenny, C., 2004. Geology and correlation of the Ezine zone: a Rhodope fragment in NW Turkey? Turkish Journal of Earth Sciences, 13, pp. 145-176.

Bortolotti, V., Marroni, M., Pandolfi, L., Principi, G., 2005. Mesozoic to Tertiary tectonic history of the Mirdita ophiolites, northern Albania. Island Arc, 14, pp. 471-493.

Carosi, R., Cortesogno, L., Gaggero, L., Marroni, M., 1996. Geological and petrological features of the metamorphic sole from the Mirdita nappe, northern Albania. Ofioliti, 21, pp. 21-40.

Çelik, O.F., 2007. Metamorphic sole rocks and their mafic dykes in the eastern Tauride belt ophiolites (southern Turkey): implications for OIB-type magma generation following slab break-off. Geological Magazine, 144, pp. 849-866.

Çelik, Ö.F., Delaloye, M.F., 2003. Origin of metamorphic soles and their post-kinematic mafic dike swarms in the Antalya and Lycian ophiolites, SW Turkey. Geological Journal, 38, pp. 235-256.

Çelik, Ö.F., Delaloye, M.F., 2004. Mineral chemistry and P–T conditions of metamorphic sole rocks from the Lycian and the Antalya ophiolites, western Taurides (SW Turkey). In: Chatzipetros, A.A., Pavlides, S.B. (Eds.), Proceedings of 5th International Symposium on Eastern Mediterranean Geology, Thessaloniki, Greece, p. 241.

Çelik, Ö.F., Delaloye, M.F., 2006. Characteristics of ophiolite-related metamorphic rocks in the Beyşehir ophiolitic mélange (Central Taurides, Turkey), deduced from whole rock and mineral chemistry. Journal of Asian Earth Sciences, 26, pp. 461-476.

Çelik, Ö.F., Delaloye, M.F., Feraud, G., 2006. Precise $^{40}Ar/^{39}Ar$ ages from the metamorphic sole rocks of the Tauride Belt Ophiolites, southern Turkey: implications for the rapid cooling history. Geological Magazine, 143, pp. 213-227.

Çelik, O.F., Marzoli, A., Marschik, R., Chiaradia, M., Neubauer, F., Öz, I., 2011. Early–Middle Jurassic intra-oceanic subduction in the İzmir-Ankara-Erzincan Ocean, Northern Turkey, Tectonophysics 509, 120-134, doi: 10.1016/j.tecto.2011.06.007.

Cloos, M., Shreve, R.L., 1988. Subduction-Channel Model of Prism Accretion, Melange Formation, Sediment Subduction, and Subduction Erosion at Convergent Plate Margins : 1. Background and Description. Physical Applied Geophysics, 128, pp. 456-500.

Coleman, R.G., 1981. Tectonic setting for ophiolite obduction in Oman. Journal of Geophysical Research, 86, pp. 2497-2508.

Collaku, A., Bonneau, M., Cadet, J.-P., Kienast, J.-R., 1991. The metamorphic sole at the base of the Mirdita ophiolitic nappe, its reverse metamorphism and its relationships with the underlying volcano-sedimentary sequence (vicinity of Lura, Northern Albania). Comptes rendus de l'Académie des sciences. Série 2, Mécanique, Physique, Chimie, Sciences de l'univers, Sciences de la Terre, 313, pp. 251-258.

Connolly, J.A.D., 2009. The geodynamic equation of state: what and how. Geochemistry, Geophysics, Geosystems, 10.

Connolly, J.A.D., Kerrick, D.M., 2002. Metamorphic controls on seismic velocity of subducted oceanic crust at 100–250 km depth. Earth and Planetary Science Letters, 204, pp. 61-74.

Danelian, T., Asatryan, G., Sahakyan, L., Galoyan, G., Sosson, M., Avagyan, A., 2010. New and revised radiolarian biochronology for the sedimentary cover of ophiolites in the Lesser Caucasus (Armenia). Geological Society, London, Special Publications, 340, pp. 383-391.

Dercourt, J., Zonenshain, L.P., Ricou, L.-E., Kazmin, V.G., Le Pichon, X., Knipper, A.L., Grandjacquet, C., Sbortshikov, I.M., Geyssant, J., Lepvrier, C., Pechersky, D.H., Boulin, J., Sibuet, J.-C., Savostin, L.A., Sorokhtin, O., Westphal, M., Bazhenov, Lauer, J.P., Biju-Duval, B., 1986. Geological evolution of the Tethys belt from the Atlantic to the Pamirs since the Lias. Tectonophysics, 123, pp. 241-315.

Dilek, Y., Whitney, D., 1997. Counterclockwise P-T-t trajectory from the metamorphic sole of a Neo-Tethyan ophiolite (Turkey). Tectonophysics, 280, pp. 295-310.

Ding, L., Kapp, P., Wan, X., 2005. Paleocene–Eocene record of ophiolite obduction and initial India-Asia collision, south central Tibet. Tectonics, 24, pp. 1-9.

Domanik, K.J., Holloway, J.R., 2000. Experimental synthesis and phase relations of phengitic muscovite from 6.5 to 11 GPa in a calcareous metapelite from the Dabie Mountains, China. Lithos, 52, pp. 51-77.

Domanik, K.J., Holloway, J.R., 1996. The stability and composition of phengitic muscovite and associated phases from 5.5 to 11 GPa: implications for deeply subducted sediments. Geochimica and Cosmochimica Acta, 60, pp. 4133-4150.

Dubacq, B., Vidal, O., De Andrade, V., 2010. Dehydration of dioctahedral aluminous phyllosilicates: thermodynamic modelling and implications for thermobarometric estimates. Contributions to Minerology and Petrology, 159, pp. 159-174.

Elitok, Ö., Drüppel, K., 2008. Geochemistry and tectonic significance of metamorphic sole rocks beneath the Beyşehir-Hoyran ophiolite (SW-Turkey). Lithos, 100, pp. 322-353.

Ellis, D.J., Green, D.H., 1979. An Eperimental Study of the Effect of Ca upon Garbet-Clinopyroxene Fe-Mg Exchange Equilibria. Contributions to Mineralogy and Petrology, 71, pp. 19-22.

Ellis, S., Beaumont, C., Pfiffner, O.A., 1999. Geodynamic models of crustal-scale episodic tectonic accretion and underplating in subduction zones. Journal of Geophysical Research, 104, pp. 15169-15190.

Engi, M., Berger, A., Roselle, G.T., 2001. Role of the tectonic accretion channel in collisional orogeny. Geology, 29, pp. 1143-1146.

Federico, L., Crispini, L., Scambelluri, M., Capponi, G., 2007. Ophiolite mélange zone records exhumation in a fossil subduction channel. Geology, 35, pp. 499-502.

Ferry, J.M., Spear, F.S., 1978. Experimental Calibration of the Partitioning of Fe and Mg Between Biotite and Garnet. Contributions to Mineralogy and Petrology, 66, pp. 113-117.

Festa, A., Pini, G.A., Dilek, Y., Codegone, G., 2010. Mélanges and mélange-forming processes: a historical overview and new concepts. International Geology Review, 52, pp. 1040-1105.

Floyd, P.A., Winchester, J.A., 1975. Magma type and tectonic setting discrimination using immobile elements. Earth and Planetary Science Letters, 27, pp. 211-218.

Floyd, P.A., Winchester, J.A., 1978. Identification and discrimination of altered and metamorphosed volcanic rocks using immobile elements. Chemical Geology, 21, pp. 291-306.

Gaggero, L., Marroni, M., Pandolfi, L., Buzzi, L., 2009. Modeling the oceanic lithosphere obduction: Constraints from the metamorphic sole of Mirdita ophiolites (Northern Albania). Ofioliti, 34, pp. 17-42.

Galoyan, G., 2008. Etude Pétrologiques, Géochimiques et Géochronologiques des Ophiolites du Petit Caucase (Arménie). PhD thesis, University of Nice–Sophia Antipolis.

Galoyan, G., Rolland, Y., Sosson, M., Corsini, M., Melkonyan, R., 2007. Evidence for superposed MORB, oceanic plateau and volcanic arc series in the Lesser Caucasus (Stepanavan, Armenia). Comptes Rendus Geosciences, 339, pp. 482-492.

Galoyan, G., Rolland, Y., Sosson, M., Corsini, M., Billo, S., Verati, C., Melkonyan, R., 2009. Geology, geochemistry and $^{40}Ar/^{39}Ar$ dating of Sevan ophiolites (Lesser Caucasus, Armenia): Evidence for Jurassic Back-arc opening and hot spot event between the South Armenian Block and Eurasia. Journal of Asian Earth Sciences, 34, pp. 135-153.

Göncüoğlu, M.C., Turhan, N., 1984, Geology of the Bitlis metamorphic belt. In "Geology of the Taurus Belt", O. Tekeli and M.C. Göncüoğlu (eds.), Proccedings of the Int. Symp. on the Geology of the Taurus Belt, 26-29.9.1983, Ankara, pp. 237-244.

Graham, C., Powell, R., 1984. A garnet–hornblende geothermometer: calibration, testing, and application to the Pelona Schist, Southern California. Journal of Metamorphic Geology, 2, pp. 13-31.

Gray, D.R., Gregory, R.T., 2000. Implications of the structure of the Wadi Tayin metamorphic sole, the Ibra-Dasir block of the Samail ophiolite, and the Saih Hatat window for late stage extensional ophiolite emplacement, Oman. Marine Geophysical Researches, 21, pp. 211-227.

Green, T.H., Hellman, P.L., 1982. Fe-Mg partitioning between coexisting garnet and phengite at high pressure, and comments on a garnet-phengite geothermometer. Lithos, 15, pp. 253-266.

Gücer, M.A., Aslan, Z., Bektas, O., 2007. Petrology and Geochemistry Features of the Yoncayolu Metamorphics in Erzincan, NE Turkey. Goldschmidt Conference Abstracts, p. A360.

Guilmette, C., Hébert, R., Wang, C., Villeneuve, M., 2009. Geochemistry and Geochronology of the metamorphic sole underlying the Xigaze Ophiolite, Yarlung Zangbo Suture Zone, South Tibet. Lithos, 112, pp. 149-162.

Hacker, B.R., 1991. The role of deformation in the formation of metamorphic field gradients: Ridge subduction beneath the Oman ophiolite, Tectonics, 10, pp. 455-473.

Hacker, B.R., Mosenfelder, J.L., Gnos, E., 1996. Rapid emplacement of the Oman ophiolite: Thermal and geochronologic constraints. Tectonics, 15, pp. 1230-1247.

Harper, G.D., Grady, K., Coulton, A.J., 1996. Origin of the amphibolite "sole" of the Josephine ophiolite: Emplacement of a cold ophiolite over a hot arc. Tectonics, 15, pp. 296-313.

Hart, S.R., Erlank, A.J., Kable, E.J.D., 1974. Sea floor basalt alteration: some chemical and Sr isotopic effects. Contributions to Mineralogy and Petrology, 44, pp. 219-230.

Hässig, M., Rolland, Y., Sosson, M., Galoyan, G., Müller, C., Avagyan, A., Sahakyan, L., 2013. New structural and petrological data on the Amasia ophiolites (NW Sevan-Akera suture zone, Lesser Caucasus): Insights for a large-scale obduction in Armenia and NE Turkey. Tectonophysics, 588, pp. 135-153.

Hässig, M., Rolland, Y., Sosson, M., Galoyan, G., Sahakyan, L., Topuz, G., Çelik, Ö.F., Avagyan, A., Müller, C., (2014). Linking the NE Anatolian and Lesser Caucasus ophiolites: evidence for large scale obduction of oceanic crust and implications for the formation of the Lesser Caucasus-Pontides Arc. Geodinamica Acta, (just-accepted), pp. 1-52.

Hempton, M.R., 1985. Structure and deformation history of the Bitlis Suture near Lake Hazar, SE Turkey. Geological Society of America Bulletin, 96, pp. 223-243.

Holland T.J.B., Powell R., 2003. Activity-composition relations for phases in petrological calculations: an asymmetric multicomponent formulation. Contributions to Mineralogy and Petrology, 145, pp. 492-501.

Huene, R., Ranero, C., Vannucchi, P., 2004. Generic model of subduction erosion. Geology, 32, pp. 913-916.

Humphris, S.E., Thompson, G., 1978. Hydrothermal alteration of oceanic basalts by seawater. Geochimica et Cosmochimica Acta, 42, pp. 107-125.

Jaillard, E., Benítez, S., Mascle, G., 1997. Les deformations paléogènes de la zone d'avant-arc sud-équatorienne en relation avec l'évolution géodynamique. Bulletin de la Société Géologique de France, 168, pp. 403-412.

Jourdan, F., Feraud, G., Bertrand, H., Kampunzu, A.B., Tshoso, G., Le Gall, B., Tiercelin, J.J., Capiez, P., 2004. The Karoo triple junction questioned: evidence from Jurassic and Proterozoic $^{40}Ar/^{39}Ar$ ages and geochemistry of the giant Okavango dyke swarm (Botswana). Earth and Planetary Science Letters, 222, pp. 989-1006.

Knipper, A.L., 1975. The oceanic crust in the structure of the Alpine Folded Belt (South Europe, western part of Asia and Cuba). Transactions, 267, Moscow 'Nauka', 207 p. (in Russian).

Knipper, A.L., Sokolov, S.D., 1977. Vedi ophiolites (Armenia): autochthone or allochtone? Geotektonica, 10, pp. 55–66 (in Russian).

Knipper, A.L., Khain, E.V., 1980. Structural position of ophiolites of the Caucasus. Ofioliti, Special Issue, 2, pp. 297–314.

Knipper, A.L., Ricou, L.E., Dercourt, J., 1986. Ophiolites as indicators of the geodynamic evolution of the Tethyan ocean. Tectonophysics, 123, pp. 213–240.

Knipper, A.L., Bragin, N.Y., Satian M.A., 1997. Upper Triassic-Lower Jurassic volcanogenic and sedimentary deposits of the Old Zod Pass (Transcaucasia). Stratigraphy and Geological Correlation, 5, pp. 58–65 (in Russian).

Kretz, R., 1983. Symbols of rock-forming minerals. American Mineralogist, 68, pp. 227-279.

Krogh, E.J., Råheim, A., 1978. Temperature and pressure dependence of Fe-Mg partitioning between garnet and phengite, with particular reference to eclogites. Contributions to Mineralogy and Petrology, 66, pp. 75-80.

Leake, B.E., Woolley, A.R., Arps, C.E.S., Birch, W.D., Gilbert, M.C., Grice, J.D., Hawthrne, F.C., Kato, A., Kisch, H.J., Krivovichiev, V.G., Linthout, K., Laird, J., Mandarino, J.A., Maresch, W.V., Nickel, E.H., Rock, N.M.S., Schumacher, J.C., Smith, D.C., Stephenson, N.C.N., Ungaretti, L., Whittaker, E.J.W., Youzhi, G., 1997. Nomenclature of amphiboles: report of the subcommittee on amphiboles of the international mineralogical association, commission on new minerals and mineral names. Canadian Mineralogist, 35, pp. 219-246.

Lytwyn, J.N., Casey, J.F., 1995. The geochemistry of postkinematic mafic dike swarms and subophiolitic metabasites, Pozantı–Karsantı ophiolite, Turkey: evidence for ridge subduction. Geological Society of America Bulletin, 107, pp. 830-850.

Massone, H-J., Schreyer, W., 1987. Phengite geobarometry based on the limiting assemblage with K-feldspar, phlogopite, and quartz. Contributions to Mineralogy and Petrology, 96, pp. 212-224.

Meijers, M., Sosson, M., Rolland, Y., Smith, B., Mensink, M., Grigoryan, A., Avagyan, A., Sahakyan, L., Sadradze, N., Adamia, S., Müller, C., 2012. Paleomagnetism of the Armenian Block and its foreland: constraints on the Tethyan Plate reconstructions and oroclinal bending during the Phanerozoic. 65th Geological Congress of Turkey.

Meijers, M., Smith, B., Sosson, M., Rolland, Y., Grigoryan, A., Sahakyan, L., Avagyan, A., Adamia, S., Sadradze, N., Asanidze, B., Langereis, C., Kircher, U., Mensink, M., Müller, C., 2013. A paleolatitude reconstruction of the South Armenian Block (SAB) since the late Cretaceous: constraints on the Tethyan realm. Darius Programme, Tbilisi Meeting, Eastern Black Sea and Caucasus Workshop.

Michard, A., Boudier, F., Goffé, B., 1991. Obduction versus subduction and collision in the Oman case and other Tethyan settings. Petrology and Structural Geology, 5, 1991, pp. 447-467.

Oberhänsli, R., Candan, O., Bousquet, R., Rimmele, G., Okay, A., Goff, J., 2010. Alpine HP evolution of the eastern Bitlis complex, SE Turkey. In: Sosson, M., Kaymakci, N., Stephanson, R., Bergarat, F., Storatchenoko, V., (eds.), Sedimentary Basin Tectonics from the Black Sea and Caucasus to the Arabian Platform. Geological Society, London, Special Publication, 340, pp. 461-483.

Obernänsli, R., Koralay, E., Candan, O., Pourteau, A., Bousquet, R., 2014. Late Cretaceous ecologitic high-pressure relics in the Bitlis Massif. Geodinamica Acta, (ahead-of-print), pp. 1-17.

Okay, A.I., Tüysüz, O., 1999. Tethyan sutures of northern Turkey. In "The Mediterranean Basins: Tertiary extension within the Alpine orogen" (eds. B. Durand, L. Jolivet, F. Horváth and M. Séranne), Geological Society, London, Special Publication, 156, pp. 475-515.

Okay, A.I., Tansel, I., Tüysüz, O., 2001. Obduction, subduction and collision as reflected in the Upper Cretaceous–Lower Eocene sedimentary record of western Turkey. Geological Magazine, 138, pp. 117-142.

O'Neill, H.St-C., Wood, B.J., 1979. An Eperimental Study of Fe-Mg Partitioning Between Garnet and Olivine and Its Calibration as a Geothermometer. Contributions to Mineralogy and Petrology, 70, pp. 59-70.

Palandjyan, S.A., 1971. The petrology of ultrabasic and gabbroic rocks of the Sevan mountain range. Izdatelstvo NAS Arm.SSR, 201 p. (in Russian).

Parlak, O., Delaloye, M., Bingöl, E., 1995. Origin of sub-ophiolitic metamorphic rocks beneath the Mersin ophiolite, southern Turkey. Ofioliti, 20, pp. 97-110.

Parlak, O., Yılmaz, H., Boztuğ, D., 2006. Origin and tectonic significance of the metamorphic sole and isolated dikes of the Divriği Ophiolite (Sivas, Turkey): evidence for slab break-off prior to ophiolite emplacement. Turkish Journal of Earth Sciences, 15, pp. 25-45.

Parlak, O., Çolakoğlu, A., Dönmez, C., Sayak, H., Yildirim, N., Türkel, A., Odabaşi, İ., 2012. Geochemistry and tectonic significance of ophiolites along the Ankara-Erzincan suture zone in northeastern Anatolia. Geological Society, London, Special Publications, 372.

Pearce, J.A., 1982. Trace element characteristics of lava from destructive plate boundaries. In: Thorpe, R.S. (Ed.), Andesites. Wiley, New York, pp. 525-548.

Pearce, J.A., 1983. Role of the sub-continental lithosphere in magma genesis at active continental margins. In: Hawkesworth, C.J., Norry, M.J. (Eds.), Continental Basalts and Mantle Xenoliths. Shiva, Nantwich, pp. 30-249.

Pearce, J.A., 1996. A users guide to basalt discrimination diagrams. In: Wyman, D.A. (eds.) Trace element geochemistry of volcanic rocks: applications for massive sulphide exploration. Geochemistry short course notes. Geological Association of Canada, 12, pp. 79-113.

Pearce, J.A., Cann, J.R., 1973. Tectonic setting of basaltic volcanic rocks determined using trace element analysis. Earth and Planetary Science Letters, 19, pp. 290-300.

Pearce, J.A., Norry, M.J., 1979. Petrogenetic implications of Ti, Zr, Y and Nb variations in volcanic rocks. Contributions to Mineralogy and Petrology, 69, pp. 33–47.

Pearce, J.A., Lippard, S.J., Roberts, S., 1984. Characteristics and tectonic significance of suprasubduction zone ophiolite. In: Kokelaar, B.P., Howells, M.F. (Eds.), Marginal Basin Geology. Geological Society, London, Special Publication, 16, pp. 77-94.

Perchuk, L.L., Aranovich, L.Y., Podlesskii, K.K., Lavrant'eva, I.V., Gerasimov, V.Y., Fed'Kin, V.V., Kitsul, V.I., Karsakov, L.P., Berdnikov, N.V., 1985. Precambrian granulites of the Aldan shield, eastern Siberia, USSR. Journal of metamorphic Geology, 3, pp. 265-310.

Perfit, M.R., Gust, D.A., Bence, A.E., Arculus, R.J., Taylor, S.R., 1980. Chemical characteristics of island-arc basalts: implications for mantle sources. Chemical Geology, 30, pp. 227-256.

Pourteau, A., Sudo, M., Candan, O., Lanari, P., Vidal, O., Oberhänsli, R., 2013. Neotethys closure history of Anatolia: insights from 40Ar–39Ar geochronology and P–T estimation in high-pressure metasedimentary rocks. Journal of Metamorphic Geology 31, 585–606.

Råheim, A., Green, D.H. 1974. Experimental determination of the temperature and pressure dependence of the Fe-Mg partition coefficient for coexisting garnet and clinopyroxene. Contributions to Minerology and Petrology, 48, pp. 179-203.

Rice, S.P., Robertson, A.H.F., Ustaömer, T., Inan, N., Tasli, K., 2009. Late Cretaceous–Early Eocene tectonic development of the Tethyan suture zone in the Erzincan area, Eastern Pontides, Turkey. Geological Magazine, 146, pp. 567-590.

Ricou, L.E., 1994. Tethys reconstructed: plates, continental fragments and their bounderies since 260 Ma from Central America to South-eastern Asia. Gedinamica Acta, 7, pp. 169-218.

Ricou, L.E., Dercourt, J., Geyssant, J., Grand-Jaquet, C., Lepcrier, C., Biju-Duval, B., 1986. Geological constraints on the Alpine evolution of the Mediterranean Tethys. Tectonophysics, 123, pp. 83-122.

Ricou, L.E., Zonenshain, L.P., Dercourt, J., Kazmin, V.G., Le Pichon, X., Knipper, A.L., Grandjacquet, C., Sborshchikov, I.M., Geyssant, J., Lepvrier, C., Pechersky, D.M., Boulin, J., Sibuet, J.C., Savostin, L.A., Sorokhtin, O., Westphal, M., Bazhenov, M.L., Lauer, J.P., Biju-Duval, B., 1985. Méthodes pour l'établissement de neuf cartes paléogéographiques de l'Atlantique au Pamir depuis le Lias. Bulletin de la Société Géologique de France, 8, pp. 625-635.

Robertson, A., 2004. Development of concepts concerning the genesis and emplacement of Tethysan ophiolites in the Eastern Mediterranean and Oman regions. Earth-Science Reviews, 66, pp. 331-387.

Robertson, A.H.F., Karamata, S., 1994. The role of subduction-accretion processes in the tectonic evolution of the Mesozoic Tethys in Serbia. Tectonophysics, 234, pp. 73-94.

Rolland, Y., Billo, S., Corsini, M., Sosson, M., Galoyan, G., 2009a. Blueschists of the Amasia-Stepanavan Suture Zone (Armenia): linking Tethys subduction history from E-Turkey to W-Iran. International Journal Earth Sciences (Geologische Rundschau), 98, pp. 533-550.

Rolland, Y., Galoyan, Gh., Bosch, D., Sosson, M., Corsini, M., Fornari, M., Vérati, C., 2009b. Jurassic Back-arc and hot-spot related series in the Armenian ophiolites – Implications for the obduction process. Lithos, 112, pp. 163-187.

Rolland Y., Galoyan G., Sosson, M., Melkonian R., Avagyan A., 2010. The Armenian ophiolites : insights for Jurassic Back-arc formation, Lower Cretaceous hot-spot magmatism, and Upper Cretaceous obduction over the South Armenian Block. In: M.Sosson, N. Kaymakci, R. Stephanson, F. Bergarat, and V. Storatchenoko (eds.) Sedimentary basin tectonics from the Black Sea and Caucasus to the Arabian Platform. Geological Society, London, Special Publication, 340, pp. 353–382.

Rolland, Y., Sosson, M., Adamia, Sh., Sadradze, N., 2011. Prolonged Variscan to Alpine history of an active Eurasian margin (Georgia, Armenia) revealed by $^{40}Ar/^{39}Ar$ dating. Gondwana Research, 20, pp. 798-815.

Rolland, Y., Perincek, D., Kaymakci, N., Sosson, M., Barrier, E., Avagyan, A., 2012. Evidence for ~80-75 Ma subduction jump during Anatolide-Tauride-Armenian block accretion and ~48 Ma Arabia-Eurasia collision in Lesser Caucasus-East Anatolia. Journal of Geodynamics, 56-57, pp. 76-85.

Rollinson, H.R., 1993. Using geochemical data: evaluation, presentation, interpretation. Longman Scientific & Technical, 352 p.

Sage, F., Collot, J-.Y., Ranero, C.R., 2006. Interplate patchiness and subduction-erosion mechanisms: Evidence from depth-migrated seismic images at the central Ecuador convergent margin. Geology, 34, pp. 997-1000.

Shemenda, A.I., 1994. Subduction: Insights from Physical Modeling. Kluwer Academic Publishers, p. 215.

Searle, M., Cox, J., 1999. Tectonic setting, origin, and obduction of the Oman ophiolite. Geological Society of America Bulletin, 111, pp. 104-122.

Sengör, A.M.C., Yilmaz, Y., 1981. Tethyan evolution of Turkey: A plate tectonic approach. Tectonophysics, 75, pp. 181-241.

Sokolov, 1977. The olistostromes and ophiolitic nappes of the Lesser Caucasus. Izdatelstvo 'Nauka', Moscow, 92 p. (in Russian).

Sosson, M., Rolland, Y., Danelian, T., Muller, C., Melkonyan, R., Adamia, S., Kangarli, T., Avagyan, A., Galoyan, G., 2010. Subductions, obduction and collision in the Lesser Caucasus (Armenia, Azerbaijan, Georgia), new insights. Geological Society, London, Special Publications, 340, pp. 329-352.

Spray, J.G., 1983. Lithosphere- asthenosphere decoupling at spreading centers and initiation of obduction. Nature, 304, pp. 253-255.

Stampfli, G.M., Borel, G.D., Cavazza, W., Mosar, J., Ziegler, P.A., 2001. Palaeotectonic and palaeogeographic evolution of the western Tethys and PeriTethyan domain (IGCP Project 369). Episodes, 24, pp. 222-228.

Stampfli, G.M., Borel, G.D., 2002. A plate tectonic model for the Paleozoic and Mesozoic constrained by dynamic plate boundaries and restored synthetic oceanic isochrones. Earth and Planetary Science Letters, 196, pp. 17-33.

Steiger, R.H., Jäger, E., 1977. Subcommission on geochronology: convention on the use of decay constants in geo- and cosmochronology. Earth and Planetary Science Letters, 36, pp. 359-362.

Sun, S.S., McDonough, W.F., 1989. Chemical and isotopic systematic of oceanic basalts: implications for mantle composition and processes. In: Saudners A.D., Norry, M.J. (Eds.), Magmatism in Ocean Basins, Geological Society, London, Special Publications, 42, pp. 313-345.

Topuz, G., Göçmengil, G., Rolland, Y., Çelik, Ö. F., Zack, T., Schmitt, A.K., 2013a. Jurassic accretionary complex and ophiolite from northeast Turkey: No evidence for the Cimmerian continental ribbon. Geology, 41, pp. 255-258.

Topuz, G., Çelik, O.F., Şengör, C., Altıntaş, E., Zack, T., Rolland, Y., Barth M., 2013b. Jurassic ophiolite formation and emplacement as backstop to a subduction-accretion complex in NE Turkey and relation to the Balkan ophiolites. American Journal of Science 10/2013; DOI:DOI 10.2475/09.2013.00

Turner, G., Huneke, J.C., Podose, F.A., Wasserburg, G.J., 1971. $^{40}Ar/^{39}Ar$ ages and cosmic ray exposure ages of Apollo 14 samples. Earth and Planetary Science Letters, 12, pp. 15-19.

Uysal, I.E., Ersoy, Y., Dilek, Y., Escayola, M., Sarıfakıoğlu, E., Saka, S., Hirata, T., 2013. Depletion and refertilization of the Tethyan oceanic upper mantle as revealed by the early

Jurassic Refahiye ophiolite, NE Anatolia—Turkey. Gondwana Research, (ahead-of-print), pp. 1-18)

Velde, B., 1965. Phengote micas: synthesis, stability and natural occurrence. American Journal of Science, 263, pp. 886-913.

Vergili, Ö., Parlak, O., 2005. Geochemistry and tectonic significance of metamorphic sole rocks and mafic dikes from the Pınarbaşı (Kayseri) ophiolite, central Anatolia (Turkey). Ofioliti, 30, pp. 37-52.

Wakabayashi, J., Dilek, Y., 2000. Spatial and temporal relationships between ophiolites and their metamorphic soles: a test of models of forearc ophiolite genesis. In: Dilek, Y., Moores, E.M., Elthon, D., Nicolas, A. (Eds.), Ophiolites and Oceanic Crust: New Insight from Field Studies and the Ocean Drilling Program:Boulder Colorado. Geological Society of America Special Paper, 349, pp. 53-64.

Wakabayashi, J., Dilek, Y., 2003. What constitutes 'emplacement' of an ophiolite?: Mechanisms and relationship to subduction initiation and formation of metamorphic soles. Geological Society, London, Special Publications, 218, pp. 427-447.

Whitechurch, H., Juteau, T., Montigny, R., 1984. Role of the Eastern Mediterranean ophiolites (Turkey, Syria, Cyprus) in the history of the Neo-Tethys. Geological Society, London, Special Publications, 17, pp. 301-317.

Yamamoto, S., Senshu H., Rino, S., Omori, S., Maruyama, S., 2009. Granite subduction: Arc subduction, tectonic erosion and sediment subduction. Gondwana Research, 15, pp. 443-453.

Yılmaz, A., Adamia, S., Yılmaz, H., 2013. Comparison of the suture zones along a geotravse from the Scythian Platform to the Arabian Platform. Geoscience Frontiers, (ahead-of-print), pp. 1-21.

Yılmaz, Y. 1993. New evidence and model on the evolution of the southeast Anatolian orogen. Bulletin of the Geological Society of America, 105, pp. 252-271.

Yılmaz, Y., Yiğitbaş, E., Can Genç, S., 1993. Ophiolitic and metamorphic assemblages of Southeast Anatolia and their significance in the geological evolution of the orogenic belt. Tectonics, 10, pp. 1280-1297.

Zakariadze, G.S., Knipper, A.L., Sobolev A.V., Tsamerian, O.P., Dmitriev, L.V., Vishnevskaya, V.S., Kolesov, G.M., 1983. The ophiolite volcanic series of the Lesser Caucasus. Ofioliti, 8, pp. 439-466.

Zakariadze G.S., Knipper A.L., Bibikova E.V., Silantiev S.A., Zlobin S.K., Gracheva T.V., Makarov S.A., Kolesov T.M., 1990. The setting and age of the plutonic part of the NE Sevan ophiolite complex. Izvestia NAS USSR, Geological series 3, pp. 17-30, (in Russian).

Zakariadze, G.S., Dilek, Y., Bogdanovsky, O.G., Karpenko, S.F., Vishnevskaya, V.S., Solov'eva, N.V., 2005. Age limits of the Lesser Caucasus paleooceanic allochthon. Abstracts of the International Symposium on the Geodynamics of Eastern Mediterranean: Active Tectonics of the Aegean Region, 15–18 June 2005, Kadir Has University, Istanbul, Turkey, p. 229.

Tables

Sample	AR-09-02	AR-09-03	AR-09-06	AR-09-12	AR-09-14	AR-09-17	AR-10-12
Formation	Plagiogranite	Basalt	Garnet Amphibolite	Gabbro	Basalt	Gabbro	Basalte
SiO2	72.70	50.18	46.09	56.91	51.98	47.81	58.85
TiO2	0.65	2.39	3.00	0.93	3.04	0.57	0.52
Al2O3	10.19	15.36	14.06	15.65	14.36	15.45	18.47
Fe203	0.79	1.95	1.88	1.67	1.76	1.32	0.99
FeO	4.03	9.93	9.59	8.53	8.97	6.74	5.05
MnO	0.10	0.19	0.09	0.17	0.22	0.16	0.16
MgO	2.22	3.63	2.38	5.11	4.12	7.99	2.52
CaO	5.93	9.27	15.08	4.95	11.69	19.42	7.27
Na2O	2.09	3.66	4.54	5.04	2.56	0.42	4.02
K2O	1.20	2.91	2.49	0.93	0.85	0.07	1.91
P2O5	0.09	0.55	0.79	0.10	0.45	0.05	0.24
Total	100.00	100.00	100.00	100.00	100.00	100.00	99.99
Ba	122.40	315.90	157.00	93.91	304.90	7.12	683.40
Rb	36.88	61.18	66.02	6.43	9.98	0.81	44.23
Sr	62.92	115.50	287.50	122.70	407.20	82.16	732.60
Ta	0.83	3.03	2.66	0.20	2.38	0.04	0.40
Th	6.46	3.83	2.95	0.65	2.36	0.13	5.77
Zr	194.30	204.70	201.40	52.50	176.80	30.50	120.90
Nb	9.89	40.52	35.66	2.38	30.76	0.45	5.82
Y	17.05	21.23	29.86	20.76	27.02	14.68	16.04
Hf	5.01	4.55	4.67	1.51	4.17	1.07	2.99
V	75.58	187.40	294.40	286.80	244.10	240.10	110.60
Cr	169.50	83.64		13.24	44.39	77.09	6.34
Ni	50.63	62.66	25.47	23.62	50.84	65.31	5.07
Co	8.97	19.96	32.74	30.39	31.08	35.43	13.83
U	1.51	0.86	0.91	0.22	0.52	0.06	2.13
Cu	13.48	8.10	41.51	37.35	61.91	10.59	31.48
Zn	57.65	79.63	154.90	42.99	87.58	63.26	70.12
Pb	11.91	4.89	3.96		3.59		7.62
Cs	1.17	1.73	2.03		0.21		0.48
La	21.08	28.78	32.08	3.83	24.98	1.32	27.03
Ce	41.27	60.41	64.86	8.89	50.84	4.06	47.78
Pr	4.69	7.15	7.85	1.29	6.24	0.68	5.36
Nd	17.45	27.76	31.64	6.33	26.07	3.65	19.88
Sm	3.53	5.62	6.87	2.07	6.00	1.26	3.80
Eu	0.73	1.83	2.22	0.74	2.05	0.51	1.19
Gd	3.11	5.03	6.62	2.70	5.68	1.82	3.15
Tb	0.51	0.74	0.97	0.48	0.89	0.34	0.47
Dy	3.06	4.04	5.57	3.31	5.17	2.31	2.71
Ho	0.60	0.75	1.04	0.73	0.97	0.52	0.53
Er	1.73	2.01	2.78	2.14	2.50	1.55	1.55
Tm	0.26	0.29	0.39	0.33	0.35	0.24	0.24
Yb	1.81	1.83	2.48	2.25	2.24	1.67	1.70
Lu	0.28	0.28	0.37	0.36	0.33	0.27	0.26

Table 6 - Representative whole-rock analyses of samples from ophiolitic complex of Amasia.

Sample	AR-08-09c	AR-08-13	AR-08-22	AR-08-29	AR-10-13
Formation	Garnet Amphibolite	Gabbro	Gabbro	Gabbro	Garnet Amphibolite
SiO2	54.37	54.68	55.90	47.73	45.23
TiO2	0.98	0.24	0.95	2.45	1.64
Al2O3	19.43	20.44	15.85	14.21	18.31
Fe203	1.73	0.88	1.72	2.10	1.92
FeO	8.83	4.51	8.76	10.72	9.78
MnO	0.13	0.10	0.17	0.15	0.20
MgO	3.65	5.36	5.02	6.35	7.38
CaO	6.34	9.79	5.81	11.66	15.36
Na2O	3.12	3.75	5.57	4.05	1.62
K2O	1.35	0.23	0.19	0.31	0.47
P2O5	0.06	0.01	0.05	0.28	0.17
Total	100.00	100.00	100.00	100.00	102.09

Table 6 - Representative whole-rock analyses of samples from ophiolitic complex of Amasia (continued).

Sample	AR 08 09c										
Analysis	98 / 1 .	99 / 1 .	100 / 1 .	104 / 1 .	105 / 1 .	107 / 1 .	65 / 1 .	66 / 1 .	31 / 1 .	32 / 1 .	42 / 1 .
SiO2	37.84	37.91	37.76	37.63	37.74	37.87	38.11	37.97	35.76	36.11	38.09
Al2O3	20.83	21.15	20.63	20.97	20.87	21.01	20.98	20.98	20.00	20.24	21.09
MgO	3.31	3.36	3.38	3.47	3.38	3.34	3.42	3.51	3.44	3.23	3.33
FeO	31.46	31.14	31.42	31.59	31.76	31.66	31.38	31.33	31.51	31.12	31.24
MnO	0.44	0.48	0.49	0.53	0.60	0.56	0.24	0.11	1.14	1.42	1.29
Cr2O3				0.01			0.01	0.04	0.00		0.03
TiO2	0.07	0.17	0.15	0.20	0.17	0.12	0.13	0.11	0.15	0.16	0.16
CaO	6.64	6.83	6.75	6.36	6.38	6.24	6.61	6.67	6.29	6.38	6.48
Na2O		0.06	0.05	0.05	0.07	0.03	0.05		0.03	0.02	0.04
K2O	0.02			0.01	0.03		0.01				
Total	100.61	101.09	100.63	100.81	101.01	100.83	100.94	100.71	98.33	98.68	101.74
Almandine	67.9	67.2	67.4	68.0	68.2	68.6	67.9	67.8	67.3	66.9	66.8
Spessartine	1.0	1.0	1.1	1.1	1.3	1.2	0.5	0.2	2.5	3.1	2.8
Pyrope	12.8	12.9	12.9	13.3	12.9	12.9	13.2	13.5	13.1	12.4	12.7
Grossular	18.4	18.9	18.6	17.5	17.5	17.3	18.3	18.5	17.2	17.6	17.7

Sample	AR 09 08										
Analysis	158 / 1 .	158 / 2 .	158 / 3 .	158 / 4 .	158 / 5 .	158 / 6 .	158 / 7 .	158 / 8 .	158 / 9 .	158 / 10 .	158 / 11 .
SiO2	37.24	37.37	37.48	37.66	37.61	37.54	37.77	37.70	37.28	37.69	37.23
Al2O3	21.28	20.92	20.99	20.86	20.99	20.90	20.81	20.90	20.80	20.85	20.99
MgO	6.76	6.35	6.27	6.47	6.55	6.60	6.49	6.76	6.52	6.29	6.33
FeO	30.29	29.29	29.23	29.89	29.32	29.77	29.42	29.77	29.94	29.24	29.47
MnO	0.53	0.48	0.58	0.49	0.49	0.52	0.59	0.52	0.51	0.40	0.53
Cr2O3											
TiO2	0.11	0.11	0.08	0.09	0.02	0.16	0.10	0.04	0.04	0.00	0.07
CaO	3.21	4.55	4.55	4.44	4.15	3.81	3.70	3.66	4.05	4.28	4.51
Na2O	0.13	0.04	0.06	0.06	0.08	0.11	0.07	0.07	0.06	0.17	0.05
K2O											
Total	99.54	99.10	99.25	99.95	99.22	99.41	98.95	99.43	99.20	98.92	99.20
Almandine	64.5	62.4	62.4	62.8	62.6	63.4	63.5	63.3	63.3	63.1	62.6
Spessartine	1.1	1.0	1.3	1.0	1.1	1.1	1.3	1.1	1.1	0.9	1.1
Pyrope	25.6	24.1	23.9	24.2	24.9	25.1	25.0	25.6	24.6	24.2	24.0
Grossular	8.8	12.4	12.4	11.9	11.4	10.4	10.2	10.0	11.0	11.8	12.3

Sample	AR 09 08										
Analysis	158 / 12 .	158 / 13 .	158 / 14 .	158 / 16 .	158 / 17 .	158 / 18 .	158 / 19 .	158 / 20 .	158 / 21 .	158 / 22 .	158 / 23 .
SiO2	37.93	37.66	37.64	36.33	36.85	37.93	37.62	35.85	37.99	35.85	37.66
Al2O3	21.03	20.97	20.88	20.83	20.56	21.31	21.03	23.09	21.24	19.91	21.20
MgO	6.52	6.51	6.33	6.26	6.23	6.72	6.34	5.71	6.74	6.03	6.49
FeO	29.92	29.55	29.67	27.98	28.73	29.98	29.46	29.01	29.96	29.16	29.18
MnO	0.55	0.48	0.54	0.59	0.47	0.56	0.61	0.51	0.58	0.57	0.57
Cr2O3											
TiO2	0.11	0.10	0.07	0.04	0.04	0.03	0.04	0.03	0.09	0.11	0.05
CaO	3.68	4.22	4.15	4.66	4.73	3.57	4.54	4.31	3.55	4.18	4.62
Na2O	0.09	0.06	0.06	1.27	0.52	0.14	0.07	0.07	0.02	0.08	0.05
K2O											
Total	99.82	99.55	99.33	97.97	98.12	100.25	99.70	98.58	100.17	95.89	99.83
Almandine	63.9	62.8	63.4	61.2	62.0	63.6	62.4	64.1	63.6	63.6	61.8
Spessartine	1.2	1.0	1.2	1.3	1.0	1.2	1.3	1.1	1.3	1.3	1.2
Pyrope	24.8	24.7	24.1	24.4	23.9	25.4	24.0	22.5	25.5	23.5	24.5
Grossular	10.1	11.5	11.4	13.1	13.1	9.7	12.3	12.2	9.6	11.7	12.5

Table 7 - Electron microprobe analyses of representative garnets from metamorphic rocks of the Amasia ophiolite complex. Oxydes and end-member proportions are given in percentages.

Sample	AR 09 08										
Analysis	158 / 24 .	158 / 25 .	158 / 26 .	158 / 28 .	158 / 29 .	158 / 30 .	158 / 31 .	158 / 32 .	158 / 33 .	158 / 34 .	158 / 35 .
SiO2	37.54	37.81	37.64	37.90	38.04	37.87	38.08	37.88	38.00	37.68	37.47
Al2O3	21.26	21.28	20.96	20.96	20.83	21.39	21.07	21.37	21.14	21.05	20.96
MgO	6.60	6.45	6.45	6.80	6.81	6.93	6.92	6.96	6.68	6.64	6.51
FeO	29.36	29.05	29.07	29.37	29.25	29.81	29.46	29.71	29.45	29.13	30.68
MnO	0.58	0.49	0.58	0.49	0.53	0.54	0.52	0.53	0.51	0.55	0.52
Cr2O3											
TiO2	0.03	0.08	0.10	0.05	0.05	0.07	0.13	0.03	0.05	0.06	0.16
CaO	4.44	4.36	4.48	3.81	3.94	3.45	3.79	3.24	3.91	3.99	3.29
Na2O	0.08	0.10	0.09	0.02	0.09	0.02	0.03	0.04	0.07	0.23	0.06
K2O											
Total	99.90	99.62	99.36	99.40	99.54	100.08	99.99	99.76	99.81	99.32	99.65
Almandine	61.9	62.3	62.0	62.7	62.3	63.2	62.4	63.5	62.8	62.5	65.2
Spessartine	1.2	1.1	1.2	1.1	1.1	1.2	1.1	1.1	1.1	1.2	1.1
Pyrope	24.8	24.7	24.5	25.9	25.8	26.2	26.1	26.5	25.4	25.4	24.7
Grossular	12.0	12.0	12.2	10.4	10.8	9.4	10.3	8.9	10.7	10.9	9.0

Sample	AR 09 08										
Analysis	158 / 37 .	158 / 38 .	158 / 39 .	158 / 40 .	158 / 41 .	158 / 42 .	158 / 43 .	158 / 44 .	158 / 45 .	158 / 46 .	158 / 47 .
SiO2	37.91	37.64	37.71	37.74	38.27	38.37	37.88	37.89	38.37	38.03	38.25
Al2O3	21.21	21.33	21.16	21.01	21.48	21.13	21.15	21.28	21.37	21.08	21.66
MgO	6.82	7.21	7.39	7.28	7.46	7.45	7.51	7.36	7.36	7.44	7.32
FeO	29.67	29.73	30.09	29.68	29.77	29.89	29.70	29.92	30.09	29.52	29.54
MnO	0.51	0.54	0.46	0.52	0.36	0.39	0.41	0.35	0.36	0.37	0.34
Cr2O3											
TiO2	0.11	0.05	0.00	0.10	0.04	0.09	0.06	0.04	0.08	0.07	0.05
CaO	3.85	3.39	2.70	3.09	2.93	2.93	2.73	3.07	2.99	2.79	3.57
Na2O	0.09	0.08	0.04	0.08	0.06	0.07	0.07	0.07	0.02	0.10	0.06
K2O											
Total	100.17	99.97	99.54	99.49	100.37	100.33	99.52	99.98	100.64	99.41	100.79
Almandine	62.7	62.6	63.8	63.0	63.1	63.1	63.2	63.2	63.5	63.2	62.2
Spessartine	1.1	1.1	1.0	1.1	0.8	0.8	0.9	0.7	0.8	0.8	0.7
Pyrope	25.7	27.1	27.9	27.5	28.2	28.1	28.5	27.7	27.7	28.4	27.5
Grossular	10.4	9.2	7.3	8.4	7.9	7.9	7.4	8.3	8.1	7.6	9.6

Sample	AR 09 08										
Analysis	158 / 48 .	158 / 49 .	158 / 50 .	158 / 52 .	158 / 54 .	158 / 55 .	158 / 56 .	158 / 57 .	158 / 58 .	158 / 60 .	158 / 61 .
SiO2	38.25	38.11	37.92	37.95	38.03	38.15	37.64	38.16	38.13	38.02	38.21
Al2O3	21.18	21.19	21.43	21.37	21.45	21.53	21.14	21.35	21.23	21.54	21.57
MgO	7.43	7.53	7.60	7.45	7.49	7.16	6.94	7.30	7.04	7.22	7.66
FeO	29.54	29.76	29.78	29.06	29.29	29.14	28.79	29.28	29.36	28.33	28.66
MnO	0.29	0.22	0.19	0.21	0.23	0.13	0.10	0.05	0.12	0.03	0.11
Cr2O3											
TiO2	0.05	0.12	0.05	0.13	0.10	0.17	0.10	0.12	0.16	0.11	0.04
CaO	2.95	3.06	3.05	3.31	3.65	3.85	4.10	3.90	4.12	4.23	3.96
Na2O	0.03	0.05	0.03	0.05	0.06	0.07	0.09	0.02	0.03	0.06	0.04
K2O											
Total	99.72	100.05	100.04	99.52	100.30	100.21	98.90	100.18	100.18	99.54	100.24
Almandine	63.0	62.9	62.8	62.1	61.6	62.0	61.9	61.8	62.1	60.7	60.3
Spessartine	0.6	0.5	0.4	0.5	0.5	0.3	0.2	0.1	0.3	0.1	0.2
Pyrope	28.3	28.4	28.6	28.4	28.1	27.2	26.6	27.5	26.5	27.6	28.7
Grossular	8.1	8.3	8.2	9.1	9.8	10.5	11.3	10.5	11.1	11.6	10.7

Table 7 - Electron microprobe analyses of representative garnets from metamorphic rocks of the Amasia ophiolite complex. Oxydes and end-member proportions are given in percentages (continued).

Sample	AR 09 08										
Analysis	158 / 62 .	158 / 63 .	158 / 64 .	173 / 1.	179 / 1.	187 / 1 .	187 / 2 .	187 / 3 .	187 / 4 .	187 / 5 .	187 / 6 .
SiO2	38.09	38.40	38.55	37.79	38.29	37.50	37.49	37.81	38.17	38.02	35.98
Al2O3	21.33	21.40	21.62	21.41	21.27	20.83	21.13	21.53	21.43	21.14	21.63
MgO	7.68	7.65	7.97	7.94	8.15	6.98	6.88	6.90	6.76	6.66	6.01
FeO	27.96	28.08	27.90	28.08	27.92	29.35	28.72	29.28	29.16	29.62	29.57
MnO	0.13	0.12	0.17	0.14	0.13	0.10	0.10	0.07	0.08	0.04	0.06
Cr2O3											
TiO2	0.15	0.08	0.15	0.04	0.08	0.20	0.19	0.13	0.15	0.16	0.15
CaO	4.06	4.12	4.00	3.17	3.35	3.91	4.23	4.20	4.25	4.29	4.20
Na2O	0.07	0.03	0.11	0.08	0.05	0.08	0.04	0.04	0.05	0.02	0.04
K2O											
Total	99.47	99.89	100.46	98.64	99.24	98.93	98.78	99.96	100.03	99.95	97.64
Almandine	59.5	59.6	58.9	60.5	59.5	62.6	61.8	62.2	62.4	63.0	64.7
Spessartine	0.3	0.3	0.4	0.3	0.3	0.2	0.2	0.1	0.2	0.1	0.1
Pyrope	29.2	28.9	30.0	30.5	31.0	26.5	26.4	26.2	25.8	25.2	23.4
Grossular	11.1	11.2	10.8	8.7	9.2	10.7	11.6	11.4	11.6	11.7	11.8

Sample	AR 09 08										
Analysis	187 / 7 .	187 / 8 .	187 / 9 .	187 / 10 .	187 / 11 .	187 / 12 .	187 / 13 .	187 / 14 .	187 / 15 .	187 / 16 .	187 / 17 .
SiO2	37.76	37.55	38.01	38.11	37.92	37.79	37.74	37.85	37.91	38.00	37.95
Al2O3	20.84	20.89	20.90	21.22	21.20	20.81	21.30	20.69	20.85	21.36	21.43
MgO	6.77	6.83	6.82	6.78	6.81	6.57	6.54	6.57	6.51	6.39	6.55
FeO	30.51	30.17	29.92	30.62	30.55	30.09	30.31	30.16	30.41	30.26	30.19
MnO	0.06	0.07	0.07	0.03	0.09	0.06	0.13	0.12	0.05	0.11	0.15
Cr2O3											
TiO2	0.20	0.21	0.19	0.24	0.15	0.19	0.17	0.16	0.17	0.16	0.12
CaO	3.71	3.65	3.78	3.67	3.43	4.13	4.06	3.90	4.01	4.06	3.91
Na2O	0.04	0.09	0.07	0.04	0.07	0.04	0.06	0.02	0.04	0.07	0.06
K2O											
Total	99.90	99.45	99.76	100.71	100.23	99.67	100.31	99.48	99.95	100.40	100.35
Almandine	64.4	64.1	63.7	64.6	64.7	63.8	64.1	64.2	64.4	64.4	64.2
Spessartine	0.1	0.1	0.1	0.1	0.2	0.1	0.3	0.3	0.1	0.2	0.3
Pyrope	25.5	25.9	25.9	25.5	25.7	24.8	24.7	24.9	24.6	24.2	24.8
Grossular	10.0	9.9	10.3	9.9	9.3	11.2	11.0	10.6	10.9	11.1	10.7

Sample	AR 09 08			AR 09 09			
Analysis	187 / 18 .	187 / 19 .	187 / 20 .	192 / 1 .	198 / 1 .	203 / 1 .	204 / 1 .
SiO2	37.99	38.21	37.76	37.05	36.82	37.31	37.04
Al2O3	21.12	20.98	21.07	20.47	20.93	20.71	20.53
MgO	6.64	6.88	6.87	2.15	2.56	2.52	2.60
FeO	30.21	30.32	29.84	28.03	30.21	28.17	30.67
MnO	0.06	0.16	0.11	2.36	1.78	1.96	1.93
Cr2O3							
TiO2	0.15	0.10	0.09	0.26	0.06	0.06	0.14
CaO	3.49	3.83	3.53	10.18	7.11	9.47	7.21
Na2O	0.06	0.10	0.05	0.03		0.04	0.01
K2O							
Total	99.71	100.58	99.32	100.55	99.48	100.25	100.13
Almandine	64.9	63.6	63.9	59.3	66.1	60.2	66.0
Spessartine	0.1	0.3	0.2	5.1	4.0	4.2	4.2
Pyrope	25.4	25.7	26.2	8.1	10.0	9.6	10.0
Grossular	9.6	10.3	9.7	27.6	19.9	25.9	19.9

Table 7 - Electron microprobe analyses of representative garnets from metamorphic rocks of the Amasia ophiolite complex. Oxydes and end-member proportions are given in percentages (continued).

Sample	AR 08 09c										
Analysis	37 / 1 .	39 / 1 .	40 / 1 .	46 / 1 .	47 / 1 .	59 / 1 .	60 / 1 .	115 / 1 .	115 / 2 .	115 / 3 .	115 / 4 .
SiO2	40.75	41.27	41.33	41.83	41.44	40.94	41.52	40.67	40.67	40.45	40.84
Al2O3	16.08	15.85	16.17	15.62	15.82	15.57	15.63	15.57	15.67	15.66	15.71
MgO	7.56	7.54	7.69	7.74	7.88	7.76	8.62	7.31	7.57	7.54	7.91
FeO	18.62	18.99	19.01	18.12	18.15	17.91	17.08	18.89	18.55	18.22	18.06
MnO	0.15	0.20	0.16	0.00	0.04	0.02	0.06	0.17	0.09	0.10	0.08
Cr2O3	0.00	0.00	0.00	0.00	0.00	0.00	0.03	0.00	0.00	0.01	0.03
TiO2	0.35	0.23	0.32	0.54	0.67	0.39	0.39	0.25	0.25	0.34	0.34
CaO	10.86	10.92	10.49	9.60	9.63	10.58	10.31	10.58	10.75	10.69	10.73
Na2O	2.01	1.94	1.95	2.38	2.49	2.30	2.08	1.95	2.01	2.01	1.88
K2O	0.36	0.30	0.37	0.53	0.52	0.42	0.36	0.43	0.41	0.43	0.41
Total	96.73	97.24	97.50	96.37	96.65	95.88	96.07	95.81	95.96	95.46	95.97
Al/(Al+Si)	0.25	0.24	0.25	0.31	0.32	0.28	0.27	0.25	0.25	0.25	0.24
Na/(Na+Ca)	0.32	0.31	0.32	0.31	0.31	0.31	0.31	0.31	0.31	0.31	0.31

Sample	AR 08 09c										
Analysis	115 / 5 .	115 / 6 .	115 / 7 .	115 / 8 .	115 / 9 .	115 / 10 .	115 / 11 .	115 / 13 .	115 / 14 .	115 / 15 .	115 / 16 .
SiO2	41.20	41.06	41.89	40.92	41.48	41.74	41.70	41.75	41.66	41.21	41.33
Al2O3	15.76	15.91	15.98	15.39	15.21	15.07	15.38	15.20	15.22	15.28	15.23
MgO	8.10	7.91	8.37	8.06	8.21	8.45	8.53	8.20	7.98	7.96	7.81
FeO	18.37	17.97	17.90	17.91	17.97	17.50	17.25	18.24	18.40	18.26	18.30
MnO	0.11	0.11	0.05	0.04	0.13	0.09	0.07	0.12	0.11	0.11	0.14
Cr2O3	0.00	0.00	0.02	0.01	0.00	0.04	0.04	0.03	0.00	0.02	0.06
TiO2	0.47	0.41	0.38	0.36	0.41	0.36	0.31	0.36	0.31	0.44	0.47
CaO	10.46	10.51	10.41	10.40	10.39	10.59	10.39	10.45	10.36	10.45	10.47
Na2O	2.00	2.11	2.06	2.14	2.05	2.02	1.92	2.02	2.07	2.09	2.00
K2O	0.36	0.42	0.44	0.47	0.44	0.41	0.38	0.43	0.37	0.38	0.39
Total	96.82	96.41	97.49	95.71	96.29	96.29	95.97	96.79	96.49	96.18	96.21
Al/(Al+Si)	0.26	0.27	0.26	0.27	0.26	0.26	0.25	0.26	0.27	0.27	0.26
Na/(Na+Ca)	0.31	0.31	0.31	0.31	0.30	0.30	0.30	0.30	0.30	0.30	0.30

Sample	AR 08 09c								AR 08 22	
Analysis	115 / 17 .	115 / 20 .	115 / 22 .	115 / 23 .	115 / 24 .	115 / 26 .	115 / 29 .	115 / 30 .	68 / 1 .	72 / 1 .
SiO2	42.25	41.91	41.08	41.00	41.75	41.58	40.49	40.89	42.98	43.14
Al2O3	14.82	16.14	15.39	15.39	14.77	14.74	15.62	15.79	14.79	13.93
MgO	7.52	8.37	7.83	7.70	7.59	8.08	7.27	7.34	9.12	9.25
FeO	17.75	17.55	18.67	18.39	18.84	17.34	18.42	18.57	16.53	17.14
MnO	0.16	0.08	0.12	0.13	0.08	0.10	0.14	0.11	0.29	0.29
Cr2O3	0.00	0.01	0.00	0.00	0.01	0.33	0.03	0.00	0.02	0.01
TiO2	0.37	0.53	0.32	0.36	0.26	0.55	0.31	0.37	0.68	0.39
CaO	10.69	10.29	10.45	10.56	10.61	10.18	10.52	10.52	8.88	8.61
Na2O	2.36	2.19	2.03	1.94	2.01	2.27	2.16	1.97	2.96	2.78
K2O	0.39	0.46	0.44	0.46	0.36	0.45	0.43	0.40	0.49	0.22
Total	96.31	97.54	96.33	95.93	96.28	95.62	95.39	95.96	96.75	95.75
Al/(Al+Si)	0.29	0.28	0.26	0.25	0.26	0.29	0.27	0.25	0.38	0.37
Na/(Na+Ca)	0.29	0.31	0.31	0.31	0.29	0.29	0.31	0.31	0.29	0.28

Table 8 - Electron microprobe analyses of representative amphiboles from metamorphic rocks of the Amasia ophiolite complex.

Sample	AR 08 21				AR 08 25B					
Analysis	57 / 1 .	58 / 1 .	60 / 1 .	62 / 1 .	74 / 1 .	75 / 1 .	87 / 1 .	87 / 2 .	87 / 3 .	87 / 4 .
SiO2	44.63	44.81	44.96	43.57	45.05	44.37	42.27	26.07	44.84	42.97
Al2O3	13.50	13.93	12.01	14.76	13.90	13.89	15.05	19.57	14.10	17.08
MgO	10.10	10.65	10.90	10.04	10.50	9.95	8.62	15.69	10.27	9.52
FeO	16.61	15.66	16.17	15.55	15.47	15.70	16.67	24.61	15.37	14.84
MnO	0.13	0.12	0.17	0.11	0.22	0.41	0.38	0.31	0.20	0.29
Cr2O3	0.00	0.00	0.00	0.00	0.00	0.00	0.00	0.01	0.00	0.01
TiO2	0.44	0.55	0.39	0.67	0.45	0.36	0.46	0.13	0.45	0.48
CaO	8.69	8.59	9.95	9.05	8.60	9.38	9.90	0.19	9.19	8.73
Na2O	2.90	2.75	2.12	2.92	2.71	3.03	2.82	0.00	2.79	3.83
K2O	0.13	0.13	0.12	0.24	0.23	0.26	0.34	0.02	0.19	0.27
Total	97.13	97.19	96.78	96.90	97.14	97.33	96.51	86.60	97.40	98.03
Al/(Al+Si)	0.38	0.37	0.28	0.37	0.36	0.37	0.34	0.00	0.35	0.44
Na/(Na+Ca)	0.26	0.27	0.24	0.29	0.27	0.27	0.30	0.47	0.27	0.32

Sample	AR 08 25B										
Analysis	87 / 5 .	87 / 6 .	87 / 7 .	87 / 8 .	87 / 9 .	87 / 11 .	87 / 12 .	87 / 13 .	87 / 18 .	87 / 19 .	87 / 20 .
SiO2	43.62	45.44	49.36	43.59	45.58	46.88	30.72	43.57	44.59	34.40	42.98
Al2O3	15.12	13.47	11.68	13.90	10.91	12.11	14.85	14.12	15.62	13.80	14.68
MgO	10.02	9.58	11.51	9.67	10.14	7.08	9.89	9.28	8.89	7.23	9.84
FeO	15.19	16.21	15.52	15.79	16.11	18.56	17.23	15.90	16.08	17.53	15.35
MnO	0.21	0.31	0.41	0.40	0.43	0.32	0.39	0.47	0.36	0.33	0.32
Cr2O3	0.01	0.03	0.00	0.00	0.00	0.00	0.00	0.03	0.00	0.02	0.00
TiO2	0.47	0.53	0.54	0.43	0.39	0.42	0.48	0.51	0.41	0.26	0.48
CaO	8.80	8.69	8.85	9.94	10.48	9.63	9.12	9.42	10.74	8.28	8.83
Na2O	3.02	3.16	1.91	2.66	1.85	1.76	3.39	2.94	2.93	1.48	2.92
K2O	0.26	0.21	0.25	0.26	0.20	0.37	0.19	0.26	0.21	0.30	0.18
Total	96.73	97.62	100.04	96.63	96.10	97.13	86.27	96.50	99.83	83.62	95.58
Al/(Al+Si)	0.38	0.40	0.28	0.33	0.24	0.25	0.40	0.36	0.33	0.24	0.37
Na/(Na+Ca)	0.29	0.26	0.22	0.27	0.22	0.23	0.36	0.28	0.29	0.32	0.29

Sample	AR 08 25B										
Analysis	87 / 21 .	87 / 23 .	87 / 24 .	87 / 25 .	87 / 26 .	87 / 27 .	87 / 28 .	87 / 29 .	87 / 30 .	87 / 32 .	87 / 33 .
SiO2	43.75	43.76	43.89	39.44	44.78	41.45	36.11	46.57	50.83	27.18	46.81
Al2O3	14.34	14.10	15.26	15.24	10.74	16.13	16.58	14.35	13.95	18.94	12.49
MgO	9.68	9.17	10.62	11.17	10.10	10.82	11.08	11.39	10.65	16.59	10.48
FeO	15.51	15.89	14.53	18.76	20.51	15.25	17.99	14.83	13.70	22.94	15.82
MnO	0.47	0.36	0.17	0.18	0.15	0.18	0.30	0.16	0.17	0.40	0.47
Cr2O3	0.03	0.05	0.00	0.01	0.02	0.02	0.00	0.00	0.02	0.01	0.00
TiO2	0.43	0.42	0.37	0.40	0.26	0.31	0.11	0.41	0.42	0.06	0.50
CaO	9.45	9.38	8.91	9.01	6.61	6.93	1.73	8.93	9.62	0.19	9.43
Na2O	2.84	2.97	2.77	2.10	2.24	3.27	0.07	2.67	2.76	0.01	2.55
K2O	0.20	0.17	0.18	0.19	0.09	0.10	0.12	0.21	0.20	0.01	0.30
Total	96.71	96.26	96.69	96.48	95.49	94.46	84.10	99.51	102.32	86.33	98.84
Al/(Al+Si)	0.35	0.36	0.36	0.30	0.38	0.46	0.07	0.35	0.34	0.12	0.33
Na/(Na+Ca)	0.28	0.28	0.29	0.31	0.22	0.31	0.35	0.27	0.24	0.45	0.24

Table 8 - Electron microprobe analyses of representative amphiboles from metamorphic rocks of the Amasia ophiolite complex (continued).

Sample	AR 08 25B							AR 09 08		
Analysis	87 / 34 .	87 / 35 .	87 / 36 .	87 / 37 .	87 / 38 .	87 / 39 .	87 / 40 .	159 / 1 .	167 / 1 .	169 / 1 .
SiO2	44.04	34.00	41.59	43.69	42.90	44.80	44.30	44.91	43.13	44.66
Al2O3	14.33	12.49	15.83	13.55	14.55	14.56	15.07	14.89	14.22	14.75
MgO	9.28	6.54	9.12	9.29	9.70	10.26	8.95	11.90	11.54	12.25
FeO	15.89	15.89	15.68	15.05	15.14	15.47	15.95	13.48	13.32	13.41
MnO	0.42	0.37	0.24	0.25	0.32	0.27	0.42	0.05	0.07	0.04
Cr2O3	0.01	0.00	0.00	0.04	0.00	0.00	0.00	0.01	0.06	0.01
TiO2	0.44	0.43	0.52	0.48	0.47	0.50	0.46	0.51	0.54	0.52
CaO	9.02	8.19	8.69	8.98	10.03	8.76	9.49	8.69	8.67	8.89
Na2O	3.02	2.45	3.53	2.99	2.50	3.08	3.19	2.58	2.32	2.32
K2O	0.20	0.16	0.19	0.29	0.26	0.23	0.25	0.21	0.25	0.17
Total	96.65	80.52	95.41	94.59	95.85	97.92	98.08	97.23	94.12	97.00
Al/(Al+Si)	0.38	0.35	0.42	0.38	0.31	0.39	0.38	0.35	0.33	0.32
Na/(Na+Ca)	0.28	0.30	0.31	0.27	0.29	0.28	0.29	0.28	0.28	0.28

Sample	AR 09 08										
Analysis	178 / 1 .	181 / 1 .	184 / 1 .	186 / 4 .	186 / 5 .	186 / 6 .	186 / 7 .	186 / 8 .	186 / 9 .	186 / 10 .	186 / 11 .
SiO2	44.96	44.53	44.68	49.52	44.96	44.42	45.02	45.35	45.04	44.91	44.61
Al2O3	14.40	14.70	14.97	11.49	13.93	13.65	15.21	14.84	14.68	14.93	15.03
MgO	12.12	11.80	12.24	13.25	11.87	11.74	12.05	11.95	12.46	12.18	11.87
FeO	13.33	13.26	12.90	14.75	13.94	12.87	12.78	12.61	12.92	12.91	13.24
MnO	0.03	0.00	0.04	0.06	0.01	0.00	0.00	0.00	0.03	0.00	0.02
Cr2O3	0.02	0.00	0.02	0.00	0.00	0.05	0.03	0.06	0.01	0.01	0.01
TiO2	0.50	0.41	0.49	0.38	0.43	0.44	0.55	0.52	0.50	0.49	0.51
CaO	8.99	9.37	8.81	9.65	8.95	9.43	8.52	8.79	8.53	8.76	8.44
Na2O	2.57	2.52	2.49	1.47	2.28	2.07	2.56	2.54	2.48	2.63	2.82
K2O	0.13	0.22	0.19	0.16	0.20	0.20	0.20	0.16	0.21	0.24	0.16
Total	97.05	96.80	96.84	100.72	96.57	94.87	96.93	96.82	96.86	97.06	96.72
Al/(Al+Si)	0.34	0.33	0.34	0.22	0.32	0.28	0.35	0.34	0.35	0.35	0.38
Na/(Na+Ca)	0.27	0.28	0.28	0.21	0.27	0.27	0.28	0.28	0.28	0.28	0.28

Sample	AR 09 08								
Analysis	186 / 12 .	186 / 13 .	186 / 14 .	186 / 15 .	186 / 16 .	186 / 17 .	186 / 18 .	186 / 19 .	186 / 20 .
SiO2	44.65	43.97	45.26	44.91	45.37	45.04	44.93	43.60	42.86
Al2O3	14.67	14.11	14.80	15.14	15.21	14.86	14.96	16.11	15.93
MgO	12.10	13.14	12.35	12.14	12.20	12.01	12.01	10.91	9.94
FeO	12.85	12.68	12.78	12.62	12.76	12.76	13.06	14.24	15.12
MnO	0.04	0.00	0.01	0.00	0.00	0.00	0.02	0.02	0.00
Cr2O3	0.02	0.00	0.01	0.00	0.00	0.02	0.00	0.00	0.03
TiO2	0.55	0.56	0.58	0.52	0.52	0.55	0.48	0.55	0.44
CaO	8.67	8.89	9.00	8.77	8.77	9.03	8.98	8.85	9.35
Na2O	2.56	2.00	2.48	2.58	2.54	2.53	2.55	2.95	2.57
K2O	0.18	0.13	0.17	0.24	0.22	0.19	0.16	0.19	0.17
Total	96.29	95.49	97.44	96.92	97.59	96.98	97.15	97.42	96.42
Al/(Al+Si)	0.35	0.29	0.33	0.35	0.34	0.34	0.34	0.38	0.33
Na/(Na+Ca)	0.28	0.27	0.28	0.28	0.28	0.28	0.28	0.30	0.30

Table 8 - Electron microprobe analyses of representative amphiboles from metamorphic rocks of the Amasia ophiolite complex (continued).

Sample	AR 09 09				
Analysis	190 / 1 .	193 / 1 .	194 / 1 .	195 / 1 .	201 / 1 .
SiO2	41.74	42.07	42.21	41.73	41.08
Al2O3	13.32	12.70	12.78	12.93	13.77
MgO	7.03	7.47	7.12	7.06	6.78
FeO	21.78	20.78	20.47	20.62	21.64
MnO	0.31	0.38	0.37	0.32	0.32
Cr2O3	0.01	0.04	0.02	0.02	0.00
TiO2	0.54	0.71	0.99	0.70	0.74
CaO	10.64	10.40	9.49	10.26	10.62
Na2O	2.11	2.13	2.47	2.26	2.19
K2O	0.19	0.18	0.17	0.19	0.20
Total	97.67	96.87	96.09	96.07	97.35
Al/(Al+Si)	0.26	0.27	0.32	0.28	0.27
Na/(Na+Ca)	0.27	0.26	0.26	0.27	0.28

Table 8 - Electron microprobe analyses of representative amphiboles from metamorphic rocks of the Amasia ophiolite complex (continued).

Sample	AR 08 09c							AR 08 25B		
Analysis	41 / 1 .	45 / 1 .	67 / 1 .	68 / 1 .	101 / 1 .	102 / 1 .	103 / 1 .	83 / 1 .	83 / 2 .	83 / 3 .
SiO2	25.88	25.89	25.35	24.82	23.31	23.35	23.23	30.99	36.52	33.78
Al2O3	21.25	19.07	21.54	20.65	19.78	19.89	19.38	17.12	15.69	15.74
MgO	14.70	14.02	15.68	11.55	11.99	12.15	9.25	15.77	14.25	14.18
FeO	25.83	27.27	24.48	30.03	27.42	28.03	32.00	22.40	17.72	20.73
MnO	0.29	0.06		0.03	0.19	0.16	0.24	0.18	0.22	0.19
Cr2O3	0.01					0.02		0.06	0.03	0.07
TiO2	0.07	0.03	0.07	0.03	0.02	0.03	0.03	0.38	0.15	0.89
CaO	0.06	0.14	0.00	0.06	0.06	0.08	0.13	0.43	0.66	0.56
Na2O	0.00	0.02		0.03	0.01	0.02	0.01		0.05	0.08
K2O	0.11	0.03	0.00	0.02		0.01	0.03	1.24	8.53	3.60
Total	88.20	86.53	87.14	87.22	82.77	83.75	84.31	88.57	93.83	89.82

Sample	AR 08 25B										
Analysis	83 / 4 .	83 / 5 .	83 / 6 .	83 / 7 .	83 / 8 .	83 / 9 .	83 / 10 .	83 / 11 .	83 / 12 .	83 / 13 .	83 / 14 .
SiO2	32.97	32.94	29.82	34.12	28.11	28.97	22.33	28.50	33.04	35.83	32.24
Al2O3	15.30	12.72	16.45	15.17	18.33	16.23	9.13	17.97	14.40	16.44	16.69
MgO	11.08	12.96	15.24	15.82	17.33	18.23	9.08	17.04	12.21	13.58	15.00
FeO	15.16	20.39	21.61	19.48	22.91	23.26	13.36	23.88	19.38	18.04	24.11
MnO	0.14	0.13	0.21	0.28	0.24	0.30	0.16	0.28	0.09	0.18	0.25
Cr2O3	0.01	0.07	0.02		0.01	0.03	0.02	0.04	0.06	0.03	0.01
TiO2	1.87	1.21	2.22	0.08	0.07	0.05	0.71	0.15	3.90	1.49	0.09
CaO	0.41	2.30	2.88	1.66	0.18	0.26	0.70	0.14	4.45	0.47	0.54
Na2O	0.10	0.04	0.01		0.03		0.02	0.03	0.03	0.04	0.01
K2O	6.30	0.73	0.07	0.03		0.03	0.34	0.06	1.67	5.44	0.41
Total	83.35	83.48	88.53	86.64	87.20	87.36	55.84	88.09	89.24	91.55	89.36

Sample	AR 08 25B										
Analysis	83 / 15 .	83 / 16 .	83 / 17 .	83 / 18 .	83 / 19 .	83 / 20 .	83 / 21 .	83 / 22 .	83 / 23 .	83 / 24 .	83 / 25 .
SiO2	32.89	27.71	29.48	28.34	30.34	32.13	31.75	33.24	33.76	25.74	30.29
Al2O3	16.36	17.14	16.95	18.85	16.96	16.47	16.92	17.54	16.18	15.76	17.30
MgO	14.76	14.70	15.33	14.33	15.00	15.63	14.69	14.06	14.03	10.27	16.47
FeO	22.15	16.38	24.88	24.60	23.93	21.32	21.66	19.84	21.64	19.90	22.78
MnO	0.22	0.14	0.23	0.21	0.19	0.20	0.22	0.17	0.13	0.20	0.26
Cr2O3		0.00		0.00					0.04		
TiO2	0.57	0.81	0.05		0.13	0.56	0.53	0.82	0.08	0.87	0.20
CaO	0.84	0.81	0.52	0.42	0.74	0.86	0.96	1.10	1.66	1.31	0.50
Na2O	0.00	0.02			0.01	0.02		0.04			0.03
K2O	1.69	4.11	0.06	0.07	0.05	0.50	0.30	0.82	0.24	1.30	0.35
Total	89.49	81.82	87.50	86.83	87.35	87.67	87.02	87.63	87.74	75.36	88.16

Sample	AR 08 25B										
Analysis	83 / 26 .	83 / 27 .	83 / 28 .	83 / 29 .	83 / 30 .	86 / 11 .	86 / 12 .	86 / 13 .	86 / 14 .	86 / 15 .	86 / 16 .
SiO2	26.50	27.90	27.00	26.92	43.71	26.32	26.20	38.29	32.86	26.70	26.33
Al2O3	19.83	20.06	20.43	18.86	15.31	23.14	22.77	24.65	30.29	21.19	21.06
MgO	17.33	18.90	18.93	17.30	9.90	18.92	18.86	14.78	3.73	17.12	16.90
FeO	21.47	20.88	20.09	19.81	15.11	19.20	18.94	10.60	15.27	19.84	20.60
MnO	0.28	0.31	0.35	0.29	0.20	0.27	0.20	0.25	0.01	0.40	0.31
Cr2O3	0.00		0.00			0.03		0.02		0.03	0.04
TiO2	0.08	0.04	0.06	0.08	0.39	0.03	0.03	0.13	0.31	0.06	0.01
CaO	0.16	0.02	0.01	0.39	9.35	0.05	0.06	0.03	0.01	0.22	0.22
Na2O	0.03	0.00	0.02		3.03	0.00	0.00	0.43	0.02	0.02	0.02
K2O	0.01	0.05	0.04	0.00	0.25	0.12	0.03	5.57	2.68	0.06	0.05
Total	85.68	88.17	86.91	83.65	97.23	88.09	87.09	94.75	85.17	85.64	85.54

Table 9 - Electron microprobe analyses of representative chlorites from metamorphic rocks of the Amasia ophiolite complex.

Sample	AR 08 25B						AR-09-08			
Analysis	86 / 17 .	86 / 18 .	86 / 19 .	86 / 20 .	86 / 21 .	86 / 22 .	168 / 1 .	172 / 1 .	175 / 1 .	176 / 1 .
SiO2	25.85	25.04	26.39	27.41	30.62	31.41	26.60	26.85	26.46	25.93
Al2O3	22.84	24.63	22.65	21.95	25.45	25.54	21.98	22.93	21.69	22.62
MgO	17.87	17.17	17.79	19.64	14.93	14.26	20.94	20.55	20.80	20.37
FeO	20.01	20.42	20.10	19.92	17.38	17.25	16.54	17.02	17.11	17.30
MnO	0.35	0.36	0.32	0.36	0.32	0.15		0.02	0.08	
Cr2O3	0.02	0.02	0.00	0.01	0.01	0.03			0.02	0.07
TiO2	0.04	0.05	0.06	0.04	0.13	0.13	0.13	0.12	0.09	0.08
CaO	0.09	0.11	0.11	0.13	0.10	0.18	0.04	0.03	0.05	
Na2O	0.01	0.05	0.02	0.10	0.04	0.05		0.13	0.14	0.07
K2O		0.04	0.04	0.11	1.62	1.80	0.03	0.01	0.04	0.03
Total	87.07	87.89	87.49	89.66	90.59	90.80	86.26	87.65	86.47	86.45

Sample	AR-09-08										
Analysis	182 / 1 .	183 / 1 .	185 / 1 .	185 / 2 .	185 / 4 .	185 / 5 .	185 / 6 .	185 / 7 .	185 / 8 .	185 / 9 .	185 / 10 .
SiO2	26.76	26.53	27.37	27.04	25.31	27.46	27.37	26.85	26.75	26.74	26.55
Al2O3	21.88	22.54	22.16	22.17	20.43	21.79	21.90	21.81	21.85	21.84	21.21
MgO	20.81	20.38	21.17	20.50	19.32	19.92	20.93	20.98	20.97	21.01	20.93
FeO	16.77	16.15	17.23	17.61	17.13	17.73	17.64	17.18	17.36	17.44	17.50
MnO	0.03	0.04			0.03	0.03	0.04	0.00		0.03	0.04
Cr2O3	0.04	0.05	0.02		0.06	0.03	0.01		0.03	0.05	
TiO2	0.11	0.11	0.13	0.09	0.11	0.07	0.02	0.04	0.09	0.12	0.04
CaO	0.03	0.04	0.05	0.05	0.09	0.03	0.01	0.03	0.01		0.01
Na2O	0.04	0.03			0.00	0.02	0.03	0.01		0.01	
K2O	0.05		0.02	0.02		0.09	0.02	0.00	0.01	0.01	
Total	86.53	85.88	88.14	87.47	82.49	87.17	87.98	86.91	87.07	87.25	86.29

Sample	AR-09-08										
Analysis	185 / 11 .	185 / 12 .	185 / 13 .	185 / 14 .	185 / 15 .	185 / 16 .	185 / 17 .	185 / 18 .	185 / 19 .	185 / 20 .	185 / 21 .
SiO2	27.00	25.11	27.15	26.80	27.47	26.99	24.75	26.98	26.48	27.30	26.56
Al2O3	22.17	19.95	21.27	21.81	19.58	21.82	21.28	21.77	21.54	21.05	21.16
MgO	21.05	17.06	20.48	20.70	21.47	20.82	18.17	20.75	20.46	21.15	20.42
FeO	17.25	16.94	17.76	17.68	17.10	17.24	17.22	17.41	16.65	17.23	17.06
MnO	0.05	0.04	0.00			0.01	0.04	0.02	0.03	0.02	
Cr2O3		0.04		0.02	0.03	0.04		0.01			
TiO2	0.06	0.08	0.10	0.09	0.10	0.07	0.05	0.14	0.00	0.12	0.09
CaO	0.01	0.42	0.04	0.03	0.05	0.02	0.04		0.05	0.01	0.05
Na2O	0.02	0.02	0.02	0.03		0.00	0.01	0.00		0.02	0.01
K2O	0.00	0.13	0.03			0.02	0.03	0.01	0.02		0.00
Total	87.60	79.77	86.86	87.16	85.80	87.03	81.59	87.09	85.23	86.90	85.34

Sample	AR-09-08				AR-09-09			
Analysis	185 / 22 .	185 / 23 .	185 / 24 .	185 / 25 .	191 / 1 .	199 / 1 .	200 / 1 .	202 / 1 .
SiO2	26.87	25.88	26.82	26.85	25.12	26.54	23.72	25.26
Al2O3	21.60	20.98	21.75	21.07	19.79	19.15	19.83	19.93
MgO	20.21	17.48	19.79	20.17	4.53	5.98	6.51	11.94
FeO	17.95	17.56	17.53	17.64	37.33	33.85	37.50	29.70
MnO	0.01	0.03	0.05		0.44	0.72	0.99	0.36
Cr2O3	0.02		0.03	0.02	0.00	0.03	0.01	0.02
TiO2	0.08	0.05	0.11	0.03	0.09	0.04	0.11	0.08
CaO	0.16	0.32	0.11	0.13	0.35	0.50	0.04	0.07
Na2O						0.06		
K2O	0.02	0.04	0.05	0.07	0.45	0.53	0.04	
Total	86.93	82.33	86.22	85.98	88.10	87.40	88.75	87.36

Table 9 - Electron microprobe analyses of representative chlorites from metamorphic rocks of the Amasia ophiolite complex (continued).

Sample	AR 08 09c										
Analysis	35 / 1 .	48 / 1 .	49 / 1 .	50 / 1 .	51 / 1 .	52 / 1 .	53 / 1 .	54 / 1 .	55 / 1 .	56 / 1 .	61 / 1 .
SiO2	49.89	46.56	46.45	46.00	46.49	46.93	45.91	46.30	46.37	46.66	46.44
Al2O3	32.95	31.87	32.39	34.64	39.76	32.99	37.97	34.45	34.69	34.39	31.80
MgO	0.03	1.29	1.44	0.77	0.10	0.93	0.15	0.61	0.85	0.88	1.19
FeO	1.06	4.40	3.74	2.66	1.04	3.49	1.52	2.55	2.70	2.67	3.03
MnO					0.02		0.03	0.04	0.00	0.02	
Cr2O3	0.02	0.04			0.04	0.02				0.02	
TiO2		0.69	0.39	0.38	0.18	0.25	0.14	0.30	0.31	0.37	0.53
CaO	0.52	0.04	0.03	0.04	0.55	0.02	0.41	0.03	0.02	0.00	0.23
Na2O	1.97	0.63	0.82	1.87	5.62	0.75	5.33	2.07	1.68	1.69	1.70
K2O	9.67	10.36	10.37	8.81	1.26	10.41	2.15	8.28	8.94	8.81	8.63
Total	96.10	95.87	95.63	95.16	95.05	95.79	93.60	94.62	95.56	95.51	93.56
Al total	2.56	2.53	2.57	2.73	3.02	2.61	2.95	2.72	2.72	2.70	2.56
Si^{4+}	3.29	3.14	3.13	3.08	3.00	3.15	3.02	3.10	3.09	3.10	3.17

Sample	AR 08 09c										
Analysis	109 / 1 .	110 / 1 .	111 / 1 .	111 / 2 .	111 / 3 .	111 / 4 .	111 / 5 .	111 / 6 .	111 / 7 .	111 / 8 .	111 / 9 .
SiO2	46.97	44.05	46.14	45.62	45.22	44.79	46.33	46.12	45.97	46.33	46.69
Al2O3	33.10	32.59	33.54	32.40	33.44	31.63	33.42	33.84	33.85	33.46	33.01
MgO	1.02	1.06	1.00	1.11	0.90	0.90	1.08	0.94	0.80	1.19	1.17
FeO	3.09	2.68	2.98	2.99	2.80	2.79	3.02	2.94	2.84	3.07	3.04
MnO									0.05	0.03	
Cr2O3	0.04	0.01	0.04	0.04	0.05		0.03	0.02	0.01	0.05	0.02
TiO2	0.39	0.60	0.55	0.63	0.54	0.54	0.46	0.47	0.32	0.61	0.61
CaO	0.08	0.06	0.01	0.07	0.06	0.12	0.02	0.03	0.08	0.04	0.03
Na2O	1.91	1.60	1.90	1.78	1.52	1.74	2.01	2.21	2.33	1.76	1.91
K2O	8.20	8.30	8.82	8.79	8.64	8.00	8.21	7.78	7.66	8.45	8.36
Total	94.81	90.95	94.98	93.44	93.19	90.51	94.59	94.36	93.91	94.99	94.83
Al total	2.62	2.69	2.66	2.61	2.69	2.62	2.65	2.68	2.69	2.64	2.61
Si^{4+}	3.15	3.08	3.10	3.12	3.09	3.15	3.11	3.10	3.10	3.11	3.13

Sample	AR 08 09c										
Analysis	111 / 10 .	111 / 11 .	111 / 12 .	111 / 13 .	111 / 14 .	111 / 15 .	111 / 16 .	111 / 17 .	111 / 18 .	111 / 19 .	111 / 20 .
SiO2	46.86	46.21	46.21	46.55	46.44	47.13	46.54	46.39	46.62	46.16	47.18
Al2O3	31.96	33.18	33.24	32.99	33.47	32.21	32.21	32.77	32.46	33.16	32.79
MgO	1.13	1.12	1.16	1.20	1.19	1.18	1.21	1.21	1.16	1.04	1.26
FeO	2.94	3.04	2.94	2.93	3.09	3.10	3.31	3.05	3.18	3.15	3.02
MnO										0.05	
Cr2O3	0.03	0.02					0.01	0.02	0.06	0.04	
TiO2	0.64	0.61	0.54	0.61	0.61	0.63	0.67	0.60	0.66	0.60	0.61
CaO	0.01		0.05	0.05	0.04	0.04	0.01	0.05	0.05	0.06	0.04
Na2O	1.80	1.91	1.78	1.79	1.92	1.80	1.84	1.92	1.75	1.92	1.81
K2O	8.46	8.41	8.59	8.54	8.52	8.35	8.41	8.72	8.35	8.22	8.63
Total	93.82	94.50	94.51	94.66	95.29	94.44	94.20	94.73	94.30	94.40	95.33
Al total	2.55	2.63	2.64	2.61	2.64	2.56	2.57	2.60	2.58	2.64	2.58
Si^{4+}	3.18	3.11	3.11	3.13	3.11	3.17	3.15	3.13	3.15	3.11	3.15

Table 10 - Electron microprobe analyses of representative micas from metamorphic rocks of the Amasia ophiolite complex.

Sample	AR-08-25B										
Analysis	77 / 1 .	78 / 1 .	80 / 1 .	81 / 1 .	86 / 1 .	86 / 2 .	86 / 3 .	86 / 4 .	86 / 5 .	86 / 6 .	86 / 7 .
SiO2	46.31	45.68	46.74	45.87	46.92	46.26	46.09	45.71	46.16	45.99	45.86
Al2O3	31.97	28.99	35.80	37.46	31.71	33.92	33.35	34.61	34.03	34.27	34.60
MgO	1.12	1.69	0.63	0.35	1.53	1.18	1.20	1.21	1.20	1.08	0.96
FeO	3.43	4.15	1.56	1.39	3.02	2.63	2.64	2.66	2.47	2.76	2.64
MnO		0.03	0.00	0.01	0.03			0.05	0.02		
Cr2O3	0.07					0.04	0.01		0.02		0.01
TiO2	0.38	0.35	0.11	0.10	0.34	0.35	0.37	0.45	0.34	0.45	0.44
CaO	0.06	0.19	0.11	0.02	0.02	0.01		0.00	0.01	0.04	0.04
Na2O	1.16	0.58	0.18	1.25	0.55	0.97	1.18	0.91	1.02	0.86	1.07
K2O	8.32	7.77	11.02	9.89	10.38	9.63	10.01	9.89	9.84	9.90	9.67
Total	92.81	89.44	96.15	96.35	94.52	94.99	94.85	95.50	95.10	95.35	95.28
Al total	2.58	2.43	2.79	2.90	2.53	2.68	2.65	2.73	2.69	2.71	2.73
Si^{4+}	3.17	3.25	3.09	3.02	3.18	3.10	3.11	3.06	3.10	3.08	3.07

Sample	AR-08-25B										
Analysis	86 / 8 .	86 / 9 .	86 / 10 .	86 / 23 .	86 / 24 .	86 / 25 .	86 / 26 .	86 / 27 .	86 / 28 .	86 / 29 .	86 / 30 .
SiO2	46.25	46.00	49.09	46.55	46.83	45.38	48.12	46.19	47.13	46.81	47.42
Al2O3	33.79	34.43	29.86	32.59	31.65	30.82	27.64	33.93	31.85	31.47	31.24
MgO	1.18	1.29	2.29	1.53	1.88	2.26	1.97	1.22	1.67	1.83	1.97
FeO	2.58	2.62	3.70	2.99	3.52	3.43	3.39	2.84	2.98	3.11	3.42
MnO	0.02		0.00	0.04	0.01	0.05		0.02	0.02	0.03	
Cr2O3					0.02		0.04	0.03	0.04		0.03
TiO2	0.48	0.42	0.34	0.40	0.50	0.46	0.43	0.48	0.42	0.47	0.47
CaO	0.03	0.04	0.16	0.06	0.09	0.05	0.12	0.02	0.08	0.08	0.23
Na2O	0.89	0.86	0.49	0.35	0.41	0.58	0.44	0.76	0.43	0.42	0.42
K2O	9.53	9.64	9.40	10.08	10.47	9.57	10.34	10.12	10.43	10.10	9.77
Total	94.76	95.30	95.34	94.60	95.38	92.60	92.48	95.61	95.04	94.32	94.96
Al total	2.68	2.71	2.36	2.60	2.52	2.52	2.26	2.68	2.53	2.52	2.48
Si^{4+}	3.11	3.08	3.29	3.15	3.16	3.14	3.34	3.09	3.18	3.18	3.20

Sample	AR-09-08				
Analysis	161 / 1 .	162 / 1 .	163 / 1 .	170 / 1 .	171 / 1 .
SiO2	46.61	46.32	46.29	46.43	46.15
Al2O3	39.04	39.43	39.56	39.72	40.80
MgO	0.12	0.15	0.13	0.13	0.18
FeO	0.87	1.22	0.75	0.79	1.03
MnO			0.01		
Cr2O3	0.04		0.01		
TiO2	0.20	0.21	0.27	0.30	0.24
CaO	0.45	0.43	0.60	0.59	0.51
Na2O	6.76	6.53	6.70	6.55	7.01
K2O	0.61	0.73	0.65	0.39	0.53
Total	94.69	95.01	94.96	94.90	96.43
Al total	2.97	3.00	3.01	3.01	3.06
Si^{4+}	3.01	2.99	2.99	2.99	2.94

Table 10 - Electron microprobe analyses of representative micas from metamorphic rocks of the Amasia ophiolite complex (continued).

Step	Laser power (mW)	Atmospheric cont (%)	^{39}Ar (%)	$^{37}Ar_{Ca}/^{39}Ar_K$	$^{40}Ar^*/^{39}Ar_K$	Age (Ma ± 2σ)
Muscovite AR-08-09c, J = 0.02, plateau age: 89.7 ± 1.12 Ma (97 % ^{39}Ar) (MSDW: 0.80)						
1	400		3.01	0.06	2.95	98.38 ± 7.48
2	460		18.48	0.02	2.71	90.58 ± 1.99
3	493		13.40	0.01	2.68	89.72 ± 2.40
4	523		27.19	0.03	2.66	89.07 ± 1.75
5	544		4.55	0.04	2.67	89.51 ± 1.83
6	616		12.24	0.03	2.65	88.75 ± 1.76
7	695		10.69	0.04	2.68	89.57 ± 1.78
8	1111		10.43	0.11	2.72	91.04 ± 1.78
Amphibole AR-08-09c, J = 0.02, plateau age: 90.3 ± 3.04 Ma (92.7 % ^{39}Ar), inverse isochron age: 90.2 ± 2.0 Ma (MSDW: 0.01)						
1	450		3.49	4.65	0.25	8.65 ± ± 81.95
2	500		1.82	3.78	0.76	26.04 ± ± 92.44
3	552		1.89	4.60	1.52	51.53 ± ± 45.35
4	600		2.37	6.51	2.71	90.92 ± ± 24.05
5	651		7.92	8.92	2.71	90.76 ± ± 10.96
6	694		24.63	9.50	2.70	90.32 ± ± 6.01
7	726		2.81	8.74	2.64	88.64 ± ± 17.40
8	1111		55.06	8.87	2.69	90.24 ± ± 3.60
Amphibole AR-09-15, J = 0.02, plateau age: 91.2 ± 3.1 Ma (98.1 % ^{39}Ar), inverse isochron age: 89.3 ± 3.9 Ma (MSDW: 0.74)						
1	400		0.05	1.65	12.09	8.65 ± 81.95
2	600		0.25	11.73	0.74	26.04 ± 92.44
3	661		1.08	14.66	2.72	51.53 ± 45.35
4	720		6.76	14.59	2.84	90.92 ± 24.05
5	770		70.55	12.97	2.71	90.76 ± 10.96
6	820		19.62	12.02	2.66	90.32 ± 6.01
7	1111		1.69	12.49	2.88	88.64 ± 17.40
Amphibole AR-09-08, J = 0.02, plateau age: 87.7 ± 5.6 Ma (94.7 % ^{39}Ar), inverse isochron age: 86.1 ± 7.1 Ma (MSDW: 0.02)						
1	400		0.40	10.08	5.60	182.99 ± 390.11
2	500		0.98	3.58	3.33	110.98 ± 201.40
3	551		1.78	8.69	5.36	175.59 ± 54.69
4	601		2.19	19.33	3.55	117.94 ± 44.62
5	659		32.48	24.34	2.65	88.85 ± 9.37
6	712		51.42	24.01	2.58	86.66 ± 8.41
7	999		10.76	22.98	2.62	87.95 ± 11.82

Table 11 - $^{40}Ar/^{39}Ar$ dating results.

<u>Chapitre 4</u> - Relations entre les ophiolites du N-E de l'Anatolie et du Petit Caucase : arguments pour une obduction de grande échelle de croute océanique.

« L'ordre et la connexion des idées est le même que l'ordre et la connexion des choses. »

Spinoza, extrait d'*Ethique II*

IV.1 Article 3 – Linking the NE Anatolian and Lesser Caucasus ophiolites: evidence for large scale obduction of oceanic crust and implications for the formation of the Lesser Caucasus-Pontides Arc

Une des difficultés majeures de la reconstruction des évènements géodynamiques ayant abouti à la mise en place des ophiolites dans la région du Petit Caucase-Pontides est due à l'intermittence des affleurements. En effet, un épais dépôt de sédiments et de roches volcaniques post-obduction (Eocène à Quaternaire) recouvre ces régions (Avagyan *et al.*, 2010; Gürer & Aldanmaz, 2002; Sosson *et al.*, 2010). Par conséquent, pour relier les domaines ophiolitiques de l'Arménie et du NE de la Turquie et valider la continuité des unités structurales principales nous cherchons à répondre à trois questions au cours de cette étude :

(1) Toutes les ophiolites du Petit Causase-NE Anatolie sont-elles des restes de la même lithosphère océanique ?

(2) Furent-elles obduites sur un ruban continental continu (comprenant les SAB et Taurides-Anatolides au sud) ?

et (3) Est-ce que ce domaine océanique fut subduit sous une même marge continentale au nord?

Nos études précédemment exposées ont montré que l'ensemble des âges de formation ainsi que les compositions des roches analysées sont similaires à ceux des autres ophiolites arméniennes (Galoyan *et al.*, 2009; Rolland *et al.*, 2009a; 2009b; Sosson *et al.*, 2010). Ceci est également vrai pour les affleurements de roches ophiolitiques en Turquie du NE (Çelik *et al.*, 2011; 2013; Topuz *et al.*, 2013a; 2013b). Ces comparaisons soutiennent l'hypothèse que l'échelle du chevauchement de lithosphère océanique sur la lithosphère continentale est exceptionnelle. Selon toute vraisemblance la ceinture ophiolitique anatolienne (suture d'Izmir-Ankara-Erzincan) se prolonge bien dans le Petit Caucase (suture de Sevan-Akera) (Knipper, 1975; Knipper & Khain, 1980; Adamia *et al.*, 1981; Şengör & Yılmaz, 1981; Adamia *et al.*, 1987; Yılmaz *et al.*, 2000; Galoyan, 2008).

Les ophiolites ont des compositions géochimiques montrant des affinités avec un contexte de supra-subduction. La composition géochimique des unités métamorphiques sous les ophiolites Stépanavan, Amasia et Erzincan a une affinité calco-alcaline à alcaline distincte, attribuée à des processus magmatiques anté-obduction (Galoyan, 2008; Galoyan *et al.*, 2007;

2009; Rolland *et al.*, 2010; Rolland *et al.*, 2009; Sosson *et al.*, 2010). Toutefois, lorsque l'on considère un modèle dans lequel les ophiolites se forment en position supra-subduction à arrière-arc dans un contexte de subduction intra-océanique, avec une ouverture lente, les observations amènent à conclure que l'arc volcanique insulaire est manquant.

Il a été suggéré que les ophiolites sont représentatives d'un environnement avant-arc en raison de certaines signatures chimiques boninitiques (Crawford, 1989; Falloon & Crawford, 1991), et de l'absence de l'arc insulaire (Parlak *et al.*, 2013). Cependant, des études plus récentes ont montré que des boninites se mettent non seulement en place dans un domaine d'avant-arc, mais aussi dans des environnements d'arrière-arc (Deschamps & Lallemand, 2003; Falloon *et al.*, 1992; Teklay, 2006). Deschamps & Lallemand (2003) attribuent même les boninites davantage à un environnement d'arrière-arc. Il est possible que l'arc ait disparu au cours d'un processus d'accrétion/subduction comme le décrivent Boutelier *et al.* (2003), Shemenda (1994), et Ellis *et al.* (1999), lors de sa rencontre avec la marge continentale plus au sud. Ceci expliquerait les tendances géochimiques d'arc des roches composant la semelle de l'obduction.

Ainsi, cette nouvelle contribution à la compréhension de l'évolution géodynamique des ophiolites du Petit Caucase et du NE de l'Anatolie soutient la présence de deux zones de subduction plongeant vers le nord : (1) une sous la marge eurasienne et (2) plus au sud, une autre, intra-océanique à l'origine des ophiolites, conduisant à la mise en place ophiolite. Cela étend le modèle géodynamique proposé précédemment vers l'est pour inclure le NE de l'Anatolie, et pourrait être généralisé à l'ensemble de celle-ci.

L'ensemble des données (structurales, stratigraphiques, géochimiques et géochronologiques) provenant de toute la zone d'étude, concernant la mise en place de ces différentes ophiolites, amènent à la conclusion qu'elles appartiennent à une seule nappe ophiolitique. Cette analyse nous permet de proposer un modèle dans lequel ce domaine océanique obduit, continu d'est en ouest entre le SAB-TAP et au sud et les Pontides et Somkheto-Karabagh au nord, s'est formé et mis en place selon les mêmes modalités et dans le même intervalle de temps. Par conséquent, nous suggérons la mise en place d'une nappe ophiolitique, d'une extension latérale de plusieurs centaines de kilomètres (>600 km) et d'un rejet horizontal de 100 à 200 kilomètres, dans un modèle commund'obduction.

Cette étude a fait l'objet d'un article publié dans *Geodinamica Acta*.

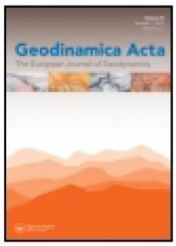

Geodinamica Acta

Linking the NE Anatolian and Lesser Caucasus ophiolites: evidence for large scale obduction of oceanic crust and implications for the formation of the Lesser Caucasus-Pontides Arc

Marc Hässig[a], Yann Rolland[a], Marc Sosson[a], Ghazar Galoyan[b], Lilit Sahakyan[b], Gültekin Topuz[c], Ömer Faruk Çelik[d], Ara Avagyan[b] & Carla Müller[e]

[a] Géoazur, Université Nice-Sophia Antipolis, Centre National de la Recherche Scientifique (UMR 7329), Observatoire de la Côte d'Azur, 250 av Einstein 06560 Valbonne, France

[b] Institute of Geological Sciences, National Academy of Sciences of Armenia, 24a Baghramian Avenue, 375019 Yerevan, Armenia

[c] İstanbul Teknik Üniversitesi, Avrasya Yerbilimleri Enstitüsü, TR-34469 Maslak, İstanbul, Turkey

[d] Kocaeli Üniversitesi, Jeoloji Mühendisliği Bölümü, 41150 Kocaeli, Turkey

[e] 6 bis rue Haute, 92500 Rueil Malmaison, France

Accepted author version posted online: 08 Jan 2014.Published online: 08 Jan 2014.

Abstract

In the Lesser Caucasus and NE Anatolia three domains are distinguished from south to north: (1) Gondwanian-derived continental terranes represented by the South Armenian Block (SAB) and the Tauride-Anatolide Platform (TAP), (2) scattered outcrops of Mesozoic ophiolites, obducted during the Upper Cretaceous times, marking the northern Neotethys suture, and (3) the Eurasian plate, represented by the Eastern Pontides and the Somkheto-Karabagh Arc. At several locations along the northern Neotethyan suture, slivers of preserved unmetamorphozed relics of now disappeared Northern Neotethys oceanic domain (ophiolite bodies) are obducted over the northern edge of the passive SAB and TAP margins to the south. There is evidence for thrusting of the suture zone ophiolites towards the north, however we ascribe this to retro-thrusting and accretion onto the active Eurasian margin during the latter stages of obduction. Geodynamic reconstructions of the Lesser Caucasus feature two north dipping subduction zones: (1) one under the Eurasian margin and (2) farther south, an intra-oceanic subduction leading to ophiolite emplacement above the northern margin of SAB. We extend our model for the Lesser Caucasus to NE Anatolia by proposing that the ophiolites of these zones originate from the same oceanic domain, emplaced during a common obduction event. This would correspond to the obduction of non-metamorphic oceanic domain along a lateral distance of more than 500 km and overthrust up to 80 km of passive continental margin. We infer that the missing volcanic arc, formed above the intra-oceanic subduction, was dragged under the obducting ophiolite through scaling by faulting and tectonic erosion. In this scenario part of the blueschists of Stepanavan, the garnet

amphibolites of Amasia and the metamorphic arc complex of Erzincan correspond to this missing volcanic arc. Distal outcrops of this exceptional object were preserved from latter collision, concentrated along the suture zones.

Keywords : Lesser Caucasus; NE Anatolia; Tethys; Ophiolite; Obduction

1.1 Introduction

During the Mesozoic, the southern margin of the Eurasian continent was involved in the closure of Paleotethys and the opening of Neotethys oceans. Later, from the Jurassic to the Eocene, subductions, obductions, micro-plate accretions, and finally continent-continent collision occurred between Eurasia and Arabia, and resulted in the closure of Neotethys.

In order to better understand the different phases linked with the opening and closing of the Tethyan Ocean leading to the current structure of the Lesser Caucasus and the Eastern Pontides (Figure 1), it is important to identify the different units involved in the Tethyan suture *s.l.* and their corresponding geodynamic context including the lateral continuation of the structures. The evolution of northern Neotethys can be deduced from the structural, geochemical and geochronological studies of preserved oceanic crust domains obducted (ophiolites) in the Lesser Caucasus and in NE Anatolia and of the metamorphic rocks beneath these ophiolites. These studies yield key time and paleogeographic data from the East Mediterranean area to the NW Himalayan belt (Barrier & Vrielynck, 2008; Dercourt et al., 1986; Galoyan et al., 2009; Hafkenscheid et al., 2006; Hässig et al., 2013; Okay & Tüysüz, 1999; Ricou, 1994; Ricou et al., 1985; Robertson, 2004; Rolland et al., 2010; Şengör & Yılmaz, 1981; Sosson et al., 2010; Stampfli et al., 2001). Supra-subduction zone (SSZ) ophiolites provide chronologic constraints related to oceanic crust formation by repetitive extension in a fore- and/or back-arc context, linked to the behavior of an intraoceanic subduction, by the dating of related magmatic rocks. The study of these remarkable objects also contributes to understand oceanic closure, particularly ophiolite emplacement processes, by the dating of metamorphic rocks underlying the preserved (non-metamorphic) ophiolites and post-accretionary sedimentary series unconformably overlying the suture zone. Datings undertaken along the Ankara–Erzincan–Sevan-Akera suture zone suggest a similar Lower to Middle Jurassic age of the oceanic crust of c. 180-150 Ma (Çelik et al., 2011, 2013; Dilek & Thy, 2006; Galoyan, 2008; Galoyan et al., 2009; Hässig et al., 2013; Rolland et al., 2009b, 2010; Topuz et al., 2013a). A major difficulty in Mesozoic geodynamic reconstruction of the Lesser Caucasus-Eastern Pontides is the paucity of outcrops due to thick post-obduction (Eocene to Quaternary) deposit of sediments and volcanics that overly the ophiolitic nappe (Avagyan et al., 2010; Gürer & Aldanmaz, 2002; Sosson et al., 2010). Therefore, to link the NE Turkey and Armenia ophiolitic domains, three questions are posed in this study concerning the continuity of the main structural units: (1) are all the NE Turkey–Armenia

ophiolites remnants of the same oceanic lithosphere, (2) are they partly obducted over a continuous continental ribbon (including the South Armenian and Tauride-Anatolide blocks to the south), and (3) does the oceanic domain subduct under a common margin?

In this paper we present field geological, structural and whole-rock geochemical data on the crustal rocks of the NE Anatolian and Armenian ophiolites. These data in conjunction with those from the literature strongly suggest a common origin and Late Cretaceous emplacement onto the leading edge of the passive continental margin leading to the current positioning of NE Anatolian and Lesser Caucasus ophiolites.

1.2 Previous works across the NE Anatolia-Lesser Caucasus region

1.2.1 Lesser Caucasus

Previous geological, petrological and geochemical works on the Lesser Caucasus ophiolites were carried out mostly during the 1970s and 1980s (Adamia et al., 1981; Knipper, 1975; Knipper & Khain, 1980; Knipper & Sokolov, 1977; Knipper et al., 1986, 1997; Satian, 2005; Sokolov, 1977; Zakariadze et al., 1983, 1990, 2005). These works mainly showed a Jurassic age for the ophiolite bodies, and variable geochemical affinities (ranging from tholeiitic to calc-alkaline and alkaline), which was interpreted as a complex oceanic context with variable magmatic sources, and closed mainly by subduction in the Late Cretaceous (e.g., Zakariadze et al., 1990). More recent works along the Neotethys domain evidence processes which include Neotethyan oceanic crust obduction and the collision–accretion of microplates to the Eurasian margin before the final Arabia–Asia collision or India-Asia collision (Agard et al., 2010; Avagyan et al., 2010; de Sigoyer et al., 2004; Ding et al., 2005; Galoyan et al., 2009; Hacker, 1991; Hacker et al., 1996; Harper et al., 1996; Okay et al., 2001; Rice et al., 2009; Rolland et al., 2009a,b, 2011, 2012; Searle and Cox, 1999; Sosson et al., 2010; Stampfli et al., 2001; Yılmaz et al., 1993). In these works, the presence of several geochemical suites in a given suture zone is interpreted as the tectonic collage of petrological slivers originating from various oceanic environments: volcanic arc, oceanic islands and seamounts, oceanic crust from Mid Oceanic Ridge (MOR) or from back-arcs.

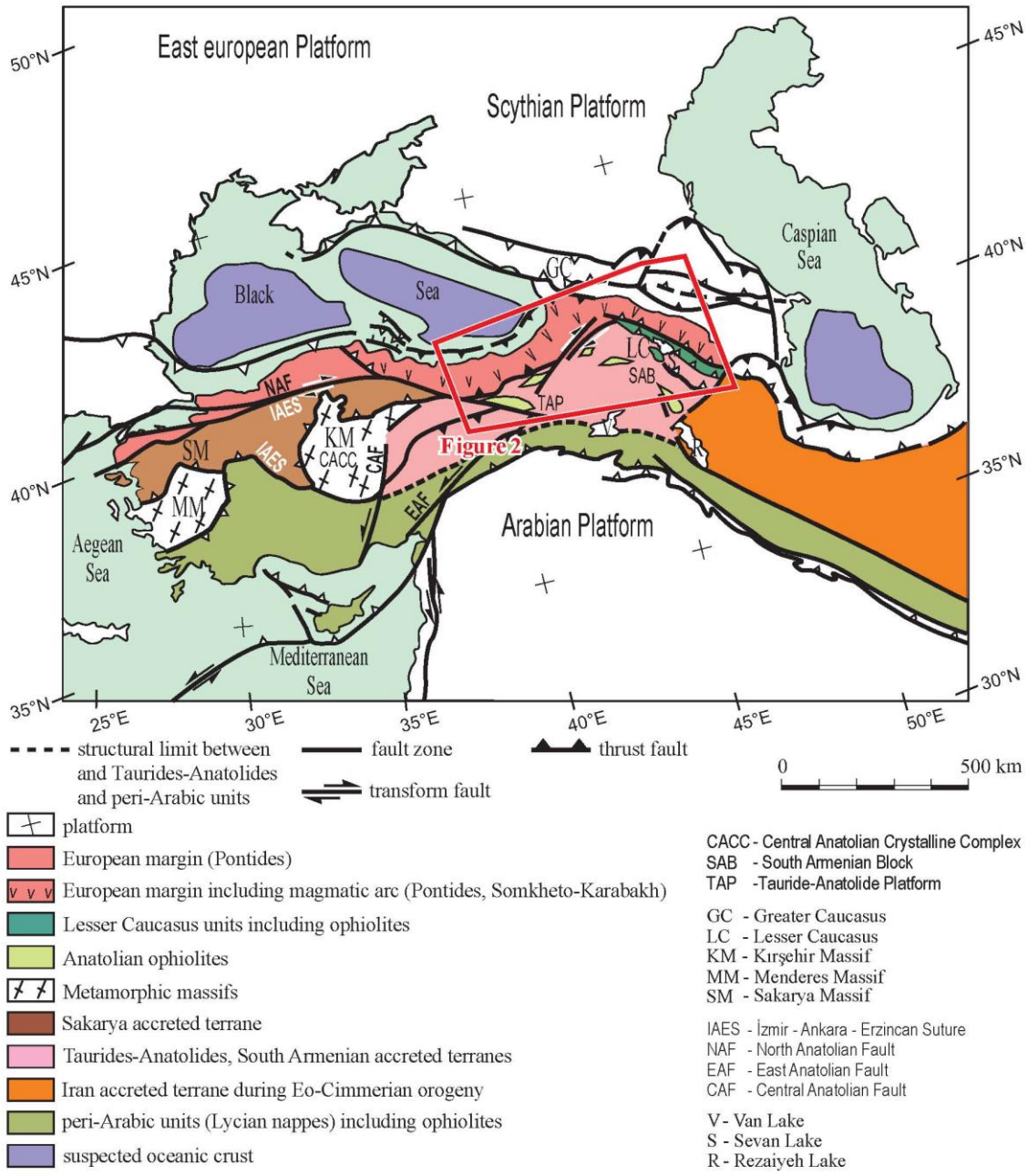

Figure 42 - Structural sketch map of the Tauride-Anatolides, Caucasus and Iranian belts (modified after Avagyan et al., 2005). Location of Figure 43 is indicated.

North of the obduction zone, in the Eurasian part of the Lesser Caucasus the subduction of the Tethys is evidenced by a thick and mainly calc-alkaline volcanogenic and volcanoclastic series of Bajocian to Santonian age (e.g., Adamia et al., 1981 for a review). At this period of time the northern Lesser Caucasus was characterized by an island arc domain called the Somkheto–Karabakh Island Arc (Adamia et al., 1977; 1987; Knipper, 1975; Ricou et al., 1986; Sosson et al., 2010). During Early Cretaceous, a part of the plutonic unit of this arc was unroofed due to tectonic erosion which was the result of significant uplift and

denudation along the subduction zone (Rolland et al., 2011). Such a change in the Eurasian active margin strain field could be, and subsequent development of this unconformity, is ascribed to the subduction of more buoyant crustal domain such as the spreading ridge of the back-arc basin (Rolland et al., 2011). The basement formations are quite similar to those known all along the Eurasian margin (Sosson et al., 2010 for a review).

South of the obduction zone, the South Armenian Block (SAB) (Knipper, 1975; Knipper & Khain, 1980) is a microplate which also corresponds to the Turkish and Iranian platforms (Şengör & Yılmaz, 1981; **Figure 42**). In Armenia the SAB is represented by a Proterozoic metamorphic basement well exposed north of Yerevan. An incomplete Paleozoic sedimentary succession (mainly represented by Upper Devonian to Upper Permian carbonates and shales) in the SW (north of the Araks Valley), widespread Triassic limestones and sandstones and some Jurassic sedimentary and volcanogenic formations unconformably covered by Cenomanian to Turonian limestone and flysch (Nalivkin, 1976; Sosson et al., 2010; **Figure 43**).

Upper Cretaceous obduction on the SAB is deduced from Upper Coniacian to Santonian flysch (reworking the ophiolites), which conformably covers Cenomanian–Turonian reef limestones and flysch of the SAB (Sokolov, 1977; Sosson et al., 2010). This obduction took place while a magmatic arc occurred along the southern edge of Eurasia (Somkheto–Karabakh island arc, Lesser Caucasus, **Figure 43**), which implies that at least two subduction zones were active at the same time (Rolland et al., 2011). The onset of collision or the continental subduction of the SAB below the Eurasian margin is dated as Late Cretaceous–Paleocene. This process occurred around 20 Ma later than the obduction (Late Coniacian–Santonian, 88–83 Ma) of the marginal basin over the SAB (Sosson et al., 2010). Oceanic closure is indicated by the Late–Middle Eocene unconformity on the SAB, the suture zone and the Eurasia margin. Ending of subduction and subsequent accretion of the SAB to the Eurasian margin resulted in the subduction jump to the south of the SAB (Rolland et al., 2012). Evidence for this southward jump in subduction can be found between the Bitlis–Pütürge massifs and SAB. There, HP metamorphic evolution due to continental subduction is bracketed between 74 and 71 Ma (Göncüoğlu & Turhan, 1984; Hempton, 1985; Oberhänsli et al., 2010). This metamorphic age is thus in agreement with a continental subduction event that occurred before the final closure of the southern Neotethys and Arabian–Eurasian collision. $^{40}Ar/^{39}Ar$ dates agree for initial subduction of the Eastern Bitlis massif at 74 Ma followed by

underthrusting of the Pütürge massif under blueschists conditions at 71 Ma (Rolland et al., 2012).

For a compilation of works about the ophiolites of the Lesser Caucasus, the reader is referred to Galoyan et al. (2007, 2009), Rolland et al. (2009b, 2010), Sosson et al. (2010) and Hässig et al. (2013). These authors have shown the following geochemical affinities in the ophiolite-related nappes: (1) the basalts and gabbros mainly bear an enriched tholeiitic composition, contaminated by subduction components, (2) above these series, a layer of alkaline basalt lava flows with large pillows is supposed to represent Ocean Island Basalts (OIB) erupted in seamounts or oceanic plateau(s), and (3) locally some arc-related basalts have been described. In Armenia, the oceanic gabbros of the tholeiitic series were dated to 170–150 Ma similar to radiolarian ages (Danelian et al., 2010), while the alkaline series were dated at c. 117 Ma (Rolland et al., 2009b).

1.2.2 Northeast Anatolia

The East Anatolian Platform (EAP) represents a continental platform between the northern and southern branches of Neotethys (Bozkurt and Mittwede, 2001). As for the SAB, the EAP represents a sliver of continental crust having rifted off northern Gondwana, which drifted to the north, which resulted into collision with Eurasia (Adamia et al., 1977; Biju-Duval et al., 1977; Dercourt et al., 1986; Şengün, 2006; Stöcklin, 1974; Stöcklin & Bhattarai, 1977).

The Eastern Pontides are interpreted as a part of the Sakarya Zone (Okay & Şahintürk, 1997). It represents an active continental margin of Eurasia, which was formed as a result of northward subduction of Neotethys during Late Cretaceous (Akıncı, 1984; Okay & Şahintürk, 1997; Şengör and Yılmaz, 1981). There is no consensus concerning onset age of subduction, since Jurassic (Adamia et al., 1981; Hess et al., 1995; Nikishin et al., 2003; Topuz et al., 2013b), Cenomanian–Turonian (Okay & Şahintürk, 1997; Yılmaz et al., 1997) or Albian (Okay et al., 2006) ages have been proposed. The lack of consensus equally stands when considering the end of subduction and the onset of continental collision; as proposed range stretches out from the end of Eocene (Peccerillio & Taylor, 1976; Robinson et al., 1995; Şengör & Yılmaz, 1981), to the Middle Eocene (Yılmaz et al., 1997) and even the Paleocene (Okay & Şahintürk, 1997).

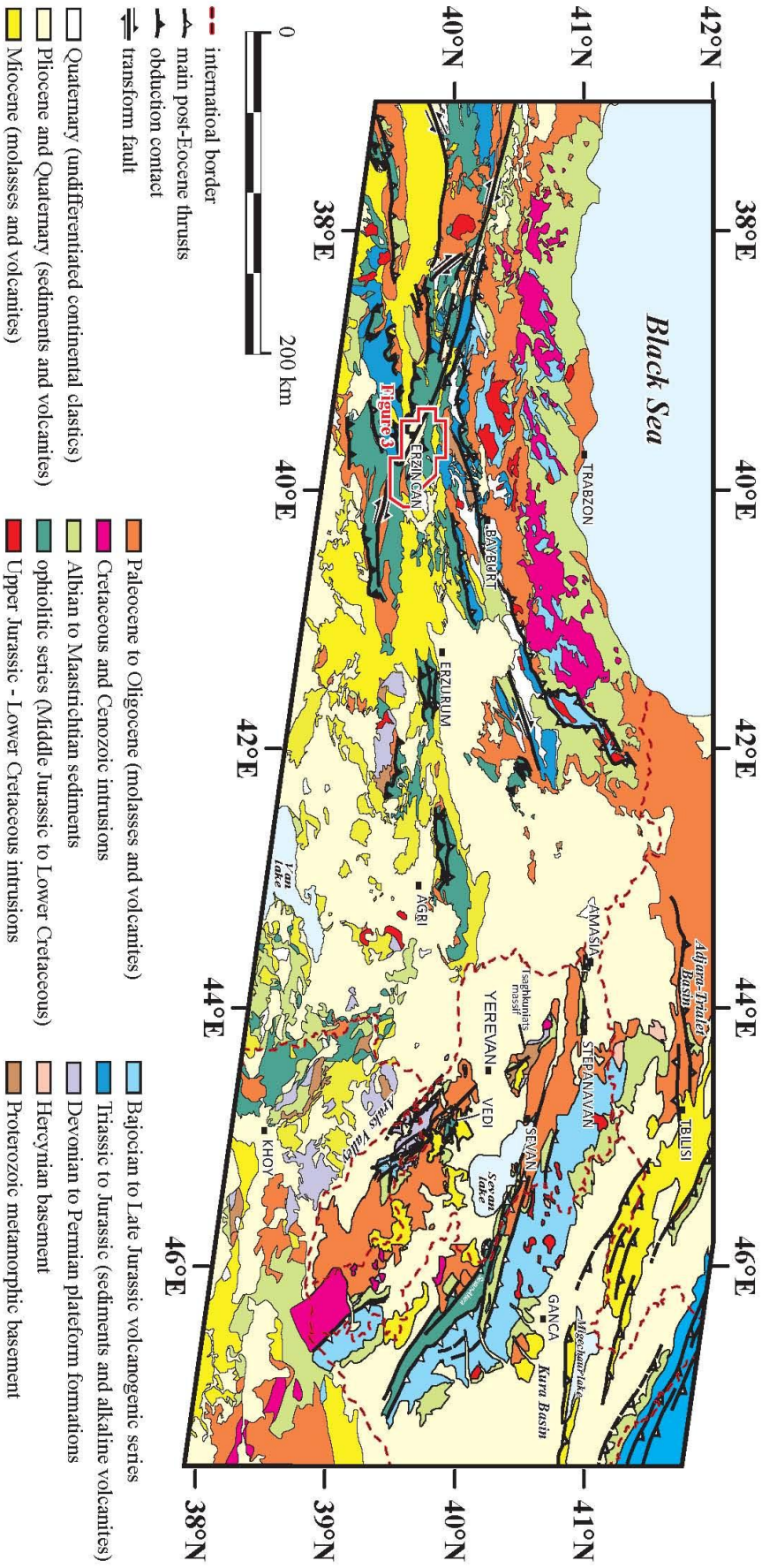
Black Sea
TRABZON
BAYBURT
ERZINCAN
ERZURUM
AGRI
AMASIA
YEREVAN
STEPANAVAN
TBILISI
SEVAN
VEDI
KHOY
GANCA
Adjara-Trialet Basin
Kura Basin
Sevan lake
Van lake
Arats Valley
Figure 3
0
200 km
38°E
40°E
42°E
44°E
46°E
38°N
39°N
40°N
41°N
42°N
international border
main post-Eocene thrusts
obduction contact
transform fault
Quaternary (undifferentiated continental clastics)
Pliocene and Quaternary (sediments and volcanites)
Miocene (molasses and volcanites)
Paleocene to Oligocene (molasses and volcanites)
Cretaceous and Cenozoic intrusions
Albian to Maastrichtian sediments
ophiolitic series (Middle Jurassic to Lower Cretaceous)
Upper Jurassic - Lower Cretaceous intrusions
Bajocian to Late Jurassic volcanogenic series
Triassic to Jurassic (sediments and alkaline volcanites)
Devonian to Permian plateform formations
Hercynian basement
Proterozoic metamorphic basement

Figure 43 - Structural map of the Lesser Caucasus-Eastern Pontides-Northeast Anatolides regions. Turkish zone modified from the 1:1 250 000 geological map of Turkey (MTA 2011); the Georgian-Armenian zone of the Caucasus after Sosson et al. (2010); the Iranian zone from Mederer (2013).

The NE Anatolian ophiolites have been studied to characterize their geodynamic environments (Eyüboğlu et al., 2007; Parlak et al., 2013; Rice et al., 2006; Sarifakioğlu et al., 2009; Topuz et al., 2013b; Yılmaz et al., 2010). Geochemical analyses of these ophiolites show similar rock types as in Armenia as well as most of the ophiolites worldwide, that is to say Mid Ocean Ridge Basalt (MORB) to volcanic arc rocks and Within-Plate Basalts (WPB). Lateral continuity between NE Anaolia and Armenia through the comparison of lithostratigraphic colons illustrates similar successions and relations as those well identified in the Lesser Caucasus, especially the timing of the emplacement of tectonic thrusts and related sedimentary deposits. Our field investigations to the north of the Erzincan basin has also shed light on an outcrop of low-grade metamorphic rocks of volcanic origin overthrusted by the ophiolites towards the south on the northern side of the Erzincan basin, along the North Anatolian Fault (NAF) and Northeast Anatolian Fault (NEAF) (**Figure 44**).

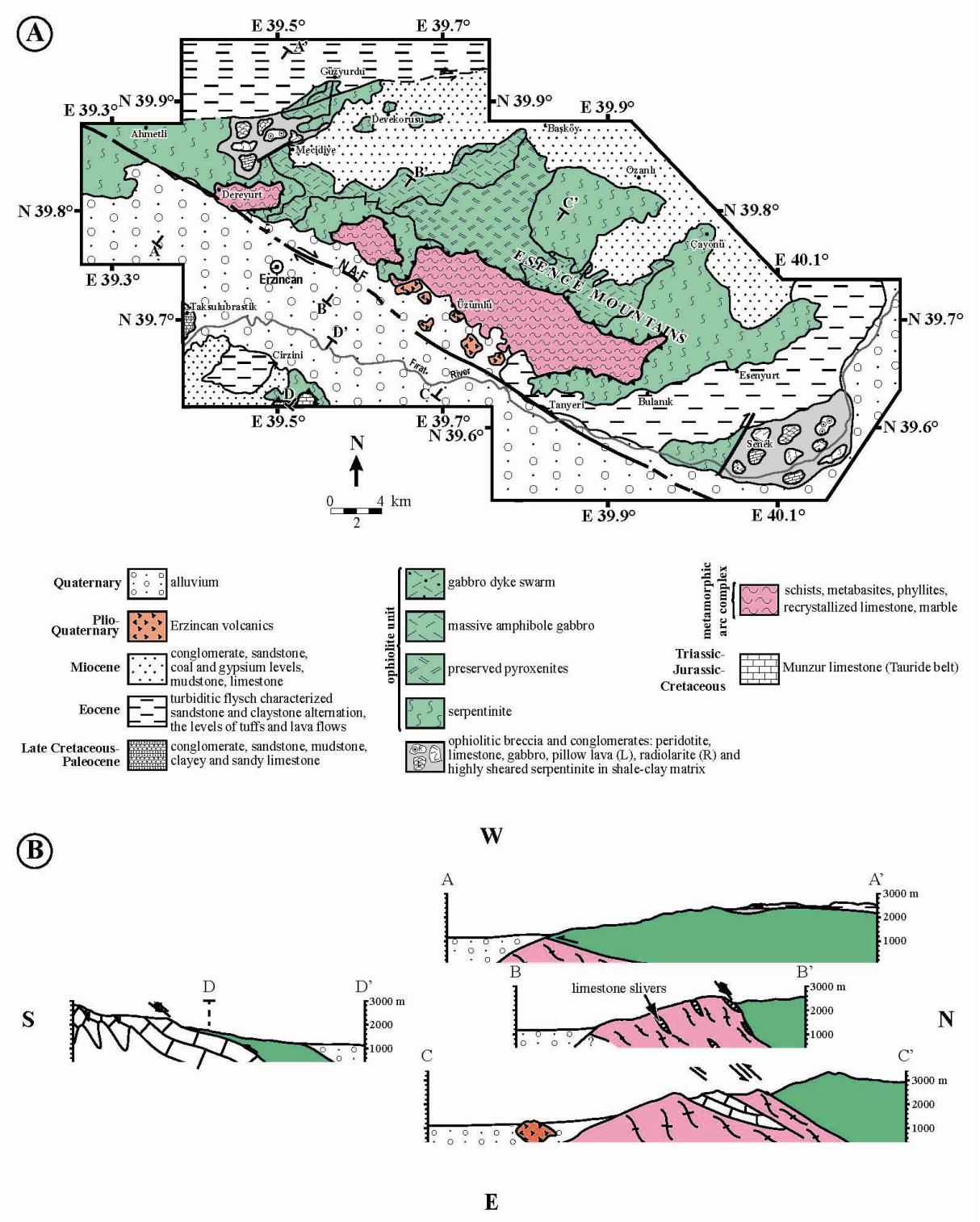

Figure 44 - Geological map and cross-sections of the Refahiye ophiolite in the vicinity of Erzincan. A: Geological map featuring the position of the cross-sections (modified after Aktimur et al., 1995; Özen et al., 2006; Sarıfakıoğlu et al., 2009). B: Geological cross-section illustrating the positioning and structural relationships between the main units based on field observations.

1.3 Structural Continuity

In order to highlight the main structural, geochemical and temporal evidences toward structural continuity between the Lesser Caucasus and NE Anatolia we present new data pertaining to the ophiolites and potential sole lithologies of these bodies, as well as published data used to complete our data set.

1.3.1 Lithostratigraphic sections

In this paper we overview the lithostratigraphic sections compiled from Bergougnan (1987), Bozkuş (1998), Bozkurt & Mittwede (2001), Gedik (2008), Moix et al. (2008), Özgül & Turşucu (1984), Okay & Tüysüz (1999) and Sokolov (1977) for the Turkish and Armenian domains and their implications for the geological evolution of that region. These data are completed by investigations carried out during a field campaign in 2011 (**Figure 45**). This input from pervious works offers a series of well-constrained data on the ophiolites, with precise and modern dating of the magmatic and metamorphic events. Structural/paleogeographic units are linked to one another in order to precise their lateral continuation. Integrated in a larger tectonic framework we use these lithostratigraphic sections to constrain the origin of the NE Anatolian ophiolite nappe as a portion a greater nappe, including the Lesser Caucasus ophiolites.

In the Lesser Caucasus, all ophiolite outcrops feature three main superposed lithotectonic units (Galoyan, 2008; Hässig et al., 2013; Rolland et al., 2009a; 2009b; 2010; Sosson et al., 2010). An upper unit with serpentinite, gabbro, pillow lava and volcanic rocks with interlayered reefal limestone is ascribed to the ophiolite. A Coniacian–Santonian detrital deposit, reworking elements from the entire ophiolitic unit is also included in this unit. Below the ophiolite unit is a tectonic melange including rock types ranging from low grade (greenschist facies) meta-basalts, meta-cherts, metamorphosed serpentinites, lenses of ophiolites, garnet bearing amphibolites and/or alkali basalts. The lower unit comprises basalts, overlain by Lower Cretaceous (Valanginian–Barremian) limestones, which are in turn unconformably covered by Late Paleocene flysch to Lower Eocene limestone as well as Middle to Upper Eocene volcanogenic deposits.

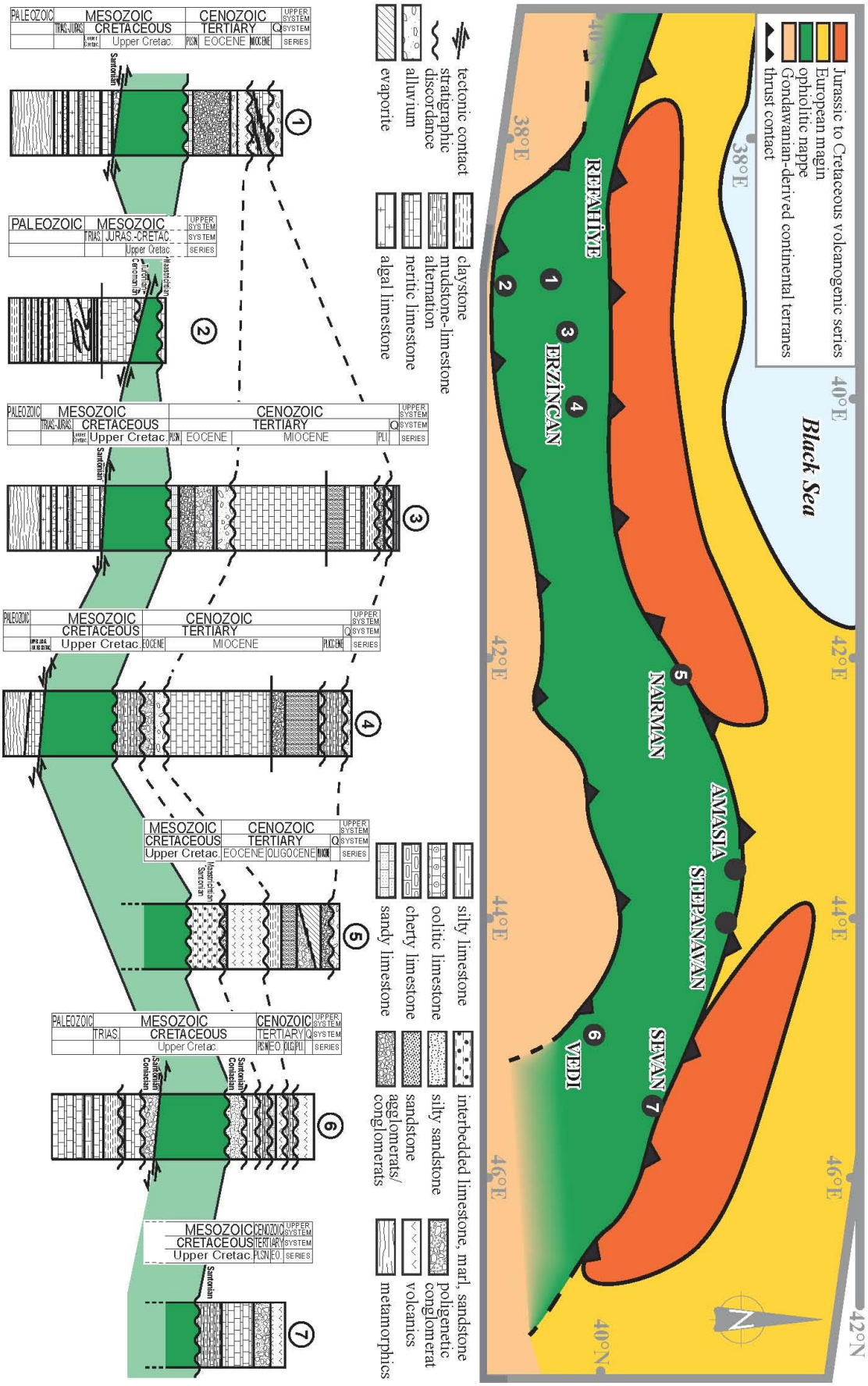
Jurassic to Cretaceous volcanogenic series
European magin
ophiolitic nappe
Gondawanian-derived continental terranes
thrust contact
Black Sea
REFAHİYE
ERZİNCAN
NARMAN
AMASIA
SEEANAVAN
SEVAN
VEDI
1
2
3
4
5
6
7
38°E
40°E
42°E
44°E
46°E
40°N
42°N
tectonic contact
stratigraphic discordance
alluvium
evaporite
claystone
mudstone-limestone alternation
neritic limestone
algal limestone
silty limestone
oolitic limestone
cherty limestone
sandy limestone
interbedded limestone, marl, sandstone
silty sandstone
sandstone
agglomerats/ conglomerats
poligenetic conglomerat
volcanics
metamorphics

Figure 45 - Synthetic lithostratigraphic sections throughout the study area. 1, 3 and 4: modified after Gedik (2008); 2: modified after Moix et al. (2008); 5: modified after Bozkuş (1998); 6 and 7: modified after Sokolov (1977).

In NE Anatolia, the TAP is made up of a succession of thrust sheets (Okay, 2008). The topmost thrust sheet is made up of ophiolite and/or ophiolitic melange forming large isolated bodies (e.g. Gutnic et al. 1979; Özgül 1984; Özgül & Turşucu, 1984). The thrusting occurred in the Late Cretaceous, in the Eocene and in the Early Miocene. The obduction of preserved ophiolite was associated with subduction and high pressure metamorphism of the northern margin of the TAP. The more distal portions of the obducted ophiolite were emplaced over the Cretaceous sedimentary rocks.

The continental collision during the late Palaeocene-Early Eocene between the TAP and the Eastern Pontides led to a second phase of convergence by folding and thrusting.

1.3.2 Geochemical analyses

Samples from the Lesser Caucasus and NE Anatolian ophiolites and related metamorphics were analyzed for major elements, trace and Rare Earth Elements (REE; **Table 12**). Samples were analyzed at the C.R.P.G. (Nancy, France). ICP-MS analytical procedures and analyses of standards for can be found on the following website (http://www.crpg.cnrs-nancy.fr/SARM).

The sampling was undertaken during a field campaign in 2011. Additional data pertaining to the other Armenian ophiolites along with the Turkish ophiolites are published in Galoyan (2008), Hässig et al. (2013), Parlak et al. (2013) and Rolland et al. (2009a; 2009b; 2010). In order to designate rock groups, trends and tectonic environments (Floyd & Winchester, 1975, 1978; Pearce, 1982, 1983, 1996; Peace & Cann, 1973; Pearce & Norry, 1979) relatively immobile elements, such as Ti, Zr, Y, Nb, Ta, Th, V and REEs, were chosen since the immobility of these elements during low grade submarine alteration has been constrained in a number of studies (e.g., Hart et al., 1974; Humpris et al., 1978). We analyzed three types of rocks: (1) gabbro (**Figures 46 A1**; **A2**; **A3**) and (2) basalt (**Figure 46 B1**; **B2**; **B3**) from the ophiolite unit, as well as (3) metamorphic rocks (mainly amphibolites but also greenschist) (**Figure 46 C1**; **C2**; **C3**) from the metamorphic rocks.

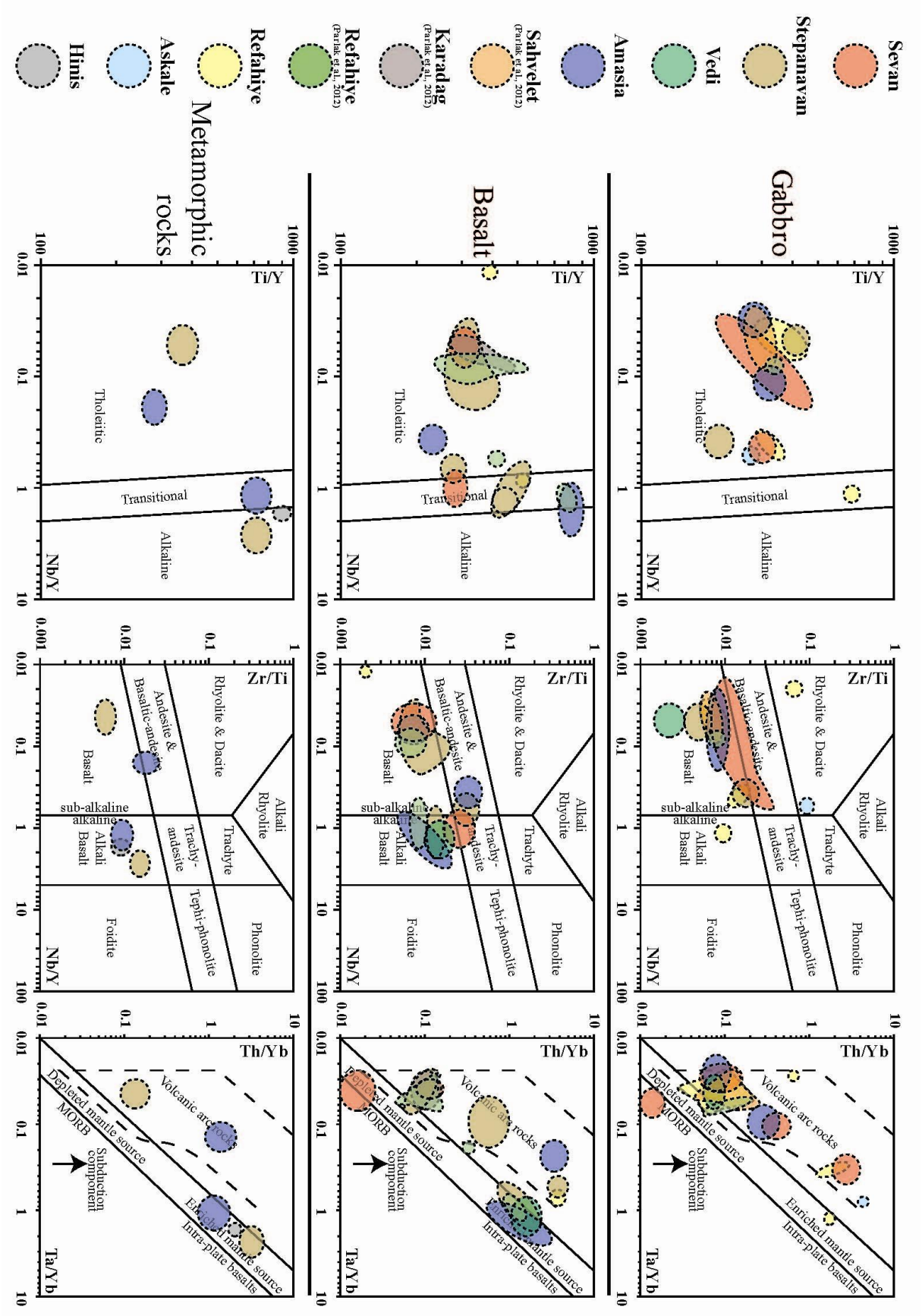
Sevan
Stepanavan
Vedi
Amasia
Salvelet (Parlak et al., 2012)
Karadag (Parlak et al., 2012)
Refahiye (Parlak et al., 2012)
Refahiye
Askale
Hinis
Metamorphic rocks
Gabbro
Basalt
Ti/Y
Nb/Y
Tholeiitic
Transitional
Alkaline
Zr/Ti
Rhyolite & Dacite
Andesite & Basaltic-andesite
Basalt
sub-alkaline
alkaline
Alkali Rhyolite
Tradyte
Trachy-andesite
Tephri-phonolite
Foidite
Phonolite
Alkali Basalt
Th/Yb
Ta/Yb
Volcanic arc rocks
Depleted mantle source
MORB
Subduction component
Enriched mantle source
Intra-plate basalts

Figure 46 - Diagrams for crustal rocks of the ophiolites. Data concerning Erzincan–Erzurum region (Refahiye, Şahvelet and Karadağ) are from Parlak et al. (2013) and this study. Data concerning Amasia, Stepanavan, Sevan and Vedi are from Hässig et al. (2013), Galoyan et al. (2007, 2009) and Rolland et al. (2009, 2010). A1, B1, C1: Ti/Y vs. Nb/Y discrimination diagram (after Pearce, 1982). A2, B2, C2: Zr/Ti vs. Nb/Y classification diagram (after Pearce, 1996). A3, B3, C3: Ta/Yb vs. Th/Yb tectonic emplacement diagram (after Pearce, 1982).

A tholeiitic (MORB-type) affiliation is found in samples, some with variable enrichment in Large Ion Lithophile Elements (LILE). In Ti/Y vs. Nb/Y and Zr/Ti vs. Nb/Y diagrams these samples plot as basaltic tholeiites. The trace element patterns show generally marked negative anomalies in Ta–Nb and enrichment in Large Ion Lithophile Elements (LILE) (**Figure 47**). The gabbros have rather flat spectra. This variable enrichment is interpreted as a contamination of a depleted mantle source by a subduction component. The association of serpentinites, gabbros, plagiogranites and basalts is typical of ophiolite assemblages, suggestive of an oceanic crust. Therefore, ophiolite rocks, as ophiolite mélange rocks, probably represent supra-subduction back- or fore-arc basins. The second tendency observed is formed by rocks with an alkaline basalt composition.

The metamorphic rocks have a very similar composition to that of alkaline basalts either plotting in Ti/Y vs. Nb/Y and Zr/Ti vs. Nb/Y diagrams as alkaline or transitional rocks. Spidergrams show neat enrichments in LILE, LREE, Ti and Pb for these samples, with no Nb–Ta negative anomalies in respect to LREE enrichment (**Figure 47**). The sub-ophiolitic metamorphic rocks also displays similar patterns as alkaline basalts in spider diagrams. The basalt MORB-normalized spider-diagrams are consistent with an Ocean Island Basalt (OIB) signature, characterized by lack of Nb and Ta negative anomalies and general enrichment in incompatible elements. As quoted by Galoyan (2008) and Galoyan et al. (2009), we interpret these features as representing an OIB signature.

Similar trends have been described by Eyüboğlu et al. (2007) and Sarıfakıoğlu et al. (2008; 2009; 2010). The likeness of these data sets strongly enforces the parallel between NE Anatolia and the Lesser Caucasus and argues that the ophiolites originate from a common supra-subduction oceanic domain.

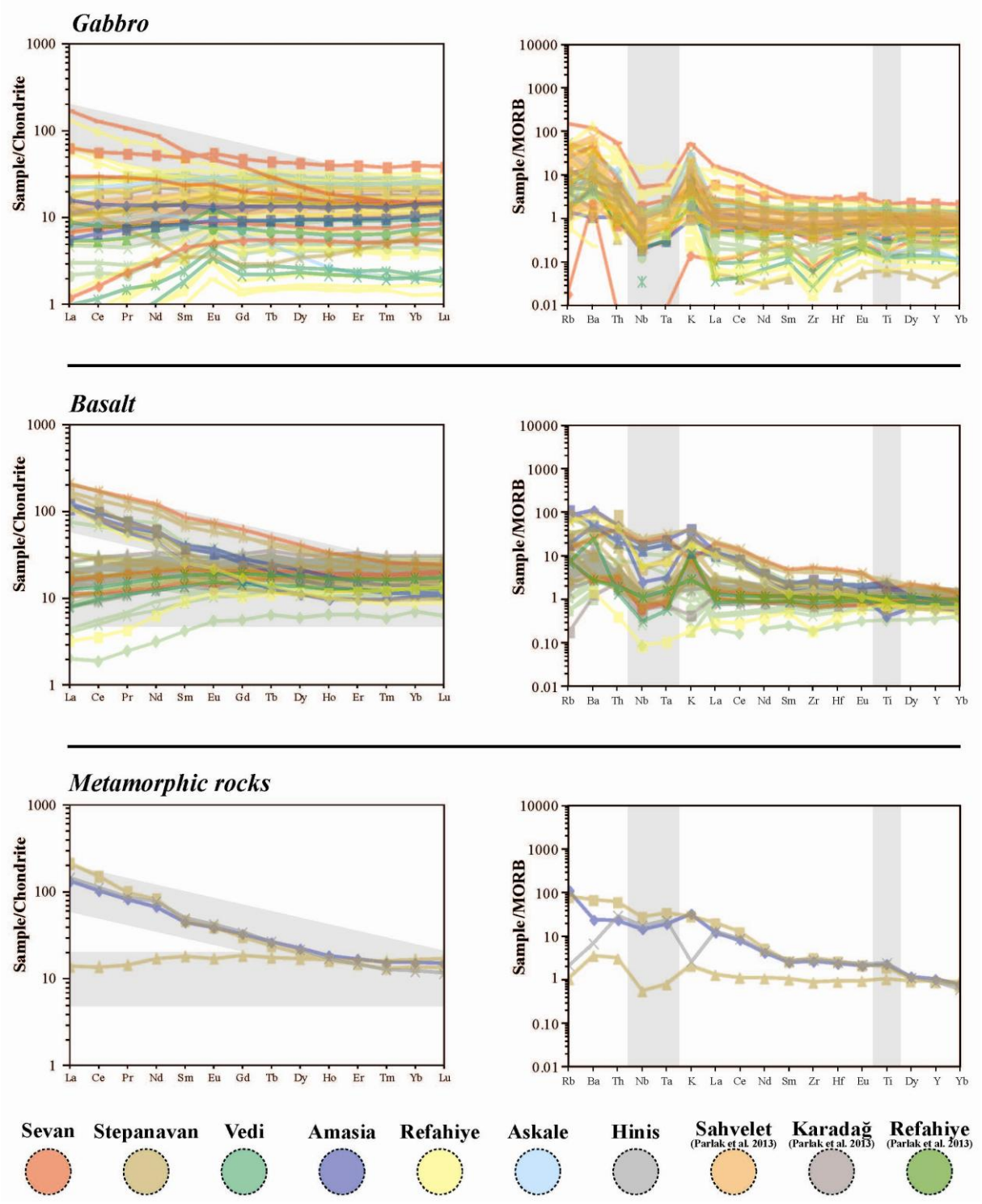

Figure 47 - Chondrite normalized REE spider diagrams and N-MORB normalized multi-element spider diagrams. Data concerning Erzincan–Erzurum region (Refahiye, Şahvelet and Karadağ) from Parlak et al. (2013) and concerning Stepanavan, Sevan and Vedi from Galoyan et al. (2007, 2009) and Rolland et al. (2009b, 2010). Normalizing values are from Sun and McDonough (1989).

1.3.3 Datings

Ophiolite gabbro containing amphiboles, hydrated during hydrothermal circulation throughout rifting commonly occurs in ophiolite mélange units and massif gabbro outcrops of both NE Anatolia and Lesser Caucasus, and are of particular interest because they may provide constraints on the timing of oceanic accretion and/or of further ophiolite obduction. Similarly, palaeontological dating of the sedimentary cover of ophiolites (i.e. radiolarites) provide minimum age constraint on the timing of ocean opening (Bill et al., 2001; Chiari et al., 1997, 2000; Danelian et al., 2000; De Wever et al., 1987; Göncüoğlu et al., 2006). Published geochronological data from ophiolite rocks of the İzmir-Ankara-Erzincan and Sevan-Akera suggest Middle to Upper Jurassic ages. Cretaceous ages are generally obtained from the metamorphic sole rocks (e.g. Harris et al., 1994; Önen, 2003) suggesting emplacement throughout these times.

These data (**Figure 48**) are suggestive of the formation of a continuous oceanic domain between the TAP and SAB to the south and the Pontides and Somkheto-Karabagh arc to the north. These ages also indicate emplacement due to a common obduction event.

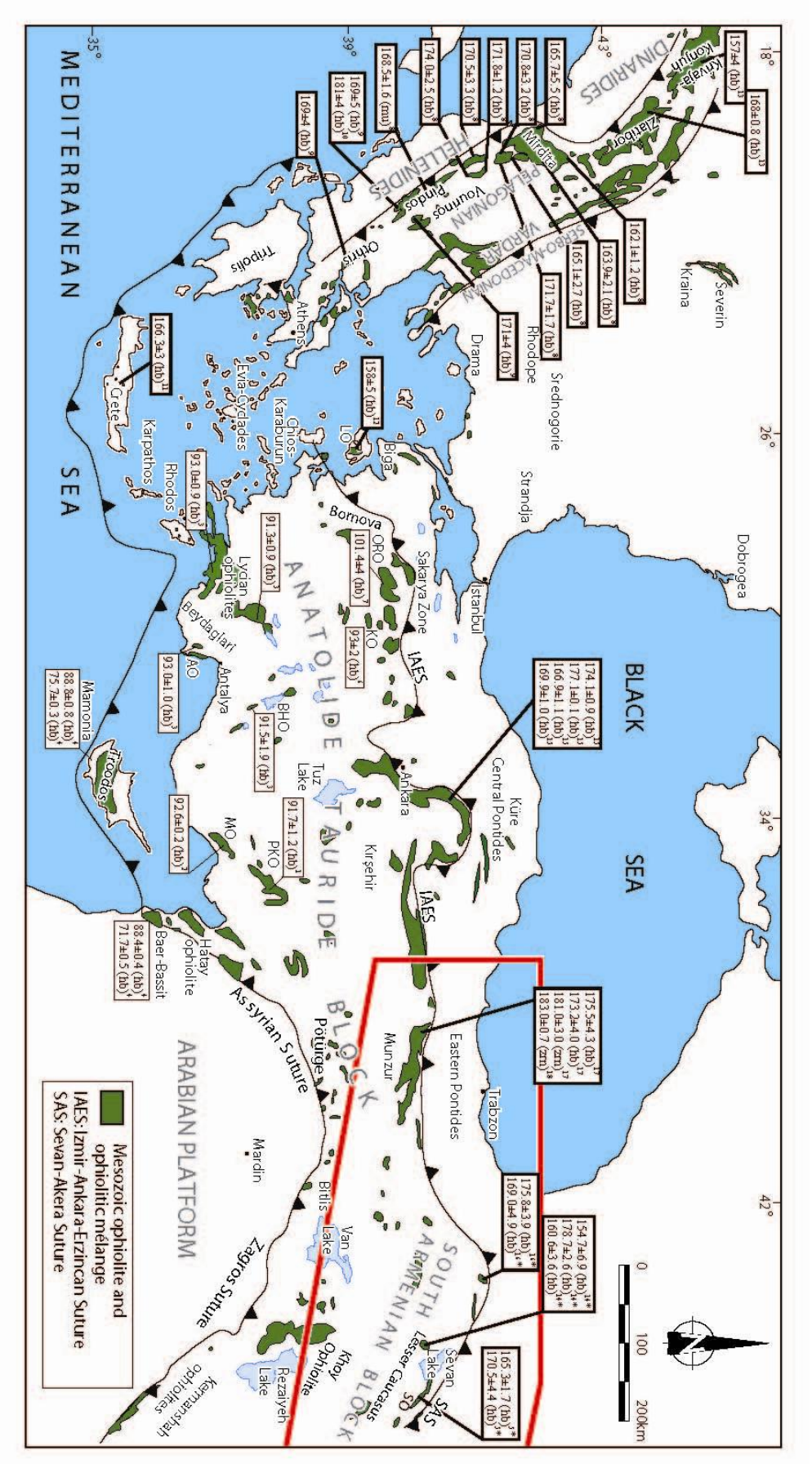
MEDITERRANEAN SEA
BLACK SEA
ANATOLIDE TAURIDE BLOCK
ARABIAN PLATFORM
SOUTH ARMENIAN BLOCK
DINARIDES
HELLENIDES
PELAGONIAN
VARDAR
SERBO-MACEDONIAN
Mesozoic ophiolite and ophiolitic mélange
IAES: Izmir-Ankara-Erzincan Suture
SAS: Sevan-Akera Suture
Assyrian Suture
Zagros Suture
Kermanshah ophiolites
Khoy Ophiolite
Rezaiyeh Lake
Van Lake
Bitlis
Mardin
Pötürge
Munzur
Eastern Pontides
Trabzon
Küre
Central Pontides
Ankara
Kırşehir
Tuz Lake
Istanbul
Sakarya Zone
Bornova
Biga
Strandja
Dobrogea
Sevan Lake
Lesser Caucasus
Kraina
Severin
Drama
Rhodope
Srednogorie
Athens
Tripolis
Othris
Pindos
Vourinos
Mirdita
Zlatibor
Konjuh
Krivaja
Crete
Karpathos
Rhodos
Evia-Cyclades
Chios-Karaburun
Lycian ophiolites
Beydagiari
Antalya
Mamonia
Troodos
Hatay ophiolite
Baer-Bassit
0
100
200km

Figure 48 - Tectonic map of Mesozoic Ophiolites and ophiolitic mélanges from the Tethyan realm in Turkey and adjacent areas (modified after Stampfli, 2000) and representative geochronological data from rocks of the ophiolitic mélanges as well as from metamorphic soles (modified after Çelik et al., 2011). All data are from 40Ar/39Ar analyses except where stated otherwise: (1) Dilek et al. (1999); (2) Parlak and Delaloye (1999); (3) Çelik et al. (2006); (4) Chan et al. (2007); (5) Galoyan et al. (2009); (6) Önen (2003); (7) Harris et al. (1994); (8) Dimo-Lahitte et al. (2001); (9) Spray et al. (1984); (10) Roddick et al. (1979); (11) Koepke et al. (2002), K-Ar age data; (12) Hatzipanagiotou and Pe-Piper (1995), K-Ar age data; (13) Lanphere et al. (1975), K-Ar age data; (14) Rolland et al. (2010); (15) Çelik et al. (2011); (16) Hässig et al. (2013); (17) Topuz et al. (2013a), (18) Topuz et al. (2013b). Abbreviations, AO: Antalya Ophiolite; BHO: Beyşehir-Hoyran Ophiolite; EO: Eldivan ophiolite; KO: Kınık Ophiolite; LO: Lesvos Ophiolite; MO: Mersin Ophiolite; ORO: Orhaneli Ophiolite; PKO: Pozantı-Karsantı Ophiolite; SO: Sevan Ophiolite; mu: muscovite; hb: hornblende. (*) age data from gabbro.

1.4 Discussion and Geodynamic implications

The emplacement of NE Anatolia and Lesser Caucasus ophiolites, now linked together, over the passive continental margin to the south requires at least 60 km tectonic transport from the northern Neotethyan suture to their emplacement in their current position, 60 km from Sevan–Akera suture to Vedi for the Lesser Caucasus and at least 80 km from Ankara-Erzurum suture to Hınıs for NE Anatolia. In all these areas the obducted ophiolite sequences display supra-subduction affinities. The geochemical composition of the amphibolites in the metamorphic units beneath the Stepanavan, Amasia and Hınıs ophiolites shows a distinct alkaline affinity similar to the alkaline oceanic island basalts (OIB) suite ascribed to magmatic processes prior to obduction and so part of the ophiolites in Armenia (Vedi, Stepanavan and Amasia) (Galoyan et al., 2007, 2009; Galoyan, 2008; Rolland et al., 2009b, 2010; Sosson et al., 2010).

The alkaline rocks in both regions (NE Anatolia and Lesser Caucasus) are not related to the generation of the SSZ type oceanic crust. We consider these alkaline rocks, found directly on the ophiolite body in Armenia, outcropping as preserved metric pillow lavas as markers of an ocean environment at the time of alkaline volcanism dated c. 117 Ma (mid-Early Cretaceous) by Rolland et al. (2009b). Consequently, the alkaline lithologies are regarded as formations emplaced on the oceanic crust prior to the obduction event, thus, typical of the ophiolite series of this area.

When considering an intra-oceanic subduction model for the origin of slow spreading ophiolites, observations lead to conclude that the volcanic arc is missing. The only evidence of any remains of such a volcanic arc structure can be found in the ophiolitic sole lithologies evidenced by geochemical tendencies. Determining whether ophiolites are of fore- or back-arc origin is not simple because of intricate obduction initiation as well as syn- and post-obduction processes. Both scenarios, fore- or back-arc origin, suggest the existence of an

intra-oceanic arc. The structural and geochemical processes leading to their formation are almost identical, except for less important subduction contamination for back-arc tholeiites.

It has been suggested that the Karadağ ophiolites are representative of a fore-arc environment due to boninitic chemical signatures (Crawford, 1989; Falloon & Crawford, 1991), typical of SSZ magmatism (Parlak et al., 2013). In this scenario the arc would then be either accreted to the Pontides margin (to the north) or subducted under it. There is no evidence of this arc to the north of the ophiolites, except for U-Pb ages which are ascribe to a continuous activity along the southern margin of Eurasia (Rolland et al., 2011; Ustaömer et al., 2012). The only arc is the Pontides and Somkheto-Karabakh, which are limited to the south by the north dipping subduction of ophiolites evidenced by eclogite facies metamorphism (Topuz et al., 2013b) in the Refahiye area.

However, more recent investigations have shown that boninites are not solely found in fore-arc but also in back-arc environments (Deschamps & Lallamend, 2003; Falloon et al., 1992; Teklay, 2006). In addition, Deschamps & Lallemand (2003) tends to ascribe boninites more to a back-arc environment. Furthermore, observations made by Rice et al. (2009) state that the Karadağ ophiolites show proof of the presence of an intra-oceanic arc. The ages found for this formation are Upper Cretaceous but the authors also remarked by Rice et al. (2009) that *"As no plutonic bodies were observed, it is inferred that only the upper part of the arc is preserved, possibly because the lower part of the arc was detached and subducted."* It is then arguable that the older part of the arc, older than Upper Cretaceous, has disappeared through a continent-arc accretion/subduction process as described in Boutelier et al. (2003) and Shemenda (1994), or Ellis et al. (1999).

The mélanges found under the ophiolitic units represent, in part, dismembered pieces of the thrusted ophiolites which fell in front of the obduction front throughout obduction (Festa et al., 2010; Huene et al., 2004; Vannucchi et al., 2008), as well as scraped off features of the underthrusted unit (Cloos & Shreve, 1988; Dilek & Whitney, 1997; Elitok & Drüppel, 2008). This lithologic blend was then overthrusted by the ophiolitic body during emplacement and incorporated and metamorphosed throughout thrusting with other metamorphics beneath the ophiolites (Engi et al., 2001).

In the Erzincan area bibliographic sources as well as field observations evidence the presence of a dismembered thrust sheet of meta-carbonate rock containing Permian foraminifers (Özgül, 1981) topping highly schistosed metamorphosed magmatic rocks, directly under the obduction contact. These marbles could represent mega-lenses emplaced

through tectonic transport due to differential movements between over-thrusted upper ophiolite unit and under-thrusted Tauride Anatolide Platform unit (TAP) or mega-olistolites. This interpretation only leads us to say that the foraminifers evidence that an oceanic domain existed during the Permian between the northern passive margin of the TAP and the area where the future ophiolite will be generated or formed, thus the existence of Neotethys during the Permian.

As for the metamorphic rocks, they may have originally been emplaced anywhere between the passive continental margin (to the south) and the future obducted ophiolite (to the north).We ascribe their schistosity to the intense shearing endured by these rocks throughout ophiolite emplacement. The basal contact of this unit being shielded by Cenozoic deposits of the Erzincan Basin renders it difficult to affirm that these rocks were originally located on the passive (continental or oceanic) margin. This includes a fore- or back-arc environment which is now only testified by sub-ophiolitic metamorphics caught between the underthrusted continent and overthrusted ophiolites. Analyses of these Erzincan metamorphic rocks, phyllite with calc-alkaline affinities, are documented by Gücer et al. (2007). Their geochemistry testifies of meta-basalts with tholeiitic as well as calc-alkaline tendencies. Even if there is no geochronologic data to bracket the original emplacement of these rock types before obduction, the presence of these rocks argues the occurrence of a volcanic arc between the passive continental margin to the south and the future ophiolites to the north, prior to obduction. This further argues an intra-oceanic subduction which accounts for the creation of oceanic crust in a supra-subduction setting.

The geochemical affinities and corresponding protoliths determined for all of these metamorphic rocks are compatible with a volcanic arc environment (Gücer & Aslan, 2009). Also recent $^{40}Ar/^{39}Ar$ ages have been calculated by Aslan et al. (2011) for plagioclases populations which yield ages of 94.1±3.3 Ma and 60.7±4.9 Ma for the metamorphism of this unit. Let us point out that these ages are similar to those of Stepanavan metamorphic unit (95-91 Ma and 71 Ma; Rolland et al., 2009a).

The field relations are thus compatible with a model of obduction of a back-arc domain with oceanic crust slicing after OIB emplacement, which explains why we find alkaline rocks both underneath and on top of the ophiolite. The alkaline outcrops would have been under-thrusted as the ophiolite underwent an intra-oceanic scaling process. Two hypotheses can account for the absence of the expected intra-oceanic island arc: (1) the progressive slicing and alteration by tectonic erosion of the volcanic arc during the obduction or (2) a subduction

"jump" behind the fore-arc block, dragging the volcanic arc with it as proposed by Shemenda (1994). This latter model is suggested by some volcanic blocks in the Stepanavan blueschists and by the paleo-arc complex overprinted by low grade metamorphism found under the obducted ophiolite sequence to the north of the Erzincan basin. In central and eastern Turkey, remnants for such intra-oceanic subduction have also been documented between 169.91+/- 0.8 and 177.08 +/- 0.96 Ma (Çelik et al., 2011).

From all the available geological data, we propose the following model for the evolution of the NE Anatolian and Lesser Caucasus regions (**Figure 49**):

1- The magmatic and metamorphic rocks of all the ophiolites have similar geochemical compositions. The ophiolitic rocks are all of similar age (between 150 and 170 Ma; Çelik et al., 2011; 2013; Galoyan et al., 2009; Rolland et al., 2009a, 2009b; Sosson et al., 2010; Topuz et al., 2013a, 2013b).

2- The two magmatic suites were emplaced one on top of the other: a gabbroic basement of supposedly back-arc oceanic crust topped by thick basaltic flows with an alkaline tendency. This confirms the hypothesis of a single ophiolitic nappe (Galoyan, 2008) over the SAB topped by a volcanic series of hot-spot type, dated c. 117 Ma in Rolland et al. (2009b).

3- The ages of the syn-tectonic sedimentary deposits limit the beginning of obduction of this oceanic domain to Coniacian–Santonian times. Datings on the flysch at Sevan and Vedi indicate similar dates as well as those found in the literature for the NE Anatolian domain (Dilek & Thy, 2006; Okay, 2008). This is compatible with the context of the closure of Neotethys.

4- This new contribution in the comprehension of the geodynamic evolution of NE Anatolia and the Lesser Caucasus supports the presence of two north dipping subduction zones: (1) a subduction under the Eurasian margin and (2) farther south, an intra-oceanic subduction allowing the continental domain to subduct under the oceanic lithosphere, thus leading to ophiolite emplacement. This extends recent geodynamic models for the Lesser Caucasus (Hässig et al., 2013; Rolland et al., 2010; Sosson et al., 2010) eastwards to include NE Anatolia.

5- The missing of the volcanic arc formed above the intra-plate subduction may be explained by its dragging under the obducting ophiolite with scaling by faulting and tectonic erosion. It is hypothesized that the part of the blueschists of Stepanavan corresponds to this missing volcanic arc (Galoyan et al., 2007; Rolland et al., 2009a). In the Erzincan region geochemical traces (Parlak et al., 2013) and field observations lead to the confirmation of this

hypothesis because of the presence of low-grade metamorphic rocks of volcanic origin that are found under the ophiolitic rocks obducted from north to south along the northern edge of the Erzincan basin.

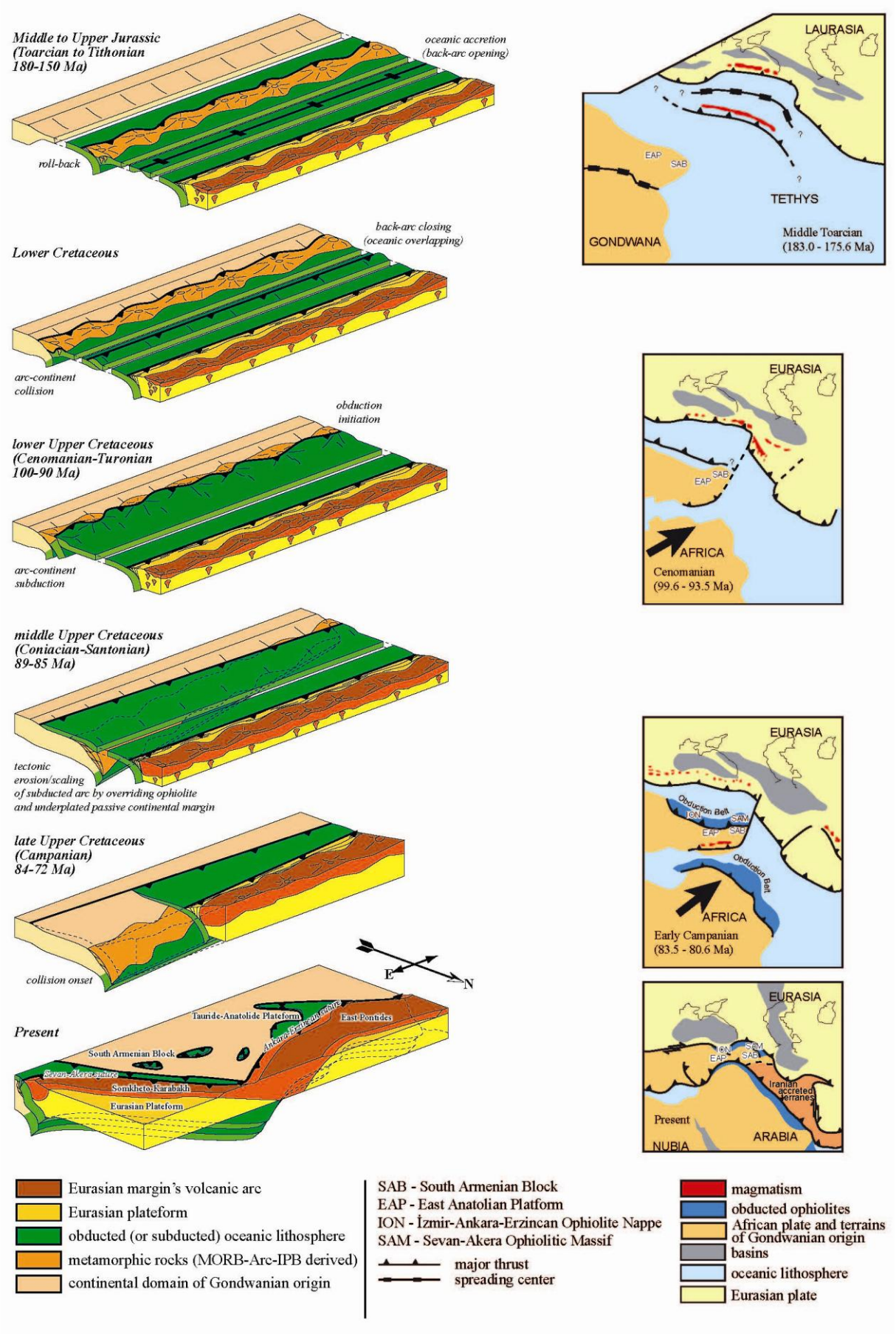
Middle to Upper Jurassic
(Toarcian to Tithonian
180-150 Ma)
oceanic accretion
(back-arc opening)
roll-back
LAURASIA
EAP
SAB
TETHYS
GONDWANA
Middle Toarcian
(183.0 - 175.6 Ma)
Lower Cretaceous
back-arc closing
(oceanic overlapping)
arc-continent
collision
EURASIA
EAP
SAB
AFRICA
Cenomanian
(99.6 - 93.5 Ma)
obduction
initiation
lower Upper Cretaceous
(Cenomanian-Turonian
100-90 Ma)
arc-continent
subduction
middle Upper Cretaceous
(Coniacian-Santonian)
89-85 Ma)
tectonic
erosion/scaling
of subducted arc by overriding ophiolite
and underplated passive continental margin
EURASIA
Obduction Belt
ION
SAM
EAP
SAB
Obduction Belt
AFRICA
Early Campanian
(83.5 - 80.6 Ma)
late Upper Cretaceous
(Campanian)
84-72 Ma)
collision onset
E
N
Present
Tauride-Anatolide Plateform
East Pontides
Ankara-Erzincan suture
South Armenian Block
Sevan-Akera suture
Somkheto-Karabakh
Eurasian Plateform
EURASIA
ION
SAM
EAP
SAB
Iranian
accreted
terranes
Present
NUBIA
ARABIA
Eurasian margin's volcanic arc
Eurasian plateform
obducted (or subducted) oceanic lithosphere
metamorphic rocks (MORB-Arc-IPB derived)
continental domain of Gondwanian origin
SAB - South Armenian Block
EAP - East Anatolian Platform
ION - İzmir-Ankara-Erzincan Ophiolite Nappe
SAM - Sevan-Akera Ophiolitic Massif
major thrust
spreading center
magmatism
obducted ophiolites
African plate and terrains
of Gondwanian origin
basins
oceanic lithosphere
Eurasian plate

Figure 49 - Middle Toarcian (c. 180 Ma) to present day palaeotectonic evolution of the NE Anatolian-Lesser Caucasus region. Maps modified from Middle East Basins Evolution Programme palaeotctonic maps of the Middle East (Barrier and Vrielynck, 2008) illustrating our new interpretation.

When considering the discontinuous occurrences of metamorphic rocks with calc-alkaline tendencies along the northern Neotethyan suture, we do not see the problem with punctual occurrences of arc volcanism due to the intra-oceanic subduction, as opposed to a continuous uninterrupted volcanic arc.

Acknowledgements

This work was supported by the MEBE (Middle East Basin Evolution) and the DARIUS programs jointly supported by a consortium including oil companies, the University Pierre and Marie Curie and the INSU/CNRS. Fieldwork was partly facilitated by the support of the Armenian Academy of Science (Institute of Geological Sciences). We gratefully acknowledge help of M. Manetti and S. Gallet in Nice during sample preparation and data acquisition, respectively. Osman Parlak and anonymous reviewer are thanked for their valuable comments and suggestions that improved the manuscript. This publication is a contribution of "GEOAZUR", University of Nice–Sophia Antipolis, and CNRS, France.

References

Adamia, S. A., Lordkipanidze, M. B., & Zakariadze, G. S. (1977). Evolution of an active continental margin as exemplified by the Alpine history of the Caucasus. *Tectonophysics, 40,* 183–189.

Adamia, Sh. A., Chkhotua, T., Kekelia, M., Lordkipanidze, M., Shavishvili, I., & Zakariadze, G. (1981). Tectonics of Caucasus and adjoining regions: implications for the evolution of the Tethys ocean. *Journal of Structural Geology,* 3, 437–447.

Adamia, Sh. A., Belov, A., Kekelia, M., & Shavishvili, I. (1987). Paleozoic tectonic development of the Caucasus and Turkey (Geotraverse C). In Flugel, H. W., Sassi, F. P., & Grecula, P. (Eds.), *Pre-Variscan and Variscan Events in the Alpine–Mediterranean Mountain Belts* (pp. 22–50). Mineralia Slovaca: Alfa Bratislava.

Agard, P., Searle, M. P., Alsop, G. I., & Dubacq, B. (2010). Crustal stacking and expulsion tectonics during continental subduction: P–T deformation constraints from Oman. *Tectonics,*

Akıncı, Ö. T. (1984). The eastern Pontide volcanosedimentary belt and associated massive sulphide deposits. In Dixon, J. E. & Robertson, A. H. F. (Eds.), *The Geological Evolution of the Eastern Mediterranean* (pp. 415–428). Geological Society, London: Special Publication, 17.

Aktimur, H. T., Sarıaslan, M., Keçer, M., Turşucu, A., Ölçer, S., Yurdakul, M. E.,… Yıldırım, T. (1995). Geology of Erzincan Surrounding. *Mineral Research and Exploration Institute (MTA) of Turkey Report no. 9792* (unpublished, in Turkish).

Aslan, Z., Gücer, M. A., & Arslan, M. (2011). ^{39}Ar-^{40}Ar dating on plagioclases of metabasic metagranitic rocks in the Yoncayolu metamorphic, NE Turkey. *Goldschmidt Conference Abstracts*, 460.

Avagyan, A., Sosson, M., Philip, M. H., Karakhanian, A., Rolland, Y., Melkonyan, R., Rebai, S., & Davtyan, V. (2005). Neogene to quaternary stress field evolution in Lesser Caucasus and adjacent regions using fault kinematics analysis and volcanic cluster data. *Geodinamica Acta, 18,* 401–416.

Avagyan, A., Sosson, M., Karakhanian, A., Philip, H., Rebai, S., Rolland, Y., Melkonyan, R., & Davtyan, V. (2010). Recent tectonic stress evolution in the lesser Caucasus and adjacent regions. *Geological Society, London: Special Publications, 340,* 393–408.

Barrier, E. & Vrielynck, B. (2008). Palaeotectonic map of the Middle East, Atlas of 14 maps, Tectonosedimentary–Palinspastic maps from Late Norian to Pliocene. *Commission for the Geologic Map of the World (CCMW, CCGM), Paris, France.*

Bergougnan, H. (1987). *Etudes géologiques dans l'Est-Anatolien* (Doctoral dissertation). Université Pierre et Marie Curie, Paris VI, France.

Biju-Duval, B., Dercourt, J., & Le Pichon, X. (1977). From the Tethys Ocean to the Mediterranean Seas: a plate tectonic model of the evolution of the western Alpine System. In Biju-Duval, B. & Montadert, L. (Eds.), *Structural History of the Mediterranean basins* (pp. 143-164. Editions Technip: Paris.

Bill, M., O'Dogherty, L., Guex, J., Baumgartner, P. O., & Masson, H. (2001). Radiolarite ages in Alpine-Mediterranean ophiolites: Constraints on the oceanic spreading and the Tethys-Atlantic connection. *Geological Society of America Bulletin, 113,* 129-143.

Boutelier, D., Chemenda, A., Burg, J. -P., (2003). Subduction versus accretion of intra-oceanic volcanic arcs: insight from thermo-mechanical analogue experiments. *Earth and Planetary Science Letters, 212,* 31-45.

Bozkuş C. (1998). Stratigraphy and structural evolution of Pontid/Anatolid suture zone in NE Anatolia (between Oltu-Narman). *Journal of Engineering Sciences, 4,* 487-499.

Bozkurt, E. & Mittwede, S. K. (2001). Introduction to the geology of Turkey — a synthesis. *International Geology Review 43,* 578–594.

Çelik, Ö. F., Delaloye, M., & Feraud, G. (2006). Precise ^{40}Ar/^{39}Ar ages from the metamorphic sole rocks of the Tauride Belt ophiolites, southern Turkey: implications for the rapid cooling history. *Geological Magazine, 143,* 213–227.

Çelik, Ö. F., Marzoli, A., Marschik, R., Chiaradia, M., Neubauer, F., & Öz, I. (2011). Early-Middle Jurassic intra-oceanic subduction in the İzmir–Ankara–Erzincan Ocean, Northern Turkey. *Tectonophysics, 509,* 120–134.

Çelik, Ö. F., Chiaradia, M., Marzoli, A., Billor, Z., & Marschik, R. (2013). The Eldivan ophiolite and volcanic rocks in the İzmir–Ankara–Erzincan suture zone, Northern Turkey: Geochronology, whole-rock geochemical and Nd–Sr–Pb isotope characteristics. *Lithos, 172–173,* 31-46.

Chan, G. H. N., Malpas, J., Xenophontos, C., & Lo, C. H. (2007). Timing of subduction zone metamorphism during the formation and emplacement of Troodos and Baër-Bassit ophiolites: insights from $^{40}Ar/^{39}Ar$ geochronology. *Geological Magazine, 144,* 797–810.

Chiari, M., Cortese, G., Marcucci, M., & Nozzoli, N. (1997). Radiolarian biostratigraphy in the sedimentary cover of the ophiolites of south-western Tuscany, Central Italy. *Eclogae Geologicae Helvetiae, 90,* 55–77.

Chiari, M., Marcucci, M., & Principi, G. (2000). The age of Radiolarian Cherts associated with the ophiolites in the Apennines (Italy) and Corsica (France): a revision. *Ofioliti, 25,* 141-146.

Cloos, M., & Shreve, R. L., (1988). Subduction-Channel Model of Prism Accretion, Melange Formation, Sediment Subduction, and Subduction Erosion at Convergent Plate Margins : 1. Background and Description. *Physical Applied Geophysics*, 128, 456-500.

Crawford, A. J., (1989). *Boninites*. Allen & Unwin Australia.

Danelian, T., Lekkas, S., & Alexopoulos, A (2000). Découverte de radiolarites triasiques dans un complexe ophiolitique à l'extrême sud du Péloponnèse (Agelona, Lakonie, Grèce). *Comptes Rendus de l'Académie des Sciences, Paris, 330,* 639–644.

Dercourt, J., Zonenshain, L. P., Ricou, L.-E., Kazmin, V. G., Le Pichon, X., Knipper, A. L., … Biju-Duval, B. (1986). Geological evolution of the Tethys belt from the for the Atlantic to the Pamirs since the Lias. *Tectonophysics, 123,* 241–315.

Deschamps, A., & Lallemand, S. (2003). Geodynamic setting of Izu-Bonin-Mariana boninites. *Geological Society, London, Special, 219,* 163-186.

De Sigoyer, J., Guillot, S., & Dick, P. (2004). Exhumation of the ultrahigh-pressure Tso Morari unit in eastern Ladakh (NW Himalaya): a case study. *Tectonics, 23,* 1–18.

De Wever, P., Danelian, T., Durand-Delga, M., Cordey, F., & Kito, N. (1987). Datations des radiolarites post-ophiolitiques de Corse alpine à l'aide des Radiolaires. *Comptes Rendus de l'Académie des Sciences, Paris, 305,* 893-900.

Dilek, Y., & Whitney, D. L. (1997). Counterclockwise PTt trajectory from the metamorphic sole of a Neo-Tethyan ophiolite (Turkey). *Tectonophysics, 280,* 295-310.

Dilek, Y., Thy, P., Hacker, B., & Grundvig, S. (1999). Structure and petrology of Tauride ophiolites and mafic dike intrusions (Turkey): Implications for the Neotethyan ocean. *Geological Society of America Bulletin, 111,* 1192-1216.

Dilek, Y., & Thy, P. (2006). Age and petrogenesis of plagiogranite intrusions in the Ankara mélange, central Turkey. *Island Arc, 15,* 44-57.

Dimo-Lahitte, A., Monié, P., & Vergély, P. (2001). Metamorphic soles from the Albanian ophiolites: Petrology, $^{40}Ar/^{39}Ar$ geochronology, and geodynamic evolution. *Tectonics, 20,* 78-96.

Ding, L., Kapp, P., & Wan, X. (2005). Paleocene–Eocene record of ophiolite obduction and initial India–Asia collision, south central Tibet. *Tectonics, 24,* 1–9.

Elitok, Ö., & Drüppel, K. (2008). Geochemistry and tectonic significance of metamorphic sole rocks beneath the Beyşehir–Hoyran ophiolite (SW-Turkey). *Lithos, 100,* 322-353.

Ellis, S., Beaumont, C., & Pfiffner, A., (1999). Geodynamic models of crustal-scale episodic tectonic accretion and underplating in subduction zones. *Journal of Geophysical Research, 104,* 15169-15190.

Engi, M., Berger, A., & Roselle, G.T. (2001). Role of the tectonic accretion channel in collisional orogeny. *Geology, 29,* 1143-1146.

Eyüboğlu, Y., Bektas, O., & Pul, D., (2007). Mid-Cretaceous Olistostromal Ophiolitic Mélange Developed in the Back-arc Basin of the Eastern Pontide Magmatic Arc, Northeast Turkey. *International Geology Review, 49,* 1103–1126.

Falloon, T. J., & Crawford, A.J., (1991). The petrogenesis of high-Ca boninite lavas dredged from the northern Tonga ridge. *Earth Planetary Science Letters, 102,* 375–394.

Falloon, T. J., Malahoff, A., Zonenshaina, L. P., & Bogdanova, Y., (1992). Petrology and geochemistry of back-arc basin basalts from Lau Basin spreading ridges at 15°, 18° and 19°S. *Mineralogy and Petrology, 47,* 1-35.

Festa, A., Pini, G. A., Dilek, Y., & Codegone, G. (2010). Mélanges and mélange-forming processes: a historical overview and new concepts. *International Geology Review, 52,* 1040-1105.

Floyd, P. A. & Winchester, J. A. (1975). Magma type and tectonic setting discrimination using immobile elements. *Earth and Planetary Science Letters, 27,* 211–218.

Floyd, P. A., & Winchester, J. A. (1978). Identification and discrimination of altered and metamorphosed volcanic rocks using immobile elements. *Chemical Geology, 21,* 291-306.

Galoyan, G., Rolland, Y., Sosson, M., Corsini, M., & Melkonyan, R. (2007). Evidence for superposed MORB, oceanic plateau and volcanic arc series in the Lesser Caucasus (Stepanavan, Armenia). *Comptes Rendus Geoscience, 339,* 482-492.

Galoyan, G. (2008). *Etude Pétrologiques, Géochimiques et Géochronologiques des Ophiolites du Petit Caucase (Arménie)* (Doctoral dissertation). Université Nice–Sophia Antipolis, Nice, France.

Galoyan, G., Rolland, Y., Sosson, M., Corsini, M., Billo, S., Verati, C., & Melkonyan, R. (2009). Geology, geochemistry and $^{40}Ar/^{39}Ar$ dating of Sevan ophiolites (Lesser Caucasus, Armenia): evidence for Jurassic Back-arc opening and hot spot event between the South Armenian Block and Eurasia. *Journal of Asian Earth Sciences, 34,* 135–153.

Gedik, A. (2008). Geology of the Tertiary rocks around Kemah-Erzincan-Çayirli region and their source rock characteristics. *Türkiye Mineral Resource Exploration Bulletin, 137,* 1-27
Geology, 156, 149–168.

Göncüoğlu, M. C. & Turhan, N. (1984). Geology of the Bitlis metamorphic belt: International Symposium. In Tekeli, O. & Göncüoglu, M.C. (Eds.), *Proceedings of the International Symposium on the Geology of the Taurus Belt* (pp. 237–244). Mineral Research and Exploration Institute: Ankara, Turkey.

Göncüoğlu, M. C., Yalınız, K., & Tekin, U. K. (2006). Geochemistry, tectono-magmatic discrimination and radiolarian ages of basic extrusives within the Izmir-Ankara suture belt (NW Turkey); time constraints for the Neotethyan evolution. *Ofioliti, 31,* 25-38.

Gücer, M. A., Aslan, Z., & Bektas, O., (2007). Petrography and Geochemistry Freatures of the Yoncayolu Metamorphics in Erzincan, NE Turkey. *Glodschmidt Conference Abstracts*, A360.

Gücer, M. A., & Aslan, Z., (2009).Yoncayolu Metamorfitleri'nin (Üzümlü-Erzincan) Mineralojisi, Jeokimyası ve Kökeni: Yeşilşist Fasiyesinin Metamorfizma Özellikleri. Türkiye Jeoloji Kurultayı, MTA – Ankara.

Gürer, Ö. F. & Aldanmaz, E. (2002). Origin of the Upper Cretaceous-Tertiary sedimentary basins within the Tauride-Anatolide platform in Turkey. *Geological Magazine, 139,* 191-197. doi:10.1017/S0016756802006295

Gutnic, M., Monod, O., Poisson, A., & Dumont, F.-D. (1979). Géologie des Taurides occidentales (Turquie). *Mémoires de la Société Géologique de France, Numéro Spécial, 58,* 112.

Hacker, B. R. (1991). The role of deformation in the formation of metamorphic field gradients: Ridge subduction beneath the Oman ophiolite. *Tectonics, 10,* 455–473.

Hacker, B. R., Mosenfelder, J. L., & Gnos, E. (1996). Rapid emplacement of the Oman ophiolite: thermal and geochronologic constraints. *Tectonics, 15,* 1230–1247.

Hafkenscheid, E., Wortel, M. J. R., & Spakman, W. (2006). Subduction history of the Tethyan region derived from seismic tomography and tectonic reconstructions. *Journal of Geophysical Research, 111*(B8), B08401.

Harper, G. D., Grady, K., & Coulton, A.J. (1996). Origin of the amphibolite "sole" of the Josephine ophiolite: emplacement of a cold ophiolite over a hot arc. *Tectonics, 15,* 296–313.

Harris, N. B., Kelley, S., & Okay, A. I. (1994). Post-collision magmatism and tectonics in northwest Anatolia. *Contribution to Mineralogy and Petrology, 117,* 241–252.

Hart, S. R., Erlank, A. J., & Kable, E. J. D. (1974). Sea floor basalt alteration: some chemical and Sr isotopic effects. *Contributions to Mineralogy and Petrology, 44,* 219-230.

Hässig, M., Rolland, Y., Sosson, M., Galoyan, G., Müller, C., Avagyan, A., & Sahakyan, L. (2013). New structural and petrological data on the Amasia ophiolites (NW Sevan–Akera suture zone, Lesser Caucasus): Insights for a large-scale obduction in Armenia and NE Turkey. *Tectonophysics, 588,* 135-153.

Hatzipanagiotou, K., & Pe-Piper, G. (1995). Ophiolitic and sub-ophiolitic metamorphic rocks of the Vatera area, southern Lesbos (Greece): geochemistry and geochronology. *Ofioliti, 20,* 17-29.

Hempton, M. R. (1985). Structure and deformation history of the Bitlis Suture near Lake Hazar, SE Turkey. *Geological Society of America Bulletin, 96,* 223–243.

Hess, J. C., Aretz, J., Gurbanov, A. G., Emmermann, R., Lippolt, & H. J. (1995). Subduction related Jurassic andesites in the northern Great Caucasus. *Geologische Rundschau, 84,* 319-333.

Huene, R., Ranero, C. R., & Vannucchi, P., (2004). Generic model of subduction erosion. Geology, 32, 913-916.

Humphris, S. E., Morrison, M., & Thompson, R. N. (1978). Influence of rock crystallization history upon subsequent lanthanide mobility during hydrothermal alteration of basalts. *Chemical Geology, 23,* 125-137.

Knipper, A. L. (1975). The oceanic crust in the structure of the Alpine Folded Belt (South Europe, western part of Asia and Cuba). *Tr. GIN NAS USSR, 267,* 207. (in Russian).

Knipper, A. L. & Sokolov, S. D. (1977). Vedi ophiolites (Armenia) autochton or allochton? *Geotektonica, 10,* 55–66. (in Russian)

Knipper, A. L. & Khain, E. V. (1980). Structural position of ophiolites of the Caucasus. *Ofioliti, Special Issue, 2,* 297–314.

Knipper, A. L., Ricou, L. E., & Dercourt, J. (1986). Ophiolites as indicators of the geodynamic evolution of the Tethyan ocean. *Tectonophysics, 123,* 213–240.

Knipper, A. L., Bragin, N. Y., & Satian, M. A. (1997). Upper Triassic–Lower Jurassic volcanogenic and sedimentary deposits of the Old Zod Pass (Transcaucasia). Stratigraphy, *Geological Correlation, 5,* 58–65. (in Russian)

Koepke, J., Seidel, E., & Kreuzer, H. (2002). Ophiolites on the Southern Aegean islands Crete, Karpathos and Rhodes: composition, geochronology and position within the ophiolite belts of the Eastern Mediterranean. *Lithos, 65,* 183-203.

Lanphere, M. A., Coleman, R. G., Karamata, S., & Pamić, J. (1975). Age of amphibolites associated with Alpine peridotites in the Dinaride ophiolite zone, Yugoslavia. *Earth and Planetary Science Letters, 26,* 271-276.

Mederer, J., (2013). *Regional setting, geological context and genetic aspects of polymetallic hydrothermal ore deposits from the Kapan ore district, southern Armenia: a contribution to the Mesozoic island arc metallogeny of the Lesser Caucasus* (Doctoral dissertation). Université de Genève, Geneva, **Switzerland.**

Moix, P., Beccaletto, L., Kozur, H. W., Hochard, C., Rosseletd, F., & Stampfli, G. M. (2008). A new classification of the Turkish terranes and sutures and its implication for the paleotectonic history of the region. *Tectonophysics, 451,* 7–39.

Nalivkin, V. D. (1976). Dynamics of the development of the russian platform structures. *Tectonophysics, 36,* 247–262.

Nikishin, A. M., Korotaev, M. V., Ershov, A. V., & Brunet, M. F. (2003). The Black Sea Basin: tectonic history and Neogene–Quaternary rapid subsidence modelling. *Sedimentary*

Oberhänsli, R., Candan, O., Bousquet, R., Rimmele, G., Okay, A., & Goff, J. (2010). Alpine HP evolution of the eastern Bitlis complex, SE Turkey. *Geological Society, London, Special Publication, 340,* 461-483.

Okay, A. İ. & Şahintürk, Ö. (1997). Geology of the eastern Pontides. In Robinson, A.G. (Ed.), *Regional and Petroleum Geology of the Black Sea and Surrounding Region: American Association of Petroleum* (pp. 291–311). Geologists Memoir, 68: Tulsa, Oklahoma.

Okay, A. I. & Tüysüz, O. (1999). Tethyan sutures of northern Turkey. *Geological Society, London, Special Publication, 156,* 475–515.

Okay, A. I., Tansel, I., & Tüysüz, O. (2001). Obduction, subduction and collision as reflected in the Upper Cretaceous–Lower Eocene sedimentary record of western Turkey. *Geological Magazine, 138,* 117–142.

Okay, A. I., Tüysüz, O., Satır, M., Özkan-Altıner, S., Altıner, D., Sherlock, S., & Eren, R. E. (2006). Cretaceous and Triassic subduction-accretion, HP-LT metamorphism and continental growth in the Central Pontides, Turkey. *Geological Society of America Bulletin, 118,* 1247–1269.

Okay, A. I. (2008). Geology of Turkey: a synopsis. *Anschnitt, 21,* 19-42.

Önen, A. P. (2003). Neotethyan ophiolitic rocks of the Anatolides of NW Turkey and comparison with Tauride ophiolites. *Journal of the Geological Society, 160,* 947-962.

Özen, H., Çolakoğlu, A., Sayak, H., Dönmez, C., Türkel, A., Odabaşı, İ.,… Winchester, J. A. (2006). The petrogenesis of tectonites and cumulate rocks from the ophiolites, north of Erzincan. *59th Geological Congress of Turkey, Abstracts,* 100–101.

Özgül, N. (1981). Munzur Dağlarının Jeolojisi. *General Directorate of Mineral Research and Exploration (MTA),* Report 6995. (in Turkish)

Özgül, N. (1984). Stratigraphy and tectonic evolution of the Central Taurides. *Geology of the Taurus Belt,* 77-90.

Özgül, N., and Turşucu, A., 1984, Stratigraphy of the Mesozoic carbonate sequence of the Munzur Mountains (Eastern Taurides), *in* Tekeli, O., and Göncüoğlu, M. C., editors, Geology of the Taurus Belt, Ankara, Maden Tetkit Arama Enstitüsü, p. 173–181.

Parlak, O. & Delaloye, M. (1999). Precise $^{40}Ar/^{39}Ar$ ages from the metamorphic sole of the Mersin Ophiolite (southern Turkey). *Tectonophysics*, *301,* 145-158. doi:10.1016/S0040-1951(98)00222-4

Parlak, O., Çolakoğlu, A., Dönmez, C., Sayak, H., Yıldırım, N., Türkel, A., & Odabaşı, İ. (2013). Geochemistry and tectonic significance of ophiolites along the Ankara–Erzincan suture zone in northeastern Anatolia. In: Robertson, A. H. F., Parlak, O. & Ünlügenç, U. C. (Eds). *Geological Development of Anatolia and the Easternmost Mediterranean Region* (pp. 75–105). Geological Society, London, Special Publications, 372.

Pearce, J. A. & Cann, J. R. (1973). Tectonic setting of basic volcanic rocks determined using trace element analyses. *Earth and Planetary Science Letters*, *19,* 290-300. doi:10.1016/0012-821X(73)90129-5

Pearce, J. A., & Norry, M. J. (1979). Petrogenetic implications of Ti, Zr, Y, and Nb variations in volcanic rocks. *Contributions to mineralogy and petrology*, *69,* 33-47. doi:10.1007/BF00375192

Pearce, J. A. (1982). Trace element characteristics of lavas from destructive plate boundaries. *Orogenic andesites and related rocks,* 528-548.

Pearce, J. A. (1983). Role of the sub-continental lithosphere in magma genesis at active continental margins. In Hawkesworth, C. J. & Norry, M. J. (Eds.), *Continental basalts and mantle xenoliths* (pp. 230-249). Nantwich, Cheshire: Shiva Publications.

Pearce, J. A. (1996). A user's guide to basalt discrimination diagrams. *Trace element Geochemistry of volcanic rocks: applications for massive sulphide exploration. Geological Association of Canada, Short Course Notes, 12,* 79-113.

Peccerillo, A. & Taylor, S. R. (1976). Geochemistry of Eocene calc-alkaline volcanic rocks from the Kastamonu area, northern Turkey. *Contributions to Mineralogy and Petrology, 58,* 63–81. doi:10.1007/BF00384745

Rice S. P., Robertson, A.H.F., & Ustaömer, T (2006). Late-Certaceous-Early Cenozoic tectonic evolution of the Eurasian active margin in the Central and Esatern Pontides, north

Turkey. In Robertson, A. H. F. & Mountrakis, D. (Eds.), *Tectonic Development of the Eastern Mediterranean Region* (pp.413-445). Geological Society, London, Special Publications, 260.

Rice, S. P., Robertson, A. H. F., Ustaömer, T., İnan, N., & Taslı, K. (2009). Late Cretaceous–Early Eocene tectonic development of the Tethyan suture zone in the Erzincan area, Eastern Pontides, Turkey. *Geological Magazine, 146,* 567–590.

Ricou, L. E., Zonenshain, L. P., Dercourt, J., Kazmin, V. G., Le Pichon, X., Knipper, A. L., … Biju-Duval, B. (1985). Méthodes pour l'établissement de neuf cartes paléogéographiques de l'Atlantique au Pamir depuis le Lias. *Bulletin de la Société Géologique de France, 8,* 625–635.

Ricou, L. E., Dercourt, J., Geyssant, J., Grand-Jaquet, C., Lepcrier, C., & Biju-Duval, B. (1986). Geological constraints on the Alpine evolution of the Mediterranean Tethys. *Tectonophysics, 123*, 83–122.

Ricou, L. E. (1994). Tethys reconstructed: plates, continental fragments and their Boundaries since 260 Ma from Central America to South-eastern Asia. *Geodinamica Acta-Revue de Geologie Dynamique et de Geographie Physique*, *7*(4), 169-218.

Robertson, A. (2004). Development of concepts concerning the genesis and emplacement of Tethyan ophiolites in the Eastern Mediterranean and Oman regions. *Earth-Science Reviews, 66,* 331–387.

Robinson, A., Spadini, G., Cloetingh, S., & Rudat, J. (1995). Stratigraphic evolution of the Black Sea: inferences from basin modelling. Marine and Petroleum Geology, 12, 821–835.

Roddick J. C., Cameron, W. E., & Smith, A. G. (1979). Permo-Triassic and Jurassic $^{40}Ar/^{39}Ar$ ages from Greek ophiolites and associated rocks. Nature, 279, 788-790.

Rolland, Y., Billo, S., Corsini, M., Sosson, M., & Galoyan, G. (2009a). Blueschists of the Amasia–Stepanavan Suture Zone (Armenia): linking Tethys subduction history from E Turkey to W-Iran. *International Journal Earth Sciences (Geologische Rundschau), 98,* 533-550.

Rolland, Y., Galoyan, Gh., Bosch, D., Sosson, M., Corsini, M., Fornari, M., & Vérati, C. (2009b). Jurassic back-arc and hot-spot related series in the Armenian ophiolites - implications for the obduction process. *Lithos, 112,* 163–187.

Rolland, Y., Galoyan, G., Sosson, M., Melkonian, R., & Avagyan, A. (2010). The Armenian ophiolites: insights for Jurassic back-arc formation, Lower Cretaceous hot-spot magmatism, and Upper Cretaceous obduction over the South Armenian Block. *Geological Society, London, Special Publication, 340,* 353–382.

Rolland, Y., Sosson, M., Adamia, Sh., & Sadradze, N. (2011). Prolonged Variscan to Alpine history of an active Eurasian margin (Georgia, Armenia) revealed by $^{40}Ar/^{39}Ar$ dating. *Gondwana Research, 20,* 798–815.

Rolland, Y., Perincek, D., Kaymakçı, N., Sosson, M., Barrier, E., & Avagyan, A. (2012). Evidence for 80–75 Ma subduction jump during Anatolide–Tauride–Armenian Block accretion and 48 Ma Arabia–Eurasia collision in Lesser Caucasus–East Anatolia. *Journal of Geodynamics, 56–57,* 76–85.

Sarıfakıoğlu, E., Özen, H., Çolakoğlu, A., & Sayak, H. (2008). İzmir-Ankara-Erzincan Kenet Zonundaki Suprasübdüksiyon Ofiyolitleri: petrolojisi, mineral kimyası ve tektonomagmatik ortamı. *GeoSound, 52*.

Sarıfakıoğlu, E., Özen, H., & Winchester, J. A. (2009). Whole Rock and Mineral Chemistry of Ultramafic-mafic Cumulates from the Orhaneli (Bursa) Ophiolite, NW Anatolia. *Turkish Journal of Earth Sciences, 18,* 55-83.

Sarıfakıoğlu, E., Özen, H., Çolakoğlu, A., & Sayak, H. (2010). The Suprasubduction Zone Ophiolites From Izmir-Ankara Suture Zone: petrology, mineral chemistry and tectonomagmatic setting. *GeoSound, 52*.

Satian, M. A. (2005). Mesozoic ophiolite basins of the Transcaucasian geotraverse. Izvestia of National Academy of Science of Armenia, Nauki o Zemle 1, 3–8. (in Russian)

Searle, M. & Cox, J. (1999). Tectonic setting, origin, and obduction of the Oman ophiolite. *Geological Society of America Bulletin, 111,* 104–122.

Şengör, A. M. C. & Yılmaz, Y. (1981). Tethyan evolution of Turkey: a plate tectonic approach. *Tectonophysics, 75,* 181–241.

Şengün, M. (2006). A critical review of the Anatolian geology: a dialectic to sutures and evolution of the Anatolian Tethys and Neotethys. *Mineral Research Exploration Bulletin, 133,* 1–29.

Shemenda, A. I. (1994). *Subduction: Insights from physical modeling.* Kluwer Academic Pub.

Spray, J. G., Bébien, J., Rex, D. C., & Roddick, J. C. (1984). Age constraints on the igneous and metamorphic evolution of magmatism in the Hellenic–Dinaric ophiolites. In Dixon, J.E. & Robertson, A.H.F. (Eds.), *The Geological Evolution of the Eastern Mediterranean* (pp. 619–627), Geological Society of London, Special Publication, 17.

Sokolov, S. D. (1977). The Olistostromes and Ophiolitic Nappes of the Lesser Caucasus. Izdatelstvo 'Nauka', Moscow. (in Russian).

Sosson, M., Rolland, Y., Danelian, T., Muller, C., Melkonyan, R., Adamia, S., … Galoyan, G., 2010. Subductions, obduction and collision in the Lesser Caucasus (Armenia, Azerbaijan, Georgia), new insights. *Geological Society, London, Special Publications, 340,* 329–352.

Stampfli, G. M., Borel, G. D., Cavazza, W., Mosar, J., & Ziegler, P.A. (2001). Palaeotectonic and palaeogeographic evolution of the western Tethys and PeriTethyan domain (IGCP Project 369). *Episodes*, *24,* 222–228.

Stocklin, J. (1974). Possible ancient continental margins in Iran. *The geology of continental margins*, 873-887.

Stöcklin, J., & Bhattarai, K. D. (1977). Geology of the Kathmandu area and central Mahabharat range. *Nepal: Nepal Department of Mines and Geology, Himalayan Report*.

Sun, S. S., & McDonough, W. F., (1989). Chemical and isotopic systematic of oceanic basalts: implications for mantle composition and processes. In: Saudners A. D., & Norry, M. J. (Eds.), *Magmatism in Ocean Basins* (pp. 313-345), Geological Society, London, Special Publications, 42.

Topuz, G., Çelik, Ö. F., Şengör, A. M. C., Altıntaş, İ. E., Zack, T., Rolland, Y., & Barth, M. (2013a). Jurassic ophiolite formation and emplacement as backstop to a subduction-accretion complex in Northeast Turkey, the Refahiye ophiolite, and relation to the Balkan ophiolites. *American Journal of Science*, 313.

Topuz, G., Göçmengil, G., Rolland, Y., Çelik, Ö. F., Zack, T. & Schmitt, A. K. (2013b). Jurassic accretionary complex and ophiolite from northeast turkey: no evidence for the Cimmerian continental ribbon. *Geology, 41*, 255-258.

Ustaömer, P. A., Ustaömer, T., & Robertson, A. H. (2012). Ion Probe U-Pb dating of the Central Sakarya Basement: a peri-Gondwana terrane intruded by Late Lower Carboniferous subduction/collision-related granitic rocks. *Turkish Journal of Earth Sciences, 21,* 905-932.

Vannucchi, P., Remitti, F., Bettelli, G., (2008). Geologic record of fluid flow and seismogenesis along an erosive subducting plate boundary. *Nature, 451*, 699-703.

Yılmaz, Y., Yiğitbaş, E., & Can Genç, Ş. (1993). Ophiolitic and metamorphic assemblages of Southeast Anatolia and their significance in the geological evolution of the orogenic belt. *Tectonics, 10,* 1280–1297.

Yılmaz, Y., Tüysüz, O., Yiğitbaş, E., Genç, Ş. C. & Şengör, A. M. C. (1997). Geology and tectonic evolution of the Pontides. In Robinson, A.G. (Ed.), *Regional and Petroleum Geology of the Black Sea and Surrounding Region: American Association of Petroleum* (pp. 183–226). Geologists Memoir, 68: Tulsa, Oklahoma.

Yılmaz, A., Yılmaz, H., Kaya, C., Boztuğ, D., (2010). The Nature of the Crustal Structure of the Eastern Anatolian Plateau, Turkey. *Geodinamica Acta, 23*, 167-183.

Zakariadze, G. S., Knipper, A. L., Sobolev, A. V., Tsamerian, O. P., Dmitriev, L. V., Vishnevskaya, V. S., & Kolesov, G. M. (1983). The ophiolite volcanic series of the Lesser Caucasus. *Ofioliti*, *8*(3), 439-466.

Zakariadze, G. S., Knipper, A. L., Bibikova, E. V., Silantiev, S. A., Zlobin, S. K., Gracheva, T. V., … Kolesov, T. M., 1990. The setting and age of the plutonic part of the NE Sevan ophiolite complex. *Izvestia NAS USSR, Geological, 3,* 17–30. (in Russian)

Zakariadze, G. S., Dilek, Y., Bogdanovsky, O. G., Karpenko, S. F., Vishnevskaya, V. S., Solov'eva, N. V. (2005). Age limits of the Lesser Caucasus paleooceanic allochthon. Abstracts of the International Symposiumon the Geodynamics of EasternMediterranean: Active Tectonics of the Aegean Region, 15–18 June 2005, Kadir Has University, Istanbul, Turkey, p.229.

Table

Lab No.		700a	701a	713c	729b	730	733	737	743b	745b	746c	746d	751	755a
Locality		Kemah	Kemah	Kemah	Kemah	Kemah	Kemah	Erzincan	Erzincan	Erzincan	Erzincan	Erzincan	Erzincan	Erzincan
Latitude		39.61185° N	39.60997° N	39.54635° N	39.54635° N	39.54635° N	39.69487° N	39.60615° N	39.83641° N	39.88024° N	39.79576° N	39.79576° N	39.64722° N	39.58129° N
Longitude		39.22681° E	39.22995° E	38.96879° E	38.96879° E	38.96879° E	39.05207 E	39.19323° E	39.33277° E	39.16705° E	39.48271° E	39.48271° E	39.51133° E	39.62554° E
Formation		Gabbro	Gabbro	Gabbro	Gabbro	Gabbro	Gabbro	Gabbro	Gabbro	Gabbro	Gabbro	Gabbro	Gabbro	Gabbro
SiO_2	%	46.96	46.52	47.09	49.40	48.58	53.87	48.87	48.49	46.40	76.50	47.90	50.93	47.96
TiO_2	%	0.13	0.09	2.65	0.69	0.95	0.85	0.25	1.85	2.52	0.14	0.15	0.97	0.25
$AlZO_3$	%	18.05	19.13	15.29	15.61	18.72	17.61	18.65	14.43	14.39	13.09	21.08	15.62	16.39
$Fe2O_3$	%	3.96	3.39	9.70	9.49	9.53	8.38	4.69	13.74	16.94	0.24	6.76	9.95	7.27
MnO	%	0.07	0.06	0.12	0.16	0.17	0.15	0.09	0.21	0.26	0.00	0.13	0.16	0.12
MgO	%	10.97	9.95	5.21	7.01	4.71	4.49	7.83	5.69	5.66	0.18	8.77	5.79	10.24
CaO	%	16.49	17.53	11.58	10.68	8.62	7.10	17.06	7.38	9.67	4.66	14.53	6.96	14.65
Na_2O	%	0.88	0.71	3.89	3.76	4.03	4.97	1.59	4.70	3.09	2.83	0.78	5.28	1.62
K_2O	%	0.02	0.01	1.08	0.12	1.55	0.95	0.05	0.20	0.10	0.15	0.07	0.38	0.02
P_2O_5	%	< L.D.	< L.D.	1.28	0.06	0.22	0.19	< L.D.	0.16	0.25	< L.D.	< L.D.	0.09	< L.D.
LOI	%	1.82	1.42	1.15	3.01	3.26	2.45	1.41	2.28	0.60	0.71	0.80	3.34	0.86
Total	%	99.34	98.81	99.04	99.97	100.35	101.00	100.49	99.11	99.87	98.51	100.97	99.47	99.38
Ba	ppm	1.54	< L.D.	184.20	202.40	876.50	381.00	23.33	91.43	50.72	37.34	8.24	42.56	< L.D.
Rb	ppm	0.38	0.30	18.53	2.88	28.08	20.12	0.80	1.74	0.79	2.03	1.23	7.09	0.50
Sr	ppm	63.35	85.09	873.00	119.30	659.70	555.00	132.90	151.10	132.30	206.20	147.80	139.80	96.47
Ta	ppm	< L.D.	< L.D.	2.29	0.06	0.75	0.63	< L.D.	0.15	0.25	0.14	< L.D.	0.06	< L.D.
Th	ppm	< L.D.	< L.D.	3.10	0.15	2.88	4.96	< L.D.	0.17	0.04	3.27	< L.D.	0.20	< L.D.
Zr	ppm	1.68	< L.D.	190.70	29.65	91.22	105.10	2.73	94.67	133.00	67.76	1.12	52.96	3.09
Nb	ppm	< L.D.	< L.D.	33.13	0.69	9.19	7.57	< L.D.	1.81	3.18	1.00	< L.D.	0.67	< L.D.
Y	ppm	3.32	2.18	28.38	17.16	19.99	20.31	6.46	37.68	50.67	49.31	2.42	21.46	6.41
Hf	ppm	0.08	0.04	4.44	0.98	2.33	2.76	0.15	2.70	3.27	2.76	0.06	1.61	0.16
V	ppm	102.60	92.43	162.80	264.30	310.80	259.00	176.60	414.90	530.30	5.87	153.40	280.50	153.70
Cr	ppm	1493.00	957.40	169.70	97.08	34.21	24.24	398.60	27.32	32.15	7.14	69.50	34.81	551.10
Ni	ppm	162.10	173.50	114.10	50.63	34.94	24.89	96.62	14.91	29.65	< L.D.	43.42	26.79	145.30
Co	ppm	30.56	28.07	38.49	34.92	32.25	24.88	25.43	33.76	46.33	1.05	36.50	31.73	46.26
U	ppm	< L.D.	< L.D.	1.71	0.06	1.36	1.42	< L.D.	0.09	< L.D.	0.50	< L.D.	0.09	< L.D.
Sc	ppm	38.28	38.37	24.61	39.47	21.59	24.14	53.99	36.67	45.64	2.20	38.03	35.43	46.63
Cu	ppm	25.29	109.80	33.00	75.20	148.60	82.69	< L.D.	47.16	64.40	< L.D.	27.12	63.52	118.90
Zn	ppm	20.71	14.12	124.70	65.76	85.75	67.60	14.78	112.30	131.60	< L.D.	29.01	81.02	38.28
Pb	ppm	< L.D.	< L.D.	3.27	< L.D.	8.65	15.50	< L.D.	< L.D.	< L.D.	< L.D.	< L.D.	< L.D.	< L.D.
Cs	ppm	< L.D.	< L.D.	0.08	7.48	0.21	0.15	0.10	0.14	0.11	0.15	< L.D.	0.53	0.24
La	ppm	< L.D.	< L.D.	32.60	1.22	13.62	16.47	0.14	3.85	5.04	11.57	0.19	2.25	0.14
Ce	ppm	0.32	0.15	61.02	3.31	26.62	32.07	0.48	11.44	15.59	26.05	0.44	6.71	0.55
Pr	ppm	0.06	0.03	7.01	0.53	3.14	3.63	0.10	1.85	2.57	3.30	0.07	1.09	0.12
Nd	ppm	0.44	0.26	32.19	3.36	14.36	16.03	0.80	10.49	15.17	16.11	0.45	6.25	0.91
Sm	ppm	0.22	0.14	6.76	1.41	3.54	3.62	0.49	3.72	5.36	4.27	0.20	2.18	0.50
Eu	ppm	0.17	0.11	2.32	0.58	1.16	1.05	0.33	1.39	1.86	0.23	0.17	0.97	0.34
Gd	ppm	0.37	0.26	6.28	1.98	3.40	3.52	0.83	5.01	6.87	5.42	0.30	2.97	0.83
Tb	ppm	0.07	0.05	0.87	0.39	0.56	0.57	0.16	0.90	1.25	0.97	0.06	0.52	0.16
Dy	ppm	0.54	0.38	4.83	2.67	3.42	3.41	1.11	6.08	8.22	6.82	0.41	3.48	1.08
Ho	ppm	0.12	0.08	0.88	0.60	0.69	0.70	0.24	1.32	1.79	1.54	0.09	0.76	0.24
Er	ppm	0.34	0.23	2.21	1.76	1.97	1.95	0.65	3.78	5.05	4.69	0.26	2.17	0.65
Tm	ppm	0.05	0.04	0.30	0.28	0.30	0.30	0.10	0.59	0.79	0.75	0.04	0.34	0.09
Yb	ppm	0.33	0.21	1.83	1.87	2.04	2.04	0.61	3.88	5.23	5.04	0.27	2.24	0.62
Lu	ppm	0.05	0.03	0.27	0.29	0.31	0.31	0.09	0.61	0.79	0.82	0.04	0.36	0.09

Table 12 - Representative whole-rock analyses of samples from ophiolitic complexes of NE Anatolia and Lesser Caucasus. "< L.D.": under detection level.

Lab No.		774	776	777	780	788	796a	797a	T-11-01	T-11-02	T-11-04	T-11-08	T-11-22	T-11-27
Locality		Erzincan	Erzincan	Erzincan	Erzincan	Erzincan	Aşkale	Aşkale	Refahiye	Refahiye	Erzincan	Erzincan	Erzincan	Hınıs
Latitude		39.79455° N	39.78600° N	39.78463° N	39.80939° N	39.76208° N	40.01914° N	40.01914° N	39.81766° N	39.81766° N	39.64293° N	39.64722° N	39.72808° N	39.45520° N
Longitude		39.59068° E	39.51395° E	39.51402° E	39.54614° E	39.73071° E	40.53653° E	40.53653° E	38.85969° E	38.85969° E	39.51794° E	39.51133° E	39.71039° E	42.09869° E
Formation		Peridotite	Gabbro	Gabbro	Gabbro	Gabbro	Gabbro	Gabbro	Plagiogranite	Gabbro	Basalt	Gabbro	Meta-Basalt	Amphibolite
SiO_2	%	42.68	39.14	50.00	47.54	44.11	46.14	50.69	51.58	47.10	46.86	50.84	54.27	43.70
TiO_2	%	0.02	1.90	1.74	0.67	1.22	1.95	0.05	0.59	1.62	1.14	0.91	0.97	3.26
$AlZO_3$	%	1.23	15.29	14.72	14.94	14.17	14.42	0.69	22.72	13.86	15.36	15.59	15.05	12.56
$Fe2O_3$	%	8.68	13.21	12.57	10.19	11.47	14.07	3.70	4.32	13.59	6.54	9.69	12.26	13.69
MnO	%	0.13	0.23	0.21	0.16	0.19	0.21	0.08	0.07	0.22	0.10	0.15	0.14	0.18
MgO	%	38.99	8.15	4.71	9.54	7.36	5.26	23.75	2.26	6.74	6.52	6.39	5.41	9.94
CaO	%	1.66	15.05	10.21	11.81	14.09	7.59	17.76	9.98	9.81	14.49	8.30	5.22	11.70
Na_2O	%	0.03	0.46	4.39	2.49	2.37	4.46	0.12	5.79	3.17	2.80	3.59	2.72	3.15
K_2O	%	0.02	0.04	0.27	0.04	0.06	1.14	< L.D.	0.06	0.18	1.29	1.08	0.01	0.20
P_2O_5	%	< L.D.	0.16	0.20	< L.D.	0.11	0.17	< L.D.	0.09	0.15	0.34	0.09	0.08	0.39
LOI	%	6.08	6.27	1.46	2.79	3.41	3.52	2.28	3.00	3.49	4.96	3.26	3.51	1.15
Total	%	99.51	99.91	100.47	100.17	98.55	98.94	99.13	100.46	99.94	100.39	99.89	99.64	99.89
Ba	ppm	< L.D.	10.25	110.60	5.90	83.32	69.63	< L.D.	27.94	54.49	490.20	42.92	9.84	46.31
Rb	ppm	0.65	0.48	3.28	< L.D.	1.04	19.27	< L.D.	1.43	2.34	38.73	14.24	< L.D.	1.30
Sr	ppm	< L.D.	38.11	185.60	103.00	121.10	131.80	8.80	340.10	1298.00	1014.00	267.40	195.70	542.40
Ta	ppm	< L.D.	0.18	0.23	< L.D.	0.09	0.19	< L.D.	0.05	0.15	1.00	0.06	0.02	3.37
Th	ppm	< L.D.	0.21	0.51	< L.D.	< L.D.	0.48	< L.D.	0.05	0.11	5.57	0.20	0.05	3.90
Zr	ppm	< L.D.	96.90	122.70	7.09	46.48	107.60	< L.D.	74.15	86.26	129.30	59.28	14.90	226.20
Nb	ppm	< L.D.	2.24	2.79	< L.D.	1.18	2.29	< L.D.	0.73	1.95	14.34	0.71	0.21	44.75
Y	ppm	< L.D.	34.99	41.47	10.24	27.23	39.27	0.69	9.52	33.97	16.19	22.56	18.55	26.52
Hf	ppm	< L.D.	2.67	3.32	0.30	1.40	2.96	< L.D.	1.70	2.34	2.88	1.73	0.60	5.39
V	ppm	59.15	437.50	301.10	354.20	333.30	440.20	52.42	113.50	412.00	147.50	268.30	391.00	299.00
Cr	ppm	3030.00	71.83	57.83	447.10	148.90	38.65	3877.00	18.61	94.26	182.60	58.06	7.19	407.50
Ni	ppm	1793.00	39.16	35.16	113.80	52.51	13.56	379.10	17.18	38.38	65.21	36.94	11.00	192.60
Co	ppm	107.70	39.74	35.27	58.23	39.90	37.40	45.46	12.73	40.89	26.35	35.29	29.27	56.68
U	ppm	< L.D.	0.10	0.16	< L.D.	< L.D.	0.16	< L.D.	0.04	0.04	1.51	0.09	< L.D.	1.10
Sc	ppm	13.44	43.55	35.57	52.54	45.65	38.91	26.55	8.94	45.20	22.80	36.72	47.84	31.62
Cu	ppm	19.39	34.00	60.48	187.70	94.54	188.00	39.26	11.49	55.11	39.30	56.93	64.79	113.20
Zn	ppm	49.10	91.43	98.15	47.07	89.08	98.96	< L.D.	28.03	100.40	50.93	71.25	103.60	118.80
Pb	ppm	< L.D.	1.11	< L.D.	< L.D.	< L.D.	< L.D.	< L.D.	< L.D.	< L.D.	4.66	0.79	1.78	4.55
Cs	ppm	0.76	0.19	11.06	< L.D.	0.31	9.56	< L.D.	0.27	0.24	0.96	0.12	0.14	< L.D.
La	ppm	< L.D.	4.23	5.81	0.31	2.23	5.39	< L.D.	1.92	4.45	26.41	2.39	0.78	35.62
Ce	ppm	< L.D.	11.91	15.73	1.14	7.15	14.33	< L.D.	4.31	11.99	46.38	6.87	2.25	70.88
Pr	ppm	< L.D.	1.88	2.37	0.23	1.22	2.23	< L.D.	0.60	1.83	4.87	1.08	0.41	8.29
Nd	ppm	< L.D.	10.77	13.53	1.65	7.26	11.98	0.09	3.25	10.36	20.00	6.40	2.95	36.55
Sm	ppm	< L.D.	3.65	4.40	0.81	2.67	4.02	0.05	0.92	3.53	3.92	2.27	1.42	7.59
Eu	ppm	< L.D.	1.26	1.58	0.43	1.03	1.69	0.02	0.97	1.26	1.25	0.89	0.66	2.45
Gd	ppm	< L.D.	4.88	5.59	1.23	3.70	5.29	0.08	1.17	4.53	3.46	2.97	2.10	6.96
Tb	ppm	< L.D.	0.86	1.02	0.24	0.66	0.93	0.01	0.21	0.82	0.52	0.55	0.41	0.99
Dy	ppm	0.04	5.74	6.69	1.71	4.40	6.28	0.11	1.45	5.60	2.96	3.64	2.93	5.44
Ho	ppm	0.01	1.24	1.46	0.38	0.96	1.36	0.03	0.32	1.19	0.56	0.78	0.64	0.95
Er	ppm	0.04	3.55	4.17	1.04	2.71	3.91	0.07	0.96	3.42	1.51	2.25	1.95	2.42
Tm	ppm	0.01	0.54	0.64	0.16	0.42	0.60	0.01	0.16	0.53	0.22	0.35	0.31	0.32
Yb	ppm	0.06	3.64	4.33	1.03	2.77	4.01	0.07	1.13	3.50	1.43	2.37	2.10	1.97
Lu	ppm	0.01	0.57	0.68	0.16	0.43	0.63	0.01	0.18	0.54	0.22	0.37	0.33	0.29

Table 12 - Representative whole-rock analyses of samples from ophiolitic complexes of NE Anatolia and Lesser Caucasus. "< L.D.": under detection level (continued).

Lab No.		T-11-34	T-11-36	T-11-39	ARM-11-01	ARM-11-02	ARM-11-06	ARM-11-08	ARM-11-09	ARM-11-10	ARM-11-13	ARM-11-26	ARM-11-27
Locality		Aşkale	Aşkale	Aşkale	Stepanavan	Stepanavan	Stepanavan	Stepanavan	Stepanavan	Stepanavan	Stepanavan	Vedi	Vedi
Latitude		40.01676° N	40.02484° N	39.95417° N	40.95105° N	40.95061° N	40.95727° N	40.95444° N	40.95465° N	40.96111° N	40.97181° N	39.98949° N	39.9861° N
Longitude		43.53854° E	40.53245° E	40.23643° E	44.33044° E	44.33114° E	44.34209° E	44.30867° E	44.30893° E	44.36245° E	44.34361° E	44.97837° E	44.97505° E
Formation		Gabbro	Plagiogranite	Gabbro	Basalt	Basalt	Meta-Basalt	Gabbro	Plagiogranite	Blueschist	Amphibolite	Gabbro	Gabbro
SiO_2	%	47.28	75.81	47.86	63.10	51.32	64.50	43.73	77.22	43.74	55.08	45.56	46.38
TiO_2	%	1.95	0.15	0.17	0.71	0.95	0.71	0.07	0.16	2.29	1.31	2.30	0.15
$Al2O_3$	%	14.14	12.99	23.84	10.95	16.45	15.04	20.55	11.27	16.22	14.66	16.90	18.89
$Fe2O_3$	%	13.74	2.36	0.99	5.05	10.62	5.34	8.10	2.32	8.68	12.68	13.33	4.19
MnO	%	0.21	0.05	0.02	0.10	0.17	0.08	0.12	0.03	0.11	0.23	0.21	0.08
MgO	%	4.45	0.34	0.91	2.41	3.69	3.22	9.19	0.81	4.53	3.32	5.67	9.11
CaO	%	8.72	0.57	2.12	5.90	4.59	0.79	9.50	2.06	10.05	3.34	10.45	16.42
Na_2O	%	4.54	6.41	15.41	1.89	5.27	6.31	1.50	4.85	3.83	6.86	2.90	1.27
K_2O	%	2.22	0.23	0.13	1.70	0.92	0.39	1.32	0.02	1.98	0.15	0.13	0.48
P_2O_5	%	0.18	0.04	< L.D.	0.14	0.17	0.13	< L.D.	< L.D.	0.67	0.11	0.05	< L.D.
LOI	%	2.56	1.34	9.19	7.69	5.09	2.83	5.14	1.20	6.68	1.27	2.69	3.78
Total	%	99.98	100.29	100.65	99.64	99.23	99.35	99.21	99.93	98.78	99.02	100.20	100.74
Ba	ppm	83.25	30.42	153.00	194.90	217.60	59.84	170.70	9.05	442.10	23.21	27.28	79.39
Rb	ppm	17.75	4.48	0.61	58.43	16.52	13.79	27.25	< L.D.	46.43	0.59	0.92	5.42
Sr	ppm	118.10	134.10	125.60	110.70	327.30	55.01	449.00	73.08	445.20	56.81	234.20	199.50
Ta	ppm	0.20	0.19	0.26	1.05	0.26	0.96	< L.D.	< L.D.	4.71	0.11	0.06	< L.D.
Th	ppm	0.47	19.06	1.46	8.10	1.64	10.02	0.04	< L.D.	7.58	0.38	0.11	< L.D.
Zr	ppm	113.80	135.10	122.00	175.40	89.06	174.30	< L.D.	1.42	238.40	65.41	34.08	1.98
Nb	ppm	2.38	1.83	2.38	12.58	3.19	11.15	< L.D.	< L.D.	66.57	1.31	0.68	< L.D.
Y	ppm	39.88	22.15	4.76	20.02	23.02	22.18	0.93	1.70	25.32	25.93	14.16	3.29
Hf	ppm	3.09	3.84	3.35	4.50	2.50	4.48	0.05	0.04	5.10	1.93	1.00	0.09
V	ppm	451.10	4.09	9.82	81.88	261.40	95.65	141.90	25.03	177.60	358.40	379.20	123.50
Cr	ppm	19.82	8.09	5.52	92.19	14.11	114.40	17.38	11.97	122.40	19.39	9.09	1113.00
Ni	ppm	15.06	< L.D.	< L.D.	41.04	18.53	60.48	31.01	< L.D.	127.00	14.30	13.53	136.00
Co	ppm	36.88	1.32	1.06	9.33	24.56	16.86	47.56	4.80	37.25	30.97	38.97	30.03
U	ppm	0.16	0.82	1.61	1.93	0.36	2.32	< L.D.	< L.D.	2.21	0.13	< L.D.	< L.D.
Sc	ppm	38.00	2.67	1.96	11.43	29.14	13.08	50.13	6.47	20.96	35.89	46.08	46.72
Cu	ppm	55.48	40.32	< L.D.	18.94	65.07	47.35	69.90	23.38	49.75	31.80	13.97	124.00
Zn	ppm	96.65	172.80	17.60	71.52	117.90	76.51	45.07	11.09	87.01	110.80	71.42	12.31
Pb	ppm	< L.D.	7.87	36.75	5.80	5.94	3.25	< L.D.	< L.D.	3.42	2.44	< L.D.	1.02
Cs	ppm	3.24	0.56	0.90	1.77	0.27	0.60	0.90	< L.D.	1.06	< L.D.	< L.D.	0.27
La	ppm	5.20	80.14	1.79	25.86	7.85	37.52	0.13	2.06	51.32	3.34	1.26	0.09
Ce	ppm	14.04	173.30	5.67	54.11	17.19	70.97	0.30	3.10	95.26	8.67	3.34	0.31
Pr	ppm	2.12	19.76	0.95	5.69	2.35	7.13	0.04	0.32	9.52	1.38	0.53	0.06
Nd	ppm	11.92	73.90	5.11	23.74	11.36	28.78	0.23	1.34	38.75	8.05	3.09	0.49
Sm	ppm	4.08	12.41	1.52	4.65	3.14	5.36	0.11	0.24	7.07	2.76	1.22	0.27
Eu	ppm	1.45	0.85	0.53	0.89	0.96	1.27	0.06	0.52	2.25	0.98	0.71	0.19
Gd	ppm	5.31	8.13	1.29	3.92	3.55	4.57	0.17	0.25	6.17	3.72	1.80	0.43
Tb	ppm	0.95	1.03	0.18	0.61	0.59	0.69	0.03	0.03	0.88	0.65	0.33	0.08
Dy	ppm	6.36	4.92	0.90	3.58	3.79	4.07	0.24	0.20	4.89	4.27	2.33	0.57
Ho	ppm	1.39	0.82	0.15	0.70	0.81	0.79	0.06	0.05	0.90	0.92	0.51	0.12
Er	ppm	4.02	2.27	0.37	2.00	2.34	2.20	0.17	0.15	2.43	2.66	1.48	0.34
Tm	ppm	0.61	0.34	0.05	0.31	0.36	0.33	0.03	0.03	0.33	0.41	0.22	0.05
Yb	ppm	4.27	2.47	0.33	2.09	2.39	2.24	0.19	0.20	2.24	2.74	1.50	0.32
Lu	ppm	0.65	0.39	0.05	0.32	0.38	0.35	0.03	0.04	0.34	0.43	0.24	0.05

Table 12 - Representative whole-rock analyses of samples from ophiolitic complexes of NE Anatolia and Lesser Caucasus. "< L.D.": under detection level (continued).

<u>Chapitre 5</u> - Métamorphisme du Bloc Sud Arménien (Jurassique Supérieur - Crétacé Inférieur) : subduction à vergence sud de la branche nord de la Néotéthys.

« L'expérience est une lanterne attachée dans notre dos, qui n'éclaire que le chemin parcouru. »

Confucius

V.1 Article 4 – Multi-stage metamorphism in the South Armenian Block during the Late Jurassic to Early Cretaceous: tectonics over south-dipping subduction of Northern branch of Neotethys

Afin de mieux déterminer les modalités de mise en place des ophiolites dans le Petit Caucase, nous nous sommes intéressés au socle cristallin du bloc sud arménien (SABCB). C'est sur ce domaine que les ophiolites arméniennes se sont mises en place dans le Petit Caucase. Cette étude fournit ainsi des informations clés et sans précédent concernant la fermeture du domaine océanique téthysien au nord de la plate-forme SAB-TAP. Le SABCB a une histoire géologique complexe et mal contrainte comprenant :

(1) un métamorphisme présumé panafricain de haut dégré (Baghdasarian & Ghoukasian, 1983; Aghamalyan *et al.*, 2011a; 2011b),

(2) une phase de rifting conduisant à l'ouverture de l'océan Néotéthys ainsi qu'à la dérive à partir de Gondwana au cours du Permien jusqu'au début du Mésozoïque (Sosson *et al.*, 2010 *et les références qui y sont citées*),

(3) l'obduction de croûte océanique dans le milieu du Crétacé supérieur (Galoyan *et al.*, 2009; Rolland *et al.*, 2009b),

(4) suivie par la fermeture totale du domaine océanique et la subduction continental/collision à la fin du Crétacé (Rolland *et al.*, 2009a; 2011; Sosson *et al.*, 2010).

Le SABCB affleure uniquement dans une étroite fenêtre tectonique au nord-ouest de Erevan, dans le massif de Tsaghkuniats près du village de Bjni (Belov & Sokolov, 1973; Aghamalyan, 1978; 1998; Shengelia *et al.*, 2006). Pour obtenir des limites temporelles concernant l'enchaînement ainsi que la durée des événements géologiques affectant cette zone, nous avons mené une étude structurale, pétrologique et géochronologique de ce massif.

Dans le massif de Tsaghkuniats le socle cristallin est constitué de gneiss granitiques (orthogneiss) et de micaschistes paradérivés intrudés par des granodiorites et leucogranites. Ceux-ci sont recouverts en discordance par une série sédimentaire datée du Crétacé supérieur au Paléocène composée de conglomérats remaniant des roches ophiolitiques, des grès ainsi que de marnes. Ces formations sont à leur tour recouvertes en discordance par des sédiments volcanogéniques de l'Eocène moyen-supérieur et des basaltes du Plio-Quaternaire au Présent.

Nous présentons de nouvelles datations (U-Pb et $^{40}Ar/^{39}Ar$) concernant la mise en place d'un corps granodioritique et son encaissant métamorphique. Le métamorphisme régional est interprété comme témoin :

(1) des conditions d'enfouissement et d'épaississement dans un gradient régional barrovien MP-MT (staurotide-disthène, M1) à c. 160-157 Ma, avec la mise en place de magmas dioritiques à c. 156-150 Ma,

(2) d'une décompression adiabatique caractéristique de fusion partielle et de production de leucogranites à c. 153 Ma, suivie par des conditions HT-BP (andalousite-K-feldspath, M2),

(3) d'une phase de cisaillement et de recristallisation attribuées à un bombement au c. 130-150 Ma et à un refroidissement à 400°C à c. 123 Ma (M3).

Nous montrons, pour la première fois, une évolution métamorphique polyphasée étonnamment jeune pour cette région préservée dans le SABCB. Nous ne notons pas dans les âges obtenus d'héritage panafricain comme il avait été suggéré par les datations Rb-Sr précédentes (Shengelia *et al.*, 2006). Cette évolution métamorphique, le magmatisme calco-alcalin qui lui est associée et les marqueurs cinématiques sont interprétés comme les témoins d'une subduction plongeant vers le sud, sous le SAB.

Ces résultats et interprétations sont intégrés dans un modèle illustrant l'évolution géodynamique de la marge nord du SAB. Que cette zone de subduction se prolonge plus à l'ouest reste à être prouvé, car les affleurements de socle cristallin en NE Anatolie et/ou sur la TAP sont rares. Nous avons cependant pu observer une forte empreinte métamorphique thermique accompagnée d'intrusifs granitiques sous la nappe ophiolitique non métamorphique dans les Taurides au SE d'Erzurum, mais nous n'avons pas encore pu ni étudier en détail cette zone, ni obtenir d'âge préliminaire.

Cette étude a fait l'objet d'une publication en révision dans le *Journal of Asian Earth Sciences*.

Multi-stage metamorphism in the South Armenian Block during the Late Jurassic to Early Cretaceous: tectonics over south-dipping subduction of Northern branch of Neotethys

M. HÄSSIG[1]*, Y. ROLLAND[1], L. SAHAKYAN[2], M. SOSSON[1], G. GALOYAN[2], A. AVAGYAN[2], D. BOSCH[3], C. MÜLLER[4]

[1] Géoazur, Université de Nice Sophia-Antipolis, CNRS, IRD, Observatoire de la Côte d'Azur, 250 rue Albert Einstein, 06560, Sophia Antipolis - France.

[2] Institute of Geological Sciences, National Academy of Sciences of Armenia, 24a Baghramian Avenue, Yerevan 375019 - Armenia.

[3] Géosciences Montpellier, UMR 5243 - CC 60, Université Montpellier 2, Place E. Bataillon, 34095 Montpellier cedex 5 - France.

[4] 6 bis rue Haute 92500 Rueil Malmaison - France.

Abstract

The geologic evolution of the South Armenian Block (SAB) in the Mesozoic is reconstructed from a structural, metamorphic, and geochronologic study including U-Pb and $^{40}Ar/^{39}Ar$ dating. The South Armenian Block Crystalline Basement (SABCB) outcrops solely in a narrow tectonic window, NW of Yerevan. The study of this zone provides key and unprecedented information concerning closing of the Tethys oceanic domain north of the Taurides-Anatolides platform from Middle Jurassic to Early Cretaceous times. The basement comprises of presumed Proterozoic orthogneiss overlain by metamorphosed pelites as well as intrusions of granodiorite and leucogranite. During the Late Jurassic and Early Cretaceous times structural, geochronological and petrological observations show a multiphased evolution of the northern margin of the SAB. A south-dipping subduction under the EAP-SAB is proposed in order to suit recent findings pertaining emplacement of relatively hot subduction related granodiorite as well as the metamorphic evolution of the crystalline basement in the Lesser Caucasus area.The metamorphism is interpreted as evidencing: (1) M1 Barrovian MP-MT conditions (staurolite-kyanite) at c. 157-160 Ma and intrusion of dioritic magmas at c. 150-156 Ma, (2) near-adiabatic decompression is featured by partial melting and production of leucogranites at c. 153 Ma, followed by M2 HT-BP conditions (andalusite-K-feldspar). A phase of shearing and recrystallization is ascribed to doming at c. 130-150 Ma and cooling at 400°C by c. 123 Ma (M3). Structural observations show (1) top to the north shearing during M1 and (2) radial extension during M2. The extensional event ends by emplacement of a thick detrital series along radial S, E and W-dipping normal faults. Further, the crystalline basement is unconformably covered by Upper Cretaceous-Paleocene series dated by nannofossils, evolving from Maastrichtian marly sandstones to Paleocene limestones.

keywords : Lesser Caucasus; subduction; South Armenian Block; geochronology

1.1 Introduction

The Crystalline Basement of the South Armenian Block (SAB) (**Figures 50A** & **B**) has a geological history poorly constrained. The SAB was involved in a long and complex tectonic evolution including (1) presumed Panafrican high-grade metamorphism (Baghdasarian and Ghukasian, 1983, Aghamalyan et al., 2011a; 2011b). However, contrary to other occurrences of Paleozoic sedimentary rocks SE of Yerevan (Sosson et al., 2010), the presumed Paleozoic sediments of the Tsaghkuniats crystalline massif are metamorphosed. Both the metamorphic basement and cross-cutting intrusions are unconformably covered by Upper Cretaceous deposits (**Figures 51A**, **B** & **C**). This observation leads us to question the Precambrian age forwarded for metamorphism, as well as the tectonic setting and its geodynamic cause. Indeed, several geodynamic processes can explain the metamorphic history of this basement, including (2) a rifting stage leading to Neotethys ocean opening and drifting from Gondwana in the Permian to Early Mesozoic times (Sosson et al., 2010 and references herein), (3) oceanic closure by subduction of Paleotethys from the Early to late Mesozoic and (4) subsequent continental subduction/ocean crust obduction in the middle-Late Cretaceous (Galoyan et al., 2009; Rolland et al., 2009b), followed by (5) continental collision or accretion to the Eurasian margin in Late Mesozoic/Early Cenozoic times (Sosson et al., 2010) and depending on authors the Arabia-Eurasia collision from middle to late Eocene up to Oligocene (Hempton, 1985; Robertson et al., 2012; Rolland et al., 2009a; 2012; Yılmaz, 1993). Moreover, the influence of the Cimmerian orogeny, known more eastward in Iran, is also a possible cause of this metamorphism. Consequently, the SAB Crystalline Basement (SABCB) needs to be investigated by detailed geochronological and petro-metamorphic (P-T-t) studies to evaluate the importance of these post-Paleozoic events in this part of the Caucasus region.

In order to constrain the timing of these geological events, field geology and sampling were undertaken in the SABCB, which outcrops in a narrow tectonic window to the NW of Yerevan, in the Tsaghkuniats massif (Aghamalyan, 1983; **Figures 50B** & **51A**). This study presents new U-Pb and $^{40}Ar/^{39}Ar$ age data to temporally constrain the metamorphism and magmatism of the basement. This study is complemented by a petrologic and Pressure-Temperature (P-T) analysis to interpret the metamorphic significance of these rocks. Subsequently, we propose a tectonic and geodynamic reconstruction of the evolution of the SAB throughout the closing of the northern Neotethys oceanic domain.

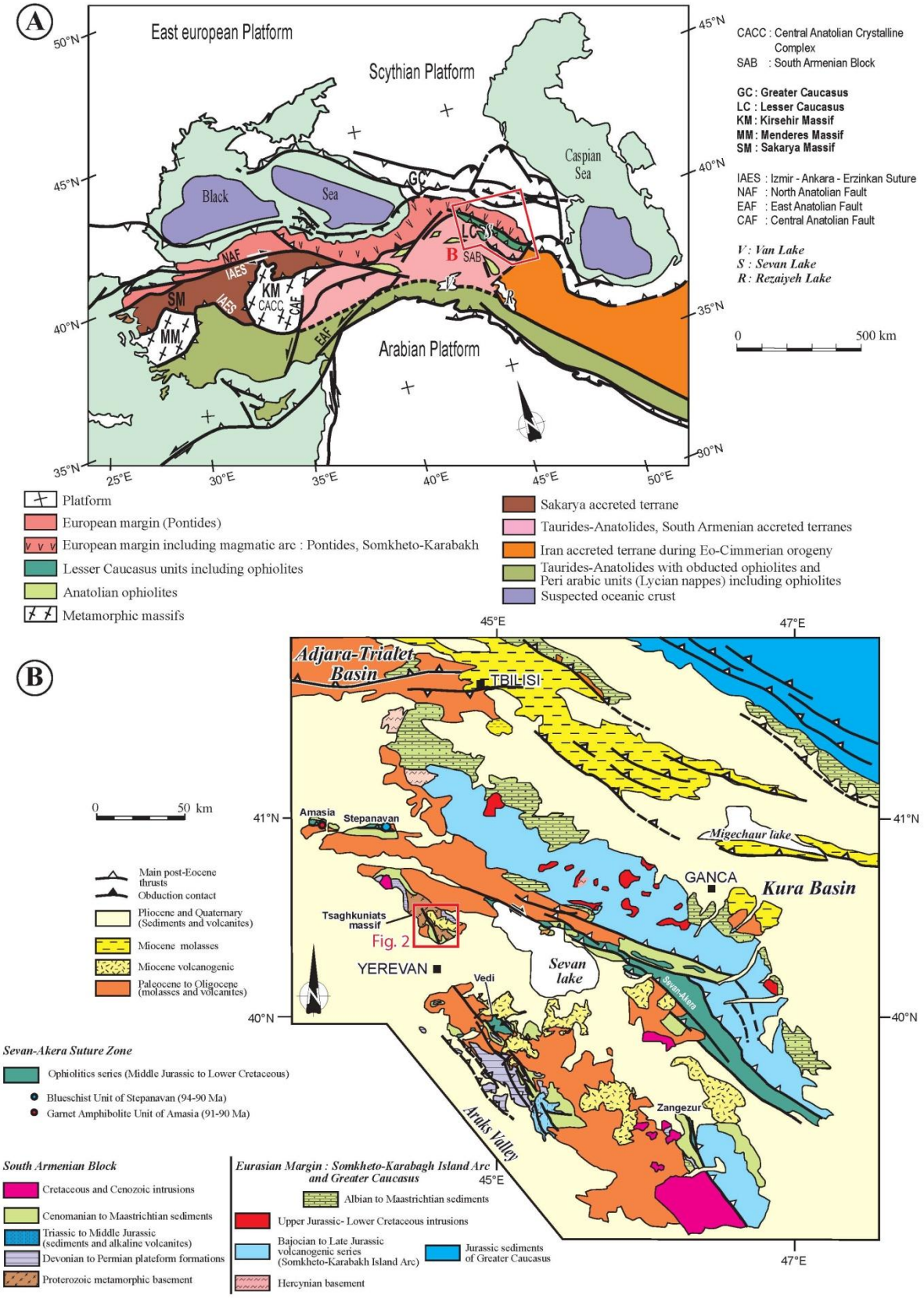

Figure 50 - A, tectonic map of the Middle East–Caucasus area, with main blocks and suture zones, after Avagyan et al. (2005), modified. Location of Figure 1B is indicated. B, structural map of the Lesser Caucasus, modified from Sosson et al. (2010). Location of figure 51A is indicated.

1.2 Geological Setting

1.2.1 Origin of the SAB

Palaeomagnetic analyses indicate palaeo-latitudes for the SAB during the Early and Middle Jurassic at least 2000 km farther south than its current position (Bazhenov et al., 1996; Meijers et al., 2013). This argues a Gondwanian origin of the SAB, as also suggested by the dating undergone by Baghdasarian and Ghukasian (1983) and palaeogeoraphic reconstructions (Barrier and Vrielynck, 2008; Knipper and Khain, 1980; Monin and Zonenshain, 1987; Robertson and Mountrakis, 2006; Şengör et al., 1988). The rifting of the Taurides-Anatolides (including the SAB) from Gondwana is documented as initiating during Triassic times (Gealey, 1988; Kazmin, 1991; Mart, 1987).

1.2.2 Post-Paleozoic tectonic events

1.2.3 Tethys subduction – Cimmerian orogeny

Throughout the Mesozoic and Cenozoic, the northern margin of the SAB, as well as the southern Eurasian margin, was involved in subduction and accretion/collision processes resulting in closure of northern branch of the Tethys ocean (Adamia et al., 1981; 2011; Dercourt et al., 1986; Galoyan, 2008; 2009; Golonka 2004; Hässig et al., 2013; 2014; Nikishin et al., 1998; Ricou, 1994; Robertson, 2002; Rolland et al., 2009a; 2009b; 2010; 2011; 2012; Şengör and Yılmaz, 1981; Sosson et al., 2010; Stampfi et al., 2001; Topuz et al., 2013; Yilmaz et al., 2000; Zakariadze et al., 1990; 2005). The north-dipping subduction of the Tethyan oceanic domain under the southern Eurasian margin, from Middle Jurassic to middle-Late Cretaceous times (c. 170-83 Ma), is evidenced in the Pontides and Somkheto-Karabakh regions which exhibit continuous volcanic arc related to subduction throughout this period (Adamia et al., 1981; Yilmaz et al., 2000). Within the northern branch of Neotethys/Paleotethys, a period of intra-oceanic subduction has been evidenced by the presence of obducted ophiolites along the Lesser Caucasus (Adamia et al., 1981; Ahamalyan, 1978; 1998; 2011a; 2011b; Galoyan, 2008; Hässig et al., 2013; Rolland et al., 2009b; Sosson et al., 2010). These bodies of non-metamorphic obducted oceanic crust were formed in a back-arc to supra-subduction zone setting during the Middle Jurassic north of the SAB (Aghamalyan, 1998; Galoyan, 2008; Rolland et al., 2009b, 2011; Hässig et al., 2013). The intra-oceanic subduction zone is most likely north-dipping, as suggested by the overall

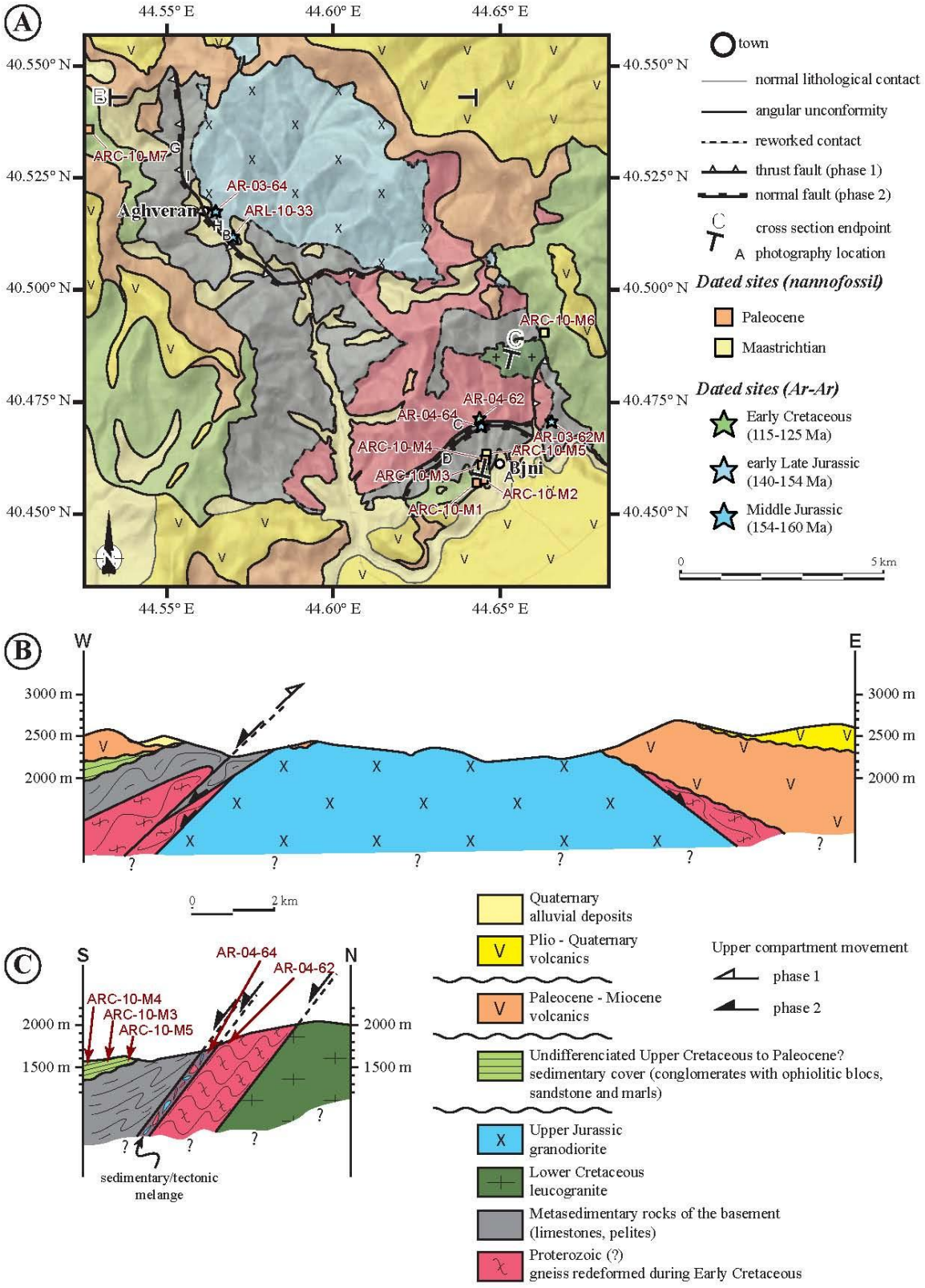

Figure 51 - A, structural map of the Tsaghkuniats massif, modified from Aghamalyan (1983). Location of this map is indicated on figure 1B. Plot of geological sections of Figure B and C along with localization of dated samples by the U-Pb and $^{40}Ar/^{39}Ar$ methods and paleontological identification. Location of field photographs of Figure 52 indicated as well. B and C, sketch geological cross sections of the Tsaghkuniats massif.

geometry of the tectonic wedge. The outcrops of blueschist and amphibolite facies rocks below the ophiolite nappe along the Sevan-Akera suture zone in the Stepanavan (Rolland et al., 2009a; Sosson et al., 2010) and Amasia areas (Hässig et al., submitted), respectively, also argue for the two north dipping subduction zones. These two northward dipping subduction zones (below the southern Eurasian margin and intra-oceanic between the southern Eurasian margin to the SAB) are considered to be synchronous, as evidenced by the timing of peak metamorphism (c. 95-91 Ma and c. 92-88 Ma) for these lithologies encompassed within the period of activity of the Pontides and Somkheto-Karabakh arc.

Recent investigations along the Pontides and Lesser Caucasus sutures have not evidenced any Cimmerian tectonic phase (Topuz et al., 2013; Rolland et al., 2012).

1.2.4 Collisional stages

The collision between the SAB and the southern Eurasian margin started during the Late Cretaceous-Paleocene as evidenced by the formations of a foreland basin in the southeastern part of the belt and by the folding, uplift and erosion of the Sevan–Akera suture zone (Sosson et al., 2010). From Middle Eocene to Miocene times, inherited normal faults of the northern SAB passive margin were reactivated as reverse faults progressively deforming molassic deposits. A fold-and-thrust belt type structure developed until the Miocene through the development and propagation of décollement faults (Sosson et al., 2010).

The south of the SAB (included in the Taurides-Anatolides) is limited from the Arabian platform by the Pütürge and Bitlis massifs marking the Misis-Andırın and Bitlis sutures (Hempton, 1985; Oberhänsli *et al*., 2010; 2014; Rolland et al., 2012). Timing of continental subduction is documented at c. 76-71 Ma (Göncüoğlu and Turhan, 1984; Hempton, 1985; Oberhänsli et al., 2010). As for the later collision between the Taurides-Anatolides and the Arabian platform, timing is still debated with authors proposing ages ranging from middle to late Eocene up to Oligocene (Hempton, 1985; Yılmaz, 1993; Robertson et al., 2012) with complete closure of the southern branch of Neotethys.

1.2.5 Metamorphism and magmatism in the SAB crystalline basement

The SABCB only outcrops in a 600 km² zone NE of Yerevan, the Tsagkhuniats massif (Aghamalyan, 1978; 1998; Belov and Sokolov, 1973; Shengelia et al., 2006). This massif

features metamorphic rocks characterized by gneisses, micaschists along with granodiorite and leucogranite intrusions (Sosson et al., 2010). It is discordantly overlain by an Upper Cretaceous to Paleocene sedimentary cover (**Table 13**; **Figures 51A**, **51C** and **52A**) comprising of conglomerats reworking ophiolitic rocks, sandstone and marls. These sediments are in turn unconformably overlain by Paleocene to Miocene volcanics and covered by discordant Plio-Quaternary volcanites present throughout the region (**Figure 51A**). Previous studies of the Tsaghkuniats massif rocks have evidenced a high-grade regional metamorphism (Aghamalyan et al., 1978; Shengelia et al., 2006) of the magmatic-derived basement, intercalated with mafic and sedimentary rocks. According to prior petrological and geochemical results, the mafic rocks are of amphibolites facies (Aghamalyan et al., 1978; 2011a). P and T conditions range between T = 420~640°C and P = 1.6~5.7 kbar, which argues for a geothermal gradient between 25 and 50 °C/km (Aghamalyan et al., 2011b).

Presumed origin of the SABCB dates back to the Proterozoic as is suggested by an age of 610 ± 36 Ma obtained by Baghdasarian and Ghukasian (1983). This age was acquired using the Rb-Sr isochron method on the Bjni migmatite-granitic massif of the Tsaghkuniats crystalline outcrop (**Figure 51A**). This age tends to supports that the SABCB is of Gondwanian origin, as suggested by Knipper and Khain (1980), Monin and Zonenshain (1987), Robertson and Mountrakis (2006), Rolland et al. (2009b), Şengör et al. (1988), Sosson et al. (2010) and Stampfli and Borel (2002). However, the Rb-Sr method applied to metamorphic rocks is subject to caution and has to be re-evaluated by other methods. Recent field observations allow to evidence structural cross-cutting relations between an undeformed granodiorite intrusion and the metamorphic basement (**Figures 51A** & **B**). U-Pb dating of the granodiorite intrusion would thus provide an upper temporal boundary for the high-grade metamorphism, while the $^{40}Ar/^{39}Ar$ method could be applied to the micaschists from the basement in order to build the P-T path deduced from the metamorphic evolution.

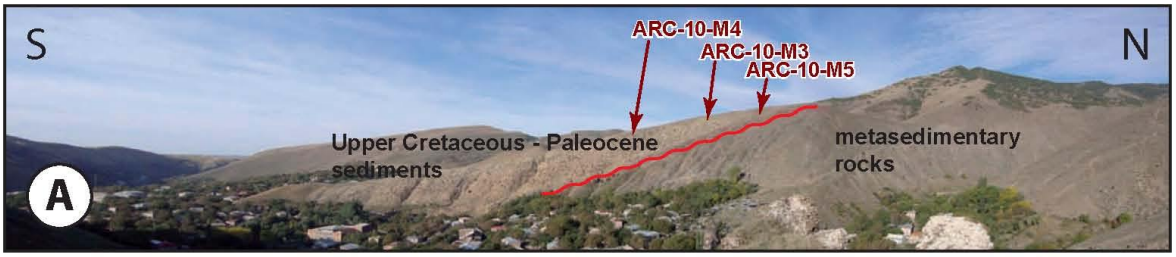
S
N
ARC-10-M4
ARC-10-M3
ARC-10-M5
Upper Cretaceous - Paleocene sediments
metasedimentary rocks
A

N
S
ARL-10-33
B

N
S
AR-04-62
AR-04-64
gneiss
metasedimentary rocks
C

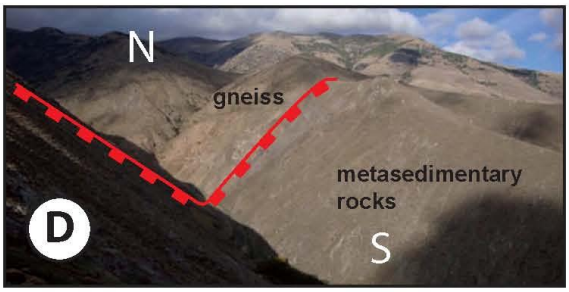
N
gneiss
metasedimentary rocks
S
D

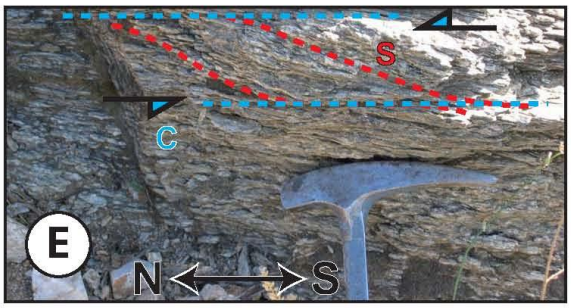
S
C
E
N
S

F

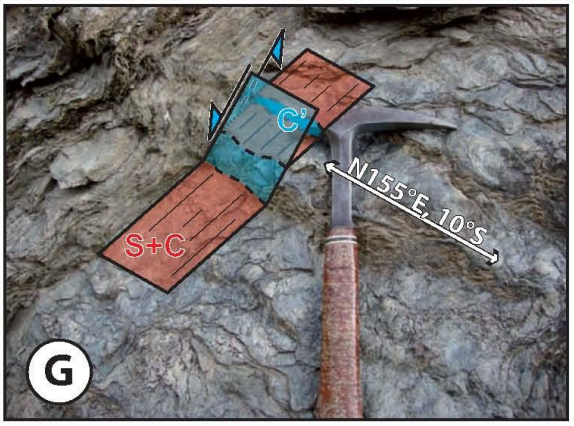
C'
S+C
N155°E, 10°S
G

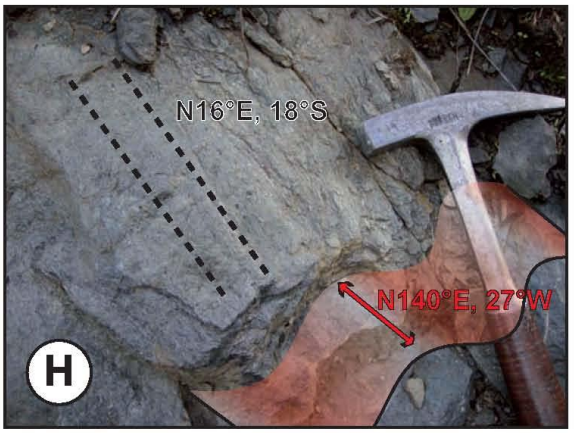
N16°E, 18°S
N140°E, 27°W
H

N 20°E
I

Figure 52 - Representative field photographs of the lithologies of the Tsaghkuniats massif and interpreted structural relationships. A, a view to the west of the unconformity of Upper Cretaceous to Paleocene sedimentary series on top of crystalline basement made of metasedimentary rocks, north of the town of Bjni below. B, outcrop of the granodiorite massif north-east of the town of Aghveran. C, normal fault contact of metasedimentary rocks on top of gneiss. D, normal fault contact of metasedimentary rocks on top of gneiss seen in another valley just west of C. E, gneiss outcrop with C-S deformation indicated. F, well deformed mica-schist with cross-cutting andalusite. G, intense deformation with coinciding C and S planes and synthetic C' planes concordant to general shearing. H, folds re-deforming in mica-schist. I, deformed pyrite indicating shear movement.

1.3 New Field Observations

The crystalline basement of the Tsaghkuniats massif is made up of metamorphic rocks characterized by para- and ortho-gneisses with micaschists cross-cut by leucogranite and granodiorite intrusions **(**Baghdasarian and Ghukasian, 1983; Aghamalyan, 1998; Shengelia et al., 2006). A stack of metasedimentary rocks mainly comprised by skarnified limestones is also evidenced. These metasedimentary rocks (**Figures 51A**, **B** & **C**) could belong to the Proterozoic formations (Aghamalyan et al., 1998) or to the Upper Devonian-Permian formations like in the other parts of the SAB, they could also belong to the Upper Devonian-Permian formations (Sosson et al., 2010), but metamorphosed. Normal faults have been observed between the gneiss and the metasedimentary units (**Figures 52C** & **52D**) as well as along a large (≈ 20 km²) outcrop of granodiorite (**Figure 52B**), which appear to be geometrically related to the emplacement of this intrusion. The mineral relationships in the metamorphic rocks (i.e. metamorphic paragenesis, deformation and orientation, as well as cross-cutting relationships; **Figures 52**, **53** & **54**) argue for significant simple-shear deformation of the crystalline basement during a barrovian metamorphic event at high-temperature and mid-to low-pressure conditions.

High-grade micaschists (samples AR-03-62M & AR-04-64) exhibit kyanite-staurolite ± sillimanite -andalusite-K-feldspar-garnet micaschists (**Figures 53F**, **53C**, **D**, **G**, **H**, **I**, **J**, **K1**, **K2**, **54E**, **F1** & **F2**). This mineral assemblage indicates burial of metasediments in the Medium-Pressure and Medium-Temperature (MP-MT) conditions of kyanite-staurolite stability field (550<T<750°C ; P>5 kbar, Johnson and Brown, 2004). Subsequent exhumation in Low-Pressure and High-Temperature (LP-HT) conditions is highlighted by K-feldspar + andalusite assemblage (T<750°C ; P>5 kbar, Soto and Platt, 1999).

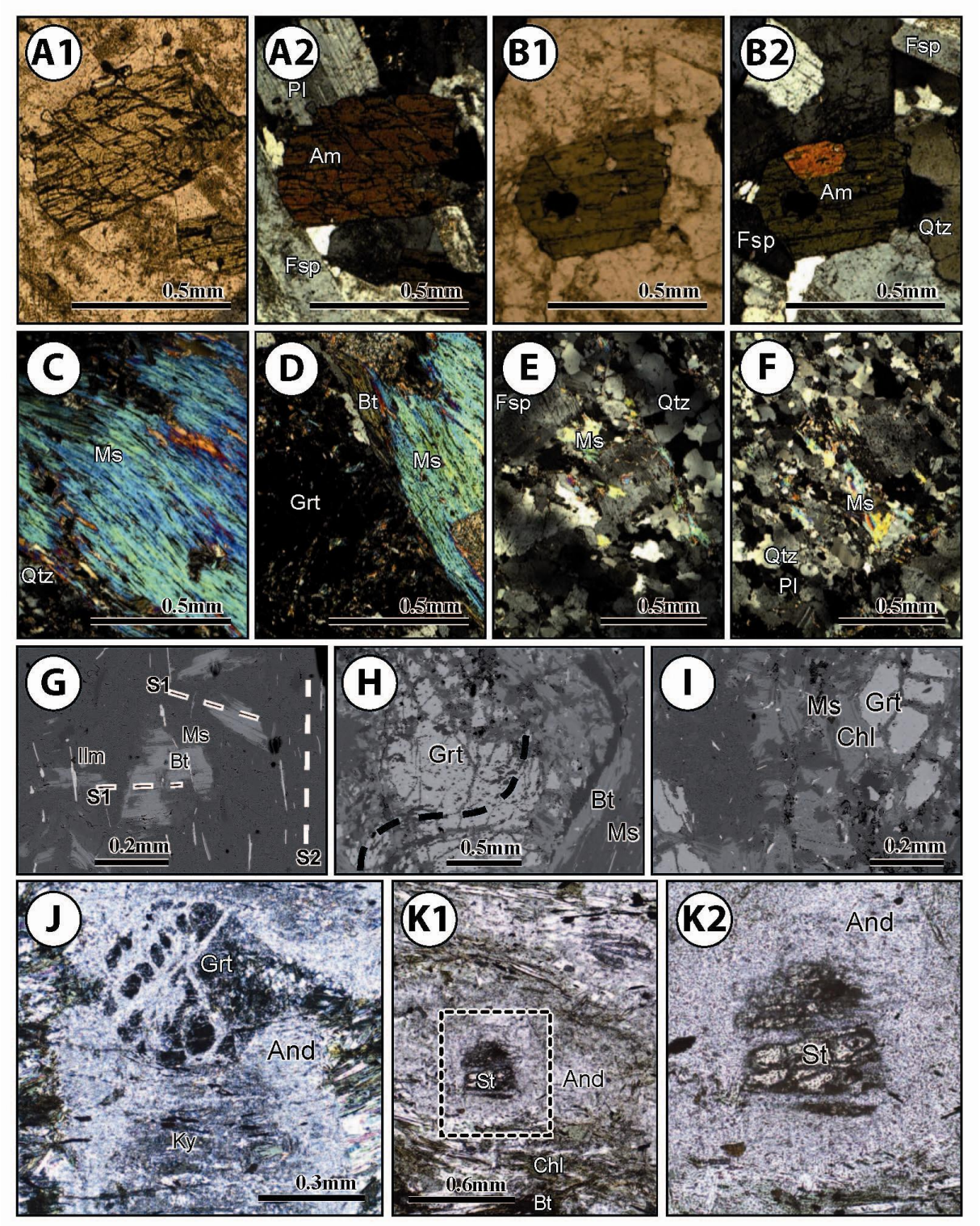

Figure 53 - Representative microphotographs of fin sections of rock samples of the Tsaghkuniats massif showing mineral relationships of $^{40}Ar/^{39}Ar$ dated mineral phases. A1 and A2, plane and cross-polarized images, respectively, centered on amphibole of granodiorite sample AR-03-64. B1 and B2, plane and cross-polarized images, respectively, centered on amphibole of granodiorite sample AR-03-64. C, cross-polarized images centered on white mica of micaschist sample AR-03-62M. D, cross-polarized image centered on white mica of micaschist sample AR-03-62M. The white mica molds the garnet and biotite. E, cross-polarized images centered on white mica of leucogranite sample AR-03-64. F, cross-polarized images centered on white mica of leucogranite sample AR-03-64. G, H and I, electron back-scatter (EBS) images of metaschist sample AR-03-64B. J, K1 and K2, optical microscope photography of sample AR-03-62M showing relics of garnet, kyanite and staurolite included in andalusite.

A top-to-north movement is generally observed in the units that are part of the basement rocks. In gneiss outcrops, this deformation is identified by shear-schistosity geometries (C-S; **Figure 52E**), illustrating top-to-north movement. It is represented by nearly north-south trending (N 16°E) shallow southward dipping (18°S) mineral lineation (**Figure 52H**). In a micaschist outcrop asymmetric pyrite clast were found (Figs. 3I & 5A) also showing top-to-north deformation. Pressure-shadow recrystallizations in one oriented sample show a concordant sense of movement with the prior observations that are in agreement with a first stage of syn-metamorphic deformation.

Along the granodiorite intrusion, the localized intense deformation lead to the formation of C and S planes with synthetic C' planes oriented concordantly with general shearing, conform to Choukroune et al. (1987), along a N155°E direction with a west dip (**Figure 52G**). This may also be observed at the mineral scale with the development of shear bands, which distinctly shift well defined and parallelized C and S planes along C' planes (**Figures 52G**, **54B**, **C1**, **C2**, **D1** & **D2**). At the NW boundary of the massif, centimetric scale folding is observed. The fold axes tendency approaches NW-SE orientation (N140°E, 27°W; **Figure 52H**). This deformation is, as for top-to-north deformation, associated with N-S mineral or stretching lineation, illustrating N-S extension, also emphasized by the dome-shape of the massif.

Brittle-ductile deformation is featured by a regional radial-extensional movement around granodiorite and leucogranite intrusions. Normal faults striking through both metasedimentary micaschists and gneiss rocks, along the SW border of the granodiorite outcrop, have strikes varying from NNW in the northwestern part to ESE for the southeastern segments. Dip directions for these faults vary from W to S, as there their strike turns from NNW to ESE, respectively. Normal faults along the SE limit of the leucogranite intrusion present a general strike direction oriented ENE to NNE from W to E, with an overall dip towards the S. In parts of the hanging-wall of these faults are found lower metamorphic grade rocks featured by white mica/biotite schists and phyllades.

We therefore interpret all these brittle ductile structures as related to an extensional event as the result of the massif's exhumation.

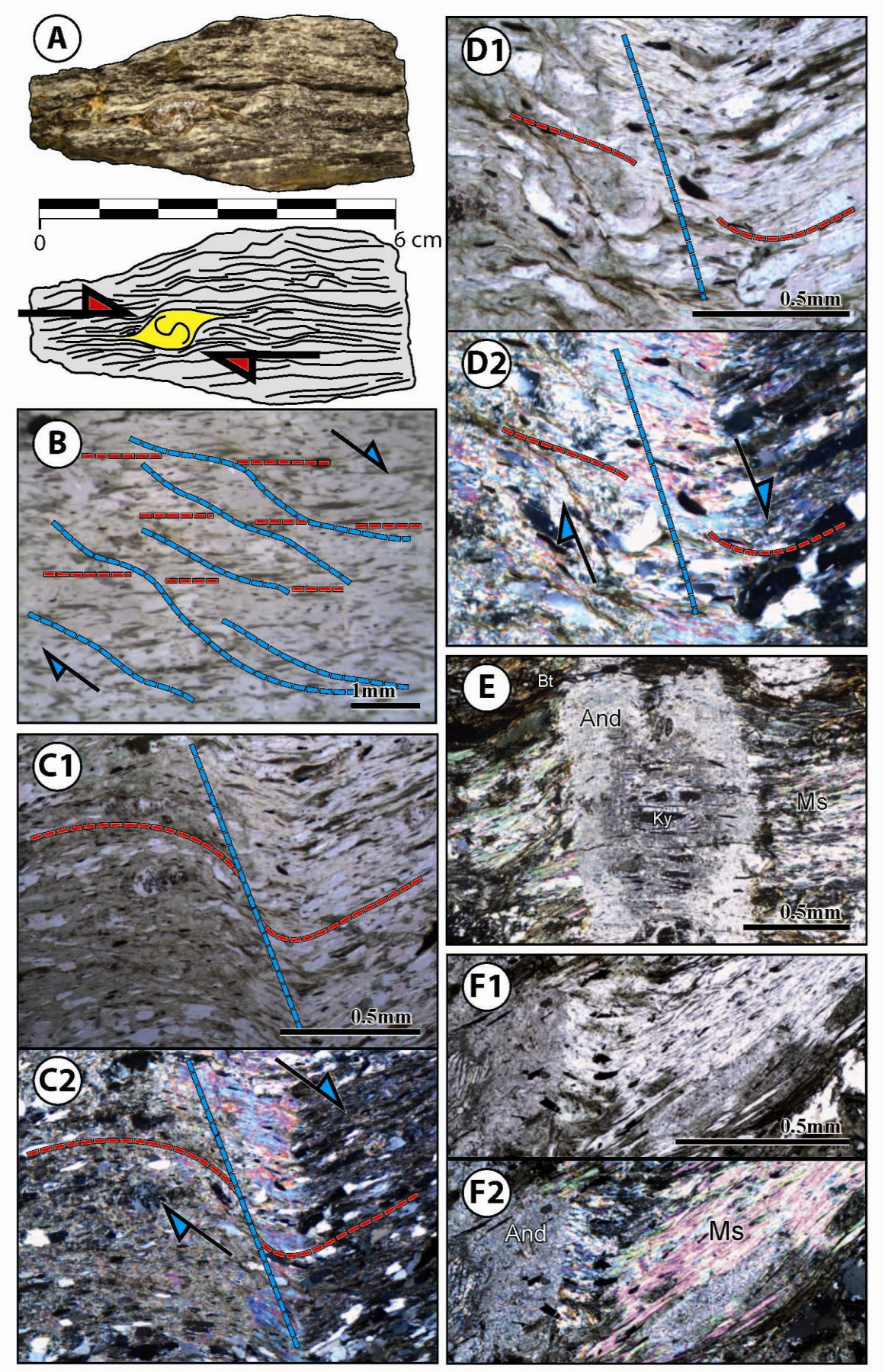
A
0
6 cm
S
B
1mm
C1
0.5mm
C2
D1
0.5mm
D2
E
Bt
And
Ky
Ms
0.5mm
F1
0.5mm
F2
And
Ms

Figure 54 - Mineral deformations and associations found in sampled outcrops. A, zoom of Figure 52I of deformed pyrite indicating shear movement in well-foliated metamorphic rock. B, C1, C2, D1 and D2, microphotographs taken with a stereo microscope of shear bands found in micaschist thin sections. B, C1 and D1, are taken in LPNA whereas C2 and D2 are in LPA. E, cross polarized microphotograph of andalusite cross-cutting preexisting white micas. The andalusite features relic kyanite mineral fragments at its core and is molded by biotite. F1 and F2, plane and cross-polarized micrographs, respectively, zoom on andalusite cross-cutting white mica lineation.

1.4 Mineralogy and Pressure-Temperature path of metamorphic rocks

The chemical compositions of minerals were obtained by Electron Microprobe Analysis (EPMA) in order to verify the homogeneity of mineral compositions from core to rim (see **Annexe 7**). A detailed mineralogical analysis of the micaschist (metapelite) sample AR-03-62M (**Table 14**; **Figures 53C**, **D**, **G**, **H**, **I**, **J**, **K1**, **K2**, **54C1**, **C2**, **D1**, **D2**, **E**, **F1** & **F2**) allows us to construct the Pressure-Temperature (PT) path followed by part of the SAB crystalline basement (**Figure 55C**), using the grid established by Holland and Powell (1998) for the KFASH system. The PT path can be described as follows from the main assemblage mineralogy. The co-stability of a Medium P - Medium T (MP-MT) paragenesis defined by (1) staurolite-kyanite-garnet (Alm 0.6)-rutile implies a pressure peak at 7-9 kbar and 500°C < T < 625°C (**Figure 55A**). The breakdown reaction of muscovite + garnet into kyanite + staurolite + quartz (2) implies re-equilibration at 6-7 kbar and 600 ± 50°C. Transformation of kyanite into andalusite, and the crystallization of andalusite + K-feldspar at the expense of muscovite (3) constrain the low P part of the PT path (P < 2 kbar, 600 < T < 650°C), in Low P - High T (LP-HT) condition. This PT evolution is compatible with the occurrence of leucogranites as the PT conditions are almost on the hydrated solidus curve of metapelites.

Rim to rim EPMA analysis of garnet is shown in **Figure 55A**. The garnet is zoned, with a homogeneous central part showing high spessartine (20~24 %) and relatively low grossular (14~16 %) and pyrope (5~7 %) contents. Symmetrical zoning is observed towards higher almandine and, in a lesser extent, pyrope contents towards the rims. The garnet is compositionally zoned in a style that strongly suggests prograde growth zoning during increasing temperature conditions (Spear, 1988; 1993). The garnet profile seems unmodified by post-growth diffusion affecting the rim. Snow-ball inclusion trails are also observed (**Figure 53H**), which is in agreement with garnet rotation and thus growth during shearing. Garnet-Biotite-Plagioclase geothermobarometry provides PT estimates in agreement with low-pressure reequilibration of these minerals, with PT estimates ranging between 360-460°C and 2 ± 1 kbar (**Figure 55B**). Post-temperature peak re-equilibration of biotite is likely as this mineral shows signs of chloritization.

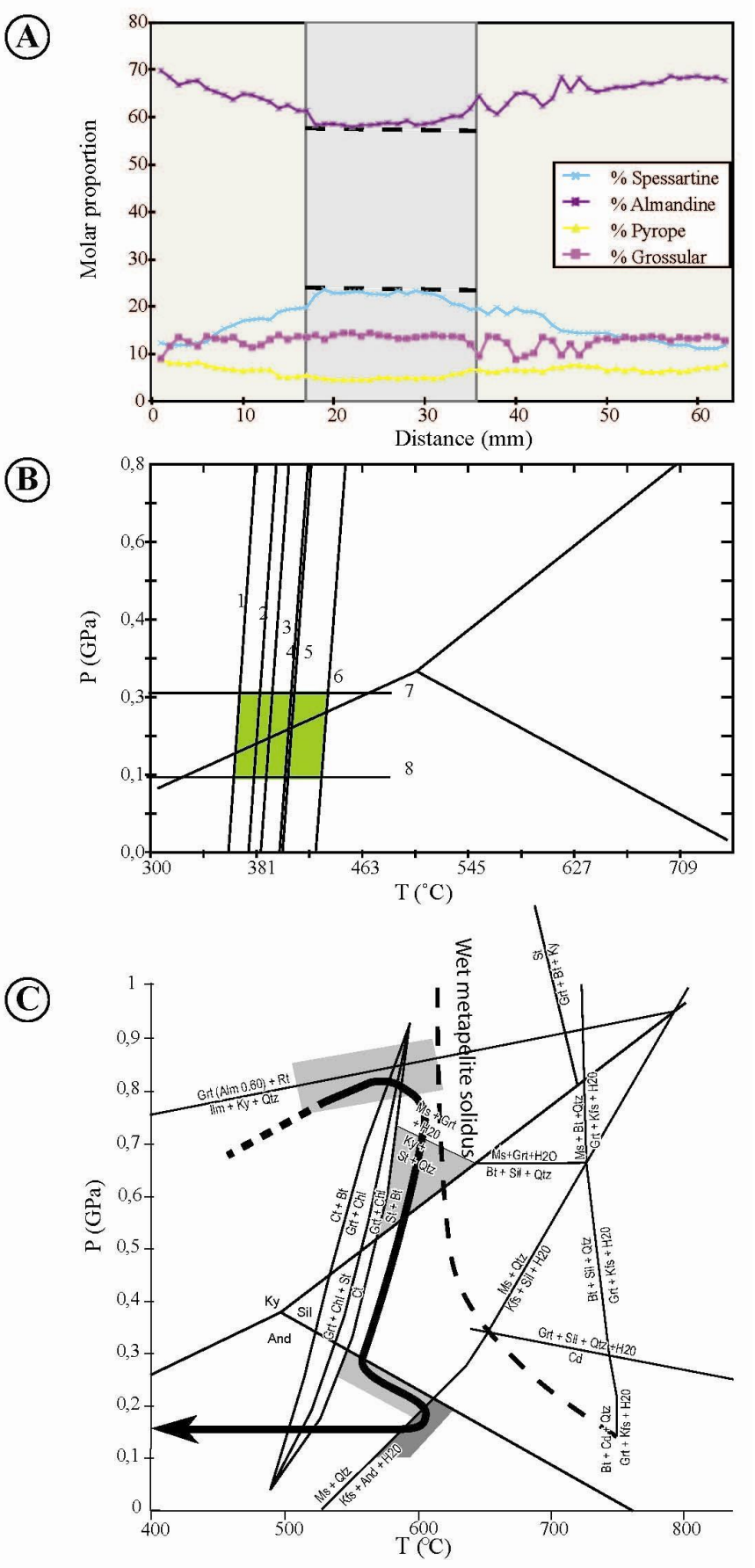
A
Molar proportion
Distance (mm)
% Spessartine
% Almandine
% Pyrope
% Grossular
B
P (GPa)
T (°C)
1
2
3
4
5
6
7
8
C
P (GPa)
T (°C)
Wet metapelite solidus
Grt (Alm 0,60) + Rt
Ilm + Ky + Qtz
Ms + Grt + H2O
Ky + St + Qtz
Ms+Grt+H2O
Bt + Sil + Qtz
St
Grt + Bt + Ky
Ms + Bt + Qtz
Grt + Kfs + H2O
Ct + Bt
Grt + Chl
Grt + Ctd
St + Bt
Ky
Sil
And
Grt + Chl + St
Ctd
Ms + Qtz
Kfs + Sil + H2O
Bt + Sil + Qtz
Grt + Kfs + H2O
Grt + Sil + Qtz + H2O
Cd
Bt + Cd + Qtz
Grt + Kfs + H2O
Ms + Qtz
Kfs + And + H2O

Figure 55 - A, profile of a garnet from sample AR-03-62M, (see Figures 55C4 and 55D1). B, Garnet-Biotite-Plagioclase thermobarometry using representative rim biotite and garnet compositions with associated plagioclase within sample AR-03-62M. Calibrations from: 1, Ganguly and Saxena (1984) ; 2, Hodges and Spear (1982) ; 3, Hodges and Crowley (1985) ; 4, Perchuk and Lavrent'eva (1983) ; 5, Ferry and Spear (1978); 6, Hoisch (1990); 7, Hodges and Crowley (1985); 8, Ghent and Stout (1981). C, PT path mineralogical evolution within the same sample (AR-03-62M), using the grid established by Holland and Powell (1998) for the system KFASH. Mineral abbreviations after Kretz (1983).

1.5 Geochronology and Geochemistry

1.5.1 Analytical procedures

1.5.1.1 $^{40}Ar/^{39}Ar$ dating

Pure minerals less than 1mm in diameter (between 800µm and 500µm) were obtained using a mortar and pestle and multiple sieving. Datable minerals were separated by careful hand-picking under a binocular microscope to avoid altered grains or inclusions. All samples were irradiated for around 70h (J1) and 10h (J2, J3) in the nuclear reactor at McMaster University in Hamilton (Canada), in position 5c along with Hb3gr hornblende fluence monitor (1073.6 Ma ± 5.30 Ma; Jourdan et al., 2006) and Fish Canyon sanidine monitor (28.03 ± 0.08 Ma; Jourdan and Renne, 2007) for J1 and J2, J3 respectively. The estimated errors of $^{40}Ar^*/^{39}Ar_K$ ratios range between ± 0.1% (2σ), and ± 0.6% (2σ) in the volume where the samples were included.

Samples were analyzed by single-grain CO_2 laser analysis or by furnace step-heating analysis, at the University Nice Sophia Antipolis (Géoazur UMR 7329). Laser analyses were undertaken by step heating with a 50 W CO_2 Synrad 48-5 continuous laser beam. Measurement of isotopic ratios was done with a VG3600 mass spectrometer, equipped with a Daly detector system. Detailed procedures are given in Jourdan et al. (2004). The typical blank values for extraction and purification of the laser system are in the range 4.2-8.75, 1.2-3.9, and 2-6 cc STP for masses 40, 39 and 36, respectively. Furnace analyses were undertaken with a step-heating technique using a double-vacuum high-frequency furnace and a mass spectrometer composed of a 120° M.A.S.E.E. tube, a Baur-Signer GS98 source and a Blazers electron multiplier. Heating lasted 20 min for each temperature step, followed by 5 min for clean-up of the released gas, before introducing the gas into the spectrometer. Ar isotopes were of the order of 100-2000, 100-1000 and 2-200 times the blank for masses 40, 39 and 36, respectively. All measurements were undertaken at the University of Nice (Géoazur UMR 7327). For both $^{40}Ar/^{39}Ar$-dating techniques, the mass-discrimination was monitored by regularly analyzing air pipette volume. Decay constants are those of Steiger and Jäger (1977).

The criteria used for defining a plateau age are those described in McDougall and Harrison (1988). Uncertainties on apparent ages, plateau and isochron ages are given at 2σ level, which includes the error on the $^{40}Ar^*/^{39}Ar_k$ ratio of the monitor. For the muscovite datings, the restricted spread in $^{36}Ar/^{40}Ar$ vs. $^{39}Ar/^{40}Ar$ values does not allow the use of inverse isochron method (see **Annexes 8**, **9**, **10**, **11**, **12** and **13**).

1.5.1.2 **U-Pb dating**

LA-ICP-MS U-Th-Pb zircon dating was performed at the University of Montpellier II using a Lambda Physik CompEx 102 excimer laser generating 15 nanoseconds duration pulses of radiation at a wavelength of 193 nm. Approximately thirty zircons were handpicked from the least magnetic concentrates using a binocular microscope, in order to obtain an assortment of the best quality grains. Crystals were then embedded in epoxy resin together with chips of the 91500 standard zircon (Wiedenbeck et al., 1995), grounded and polished to expose their internal structure. For analyses, the laser was coupled to a an Element XR sector field ICP-MS. Laser spot sizes were 50 µm. Samples were ablated under helium in a 15 cm^3, circular shaped cell using an energy density of 15 J/cm² at a frequency of 4 Hz. Analytic signal was acquired during 45 seconds and the blank was measured before each sample during 15 seconds. All isotopes (^{202}Hg, ^{204}Pb+Hg, ^{206}Pb, ^{207}Pb, ^{208}Pb, ^{238}U and ^{232}Th) were measured in pulse counting mode. The isotopes were measured using 15 points per peak and a 20% mass window resulting in 3 measured points for each mass station. Unknowns were bracketed by measurements of the G91500 standard (Wiedenbeck et al., 1995), which were used to calculate a mass bias factor (Pb/Pb ratio) and the inter-element fractionation (U/Pb ratios). The calculated bias factors and their associated errors were then added in quadrature to individual errors measured on each unknown following the procedure described in Horstwood et al. (2003). The decay constants and present-day $^{238}U/^{235}U$ value given by Steiger and Jäger (1977) were used and ages were calculated using the program Isoplot/Ex of Ludwig (2002).

1.5.1.3 **Geochemistry**

The Sr, Pb and Nd isotope analyses were determined using the VG354 5-collector mass spectrometer at the Lyon University following conventional chemical separation at the University Montpellier 2 radiogenic isotope facility. Major and trace element analysis was undertaken at Centre de Recherches Pétrographiques et Géochimiques (CRPG) Nancy (http://www.crpg.cnrs-nancy.fr/SARM/).

Major elements were analyzed on the basis of optical emission spectrum (ICP-OES) using an inductively coupled argon plasma source. The trace elements were obtained using mass spectrometry (ICP-MS), according to the following analytical procedure: solutions are prepared with the addition of $LiBO_2$ and dissolved in HNO_3. The spectrometer inductively coupled to a plasma source (ICP) allows the rapid simultaneous analysis of multiple elements with great precision. The source is constituted by a flame in which the samples are introduced in aerosol form.

1.5.2 Results

Dating performed on the SABCB has been focused on several lithologies. The same metapelitic sample that was studied for metamorphism (AR-03-62M) was also selected for $^{40}Ar/^{39}Ar$ dating, to perform a PTt path. A basement orthogneiss (AR-04-62) and a leucogranite (AR-04-64) were also analyzed in order to further constrain the thermal history of the study area. Finally, two granodiorite samples were also selected for U-Pb zircon and $^{40}Ar/^{39}Ar$ dating on amphibole, respectively ARL-10-33 and AR-03-64, to fix the pluton emplacement age as well as the early cooling history. $^{40}Ar/^{39}Ar$ and U-Pb dating samples and corresponding age results are found in **Tables 15** and **16**, respectively. Results are shown on **Figures 57** and **58**, compiled in the **Table 17**.

1.5.2.1 Geochronology and geochemistry of the granodiorite pluton

1.5.2.1.1 U–Pb dating

A photography of the dated zircon using a scanning electron microscope is provided in **Figures 57C1**, **C2**, **C3** & **C4**. The zircons show zonation compatible with a magmatic origin. Zircon dating using U-Pb laser ICP-MS ablation of granodiorite sample ARL-10-33 (**Table 15**) yields a concordia age of 150 ± 6 Ma (2σ) (**Figure 57A**) and a Tera-Wasserburg age of 153 ± 2 Ma (2σ) (**Figure 57B**).

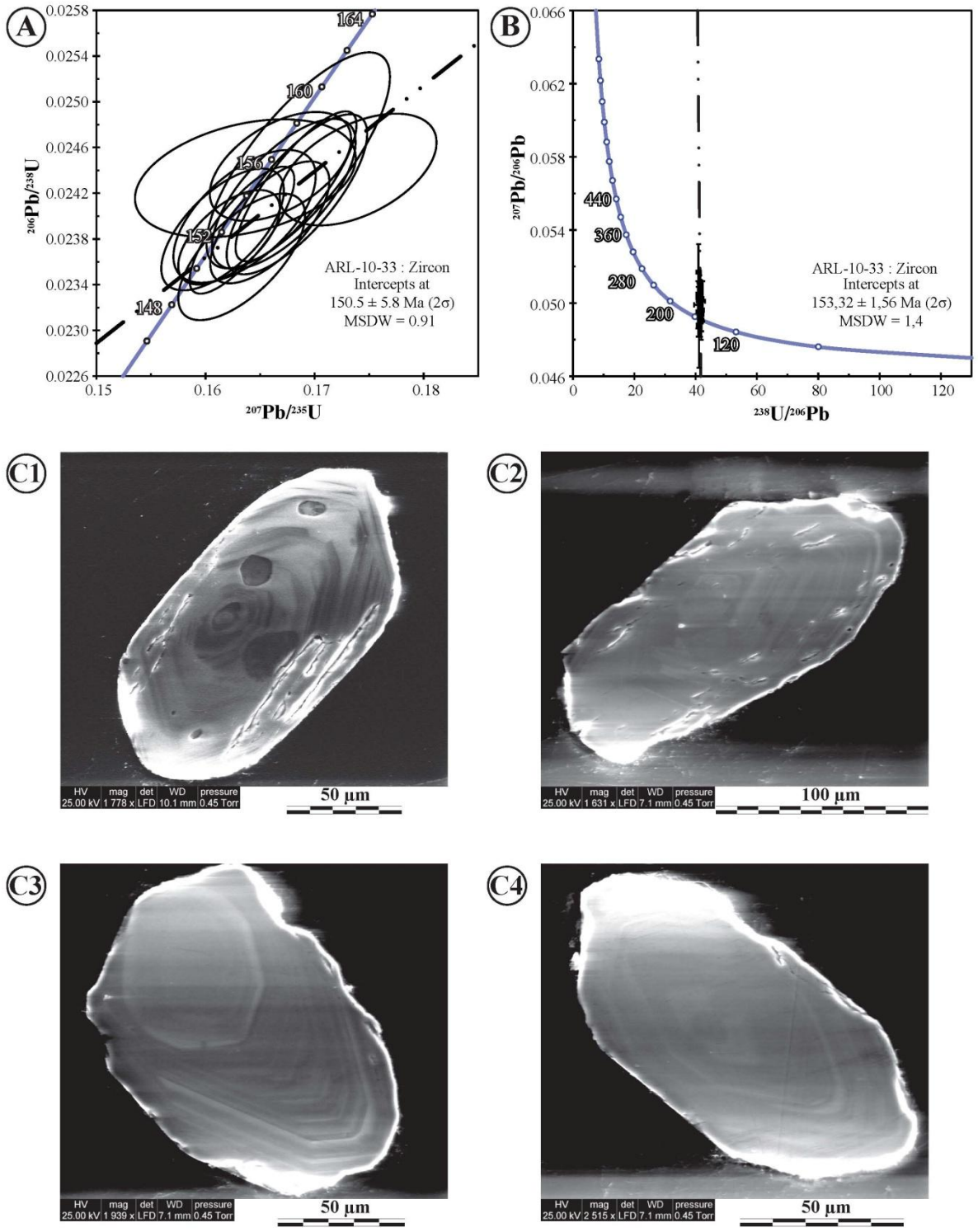

Figure 56 - U-Pb laser ICP-MS ablation concordia, A, and Tera-Wasserburg age diagrams, B, for the samples ARL10-33. C1, C2, C3 and C4 scanning electron microscope photography of dated granodiorite zirons corresponding to numbered analyses of table 15, respectfully. Location of the sample is shown on Figure 52.

1.5.2.1.2 **40Ar/39Ar dating**

The laser dating of the granodiorite sample AR-03-64 amphibole provides a relatively flat $^{40}Ar/^{39}Ar$ spectra with (1) steps 1-2 at 62 Ma representing less than 4% of released ^{39}Ar, (2) a high K/Ca ratio (K/Ca ~ 8) with ages between 147 and 152 Ma representing a total of 41.4% of degassed ^{39}Ar (steps 3-6) and (3) a low K/Ca ratio at high temperatures (K/Ca ~ 1-2) with ages between 157 Ma and 160 Ma representing a total of 54.7% of degassed ^{39}Ar (steps 7-14) (**Figure 58**, **Table 16**). The calculation of the weighted mean age of the spectrum except steps 1-2 gives an age of 156 ± 2 Ma (2σ) with a MSWD of 4.38. The isochron age gives an age of 158 ± 3 Ma (2σ) (MSWD 4.13) and the inverse isochron age is of 157 ± 3 Ma (2σ) (MSWD 4.21), with an intercept $(^{40}Ar/^{36}Ar)_0$ close to air value (266 ± 23). Therefore there is a good agreement between these different age calculations. We ascribe the variation in K/Ca ratio versus cumulative released $^{39}Ar(\%)$ in the high temperature part of the spectrum either to (1) a first phase of amphibole crystallization between 160 Ma and 152 Ma (steps 7-14) and the lower temperature part (steps 3-6) to a second amphibole growth between 152 Ma and 147 Ma, or (2) to recoil effects on the ^{39}K-^{39}Ar reaction in terms of ^{39}Ar distribution. However the two U-Pb and $^{40}Ar/^{39}Ar$ age provide within-error overlapping, which suggests sub-synchronous crystallization of amphibole and zircon at c. 153 Ma.

1.5.2.1.3 **Geochemistry**

The geochemical analysis of granodiorite sample ARL-10-33 (**Table 18**) was done in order to constrain its related geodynamic context. The result shows significant enrichments in Large Ion Lithophile Elements (LILE) and in Light Rare Earth Elements (LREE) as compared to Heavy Rare Earth Elements (HREE). The chondrite-normalized patterns have $(La/Sm)_N$ of 4.9 and $(La/Yb)_N$ ratios of 23.2. A well-marked negative Nb-Ta anomaly is observed and may be accounted by contribution of a subduction (or crustal) component in the source (Jacobsen and Wasserburg, 1980; **Figure 56**; **Table 18**).

Radiogenic isotopic analysis shows (1) $^{87}Sr/^{86}Sr_{(i)}$ value of 0.70341, (2) a $^{144}Nd/^{144}Nd_{(i)}$ equal to 0.51264 ($\varepsilon_{Nd(i)}$ = + 3.7), (3) a $^{206}Pb/^{204}Pb_{(i)}$ value of 18.24, $^{207}Pb/^{204}Pb_{(i)}$ of 15.55 and $^{208}Pb/^{204}Pb_{(i)}$ ratio of 38.01. These values are comparable to enriched mantle sources, suggesting that the grano-diorite originated from a mantle source contaminated by continental crust. The bulk chemical composition of the SAB crystalline basement granodiorite is thus

compatible with that of arc magmas resulting from mixing of different proportions of a mantle component with a subduction/crustal component (e.g. Marchesi et al., 2007).

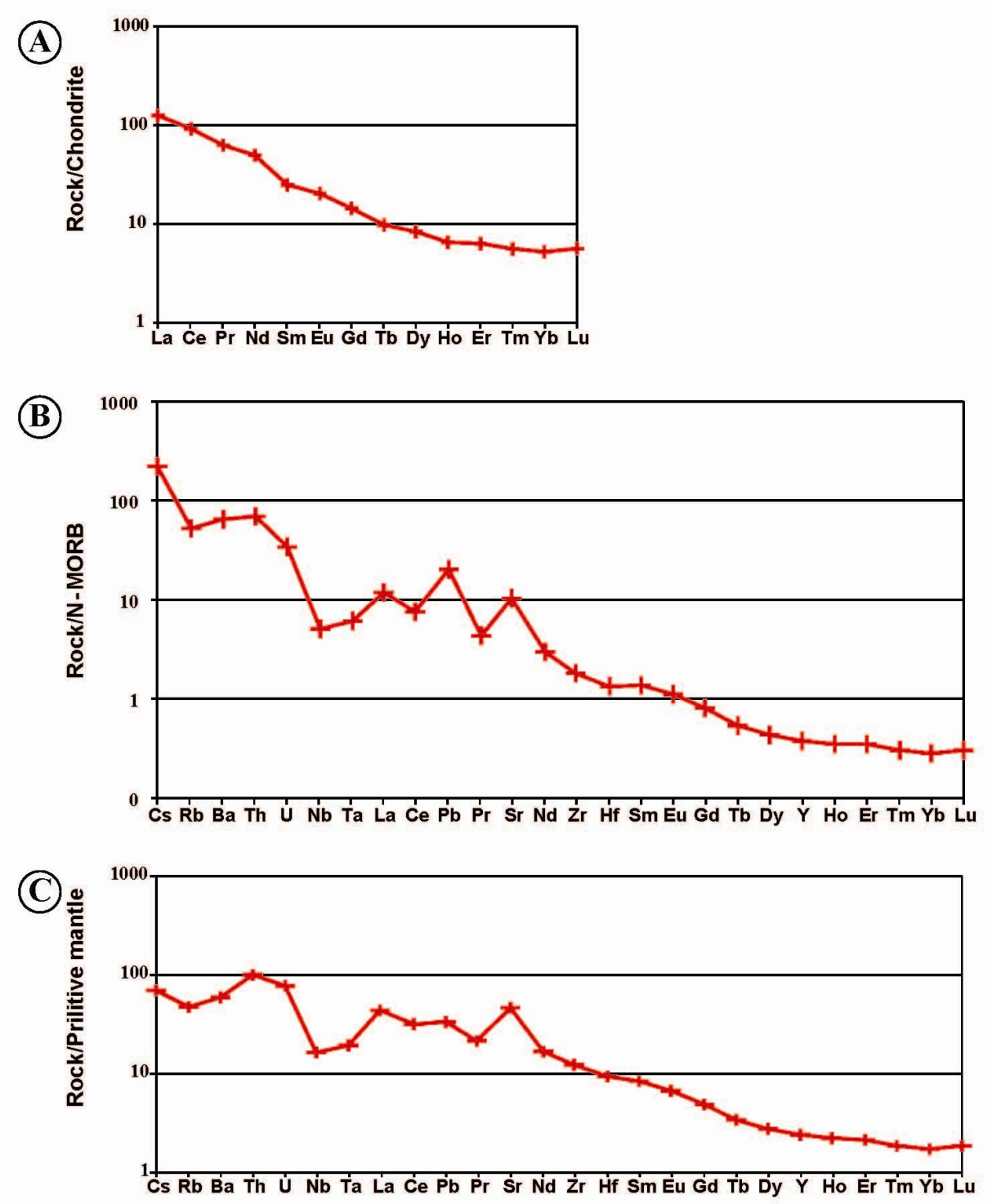

Figure 57 - Chondrite normalized REE and N-MORB and primitive mantle normalized multi-element spider diagrams of the granodiorite sample ARL-10-33. Normalizing values are from Sun and McDonough (1989).

1.5.2.2 $^{40}Ar/^{39}Ar$ Geochronology of sample AR-04-64 leucogranite

Two experiments have been undertaken on this sample (1) a single-grain laser experiment (H446) and (2) a furnace experiment (M1907) (**Figure 58**, **Table 16**). Identically as for sample AR-03-62 exposed below, the two (laser and furnace) experiments show a double hump shape. Experiment H446 shows (1) a low temperature part with younger age steps (~149 Ma), which represents less than 4% of released ^{39}Ar (steps 9-10). The rest of the spectra is comprised between 149 and 158 Ma, with (1) a low temperature age maximum of c. 156 Ma; (2) a medium temperature age minimum of c. 147-148 Ma in steps 9-10; (3) a HT maximum of c. 157-158 Ma (for the last three steps). Despite this spread, a weighted mean age of 153 ± 2 Ma (2σ) (MSWD 4.95) is calculated. The normal isochron is within error, with an age of 154 ± 2 Ma (2σ) (MSWD 1.78). The good agreement between these two ages, and the proximity with minimum age of HT steps validates an Upper Jurassic age for muscovite of the leucogranite body.

Similarly to this laser experiment, the furnace experiment (M1907) shows a minimum age of 150 Ma in the last three steps, with a weighted mean age of 142 ± 4 Ma (2σ) (MSWD 12) and an isochron age of 139 ± 5 Ma (2σ) (MSWD 9.0). The spread in ages along with a greater MSWD value shows a more important resetting in this sample than in experiment H446, which is therefore variable from one sample to another. Nonetheless, the minimum age of ~150 Ma is in agreement with the laser results (experiment H446).

1.5.2.3 $^{40}Ar/^{39}Ar$ geochronology of sample AR-03-62M micaschist

Muscovite AR-03-62M laser $^{40}Ar/^{39}Ar$ spectrum is complex (**Figure 58**, **Table 16**), showing a double-hump shape. It shows: (1) a low temperature part with a younger age step (105 Ma), which represents less than 5% of released ^{39}Ar (step 1). The rest of the spectra is comprised between 131 and 148 Ma, with (1) a low temperature age maximum of c. 140 Ma (obtained for two consecutive steps in **Figure 58**, steps 4-5); (2) a medium temperature age minimum of c. 130 Ma (steps 7-8); (3) a HT maximum of c. 148 Ma (steps 11-12). This latter age is considered as a minimum age for muscovite closure. No correlation is found between the K/Ca ratios and ages of individual steps, therefore it does not seem possible to discriminate between several muscovite generations from this dataset as is illustrated by fine section observations (**Figures 53C** & **D**). The isochron age of 149 ± 5 Ma (2σ) (MSWD 2.5) supports the interpretation of a minimum age of crystallization at c. 149 Ma.

1.5.2.4 $^{40}Ar/^{39}Ar$ geochronology of sample AR-04-62 orthogneiss

The gneiss muscovite furnace $^{40}Ar/^{39}Ar$ dating experiment (M1905) (**Figure 58**, **Table 16**) exhibits a double-hump shape with (1) low temperature steps 1-3 < 135 Ma, representing less than 4% of released ^{39}Ar, (2) a LT maximum of 155 Ma (step 5), (3) a MT minimum of 142 Ma (steps 7-8) and (4) a HT maximum of 152-153 Ma in the steps 12-14. Despite this spread a weighted mean age of 148 ± 3 Ma (2σ) (MSWD 10) and a corresponding isochron of 150 ± 3 Ma (2σ) (MSWD 7.2) can be calculated. This latter isochron age is within error of the HT spectra minimum age. The gneiss biotite exhibits a flat spectrum, with a plateau age using 95% of released ^{39}Ar, of 123 ± 2 Ma (2σ) (MSWD 1.4). The isochron plot provides a similar within-error age estimate of 121 ± 4 Ma (MSWD 1.3) and the inverse isochron gives an age of 121 ± 5 Ma (2σ) (MSWD 1.4) with an upper intercept $(^{40}Ar/^{36}Ar)_0$ = 320 ± 19 close to atmospheric value. These ages are in good agreement, which gives good insight in the cooling process of the orthogneiss with biotite closure at 120-123 Ma. We interpret this to occur during gneiss retrogression at T ≈ 400°C (Villa, 1998), which temperature is coherent by garnet-biotite thermometry (section 4).

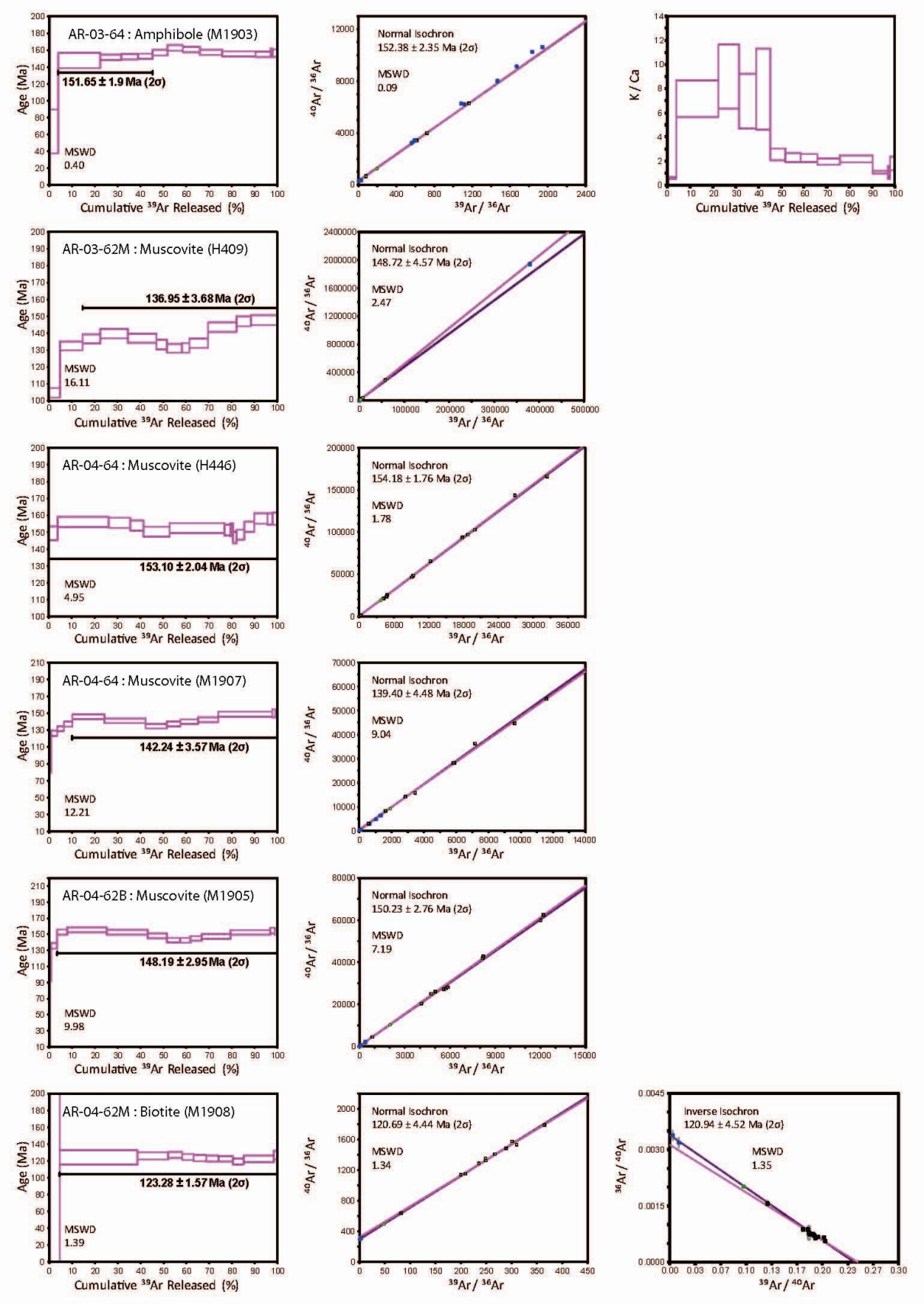

Figure 58 - ^{40}Ar/^{39}Ar age spectra, normal isochrones and Ca/K spectra of dated samples. Locations of samples are shown on Figure 52.

1.6 Discussion

The origin of the different rock types found in the Tsaghkuniats region is unconstrained in time as well as the geodynamic processes responsible for their formation. Before the present paper, only the age obtained by Baghdasarian and Ghukasian (1983) obtained using the Rb-Sr isochron method on the Bjni migmatite-granite suggests a Proterozoic (610 ± 36 Ma) origin for the metamorphism and magmatism undergone by the SABCB. The metamorphic evolution of the SABCB is investigated here for the first time with combined U/Pb and $^{40}Ar/^{39}Ar$ geochronological data. In addition, we also show here for the first time a well-constrained PT evolution featured by a decompression path from mid-crustal (M1) MP-MT conditions to sub-surface (M2) HT-BP conditions. This metamorphic history coincides with calc-alkaline magmatism along the northern margin of the SAB. In the following discussion we propose significance for the above ages as well as structural observations, and their implication for the tectonic evolution of the SAB.

1.6.1 Significance of double-hump shaped muscovite Ar spectra

The HT part of the white mica spectra all show minimum ages similar within error to the age of the granodiorite, which is interpreted as a M1 regional metamorphic imprint coinciding with intrusion emplacement at c. 153 Ma. Granodiorite intrusion occurred at c. 153 Ma, as shown by within error U/Pb Tera-Wasserburg age of 153 ± 2 Ma on zircon and amphibole $^{40}Ar/^{39}Ar$ weighted mean average of 150 ± 6 Ma (see section 5.2.1). The M1 event is featured by complex $^{40}Ar/^{39}Ar$ ages in intruded schists, as shown by the 153 Ma, 142 Ma and 149 Ma mean weighted averages of two leucogranite muscovites and a micaschist muscovite sample, respectfully AR-04-64 and AR-04-62 (**Figure 59**). However, mylonitic muscovites exhibit complex spectra with two age maxima, in the LT and HT steps. This shape does not coincide with variations in K/Ca and Cl/K ratios of the sample (see Supplementary Data 2). It is interpreted as resulting from argon diffusion during mylonitization, which lowers the age (e.g. Dodson, 1973; Kramar et al., 2001; Mulch et al., 2002 and Sanchez et al., 2011 for a complete analysis of the effect of mylonitic deformation on argon spectra). Chemically zoned grains (or grain populations) may contain heterogeneous argon compositions because of zonation induced by recrystallization and re-equilibration with their environment (Giorgis et al., 2000; Vance et al., 2003) or because of

chemically diverse zones of the grain having different retention properties (Villa et al., 1996). Such lattice defects form the boundaries of micro-structurally controlled diffusion segments and reduce the physical (observed) grain size and, hence, the characteristic length scale for argon diffusion (Reddy and Potts, 1999). This conclusion is consistent with the results of Dunlap and Kronenberg (2001) who speculated that grain segmentation affects the ability to retain argon in micas deformed under laboratory conditions. However, there are currently no experimental data in the earth science literature for noble gas behavior in strained solids. Field structural observations and microscope or Electron back-scatter (EBS) imaging of sample AR-04-64 (**Figure 53C**, **D** & **G**) provide further insights into the internal deformation and recrystallization of micas. Mylonitic deformation is found to occur during (1) top-to-north deformation and (2) normal sense of shear during doming. The top-to-north deformation is mainly featured by growth of M1 muscovite neo-cysts within the foliation forming at T > 500°C. Therefore, this should not be responsible of argon diffusion. In contrast, the extensional phase starts in HT conditions, and ends with brittle deformation. Therefore, M1 muscovite has been severely deformed during M2 (150-130 Ma) at a temperature between 200°C and 500°C, which has been noted to be a temperature range in which ductile deformation may partially reset muscovite grains by neo-crystallization and diffusion in intra-granular micro-fractures especially between 380°C and 400°C (Kramar, 2002; Mulch et al., 2002). This phase of mylonitization ends before the post-kinematic (M3) biotite AR-03-62b that crystallized at 360-460°C and 2 ± 1 kbar (section 4), which yields plateau age of 123 ± 2 Ma.

Therefore, from the example of the SABCB, we propose that mylonitic deformation can be bracketed in time by the $^{40}Ar/^{39}Ar$ dating method, because we were able to date minerals formed before (the M1 granodiorite minerals) and after (M3 biotite) the main mylonitization phase. The HT part of the spectra yields a minimum age for muscovite crystallization, here ~155 Ma during the M1 metamorphic phase (AR-04-64 muscovite). The medium temperature minimum of the spectra yields a maximum age for the low temperature stage of mylonitization, here ~130 Ma (from sample AR-03-62 muscovite). Nevertheless, it is still questionable whether ages obtained correspond to the original formation of the micaschists or their metamorphism/deformation.

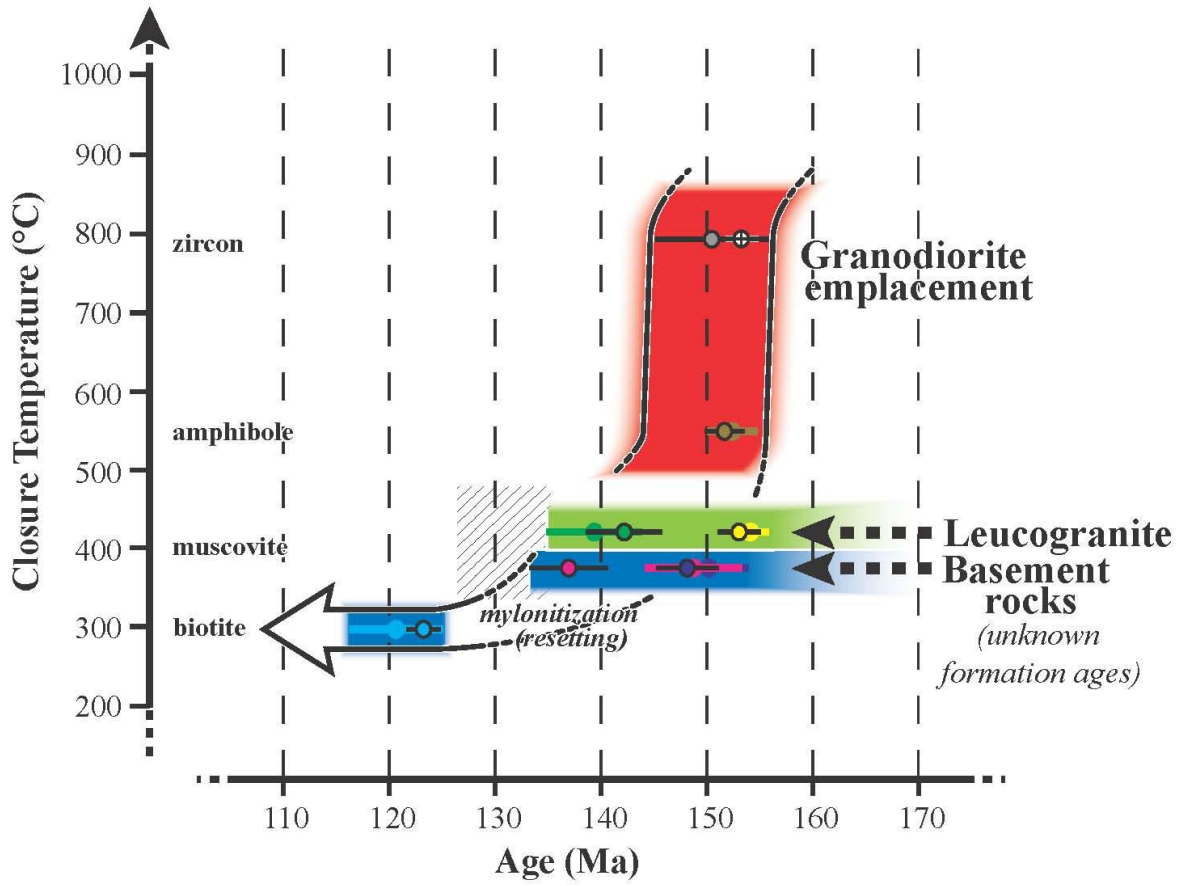

	U-Pb	$^{40}Ar/^{39}Ar$	normal isochrone	weighted mean average
Grano-diorite	ARL-10-33 concordia age Tera-Wasserburg age	AR-03-64 (H1903)		
Leucogranite		AR-04-64 (H1907) AR-04-64 (H446)		
Proterozoic basement (orthogneiss and metasedimentary micaschist)		AR-04-62B (H1905) AR-03-62M (H409) AR-04-62B (M1908)		plateau age

Figure 59 - Cooling model for $^{40}Ar/^{39}Ar$ and U-Pb dating results with error margins.

It is important to point out that despite efforts to constrain the entire metamorphic evolution of the Tsaghkuniats massif the protolith age of these micaschists is still to be determined. Two scenarios may be suggested, either (1) the micaschists were indeed originally deposited and incorporated within the Proterozoic basement as forwarded by Baghdasarian and Ghukasian (1983), and later metamorphosed through the regional metamorphism described above or (2) they represent the lateral equivalent of Upper Devonian-Permian formations in this area which are preserved (unmetamorphosed) farther

south along the northern edge of the Araks Valley (Sosson et al., 2010). To solve this issue, punctual U-Pb dating of zircon and/monazite mineral phases in these micaschists should be undertaken.

1.6.2 Tectonic significance of the PT-t history

The above age data are correlated together (**Figure 59**) and to the PT path to define a PTt path on **Figure 60**. The entire metamorphic cycle determined, from burial to exhumation, can be bracketed between 160 Ma and 120 Ma. Minimum ages preserved in M1 muscovite of metapelites imply initial burial of metasediments between 160 Ma and 155 Ma at M1 peak in MP-MT conditions (25°C/km). Rapid exhumation is suggested by decompressional melting and formation of leucogranites with injection of grano-diorites at c. 153 Ma. Exhumation is more or less isothermal and is followed by M2 doming at LP-HT conditions, which is bracketed between 150 Ma and 130 Ma, from muscovite $^{40}Ar/^{39}Ar$ spectra. Further cooling is featured by age of M3 biotite recrystallization at 123 Ma, which is linked to temperatures of 400°C from garnet-biotite exchange thermometry.

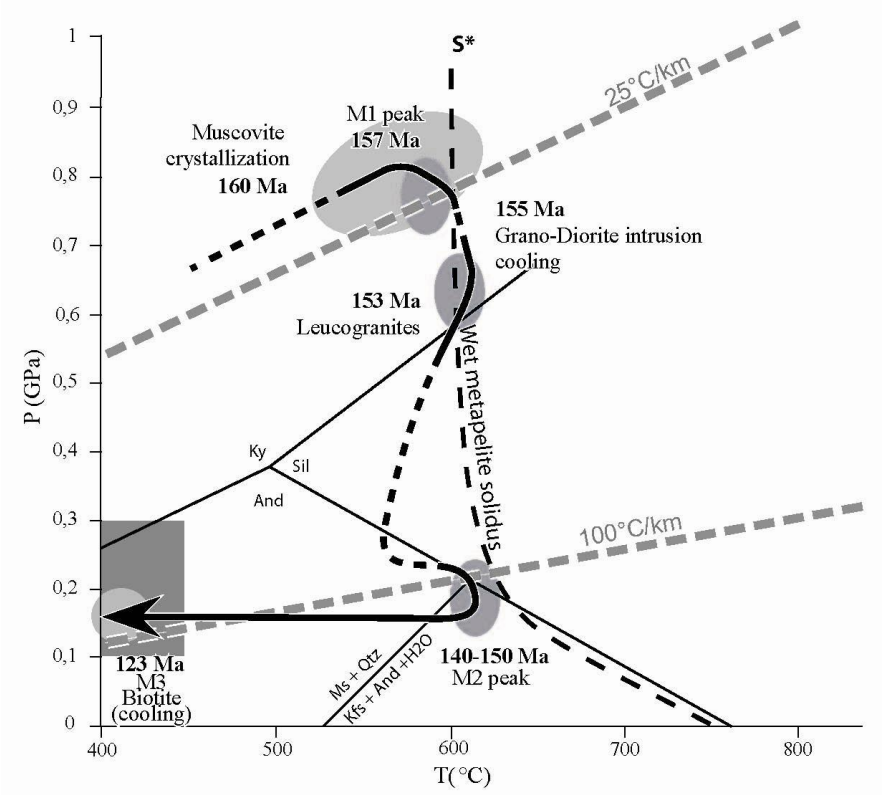

Figure 60 - PT-t path including metamorphic (Figure 55C), $^{40}Ar/^{39}Ar$ and U-Pb age data.

This PT path is quite uncommon, though it can be supported by the peculiar tectonic context of the Tethys-Caucasus region during the Late Jurassic to Early Cretaceous (**Figure**

61). The region is characterized by north-dipping subduction of the Tethyan oceanic domain below the southern Eurasian margin since the Carboniferous, and until the Middle Cretaceous (Rolland et al., 2011; 2012). A north-dipping intra-oceanic subduction is evidenced by the presence of an ophiolite formed in a back-arc setting during the Late Jurassic north of the SAB (Galoyan, 2008; Rolland et al., 2009a; 2009b, 2011; Hässig et al., 2013; Topuz et al., 2013). Such north-dipping subductions are also suggested at the scale of the Northern Paleotethys Ocean, which would be totally subducted by the Middle Cretaceous times. Here, the north sense of shear and MP-MT metamorphism, correlated to calc-alkaline magmatism, are in agreement with a south-dipping subduction zone below the SAB since at least 160 Ma, which evidence vanishes in the Early Cretaceous at 123 Ma. The magmatics could alternatively be explained by hot-spot activity. We discard this possibility, however, because of the long duration (minimum 37 Ma) of the metamorphic episode. In this period the SAB was a mobile tectonic block in the Tethyan realm that had separated from Africa. This is not in agreement with a stable position above a hot-spot during ~40 Ma. Further, the calc-alkaline nature of magmatic rocks is not in agreement with hot-spot geochemistry. North-dipping subduction below the southern margin of SAB is equally unlikely at this time as such a subduction would have led to convergence of SAB with Gondwana.

Therefore, we propose the presence of a third subduction zone in the Neotethyan realm between the SAB and the north-dipping intraoceanic subduction zone from Middle Jurassic to Early Cretaceous. We suggest that this south-dipping subduction below the SAB may have also been a motor of SAB-Eurasia convergence. This subduction, which is not observed along the rim of Taurides, may (1) be hidden by latter sedimentary deposits and/or nappe structures, or still to be evidenced, or (2) be due to a corner effect of the northward drifting SAB at the boundary with the Iranian part of Eurasian margin.

The two-stage metamorphic evolution observed in the SABCB resembles that observed in the active margin of retreating subduction zones such as in the Agean domain in the E-Mediterranean Sea (e.g. Jolivet and Brun, 2010) and may also be compared to multistage metamorphism linked to crustal deformation in Trans-amazonian and Brasiliano metamorphism (Neves et al., 2006). In these contexts, HT metamorphism is shown to occur shortly after HP-BT metamorphism, and is correlated to back-arc type extension. The retreat of the subducting slab, the steepening of the subduction due to slab pull, would result in the vanishing of metamorphism after a short period (approximately 10-20 Ma as throughout the

Agean domain). A similar scenario is proposed for the northern margin of the SAB in the Late Jurassic to Early Cretaceous: firstly, because of a similar timing and PT path, with a final extensional context featured by metamorphic domes, and secondly by the subduction of the old oceanic crust that is likely to behave in a similar way as the Neotethys in E-Mediterranean domain in the Cenozoic. In such contexts, the slab density is assumed to drive the subduction.

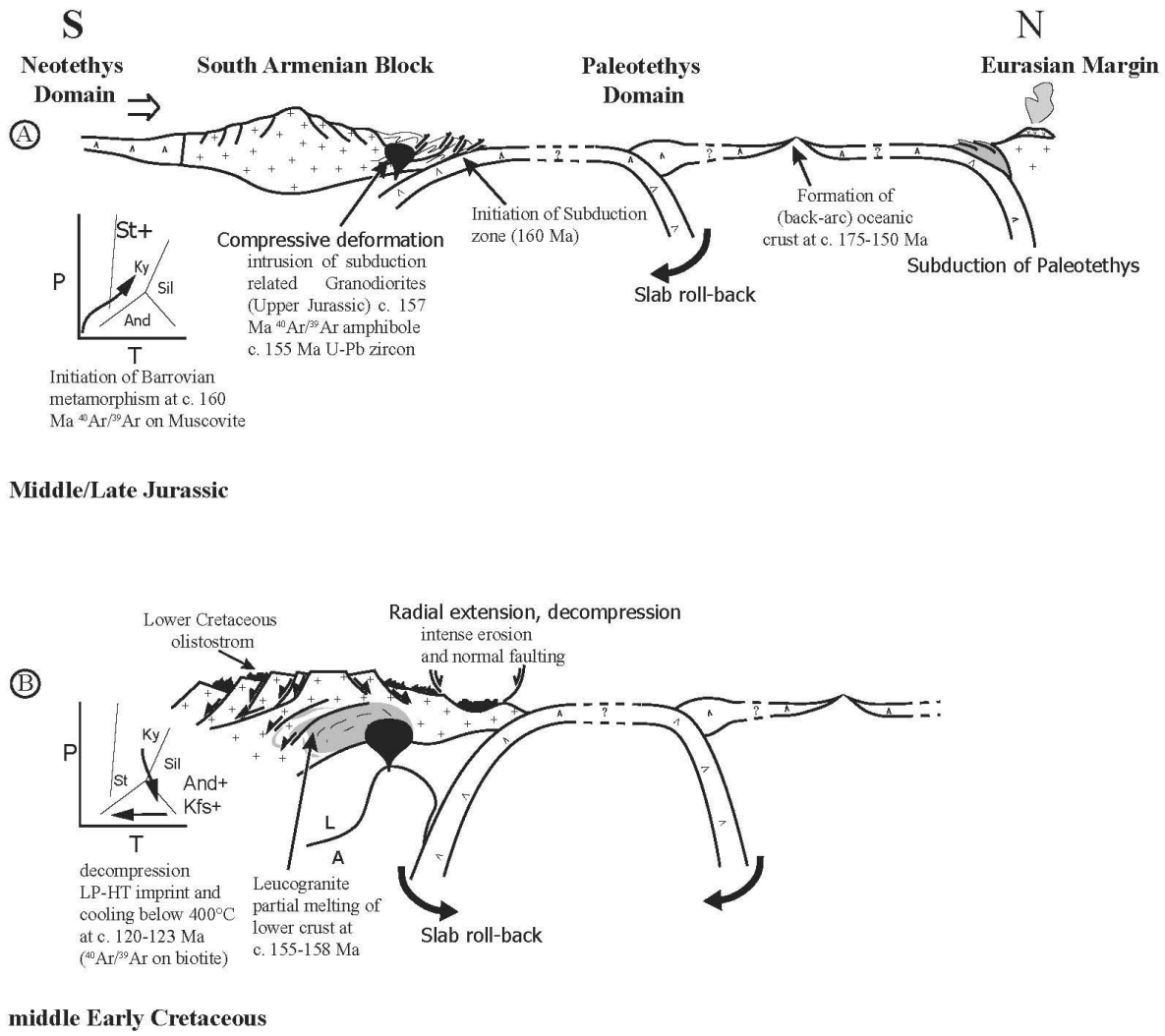

Figure 61 - Sketch geodynamic model proposed for the SAB (Lesser Caucasus) from Middle Jurassic to Upper Cretaceous-Paleocene times.

1.7 Conclusion

We show here for the first time an amazingly young multi-stage metamorphic evolution for this region preserved in the SABCB, fully occurring during the Late Jurassic and Early Cretaceous times. Geochronological data show it to be unrelated to the Cimmerian

orogeny. (1) First M1 metamorphism is featured by Barrovian (staurolite-kyanite) MP-MT conditions at 157-160 Ma and intrusion of dioritic magmas at 150-156 Ma. (2) Near-adiabatic decompression PT path is featured by partial melting and production of leucogranites at 153 Ma, followed by M2 (andalusite-K-feldspar) HT-BP metamorphism. This phase of shearing and recrystallization is ascribed to doming at 130-150 Ma and cooling at 400°C by 123 Ma (M3). Structural evidence shows (1) north-verging shearing during M1 and (2) radial extension during M2. This metamorphic evolution is interpreted as featuring south-dipping subduction below the SAB, as evidenced by emplacement of relatively hot subduction related granodiorite in a way similar to Mediterranean subduction zones in the Cenozoic.

Acknowledgements

This work was supported by the MEBE (Middle East Basin Evolution) and DARIUS programs jointly supported by a consortium including oil companies, UMPC and the INSU/CNRS. Fieldwork was facilitated by the support of the Armenian National Academy of Science (Institute of Geological Sciences). We wish to thank J.L. Devidal in Clermont-Ferrand for their involvement during data acquisition. The technical help of G. Delanoy for thin sections as well as the help from S. Gallet and C. Verati in utilizing available $^{40}Ar/^{39}Ar$ analyses is acknowledged. This publication is a contribution of "GEOAZUR", University of Nice Sophia Antipolis, CNRS, France.

References

Adamia, Sh.A., Chkhotua, T., Kekelia, M., Lordkipanidze, M., Shavishvili, I., Zakariadze, G., 1981. Tectonics of Caucasus and adjoining regions: implications for the evolution of the Tethys ocean. Journal of Structural Geology 3, 437–447.

Adamia, Sh.A., Zakariadze, G., Chkhouta, T., Sadradze, N., Tsereteli, N., Chabukiani, A., Gventsadze, A., 2011. Geology of the Caucasus: a review. Turkish Journal of Earth Sciences 20, 489-544.

Aghamalyan, V.A., 1978. The old metamorphic complexes of the territory of Armenian SSR and their tectonic disposition. Proceedings of reports of the Second Regional Petrographic Symposium on Caucasus, Crimea and Carpathians. Tbilisi, 109-115. (in Russian)

Aghamalyan V.A., 1983. Pre-Cambrian stratigraphy of the Armenian SSR. Izvestia NAS of Arm. SSR, Nauki o Zemle 4, 26-39. (in Russian)

Aghamalyan, V.A., 1998. The Basement Crystalline of Armenia. PhD thesis, Institute of Geological Sciences, National Academy of Sciences of Armenia. Yerevan. (in Russian)

Aghamalyan V., Mayringer F., Lorsabyan T., Israelyan A., 2011a. Geochemical features of pre-Cambrian amphibolites of the Armenian crystalline massif as a fragment of metamorphosed basalts of the pan-African oceanic crust. Proceedings of the National Academy of Sciences, Armenia, Earth Sciences 64, 15-23. (in Russian)

Aghamalyan V., Schulz B., Renno A., Lange J., Lorsabyan T., 2011b. Geochemical features of pre-Cambrian amphibolites of the Armenian crystalline massif as a fragment of metamorphosed basalts of the pan-African oceanic crust. Proceedings of Yerevan State University, Armenia, Geology and Geography 3, 3-8. (in Russian)

Avagyan, A., Sosson, M., Philip, M.H., Karakhanian, A., Rolland, Y., Melkonyan, R., Rebai, S., Davtyan, V., 2005. Neogene to Quaternary stress field evolution in Lesser Caucasus and adjacent regions using fault kinematics analysis and volcanic cluster data. Geodinamica Acta 18, 401-416.

Baghdasarian, G.P., Ghukasian, R.Kh., 1983. The age of Bdjni migmatite-granitic massif (By the Rb-Sr Isochron radiometric data and geological ideas. Izvestia NAS of Armenian SSR, Nauki o Zemle 6, 15-29. (in Russian)

Barrier, E., Vrielynck, B., 2008. Palaeotectonic map of the Middle East, atlas of 14 maps, tectonosedimentary-palinspastic maps from late norian to pliocene. Commission for the Geologic Map of the World (CCMW, CCGM), Paris.

Bazhenov, M., Burtman, V.S., Levashova, N.M., 1996. Lower and Middle Jurassic paleomagnetic results from the south Lesser Caucasus and the evolution of the Mesozoic Tethys ocean. Earth and Planetary Science Letters 141, 79-89.

Belov, A.A., Sokolov, S.D., 1973. Relicts of Mesozoic oceanic crust among the crystalline complexes of the Miskhana massif of Armenia. Sovetskaya Geologia 8, 26-41 (in Russian).

Choukroune, P., Gapais, D., Merle, O., 1987. Shear criteria and structural symmetry. Journal of Structural Geology 9, 525-530.

Dercourt, J., Zonenschain, L.P., Ricou, L.-E., Kazmin, V.G., Le Pichon, X., Knipper, A.L., Grandjacquet, C., Sbortshikov, I.M., Geyssant, J., Lepvir, C., Pechersky, D.H., Boulin, J., Sibuet, J.-C., Savostin, L.A., Sorokhtin, O., Westphal, M., Bazhenov, M.L., Lauer, J.P., Biju-Duval, B., 1986. Geological evolution of the Tethys belt from the Atlantic to the Pamirs since the Lias. Tectonophysics 123, 241-315.

Dodson, M.H., 1973. Closure temperature in cooling geochronological systems. Contributions to Mineralogy and Petrology 40, 259-274.

Dunlap, W.J., Kronenberg, A.K., 2001. Argon loss during deformation of micas: constraints from laboratory deformation experiments. Contributions to Mineralogy and Petrology 141, 174-185.

Ferry, J.M., Spear, F.S., 1978. Experimental calibration of the partitioning between biotite and garnet. Contributions to Mineralogy Petrology 66, 113-117.

Galoyan, G., 2008. Etude pétrologique, géochimique et géochronologique des ophiolites du Petit Caucase (Arménie). PhD thesis, Université de Nice-Sophia Antipolis.

Galoyan, G., Rolland, Y., Sosson, M., Corsini, M., Billo, S., Verati, C., Melkonian, R., 2009. Geology, geochemistry and 40Ar/39Ar dating of Sevan ophiolites (Lesser Caucasus, Armenia): Evidence for Jurassic Back-arc opening and hot spot event between the South Armenian Block and Eurasia. Journal of Asian Earth Sciences 34, 135-153.

Ganguly, J., Saxena, S.K., 1984. Mixing properties of aluminosilicate garnets: constraints from natural and experimental data, and applications to geothermo-barometry. American Mineralogist 69, 88-97.

Gealey, W.K., 1988. Plate tectonic evolution of the Mediterranean-Middle East region. Tectonophysics 155, 285-306.

Ghent, E.D., Stout, M.Z., 1981. Geobarometry and geothermometry of plagioclase-biotite-garnet-muscovite assemblages. Contributions to Mineralogy and Petrology 76, 92-97.

Giorgis, D., Cosca, M.A., Li, S., 2000. Distribution and significance of extraneous argon in UHP eclogite (Sulu terrain, China): insights from in situ $^{40}Ar/^{39}Ar$ UV-laser ablation analysis. Earth Planet Science Letters, 181, 605-615.

Golonka, J., 2004. Plate tectonic evolution of the southern margin of Eurasia in the Mesozoic and Cenozoic. Tectonophysics 381, 235-273.

Göncüoğlu, M.C., Turhan, N., 1984. Geology of the Bitlis metamorphic belt: International symposium. In O. Tekeli & M. C. Göncüoglu (Eds.), Proceedings of the international symposium on the geology of the Taurus belt (pp. 237-244). Ankara: Mineral Research and Exploration Institute.

Hässig, M., Rolland, Y., Sosson, M., Galoyan, G., Müller, C., Avagyan, A., Sahakyan, L., 2013. New structural and petrological data on the Amasia ophiolites (NW Sevan–Akera suture zone, Lesser Caucasus): Insights for a large-scale obduction in Armenia and NE Turkey. Tectonophysics 588, 135-153.

Hässig, M., Rolland, Y., Sosson, M., Galoyan, G., Sahakyan, L., Topuz, G., Çelik, Ö.F., Avagyan, A., Müller, C., 2014. Linking the NE Anatolian and Lesser Caucasus ophiolites: evidence for large scale obduction of oceanic crust and implications for the formation of the Lesser Caucasus-Pontides Arc. Geodinamica Acta (just-accepted), 1-52.

Hässig, M., Rolland, Y., Sosson, M., Galoyan, G., Avagyan, A., in review. P-T-t history of the Amasia ophiolite 'metamorphic sole' (Armenia, Lesser Caucasus): implications for the obduction process of an old oceanic lithosphere. Journal of metamorphic Geology.

Hempton, M.R., 1985. Structure and deformation history of the Bitlis Suture near Lake Hazar, SE Turkey. Geological Society of America Bulletin 96, 223-243.

Hodges, K.V., Crowley, P.D., 1985. Error estimation and empirical geothermobarometry for pelitic systems. American Mineralogist 70, 702-709.

Hodges, K.V., Spear, F.S., 1982. Geothermometry, geobarometry and the Al2SiO5 triple point at Mt. Moosilauke, New Hampshire. American Mineralogist 67, 1118-1134.

Hoisch, T.D., 1990. Empirical calibration of six geobarometers for the mineral assemblage quartz+muscovite+biotite+plagioclase+garnet. Contributions to Mineralogy and Petrology 104, 225-234.

Holland, T.J.B., Powell, R., 1998. An internally consistent thermodynamic data set for phases of petrological interest. Journal of Metamorphic Geology 16, 309-343.

Horstwood, M.S.A., Parrish, R.R., Nowell, G.M., Noble, S.R., 2003. Accessory mineral U-Th-Pb geochronology by laser-ablation plasma-ionisation multi-collector mass spectrometry (LA-PIMMS). Journal of Analytical Atomic Spectrometry 18, 837-846.

Jacobsen, S., Wasserburg, G.J., 1980. Sm-Nd isotopic evolution of chondrites. Earth and Planetary Science Letters 40, 139-155.

Johnson, T., Brown, M., 2004. Quantitative constraints on metamorphism in the Variscides of southern Brittany – a complementary pseudosection approach. Journal of Petrology 45, 1237-1259.

Jolivet, L., Brun, J.-P., 2010. Cenozoic geodynamic evolution of the Aegean. International Journal of Earth Sciences 99, 109-138.

Jourdan, F., Féraud, G., Bertrand, H., Kampunzu, A.B., Tshoso, G., Le Gall, B., Tiercelin, J.J., Capiez, P., 2004. The Karoo triple junction questioned: evidence from $^{40}Ar/^{39}Ar$ Jurassic and Proterozoïc ages and geochemistry of the Okavango dyke swarm (Botswana). Earth and Planetary Sciences Letters 222, 989-1006.

Jourdan, F., Verati, C., Féraud, G., 2006. Intercalibration of the Hb3gr $^{40}Ar/^{39}Ar$ dating standard. Chemical Geology 231, 77-189.

Jourdan, F., Renne, P.R., 2007. Age calibration of the Fish Canyon sanidine $^{40}Ar/^{39}Ar$ dating standard using primary K–Ar standards. Geochimica et Cosmochimica Acta 71, 387-402.

Kazmin, V.G., 1991. Collision and rifting in the Tethys Ocean: Geodynamic implication. Tectonophysics 196, 371-384.

Knipper, A.L., Khain, E.V., 1980. Structural position of ophiolites of the Caucasus. Ofioliti 2, 297-314. Special Issue.

Kramar, N., Cosca, M., Hunziker, J., 2001. Heterogeneous $^{40}Ar^*$ distribution in naturally deformed muscovite: in situ UV-laser ablation evidence for microstructurally controlled intragrain diffusion. Earth and Planetary Science Letters 192, 337-388.

Kramar, N., 2002. Microstructural controls on intragranular argon diffusion in naturally deformed muscovites. PhD thesis, Université de Lausanne.

Kretz, R., 1983. Symbols for rock-forming minerals. American Mineralogist 68, 277-279.

Ludwig, K.R., 2002. Isoplot/Ex version 2.4. A geochronological toolkit for Microsoft Excel. Berkeley Geochronological Center, Special Publication 56.

Marchesi, C., Garrido, C.J., Bosch, D., Proenza, J.A., Gervilla, F., Monié, P., Rodríguez-Vega, A., 2007. Geochemistry of Cretaceous Magmatism in Eastern Cuba: Recycling of North American Continental Sediments and Implications for Subduction Polarity in the Greater Antilles Paleo-arc. *Journal of Petrology* 48, 1813-1840.

Mart, Y., 1987. Superpositional tectonic patterns along the continental margin of the southeastern Mediterranean: a review. Tectonophysics 140, 213-232.

McDougall, I., Harrison, T.M., 1988. Geochronology and Thermochronology by the $^{40}Ar/^{39}Ar$ Method. Oxford University Press, New York.

Meijers, M., Smith, B., Sosson, M., Rolland, Y., Grigoryan, A., Sahakyan, L., Avagyan, A., Adamia, S., Sadradze, N., Asanidze, B., Langereis, C., Kircher, U., Mensink, M., Müller, C., 2013. A paleolatitude reconstruction of the South Armenian Block (SAB) since the late Cretaceous: constraints on the Tethyan realm. Darius Programme, Tbilisi Meeting, Eastern Black Sea and Caucasus Workshop.

Monin, A.S., Zonenshain, L.P., (eds) 1987. History of the Ocean Tethys. Moscow Institute of Oceanology (in Russian).

Mulch, A., Cosca, M.A., Handy, M.R., 2002. In-situ UV-laser $^{40}Ar/^{39}Ar$ geochronology of a micaceous mylonite: an example of defect-enhanced argon loss. Contributions to Mineralogy and Petrology 142, 738–752.

Neves, S.P., Bruguier, O., Vauchez, A., Bosch, D., Rangel da Silva, J. M., Mariano, G., 2006. Timing of crust formation, deposition of supracrustal sequences, and Transamazonian and Brasiliano metamorphism in the East Pernambuco belt (Borborema province, NE Brazil): Implications for western Gondwana assembly. Precambrian Research 149, 197-216.

Nikishin, A.M., Korotaev, M.V., Ershov, A.V., Brunet, M.F., 2003. The Black Sea Basin: Tectonic history and Neogene-Quaternary rapid subsidence modelling. Sedimentary Geology 156, 149-168.

Oberhänsli, R., Candan, O., Bousquet, R., Rimmele, G., Okay, A., Goff, J., 2010. Alpine HP evolution of the eastern Bitlis complex, SE Turkey. In: Sosson, M., Kaymakci, N., Stephanson, R., Bergarat, F., Storatchenoko, V., (eds.), Sedimentary Basin Tectonics from

the Black Sea and Caucasus to the Arabian Platform. Geological Society, London, Special Publication 340, 461-483.

Obernänsli, R., Koralay, E., Candan, O., Pourteau, A., Bousquet, R., 2014. Late Cretaceous ecologitic high-pressure relics in the Bitlis Massif. Geodinamica Acta (ahead-of-print), 1-17.

Perchuk, L.L., Lavrent'eva, I.V., 1983. Experimental investigation of exchange equilibria in the system cordierite-garnet-biotite. In: Saxena, S.K. (ed) Kinetics and Equilibrium in Mineral Reactions, Advances in Physical Geochemistry 3, 199-239.

Reddy, S.M., Potts, G.J., 1999. Constraining absolute deformation ages: the relationship between deformation mechanisms and isotope systematics. Journal of Structural Geology 21, 1255-1265.

Ricou, L.E., 1994. Tethys reconstructed: plates, continental fragments and their boundaries since 260 Ma from Central America to South-eastern Asia. Geodinamica Acta 7, 169-218.

Robertson, A.H., 2002. Overview of the genesis and emplacement of Mesozoic ophiolites in the Eastern Mediterranean Tethyan region. Lithos 65, 1-67.

Robertson, A.H., Mountrakis, D., 2006. Tectonic development of the Eastern Mediterranean region: an introduction. Geological Society, London, Special Publications 260, 1-9.

Robertson, A.H., Parlak, O., Ustaömer, T., 2012. Overview of the Palaeozoic-Neogene evolution of Neotethys in the Eastern Mediterranean region (southern Turkey, Cyprus, Syria). Petroleum Geosciences 18, 381-404.

Rolland, Y., Billo, S., Corsini, M., Sosson, M., Galoyan., G., 2009a. Blueschists of the Amassia-Stepanavan Suture Zone (Armenia): linking Tethys subduction history from E-Turkey to W-Iran. International Journal of Earth Sciences 98, 533-550.

Rolland, Y., Galoyan, G., Bosch, D., Sosson, M., Corsini, M., Fornari, M., Verati, C., 2009b. Jurassic back-arc and Cretaceous hot-spot series in the Armenian ophiolites - Implications for the obduction process. Lithos 112, 163-187.

Rolland, Y., Galoyan, G., Sosson, M., Melkonian, R., Avagyan, A., 2010. The Armenian ophiolite: Insights for Jurassic back-arc formation, lower Cretaceous hot spot magmatism and upper Cretaceous obduction over the South Armenian block. Geological Society, London, Special Publications 340, 353–382.

Rolland, Y., Sosson, M., Adamia, Sh., Sadradze, N., 2011. Prolonged Variscan to Alpine history of an active Eurasian margin (Georgia, Armenia) revealed by 40Ar/39Ar dating. Gondwana Research 20, 798-815.

Rolland, Y., Perincek, D., Kaymakci, N., Sosson, M., Barrier, E., Avagyan, A., 2012. Evidence for 80–75Ma subduction jump during Anatolide–Tauride–Armenian block accretion and 48Ma Arabia–Eurasia collision in Lesser Caucasus–East Anatolia. Journal of Geodynamics 56, 76-85.

Sanchez, G., Rolland, Y., Schneider, J., Corsini, M., Oliot, E., Goncalves, P., Verati, C., Lardeaux, J.-M., Marquer, D., 2011. Dating low-temperature deformation by 40Ar/39Ar on white mica, insights from the Argentera-Mercantour Massif (SW Alps), Lithos 125, 521-536.

Şengör, A.M.C., Yılmaz, Y., 1981. Tethyan evolution of Turkey: A plate tectonic approach. Tectonophysics 75, 181-241.

Şengör, A.M.C., Altıner, D., Cin, A., Ustaömer, T., Hsü, K.J., 1988. Origin and assembly of the Tethyside orogenic collage at the expense of Gondwana-Land. In: Audley-Charles, M.G., Hallam, A. (Eds.), Gondwana and Tethys. Geological Society, London, Special Publications 37, 119-181.

Shengelia, D.M., Tsutsunava, T.N., Shubitidze, L.G., 2006. New data on the structure, composition and regional metamorphism of the Tsakhkunyats and Akhum-Asrikchai massifs, the Lesser Caucasus. Doklady Earth Sciences 409A, 900-904.

Sosson, M., Rolland, Y., Müller, C., Danelian, T., Melkonyan, R., Kekelia, S., Adamia, S., Babazadeh, V., Kangarli, T., Avagyan, A., Galoyan, G., Mosar, J., 2010. Subductions, obduction and collision in the Lesser Caucasus (Armenia, Azerbaijan, Georgia), new insights. In: Sosson, M., Kaymakci, N., Stephenson, R., Bergerat, F. and Starostenko, V. (eds) Sedimentary Basin Tectonics from the Black Sea and Caucasus to the Arabian Platform. Geological Society, London, Special Publications 340, 329-352.

Soto, J.I., Platt, J.P., 1999. Petrological and structural evolution of high-grade metamorphicrocks from the floor of the Alboran Sea Basin, Western Mediterranean. Journal of Petrology 40, 21-60.

Spear, F.S., 1988. Metamorphic fractional crystallization and internal metasomatism by diffusional homogeneisation of zoned garnets. Contributions to Mineralogy and Petrology 98, 507-517.

Spear, F.S., 1993. Metamorphic Phase Equilibria and Pressure-Temperature-Time Paths. Monograph 1, Mineralogical Society of America, Chantilly, Virginia.

Stampfli, G.M., Borel, G.D., Cavazza, W., Mosar, J., Ziegler, P. A., 2001. Palaeotectonic and palaeogeographic evolution of the western Tethys and PeriTethyan domain (IGCP Project 369). Episodes 24, 222-228.

Stampfli, G.M., Borel, G.D., 2002. A plate tectonic model for the Paleozoic and Mesozoic contrained by dynamic plate boundaries and restored synthetic isochrones. Earth and Planetary Science Letters 196, 17-33.

Steiger, R. H., Jäger, E., 1977. Subcomission on geochronology: convention of the use of decay constants in geo- and cosmochronology. Earth and Planetary Science Letters 36, 359-362.

Sun, S.S., McDonough, W.F., 1989. Chemical and isotopic systematic of oceanic basalts: implications for mantle composition and processes. In: Saudners A.D. and Norry, M.J. (eds) Magmatism in Ocean Basins. Geological Society, London, Special Publications 42, 313-345.

Topuz G., Göçmengil G., Rolland Y., Çelik Ö. F., Zack T., Schmitt A. K., 2013. Jurassic accretionary complex and ophiolite from northeast Turkey: No evidence for the Cimmerian continent. Geology 41, 255-258.

Vance, D., Müller, W., Villa, I., 2003. Geochronology: linking the isotopic record with petrology and textures – an introduction. Geological Society of London, Special Publications 220, 1-24.

Villa, I.M., Grobety, B., Kelley, S.P., Trigila, R., Wieler, R., 1996. Assessing Ar transport in the McClure Mountains hornblende. Contributions to Mineralogy and Petrology 126, 67-80.

Villa, I.M., 1998. Isotopic closure. Terra Nova 10, 42–47.

Wiedenbeck, M., Allé, P., Corfu, F., Griffin, W., Meier, M., 1995. Three natural zircon standards for U-Th-Pb, Lu-Hf, trace element and REE analyses. Geostandards Newsletter 19, 1-23.

Yılmaz, Y., 1993. New evidence and model on the evolution of the southeast Anatolian orogen. Geological Society of America Bulletin 105, 251-271.

Yilmaz, A., Adamia, S., Chabukiani, A., Chkhotua, T., Erdoğan, K., Tuzcu, S., Karabiyikoğlu, M., 2000. Structural correlation of the southern Transcaucasus (Georgia)-Eastern Pontides (Turkey). Geological Society, London, Special Publications 173, 171-182.

Zakariadze, G.S., Knipper, A.L., Bibikova, E.V., Silantiev, S.A., Zlobin, S.K., Gracheva, T.V., … Kolesov, T. M., 1990. The setting and age of the plutonic part of the NE Sevan ophiolite complex. Izvestia NAS USSR, Geological 3, 17–30 (in Russian).

Zakariadze, G.S., Dilek, Y., Bogdanovsky, O.G., Karpenko, S.F., Vishnevskaya, V.S., Solov'eva, N.V., 2005. Age limits of the Lesser Caucasus paleooceanic allochtone. Active Tectonics of the Agean region. 15–18 June Istanbul, Turkey.

Tables

Location	Sample	Latitude	Longitude	Elevation (m)	Age	Nannofossil assemblage
Bijni	ARC-10-M1	N 40.45628°	E 44.64319°	1545	Paleocene	*Coccolithus pelagicus, Ericsonia subpertusa*
	ARC-10-M2	N 40.45734°	E 44.64434°	1595	Late Paleocene NP 6	*Coccolithus pelagicus, Fasciculithus tympaniformis, Heliolithus kleinpellii*
	ARC-10-M3	N 40.46090°	E 44..64457°	1675	Late Paleocene NP 5	*Coccolithus pelagicus, Ericsonia subpertusa, Fasciculithus tympaniformis*
	ARC-10-M4	N 40.46215°	E 44.64554°	1690	Early Paleocene NP 3	*Chiasmolithus danicus, Coccolithus pelagicus, Cruciplacolithus tenuis, Ericsonia subpertusa*
	ARC-10-M5	N 40.46232°	E 44.64590°	1685	Late Maastrichtian	*Micula murus, Micula staurophora, Watznaueria barnesae*
	ARC-10-M6	N 40.49014°	E 44.65865°	2020	Early Maastrichtian	*Micula staurophora, Quadrum gothicum, Watznaueria barnesae*
Aghveran	ARC-10-M7	N 40.53581°	E 44.52616°	2370	Paleocene inférieur ?	*sporatic nannofossils*

Table 13 - Nannofossil dating with (WGS84) GPS locations.

Analysis N°	#41	#43	#45	#46	#47	#48	#49	#50	#55
Mineral type	Garnet (core)	Garnet (rim)	Chlorite	Muscovite	Kyanite	Staurolite	K-Feldspar	Andalusite	Biotite
Na_2O	0.020	0.031	0.043	1.507	0.016	0.032	0.302	0.000	0.063
MgO	1.318	1.424	12.397	0.405	0.010	0.907	0.154	0.040	7.846
K_2O	0.000	0.004	0.031	8.892	0.027	0.025	10.517	0.029	9.260
CaO	4.854	4.826	0.018	0.074	0.031	0.052	0.053	0.035	0.066
TiO_2	0.130	0.085	0.115	0.365	0.000	0.555	0.128	0.100	1.686
FeO	28.687	29.112	27.335	1.788	0.271	10.691	0.634	0.861	20.898
MnO	7.944	7.170	0.409	0.000	0.000	0.590	0.003	0.003	0.217
SiO_2	37.243	36.706	24.722	46.474	36.856	27.892	45.317	36.471	34.214
Al_2O_3	20.810	20.580	21.590	36.252	62.965	53.414	37.499	62.332	19.569
Total	101.009	99.941	86.666	95.762	100.180	94.162	94.612	99.874	93.821

Obtained using Cameca Camebax SX100 electron microprobe of the Blaise Pascal University in Clermont-Ferrand. Natural samples were used as standards.

Table 14 - Electron microprobe analyses of the representative minerals of micaschist sample AR-03-62M.

Sample	Pb*	Th	U	Th/U	$^{208}Pb/^{206}Pb$	$^{207}Pb/^{206}Pb$	±	$^{207}Pb/^{235}U$	±	$^{206}Pb/^{238}U$	±	Rho	Apparent ages (Ma)				Terra Wasserburg			
	(ppm)	(ppm)	(ppm)				(1s)		(1s)		(1s)		$^{206}Pb/^{238}U$	± (1s)	$^{207}Pb/^{206}Pb$	± (1s)	$^{238}U/^{206}Pb$	±% (1s)	$^{207}Pb/^{206}Pb$	±% (1s)
ARL33																				
#1-1	5.3	131	199	0.66	0.215	0.0494	0.0006	0.1636	0.0027	0.0240	0.0002	0.61	152.9	1.5	168.7	29.9	41.67	1.0	0.0494	1.3
#1-2	5.2	122	192	0.64	0.196	0.0517	0.0008	0.1740	0.0029	0.0244	0.0002	0.48	155.5	1.3	272.2	33.5	40.97	0.8	0.0517	1.5
#1-3	2.8	49	103	0.48	0.195	0.0488	0.0012	0.1637	0.0041	0.0243	0.0002	0.34	155.0	1.3	137.5	54.8	41.10	0.9	0.0488	2.4
#2-2	7.5	217	285	0.76	0.229	0.0502	0.0005	0.1659	0.0022	0.0239	0.0002	0.68	152.5	1.4	206.5	22.8	41.76	0.9	0.0502	1.0
#2-3	5.9	145	235	0.62	0.197	0.0501	0.0005	0.1633	0.0024	0.0236	0.0002	0.66	150.6	1.4	199.6	25.2	42.30	1.0	0.0501	1.1
#3-1	3.7	75	142	0.52	0.163	0.0495	0.0007	0.1669	0.0026	0.0244	0.0002	0.50	155.6	1.2	173.0	31.7	40.93	0.8	0.0495	1.4
#3-2	6.9	194	255	0.76	0.239	0.0505	0.0005	0.1684	0.0026	0.0242	0.0003	0.76	154.1	1.8	217.3	23.5	41.34	1.2	0.0505	1.0
#3-3	5.9	128	239	0.54	0.164	0.0491	0.0005	0.1616	0.0023	0.0239	0.0002	0.64	152.1	1.4	150.9	25.3	41.87	0.9	0.0491	1.1
#3-4	11.1	366	413	0.89	0.264	0.0494	0.0005	0.1622	0.0019	0.0238	0.0002	0.60	151.7	1.1	166.2	21.7	41.99	0.7	0.0494	0.9
#3-5	12.8	397	467	0.85	0.265	0.0503	0.0004	0.1683	0.0023	0.0243	0.0003	0.82	154.5	1.7	209.5	17.7	41.22	1.1	0.0503	0.8
#4-1	9.0	292	326	0.89	0.272	0.0496	0.0004	0.1633	0.0020	0.0239	0.0002	0.79	152.1	1.4	177.0	17.0	41.88	1.0	0.0496	0.7
#4-2	5.0	148	182	0.81	0.255	0.0499	0.0006	0.1685	0.0034	0.0245	0.0004	0.77	156.0	2.4	190.6	29.8	40.84	1.6	0.0499	1.3
#4-3	12.5	387	456	0.85	0.262	0.0501	0.0006	0.1672	0.0027	0.0242	0.0003	0.69	154.1	1.7	200.5	26.8	41.33	1.1	0.0501	1.2

Table 15 - Detailed U-Pb results for dated zircons.

Step	Laser power (mW) / Vacuum oven heat (°C)	36Ar(a)	37Ar(ca)	38Ar(cl)	39Ar(k)	40Ar(r)	Age ± 2σ (Ma)	40Ar(r) (%)	39Ar(k) (%)	K/Ca ± 2σ
Amphibole AR-03-64, J = 0.02, plateau age: 151.65 ± 1.9 Ma (2 σ) (41.40 % 39Ar), isochron age: 152.38 ± 2.35 Ma (2σ) (MSWD: 0.09)										
1	650 °C	0.00123	0.00283	0.00673	0.00504	0.01035	62.33 ± 173.03	2.74	0.25	0.29 ± 0.15
2	750 °C	0.00271	0.01995	0.00158	0.07269	0.15164	63.24 ± 26.07	15.73	3.67	0.59 ± 0.08
3	850 °C	0.00476	0.00825	0.00990	0.36624	1.82309	147.38 ± 9.08	55.99	18.51	7.17 ± 1.52
4	900 °C	0.00029	0.00324	0.00495	0.18035	0.92170	151.15 ± 3.23	90.80	9.11	9.01 ± 2.67
5	950 °C	0.00021	0.00344	0.00423	0.14833	0.76214	151.94 ± 3.20	92.06	7.49	6.97 ± 2.28
6	1000 °C	0.00011	0.00253	0.00348	0.12446	0.64130	152.35 ± 3.12	94.75	6.29	7.95 ± 3.38
7	1050 °C	0.00022	0.00834	0.00368	0.13047	0.69243	156.72 ± 3.35	90.85	6.59	2.53 ± 0.50
8	1100 °C	0.00012	0.00947	0.00381	0.13265	0.73038	162.34 ± 3.28	94.75	6.70	2.26 ± 0.38
9	1150 °C	0.00008	0.01069	0.00417	0.14797	0.80458	160.41 ± 3.19	96.58	7.48	2.24 ± 0.33
10	1200 °C	0.00010	0.01633	0.00538	0.19481	1.03623	157.06 ± 3.09	96.67	9.84	1.93 ± 0.25
11	1250 °C	0.00020	0.02146	0.00798	0.28702	1.50765	155.18 ± 3.06	95.75	14.50	2.16 ± 0.29
12	1300 °C	0.00024	0.02037	0.00390	0.13248	0.69367	154.71 ± 3.33	90.32	6.69	1.05 ± 0.12
13	1350 °C	0.00001	0.00287	0.00057	0.01832	0.09709	156.52 ± 5.30	96.21	0.93	1.03 ± 0.54
14	1500 °C	0.00003	0.00348	0.00116	0.03830	0.20220	155.94 ± 4.44	94.69	1.94	1.78 ± 0.56
Muscovite AR-04-64, J = 0.02, plateau age: 153.10 ± 2.04 Ma (2 σ) (100 % 39Ar), isochron age: 154.18 ± 1.76 Ma (2σ) (MSWD: 1.78)										
1	351 mW	0.00080	0.00017	0.00028	0.19339	0.97593	149.25 ± 4.07	79.88	3.84	188 ± 82
2	358 mW	0.00023	0.00000	0.00224	1.12931	5.96882	156.02 ± 3.01	98.29	22.44	84237 ± 2626024
3	362 mW	0.00003	0.00000	0.00092	0.47163	2.48498	155.56 ± 3.00	99.12	9.37	19981 ± 372942
4	365 mW	0.00003	0.00007	0.00049	0.28852	1.50421	153.99 ± 3.02	98.83	5.73	688 ± 765
5	373 mW	0.00014	0.00018	0.00105	0.58196	2.95837	150.31 ± 2.90	98.04	11.56	534 ± 253
6	381 mW	0.00006	0.00019	0.00190	1.20678	6.22702	152.48 ± 2.93	99.14	23.98	1051 ± 511
7	385 mW	0.00001	0.00006	0.00025	0.13410	0.68599	151.22 ± 3.22	98.79	2.66	386 ± 459
8	390 mW	0.00000	0.00003	0.00012	0.05825	0.29848	151.46 ± 3.90	99.25	1.16	296 ± 443
9	402 mW	0.00002	0.00005	0.00013	0.07442	0.36937	146.90 ± 3.42	98.15	1.48	246 ± 321
10	422 mW	0.00000	0.00001	0.00034	0.17481	0.87777	148.54 ± 2.95	99.52	3.47	3023 ± 22691
11	459 mW	0.00001	0.00001	0.00038	0.21851	1.13263	153.14 ± 3.00	99.13	4.34	3251 ± 16712
12	512 mW	0.00001	0.00004	0.00063	0.28821	1.54483	158.14 ± 3.10	99.24	5.73	1119 ± 2062
13	580 mW	0.00001	0.00000	0.00025	0.11860	0.63418	157.78 ± 3.36	99.00	2.36	56745 ± 19563193
14	800 mW	0.00000	0.00009	0.00024	0.09413	0.50408	157.99 ± 3.69	99.69	1.87	173 ± 200
Muscovite AR-04-62B, J = 0.02, plateau age: 148.19 ± 2.95 Ma (2 σ) (96.58 % 39Ar), isochron age: 150.23 ± 2.76 Ma (2σ) (MSWD: 7.19)										
1	650 °C	0.00046	0.00239	0.00934	0.00599	0.01069	54.27 ± 57.66	7.18	0.19	0.4 ± 0.3
2	750 °C	0.00031	0.00514	0.00055	0.02373	0.08045	101.67 ± 10.18	46.40	0.74	0.7 ± 0.3
3	850 °C	0.00020	0.00259	0.00077	0.07998	0.36286	134.83 ± 3.47	85.35	2.49	5.0 ± 2.6
4	900 °C	0.00017	0.00210	0.00042	0.14533	0.74505	151.64 ± 3.12	93.01	4.53	11.2 ± 8.0
5	950 °C	0.00012	0.00285	0.00115	0.55264	2.89219	154.67 ± 2.97	98.26	17.23	31.3 ± 17.9
6	1000 °C	0.00007	0.00261	0.00106	0.57619	2.94794	151.35 ± 2.91	98.72	17.97	35.7 ± 15.5
7	1025 °C	0.00002	0.00213	0.00054	0.26783	1.33158	147.24 ± 2.85	98.91	8.35	20.3 ± 11.7
8	1050 °C	0.00003	0.00233	0.00036	0.19023	0.90977	141.85 ± 2.77	98.32	5.93	13.2 ± 7.9
9	1075 °C	0.00002	0.00075	0.00030	0.14068	0.67134	141.55 ± 2.89	98.34	4.39	30.1 ± 40.4
10	1115 °C	0.00003	0.00107	0.00038	0.16127	0.78277	143.88 ± 2.86	98.31	5.03	24.3 ± 30.0
11	1225 °C	0.00010	0.00375	0.00116	0.40446	1.99744	146.30 ± 2.84	97.96	12.61	17.4 ± 8.1
12	1325 °C	0.00005	0.00758	0.00143	0.55837	2.85451	151.23 ± 2.90	98.95	17.41	11.9 ± 2.4
13	1450 °C	0.00001	0.00130	0.00023	0.06088	0.31619	153.54 ± 3.48	98.74	1.90	7.6 ± 5.8
14	1550 °C	0.00001	0.00140	0.00009	0.03944	0.20277	152.05 ± 3.88	98.29	1.23	4.5 ± 3.7

Table 16 - Detailed $^{40}Ar/^{39}Ar$ results for dated amphibole, muscovites and biotite.

Step	Laser power (mW) / Vacuum oven heat (°C)	36Ar(a)	37Ar(ca)	38Ar(cl)	39Ar(k)	40Ar(r)	Age ± 2σ (Ma)	40Ar(r) (%)	39Ar(k) (%)	K/Ca ± 2σ
Muscovite AR-03-62M, J = 0.02, plateau age: 136.95 ± 3.68 Ma (2 σ) (85.09 % 39Ar), isochron age: 148.72 ± 4.57 Ma (2σ) (MSWD: 2.47)										
1	355 mW	0.00046	0.00001	0.00000	0.16806	0.60420	104.72 ± 2.85	80.89	4.96	3284 ± 41511
2	365 mW	0.00022	0.00003	0.00000	0.33738	1.54717	132.54 ± 2.62	95.36	9.95	1866 ± 6482
3	373 mW	0.00006	0.00001	0.00000	0.26450	1.25234	136.68 ± 2.66	97.94	7.80	3676 ± 21064
4	379 mW	0.00006	0.00001	0.00000	0.40677	1.97119	139.77 ± 2.73	98.43	12.00	4584 ± 22364
5	384 mW	0.00007	0.00005	0.00000	0.42518	2.01771	136.98 ± 2.67	98.33	12.54	1408 ± 2612
6	387 mW	0.00003	0.00005	0.00000	0.15721	0.72517	133.28 ± 2.82	98.34	4.64	548 ± 1069
7	398 mW	0.00007	0.00002	0.00000	0.22137	1.00356	131.08 ± 2.59	97.25	6.53	2106 ± 11171
8	416 mW	0.00004	0.00003	0.00000	0.11215	0.50944	131.32 ± 2.85	96.88	3.31	608 ± 2351
9	450 mW	0.00012	0.00003	0.00000	0.27512	1.27680	134.07 ± 2.69	96.61	8.11	1516 ± 4209
10	510 mW	0.00005	0.00005	0.00000	0.42165	2.10033	143.52 ± 2.83	98.68	12.43	1452 ± 2864
11	572 mW	0.00000	0.00005	0.00000	0.21450	1.09644	147.13 ± 2.95	99.41	6.33	663 ± 1024
12	800 mW	0.00001	0.00010	0.00000	0.38706	1.98778	147.79 ± 2.90	99.32	11.41	653 ± 740
Muscovite AR-04-64, J = 0.02, plateau age: 142.24 ± 3.57 Ma (2 σ) (89.79 % 39Ar), isochron age: 139.40 ± 4.48 Ma (2σ) (MSWD: 9.04)										
1	650 °C	0.00032	0.00022	0.00594	0.00446	0.00709	48.40 ± 57.32	6.92	0.20	3 ± 18
2	750 °C	0.00021	0.00127	0.00037	0.01570	0.04763	91.27 ± 11.54	43.00	0.70	2 ± 3
3	850 °C	0.00010	0.00210	0.00012	0.06191	0.26333	126.70 ± 3.10	89.23	2.77	5 ± 7
4	900 °C	0.00006	0.00205	0.00010	0.06399	0.28402	132.02 ± 2.86	93.28	2.86	5 ± 7
5	950 °C	0.00006	0.00264	0.00018	0.08239	0.38058	137.20 ± 2.95	94.73	3.68	5 ± 6
6	1000 °C	0.00011	0.00042	0.00051	0.31383	1.54507	145.88 ± 2.83	97.34	14.03	119 ± 408
7	1050 °C	0.00007	0.00147	0.00069	0.40458	1.92887	141.44 ± 2.73	98.34	18.08	45 ± 38
8	1100 °C	0.00006	0.00045	0.00037	0.20804	0.94391	134.85 ± 2.67	97.50	9.30	75 ± 186
9	1150 °C	0.00001	0.00063	0.00021	0.13283	0.61445	137.39 ± 2.77	98.70	5.94	34 ± 58
10	1200 °C	0.00001	0.00060	0.00033	0.17168	0.81080	140.16 ± 2.77	98.84	7.67	46 ± 94
11	1250 °C	0.00003	0.00018	0.00031	0.19920	0.95859	142.71 ± 2.83	98.34	8.90	179 ± 1095
12	1300 °C	0.00007	0.00078	0.00113	0.52866	2.66361	149.15 ± 2.87	98.60	23.63	110 ± 185
13	1400 °C	0.00002	0.00046	0.00011	0.03439	0.17455	150.19 ± 4.75	95.93	1.54	12 ± 22
14	1500 °C	0.00003	0.00075	0.00006	0.01572	0.07978	150.21 ± 4.75	89.95	0.70	3 ± 3
Biotite AR-04-62B, J = 0.02, plateau age: 123.28 ± 1.57 Ma (2 σ) (95.42 % 39Ar), isochron age: 120.69 ± 4.44 Ma (2σ) (MSWD: 1.34)										
1	650 °C	0.00486	0.00043	0.00392	0.00500	0.01297	81.84 ± 733.48	0.90	0.23	1.9 ± 4.5
2	750 °C	0.02637	0.00463	0.00451	0.09610	0.39756	123.32 ± 184.81	4.81	4.36	3.4 ± 1.1
3	850 °C	0.00918	0.00383	0.03357	0.75035	3.12505	124.13 ± 8.60	53.07	34.01	31.6 ± 25.1
4	900 °C	0.00149	0.00003	0.01332	0.29801	1.25823	125.78 ± 4.18	73.47	13.51	1479.7 ± 139078.8
5	950 °C	0.00055	0.00092	0.00608	0.13550	0.57696	126.81 ± 3.76	77.55	6.14	23.9 ± 78.9
6	1000 °C	0.00041	0.00205	0.00483	0.10839	0.45204	124.30 ± 3.61	78.40	4.91	8.5 ± 4.9
7	1050 °C	0.00049	0.00179	0.00529	0.12215	0.50407	123.03 ± 3.66	77.05	5.54	11.0 ± 10.6
8	1100 °C	0.00042	0.00138	0.00542	0.12054	0.49551	122.57 ± 3.55	79.44	5.46	14.1 ± 14.9
9	1150 °C	0.00038	0.00054	0.00627	0.13760	0.56340	122.10 ± 3.14	82.82	6.24	40.9 ± 94.7
10	1200 °C	0.00033	0.00052	0.00462	0.10372	0.41384	119.09 ± 3.45	80.06	4.70	32.3 ± 63.8
11	1300 °C	0.00140	0.00344	0.01304	0.29139	1.19415	122.21 ± 4.05	73.69	13.21	13.7 ± 4.8
12	1400 °C	0.00011	0.00156	0.00147	0.03275	0.13915	126.54 ± 5.13	80.58	1.48	3.4 ± 2.1
13	1550 °C	0.00002	0.00012	0.00025	0.00469	0.01976	125.46 ± 18.46	76.40	0.21	6.4 ± 71.4

Table 16 - Detailed $^{40}Ar/^{39}Ar$ results for dated amphibole, muscovites and biotite (continued).

Sample	Lithology	Coordinates		Age (2σ)	Mineral	Method
ARL-10-33	Granodiorite	40° 30' 27.36"N	44° 34' 20.57"E	*150.5 ± 2.9 Ma*	(zircon)	U/Pb
AR-03-64	Granodiorite (amphibole)	40°31'6.22"N	44°33'40.62"E	*151.7 ± 1.9 Ma*	(amphibole)	Ar/Ar furnace
AR04-64	Leucogranite (migmatite)	40°28'11.58"N	44°38'38.98"E	*154.2 ± 1.8 Ma* (1)	(muscovite)	Ar/Ar laser
				142.2 ± 3.6 Ma (1)	(muscovite)	Ar/Ar furnace
AR-04-62b	orthogneiss ("Protérozoic" basement)	40°28'13.43"N	44°38'38.02"E	*148.2 ± 3 Ma* (1)	(muscovite)	Ar/Ar furnace
				123.3 ± 1.6 Ma	(biotite)	Ar/Ar furnace
AR-03-62M	micaschist ("Proterozoic basement")	40°28'44.17"N	44°40'30.51"E	*≈ 148 Ma* (1)	(Muscovite)	Ar/Ar laser

(1): minimum age

Table 17 - Summary of $^{40}Ar/^{39}Ar$ and U-Pb dating results with (WGS84) GPS locations.

location	**Tsaghkuniats granodiorite**		
Sample	**ARL-10-33**		
SiO_2	63.24		
Al_2O_3	16.14		
Fe_2O_3	4.09		
MnO	0.04		
MgO	3.2		
CaO	4.47		
Na_2O	4.29		
K_2O	1.55		
TiO_2	0.66		
P_2O_5	0.25		
PF	1.79		
Total	99.7		
Na_2O+K_2O	5.84		
$F=0.8998Fe_2O_3$	3.68		
FeOT/MgO	1.15		
Na_2O+K_2O-CaO	1.36		
Mg#	46.49		
Rb	29.51	Th	8.5
Sr	958.8	U	1.61
Y	10.8	As	< L.D.
Zr	136.73	Be	1.274
Nb	11.66	Bi	< L.D.
Cs	1.59	Cd	< L.D.
Ba	411.37	Co	13.48
La	29.29	Cr	67.83
Ce	55.43	Cu	< L.D.
Pr	5.81	Ga	19.01
Nd	22.41	Ge	1.01
Sm	3.72	In	< L.D.
Eu	1.14	Mo	0.389
Gd	2.87	Ni	60.36
Tb	0.36	Sb	< L.D.
Dy	2.04	Sn	0.981
Ho	0.36	V	85.65
Er	1.02	W	0.29
Tm	0.14	Zn	28.78
Yb	0.86		
Lu	0.14	(La/Yb) N	23.15
Hf	2.85	(La /Sm) N	4.85
Ta	0.8	Ce/Pb	9.03
Pb	6.14	Nb/U	7.23

Table 18 - Major, trace and rare earth element contents of granodiorite pluton sample ARL10-33.

Chapitre 6* - *Histoire de la branche nord de Néotéthys avant son obduction.

« Une théorie ne ressemble pas plus à un fait qu'une photographie ne ressemble à son modèle. »

Edgar Watson Howe

VI.1 Article 5 – From ocean crust geneis to obduction initiation: history of the northern branch of Neotethys prior to the Late Cretaceous obduction event in NE Anatolian and Lesser Caucasus regions

Au regard des nouvelles données géologiques obtenues dans cette thèse, nous proposons une synthèse justifiant une configuration tectonique réaliste du contexte de pré-obduction dans la région du Petit Caucase-NE Anatolie. Ce travail de synthèse est rendu nécessaire pour bien fixer le cadre d'une modélisation numérique de l'obduction.

L'évolution de la branche nord de la Néotéthys, depuis sa genèse jusqu'à son obduction partielle, peut être déduite depuis les études structurales, stratigraphiques, géochimiques et géochronologiques relatives aux ophiolites préservées, au volcanisme de la marge eurasienne au nord, ainsi qu'aux roches métamorphiques en position basale sous l'ophiolite (la semelle) et celles appartenant à la marge chevauchée par la nappe ophiolitique au sud. Ces études convergent vers un modèle dans lequel une seule nappe ophiolitique, d'âge Jurassique moyen à Crétacé inférieur, se met en place au milieu du Crétacé supérieur, 90~83 Ma, sur le SAB-TAP (Sokolov, 1977; Özgül & Turşucu, 1984; Bergougnan, 1987; De Wever *et al.,* 1987; Bozkuş, 1998; Harris *et al.,* 1994; Aktimur *et al.,* 1995; Chiari *et al.,* 1997; Okay & Tüysüz, 1999; Chiari *et al.,* 2000; Danelian *et al.,* 2000; 2008; 2012; 2014; Bill *et al.,* 2001; Bozkurt & Mittwede, 2001; Önen, 2003; Göncüoğlu *et al.,* 2006; Özen *et al.,* 2006; Galoyan *et al.,* 2007; 2009; Asatryan *et al.,* 2009; 2010; 2011; Galoyan, 2008; Gedik, 2008; Moix *et al.,* 2008; Rolland *et al.,* 2009a; 2009b; 2010; Sosson *et al.,* 2010; Çelik *et al.,* 2011; Robertson & Ustaömer, 2012; Aslan *et al*., 2011; Hässig *et al.,* 2013; 2014; Moix & Goričan 2013; Parlak *et al.,* 2013). Cette nappe ophiolitique, au sud de la zone de suture Izmir-Ankara-Refahiye-Amasia-Sevan-Akera, s'étendrait sur au moins 700 km de large et chevaucherait de 100 à 200 km le bloc continental SAB-TAP (Lordkipanidze *et al.,* 1989; Galoyan, 2008; Sosson *et al.,* 2010; Rolland *et al.,* 2011; Danelian *et al.,* 2012; Hässig *et al.,* 2013; 2014).

Les roches magmatiques et ultrabasiques composant cette nappe ont une géochimie qui indique une formation dans un contexte de SSZ à arrière-arc. Nous en déduisons donc l'existence d'une subduction intra-océanique pendant la formation de l'ophiolite. Comme nous l'avons vu précédemment, celle-ci se formerait dans un contexte de dorsale océanique lente

au sein d'un domaine océanique préexistant. Par ailleurs, au cours de la phase d'accrétion océanique, au Jurassique moyen, ce domaine océanique est également en subduction sous l'Eurasie au nord comme l'indique une forte activité volcanique sur cette marge. L'action combinée du retrait de panneau plongeant, (sous la subduction intra-océanique), et de la traction du panneau plongeant sous l'Eurasie au nord peut être considérée comme le moteur de cette ouverture.

Cependant, ce modèle souffre de l'absence d'un arc volcanique préservé qui aurait été formé au droit de la subduction intra-océanique. Nous expliquons cette absence par l'écaillage de cet arc et son incorporation dans la semelle d'obduction sous l'ophiolite au cours de sa mise place. On suppose que les roches métamorphiques de bas degré de Erzincan, les schistes bleus de Stepanavan et les amphibolites à grenat d'Amasia correspondent à cet arc volcanique manquant (Galoyan *et al.*, 2007; Rolland *et al.*, 2009a; Hässig *et al.*, en revision).

Des études récentes fournissent des arguments pour un modèle intégrant une subduction vers le sud sous la bordure nord de la SAB-TAP avec la mise en place d'intrusions de granodiorites caractéristiques de ce contexte au Jurassique inférieur (c. 160 Ma). La continuité à l'ouest de cette structure en NE Anatolie est incertaine, ainsi à ce stade nous présentons une alternative, un modèle sans subduction plongeant au sud et l'autre l'incluant. En effet, cette zone de subduction pourtant étayée en Arménie pourrait n'être qu'un 'détail' de bordure à l'échelle du bloc SAB-TAP (sauf si les travaux futurs indiquent le contraire).

Dans la quasi-totalité des affleurements ophiolitiques, deux suites magmatiques sont mises en évidence : (1) la croûte océanique tholéiitique surmontée de (2) coulées basaltiques ou tufs volcaniques avec des tendances alcalines. Les datations radio-chronologiques ainsi que bio-stratigraphiques montrent que la mise en place de cette deuxième suite se produit dans un environnement océanique avant l'obduction des ophiolites du Jurassique au début du Crétacé supérieur. Ces roches alcalines plus jeunes, surmontant le plancher océanique est un élément explicatif important de l'obduction. En effet, la modélisation numérique montre qu'il est nécessaire de réchauffer la lithosphère océanique pour qu'elle puisse être obduite sur la marge continentale. Les amphibolites à grenat, dans la semelle de la croûte océanique charriée, indiquent en effet des conditions PT particulièrement chaudes.

Afin de présenter une modélisation numérique dans la partie suivante, qui permettra de tester les différents paramètres entrant en jeu dans le processus d'obduction, nous fournissons ici un modèle conceptuel argumentant la configuration pré-obduction pour la mise en place de la nappe ophiolitique de la région du Petit Caucase-NE Anatolie.

Cette analyse fait l'objet d'une publication en révision à *Geological Society of London, Special Publications.*

From ocean crust genesis to obduction initiation: history of the northern branch of Neotethys prior to the Late Cretaceous obduction event in the NE Anatolian and Lesser Caucasus regions

M. HÄSSIG[1]*, Y. ROLLAND[1], M. SOSSON[1]

[1] Université de Nice Sophia Antipolis, UMR Géoazur, CNRS, IRD, Observatoire de la Côte d'Azur, 250 rue Albert Einstein, 06560, Sophia Antipolis - France.

Abstract

In light of new geological data, we argue for an innovative tectonic setup just prior to the Northern Neotethys obduction event in the NE Anatolian and Lesser Caucasus area. At several locations along the northern Neotethyan suture (Ankara-Erzincan-Amasia-Sevan-Akera suture zone), slivers of preserved unmetamorphozed relics of now disappeared northern branch of the Neotethys oceanic domain are obducted over the northern edge of the South Armenian Block (SAB) and Taurides-Anatolides Platform (TAP) margins to the south, occurring as scatted ophiolite bodies. Recent studies have shown that the ophiolitic bodies are formed of similar lithologies of Middle Jurassic ages (c. 175~165 Ma) all bearing LILE-enriched MORB chemical compositions. This extensive data base supports a model in which these ophiolites derive from a single obducted nappe. This model is equally backed by metamorphic PT-t paths of sole lithologies under the suture zone ophiolite outcrops. Equivalent paleontological datings of sediment deposits directly under or sealing the obduction contact, respectively of pre- and post- ophiolite emplacement, also comfort this model by temporally linking the distant ophiolite outcrops. General emplacement during early-Late Cretaceous times (c. 92~88 Ma) is well argued. A south dipping subduction under the SAB which shortly predates obduction has recently been proposed from the metamorphic and magmatic evolution preserved in the SAB crystalline basement, establishing a model incorporating divergent subductions at least from late-Middle Jurassic to Early Cretaceous times (c. 160~130). Emplacement of large alkaline pillow basalts directly on the oceanic crust is dated Early to mid-Cretaceous (c. 120~100 Ma). These datings argue for the existence of mantle heat flows, which may be responsible for decrease in density of the 80 Ma old oceanic lithosphere prior to its obduction onto SAB-TAP. Still, with these snapshots of the closing of this oceanic domain, 80 Ma of history between genesis and emplacement are poorly constrained. We undergo a detailed review of recent data to further constrain the structural and geodynamic evolution of this sector in order to define a tectonic setup just prior to the obduction event.

keywords : obduction; subduction; Neotethys; ophiolite

1.1 Introduction

The evolution of northern Neotethys can be deduced from the structural, geochemical and geochronological studies pertaining to preserved oceanic crust domains (ophiolites) obducted as in the Lesser Caucasus and in NE Anatolia and of the metamorphic rocks beneath these ophiolites. These studies yield key time and paleogeographic constraints for the evolution of Neotethyan basins from the East Mediterranean area to the NW Himalayan belt (Şengör & Yılmaz 1981; Ricou *et al.* 1985; Dercourt *et al.* 1986; Ricou 1994; Okay & Tüysüz 1999; Stampfli *et al.* 2001; Robertson 2004; Hafkenscheid *et al.* 2006; Barrier & Vrielynck 2008; Galoyan *et al.* 2009; Rolland *et al.* 2010; Sosson *et al.* 2010; Hässig *et al.* 2013). In this area, ophiolites are mainly of supra-subduction zone (SSZ) type. They provide chronological constraints related to oceanic crust formation by repetitive extension in a fore- and/or back-arc context, linked to the behavior of an intra-oceanic subduction. The study of these remarkable objects also contributes to the understanding of oceanic closure, particularly ophiolite emplacement processes. Actually, (i) the timing for ophiolite obductions in the Middle East subduction zones determined by these studies supports sub-simultaneous ophiolite obductions along the several subduction zones at c. 90 Ma (Galoyan 2008; Rolland *et al.* 2009a; Topuz *et al.* 2013; Aslan *et al*., 2011; Hässig *et al.* submitted). (ii) Further, the size of the reconstructed obducted ophiolitic nappe of the northern Neotethys segment (south of the Izmir-Ankara-Refahiye-Amasia-Sevan-Akera suture zone) is of at least 700 km in length and 100-200 km in width (Lordkipanidze *et al.* 1989; Galoyan 2008; Sosson *et al.* 2010; Rolland *et al.* 2011; Danelian *et al.* 2012; Hässig *et al.* 2013, 2014). When considering the distance between the suture zone and the ophiolitic front (at its present day location), a minimum of 100 km is needed to reach areas such as Vedi (Armenia) or Hınıs (Turkey) and up to 200 km are necessary to reach Khoy (Iran), zones where obduction fronts have been identified (Galoyan 2008; Rolland *et al.* 2009; Sahakyan *et al.* 2013). The studies converge to constrain a 90~83 Ma interval of time for obduction of a single ophiolitic nappe of Middle Jurassic to Early Cretaceous age (Sokolov 1977; Özgül & Turşucu 1984; Bergougnan 1987; De Wever *et al.* 1987; Bozkuş 1998; Harris *et al.* 1994; Aktimur *et al.* 1995; Chiari *et al.* 1997; Okay & Tüysüz 1999; Chiari *et al.* 2000; Danelian *et al.* 2000, 2008, 2012, 2014; Bill *et al.* 2001; Bozkurt & Mittwede 2001; Önen 2003; Göncüoğlu *et al.* 2006; Özen *et al.* 2006; Galoyan *et al.* 2007, 2009; Asatryan et al. 2009, 2010, 2011; Galoyan 2008; Gedik 2008; Moix *et al.* 2008; Rolland *et al.* 2009a, b, 2010; Sosson *et al.* 2010; Çelik *et al.* 2011; Robertson &

Ustaömer 2012; Aslan *et al*., 2013; Hässig *et al.* 2013, 2014; Moix & Goričan 2013; Parlak *et al.* 2013).

Given the ~80 Ma time span which separates the setup of oceanic lithosphere and the onset of the obduction of the ophiolitic nappe, it seems evident that multiple geodynamic events may have affected this domain. The emplacement of vast bodies of preserved (unmetamorphosed) oceanic crust lithologies of such an old (~80 Ma) and dense oceanic crust over large distances onto a continental crust is a puzzling geological problem. In this paper we propose a review and implement new findings to build a coherent tectonic setup of obduction initiation for the Northern Neotethys ophiolite belt.

1.2 Main tectonic units

As the results of the obduction and collision stages in the Lesser Caucasus and Eastern Anatolides (**Figures 62** and **63**), four main tectonic units are classically distinguished along the belt. We present them from north to south as following.

1.2.1 The Eurasian margin

In the Eurasian part of the Lesser Caucasus, the basement formations are quite similar to those known all along the Eurasian margin (Sosson *et al.* 2010 for a review). It corresponds to the variscan basement and it is covered by thick and mainly calc-alkaline volcanogenic series of Bajocian to Santonian age evidences the subduction of the Tethys oceanic domain (e.g. Adamia *et al.* 1981 for a review). During this period, an active continental margin domain called the Somkheto–Karabakh Island Arc characterized the northern Lesser Caucasus (Knipper 1975; Adamia *et al.* 1977, 1987; Ricou *et al.* 1986; Sosson *et al.* 2010). During the Early Cretaceous, tectonic erosion unroofed part of the plutonic unit of the active margin as result of significant uplift and denudation along the subduction zone (Sosson *et al.* 2010; Rolland *et al.* 2011). Subduction of more buoyant crustal domain, a spreading ridge of the back-arc basin or seamounts for example, could be responsible for such a change in the Eurasian active margin strain field as well as subsequent development of this unconformity (Rolland *et al.* 2011).

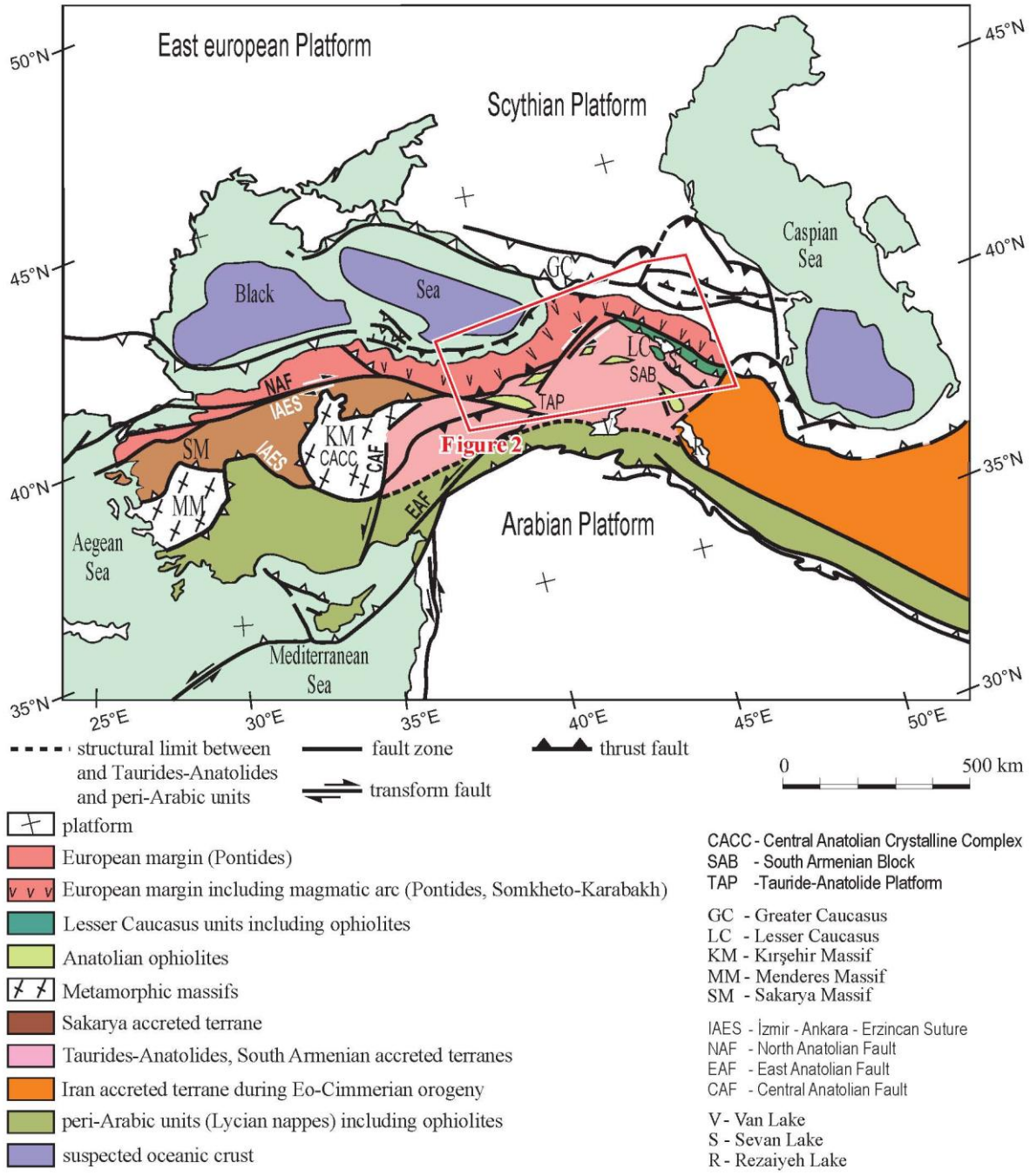

Figure 62 - Tectonic map of the Middle East–Caucasus area, with main blocks and suture zones, after Avagyan et al. (2005), modified. Location of Figure 63 is indicated.

The Eastern Pontides are interpreted as a part of the Sakarya Zone (Okay & Şahintürk 1997), and is the lateral equivalent of the Somkheto–Karabakh Island Arc. They also correspond to an active continental margin of Eurasia, which was formed as a result of northward subduction of Neotethys during the same time range spanning from Early Jurassic to Late Cretaceous (Şengör & Yılmaz 1981; Akıncı 1984; Okay & Şahintürk 1997). Onset of subduction is now well constrained. Both studies led in the Georgian side (Lesser Caucasus)

and the Turkish side (Pontides) show simultaneous calc-alkaline magmatic activity since the Early or Middle Jurassic (e.g. Adamia et al. 1981; Hess *et al.* 1995; Ustaömer & Robertson 2010; Nikishin *et al.* 2013; Ustaömer *et al.* 2013) although other ages were formerly proposed: Cenomanian–Turonian (Okay & Şahintürk 1997; Yılmaz *et al.* 1997) or Albian (Okay *et al.* 2006).

However, there is still a lack of consensus concerning the end of this subduction event in the Eastern Pontides/Eastern Anatolia region and onset of continental collision of TAP-SAB with the active margin of Eurasia. Proposals range from the end of the Late Cretaceous (Rolland *et al.* 2009, 2012) for the Lesser Caucasus, to the Paleocene (Okay & Şahintürk 1997) and the Eocene (Peccerillo & Taylor 1976; Şengör & Yılmaz 1981; Robinson *et al.* 1995; Yılmaz *et al.* 1997) for NE Anatolia.

Figure 63 - Structural map of the Lesser Caucasus-Eastern Pontides-Northeast Anatolides regions. Turkish zone modified from the 1:1 250 000 geological map of Turkey (MTA 2011); the Georgian-Armenian zone of the Caucasus after Sosson et al. (2010); the Iranian zone from Mederer (2013). The green shading represents proposed extent of the ophiolitic nappe.

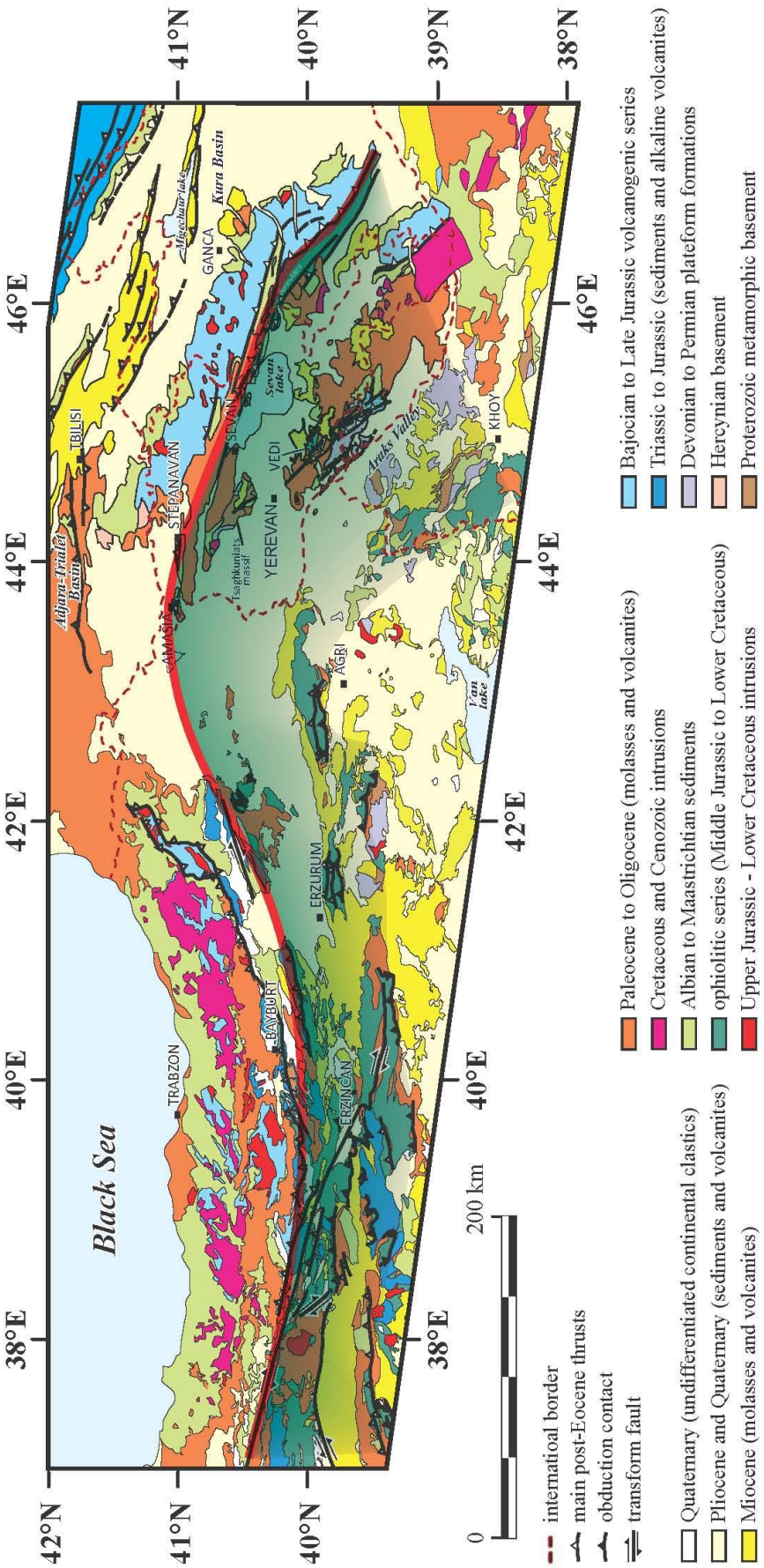
Black Sea
TRABZON
BAYBURT
ERZINCAN
ERZURUM
AMASIA
STEPANAVAN
TBILISI
GANCA
SEVAN
VEDI
YEREVAN
AGRI
KHOY
Adjara-Trialet Basin
Kura Basin
Migechaur lake
Sevan lake
Aruks Valley
Van lake
Tsaghkuniats massif
38°E
40°E
42°E
44°E
46°E
42°N
41°N
40°N
39°N
38°N
0
200 km
international border
main post-Eocene thrusts
obduction contact
transform fault
Quaternary (undifferentiated continental clastics)
Pliocene and Quaternary (sediments and volcanites)
Miocene (molasses and volcanites)
Paleocene to Oligocene (molasses and volcanites)
Cretaceous and Cenozoic intrusions
Albian to Maastrichtian sediments
ophiolitic series (Middle Jurassic to Lower Cretaceous)
Upper Jurassic - Lower Cretaceous intrusions
Bajocian to Late Jurassic volcanogenic series
Triassic to Jurassic (sediments and alkaline volcanites)
Devonian to Permian plateform formations
Hercynian basement
Proterozoic metamorphic basement

1.2.2 The ophiolites

In Armenia, this unit is mostly composed, of interbedded reef limestones embedded in volcanic tuffs and lava flows of with intercalations of Middle to Upper Jurassic radiolarites (c. 170~145 Ma; Danelian *et al.* 2007, 2008, 2010, 2012; Asatryan *et al.* 2010, 2012), serpentinized peridotites intruded by gabbros, scattered cross-cutting plagiogranites in extensional shear zones and local accumulations of pillow lava flows in scattered emission centers, all of Middle to Late Jurassic age (c. 180-150 Ma on gabbros and basalts; Galoyan *et al.* 2009; Rolland *et al.* 2010; Hässig *et al.* 2013). Similar ages have been obtained for radiochronological dating of ophiolite lithologies and biochronology farther west in the prolongation of this unit in NE Anatolia, along the Izmir-Ankara-Erzincan segment of the northern tethyan suture zone (Çelik *et al.* 2011; Danelian *et al.* 2012; Topuz *et al.* 2013, 2014; Hässig *et al.* 2014; Moix & Goričan 2013) (**Figure 64**). Topuz *et al.* (2014) dated the plagiogranites at 182 ± 3 Ma and 175 ± 4 Ma by U-Pb on zircon by the latter authors, and Topuz *et al.* (2013) dated the gabbros at 174 ± 4 Ma by $^{40}Ar/^{39}Ar$ on hornblende. This lithological association is typical of a slow-spreading oceanic ridge.

Figure 64 - Tectonic map of Mesozoic Ophiolites and ophiolitic mélanges from the Tethyan realm in Turkey and adjacent areas (modified after Stampfli, 2000) and representative geochronological data from rocks of the ophiolitic mélanges as well as from metamorphic soles (modified after Çelik et al., 2011). All data are from 40Ar/39Ar analyses except where stated otherwise: (1) Dilek *et al.* (1999); (2) Parlak and Delaloye (1999); (3) Çelik *et al.* (2006); (4) Chan *et al.* (2007); (5) Galoyan *et al.* (2009); (6) Önen (2003); (7) Harris *et al.* (1994); (8) Dimo-Lahitte *et al.* (2001); (9) Spray *et al.* (1984); (10) Roddick *et al.* (1979); (11) Koepke *et al.* (2002), K-Ar age data; (12) Hatzipanagiotou and Pe-Piper (1995), K-Ar age data; (13) Lamphere *et al.* (1975), K-Ar age data; (14) Rolland *et al.* (2010); (15) Çelik *et al.* (2011); (16) Hässig *et al.* (2013); (17) Topuz *et al.* (2013a); (18) Topuz *et al.* (2013b). Abbreviations, AO: Antalya Ophiolite; BHO: Beyşehir-Hoyran Ophiolite; EO: Eldivan ophiolite; KO: Kınık Ophiolite; LO: Lesvos Ophiolite; MO: Mersin Ophiolite; ORO: Orhaneli Ophiolite; PKO: Pozantı-Karsantı Ophiolite; SO: Sevan Ophiolite; mu: muscovite; hb: hornblende. (*) age data from gabbro. The bold numbers indicate positioning of radiolarian biostratigraphy reported in Figure 65. The red frame indicates the position of Figure 63.

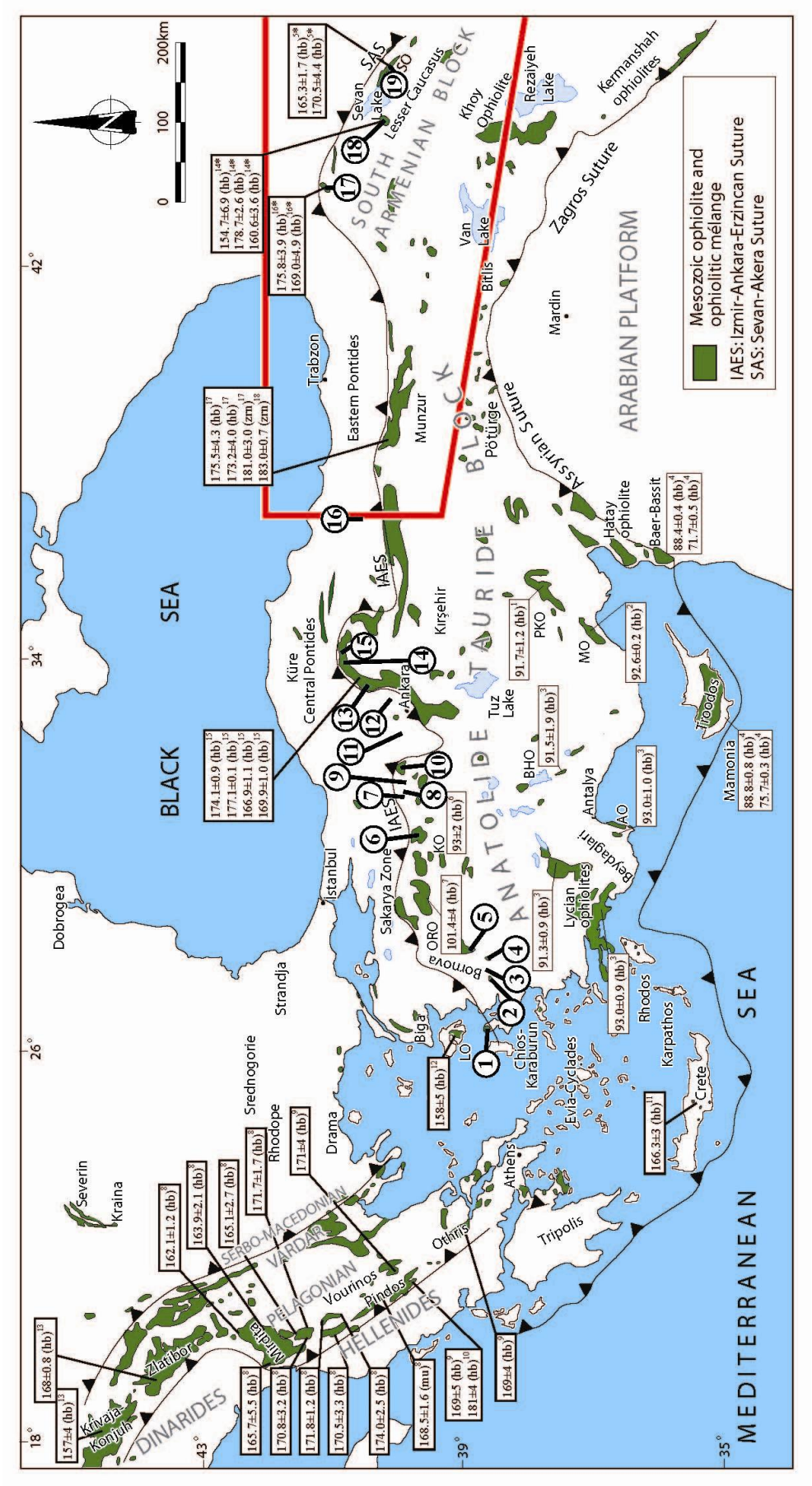
Mesozoic ophiolite and ophiolitic mélange
IAES: Izmir-Ankara-Erzincan Suture
SAS: Sevan-Akera Suture
0
100
200km
BLACK SEA
MEDITERRANEAN SEA
ARABIAN PLATFORM
SOUTH ARMENIAN BLOCK
ANATOLIDE TAURIDE BLOCK
DINARIDES
HELLENIDES
PELAGONIAN
VARDAR
SERBO-MACEDONIAN
Sevan Lake
Lesser Caucasus
Khoy Ophiolite
Rezaiyeh Lake
Kermanshah ophiolites
Zagros Suture
Van Lake
Bitlis
Mardin
Trabzon
Eastern Pontides
Munzur
Pötürge
Assyrian Suture
Hatay ophiolite
Baer-Bassit
Küre
Central Pontides
Kırşehir
Ankara
Tuz Lake
Tiroodos
Mamonia
Antalya
Beydaglari
Lycian ophiolites
Istanbul
Sakarya Zone
Bornova
Biga
Chios-Karaburun
Evia-Cyclades
Rhodos
Karpathos
Crete
Athens
Tripolis
Othris
Vourinos
Pindos
Mirdita
Zlatibor
Krivaja-Konjuh
Severin
Kraina
Dobrogea
Strandja
Srednogorie
Rhodope
Drama
IAES
SAS
SO
ORO
KO
LO
BHO
AO
MO
PKO
Mesozoic ophiolite and ophiolitic mélange
IAES: Izmir-Ankara-Erzincan Suture
SAS: Sevan-Akera Suture

1.2.2.1 **Fore- or back-arc ophiolites?**

It has been suggested that the Karadağ ophiolites (NE Anatolia) are representative of a fore-arc environment due to their boninitic chemical signatures (Crawford 1989; Falloon & Crawford 1991). However, more recent investigations have shown that boninites are not solely found in fore-arc but also in back-arc environments (Falloon *et al.* 1992; Deschamps & Lallemand 2003; Teklay 2006). In any case the SSZ nature of magmatism is well established (e.g., Topuz *et al.* 2014). The intra-oceanic subduction is also evidenced by oceanic crust rocks metamorphosed in the eclogite facies, of similar age as the SSZ ophiolites, dated at 172 ± 4 Ma by $^{40}Ar/^{39}Ar$ on phengite and by U-Pb on rutile in the Refahiye area (Topuz *et al.* 2013). In this scenario, the volcanic arc of this subduction would have then been either accreted to the Pontides margin (to the north) or subducted under it. There is yet no convincing evidence for any intra-oceanic arc to the north of the ophiolites. To the north of the Tethys oceanic domain the only arc during the Middle Jurassic to Late Cretaceous is the Pontides and Somkheto-Karabakh, which was bounded to the south by the north dipping subduction of Tethys.

Locally, Rice *et al.* (2009) show the presence of an intra-oceanic arc in the Karadağ ophiolites. However this formation is dated to the Late Cretaceous, and the authors suggest 'possibly because the lower part of the arc was detached and subducted'. However, some Upper Cretaceous calc-alkaline arc lavas are also found above an unconformity on top of Stepanavan ophiolites (Galoyan et al., 2007), just east of Karadağ ophiolites thus this arc may start in the Middle Cretaceous during of after the ophiolite obduction.

Consequently, when considering an intra-oceanic subduction model for the origin of Jurassic slow-spreading ophiolites, observations lead to conclude that the corresponding volcanic arc is missing. However, this observation may be tempered by the presence of volcanic arc remains in the ophiolitic sole lithologies / underthrusted 'mélange' unit (see dedicated following paragraph below). Determining whether ophiolites are of fore- or back-arc origin is not simple because of intricate obduction initiation as well as syn- and post-obduction processes. Both scenarios, fore- or back-arc origin, suggest the existence of an intra-oceanic arc. The structural and geochemical processes leading to their formation are almost identical, except for less important subduction contamination for back-arc tholeiites.

1.2.2.2 **Alkaline geochemical signatures**

Pillow-basalts with an Ocean Island Basalt (OIB) alkaline composition lie on top of the ophiolite series in Armenia (Galoyan *et al.* 2007, 2009; Galoyan 2008; Rolland *et al.* 2009, 2010; Hässig et al., 2013), and in NE Turkey as well (e.g., Parlak et al., GSL, and Hässig et al., 2014 for a review). These alkaline rocks are thus not related to the generation of the SSZ-type oceanic crust. They are found directly above an unconformity on top of the ophiolite body in Armenia, outcropping as fresh and large (meter-scale) pillow lavas embedded in pelagic limestones, dated at 117 Ma (mid-Early Cretaceous) by Ar-Ar on amphibole by Rolland *et al.* (2009), confirmed by radiolarian biostratigraphy (Danelian *et al.* 2012). Such occurrences of volcanism are widespread, though of variable thickness, in the various ophiolite locations. They are also described within the Karabagh and Amasia areas where late Barremian to early Aptian (~113 Ma; Asatryan *et al.* 2011) and Cenomanian (96~92 Ma; Danelian *et al.* 2014) radiolarians, respectively, bracket this submarine volcanism. Along the Sevan-Akera segment of the suture zone, between the Amasia and Karabagh zones, the Sevan ophiolite exhibits latest Tithonian to late Valanginian (135~123 Ma) radiolarians intercalated with mafic volcanic rocks (Asatryan *et al.* 2012). These datings evidence a long lasting volcanic activity from the end of the Jurassic, throughout the Early Cretaceous and up to the beginning of the Late Cretaceous not linked with the generation of the SSZ type oceanic crust. Compilations made by Moix & Goričan (2013) also show such occurrences of volcanism bracketed by Late Jurassic and Cretaceous radiolarians along the Izmir-Ankara-Erzincan segment of the northern tethyan suture zone (**Figure 65**).

The widespread occurrence of these rocks however suggests other magmatic processes than just a punctual and long-lived feature hot-spot, which may not be disconnected to subduction s.l.

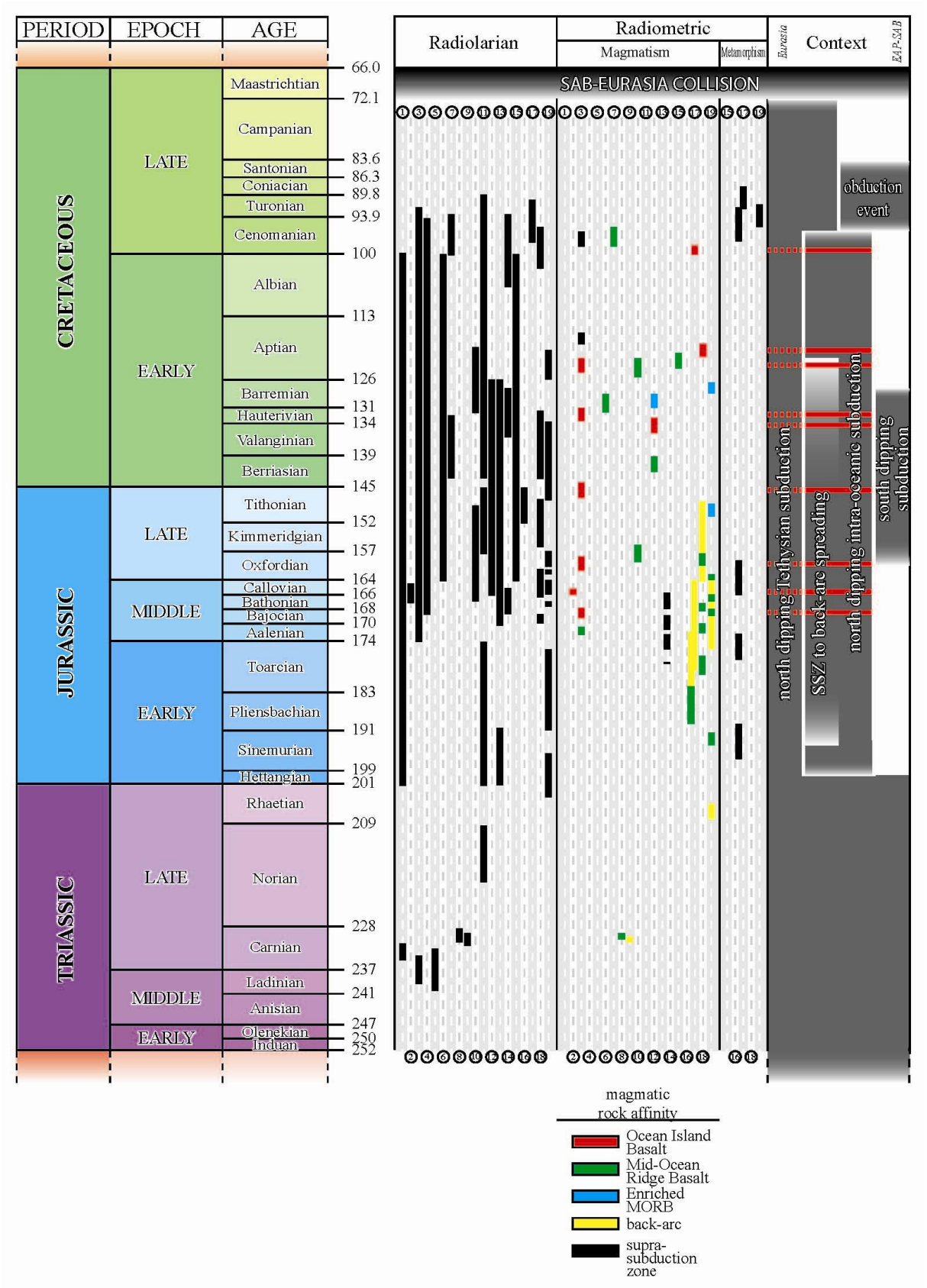

Figure 65 - Compilation of chronological data including extension of the radiolarian fauna, magmatic series of the ophiolite bodies outcropping emplaced prior to the obduction event and metamorphic lithologies marking the limit between the ophiolites and the Eurasian margin as well as between the ophiolites and the underthrusted EAP-SAB

margin from the İzmir-Ankara-Erzincan and Sevan-Akera sutures including the Bornova Zone and the Karaburun Peninsula, modified after Moix & Goričan (2013). The evolution of the various geological contexts between the Eurasian margin and the EAP-SAB is further argued by both biostratigrapghic and radiochronologic data. The red lines underline the emplacement of OIB type volcanism on the oceanic crust to be obducted. Locations are numbered and plotted on Figure 64: (1) Çakmakoğlu & Bilgin (2006); (2) Tekin & Göncüoğlu (2009); (3) Tekin *et al.* (2006) in Göncüoğlu *et al.* (2006a); (5) Tekin & Göncüoğlu (2007) and Tekin & Göncüoğlu (2008); (4) Tekin *et al.* (2012a); (10) Göncüoğlu *et al.* (2000); (7) Göncüoğlu *et al.* (2006b); (8) Göncüoğlu *et al.* (2006b); (9) Tekin *et al.* (2002) and Göncüoğlu *et al.* (2006a, 2010); (6) Servais (1982); (11) Bragin & Tekin (1996); (12) Rojay *et al.* (2004); (13) Çelik (2010) and Üner (2010) in Tekin *et al.* (2012b); (14) Tüysüz & Tekin (2007); (15) Boccaletti *et al.* (1966); (16) Bozkurt *et al.* (1997); (17) Hässig *et al.* (2013, 2014) and Danelian *et al.* (2014); (18) Danelian *et al.* (2008, 2012) and Rolland *et al.* (2010); (19) Galoyan *et al.* (2009) and Asatryan *et al.* (2010, 2012). Plots for magmatic rocks between (16) and (17) are for the Refahiye ophiolite from Topuz *et al.* (2013a, b) as for metamorphic rocks along with Aslan *et al.* (2011). Plots for metamorphic rocks between (17) and (18) are for the Stepanavan ophiolite from Rolland *et al.* (2009a).

1.2.3 The 'mélange' unit(s)

The mélanges found under the ophiolitic units represent (1) a sedimentary mélange represented by dismembered pieces of the thrusted ophiolites that fell in the obduction frontal basin (Huene *et al.* 2004; Vannucchi *et al.* 2008; Festa *et al.* 2010), as well as (2) tectonic mélanges, represented by scraped off features of the underthrusted units, tectonically intercalated with overthrusting ophiolite unit (Cloos & Shreve 1988; Dilek & Whitney 1997; Elitok & Drüppel 2008). The geochemical composition of part of the metamorphic units beneath the Stepanavan, Amasia and Hınıs ophiolites shows a distinct alkaline affinity similar to the alkaline oceanic island basalts (OIB) suite emplaced on top of the ophiolite. This lithological blend was then overthrusted by the ophiolitic unit and incorporated and metamorphosed throughout thrusting with other metamorphics beneath the ophiolites as described by Engi *et al.* (2001).

In the Erzincan area, previous works as well as field observations evidence the presence of a dismembered thrust sheet of marbles containing Permian foraminifers (fusulinids; Özgül 1981) topping highly schistosed low-grade metamorphosed magmatic rocks, directly beneath the obduction contact. These marbles could represent mega-lenses or mega-olistoliths emplaced through tectonic transport between the overthrusted upper ophiolite unit and the Tauride-Anatolide Platform unit (TAP).

1.2.3.1 Metamorphic rocks underneath the ophiolite

The metamorphic rocks below the obduction contact were originally emplaced anywhere between the SAB passive continental margin to the south and the future-obducted ophiolite in SSZ position to the north. These rocks underwent a severe deformation featured by a penetrative schistosity, shear planes and rolling structures (snowball garnets) in a simple shear strain regime, ascribed to the ophiolite emplacement (Hässig *et al.* in review). To the

north of the Erzincan Basin, the basal contact of this unit is shielded by Cenozoic deposits rendering it difficult to relate this unit to an intra-oceanic or to a continental environment (the Taurides block). Analyses of these Erzincan metamorphic rocks, phyllites with calc-alkaline affinities, are documented by Gücer *et al.* (2007). Their geochemistry testifies of meta-basalts with tholeiitic to calc-alkaline tendencies compatible with a volcanic arc environment. Even if there is no yet any convincing geochronological data to bracket the original emplacement of these rock types before obduction, the presence of these rocks argues for the occurrence of a volcanic arc between the passive continental margin to the south and the future ophiolites to the north, prior to obduction. This further argues for an intra-oceanic subduction, which accounts for the creation of oceanic crust in a supra-subduction setting.

Also recent $^{40}Ar/^{39}Ar$ ages have been calculated by Aslan *et al.* (2011) for plagioclases populations, which yield ages of 94.1 ± 3.3 and 60.7 ± 4.9 Ma for the metamorphism of this unit. Let us point out that these ages are globally similar to those of the Stepanavan metamorphic unit along the Sevan-Akera suture zone (blueschists dated at 95~91 and partially reset in greenschist facies at 71 Ma; Rolland *et al.* 2009).

1.2.4 The underthrusted continental domains (EAP-SAB)

The East Anatolian Platform (EAP) is prolonged by the SAB to the East. This domain represents a continental platform between the northern and southern branches of Neotethys (Bozkurt & Mittwede 2001). The EAP-SAB represents a sliver of a small continental plate having drifted off northern Gondwana towards the north, and then collided with Eurasia (Stocklin 1974; Adamia *et al.* 1977; Biju-Duval *et al.* 1977; Stöcklin & Bhattarai 1977; Dercourt *et al.* 1986; Şengün 2006; Barrier & Vrielynck 2008; Sosson *et al.* 2010). Palaeomagnetic analyses indicate palaeo-latitudes for the EAP-SAB during the Early and Middle Jurassic at least 2000 km farther south than its current position (Bazhenov *et al.* 1996; Meijers *et al.* 2013). This argues for a Gondwanian origin of the EAP-SAB, as also suggested by the dating undergone by Baghdasarian & Ghukasian (1983) and palaeogeographic reconstructions (Knipper & Khain 1980; Monin & Zonenshain 1987; Şengör *et al.* 1988; Robertson & Mountrakis 2006; Barrier & Vrielynck 2008). The rifting of the Taurides-Anatolides (including the SAB) from Gondwana is documented as initiating during Triassic times (Mart 1987; Gealey 1988; Kazmin 1991).

1.3 Discussion: what evolution of the geodynamic processes can explain the pre-obduction framework?

Throughout the Mesozoic and Cenozoic, the northern margin of the SAB-TAP, as well as the southern Eurasian margin, were involved in subduction and accretion/collision processes resulting in closure of the northern branch of the Tethys ocean (Adamia *et al.* 1981, 2011; Şengör & Yılmaz 1981; Dercourt *et al.* 1986; Zakariadze *et al.* 1990, 2005; Ricou 1994; Nikishin *et al.* 1998; Yilmaz *et al.* 2000; Stampfi *et al.* 2001; Robertson 2002; Golonka 2004; Galoyan 2008, 2009; Rolland *et al.* 2009a, b, 2010, 2011, 2012; Sosson *et al.* 2010; Hässig *et al.* 2013, 2014; Topuz *et al.* 2013).

Before obduction, paleomagnetic studies have shown that during Early-Middle Jurassic times the SAB-TAP was at least 2000 km south of the Eurasian margin (Bazhenov *et al.* 1996; Meijers *et al.* 2013).

After the NE Anatolian-Lesser Caucasus obduction event, during the Late Cretaceous, an oceanic domain still subsisted between the obducted ophiolite nappe and the Eurasian margin farther north. Paleomagnetic analyses indicate that a maximum of 1200~1000 km of oceanic lithosphere still separated the two continental domains during the Santonian, but the 40° rotation inferred from paleo-declinations suggest a significant rotation that may be ascribed to a highly dissymmetrical oceanic basin (Meijers *et al.* 2013). This ocean totally closed 20 Ma later as testified by the setup of a foreland basin on the obduction front and uplift and erosion along the suture zone. This continental collision event is clearly indicated by the Late-Middle Eocene unconformity on the SAB, the suture zone and the Eurasian margin, but the start of the collision occurred in the Latest Cretaceous. Then collision evolved and the domain was deformed from late-Middle Eocene to Miocene by thrusts and reverse faults (Galoyan *et al.* 2007; Rolland et al. 2009a; Sosson *et al.* 2010).

Geological data indicate that, within a convergent system, obduction occurred as the penultimate process, possibly by accommodating a slowing in subduction under the Eurasian margin, before continental collision, which may be due to underthrusting of seamounts, a thick oceanic plateau or the back-arc ridge. In order to illustrate how obduction is possible, we propose the following geodynamic reconstruction (**Figure 66**).

1.3.1 Geodynamic reconstruction

1.3.1.1 North-dipping Northern Tethys subduction under Eurasia

The north-dipping subduction of the Tethyan oceanic domain under the southern Eurasian margin ranges from Middle Jurassic to middle-Late Cretaceous times (c. 170-83 Ma). It is evidenced in the Eastern Pontides and Somkheto-Karabakh regions of the Lesser Caucasus. They correspond during this time interval to a continental magmatic arc. This is testified by occurrences of granodiorite and tonalite intrusions mainly dated to Middle Jurassic times (Sengör & Yilmaz 1981), cross cutting a crystalline basement metamorphosed in the Carboniferous (340-330 Ma, e.g., Topüz, Treloar) and covered by Upper Paleozoic to Lower Jurassic sediments (Adamia et al., 1981). Calc-alkaline volcanism is continuous throughout the Middle to Late Jurassic, even though diminishing on through to the beginning of the Late Cretaceous marked alternations with relatively deep-water sediments (Kazmin *et al.* 1986). It is noteworthy that the diminishing in volcanic arc activity broadly coincides with the onset of obduction on EAP-SAB. This subduction related volcanism is reported as intensive along the southern margin of Eurasia later during Late Cretaceous times (Sengör & Yilmaz 1981), which argues for a regained subduction just after the short-lived obduction (90-86 Ma). Volcanic arc lithologies related to subduction are exposed in the southern Pontides Arc (Adamia *et al.* 1977, 1981; Ustaömer & Robertson 1995; Rice *et al.* 2009; Dilek *et al.* 2010). This suggests that the eastern Pontides developed by northward subduction of remaining Palaeotethys and juvenile Neotethys at least from Jurassic to Late Cretaceous times (Adamia *et al.* 1981; Yilmaz *et al.* 2000).

Figure 66 - Sketch geodynamic model proposed for the oceanic domain between the northern margin of the EAP-SAB and the southern margin of Eurasia from Early Jurassic to Late Cretaceous times, from ophiolite genesis to just prior to emplacement over the EAP-SAB.

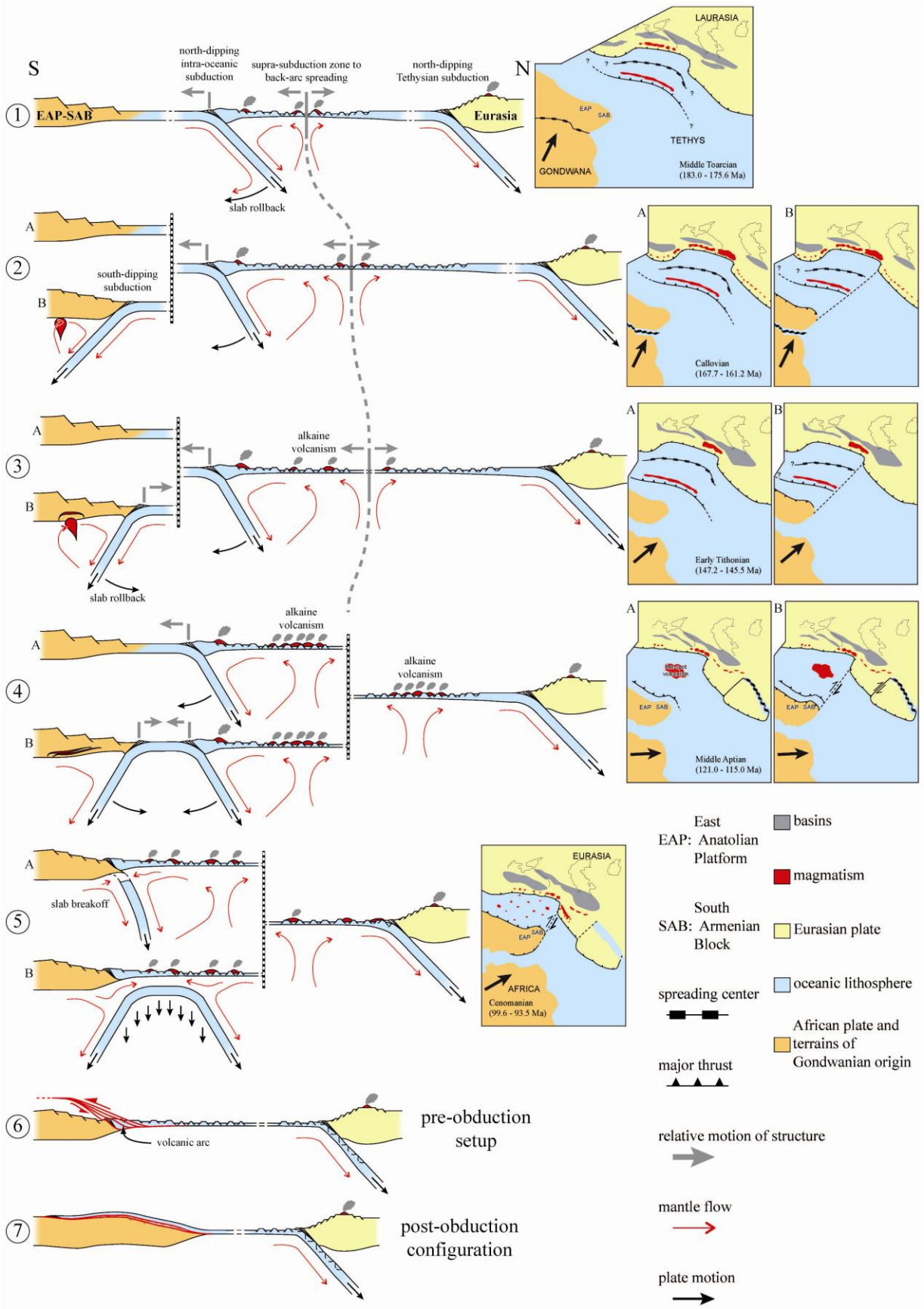
S
N
north-dipping intra-oceanic subduction
supra-subduction zone to back-arc spreading
north-dipping Tethysian subduction
1
EAP-SAB
Eurasia
slab rollback
LAURASIA
EAP
SAB
TETHYS
GONDWANA
Middle Toarcian (183.0 - 175.6 Ma)
2
A
B
south-dipping subduction
Callovian (167.7 - 161.2 Ma)
3
alkaine volcanism
slab rollback
Early Tithonian (147.2 - 145.5 Ma)
4
alkaine volcanism
alkaine volcanism
Middle Aptian (121.0 - 115.0 Ma)
5
slab breakoff
EURASIA
AFRICA
Cenomanian (99.6 - 93.5 Ma)
6
volcanic arc
pre-obduction setup
7
post-obduction configuration
East
EAP: Anatolian Platform
South
SAB: Armenian Block
spreading center
major thrust
basins
magmatism
Eurasian plate
oceanic lithosphere
African plate and terrains of Gondwanian origin
relative motion of structure
mantle flow
plate motion

1.3.1.2 **The Supra-subduction zone to back-arc domain**

An intra-oceanic subduction zone is evidenced by the preserved non-metamorphic obducted oceanic crust, the ophiolitic nappe. This oceanic crust formed in a supra-subduction to a back-arc basin setting ascribed to subducting slab roll-back. This north-dipping intra-oceanic subduction, north of the SAB, is accountable for Early Jurassic to middle-Early Cretaceous ages obtained for ophiolite lithologies (gabbros and basalts) (Aghamalyan 1998; Galoyan 2008; Rolland *et al.* 2009b, 2011; Hässig *et al.* 2013). The north-dipping of this structure is also argued by the overall geometry of the tectonic pile, as by that of the outcrops of low-grade metamorphics, blueschist and amphibolite facies rocks below the ophiolite nappe along the Ankara-Erzincan and Sevan-Akera suture zones in the Refahiye (Aslan *et al.* 2011), Stepanavan (Rolland *et al.* 2009a; Sosson *et al.* 2010) and Amasia areas (Hässig *et al.* 2013), respectively. This intra-oceanic subduction zone is considered to be synchronous with subduction under Eurasia farther north because ages obtained for the ophiolite units (gabbros and basalts) are encompassed within those of volcanism along the southern margin of Eurasia. The timing of peak metamorphism for the metamorphic units (c. 97~91 c. 95~91 Ma and c. 92~88 Ma) is considered to mark the onset of the obduction process, thus timing of the proposed pre-obduction setup.

Radiometric datings of ophiolitic lithologies are supported by occurrences of radiolarites interbedded with volcanic layers of basaltic lava flows and tuffs, representing the upper most part of the ophiolite sequence. These radiolarites yield continuous biochronologic ages either form Early Jurassic or Middle Jurassic to early-Late Cretaceous times (e.g. Danelian *et al.* 2014; **Figure 65**). We consider the Triassic radiolarian ages, either from blocks of the mélange or from the upper parts of the ophiolite's tectonic pile, to be relics of the oceanic crust that partly disappeared in the northern subduction zone.

Throughout the evolution of the future ophiolite body, from genesis to the onset of obduction, radiochronology as well as radiolarites may be used also to temporally bracket the emplacement of sediments or volcanic rocks. Occurrences of Ocean Island Basalts (OIB) have been identified dating back to the Middle Jurassic (Tekin *et al.* 2006; Tekin & Göncüoğlu 2009) but mainly spanning from Early and early-Late Cretaceous times (Aptian and Cenomanian; Rolland *et al.* 2010; Danelian *et al.* 2014). Similar Cretaceous alkaline series are also found above the Iranian ophiolites, in the region of Khoy (Ghazi & Hassanipak, 1999; Avagyan et al. this volume). Even if it is still difficult to relate these alkaline events to one another due to their geographical and temporal distribution, it is most likely from their

geochemistry that their emplacement is linked with upwelling of hot mantle material (‘plumes’; e.g. Rolland *et al.* 2009b; Parlak *et al.* 2013). We believe that this last observation may be an important factor towards solving the obduction paradox, that is to say a continental domain overthrusted by an old yet hot oceanic lithosphere. Indeed, widespread plume activity is evidenced by alkaline volcanism within 20 Ma before the obduction (Bektaş etal. 1999; Çelik 2007 Rolland *et al.* 2009b; Danelian et al. 2014). The widespread character of this event has thus potentially resulted in a significant decrease in Ocean Lithosphere thickness,density, and has produced an increase of its buoyancy..

1.3.1.3 **An active or passive northern SAB-TAP TOC margin?**

During the Late Jurassic and Early Cretaceous times structural, geochronological and petrological observations have shown a multiphase evolution of the northern margin of the SAB (Hässig *et al.* in review). A south-dipping subduction under the EAP-SAB is implemented to the model in order to suit recent findings pertaining emplacement of relatively hot subduction related granodiorite as well as the metamorphic evolution of the crystalline basement in the Lesser Caucasus area (Hässig *et al.* in review). The metamorphism is interpreted as evidencing: (1) M1 Barrovian MP-MT conditions (staurolite-kyanite) at c. 157-160 Ma and intrusion of dioritic magmas at c. 150-156 Ma, (2) near-adiabatic decompression is featured by partial melting and production of leucogranites at c. 153 Ma, followed by M2 HT-BP conditions (andalusite - K-feldspar). A phase of shearing and recrystallization is ascribed to doming at c. 130-150 Ma and cooling at 400°C by c. 123 Ma (M3). Structural observations show (1) top to the north shearing during M1 and (2) radial extension during M2.

Existence of this structure along the entire northern EAP-SAB margin is uncertain because of the lack of outcrops of basement rocks under the ophiolite nappe (**Figure 63**) and of geochronological data in NE Turkey. Accordingly, we propose two alternatives for the evolution of this zone marking the transition between ocean and continental domains (TOC), whether as a passive margin (**Figure 66A**) or as an active margin (**Figure 66B**), as this zone may still represent a local feature on the northwards drifting EAP-SAB.

1.3.1.3.1 **Passive TOC margin**

In the first case, a passive TOC margin, the intra-oceanic subduction retreats until the arrival of the EAP-SAB into the subduction. In this configuration, the north-dipping

subduction of the passive TOC provides a favorable pre-structure for later passive obduction (**Figure 66**). A similar context is described for the formation of the Antler orogen along an E-W cross-section from central California to central Utah in the United States between Middle Devonian and Late Devonian~Early Mississippian times (Speed & Sleep 1982; Ingersoll 1997, 2008; Dickinson 2000). In this model, as in ours, a relatively hot SSZ is overthrusted onto the subducting passive continental margin. This passive margin does not subduct farther than 45~25 km representing pressures between 15 and 7 kbar. Shortly following the entrance of this passive TOC into the subduction zone, shallow detachment or break-off is suggested by the end of subduction related volcanism in the overriding plate at this time.

Zedde & Wortel (2001) investigate the modalities of shallow oceanic slab detachment upon arrival of a continental slab in a subduction zone. This study concludes that depth of break-off is dependent of the thermal state of the passive TOC. This deduction is supported by numerical modelling (Duretz & Gerya 2013) showing that break-off depth is related to the coupling of the strength and the forces acting on the passive TOC, strength which is itself dependent of the rheology and thermal state of the TOC. In the scenario where the TOC margin is passive a shallow breakoff is implied, in order to fit the geological data showing only low degrees of metamorphism for the continental EAP-SAB: absence of eclogites, reset of paleomagnetic markers suggesting 200<T<400°C (Meijers et al., in review).

1.3.1.3.2 **Active TOC margin**

In the alternate possibility, an active TOC margin, the south-dipping and north-dipping intra-oceanic subductions configure a double divergent subduction setting. This framework is constituted by the EAP-SAB to the south and the future ophiolite to the north as the converging overriding plates. Models featuring divergent double subduction systems for the formation of orogens are rather rare. Still, in Thailand (Hutchison 1989), the Philippine arc (McKenzie 1969), the Nevadan belt in Western USA (Ingersoll 2008) and the Lachlan fold belt in southeastern Australia (Soesoo *et al.* 1997; Gray *et al.* 2002) such a context has been proposed.

Throughout the evolution of the two opposite convergent margins, the oceanic domain caught between the two gradually shortens. Ingersoll (2008) shows that in such a context the oceanic active margin is thrusted onto the continental active margin while the subducting intermediate portion sinks into the mantle. The entire system is unlikely to be perfectly symmetric and thus sinking will probably initiate from one side and propagate towards the

other side. As this central portion sinks, upward mantle flow has to fill the resulting gag. Decompressional melting of mantle wedge material ought to result as a response to asthenosphere uplift and tectonic underpressure due to the sinking oceanic lithosphere pulling on the overriding plates.

In the scenario comprised of an active TOC margin bordering the north of the EAP-SAB continental block, the sudden and rapid heating and melting at the base of the active overriding oceanic margin to the north is thus arguable. In the resulting setup, the former active margin of the future ophiolite overrides the continental margin towards the south. It is reasonable to propose that the occurrences of volcanism throughout Early Cretaceous times, emplaced in an oceanic environment prior to obduction, partly represents manifestations of this heating. Thus, the section of oceanic lithosphere to be obducted, just prior emplacement, is 50~80 Ma old but rather hot because of mantle flows inducted by the sinking of the divergent double subducting oceanic crust.

1.4 Conclusion

A model concerning the evolution of the northern Neotethys is argued on the base of the structural, geochemical and geochronological studies pertaining to preserved oceanic crust domains (ophiolites) obducted as in the Lesser Caucasus and in NE Anatolia and of the metamorphic rocks beneath these ophiolites. These studies provide constraints into the evolution of the Tethyan realm. As a result of this review, a geologic setup for future investigations and numerical modeling is proposed (**Figure 66**):

1- The magmatic and ultrabasic rocks composing the ophiolitic nappe originate from a SSZ basin that slowly opened in a preexisting ocean domain, While this domain subducted under Eurasia farther north. We thus infer the existence of an intra-oceanic subduction at this time and a probable rollback of the intra-oceanic subduction slab as a motor for this spreading. Radiometric dating and biostratigraphy allow us to confine this first snapshot in the Early Jurassic to Early Cretaceous times (Figures 66-1, 66-2 & 66-3).

2- Recent investigations evidence subduction under the northern margin of the SAB-EAP with emplacement of granodiorite intrusions during the early-Late Jurassic (c. 160 Ma). The western continuity of this structure into NE Anatolia is uncertain, thus we present from this point on two alternate models, one without a

south-dipping subduction and another with (**Figures 66-2A** & **66-2B**, respectively and so forth).

3- In nearly all ophiolite outcrops, two magmatic suites are evidenced one on top of the other: (1) oceanic crust topped by (2) basaltic flows or volcanic tuff with alkaline tendencies. Radiochronology and biostratigraphy both show that emplacement of this second suite occurs in an ocean environment prior to ophiolite emplacement throughout Middle to Late Jurassic and even until early-Late Cretaceous times. Geochemical analyses tend to validate the hypothesis of mantle originating hot-spot type "plumes".

4- In our scenarios (**Figures 66-4A** & **66-4B**), the intra-oceanic subduction retreats to the northern SAB-EAP margin. Since no high pressure metamorphism is evidenced in the rare outcrops of the SAB-EAP crystalline basement, this illustrates either (1) early slab breakoff or (2) intermediate slab sinking due to divergent double subduction slab rollback, respectively in the case of a passive or active north SAB-EAP margin (**Figures 66-5A** & **66-5B**). The resulting setup shows a favorable geometry for oceanic crust thrusting onto the SAB-EAP.

5- The absence of the volcanic arc formed above the intra-oceanic subduction may be explained by its dragging under the obducting ophiolite through scaling, faulting and tectonic erosion. It is hypothesized that the low-grade metamorphics of Erzincan and blueschists of Stepanavan correspond to this missing volcanic.

6- Data indicate that the oceanic domain was still subducting under Eurasia after ophiolite emplacement (**Figure 66-7**). Reconstructions of the ophiolitic nappe account for 200 km of overthrusting from the present suture zone to Khoy (Iran) hypothesized to represent the most distal obduction front. The olistostrome yields a lower chronological limite to this obduction to Coniasian - Santonian times (c. 90~86 Ma). This observation is coherent with metamorphic ages for Erzincan low-grade metamorphic unit, the Amasia garnet amphibolites and the Stepanavan blueschists.

In order to explain such an obduction event, we believe the oceanic crust thrusted in the proposed pre-obduction setup (**Figure 66-6**) must be particularly hot. The heating of the oceanic lithosphere would be due to important upwelling mantle flows, evidenced by the alkaline volcanism on the ophiolite, thus altering its rheological properties.

Acknowlegements

This work was supported by the MEBE (Middle East Basin Evolution) and DARIUS programs jointly supported by a consortium including oil companies, UMPC and the INSU/CNRS. This publication is a contribution of "GEOAZUR", University of Nice Sophia Antipolis, CNRS, France.

References

Adamia, S. A., Lordkipanidze, M. B. & Zakariadze, G. S. 1977. Evolution of an active continental margin as exemplified by the Alpine history of the Caucasus. *Tectonophysics*, **40**, 183-189.

Adamia, Sh. A., Chkhotua, T., Kekelia, M., Lordkipanidze, M., Shavishvili, I. & Zakariadze, G. 1981. Tectonics of Caucasus and adjoining regions: implications for the evolution of the Tethys ocean. *Journal of Structural Geology*, **3**, 437-447.

Adamia, Sh. A., Belov, A., Kekelia, M. & Shavishvili, I. 1987. Paleozoic tectonic development of the Caucasus and Turkey (Geotraverse C). *In:* Flugel, H. W., Sassi, F. P. & Grecula, P. (eds) *Pre-Variscan and Variscan Events in the Alpine–Mediterranean Mountain Belts*. Mineralia Slovaca: Alfa Bratislava, 22-50.

Adamia, Sh. A., Zakariadze, G., Chkhouta, T., Sadradze, N., Tsereteli, N., Chabukiani, A. & Gventsadze, A. 2011. Geology of the Caucasus: a review. *Turkish Journal of Earth Sciences*, **20**, 489-544.

Aghamalyan, V. A. 1998. *The Basement Crystalline of Armenia*. PhD thesis, Institute of Geological Sciences, National Academy of Sciences of Armenia, Yerevan. (in Russian)

Akıncı, Ö. T. 1984. The eastern Pontide volcanosedimentary belt and associated massive sulphide deposits. *In:* Dixon, J. E. & Robertson, A. H. F. (eds) *The Geological Evolution of the Eastern Mediterranean*. Geological Society, London: Special Publication, **17**, 415-428.

Aktimur, H. T., Sarıaslan, M., Keçer, M., Turşucu, A., Ölçer, S., Yurdakul, M. E.,… & Yıldırım, T. 1995. *Geology of Erzincan Surrounding*. Mineral Research and Exploration Institute (MTA) of Turkey Report no. **9792**. (unpublished, in Turkish)

Asatryan, G. 2009. *New data about the age of ophiolites in the Vedi zone on the basis of radiolarian assemblages*. Proceedings of the National Academy of Sciences of Armenia, Earth Sciences.

Asatryan, G., Danelian, T., Sosson, M., Sahakyan, L., Person, A., Avagyan, A. & Galoyan, G. 2010. Radiolarian dating of the sedimentary cover of Sevan ophiolite (Armenia, Lesser Caucasus). *Ofioliti*, **35**, 91-101.

Asatryan, G., Danelian, T., Sosson, M., Sahakyan, L. & Galoyan, G. 2011. Radiolarian evidence for Early Cretaceous (late Barremian – early Aptian) submarine volcanic activity

in the Tethyan oceanic realm preserved in Karabagh (Lesser Caucasus). *Ofioliti*, **36**, 117-123.

Asatryan, G., Danelian, T., Seyler, M., Sahakyan, L., Galoyan, G., Sosson, M., Avagyan, A., Hubert, B., Person, A. & Vantalon, S. 2012. Latest Jurassic-Early Cretaceous radiolarian assemblages constrain episodes of submarine volcanic activity in the Tethyan oceanic realm of the Sevan ophiolites (Armenia). *In:* Danelian, T. & Goričan, S. (eds) *Radiolarian biochronology as a key to tectono-stratigraphic reconstructions*. Bulletin de la Société Géologique de France, **183**, 319-330.

Aslan, Z., Arslan, M., Temizel, İ. & Kaygusuz, A. 2013. K-Ar dating, whole-rock and Sr-Nd isotope geochemistry of calc-alkaline volcanic rocks around the Gümüşhane area: implications for post-collisional volcanism in the Eastern Pontides, Northeast Turkey. *Mineralogy and Petrology*, 1-23.

Aslan, Z., Gücer, M. A. & Arslan, M. 2011. *^{39}Ar-^{40}Ar dating on plagioclases of metabasic metagranitic rocks in the Yoncayolu metamorphic, NE Turkey*. Goldschmidt Conference Abstracts, **460**.

Avagyan, A., Sosson, M., Philip, M. H., Karakhanian, A., Rolland, Y., Melkonyan, R., Rebai, S. & Davtyan, V. 2005. Neogene to Quaternary stress field evolution in Lesser Caucasus and adjacent regions using fault kinematics analysis and volcanic cluster data. *Geodinamica Acta*, **18**, 401-416.

Baghdasarian, G. P. & Ghukasian, R. Kh. 1983. The age of Bdjni migmatite-granitic massif (By the Rb-Sr Isochron radiometric data and geological ideas. *Izvestia NAS of Armenian SSR, Nauki o Zemle*, **6**, 15-29. (in Russian)

Barrier, E. & Vrielynck, B. 2008. *Palaeotectonic map of the Middle East, atlas of 14 maps, tectonosedimentary-palinspastic maps from late norian to pliocene*. Commission for the Geologic Map of the World (CCMW, CCGM), Paris.

Bazhenov, M., Burtman, V. S. & Levashova, N. M. 1996. Lower and Middle Jurassic paleomagnetic results from the south Lesser Caucasus and the evolution of the Mesozoic Tethys ocean. *Earth and Planetary Science Letters*, **141**, 79-89.

Bergougnan, H. 1987. *Etudes géologiques dans l'Est-Anatolien*. PhD thesis, Université Pierre et Marie Curie, Paris VI, France.

Biju-Duval, B., Dercourt, J. & Le Pichon, X. 1977. From the Tethys Ocean to the Mediterranean Seas: a plate tectonic model of the evolution of the western Alpine System. *In:* Biju-Duval, B. & Montadert, L. (eds) *Structural History of the Mediterranean basins*.Editions Technip: Paris, 143-164.

Bill, M., O'Dogherty, L., Guex, J., Baumgartner, P. O. & Masson, H. 2001. Radiolarite ages in Alpine-Mediterranean ophiolites: Constraints on the oceanic spreading and the Tethys-Atlantic connection. *Geological Society of America Bulletin*, **113**, 129-143.

Boccaletti, M., Bortolotti, V. & Sagri, M. 1966. Ricerche sulle ofioliti delle Catene Alpine I. Osservazioni sull'Anltara Melange nelle zona di Ankara. *Bollettino della Societa geologica Italiana*, **85**, 485-508.

Boccaletti, M., Guazzone, G. & Manetti, P. 1974. Evoluzione paleogeografica e geodinamica del Mediterraneo: i bacini marginali. *Memorie della Societa geologica italiana*, **13**, 161-169

Boutelier, D., Chemenda, A. & Burg, J. -P. 2003. Subduction versus accretion of intra-oceanic volcanic arcs: insight from thermo-mechanical analogue experiments. *Earth and Planetary Science Letters*, **212**, 31-45.

Bozkurt, E. & Mittwede, S. K. 2001. Introduction to the geology of Turkey - a synthesis. *International Geology Review*, **43**, 578-594.

Bozkurt, E. & Park, R. G. 1997. Evolution of a mid-Tertiary extensional shear zone in the southern Menderes Massif, western Turkey. *Bulletin de la Société Géologique de France*, **168**, 3-14.

Bozkuş C. 1998. Stratigraphy and structural evolution of Pontid/Anatolid suture zone in NE Anatolia (between Oltu-Narman). *Journal of Engineering Sciences*, **4**, 487-499.

Bragin, N. J. & Tekin, K. 1996. Age of radiolarian-chert blocks from the Senonian ophiolitic mélange (Ankara, Turkey). *Island Arc*, **5**, 114-122.

Çakmakoğlu, A. & Bilgin, Z. R. 2006. Pre-neogene stratigraphy of the Karaburun Peninsula (W of İzmir Turkey). *Bulletin of Mineral Research and Exploration*, **132**, 1-32.

Çelik, Ö. F., Delaloye, M. & Feraud, G. 2006. Precise $^{40}Ar/^{39}Ar$ ages from the metamorphic sole rocks of the Tauride Belt ophiolites, southern Turkey: implications for the rapid cooling history. *Geological Magazine*, **143**, 213-227.

Çelik, Ö. F., Marzoli, A., Marschik, R., Chiaradia, M., Neubauer,F. & Öz, I., 2011. Early–Middle Jurassic intra-oceanic subduction in the İzmir-Ankara-Erzincan Ocean, Northern Turkey. *Tectonophysics*, **509**, 120-134.

Chan, G. H. N., Malpas, J., Xenophontos, C. & Lo, C. H. 2007. Timing of subduction zone metamorphism during the formation and emplacement of Troodos and Baër-Bassit ophiolites: insights from $^{40}Ar/^{39}Ar$ geochronology. *Geological Magazine*, **144**, 797-810.

Chiari, M., Cortese, G., Marcucci, M. & Nozzoli, N. 1997. Radiolarian biostratigraphy in the sedimentary cover of the ophiolites of south-western Tuscany, Central Italy. *Eclogae Geologicae Helvetiae*, **90**, 55-77.

Chiari, M., Marcucci, M. & Principi, G. 2000. The age of Radiolarian Cherts associated with the ophiolites in the Apennines (Italy) and Corsica (France): a revision. *Ofioliti*, **25**, 141-146.

Cloos, M. & Shreve, R. L. 1988. Subduction-Channel Model of Prism Accretion, Melange Formation, Sediment Subduction, and Subduction Erosion at Convergent Plate Margins: 1. Background and Description. *Physical Applied Geophysics*, **128**, 456-500.

Crawford, A. J. 1989. *Boninites*. Allen & Unwin Australia.

Danelian, T., Lekkas, S. & Alexopoulos, A 2000. Découverte de radiolarites triasiques dans un complexe ophiolitique à l'extrême sud du Péloponnèse (Agelona, Lakonie, Grèce). *Comptes Rendus de l'Académie des Sciences, Paris*, **330**, 639-644.

Danelian, T., Galoyan, G., Rolland, Y. & Sosson, M. 2007. Palaeontological (Radiolarian) Late Jurassic age constraint for the Stepanavan ophiolite (Lesser Caucasus, Armenia). *Bulletin of the Geological Society of Greece*, **40**, 31-38.

Danelian, T., Asatryan, G., Sosson, M., Person, A., Sahakyan, L. & Galoyan, G. 2008. Discovery of Middle Jurassic (Bajocian) Radiolaria from the sedimentary cover of the Vedi ophiolite (Lesser Caucasus, Armenia). *Comptes Rendus PalEvol*, **7**, 327-334.

Danelian, T., Asatryan, G., Sahakyan, L., Galoyan, G., Sosson, M. & Avagyan, A. 2010. New and revised radiolarian biochronology for the sedimentary cover of ophiolites in the Lesser Caucasus (Armenia). *In:* Sosson, S., Kaymakci, N., Stephenson, R., Bergerat, F. & Starostenko, V. (eds) *Sedimentary Basin Tectonics from the Black Sea and Caucasus to the Arabian Platform*. Geological Society, London, Special Publications, **340**, 383-391.

Danelian, T., Asatryan, G., Galoyan, G., Sosson, M., Sahakyan, L., Caridroit, M. & Avagyan, A. 2012. Geological history of ophiolites in the Lesser Caucasus and correlation with the Izmir-Ankara-Erzincan suture zone: insights from radiolarian biochronology. In: Danelian, T. & Goričan, S. (eds) *Radiolarian biochronology as a key to tectono-stratigraphic reconstructions*. Bulletin de la Société Géologique de France, **183**, 331-342.

Danelian, T., Zambetakis-Lekkas, A., Galoyan, G., Sosson, M., Asatryan, G., Hubert, B. & Grigiryan, A. 2014. Reconstructing Upper Cretaceous (Cenomanian) paleoenvironments in Armenia based on radiolarian and benthic foraminifera; implications for the geodynamic evolution of the Tethyan realm in the Lesser Caucasus. *Palaeogeography, Palaeoclimatology, Palaeoecology,* (just-accepted).

De Wever, P., Danelian, T., Durand-Delga, M., Cordey, F. & Kito, N. 1987. Datations des radiolarites post-ophiolitiques de Corse alpine à l'aide des Radiolaires. *Comptes Rendus de l'Académie des Sciences, Paris*, **305**, 893-900.

Dercourt, J., Zonenschain, L. P., Ricou, L. -E., Kazmin, V. G., Le Pichon, X., Knipper, A. L., Grandjacquet, C., Sbortshikov, I. M., Geyssant, J., Lepvir, C., Pechersky, D. H., Boulin, J., Sibuet, J. -C., Savostin, L. A., Sorokhtin, O., Westphal, M., Bazhenov, M. L., Lauer, J. P. & Biju-Duval, B. 1986. Geological evolution of the Tethys belt from the Atlantic to the Pamirs since the Lias. *Tectonophysics*, **123**, 241-315.

Deschamps, A. & Lallemand, S. 2003. Geodynamic setting of Izu-Bonin-Mariana boninites. *Geological Society, London, Special Publications*, **219**, 163-186.

Dickinson, W.R. 2000. Geodynamic interpretation of Paleozoic tectonic trends oriented oblique to the Mesozoic Klamath-Sierran continental margin in California. *In:* Soreghan, M.J. & Gehrels, G.E. (eds) *Paleozoic and Triassic Paleogeography and Tectonics of Western Nevada and Northern California*. Geological Society, America, Special Paper, **347**, 209-245.

Dilek, Y. & Whitney, D. L. 1997. Counterclockwise PTt trajectory from the metamorphic sole of a Neo-Tethyan ophiolite (Turkey). *Tectonophysics*, **280**, 295-310.

Dilek, Y., Thy, P., Hacker, B. & Grundvig, S. 1999. Structure and petrology of Tauride ophiolites and mafic dike intrusions (Turkey): Implications for the Neotethyan ocean. *Geological Society of America Bulletin*, **111**, 1192-1216.

Dilek, Y., Imamverdiyev, N. & Altunkaynak, Ş. 2010. Geochemistry and tectonics of Cenozoic volcanism in the Lesser Caucasus (Azerbaijan) and the peri-Arabian region: collision-induced mantle dynamics and its magmatic fingerprint. *International Geology Review*, **52**, 536-578

Dimo-Lahitte, A., Monié, P. & Vergély, P. 2001. Metamorphic soles from the Albanian ophiolites: Petrology, $^{40}Ar/^{39}Ar$ geochronology, and geodynamic evolution. *Tectonics*, **20**, 78-96.

Duretz, T. & Gerya, T. V. 2013. Slab detachment during continental collision: Influence of crustal rheology and interaction with lithospheric delamination. *Tectonophysics*, **602**, 124-140.

Elitok, Ö. & Drüppel, K. 2008. Geochemistry and tectonic significance of metamorphic sole rocks beneath the Beyşehir–Hoyran ophiolite (SW-Turkey). *Lithos*, **100**, 322-353.

Ellis, S., Beaumont, C. & Pfiffner, A. 1999. Geodynamic models of crustal-scale episodic tectonic accretion and underplating in subduction zones. *Journal of Geophysical Research*, **104**, 15169-15190.

Engi, M., Berger, A. & Roselle, G.T. 2001. Role of the tectonic accretion channel in collisional orogeny. *Geology*, **29**, 1143-1146.

Falloon, T. J. & Crawford, A.J. 1991. The petrogenesis of high-Ca boninite lavas dredged from the northern Tonga ridge. *Earth Planetary Science Letters*, **102**, 375-394.

Falloon, T. J., Malahoff, A., Zonenshaina, L. P. & Bogdanova, Y. 1992. Petrology and geochemistry of back-arc basin basalts from Lau Basin spreading ridges at 15°, 18° and 19°S. *Mineralogy and Petrology*, **47**, 1-35.

Festa, A., Pini, G. A., Dilek, Y. & Codegone, G. 2010. Mélanges and mélange-forming processes: a historical overview and new concepts. *International Geology Review*, **52**, 1040-1105.

Galoyan, G. 2008. *Etude pétrologique, géochimique et géochronologique des ophiolites du Petit Caucase (Arménie)*. PhD thesis, Université de Nice-Sophia Antipolis.

Galoyan, G., Rolland, Y., Sosson, M., Corsini, M. & Melkonyan, R. 2007. Evidence for superposed MORB, oceanic plateau and volcanic arc series in the Lesser Caucasus (Stepanavan, Armenia). *Comptes Rendus Geoscience*, **339**, 482-492.

Galoyan, G., Rolland, Y., Sosson, M., Corsini, M., Billo, S., Verati, C. & Melkonian, R. 2009. Geology, geochemistry and $^{40}Ar/^{39}Ar$ dating of Sevan ophiolites (Lesser Caucasus, Armenia): Evidence for Jurassic Back-arc opening and hot spot event between the South Armenian Block and Eurasia. *Journal of Asian Earth Sciences*, **34**, 135-153.

Gealey, W. K. 1988. Plate tectonic evolution of the Mediterranean-Middle East region. *Tectonophysics*, **155**, 285-306.

Gedik, A. 2008. Geology of the Tertiary rocks around Kemah-Erzincan-Çayirli region and their source rock characteristics. *Türkiye Mineral Resource Exploration Bulletin*, **137**, 1-27

Golonka, J. 2004. Plate tectonic evolution of the southern margin of Eurasia in the Mesozoic and Cenozoic. *Tectonophysics*, **381**, 235-273.

Göncüoğlu, M. C., Turhan, N., Şentürk, K., Özcan, A., Uysal, Ş. & Yaliniz, M. K. 2000. A geotraverse across northwestern Turkey: tectonic units of the Central Sakarya region and their tectonic evolution. *Geological Society, London, Special Publications*, **173**, 139-161.

Göncüoğlu, M. C., Yalınız, K. & Tekin, U. K. 2006a. Geochemical features and radiolarian ages of volcanic rocks from the Izmir-Ankara Suture Belt, Western Turkey. *Proceedings of the International Symposium on Mesozoic Ophiolite Belts of the N Balkan Peninsula*, 41-44.

Göncüoğlu, M. C., Yalınız, K. & Tekin, U. K. 2006b. Geochemistry, tectono-magmatic discrimination and radiolarian ages of basic extrusives within the Izmir-Ankara Suture Belt (NW Turkey): Time Constraints for the Neotethyan Evolution. *Ofioliti*, **31**, 25-38.

Göncüoğlu, C. M., Sayit, K. & Tekin, U. K. 2010. Oceanization of the northern Neotethys: Geochemical evidence from ophiolitic melange basalts within the Izmir-Ankara suture belt, NW Turkey. *Lithos*, **116**, 175-187.

Gray, D. R., Foster, D. A. & Bierlein, F. P. 2002. Geodynamics and metallogeny of the Lachlan Orogen. *Australian Journal of Earth Sciences*, **49**, 1041-1056.

Gücer, M. A. & Aslan, Z. 2009.Yoncayolu Metamorfitleri'nin (Üzümlü-Erzincan) Mineralojisi, Jeokimyası ve Kökeni: Yeşilşist Fasiyesinin Metamorfizma Özellikleri. *Türkiye Jeoloji Kurultayı, MTA - Ankara*.

Gücer, M. A., Aslan, Z. & Bektas, O. 2007. Petrography and Geochemistry Freatures of the Yoncayolu Metamorphics in Erzincan, NE Turkey. *Glodschmidt Conference Abstracts*, A360.

Hafkenscheid, E., Wortel, M. J. R. & Spakman, W. 2006. Subduction history of the Tethyan region derived from seismic tomography and tectonic reconstructions. *Journal of Geophysical Research*, **111**, B08401.

Harris, N. B., Kelley, S. & Okay, A. I. 1994. Post-collision magmatism and tectonics in northwest Anatolia. *Contribution to Mineralogy and Petrology*, **117**, 241-252.

Hässig, M., Rolland, Y., Sosson, M., Galoyan, G., Müller, C., Avagyan, A. & Sahakyan, L. 2013. New structural and petrological data on the Amasia ophiolites (NW Sevan-Akera suture zone, Lesser Caucasus): Insights for a large-scale obduction in Armenia and NE Turkey. *Tectonophysics*, **588**, 135-153.

Hässig, M., Rolland, Y., Sosson, M., Galoyan, G., Sahakyan, L., Topuz, G., Çelik, Ö. F., Avagyan, A. & Müller, C. 2014. Linking the NE Anatolian and Lesser Caucasus ophiolites: evidence for large scale obduction of oceanic crust and implications for the formation of the Lesser Caucasus-Pontides Arc. *Geodinamica Acta*, (just-accepted).

Hässig, M., Rolland, Y., Sosson, M., Galoyan, G. & Avagyan, A. 2014. P-T-t history of the Amasia ophiolite 'metamorphic sole' (Armenia, Lesser Caucasus): implications for the obduction process of an old oceanic lithosphere. *Journal of Metamorphic Geology*, (in review).

Hässig, M., Rolland, Y., Sahakyan, L., Sosson, M., Galoyan, G., Avagyan, A., Bosch, D. & Müller, C. 2014. Multi-stage metamorphism in the South Armenian Block during the Late Jurassic to Early Cretaceous: tectonics over south-dipping subduction of Northern branch of Neotethys. *Journal of Asian Earth Sciences*, (submitted).

Hatzipanagiotou, K. & Pe-Piper, G. 1995. Ophiolitic and sub-ophiolitic metamorphic rocks of the Vatera area, southern Lesbos (Greece): geochemistry and geochronology. *Ofioliti*, **20**, 17-29.

Hess, J. C., Aretz, J., Gurbanov, A. G., Emmermann, R. & Lippolt, H. J. 1995. Subduction related Jurassic andesites in the northern Great Caucasus. *Geologische Rundschau*, **84**, 319-333.

Huene, R., Ranero, C. R. & Vannucchi, P. 2004. Generic model of subduction erosion. *Geology*, **32**, 913-916.

Hutchison, C. S. 1989. *Geological evolution of South-east Asia*. Oxford: Clarendon Press.

Ingersoll, R. V. 1997. Phanerozoic tectonic evolution of central California and environs. *International Geology Review*, **39**, 957-972.

Ingersoll, R. V. 2008. Subduction-related sedimentary basins of the USA Cordillera. *Sedimentary Basins of the World*, **5**, 395-428.

Kazmin, V. G. 1991. Collision and rifting in the Tethys Ocean: Geodynamic implication. *Tectonophysics*, **196**, 371-384.

Kazmin, V. G., Sbortshikov, I. M., Ricou, L. E., Zonenshain, L. P., Boulin, J. & Knipper, A. L. 1986. Volcanic belts as markers of the Mesozoic-Cenozoic active margin of Eurasia. *Tectonophysics*, **123**, 123-152.

Knipper, A. L. & Khain, E. V. 1980. Structural position of ophiolites of the Caucasus. *Ofioliti, Special Issue*, **2**, 297-314.

Knipper, A. L. 1975. The oceanic crust in the structure of the Alpine Folded Belt (South Europe, western part of Asia and Cuba). *Tr. GIN NAS USSR*, **267**, 207. (in Russian).

Koepke, J., Seidel, E. & Kreuzer, H. 2002. Ophiolites on the Southern Aegean islands Crete, Karpathos and Rhodes: composition, geochronology and position within the ophiolite belts of the Eastern Mediterranean. *Lithos*, **65**, 183-203.

Lanphere, M. A., Coleman, R. G., Karamata, S. & Pamić, J. 1975. Age of amphibolites associated with Alpine peridotites in the Dinaride ophiolite zone, Yugoslavia. *Earth and Planetary Science Letters*, **26**, 271-276.

Lordkipanidze, M. B., Meliksetian, B. & Djarbashian, R. 1989. Mesozoic-Cenozoic magmatic evolution of the Pontian–Crimean–Caucasian region. *In:* Rakús, M., Dercourt, J. & Nairn, A. E. M. (eds) *IGCP Project no. 198: Evolution of the Northern Margin of Tethys*. Mémoires de la Société Géologique de France, **154**, 103-124.

Mart, Y. 1987. Superpositional tectonic patterns along the continental margin of the southeastern Mediterranean: A review. *Tectonophysics*, **140**, 213-232

McKenzie, D. P. 1969. Speculations on the consequences and causes of plate motions. *Geophysical Journal International*, **18**, 1-32.

Mederer, J. 2013. *Regional setting, geological context and genetic aspects of polymetallic hydrothermal ore deposits from the Kapan ore district, southern Armenia: a contribution to the Mesozoic island arc metallogeny of the Lesser Caucasus*. PhD Thesis. Université de Genève.

Meijers, M., Smith, B., Sosson, M., Rolland, Y., Grigoryan, A., Sahakyan, L., Avagyan, A., Adamia, S., Sadradze, N., Asanidze, B., Langereis, C., Kircher, U., Mensink, M. & Müller, C. 2013. *A paleolatitude reconstruction of the South Armenian Block (SAB) since the late Cretaceous: constraints on the Tethyan realm*. Darius Programme, Tbilisi Meeting, Eastern Black Sea and Caucasus Workshop.

Moix, P. & Goričan, Š. 2013. Jurassic and Cretaceous radiolarian assemblages from the Bornova mélange in northern Karaburun Peninsula (western Turkey) and its connection to the İzmir-Ankara mélanges. *Geodinamica Acta*, (just-accepted).

Moix, P., Beccaletto, L., Kozur, H. W., Hochard, C., Rosseletd, F. & Stampfli, G. M. 2008. A new classification of the Turkish terranes and sutures and its implication for the paleotectonic history of the region. *Tectonophysics*, **451**, 7-39.

Monin, A. S. & Zonenshain, L. P. 1987. History of the Ocean Tethys. *Moscow Institute of Oceanology*. (in Russian)

Nikishin, A. M., Cloetingh, S., Brunet, M. F., Stephenson, R., Bolotov, S. N. & Ershov, A. V. 1998. Scythian platform and Black Sea region: Mesozoic-Cenozoic tectonic and dynamics. *In:* Crasquin-Soleau, S. & Barrier, E. (eds) *Peri–Tethys Memoir 3: Stratigraphy and*

Evolution of Peri–Tethyan Platforms. Mémoires du Muséum National d'Histoire Naturelle. Serie A, Paris, **177**, 163-176.

Nikishin, A. M., Khotylev, A. O., Bychkov, A. Y., Kopaevich, L. F., Petrov, E. I. & Yapaskurt, V. O. 2013. Cretaceous volcanic belts and the evolution of the Black Sea Basin. *Moscow University Geology Bulletin*, **68**, 141-154.

Okay, A. İ. & Şahintürk, Ö. 1997. Geology of the eastern Pontides. *In:* Robinson, A.G. (eds) *Regional and Petroleum Geology of the Black Sea and Surrounding Region: American Association of Petroleum*. Geologists Memoir, **68**, 291–311

Okay, A. I. & Tüysüz, O. 1999. Tethyan sutures of northern Turkey. *Geological Society, London, Special Publication*, **156**, 475-515.

Okay, A. I., Tüysüz, O., Satır, M., Özkan-Altıner, S., Altıner, D., Sherlock, S. & Eren, R. E. 2006. Cretaceous and Triassic subduction-accretion, HP-LT metamorphism and continental growth in the Central Pontides, Turkey. *Geological Society of America Bulletin*, **118**, 1247-1269.

Önen, A. P. 2003. Neotethyan ophiolitic rocks of the Anatolides of NW Turkey and comparison with Tauride ophiolites. *Journal of the Geological Society*, **160**, 947-962.

Özen, H., Çolakoğlu, A., Sayak, H., Dönmez, C., Türkel, A., Odabaşı, İ,…& Winchester, J. A. 2006. The petrogenesis of tectonites and cumulate rocks from the ophiolites, north of Erzincan. *59th Geological Congress of Turkey*, 100-101.

Özgül, N. & Turşucu, A. 1984. Stratigraphy of the Mesozoic carbonate sequence of the Munzur Mountains (Eastern Taurides). *In:* Tekeli, O. & Göncüoğlu, M. C. (eds) *Geology of the Taurus Belt*. Ankara, Maden Tetkit Arama Enstitüsü, 173-181.

Özgül, N. 1981. *Munzur Dağlarının Jeolojisi*. General Directorate of Mineral Research and Exploration (MTA) Report 6995. (in Turkish)

Parlak, O. & Delaloye, M. 1999. Precise $^{40}Ar/^{39}Ar$ ages from the metamorphic sole of the Mersin Ophiolite (southern Turkey). *Tectonophysics*, **301**, 145-158, doi:10.1016/S0040-1951(98)00222-4

Parlak, O., Çolakoğlu, A., Dönmez, C., Sayak, H., Yıldırım, N., Türkel, A. & Odabaşı, İ. 2013. Geochemistry and tectonic significance of ophiolites along the Ankara–Erzincan suture zone in northeastern Anatolia. *In:* Robertson, A. H. F., Parlak, O. & Ünlügenç, U. C. (eds) *Geological Development of Anatolia and the Easternmost Mediterranean Region*. Geological Society, London, Special Publications, **372**, 75-105.

Peccerillo, A. & Taylor, S. R. 1976. Geochemistry of Eocene calc-alkaline volcanic rocks from the Kastamonu area, northern Turkey. *Contributions to Mineralogy and Petrology*, **58**, 63-81, doi:10.1007/BF00384745

Rice, S. P., Robertson, A. H. F., Ustaömer, T., İnan, N. & Taslı, K. 2009. Late Cretaceous–Early Eocene tectonic development of the Tethyan suture zone in the Erzincan area, Eastern Pontides, *Turkey. Geological Magazine*, **146**, 567-590.

Ricou, L. E. 1994. Tethys reconstructed: plates, continental fragments and their boundaries since 260 Ma from Central America to South-eastern Asia. *Geodinamica Acta*, **7**, 169-218.

Ricou, L. E., Zonenshain, L. P., Dercourt, J., Kazmin, V. G., Le Pichon, X., Knipper, A. L., … & Biju-Duval, B. 1985. Méthodes pour l'établissement de neuf cartes paléogéographiques de l'Atlantique au Pamir depuis le Lias. *Bulletin de la Société Géologique de France*, **8**, 625-635.

Ricou, L. E., Dercourt, J., Geyssant, J., Grand-Jaquet, C., Lepcrier, C. & Biju-Duval, B. 1986. Geological constraints on the Alpine evolution of the Mediterranean Tethys. *Tectonophysics*, **123**, 83-122.

Robertson, A. H. & Mountrakis, D. 2006. Tectonic development of the Eastern Mediterranean region: an introduction. *Geological Society, London, Special Publications*, **260**, 1-9.

Robertson, A. H., Parlak, O. & Ustaömer, T. 2012. Overview of the Palaeozoic–Neogene evolution of Neotethys in the Eastern Mediterranean region (southern Turkey, Cyprus, Syria). *Petroleum Geoscience*, **18**, 381-404.

Robertson, A. H. 2002. Overview of the genesis and emplacement of Mesozoic ophiolites in the Eastern Mediterranean Tethyan region. *Lithos*, **65**, 1-67.

Robertson, A. 2004. Development of concepts concerning the genesis and emplacement of Tethyan ophiolites in the Eastern Mediterranean and Oman regions. *Earth-Science Reviews*, **66**, 331-387.

Robinson, A., Spadini, G., Cloetingh, S. & Rudat, J. 1995. Stratigraphic evolution of the Black Sea: inferences from basin modelling. *Marine and Petroleum Geology*, **12**, 821-835.

Roddick J. C., Cameron, W. E. & Smith, A. G. 1979. Permo-Triassic and Jurassic $^{40}Ar/^{39}Ar$ ages from Greek ophiolites and associated rocks. *Nature*, **279**, 788-790.

Rojay, B., Altiner, D., Altiner, S.O., Önen, P., James, S.L. & Thirlwall, M.F. 2004. Geodynamic significance of the Cretaceous pillow basalts from North Anatolian Ophiolitic Mélange Belt, Central Anatolia, Turkey: geochemical and paleontological constraints. *Geodinamica Acta*, **17**, 349-361.

Rolland, Y., Billo, S., Corsini, M., Sosson, M. & Galoyan., G. 2009a. Blueschists of the Amassia-Stepanavan Suture Zone (Armenia): linking Tethys subduction history from E-Turkey to W-Iran. *International Journal of Earth Sciences*, **98**, 533-550.

Rolland, Y., Galoyan, G., Bosch, D., Sosson, M., Corsini, M., Fornari, M. & Verati, C. 2009b. Jurassic back-arc and Cretaceous hot-spot series in the Armenian ophiolites - Implications for the obduction process. *Lithos*, **112**, 163-187.

Rolland, Y., Galoyan, G., Sosson, M., Melkonian, R. & Avagyan, A. 2010. The Armenian ophiolite: Insights for jurassic back-arc formation, lower Cretaceous hot spot magmatism and upper Cretaceous obduction over the South Armenian block. *Geological Society, London, Special Publications*, **340**, 353-382.

Rolland, Y., Sosson, M., Adamia, Sh. & Sadradze, N. 2011. Prolonged Variscan to Alpine history of an active Eurasian margin (Georgia, Armenia) revealed by 40Ar/39Ar dating. *Gondwana Research*, **20**, 798-815.

Rolland, Y., Perincek, D., Kaymakci, N., Sosson, M., Barrier, E. & Avagyan, A. 2012. Evidence for 80–75Ma subduction jump during Anatolide–Tauride–Armenian block accretion and 48Ma Arabia–Eurasia collision in Lesser Caucasus–East Anatolia. *Journal of Geodynamics*, **56**, 76-85.

Sahakyan, L., Bosch, D., Sosson, M., Avagyan, A., Shahidi, A., Galoyan, G., Danelian, T. & Müller, C. 2013. *Geochemical input on Khoy area tectonic evolution*. Darius Programme, Tbilisi Meeting, Eastern Black Sea and Caucasus Workshop.

Şengör, A. M. C. & Yılmaz, Y. 1981. Tethyan evolution of Turkey: A plate tectonic approach. *Tectonophysics*, **75**, 181-241.

Şengör, A. M. C., Altıner, D., Cin, A., Ustaömer, T. & Hsü, K.J. 1988. Origin and assembly of the Tethyside orogenic collage at the expense of Gondwana-Land. *In:* Audley-Charles, M.G. & Hallam, A. (eds) *Gondwana and Tethys*. Geological Society, London, Special Publications, **37**, 119-181.

Şengün, M. 2006. A critical review of the Anatolian geology: a dialectic to sutures and evolution of the Anatolian Tethys and Neotethys. *Mineral Research Exploration Bulletin*, **133**, 1-29.

Servais, M. 1982. *Collision et suture tethysienne en Anatolie central: étude structurale et métamorphique (H.P.B.T.) de la zone nord Kütahya*. PhD thesis, Université de Paris-Sud, Centre d'Orsay.

Shemenda, A. I. 1994. *Subduction: Insights from physical modeling*. Kluwer Academic Pub.

Soesoo, A., Bons, P. D., Gray, D. R. & Foster, D. A. 1997. Divergent double subduction: tectonic and petrologic consequences. *Geology*, **25**, 755-758.

Sokolov, S. D. 1977. *The Olistostromes and Ophiolitic Nappes of the Lesser Caucasus*. Nauka, Moscow . (in Russian).

Sosson, M., Rolland, Y., Danelian, T., Muller, C., Melkonyan, R., Adamia, S., … & Galoyan, G. 2010. Subductions, obduction and collision in the Lesser Caucasus (Armenia, Azerbaijan, Georgia), new insights. *Geological Society, London, Special Publications*, **340**, 329-352.

Speed, R. C. & Sleep, N. H. 1982. Antler orogeny and foreland basin: A model. *Geological Society of America Bulletin*, **93**, 815-828.

Spray, J. G., Bébien, J., Rex, D. C. & Roddick, J. C. 1984. Age constraints on the igneous and metamorphic evolution of magmatism in the Hellenic–Dinaric ophiolites. *In:* Dixon, J.E. & Robertson, A. H. F. (eds) *The Geological Evolution of the Eastern Mediterranean*. Geological Society of London, Special Publication, **17**, 619-627.

Stampfli, G. M. 2000. Tethyan oceans. *Geological Society, London, Special Publications*, **173**, 1-23.

Stampfli, G. M., Borel, G. D., Cavazza, W., Mosar, J. & Ziegler, P.A. 2001. Palaeotectonic and palaeogeographic evolution of the western Tethys and PeriTethyan domain (IGCP Project 369). *Episodes*, **24**, 222-228.

Stocklin, J. 1974. Possible ancient continental margins in Iran. *The geology of continental margins*, 873-887.

Stöcklin, J. & Bhattarai, K. D. 1977. *Geology of the kathmandu area and central mahabharat range, Nepal*. Nepal Department of Mines and Geology, Technical Report 86.

Tekin, U. K. & Göncüoglu, M. C. 2007. Discovery of the oldest (Upper Ladinian to Middle Carnian) radiolarian assemblages from the Bornova Flysch zone in Western Turkey: implications for the evolution of the Neotethyan Izmir–Ankara Ocean. *Ofioliti*, **32**, 131-150.

Tekin, U. K. & Göncüoğlu, C. M. 2008. Late Middle to early Late Triassic radiolarian faunas from the Izmir-Ankara suture belt in western Turkey: remarks on the evolution of the Neotethyan Izmir-Ankara Ocean. *In:* Krystyn, L. & Mandl, G. W. (eds) *Upper Triassic subdivisions, zonations and events: Meeting of the late IGCP 467 and STS, abstracts and excursion-guide*. Bad Goisern (Austria), September, 28th - October 2nd, 2008: Berichte der Geologischen Bundesanstalt 76, 59-60.

Tekin, U. K. & Göncüoğlu, C. M. 2009. Late Middle Jurassic (Late Bathonian-Early Callovian) radiolarian cherts from the Neotethyan Bornova flysch zone, Spil Mountains, western Turkey. *Stratigraphy and Geological Correlation*, **17**, 298-308.

Tekin, U. K., Göncüoglu, M. C. & Turhan, N. 2002. First evidence of Late Carnian radiolarians from the Izmir-Ankara suture complex, central Sakarya, Turkey: implications for the opening age of the Izmir-Ankara branch of Neo-Tethys. *Geobios*, **35**, 127-135.

Tekin, U. K., Göncüoğlu, C. M., & Uzuncimen, S. 2012a. Radiolarian assemblages of Middle and Late Jurassic to early Late Cretaceous (Cenomanian) ages from an olistolith record pelagic deposition within the Bornova Flysch Zone in western Turkey. *Bulletin de la Société Géologique de France*, **183**, 307-318.

Tekin, U. K., Çelik, S., Üner, T. & Arat, I. 2012b. Radiolarian Biochronology of Early Jurassic – Early Cretaceous Pelagic Deposits in Izmir – Ankara - Erzincan Suture Complex, NE and SW Çankiri, Northern Turkey: Remarks on the Evolution of Northern Branch of Neotethys. *The 13th Meeting of the International Association of Radiolarian Palaeontologists, Abstracts*, 243-244.

Teklay, M. 2006. Neoproterozoic arc–back–arc system analog to modern arc–back–arc systems: evidence from tholeiite–boninite association, serpentinite mudflows and across-arc geochemical trends in Eritrea, southern Arabian-Nubian shield. *Precambrian Research*, **145**, 81-92.

Topuz, G., Çelik, Ö. F., Şengör, A. M. C., Altıntaş, İ. E., Zack, T., Rolland, Y. & Barth, M. 2013a. Jurassic ophiolite formation and emplacement as backstop to a subduction-accretion complex in Northeast Turkey, the Refahiye ophiolite, and relation to the Balkan ophiolites. *American Journal of Science*, **313**, 1054-1087, doi:10.2475/10.2013.04

Topuz, G., Göçmengil, G., Rolland, Y., Çelik, Ö. F., Zack, T. & Schmitt, A. K. 2013b. Jurassic accretionary complex and ophiolite from northeast turkey: no evidence for the Cimmerian continental ribbon. *Geology*, **41**, 255-258.

Tüysüz, O. & Tekin, U. K. 2007. Timing of imbrication of an active continental margin facing the northern branch of Neotethys, Kargı Massif, northern Turkey. *Cretaceous Research*, **28**, 754-764.

Üner, T. 2010. *Petrology of Eldivan and Ahlat (Cankiri) ophiolites*. Ph. D. thesis, Hacettepe University (unpublished).

Ustaömer, T. & Robertson, A. H. F. 1995. Palaeotethyan tectonic evolution of the north Tethyan margin in the central Pontides, N Turkey. *In:* Erler, A., Ercan, T., Bingöl, E. & Örçen, S. (eds) *Geology of the Black Sea region*. Mineral Research and Exploration Institute, Ankara, 24-32.

Ustaömer, P. A., Ustaömer, T. & Robertson, A. H. 2012. Ion Probe U-Pb dating of the Central Sakarya Basement: a peri-Gondwana terrane intruded by Late Lower Carboniferous subduction/collision-related granitic rocks. *Turkish Journal of Earth Sciences,* **21**, 905-932.

Ustaömer, T. & Robertson, A. H. F. 2010. Late Palaeozoic–Early Cenozoic tectonic development of the Eastern Pontides (Artvin area), Turkey: stages of closure of Tethys along the southern margin of Eurasia. *In:* Sosson, M., Kaymakçı, N., Stephenson, R. A., Bergerat, F., Starostenko V. (eds) *Sedimentary Basin Tectonics from the Black Sea and Caucasus to the Arabian Platform*. Geological Society, London, Special Publications, **340**, 281-327.

Ustaömer, T., Robertson, A. H. F., Ustaömer, P. A., Gerdes, A. & Peytcheva, I. 2013. Constraints on Variscan and Cimmerian magmatism and metamorphism in the Pontides (Yusufeli-Artvin area), NE Turkey from U-Pb dating and granite geochemistry. *Geological Society, London, Special Publications*, **372**, 49-74.

Vannucchi, P., Remitti, F. & Bettelli, G. 2008. Geologic record of fluid flow and seismogenesis along an erosive subducting plate boundary. *Nature*, **451**, 699-703.

Vaughan, A. P. & Scarrow, J. H. 2003. K-rich mantle metasomatism control of localization and initiation of lithospheric strike-slip faulting. *Terra Nova*, **15**, 163-169.

Wakabayashi, J. & Dilek, Y. 2003. What constitutes 'emplacement'of an ophiolite?: Mechanisms and relationship to subduction initiation and formation of metamorphic soles. *Geological Society, London, Special Publications*, **218**, 427-447.

Yılmaz, Y., Tüysüz, O., Yiğitbaş, E., Genç, Ş. C. & Şengör, A. M. C. 1997. Geology and tectonic evolution of the Pontides. *In:* Robinson, A.G. (ed), *Regional and Petroleum*

Geology of the Black Sea and Surrounding Region: American Association of Petroleum. Geologists Memoir, **68**, 183-226.

Yilmaz, A., Adamia, S., Chabukiani, A., Chkhotua, T., Erdoğan, K., Tuzcu, S. & Karabiyikoğlu, M. 2000. Structural correlation of the southern Transcaucasus (Georgia)-Eastern Pontides (Turkey). *Geological Society, London, Special Publications*, **173**, 171-182.

Zakariadze, G. S., Knipper, A. L., Bibikova, E. V., Silantiev, S. A., Zlobin, S. K., Gracheva, T. V., … & Kolesov, T. M. 1990. The setting and age of the plutonic part of the NE Sevan ophiolite complex. *Izvestia NAS USSR, Geological*, **3**, 17-30. (in Russian)

Zakariadze, G. S., Dilek, Y., Bogdanovsky, O. G., Karpenko, S. F., Vishnevskaya, V. S. & Solov'eva, N. V. 2005. Age limits of the Lesser Caucasus paleooceanic allochtone. *Active Tectonics of the Agean region*, 15-18 June 2005, Kadir Has University, Istanbul, Turkey, 229.

Zedde, D. V. D. & Wortel, M. J. R. 2001. Shallow slab detachment as a transient source of heat at midlithospheric depths. *Tectonics*, **20**, 868-882.

Chapitre 7* - *Mise en place d'ophiolites préservées : une modélisation.

« Pour atteindre la vérité, il faut une fois dans la vie se défaire de toutes les opinions qu'on a reçues, et reconstruire de nouveau tout le système de ses connaissances. »

René Descartes

Dans cette partie nous présentons une modélisation intégrant les caractéristiques générales du domaine océanique maintenant disparu dont les ophiolites sont les seules reliques. La reconstitution géodynamique proposée avant l'obduction des ophiolites du Petit Caucase-NE Anatolie nous a permis de déterminer une structuration de la transition océan-continent (TOC) entre le SAB-TAP et la branche nord de la Néotéthys. Grace à une collaboration avec ***Thibault DURETZ*** *(Université de Lausanne), nous avons pu tester certaines hypothèses grâce à des modèles numériques thermo-mécaniques 2D. Ces modèles ont confirmé l'hypothèse principale que la lithosphère océanique devait être particulièrement chaude avant l'obduction. Cet état thermique anormalement élevé provoquerait un affaiblissement de la lithosphère facilitant le processus d'obduction. Les données géologiques fournissent des contraintes spatiales et temporelles afin de valider ou réfuter ce scénario. En replaçant cet évènement d'obduction dans le cadre de la convergence Arabie-Eurasie, nous évoquerons également d'autres hypothèses qui découlent de cette modélisation (i.e. interaction avec la subduction au nord sous l'Eurasie, résultats de datations perturbées…). En conséquence, une discussion des processus à l'origine de l'obduction est proposée pour expliquer le cas d'étude et plus généralement le mécanisme d'obduction.*

VII.1 Introduction

Les études précédentes présentées dans ce mémoire ont mis en évidence les liens entre les massifs ophiolitiques des régions du Petit Caucase et du NE de l'Anatolie. Des structures géologiques semblables, des âges identiques et des compositions géochimiques semblables vérifiées en différents points de cet ensemble ophiolitique, suggèrent qu'il s'agit d'un domaine océanique continu, d'est en ouest, séparant la marge eurasienne de celle du SAB-TAP jusqu'à la fin du Mésozoïque (voir chapitre III.1), passé en obduction sur celle-ci entre 94 et 85 Ma. La continuité de ce domaine est soutenue par des âges identiques obtenus par différentes méthodes géochronologiques ($^{40}Ar/^{39}Ar$ et U-Pb) et biochronologique (radiolaires). Elle est confirmée par des affinités et des tendances géochimiques analogues obtenues lors de comparaisons d'analyses pétrogéochimiques, montrant 2 séries magmatiques superposées d'âge distinct (voir chapitres III et IV). Un contexte de formation en SSZ à arrière-arc par ouverture lente a été déduit concernant la formation du plancher océanique des ophiolites, entre le Jurassique inférieur et Crétacé inferieur (c.180~150 Ma) (voir chapitres III et IV). La corrélation latérale de la discontinuité basale de l'obduction sur les sections lithostratigraphiques le long de la zone de suture d'Izmir-Ankara-Erzincan et Sevan-Akera à l'échelle du bloc SAB-TAP, a montré la mise en place quasi-simultanée de ces ensembles ophiolitiques au Turonien-Coniacien-Santonien (c. 94~85 Ma) (voir chapitre IV). Le métamorphisme des roches en position basale (la semelle ophiolitique) a été contraint à un intervalle de temps similaire par la datation $^{40}Ar/^{39}Ar$ des phengites et amphiboles des amphibolites à grenat (voir chapitre III.2). Il est important de remarquer que des indices sédimentaires et structuraux permettent d'affirmer qu'un bassin océanique subsistait suite à la mise en place des ophiolites et avant la collision continent–continent (voir chapitres IV et VI).

Les données paléomagnétiques indiquent qu'il était probablement dissymétrique ce qui peut expliquer un diachronisme latéral d'Est en Ouest (**Figure 67**).

En intégrant les témoins d'activité volcanique observée sur les deux marges continentales un modèle d'évolution a été proposé dans les chapitres précédents, se distinguant par une mise en place commune, telle une nappe, de l'ensemble de ces corps ophiolitiques (voir chapitres V et VI).

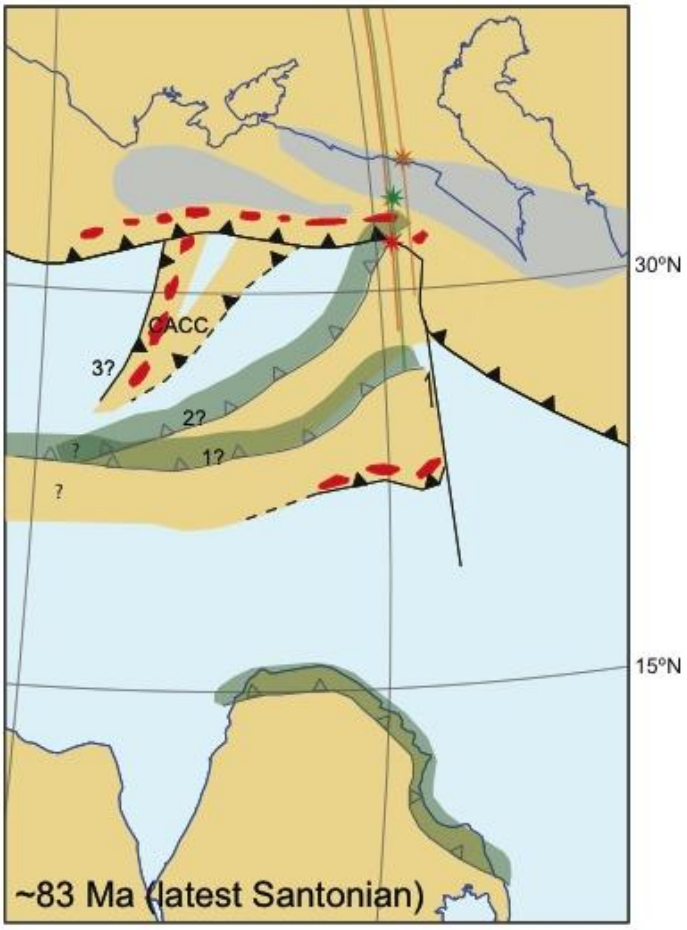

Figure 67 - Reconstitution du bloc TAP-SAB et des bassins océaniques environnants au Santonien, suite à l'obduction, d'après les données paléomagnétiques (Meijers et al., en révision). Les étoiles et marges d'erreur associées indiquent les paléo-latitudes des roches calcaires en discordance sur l'ophiolite obduite, mises en place juste après l'obduction). La position 1 décrit la position la plus méridionale et 2 la plus septentrionale du bloc TAP-SAB. L'obliquité du bloc est déduite d'une déclinaison de 40° impliquant une rotation de même valeur au moment de la fermeture de la branche nord de l'océan Téthys. La position 3 décrit la possibilité d'une zone de subduction très oblique, par rapport à la marge eurasienne, en bordure occidentale du bloc de Kirshehir (ou Central Anatolian Crystalline Complex, CACC, Lefebvre, 2011).

Dans la quasi-totalité des massifs ophiolitiques, deux suites magmatiques ont été mises en évidence l'un sur l'autre: (1) la croûte océanique surmontée de (2) coulées basaltiques ou tuf volcanique avec des tendances alcalines. Les datations radiochronologique ainsi que biostratigraphique montrent que la mise en place de cette deuxième suite se produit dans un environnement océanique l'obduction des ophiolites. Ces roches alcalines témoignent de flux mantelliques important jusqu'au début du Crétacé supérieur. Le réchauffement de la lithosphère océanique dû à ces importantes remontées de flux mantellique produirait un affaiblissement de la plaque. Cette dernière observation favorise l'hypothèse que la croûte océanique charriée doit être particulièrement chaude pour expliquer un tel événement obduction.

Afin de tester cette hypothèse, nous proposons d'effectuer, à partir de la configuration pré-obduction proposée (voir chapitre VI, **Figure 66**), une modélisation numérique thermo-mécanique. Cette démarche permettra de tester différents paramètres intervenant dans l'obduction, et de contraindre certaines grandeurs physiques se rapportant autant à la rhéologie de la lithosphère océanique obduite qu'aux mouvements relatifs de l'ensemble des structures tectoniques impliquées.

VII.2 Modélisation numérique

2.1 Configuration

Nous avons effectué des simulations à partir d'un modèle comprenant une marge continentale et un domaine océanique séparés par un niveau serpentineux (**Figure 68**). Les simulations ont été effectuées en utilisant le code thermomécanique I2VIS (Gerya & Yuen, 2003), description complète disponible dans Duretz et al. (2012). Chaque lithologie est caractérisée par une température et un état de contrainte dépendant de sa rhéologie visco-plastique, tels que listés dans le Tableau XXX. Suivant la démarche de Gerya et al. (2004), les simulations intègrent l'effet de changement de phase sur la densité des matériaux en négligeant l'effet cinétique des réactions. La taille du domaine modélisé est de 4000 x 1400 km avec un maillage variable (1361 x 351) afin d'atteindre un espacement des mailles de 1 km dans la zone de collision. Une vitesse de convergence de 5 $cm.a^{-1}$ a été initialement imposée. Après 500 km de convergence atteint, la convergence a été désactivée et nous avons imposé de l'extension à une vitesse de 5 $cm.a^{-1}$. Toutes les limites du domaine de modélisation sont à glissement libre. Une couche d'une épaisseur de 20 km d'air visqueux (ρ_{air} = 0 $kg.m^{-3}$, η_{air} = 10^{18} Pa.s) a été utilisée afin de mimer les effets d'une surface libre et ainsi de permettre le développement topographique (Schmeling et al., 2008; Crameri et al., 2012).

Figure 68 – Représentation schématique de la configuration pré-obduction (en haut) et la distribution des champs de composition de référence utilisée au cours des modélisations (en bas).

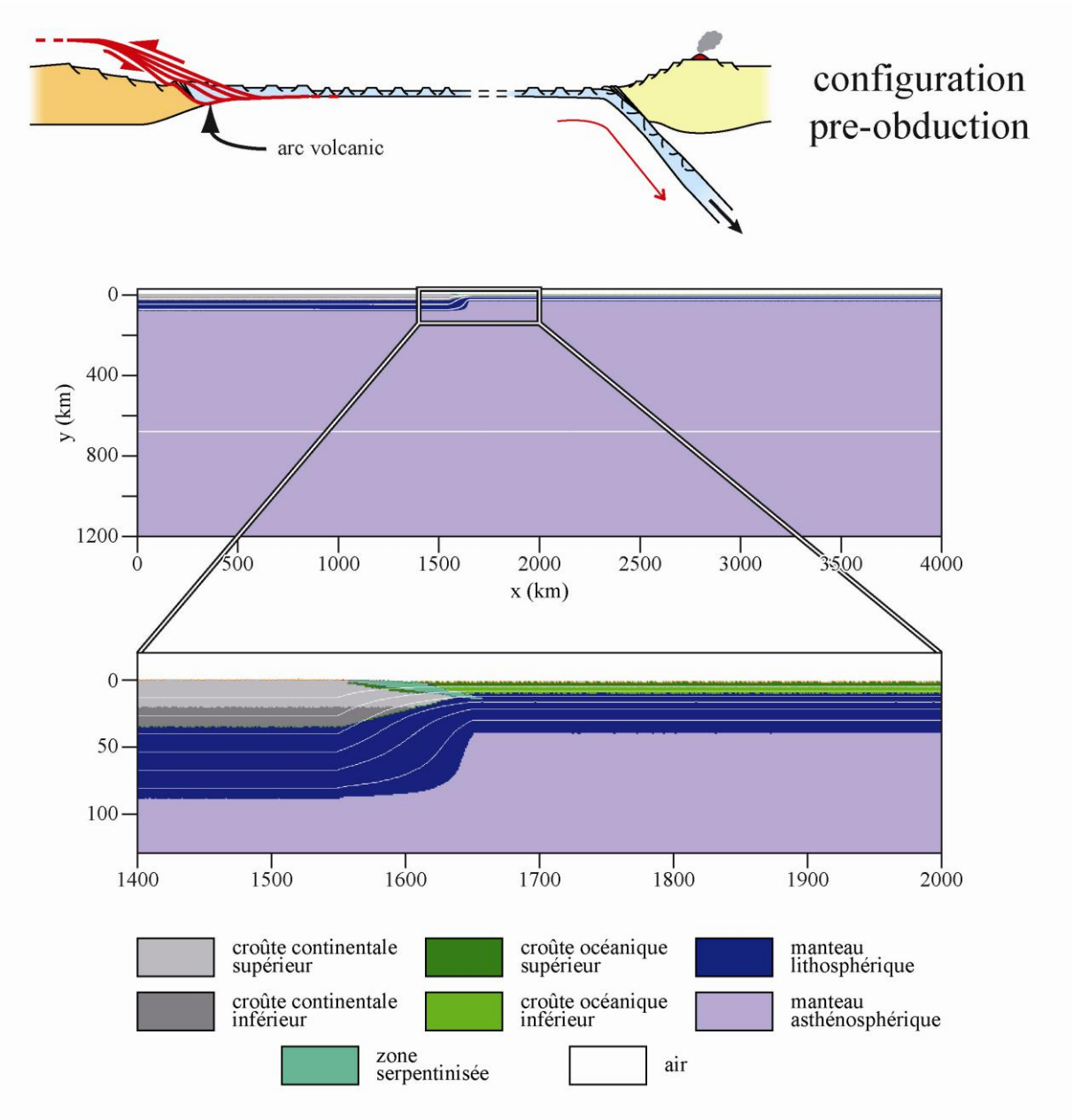

Unité	k (W/m/K)	H_r (W/m^3)	Cp (J/kg)	Loi de fluage	$\eta 0$ (Pa^n.s)	n	E_a (J)	V_a (J/bar)	sin(ϕ)	C (MPa)
Sédiments	0,64 + 807 / (T + 77)	1,50 x 10^{-6}	1000	wet Qz.	1,97 x 10^{17}	2,3	1,54 x 10^5	0,8	0,15	1
Croûte continental supérieur	0,64 + 807 / (T + 77)	1,00 x 10^{-6}	1000	wet Qz.	1,97 x 10^{17}	2,3	1,54 x 10^5	0,8	0,15	2
Croûte continental inférieur	1,18 + 474 / (T + 77)	0,25 x 10^{-6}	1000	Pl. (An75)	4,80 x 10^{22}	3,2	2,38 x 10^5	1,2	0,15	2
Croûte océanique supérieur	0,64 + 807 / (T + 77)	0,25 x 10^{-6}	1000	wet Qz.	1,97 x 10^{17}	2,3	1,54 x 10^5	0,8	0,00	2
Croûte océanique inférieur	1,18 + 474 / (T + 77)	0,25 x 10^{-6}	1000	Pl. (An75)	4,80 x 10^{22}	3,2	2,38 x 10^5	0,8	0,60	2
Manteau	0,73 + 1293 / (T + 77)	2,20 x 10^{-6}	1000	dry Ol.	3,98 x 10^{16}	3,5	5,32 x 10^5	0,8	0,60	2
Zone de faiblesse	0,73 + 1293 / (T + 77)	2,20 x 10^{-6}	1000	wet Ol.	5,01 x 10^{20}	4,0	4,70 x 10^5	0,8	0,00	1

Tableau 19 – Paramètres thermiques et rhéologique des lithologies utilisé lors des modélisations.

2.2 Modèle 1 - rajeunissement thermique étendu à tout le domaine océanique

L'évolution de ce modèle peut être décomposée en 2 étapes successives (**Figure 69**). La première étape est marquée par l'initiation d'une subduction continentale/obduction (chevauchement de lithosphère océanique sur de la lithosphère continentale ou le sous-charriage de cette dernière sous la première). Cette étape de forte compression horizontale est nécessaire pour expliquer des obductions simultanées en Oman (branche Téthys sud) et sur la branche Téthys nord. Nous avons indiqué que cette phase d'obduction s'accompagne également d'un ralentissement de la subduction sous la marge active de l'Eurasie au nord qui peut être causée par l'entrée en subduction de monts sous-marins, l'arrivée de la ride en subduction, ou encore le début de collision de l'extrêmité NE du bloc TAP-SAB (cf **Figure 67**). Par la suite, on constate une reprise de l'activité d'arc le long de la marge eurasienne. Dans cette modélisation nous avons donc imposé (1) une étape de compression où la subduction nord ne joue pas, (2) un arrêt de la compression et une reprise la subduction nord.

(1) Etape de compression

Lors de cette période les contraintes s'accumulent progressivement au cours de la convergence de deux domaines. La formation d'un bombement caractéristique d'un front de charriage se développe. La lithosphère océanique se retrouve ainsi charriée au-dessus de la lithosphère continentale. A 5 Ma la marge continentale en subduction atteint une profondeur à laquelle la flottabilité positive de sa croûte provoque une réduction de l'angle de plongement. A 6 Ma la subduction de la marge continentale progresse en une subduction plate avec un angle de plongement faible. La marge continentale est enfouie à une profondeur maximum de 50 km.

Figure 69 – Evolution temporelle du modèle 1 caractérisé par une lithosphère océanique vieille mais d'un âge thermique de 5 Ma sur la totalité de son étendu.

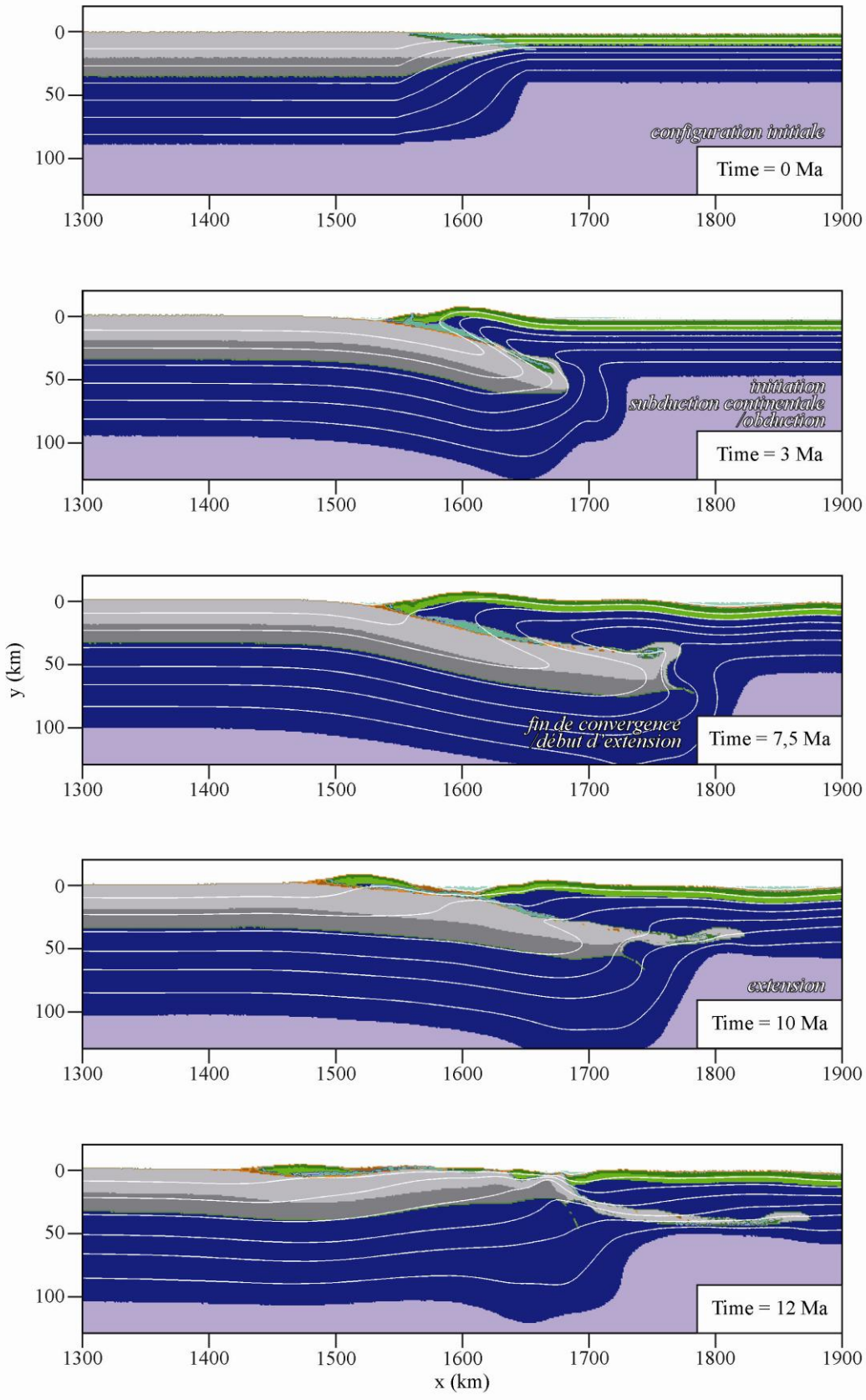

Le front de charriage est le résultat d'une zone de friction à l'interface entre les croûtes continentale et océanique. Cette friction entraîne l'érosion tectonique de la croûte océanique chevauchante et le sous-charriage de ces produits d'érosion dans le contact interplaque. Depuis l'initiation de la subduction continentale/obduction jusqu'à l'aplatissement du panneau plongeant à 6 Ma, un chenal de subduction/obduction se développe. Les sédiments et produits d'érosion sont entraînés à des profondeurs et des températures maximales de 35~40 km et 750 °C. Au cours de la formation du front de charriage, en arrière de celui-ci se forme un bassin de type 'piggy back' dans lequel s'accumulent également des sédiments.

A 7,5 Ma, les 500 km de convergence sont atteints. A ce stade la subduction continentale/obduction est terminée. Toutefois, une épaisseur non négligeable de lithosphère océanique a été charriée et mise en place (30~40 km). Or, les observations de terrain nous indiquent que les ophiolites représentent seulement une mince épaisseur de la partie crustrale de la lithosphère océanique (3~5 km). Nous ne retrouvons pas ou peu de manteau lithosphérique dans les massifs ophiolitiques.

(2) Reprise de la subduction nord

Dans la suite de la modélisation de l'extension est imposée. L'action combinée de cette traction imposée par la subduction nord sous la marge eurasienne et de la flottabilité positive de la croûte continentale subduite résultent en un amincissement vertical du système. Le manteau lithosphérique se retire sous l'effet de ces forces. L'alimentation du chenal de subduction/obduction est coupée. Les sédiments s'accumulent désormais en surface au contact inter-plaque. On constate que cette phase d'extension affecte en particulier la partie mantellique de l'ophiolite obduite. Au cours du retrait de la partie mantellique de la lithosphère océanique préalablement obduite, la partie crustale est découplée et déposée sur la lithosphère continentale. Le bombement du front d'obduction se réduit tout en s'élargissant en arrière de cette zone. Un bassin flexural se forme également en avant du bombement, reculant au fur et à mesure que la lithosphère se retire.

Au cours de cette délamination lithosphérique, des parties profondes du chenal de subduction/obduction sont exhumées sous l'effet de la remontée de la croute continentale. Ces roches métamorphiques se retrouvent ainsi en position basale de la croute océanique. Elles forment ainsi les écailles d'amphibolites à grenat identifiées dans 'la semelle ophiolitique'. Au regard de cette modélisation, nous suggérons que ces roches sont donc aussi des marqueurs d'un détachement de l'ophiolite que du passage en 'fer à repasser', en compression, de celle-ci. La zone de « Chenal d'obduction » ainsi exhumée enregistre ainsi les 2 étapes (obduction et retrait du manteau).

2.3 Modèle 2 - rajeunissement thermique du domaine océanique restreint à proximité de la marge continentale

L'évolution de ce modèle peut être décomposée en 2 étapes successives, les mêmes que pour le modèle précédent (**Figure 70**). Dans cette modélisation nous avons également imposé (1) une étape de compression où la subduction nord ne joue pas, (2) un arrêt de la compression et une reprise la subduction nord.

(1) Etape de compression

Au cours de la convergence de deux domaines les contraintes s'accumulent progressivement. Un bombement caractéristique d'un front de charriage se développe tout comme dans le modèle 1. La lithosphère océanique se retrouve ainsi charriée au-dessus de la lithosphère continentale. A 5 Ma la marge continentale en subduction atteint une profondeur à laquelle la flottabilité positive de sa croûte provoque une réduction de l'angle de plongement. Remarquons que cette profondeur est plus importante que celle constatée dans le modèle 1 dus à l'épaisseur plus importante de manteau lithosphérique la chevauchant. A 6 Ma la subduction de la marge continentale progresse en une subduction plate avec un angle de plongement faible. La marge continentale est enfouie à une profondeur maximum de 70 km.

Dans cette variante du modèle précédant, le front de charriage se forme selon les mêmes processus mais qu'il progresse plus loin sur le domaine continental. Le front de charriage est toujours le résultat d'une zone de friction à l'interface entre

les croûtes continentale et océanique. L'érosion tectonique de la croûte océanique chevauchante et le sous-charriage de ces produits d'érosion dans le contact interplaque se produit de la même manière mais l'épaisseur de la lithosphère est plus importante en arrière de la zone de charriage. Depuis l'initiation de la subduction continentale/obduction jusqu'à l'aplatissement du panneau plongeant à 6 Ma, la propagation gravitaire de l'ophiolite est plus intense. Ainsi la formation un chenal de subduction/obduction se développe plus par effet de « fer à repassé » que par entrainement du panneau plongeant. Les sédiments et produits d'érosion sont entraînés à des profondeurs et des températures maximales de 50~60 km et 750 °C. Le bassin flexural qui se forme en avant du front de charriage présentent une profondeur plus importante que dans le modèle 1 alors que celui en arrière est moins marqué.

C'est également à 7,5 Ma que les 500 km de convergence sont atteints. Le stade subduction continentale/obduction s'arrête comme dans le modèle 1. Toutefois, une épaisseur encore plus importante de lithosphère océanique a été charriée et mise en place (~50 km).

(2) Reprise de la subduction nord

L'extension est imposée, comme dans le modèle 1. Cette traction a les mêmes effets que dans le précédent modèle. Remarquons toutefois qu'il subsiste une partie du manteau lithosphérique sous la croûte océanique malgré qu'il se retire sous l'effet des mêmes forces. On constate que cette phase d'extension affecte non seulement la partie mantellique de l'ophiolite obduite mais aussi la croûte continentale en subduction. Un bombement de la croûte continentale se développe, il sépare l'ophiolite du domaine océanique chevauchant l'extrémité de la marge continentale. Il est envisageable que l'obduction passive continue de faire progresser l'ophiolite sur le domaine continental.

Figure 70 - Evolution temporelle du modèle 2 caractérisé par une lithosphère océanique vieille mais d'un âge thermique de 5 Ma sur restreint à un domaine proche de la marge continentale.

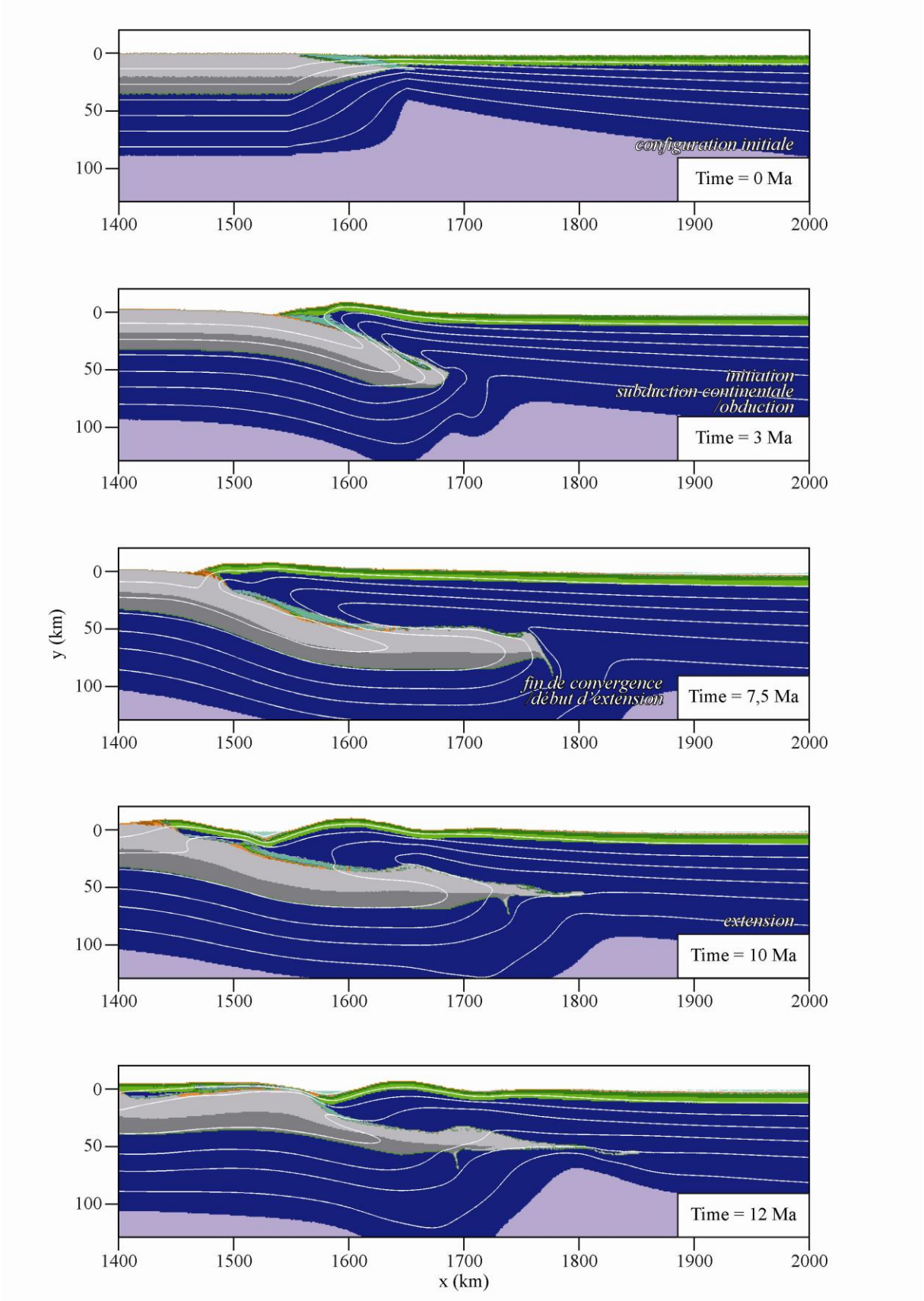

Au cours du retrait de la partie mantellique de la lithosphère océanique préalablement obduite, le bombement du front d'obduction recule au fur et à mesure que la lithosphère se retire mais ne se réduit pas pour autant.

On constant qu'au cours de cette délamination lithosphérique, le chenal de subduction/obduction est également exhumé sous l'effet de la remontée de la croûte continentale. Ces roches métamorphiques se retrouvent ainsi en position basale d'une tranche de lithosphère océanique représentée par de la croûte océanique mais également du manteau lithosphérique. Au regard de cette modélisation, nous suggérons que la complémentarité ou non des différents régimes d'obduction (cf **Figure 4**) est dû à l'état thermique de l'ophiolite.

2.4 Modèle 3 – sans rajeunissement thermique du domaine océanique

L'évolution de ce modèle peut seulement être abordée en une seule étape (**Figure 71**). Avec cette modélisation nous avons mis en évidence l'importance d'un état thermique anormalement élevé de la lithosphère océanique pour générer une obduction. Nous pouvons constater que malgré une pré-structuration favorable au chevauchement de la lithosphère continentale par de la lithosphère océanique, la densité plus élevé du domaine océanique conduit à la formation d'une subduction. Nous ne nous attarderons pas sur ce modèle car les modalités des premières étapes de la genèse d'une zone de subduction ne sont pas l'objet de ce travail et sont encore largement débattus.

Figure 71 - Evolution temporelle du modèle 3 caractérisé par une lithosphère océanique vieille n'ayant pas subi de rajeunissement thermique.

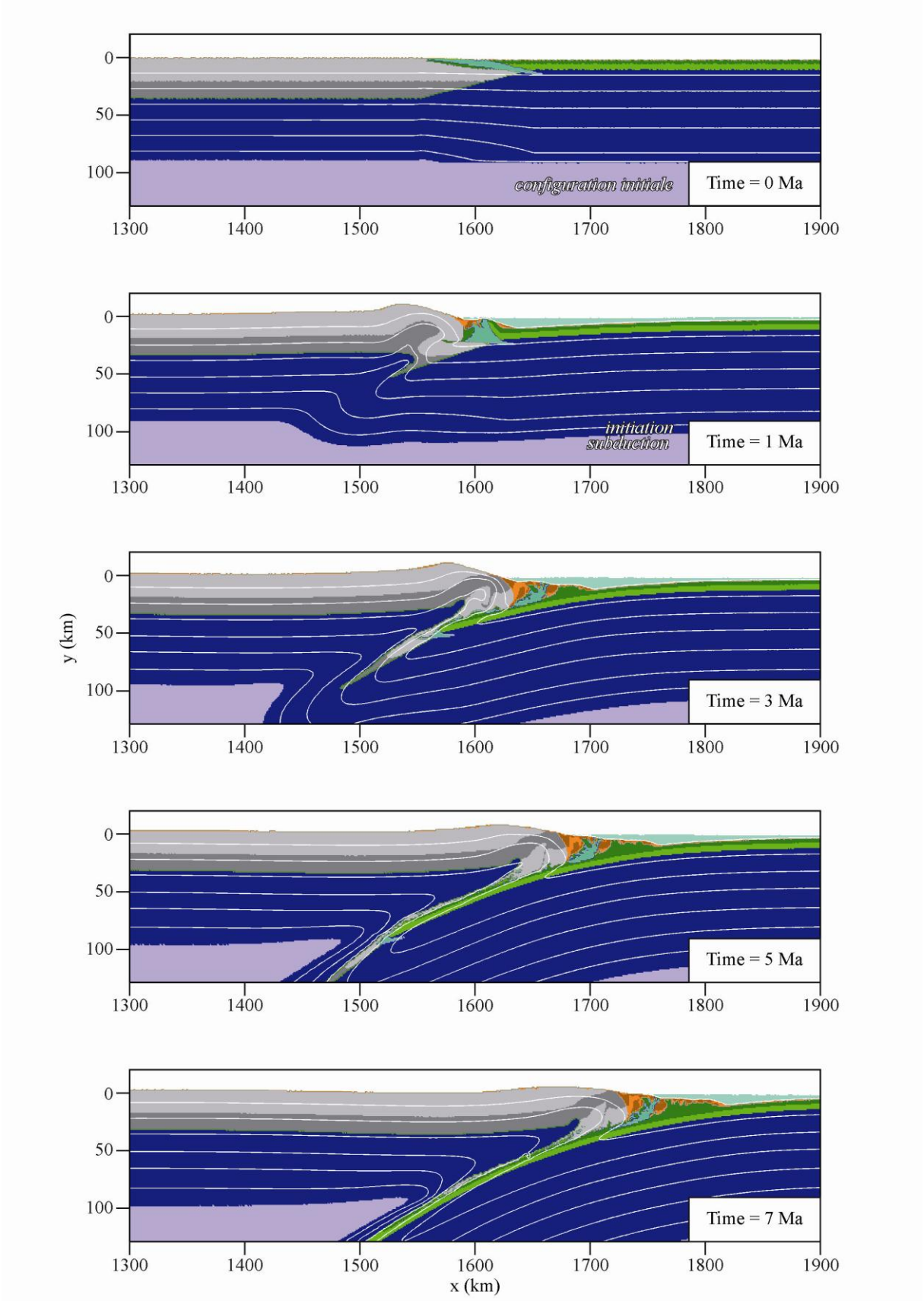

2.5 Modèle 4 – sans extension post-obduction

Tout comme la modélisation précédente l'évolution de ce modèle peut seulement être abordée en étape (**Figure 72**) puisqu'il n'y a pas d'extension imposé. Nous constatons que la flottabilité positive de la croûte continentale ne peut être seule responsable de l'extraction du manteau lithosphérique du domaine océanique.

Tout comme dans la deuxième modélisation, au cours de la convergence de deux domaines les contraintes s'accumulent progressivement. A 5 Ma la marge continentale en subduction atteint une profondeur à laquelle la flottabilité positive de sa croûte provoque une réduction de l'angle de plongement. A 6 Ma la subduction de la marge continentale progresse en une subduction plate avec un angle de plongement faible. La marge continentale est enfouie à une profondeur maximum de 70 km. A 7,5 Ma, les 500 km de convergence sont atteints. Le stade subduction continentale/obduction s'arrête. Une épaisseur importante de lithosphère océanique a été charriée et mise en place (~50 km) composé de plus de 40 km de manteau lithosphérique.

Sans extension imposée, il n'y a pas de traction de la partie mantellique de la lithosphère océanique. On constate que le modèle n'évolue plus.

Figure 72 - Evolution temporelle du modèle 2 caractérisé par une lithosphère océanique vieille mais d'un âge thermique de 5 Ma sur restreint à un domaine proche de la marge continentale. Ce modèle ce distingue du modèle 2 par l'absence de la pas d'extension post-obduction.

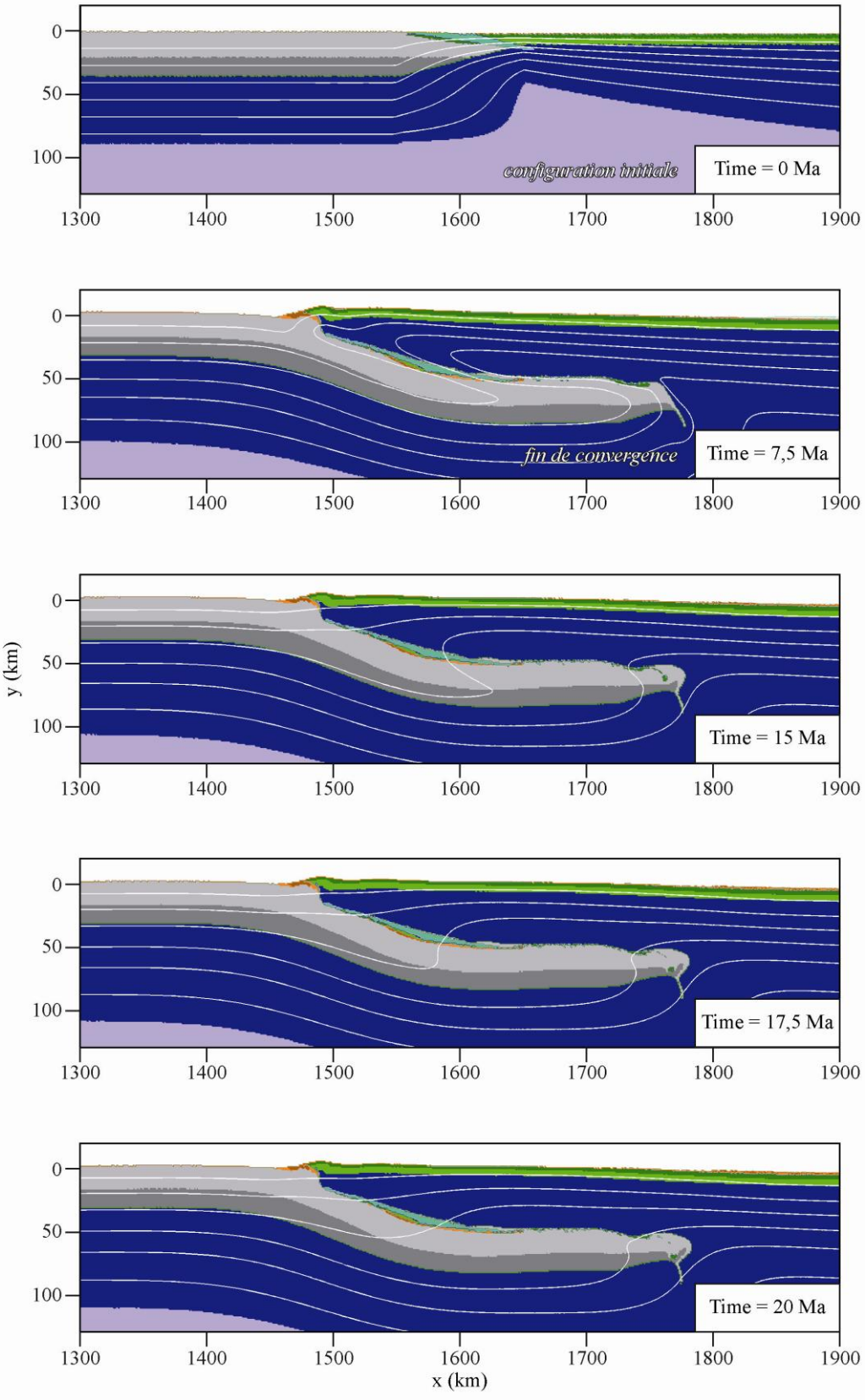

VII.3 Discussion de la modélisation

Nous testons quatre scénarios pour la mise en place d'une nappe ophiolitique. Il apparait qu'il est nécessaire d'avoir un domaine océanique relativement jeune (âge thermique de 5 Ma) pour initier une obduction le long d'une marge passive. Dans ces scénario une marge passive continentale présente une TOC marquée par un niveau de découplage possible (serpentinites) avec une lithosphère océanique. En plus du niveau de découplage à la TOC, un état thermique anormalement élevé de la lithosphère océanique est nécessaire (modèles 1 et 2). Afin d'obtenir des résultats proches des observations de terrain et des modèles conceptuels qui en découlent, il est aussi indispensable d'incorporer une phase d'extension suite à la phase compressive de subduction continentale/obduction.

Conclusions Générale

« Ecrire c'est ébranler le sens du monde, y disposer une interrogation indirecte, à laquelle l'écrivain, par un dernier suspens, s'abstient de répondre. La réponse, c'est chacun de nous qui la donne, y apportant son histoire, son langage, sa liberté. »

Roland Barthesne

Conclusion Générale

L'étude pluridisciplinaire des ophiolites du Petit Caucase et de NE Anatolie ainsi que les modélisations qui en découlent nous ont permit de préciser l'évolution des premiers stades de la fermeture néotéthysienne et en conséquence l'obduction de ces dernières, tels que :

(1) L'âge des formations sédimentaires sur les ophiolites en front est identique aux âges des sédiments remobilisés se trouvant dans l'olistrostrome. Ces âges permettent de contraindre le début du processus d'obduction. Ils sont dans la marge d'erreur des âges radiométriques obtenus pour les roches métamorphiques de la semelle d'obduction des ophiolites le long de la suture. Les ophiolites sont peu déformées et présentent une structure préservée.

(2) Les roches du socle cristallin du SAB ne présentent pas de lithologies de haute pression.

(3) En arrière de l'obduction un bassin océanique subsiste après la mise en place des ophiolites. L'extension imposée dans le modèle après 500 km de convergence représente la traction en subduction sous l'Eurasie de la lithosphère océanique.

(4) Remarquons que l'activité volcanique de la marge Eurasienne présente une période de quiescence pendant la période de mise en place des ophiolites. Ceci témoigne vraisemblablement d'une période de faible activité de la subduction à l'origine de ce volcanisme. La compression imposée pour faire converger les domaines lithosphériques a apparemment comme origine un saut de contraintes vers le sud. Ce saut de contraintes contrebalancerait le blocage/ralentissement de la subduction sous l'Eurasie. Ainsi dans un cadre globale, l'obduction compense le blocage/ralentissement la subduction en accommodant le raccourcissement en surface.

(5) Les conditions thermiques sont d'une importance capitale, et même nécessaire, car l'état thermique de la croûte océanique anormalement élevée permet de faire chevaucher un domaine de roches dense sur un domaine de roche moins dense sur de grandes distances.

L'obduction apparaît ainsi tout à la fois singulière et ordinaire, puisqu'elle semble dériver d'un système de type subduction, l'un des processus les plus spécifiques du globe (Stern, 2004; Agard et al., 2007). Dans le cas de la mise en place des ophiolites de la branche nord de la Néotéthys, elle constitue un processus géodynamique à part entière. Même si son occurrence semble appartenir à une étape bien particulière de la phase de convergence d'un cycle de type Wilson, elle ne correspond pas uniquement à la terminaison du cycle subduction

(subduction continentale). Elle est caractérisée par un ensemble de conditions propres, qui sont diffèrents de ce ceux de la subduction.

- Le cas du Petit Caucase montre qu'il est possible de déclencher l'obduction d'une croûte océanique même vieille, et même s'il reste un domaine océanique important à faire disparaitre. Pis, le déclenchement de plusieurs obductions simultanées sur plusieurs marges continentales distinctes le long d'un même transect, est en contradiction avec le principe d'une continuité entre subduction et obduction : il s'agit de deux mécanismes distincts. L'un prenant le relais de l'autre. Dans le cas du Caucase, le blocage de la subduction nord a sans doute joué un rôle déclencheur sur l'obduction.
- Notre étude montre qu'il faut prendre en compte l'état thermique du domaine océanique obducté. En effet les modélisations tendent à démontrer que le rajeunissement thermique est primordial dans le cas d'ophiolites vieilles comme le montre notre étude.
- La progression d'une obduction sur une grande distance pourrait s'expliquer par la reprise de la subduction sur l'une des limites du système (autrement dit, conduisant au retrait, et à l'aminicissement de la lithosphère obduite). La vitesse de la subduction (traction de la plaque plongeante) va alors jouer un rôle important sur l'extension et l'amincissement des ophiolites obduites.

Références

(Les références contenues dans chaque article sont données à la fin de ces derniers.)

A

Adamia, Sh. A., Belov, A., Kekelia, M. & Shavishvili, I., 1987. Paleozoic tectonic development of the Caucasus and Turkey (Geotraverse C). In: Flugel, H. W., Sassi, F. P., & Grecula, P. (Eds.), Pre-Variscan and Variscan Events in the Alpine–Mediterranean Mountain Belts (pp. 22–50). Mineralia Slovaca: Alfa Bratislava.

Adamia, Sh. A., Chkhotua, T., Kekelia, M., Lordkipanidze, M., Shavishvili, I. & Zakariadze, G., 1981. Tectonics of Caucasus and adjoining regions: implications for the evolution of the Tethys ocean. *Journal of Structural Geology*, **3**, 437–447.

Adamia, Sh. A., Lordkipanidze, M. B. & Zakariadze, G. S., 1977. Evolution of an active continental margin as exemplified by the Alpine history of the Caucasus. *Tectonophysics*, **40**, 183–189.

Agard, P., Jolivet, L., Vrielynck, B., Burov, E. & Monié, P., 2007. Plate acceleration: The obduction trigger? *Earth and Planetary Science Letters*, **258**, 428-441.

Agard, P., Monié, P., Jolivet, L. & Goffé, B., 2002. Exhumation of the Schistes Lustrés complex: in situ laser probe $^{40}Ar/^{39}Ar$ constraints and implications for the Western Alps. *Journal of Metamorphic Geology*, **20**, 599-618.

Aghamalyan, V. A., 1998. *The Basement Crystalline of Armenia*. PhD thesis, Institute of Geological Sciences, National Academy of Sciences of Armenia. Yerevan. (in Russian)

Aghamalyan, V. A., 1996. Formation and the evolution of the earth's crust of the region of the articulation of the passive and active margins of Tethys based on the example to Armenia. *Regularities of the Evolution of the Earth's Crust. Report***, 2**.

Aghamalyan, V. A., 1978. The old metamorphic complexes of the territory of Armenian SSR and their tectonic disposition. *Proceedings of reports of the Second Regional Petrographic Symposium on Caucasus, Crimea and Carpathians. Tbilisi*, 109-115. (in Russian)

Aghamalyan V. A., Mayringer F., Lorsabyan T. & Israelyan A., 2011a. Geochemical features of pre-Cambrian amphibolites of the Armenian crystalline massif as a fragment of metamorphosed basalts of the pan-African oceanic crust. *Proceedings of the National Academy of Sciences, Armenia, Earth Sciences*, **64**, 15-23. (in Russian)

Aghamalyan V. A., Schulz B., Renno A., Lange J. & Lorsabyan T., 2011b. Geochemical features of pre-Cambrian amphibolites of the Armenian crystalline massif as a fragment of metamorphosed basalts of the pan-African oceanic crust. *Proceedings of Yerevan State University, Armenia, Geology and Geography*, **3**, 3-8. (in Russian)

Aktimur, H. T., Sarıaslan, M., Keçer, M., Turşucu, A., Ölçer, S., Yurdakul, M. E., … & Yıldırım, T., 1995. Geology of Erzincan Surrounding. *Mineral Research and Exploration Institute (MTA) of Turkey Report no. 9792*. (unpublished, in Turkish)

Allègre, C. J., Dupré, B., Richard, P., Rousseau, D. & Brooks, C., 1982. Subcontinental versus suboceanic mantle, II. NdSrPb isotopic comparison of continental tholeiites with mid-ocean ridge tholeiites, and the structure of the continental lithosphere. *Earth and Planetary Science Letters*, **57**, 25-34.

Andersen, C. A. & Hinthorne, J. R., 1973. $^{207}Pb/^{206}Pb$ ages and REE abundances in returned lunar material by ion microprobe mass analysis. *Lunar and Planetary Institute Science Conference Abstracts*, **4**, 37.

Asatryan, G. 2009. New data about the age of ophiolites in the Vedi zone on the basis of radiolarian assemblages. *Proceedings of the National Academy of Sciences of Armenia, Earth Sciences*.

Asatryan, G., Danelian, T., Sosson, M., Sahakyan, L. & Galoyan, G. 2011. Radiolarian evidence for Early Cretaceous (late Barremian – early Aptian) submarine volcanic activity in the Tethyan oceanic realm preserved in Karabagh (Lesser Caucasus). *Ofioliti*, **36**, 117-123.

Asatryan, G., Danelian, T., Sosson, M., Sahakyan, L., Person, A., Avagyan, A. & Galoyan, G., 2010. Radiolarian ages for the sedimentary cover of Sevan ophiolite (Armenia, Lesser Caucausus). *Ofioliti*, **35**, 91-101.

Aslan, Z., Arslan, M., Temizel, İ. & Kaygusuz, A., 2013. K-Ar dating, whole-rock and Sr-Nd isotope geochemistry of calc-alkaline volcanic rocks around the Gümüşhane area: implications for post-collisional volcanism in the Eastern Pontides, Northeast Turkey. *Mineralogy and Petrology*, 1-23.

Aslanyan, A. T. & Satian, M. A., 1977. On the geological features of Transcaucasian ophiolitic zones. *Izvestia Acad. Sci. Armenian SSR, Nauki o Zemle*, **4**, 5.

Aubouin, J., 1965. *Geosynclines* (Vol. 1). Amsterdam: Elsevier.

Avagyan, A., Sosson, M., Karakhanian, A., Philip, H., Rebai, S., Rolland, Y., Melkonyan, R. & Davtyan, V., 2010. Recent Ectonic Stress Evolution in the Lesser Caucasus and Adjacent Regions. *Geological Society, London, Special Publications*, **340**, 393-408.

B

Baghdasarian, G. P. & Ghukasian, R. Kh., 1983. The age of Bdjni migmatite-granitic massif (By the Rb-Sr Isochron radiometric data and geological ideas. *Izvestia NAS of Armenian SSR, Nauki o Zemle*, **6**, 15-29. (in Russian)

Baghdasaryan, G. P., Ghukasyan, R. Kh., Aslanyan, A. M., Karapetyan, G. A., Dashtoyan, G. G., Mkrtchyan, D. G., Ter-Grigoryan, S. I. & Chatalyan, S. G., 1962. The results of determining the absolute age of the separate magmatic complexes of Armenian SSR. In: Proceedings of the tenth session of commission determining the absolute age of geological formations. *Academy of sciences of the USSR, Moscow*, 283-303. (in Russian)

Beccaluva, L., Coltorti, M., Premti, I., Saccani, E., Siena, F. T. & Zeda, O., 1994. Mid-ocean ridge and supra-subduction affinities in the ophiolitic belts from Albania. *Ofioliti*, **19**, 77-96.

Bédard, J. H., Lauzière, K., Tremblay, A., Sangster, A. & Tellier, M., 1998. Evidence from Betts Cove ophiolite boninites for forearc seafloor-spreading. *Tectonophysics*, **284**, 233-245.

Belov, A. A. & Sokolov, S. D., 1973. Relicts of Mesozoic oceanic crust among the crystalline complexes of the Miskhana massif of Armenia. *Sovetskaya geologia*, 8, 26-41. (in Russian)

Benson, W. N., 1926. The tectonic conditions accompanying the intrusion of basic and ultrabasic igneous rocks. *Unites States National Academy of Sciences, Memoires*, **1**, 1-90.

Bergougnan, H., 1987. *Etudes géologiques dans l'Est-Anatolien* (Doctoral dissertation). Université Pierre et Marie Curie, Paris VI, France.

Bill, M., O'Dogherty, L., Guex, J., Baumgartner, P. O. & Masson, H., 2001. Radiolarite ages in Alpine-Mediterranean ophiolites: Constraints on the oceanic spreading and the Tethys-Atlantic connection. *Geological Society of America Bulletin*, **113**, 129-143.

Black, L. P., Williams, I. S. & Compston, W., 1986. Four zircon ages from one rock: The history of a 3930 Ma-old granulite from Mount Sones, Antarctica. *Contributions to Mineralogy and Petrology*, **94**, 427-437.

Boutelier, D., Chemenda, A. & Burg, J. -P., 2003. Subduction versus accretion of intra-oceanic volcanic arcs: insight from thermo-mechanical analogue experiments. *Earth and Planetary Science Letters*, **212**, 31-45.

Bozkurt, E. & Mittwede, S.K., 2001. Introduction to the Geology of Turkey – A Synthesis. *Inernational Geology Review*, **43**, 578-594.

Bozkuş C. 1998. Stratigraphy and structural evolution of Pontid/Anatolid suture zone in NE Anatolia (between Oltu-Narman). *Journal of Engineering Sciences*, **4**, 487-499.

Božović, M., Prelević, D., Romer, R. L., Barth, M., Van Den Bogaard, P. & Boev, B., 2013. The Demir Kapija Ophiolite, Macedonia (FYROM): a Snapshot of Subduction Initiation within a Back-arc. *Journal of Petrology*, **54**, 1427-1453.

Brongniart, A., 1827. *Classifications et caractères minéralogiques des roches homogènes et hétérogènes*. Chez FG Levrault.

Brongniart, A., 1821. Sur le gisement ou position relative des ophiolites, euphotides, jaspes, etc. dans quelques parties des Apennins. *Annales des Mines* ou recueuil de *Mémoires sur l'Exploitation des Mines*, **6**.

Brongniart, A., 1813. *Essai d'une classification minéralogique des roches mélangées*. Bossande.

Brookfield, M. E., 1977. The origin of bounding surfaces in ancient aeolian sandstones. *Sedimentology*, **24**, 303-332.

Brown, D., Spadea, P., Puchkov, V., Alvarez-Marron, J., Herrington, R., Willner, A. P., ... & Juhlin, C., 2006. Arc–continent collision in the Southern Urals. *Earth Science Reviews*, **79**, 261-287.

Brunn, J. H., 1959. La dorsale médio-atlantique et les épanchements ophiolitiques. *Comptes Rendus de la Société Géologique de France*, **8**, 234-236.

C

Cady, J. W., 1975. Magnetic and gravity anomalies in the Great Valley and western Sierra Nevada metamorphic belt, California. *Geological society of America*, **168**.

Cameron, W. E., Nisbet, E. G. & Dietrich, V. J., 1979. Boninities, komatiites and ophiolitic basalts. *Nature*, **280**, 550–553.

Cann, J. R., 2003. The Troodos ophiolite and the upper ocean crust; a reciprocal traffic in scientific concepts. *Geological Society of America, Special Papers*, 309-322.

Castaing, R., 1951. *Application des sondes électroniques à une méthode d'analyse ponctuelle chimique et crystallographie* (Doctoral Dissertation). University of Paris.

Cawood, P. A. & Suhr, G.,1992. Generation and obduction of ophiolites: constraints from the Bay of Islands Complex, western Newfoundland. *Tectonics*, **11**, 884-897.

Çelik, Ö. F., Chiaradia, M., Marzoli, A., Billor, Z. & Marschik, R., 2013. The Eldivan ophiolite and volcanic rocks in the İzmir–Ankara–Erzincan suture zone, Northern Turkey: Geochronology, whole-rock geochemical and Nd–Sr–Pb isotope characteristics. *Lithos*, **172-173**, 31-46.

Çelik, Ö. F., Marzoli, A., Marschik, R., Chiaradia, M., Neubauer, F. & Öz, I., 2011. Early-Middle Jurassic intra-oceanic subduction in the İzmir–Ankara–Erzincan Ocean, Northern Turkey. *Tectonophysics*, **509**, 120-134.

Chalot-Prat F., 2005. An undeformed ophiolite in the Alps: field and geochemical evidences for a link between volcanism and shallow plate tectonic processes. *Geological Society of America, Special Papers*, **388**, 751-780

Chalot-Prat F. & Manataschal G., 2002a. Relations entre déformation et magmatisme lors de la transition rifting-accrétion océanique lente : Exemple du massif du Chenaillet (Hautes Alpes, Alpes Occidentales, France). *Groupe De Recherche Marges, Bulletin Information*, **4**, 6-7.

Chalot-Prat F. & Manatschal G., 2002b. *Oceanic volcanism, a tracer of the basement deformation during the opening of the slow spreading rate Tethys ocean (Chenaillet-Montgenèvre, Western Alps)*. Annual Meeting of the Swiss Academy of Natural Sciences

(SANW): Birth and Early Evolution of Alpine Ocean Basins, Davos, Switzerland, 19-20th Sept, 2002

Chardon, D. & Chevillotte, V., 2006. Morphotectonic evolution of the New Caledonia ridge (Pacific Southwest) from post-obduction tectonosedimentary record. *Tectonophysics*, **420**, 473-491.

Chiari, M., Marcucci, M. & Principi, G., 2000. The age of Radiolarian Cherts associated with the ophiolites in the Apennines (Italy) and Corsica (France): a revision. *Ofioliti*, **25**, 141-146.

Chiari, M., Cortese, G., Marcucci, M. & Nozzoli, N., 1997. Radiolarian biostratigraphy in the sedimentary cover of the ophiolites of south-western Tuscany, Central Italy. *Eclogae Geologicae Helvetiae*, **90**, 55–77.

Church, W. T. & Stevens, R. K., 1971. Early Paleozoic ophiolite complexes of the Newfoundland Appalachians as mantle-oceanic crust sequences. *Journal of Geophysical Research*, **76**, 1460-1466.

Cluzel, D., Jourdan, F., Meffre, S., Maurizot, P. & Lesimple, S., 2012. The metamorphic sole of New Caledonia ophiolite: $^{40}Ar/^{39}Ar$, U-Pb, and geochemical evidence for subduction inception at a spreading ridge. *Tectonics*, **31**.

Cluzel, D., Aitchison, J. C. & Picard, C., 2001. Tectonic accretion and underplating of mafic terranes in the Late Eocene intraoceanic fore-arc of New Caledonia (Southwest Pacific): geodynamic implications. *Tectonophysics*, **340**, 23-59.

Çolakoğlu, A. R., 2009. Geochemical and Mineralogical Characteristics of Fe-Ni Laterite Ore of Sariçimen (Çaldiran-Van) Area in Eastern Anatolia, Turkey. *Turkish Journal of Earth Sciences*, **18**.

Coleman, R. G., 1981. Tectonic setting for ophiolite obduction in Oman. *Journal of Geophysical Research: Solid Earth*, **86**, 2497-2508.

Coleman, R. G., 1977. *Ophiolites* (p. 229). Berlin: Springer.

Coleman, R. G., 1971. Plate tectonic emplacement of upper mantle peridotites along continental edges. *Journal of Geophysical Research*, **76**, 1212-1222.

Compston, W. & Kröner, A., 1988. Multiple zircon growth within early Archaean tonalitic gneiss from the Ancient Gneiss Complex, Swaziland. *Earth and Planetary Science Letters*, **87**, 13-28.

Compston, W. T. & Pidgeon, R. T., 1986. Jack Hills, evidence of more very old detrital zircons in Western Australia. *Nature*, **321**, 766-769.

Connolly, J. A. D., 2009. The geodynamic equation of state: what? and how? *Geochemistry, Geophysics, Geosystems*, **10**.

Connolly, J. A. D. & Kerrick, D. M., 2002. Metamorphic controls on seismic velocity of subducted oceanic crust at 100–250 km depth. *Earth and Planetary Science Letters*, **204**, 61-74.

Connolly, J. A. D., & Petrini, K. (2002). An automated strategy for calculation of phase diagram sections and retrieval of rock properties as a function of physical conditions. *Journal of Metamorphic Geology*, **20**, 697-708.

Connolly, J. A. D. & Kerrick, D. M., 1987. An algorithm and computer program for calculating composition phase diagrams. *Calphad*, **11**, 1-55.

Conrad, C. P., Lithgow-Bertelloni, C. & Louden, K. E., 2004. Iceland, the Farallon Slab, and the Dynamic Topography of the North Atlantic. *Geology*, **32**, 177-180.

Crameri, F., Schmeling, H., Golabek, G. J., Duretz, T., Orendt, R., Buiter, S. J. H., ... & Tackley, P. J., 2012. A comparison of numerical surface topography calculations in geodynamic modelling: An evaluation of the 'sticky air'method. *Geophysical Journal International*, **189**, 38-54.

Crawford, A. J., 1989. *Boninites*. Allen & Unwin Australia.

Crawford, A. J., Meffre, S. & Symonds, P. A., 2003. 120 to 0 Ma tectonic evolution of the southwest Pacific and analogous geological evolution of the 600 to 220 Ma Tasman Fold Belt System. *Geological Society of America, Special Papers*, 383-404.

Cumming, G. L. & Richards, J. R., 1975. Ore lead isotope ratios in a continuously changing earth. *Earth and Planetary Science Letters*, **28**, 155-171.

D

Danelian, T., Zambetakis-Lekkas, A., Galoyan, G., Sosson, M., Asatryan, G., Hubert, B. & Grigoryan, A., 2014. Reconstructing Upper Cretaceous (Cenomanian) paleoenvironments in Armenia based on Radiolaria and benthic Foraminifera; implications for the geodynamic evolution of the Tethyan realm in the Lesser Caucasus. *Palaeogeography, Palaeoclimatology, Palaeoecology.* (in press)

Danelian, T., Asatryan, G., Galoyan, G., Sosson, M., Sahakyan, L., Caridroit, M. & Avagyan, A., 2012. Geological history of ophiolites in the Lesser Caucasus and correlation with the Izmir-Ankara-Erzincan suture zone: insights from radiolarian biochronology. *Bulletin de la Société Géologique de France*, **183**, 331-342.

Danelian, T., Asatryan, G., Sosson, M., Person, A., Sahakyan, L. & Galoyan, G., 2008. Discovery of Middle Jurassic (Bajocian) Radiolaria from the sedimentary cover of the Vedi ophiolite (Lesser Caucasus, Armenia), *Comptes Rendus PalEvol*, **7**, 327-334.

Danelian, T., Lekkas, S. & Alexopoulos, A., 2000. Découverte de radiolarites triasiques dans un complexe ophiolitique à l'Extrême-Sud du Péloponnèse (Agelona, Lakonie, Grèce). *Comptes Rendus de l'Académie des Sciences-Series IIA-Earth and Planetary Science*, **330**, 639-644.

Davies, H. L., 1977. *Crustal Structure and Emplacement of Ophiolite in South-Eastern Papua New Guinea*. Geological Survey of Papua New Guinea.

De Capitani, C. & Brown, T. H., 1987. The computation of chemical equilibrium in complex systems containing non-ideal solutions. *Geochimica et Cosmochimica Acta*, **51**, 2639-2652.

Demoule, J. P. & Lichardus-Itten, M., 2001. Kovačevo (Bulgarie), un établissement du Néolithique le plus ancien des Balkans. Communautés villageoises du Proche-Orient à l'Atlantique (8000-2000 avant notre ère). *Paris: Séminaire du Collège de France*, 85-99.

Dercourt, J., Zonenshain, L. P., Ricou, L. -E., Kazmin, V. G., Le Pichon, X., Knipper, A. L., Grandjacquet, C., Sbortshikov, I. M., Geyssant, J., Lepvrier, C., Pechersky, D. H., Boulin, J., Sibuet, J. -C., Savostin, L. A., Sorokhtin, O., Westphal, M., Bazhenov, Lauer, J. P. & Biju-Duval, B., 1986. Geological evolution of the Tethys belt from the Atlantic to the Pamirs since the Lias. *Tectonophysics*, **123**, 241-315.

Deschamps, A. & Lallemand, S., 2003. Geodynamic setting of Izu-Bonin-Mariana boninites. *Geological Society, London, Special*, **219**, 163-186.

De Sigoyer, J., Guillot, S. & Dick, P., 2004. Exhumation of the ultrahigh-pressure Tso Morari unit in eastern Ladakh (NW Himalaya): A case study. *Tectonics*, **23**.

De Wever, P., Danelian, T., Durand-Delga, M., Cordey, F. & Kito, N., 1987. Datations des radiolarites post-ophiolitiques de Corse alpine à l'aide des Radiolaires. *Comptes Rendus de l'Académie des Sciences*, **305**, 893-900.

Dewey, J. F., 1976. Ophiolite obduction. *Tectonophysics*, **31**, 93-120.

Dewey, J. F. & Bird, J. M., 1971. Origin and emplacement of the ophiolite suite: Appalachian ophiolites in Newfoundland. *Journal of Geophysical Research*, **76**, 3179-3206.

Dewey, J. F. & Bird, J. M., 1970. Mountain belts and the new global tectonics. *Journal of Geophysical Research*, **75**, 2625-2647.

Dietz, R. S. 1963. Alpine serpentines as oceanic rind fragments. *Geological Society of America Bulletin*, **74**, 947-952.

Dilek, Y. & Furnes, H., 2011. Ophiolite genesis and global tectonics: Geochemical and tectonic fingerprinting of ancient oceanic lithosphere. *Geological Society of America Bulletin*, **123**, 387-411.

Dilek, Y. & Flower, M. F., 2003. Arc-trench rollback and forearc accretion: 2. A model template for ophiolites in Albania, Cyprus, and Oman. *Geological Society, London, Special Publications*, **218**, 43-68.

Dilek, Y., Thy, P., Hacker, B. & Grundvig, S., 1999. Structure and petrology of Tauride ophiolites and mafic dike intrusions (Turkey): Implications for the Neotethyan ocean. *Geological Society of America Bulletin*, **111**, 1192-1216

Duretz, T., Gerya, T. V., Kaus, B. J. P., & Andersen, T. B. (2012). Thermomechanical modeling of slab eduction. *Journal of Geophysical Research: Solid Earth*, **117**.

E

Ellis, S., Beaumont, C. & Pfiffner, A., 1999. Geodynamic models of crustal-scale episodic tectonic accretion and underplating in subduction zones. *Journal of Geophysical Research*, **104**, 15169-15190.

Elliott, D., 1976. The motion of thrust sheets. *Journal of Geophysical research*, **81**, 949-963.

F

Falloon, T. J., Malahoff, A., Zonenshaina, L. P. & Bogdanova, Y., 1992. Petrology and geochemistry of back-arc basin basalts from Lau Basin spreading ridges at 15°, 18° and 19°S. *Mineralogy and Petrology*, **47**, 1-35.

Falloon, T. J. & Crawford, A.J., 1991. The petrogenesis of high-Ca boninite lavas dredged from the northern Tonga ridge. *Earth Planetary Science Letters*, **102**, 375–394.

Florineth, D. & Froitzheim, N., 1994. Transtion from ccontinental to oceanic basement in the Tasna nappe (Engadine window, Graubunden, Switzerland) – Evidence for Early Cretaceous opening of the Valais ocean. *Schweizerische Mineralogische und Petrographische Mitteilungen*, **74**, 437-448.

Fouqué, F. & Lévy, A. M., 1879. *Minéralogie micrographique roches éruptives françaises* (Vol. 2). A. Quantin.

Froude, D. O., Ireland, T. R., Kinny, P. D., Williams, I. S., Compston, W., Williams, I. T. & Myers, J. S., 1983. Ion microprobe identification of 4,100–4,200 Myr-old terrestrial zircons. *Nature*, **304**, 616-618.

G

Galoyan, G., 2008. *Etude Pétrologiques, Géochimiques et Géochronologiques des Ophiolites du Petit Caucase (Arménie)* (Doctoral dissertation). Université Nice–Sophia Antipolis, Nice, France.

Galoyan, G., Rolland, Y., Sosson, M., Corsini, M., Billo, S., Verati, C. & Melkonyan, R., 2009. Geology, geochemistry and $^{40}Ar/^{39}Ar$ dating of Sevan ophiolites (Lesser Caucasus, Armenia): evidence for Jurassic Back-arc opening and hot spot event between the South Armenian Block and Eurasia. *Journal of Asian Earth Sciences*, **34**, 135-153.

Galoyan, G., Rolland, Y., Sosson, M., Corsini, M. & Melkonyan, R., 2007. Evidence for superposed MORB, oceanic plateau and volcanic arc series in the Lesser Caucasus (Stepanavan, Armenia). *Comptes Rendus Geoscience*, **339**, 482-492.

Gass, I. G., 1963. Is the Troodos Massif of Cyprus a fragment of Mesozoic ocean floor? *Nature*, **220**, 39-42.

Gealey, W. K., 1977. Ophiolite obduction and geologic evolution of the Groan Mountains and adjacent areas. *Bulletin of the Geological Society of America*, **88**, 1183-91.

Gerya, T. V., Yuen, D. A. & Maresch, W. V., 2004. Thermomechanical modelling of slab detachment. *Earth and Planetary Science Letters*, **226**, 101-116.

Gerya, T. V. & Yuen, D. A., 2003. Characteristics-based marker-in-cell method with conservative finite-differences schemes for modeling geological flows with strongly variable transport properties. *Physics of the Earth and Planetary Interiors*, **140**, 293-318.

Gedik, A., 2008. Geology of the Tertiary rocks around Kemah-Erzincan-Çayirli region and their source rock characteristics. *Turkish Mineral Resource Exploration Bulletin*, **137**, 1-27.

Glennie, K. W., Bouff, M. G. A., Hughes-Clark, M. W., Moody-Stuart, M., Pilaar, W. F. H. & Reinhardt, B. M., 1973. Late Cretaceous nappes in the Oman Mountains and their geologic evolution. *Bulletin of the American Association of Petrolium Geologists*, **57**, 5-27.

Goguel, J., 1948. *Introduction à l'étude mécanique des déformations de l'écorce terrestre.* Imprimerie nationale.

Göncüoğlu, M. C., Yalınız, K. & Tekin, U. K., 2006. Geochemistry, tectono-magmatic discrimination and radiolarian ages of basic extrusives within the Izmir-Ankara suture belt (NW Turkey); time constraints for the Neotethyan evolution. *Ofioliti*, **31**, 25-38.

Guillot, S. Hattori, K., Agard, P., Schwartz, S. & Vidal, O., 2009 Exhumation processes in oceanic and continental subduction contexts : a review. *Subduction Zone Dynamics*, 175-204.

Gürer, Ö. F. & Aldanmaz, E., 2002. Origin of the Upper Cretaceous-Tertiary sedimentary basins within the Tauride-Anatolide platform in Turkey. *Geological Magazine*, **139**, 191-197.

H

Hafkenscheid, E., Wortel, M. J. R. & Spakman, W., 2006. Subduction history of Tethyan region derived from seismic tomography and tectonic reconstructions. *Journal of Geophysical Research*, **111**, B08401.

Harper, G. D., Grady, K. & Coulton, A. J., 1996. Origin of the amphibolite "sole" of the Josephine ophiolite: emplacement of a cold ophiolite over a hot arc. *Tectonics*, **15**, 296-313.

Harris, N. B., Kelley, S. & Okay, A. I., 1994. Post-collision magmatism and tectonics in northwest Anatolia. *Contribution to Mineralogy and Petrology*, **117**, 241-252.

Hässig, M., Rolland, Y., Sosson, M., Galoyan, G., Sahakyan, L., Topuz, G., Çelik, Ö. F., Avagyan, A. & Müller, C., 2014. Linking the NE Anatolian a,d Lesser Caucasus ophiolites: evidence for large scale obduction of oceanic crust and implications for the formation of the Lesser Caucasus-Pontides Arc. *Geodinamica Acta*. (just accepted)

Hässig, M., Rolland, Y., Sosson, M., Galoyan, G., Müller, C., Avagyan, A. & Sahakyan, L., 2013. New structural and petrological data on the Amasia ophiolites (NW Sevan–Akera suture zone, Lesser Caucasus): Insights for a large-scale obduction in Armenia and NE Turkey. *Tectonophysics*, **588**, 135-153.

Hébert, R. & Laurent, R., 1990. Mineral chemistry of the plutonic section of the Troodos ophiolite: new constraints for genesis of arc-related ophiolites. Ophiolites: Oceanic Crustal Analogues. *Nicosia, Cyprus, Geological Survey*, 149-163.

Hermann, J., Müntener, O., Trommsdorff, V., Hansmann, W. & Piccardo, G. B., 1997. Fossil crust-to-mantle transition, Val Malenco (Italian Alps). *Journal of Geophysical Research: Solid Earth*, **102**, 20123-20132.

Heuret, A. & Lallemand, S., 2005. Plate motions, slab dynamics and back-arc deformation. *Physics of the Earth and Planetary Interiors*, **149**, 31-51.

Hess, H. H., 1965. Mid-oceanic ridges and tectonics of the sea-floor. *Submarine geology and geophysics, Colston Papers*, **17**, 317-334.

Hess, H. H., 1962. History of ocean basins. *Petrologic studies*, **4**, 599-620.

Hess, H. H., 1955. The oceanic crust. *Journal of Marine Research*, **14**, 423-439.

Hess, J. C., Aretz, J., Gurbanov, A. G., Emmermann, R., & Lippolt, H. J., 1995. Subduction related Jurassic andesites in the northern Great Caucasus. *Geologische Rundschau*, **84**, 319-333.

Hill, K. C. & Raza, A., 1999. Arc-continent collision in Papua Guinea: Constraints from fission track thermochronology. *Tectonics*, **18**, 950-966.

Hinthorne, J. R., Andersen, C. A., Conrad, R. L. & Lovering, J. F., 1979. Single-grain 207Pb206Pb and U/Pb age determinations with a 10-μm spatial resolution using the ion microprobe mass analyzer (IMMA). *Chemical Geology*, **25**, 271-303.

Hinton, R. W. & Long, J. V. P., 1979. High-resolution ion-microprobe measurement of lead isotopes: Variations within single zircons from Lac Seul, northwestern Ontario. *Earth and Planetary Science Letters*, **45**, 309-325.

I

Ishiwatari, A., 1994. Circum-Pacific Phanerozoic multiple ophiolite belts. In Circum-Pacific Ophiolites: *Proceedings of the 29th International Geological Congress. Part D*, 7-28.

J

Juteau, T. & Maury, R., 1997. *Geologie de la Croute Oceanique: Petrologie et Dynamique Endogenes*, p. 569.

K

Karson, J. & Dewey, J. F., 1978. Coastal Complex, western Newfoundland: an early Ordovician oceanic fracture zone. *Geological Society of America Bulletin*, **89**, 1037-1049.

Kinny, P. D., Williams, I. S., Froude, D. O., Ireland, T. R. & Compston, W., 1988. Early Archaean zircon ages from orthogneisses and anorthosites at Mount Narryer, Western Australia. *Precambrian Research*, **38**, 325-341.

Knipper, A. L., 1975. The oceanic crust in the structure of the Alpine Folded Belt (South Europe, western part of Asia and Cuba). *Moscow 'Nauka'*, **267**. (in Russian)

Knipper, A. L. & Khain, E. V., 1980. Structural position of ophiolites of the Caucasus. *Ofioliti, Special Issue*, **2**, 297–314.

Knipper, A. L., Bragin, N. Y. & Satian M. A., 1997. Upper Triassic-Lower Jurassic volcanogenic and sedimentary deposits of the Old Zod Pass (Transcaucasia). *Stratigraphy and Geological Correlation*, **5**, 58–65. (in Russian)

L

Lagabrielle, Y., 2009. Mantle exhumation and lithospheric spreading : An historical perspective from investigations in the Oceans and in the Alps-Apennines ophiolites. *Italian Journal of Geosciences*, **128**, 279-293

Lagabrielle, Y., 2005. La dorsale est-Pacifique entre 10° et 20° S. Alternance du volcanisme et de la tectonique le long de la zone active axiale. *Géomorphologie: relief, processus, environnement*, **2**, 105-120.

Lagabrielle, Y., 1987. *Les Ophiolites : marqueurs de l'histoire tectonique des domaines océaniques. Le cas des Alpes franco-italiennes (Queyras, Piémont); comparaison avec les ophiolites d'Antalya (Turquie) et du Coast Range de Californie* (Thèse de Doctorat d'Etat). U.B.O, Brest. 350 pp.

Lagabrielle, Y., Chauvet, A., Ulrich, M. & Guillot, S., 2013. Passive obduction and gravity-driven emplacement of large ophiolitic sheets: The New Caledonia ophiolite (SW Pacific) as a case study? *Bulletin de la Société Géologique de France*, **184**, 545-556.

Lagabrielle, Y. & Chauvet, A., 2008. Le role de la tectonique en extension dans l'evolution morphologique de la Nouvelle Caledonie durant le Cenozoique (10 fig.). *Bulletin de la Societe Geologique de France*, **179**, 315.

Lagabrielle, Y. & Lemoine, M., 1997. Alpine, Corsican and Apennine ophiolites: the slowspreading ridge model. *Comptes Rendus de l'Académie des Sciences, Serie II*, **325**, 909-920.

Lagabrielle, Y. & Cannat, M., 1990. Alpine Jurassic ophiolites resemble the modern central Atlantic basement. *Geology*, **18**, 319-322.

Lagabrielle, Y., Fudral, S. & Kienast, J. R., 1989. La couverture océanique des ultrabasites de Lanzo (Alpes occidentales): arguments lithostratigraphiques et pétrologiques. *Geodinamica Acta*, **3**, 43-55.

Lagabrielle, Y. & Polino, R., 1988. Un schéma structural du domaine des Schistes lustrés ophiolitifères au nord-ouest du massif du Mont Viso (Alpes Sud-Occidentales) et ses implications. *Comptes rendus de l'Académie des sciences. Série 2, Mécanique, Physique, Chimie, Sciences de l'univers, Sciences de la Terre*, **306**, 921-928.

Lardeaux, J. M., 2014. Deciphering orogeny: a metamorphic perspective. Examples from European Alpine and Variscan belts Part I: Alpine metamorphism in the western Alps. A review. *Bulletin de la Societe Geologique de France*, **185**, 93-114.

Lardeaux, J. M., Schwartz, S., Tricart, P., Paul, A., Guillot, S., Béthoux, N. & Masson, F., 2006. A crustal-scale cross-section of the south-western Alps combining geophysical and geological imagery. *Terra Nova*, **18**, 412-422.

Lefebvre, C. J. C., 2011. *The tectonics of the Central Anatolian Crystalline Complex: a structural, metamorphic and paleomagnetic study* (Doctoral dissertation). Utrecht Universiteit.

Le Pichon, X., Francheteau, J. & Bonnin, J., 1976. *Plate Tectonics*. Elsevier, Amsterdam, 312 p.

Lordkipanidze, M. B., Meliksetian, B. & Djarbashian, R., 1989. Mesozoic–Cenozoic magmatic evolution of the Pontian–Crimean–Caucasian region. *IGCP project*, **198**, 103-124.

M

Malpas, J., Moores, E. M., Panayiotou, A. & Xenophontos, C., (eds) 1990. *Ophiolites: Oceanic Crustal Analogues. Proceeding of the Symposium 'Troodos 1987'.* The Geological Survey Department, Ministry of Agriculture and Natural Resources, Nicosia, Cyprus.

Malpas, J., & Stevens, R. K., 1977. The origin and emplacement of the ophiolite suite with examples from western Newfoundland. *Geotectonics*, **11**, 453-466.

Maghakyan, R., Zakariadze, G., Dmitriev, L., Kolesov, G. & Korovina, M., 1985. Geochemistry of the Jurassic-Lower cretaceous volcanic assemblage of northern Armenia. *Journal of Volcanology and Seismology*, **3**, 39-53. (in Russian)

Manatschal, G. & Müntener, O., 2009. A type sequence across an ancient magma-poor ocean–continent transition: the example of the western Alpine Tethys ophiolites. *Tectonophysics*, **473**, 4-19.

Manatschal G., Chalot-Prat F., Edel J, -B, Coco E., Bourlier P, -Y & Warin A., 2002. *Tectono-magmatic relationships at the transition from rifting to seafloor spreading: the example of the Chenaillet massif (Western Alps, France).* Colloque GDR Marges, Paris, France, 13-14 Février 2002.

Manatschal, G. & Nievergelt, P., 1997. A continent-ocean transition recorded in the Err and Platta nappes (Eastern Switzerland). *Eclogae Geologicae Helvetiae*, **90**, 3-27.

Marroni, M., Molli, G., Montanini, A. & Tribuzio, R., 1998. The association of continental crust rocks with ophiolites in the Northern Apennines (Italy): implications for the continent-ocean transition in the Western Tethys. *Tectonophysics*, **292**, 43-66.

McDougall, I. & Harrison, T. M., 1988. *Geochronology and Thermochronology by the $^{40}Ar/^{39}Ar$ Method*. Oxford University Press, New York.

McKenzie, D. P., 1969. Speculations on the consequences and causes of plate motions. *Geophysical Journal International*, **18**, 1-32.

Meijers, M. J. M., Smith, B., Kirscher, U., Mensink, M., Sosson, M., Rolland, Y., Grigoryan, A., Sahakyan, L., Avagyan, A., Langereis, C. & Müller, C., 2014. A paleolatitude reconstruction of the South Armenian Block (SAB) since the late Cretaceous: constraints on the Tethyan realm. (submitted)

Meliksetyan, B. M., Baghdasaryan, G. P. & Ghukasyan, R. Kh., 1984. Isotopic-geochemical and geochronological investigations of Eclogite-Amphibolites associated with ophiolites of Sevan-Amasian belt (Amasian Massif). *Izvestia Acad. Sci. Armenian SSR, Nauki o Zemle*, **1**, 3-22. (in Russian)

Melikyan, L.S., 2004. Some geological and structural features of inner structure of the Amassiya-Sevan ophiolitic zone (Republic of Armenia). *Izvestia NAS of Armenia, Nauki o Zemle*, **3**, 32-38. (in Russian)

Merle, O., 1998. *Emplacement mechanisms of nappes and thrust sheets*. Springer.

Merrihue, C. & Turner, G., 1966. Potassium-argon dating by activation with fast neutrons. *Journal of Geophysical Research*, **71**, 2852-2857.

Miyashiro, A., 1973. The Troodos ophiolitic complex was probably formed in an island arc. *Earth and Planetary Science Letters*, **19**, 218-224.

Molli, G., 1996. Pre-orogenic tectonic framework of the northern Apennine ophiolites. *Eclogae Geologicae Helvetiae*, **89**, 163-180.

Moix, P. & Goričan, Š., 2014. Jurassic and Cretaceous radiolarian assemblages from the Bornova mélange in northern Karaburun Peninsula (western Turkey) and its connection to the İzmir-Ankara mélanges. *Geodinamica Acta*, 1-38. (just-accepted)

Moix, P., Beccaletto, L., Kozur, H. W., Hochard, C., Rosseletd, F. & Stampfli, G. M., 2008. A new classification of the Turkish terranes and sutures and its implication for the paleotectonic history of the region. *Tectonophysics*, **451**, 7–39.

Moores, E. M., 1969. *Petrology and structure of the Vourinos ophiolitic complex of northern Greece* (Vol. 118). Geological Society of America.

Moores, E. M., Robinson, P. T., Malpas, J. & Xenophonotos, C., 1984. Model for the origin of the Troodos massif, Cyprus, and other mideast ophiolites. *Geology*, **12**, 500-503.

Moores, E. M. & Vine, F. J. 1971. The Troodos Massif, Cyprus and other ophiolites as oceanic crust: evaluation and implications. *Philosophical Transactions of the Royal Society of London. Series A, Mathematical and Physical Sciences*, **268**, 443-467.

Morkovkina, V. F., Makarichev, G. I. & Gavrilova, S. I., 1982. The Grenade containing rocks, associated with the ophiolite - the product of the beginning of the formation to the continental crust of geosynclines. *Moscow 'Nauka'*, 117-137. (in Russian)

N

Nicolas, A., 1997. Sea floor spreading: a viewpoint from ophiolites. *Comptes rendus de l'Académie des sciences. Série 2. Sciences de la terre et des planètes*, **324**, 1-8.

Nicolas, A. 1989. *Principes de tectonique*. Masson.

Nier, A. O., 1950. A redetermination of the relative abundances of the isotopes of carbon, nitrogen, oxygen, argon, and potassium. *Physical Review*, **77**, 789.

Nikishin, A. M., Korotaev, M. V., Ershov, A. V. & Brunet, M. F. 2003. The Black Sea basin: tectonic history and Neogene–Quaternary rapid subsidence modelling. *Sedimentary Geology*, **156**, 149-168.

O

Okay, A. I., Satır, M. & Siebel, W., 2006. Pre-Alpide orogenic events in the Eastern Mediterranean region. In: Gee, D.G., Stephenson, R.A. (Eds.), European Lithosphere Dynamics. *Geological Society, London, Memoirs*, **32**, 389-405.

Okay, A. I. & Tüysüz, O., 1999. Tethyan sutures of northern Turkey. *Geological Society, London, Special Publication*, **156**, 475-515.

Okay, A. I. & Sahinturk, O., 1997. Regional and Petroleum Geology of the Black Sea and Surrounding Region, Chapter 15: Geology of the Eastern Pontides. *AAPG Memoir 68*.

Oliver, J., Sykes, L. & Isacks, B., 1969. Seismology and the new global tectonics. *Tectonophysics*, **7**, 527-541.

Önen, A. P., 2003. Neotethyan ophiolitic rocks of the Anatolides of NW Turkey and comparison with Tauride ophiolites. *Journal of the Geological Society*, **160**, 947-962.

Özen, H., Çolakoğlu, A. O., Sayak, H., Dönmez, C., Türkel, A. & Odabaşı, I., 2008. Report of Cr-Ni prospection and ophiolite geology of Erzincan-Tercan-Çayırlı region. *General Directorate of Mineral Research and Exploration*, **Report No: 11055**. (In Turkish)

Özen, H., Çolakoğlu, A., Sayak, H., Dönmez, C., Türkel, A., Odabaşı, İ, … & Winchester, J. A., 2006. The petrogenesis of tectonites and cumulate rocks from the ophiolites, north of Erzincan. *59th Geological Congress of Turkey, Abstracts*, 100–101.

Özgül, N. (1984). Stratigraphy and tectonic evolution of the Central Taurides. Geology of the Taurus Belt, 77-90.

P

Panayiotou, A., 1980. *Ophiolites*.

Parlak, O., Çolakoğlu, A., Dönmez, C., Sayak, H., Yıldırım, N., Türkel, A. & Odabaşı, İ., 2013. Geochemistry and tectonic significance of ophiolites along the Ankara–Erzincan suture zone in northeastern Anatolia. *Geological Society, London, Special Publications*, **372**, 75–105.

Pearce, J. A., 2003. Supra-subduction zone ophiolites: The search for modern analogues. *Geological Society of America, Special Papers*, 269-294.

Pearce, J. A., Lippard, S. J. & Roberts, S., 1984. Characteristics and tectonic significance of suprasubduction zone ophiolite. *Geological Society, London, Special Publication*, **16**, 77-94.

Peccerillio, A. & Taylor, S. R., 1976. Geochemistry of Eocene calc-alkaline volcanic rocks from the Kastamonu area, northern Turkey. *Contributions to Mineralogy and Petrology*, **58**, 63-81.

Penrose, C. P., 1972. Penrose field conference on ophiolites. *Geotimes*, **17**, 24-25.

Philippot, P., 1988. *Déformation et éclogitisation progressives d'une croûte océanique subductée: l'exemple du Monviso, Alpes occidentales: contraintes cinématiques durant la collision continentale alpine* (Doctoral dissertation). Montpellier 2.

Platt, J. P., 2000. Calibrating the bulk rheology of active obliquely convergent thrust belts and forearc wedges from surface profiles and velocity distributions. *Tectonics*, **19**, 529-548.

R

Rautenschlien, M., Jenner, G. A., Hertogen, J., Hoffmann, A. W., Kerrich, R., Schmincke, H. U. & White, W. M., 1985. Isotopic and trace element composition of volcanic glasses from Akaki Canyon, Cyprus: implications for the origin of the Troodos ophiolite. *Earth Planet. Science Letters*, **15**, 369-383.

Rawling, T. J. & Lister, G. S., 2002. Large-scale structure of the eclogite–blueschist belt of New Caledonia. *Journal of Structural Geology*, **24**, 1239-1258.

Rice, S. P., Robertson, A. H. F., Ustaömer, T., Inan, N. & Tasli, K., 2009. Late Cretaceous–Early Eocene tectonic development of the Tethyan suture zone in the Erzincan area, Eastern Pontides, Turkey. *Geological Magazine*, **146**, 567-590.

Rice S. P., Robertson, A. H. F. & Ustaömer, T, 2006. Late-Certaceous-Early Cenozoic tectonic evolution of the Eurasian active margin in the Central and Esatern Pontides, north Turkey. *Geological Society, London, Special Publications*, **260**, 413-445.

Ricou, L. E., 1994. Tethys reconstructed: plates, continental fragments and their Boundaries since 260 Ma from Central America to South-eastern Asia. *Geodinamica Acta-Revue de Geologie Dynamique et de Geographie Physique*, **7**, 169-218.

Ricou, L. E., 1968. Sur la mise en place au Crétacé supérieur d'importantes nappes a radiolarites et ophiolites dans les monts Zagros (Iran). *Comptes Rendus de Academie des Sciences*, **267**, 2272-2275.

Robertson, A. H., Parlak, O. & Ustaömer, T., 2012. Overview of the Palaeozoic–Neogene evolution of Neotethys in the Eastern Mediterranean region (southern Turkey, Cyprus, Syria). *Petroleum Geoscience*, **18**, 381-404.

Robertson, A. H. F. & Ustaömer, T., 2012. Testing Alternative Tectono-Stratigraphic Interpretations of the Late Palaeozoic--Early Mesozoic Karakaya Complex in NW Turkey: Support for an Accretionary Origin Related to Northward Subduction of Palaeotethys. *Turkish Journal of Earth Sciences*, **21**.

Robertson, A. H. F. & Dixon, J. E., 1984. Introduction: aspects of the geological evolution of the Eastern Mediterranean. *Geological Society, London, Special Publications*, **17**, 1-74.

Robinson, A. G., Banks, C. J., Rutherford, M. M. & Hirst, J. P. P., 1995. Stratigraphic and structural development of the Eastern Pontides, Turkey. *Journal of the Geological Society*, **152**, 861-872.

Robinson, P. T., Gibson, I. L. & Panayiotou, A., 1987. Cyprus Crustal Study Project: Initial Report, Holes CY-2 and CY-2A. *Geological Survey of Canada*, **85-29**, 381.

Rod, E., 1982. Comments on 'Tectonic setting of ophiolite obduction in Oman'by Robert Coleman. *Journal of Geophysical Research: Solid Earth*, **87**, 4759-4760.

Rolland, Y., Perincek, D., Kaymakci, N., Sosson, M., Barrier, E. & Avagyan, A., 2012. Evidence for~ 80–75Ma subduction jump during Anatolide–Tauride–Armenian block accretion and~ 48Ma Arabia–Eurasia collision in Lesser Caucasus–East Anatolia. *Journal of Geodynamics*, **56**, 76-85.

Rolland, Y., Sosson, M., Adamia, Sh. & Sadradze, N., 2011. Prolonged Variscan to Alpine history of an active Eurasian margin (Georgia, Armenia) revealed by $^{40}Ar/^{39}Ar$ dating. *Gondwana Research*, **20**, 798–815.

Rolland Y., Galoyan G., Sosson, M., Melkonian R. & Avagyan A., 2010. The Armenian ophiolites: insights for Jurassic Back-arc formation, Lower Cretaceous hot-spot magmatism, and Upper Cretaceous obduction over the South Armenian Block. *Geological Society, London, Special Publication*, **340**, 353-382.

Rolland, Y., Billo, S., Corsini, M., Sosson, M. & Galoyan, G., 2009a. Blueschists of the Amasia–Stepanavan Suture Zone (Armenia): linking Tethys subduction history from E Turkey to W-Iran. *International Journal Earth Sciences (Geologische Rundschau)*, **98**, 533-550.

Rolland, Y., Galoyan, Gh., Bosch, D., Sosson, M., Corsini, M., Fornari, M. & Vérati, C., 2009b. Jurassic back-arc and hot-spot related series in the Armenian ophiolites - implications for the obduction process. *Lithos*, **112**, 163-187.

S

Salisbury, M. H. & Christensen, N. 1., 1978, The seismic velocity structure of a traverse through the Bay of Islands ophiolite complex, Newfoundland, an exposure of oceanic crust and upper mantle. *Journal of Geophysical Research*, **83**, 805-817.

Sarıfakıoğlu, E., Özen, H. & Hall, C., 2009. Petrogenesis of extension-related alkaline volcanism in Karaburhan (Sivrihisar–Eskisehir), NW Anatolia, Turkey. *Journal of Asian Earth Sciences*, **35**, 502-515.

Satian, M. A., Stepanyan, J. H., Sahakyan, L. H., Mnatsakanyan, A. Kh. & Ghukasyan, R. Kh., 2005. The Mesozoic Lamprophyric Diatremes of Vedi Zone (Armenia). *Yerevan, Izdatelstvo 'Nairi'*. (in Russian)

Satian, M. A., 2005. Mesozoic ophiolite basins of the Transcaucasian geotraverse. *Izvestia NAS of Armenia*, **1**, 3-8.

Saunders, A. D. & Tarney, J., 1984. Geochemical characteristics of basaltic volcanism within back-arc basins. *Geological Society, London, Special Publications*, **16**, 59-76.

Schellart, W. P., Lister, G. S. & Toy, V. G., 2006. A Late Cretaceous and Cenozoic reconstruction of the Southwest Pacific region: tectonics controlled by subduction and slab rollback processes. *Earth-Science Reviews*, **76**, 191-233.

Schmeling, H., Babeyko, A. Y., Enns, A., Faccenna, C., Funiciello, F., Gerya, T., ... & Van Hunen, J., 2008. A benchmark comparison of spontaneous subduction models—towards a free surface. *Physics of the Earth and Planetary Interiors*, **171**, 198-223.

Scholz, C. H. & Campos, J., 1995. On the mechanism of seismic decoupling and back arc spreading at subduction zones. *Journal of Geophysical Research: Solid Earth*, **100**, 22103-22115.

Schwartz, S., 2000. *La zone piémontaise des Alpes occidentales: un paléocomplexe de subduction. Arguments métamorphiques, géochronologiques et structuraux* (Doctoral dissertation). Université Claude Bernard-Lyon I.

Schwartz, S., Tricart, P., Lardeaux, J. M., Guillot, S. & Vidal, O., 2009. Final exhumation of an accretionary wedge (Queyras Schistes Lustrés, Western Alps): deformation sequence and associated P-T-t path. *Geological Society of America Bulletin*, **121**, 502-518.

Searle, M. & Cox, J., 1999. Tectonic setting, origin, and obduction of the Oman ophiolite. *Geological Society of America Bulletin*, **111**, 104-122.

Searle, M. P. & Malpas, J., 1980. Structure and metamorphism of rocks beneath the Semail ophiolite of Oman and their significance in ophiolite obduction. *Transactions of the Royal Society of Edinburgh: Earth Sciences*, **71**, 247-262.

Sengör, A. M. C. & Yilmaz, Y., 1981. Tethyan evolution of Turkey: A plate tectonic approach. *Tectonophysics*, **75**, 181-241.

Shemenda, A. I., 1994. *Subduction: Insights from physical modeling*. Kluwer Academic Publishers, 215.

Shengelia, D. M., Tsutsunava, T. N. & Shubitidze, L. G., 2006. New data on the structure, composition and regional metamorphism of the Tsakhkunyats and Akhum-Asrikchai massifs, the Lesser Caucasus. *Doklady Earth Sciences*, **409A**, 900-904.

Shervais, J. W., 2006. The significance of subduction-related accretionary complexes in early Earth processes. *Geological Society of America Special Papers*, **405**, 173-192.

Smith, A. G. & Woodcock, N. H., 1976. Emplacement model for some "Tethyan" ophiolites. *Geology*, **4**, 653-656.

Sokolov, S. D., 1977. The Olistostromes and Ophiolitic Nappes of the Lesser Caucasus. *Izdatelstvo 'Nauka', Moscow*. (in Russian)

Sokolov, S. D., 1974. Tectonic mélange of Amassia region (Lesser Caucasus). *Geotectonica*, **1**, 69-77. (in Russian)

Sosson, M., Rolland, Y., Müller, C., Danelian, T., Melkonyan, R., Kekelia, S., Adamia, S., Babazadeh, V., Kangarli, T., Avagyan, A., Galoyan, G., Mosar, J., 2010. Subductions, obduction and collision in the Lesser Caucasus (Armenia, Azerbaijan, Georgia), new insights. *Geological Society, London, Special Publications*, **340**, 329-352.

Stacey, J. T. & Kramers, J. D., 1975. Approximation of terrestrial lead isotope evolution by a two-stage model. *Earth and Planetary Science Letters*, **26**, 207-221.

Steiger, R. H. & Jäger, E., 1977. Subcommission on geochronology: convention on the use of decay constants in geo- and cosmochronology. *Earth and Planetary Science Letters*, **36**, 359-362.

Stein, M. & Hofmann, A. W., 1994. Mantle plumes and episodic crustal growth. *Nature*, **372**, 63-68.

Steinmann, G., 1927. Der ophiolitischen Zonen in der mediterranean Kettengebirgen. *14th International Geological Congress in Madrid*, **2**, 638–667.

Steinmann, G., 1905. *Geologische Beobachtungen in den Alpen: die Schardtsche Überfaltungstheorie und die geologische Bedeutung der Tiefseeabsätze und der ophiolithischen Massengesteine*. Wagner.

Stern, R. J., 2004. Subduction initiation: spontaneous and induced. *Earth and Planetary Science Letters*, **226**, 275-292.

Stoneley, R., 1975. On the origin of ophiolite complexes in the southern Tethys region. *Tectonophysics*, **25**, 303-322.

Suess, E., 1909. *The face of the Earth (Vol. 4)*. Clarendon Press.

Sun, S. S. & Nesbitt, R. W., 1978. Geochemical regularities and genetic significance of ophiolitic basalts. *Geology*, **6**, 689-693.

T

Tatevosyan, T. Sh., 1950. To petrography of basic and ultrabasic rocks of the Amassia region of Armenian SSR. *Izvestia Acad. Sci. Armenian SSR, Nauki o Zemle 2*, 177-190. (in Russian)

Teklay, M., 2006. Neoproterozoic arc–back–arc system analog to modern arc–back–arc systems: evidence from tholeiite–boninite association, serpentinite mudflows and across-arc geochemical trends in Eritrea, southern Arabian-Nubian shield. *Precambrian Research*, **145**, 81-92.

Thayer, T. P., 1969. Gravity differentiation and magmatic reemplacemcnt of podiform chromite deposits. *Economic Geology Monograph A*, 132-146.

Thy, P. & Xenophontos, C., 1991. Crystallization orders and phase chemistry of glassy lavas from the pillow sequences, Troodos ophiolite, Cyprus. *Journal of Petrology*, **32**, 403-428.

Titus, S. J., Maes, S. M., Benford, B., Ferré, E. C. & Tikoff, B., 2011. Fabric development in the mantle section of a paleotransform fault and its effect on ophiolite obduction, New Caledonia. *Lithosphere*, **3**, 221-244.

Topuz, G., Çelik, Ö. F., Şengör, A. M. C., Altıntaş, İ. E., Zack, T., Rolland, Y. & Barth, M., 2013a. Jurassic ophiolite formation and emplacement as backstop to a subduction-accretion complex in Northeast Turkey, the Refahiye ophiolite, and relation to the Balkan ophiolites. *American Journal of Science*, **313**.

Topuz, G., Göçmengil, G., Rolland, Y., Çelik, Ö. F., Zack, T. & Schmitt, A. K., 2013b. Jurassic accretionary complex and ophiolite from northeast turkey: no evidence for the Cimmerian continental ribbon. *Geology*, **41**, 255-258.

Tricart, P. & Schwartz, S., 2006. A north-south section across the Queyras Schistes lustrés (Piedmont zone, western Alps): Syn-collision refolding of a subduction wedge. *Eclogae Geologicae Helvetiae*, **99**, 429-442.

Tricart, P. & Lemoine, M., 1986. From faulted blocks to megamullions and megaboudins: Tethyan heritage in the structure of the Western Alps. *Tectonics*, **5**, 95-118.

U

Ulrich, M., 2010. *Péridotites et serpentinites du complexe ophiolitique de la Nouvelle-Calédonie* (Doctoral dissertation). Université de Nouvelle Calédonie.

V

Vance, D. & Mahar, E., 1998. Pressure-temperature paths from PT pseudosections and zoned garnets: potential, limitations and examples from the Zanskar Himalaya, NW India. *Contributions to Mineralogy and Petrology*, **132**, 225-245.

Vaughan, A. P., 1995. Circum-Pacific mid-Cretaceous deformation and uplift: A superplume-related event? *Geology*, **23**, 491-494.

Vaughan, A. P. & Scarrow, J. H., 2003. K-rich mantle metasomatism control of localization and initiation of lithospheric strike-slip faulting. *Terra Nova*, **15**, 163-169.

Vissers, R.L.M. & Nicolas, A. (Eds.), 1995. *Mantle and Lower Crust Exposed in Oceanic Ridges and in Ophiolites*. Kluwer Academic, Dordrecht, the Netherlands.

Vuagnat, M. & Çoğulu, E., 1968. Quelques reflections sur le massif basique-ultrabasique du Kızıl Dagh, Hatay, Turquie. *Compte Rendu des Séances de la Société de Physique et d'Histoire Naturelle de Genève*, **2**, 210-216.

W

Waltham, D., Hall, R., Smyth, H. R. & Ebinger, C. J., 2008. Basin formation by volcanic arc loading. *Geological Society of America Special Papers*, **436**, 11.

Welland, M. J. & Mitchell, A. H. G., 1977. Emplacement of the Oman ophiolite: A mechanism related to subduction and collision. *Geological Society of America Bulletin*, **88**, 1081-1088.

Wetherill, G. W. 1956. Discordant uranium-lead ages, I. *Transactions, American Geophysical Union*, **37**, 320-326.

White W. B., Johnson S. M. & Dantzig G. B., 1958. Chemical equilibrium in complex mixtures. *Journal of Chemical Physics*, **28**, 751-755.

Williams, I. S. & Claesson, S., 1987. Isotopic evidence for the Precambrian provenance and Caledonian metamorphism of high grade paragneisses from the Seve Nappes, Scandinavian Caledonides. *Contributions to Mineralogy and Petrology*, **97**, 205-217.

Williams, H. & Smyth, W. R., 1973. Metamorphic aureoles beneath ophiolite suites and alpine peridotites; tectonic implications with west Newfoundland examples. *American Journal of Science*, **273**, 594-621.

Wilson, J. T, 1959. Geophysics and continental growth. *American Scientist*, **47**, 1-24.

Y

Yakubchuk, A. S., Nikishin, A. M. & Ishiwatari, A., 1994. A late Proterozoic ophiolite pulse. *Proc. 29th Int'l. Geol. Congr., Part D*, 273-286.

Yamato, P., Burov, E., Agard, P., Le Pourhiet, L. & Jolivet, L., 2008. HP-UHP exhumation during slow continental subduction: Self-consistent thermodynamically and thermomechanically coupled model with application to the Western Alps. *Earth and Planetary Science Letters*, **271**, 63-74.

Yamato, P., Agard, P., Goffé, B., De Andrade, V., Vidal, O. & Jolivet, L. 2007. New, high-precision P–T estimates for Oman blueschists: implications for obduction, nappe stacking and exhumation processes. *Journal of Metamorphic Geology*, **25**, 657-682.

Yılmaz, Y., Genc, S. C., Gurer, F., Bozcu, M., Yilmaz, K., Karacık, Z., Altunkayak, S. & Elmas, A., 2000. When did the western Anatolian grabens begin to develop? *Geological Society, London, Special Publication*, **173**, 353-384.

Yılmaz, Y., Tüysüz, O., Yiğitba¸S, E., Genç, ¸ S. C., ¸Sengör, A. M. C., 1997. Geology and tectonic evolution of the Pontides. *American Association of Petroleum Geologists, Memoir*, **68**, 183-226.

Annexes

Liste des Annexes

Annexe 1 – Résultats de datation (1) sur Gabbro AR-09-20. 335

Annexe 2 - Résultats de datation (1) sur Gabbro AR-08-29. 339

Annexe 3 - Résultats de datation (1) sur Amphibole AR-09-08. 343

Annexe 4 - Résultats de datation (1) sur Amphibole AR-09-15. 347

Annexe 5 - Résultats de datation (1) sur Amphibole AR-08-09c. 351

Annexe 6 - Résultats de datation (1) sur Mica AR-08-09c. 355

Annexe 7 – Données microsonde, transect Grenat de AR-03-62M. 359

Annexe 8 - Résultats de datation (2) sur Amphibole AR-03-64. 361

Annexe 9 - Résultats de datation (2) sur Muscovite AR-03-62M. 368

Annexe 10 - Résultats de datation (2) sur Muscovite AR-04-64. 374

Annexe 11 - Résultats de datation (2) sur Muscovite AR-04-64. 381

Annexe 12 - Résultats de datation (2) sur Muscovite AR-04-62B. 388

Annexe 13 - Résultats de datation (2) sur Biotite AR-04-62M. 395

Annexe 1 – Résultats de datation (1) sur Gabbro AR-09-20.

Incremental Heating		36Ar(a)	37Ar(ca)	38Ar(cl)	39Ar(k)	40Ar(r)	Age ± 1σ (Ma)	40Ar(r) (%)	39Ar(k) (%)	K/Ca ± 1σ
K388-1A	400.00 W	0.000252	0.242365	0.001513	0.000942	0.000000	0.00 ± 0.00	0.00	1.75	0.00063 ######
K388-2	480.00 W	0.000020	0.031778	0.001503	0.000511	0.000000	0.00 ± 0.00	0.00	0.95	0.00260 ######
K388-3	553.00 W	0.000054	0.641382	0.070443	0.020057	0.104560	170.99 ± 7.10	86.18	37.16	0.00505 ######
K388-4	600.00 W	0.000028	0.378075	0.041653	0.012316	0.062726	167.22 ± 6.85	87.70	22.82	0.00526 ######
K388-5	640.00 W	0.000014	0.071618	0.007092	0.002116	0.009407	146.84 ± 26.57	69.59	3.92	0.00477 ######
K388-6	999.00 W	0.000032	0.632080	0.058595	0.018035	0.093095	169.38 ± 6.95	90.18	33.41	0.00461 ######
	Σ	0.000400	1.997298	0.180799	0.053977	0.269789				

Information on Analysis
Sample = K386
Material = Amphibole (105 MC 54)
Location = Caucase
Analyst = YR-MH
Project = ROLLAND_HASSIG
Mass Discrimination Law = LIN
Irradiation = MC54
J = 0.01906980 ± 0.00009535
Hb3gr = 1074.000 ± 5.370 Ma

Results	40(r)/39(k) ± 1σ	Age ± 1σ (Ma)	MSWD	39Ar(k) (%,n)	K/Ca ± 1σ
Age Plateau	5.1383 ± 0.1268 ± 2.47%	168.64 ± 4.06 ± 2.40%	0.28	97.31 4	0.00490 ######
		Minimal External Error ± 4.07	1.10	Statistical T Ratio	
		Analytical Error ± 3.97	1.0000	Error Magnification	
Total Fusion Age	4.9982 ± 0.1269 ± 2.54%	164.25 ± 4.06 ± 2.47%		6	0.00437 ######
		Minimal External Error ± 4.07			
		Analytical Error ± 3.99			

Normal Isochron		39(k)/36(a) ± 1σ	40(a+r)/36(a) ± 1σ	r.i.
K388-1A	400.00 W	3.7 ± 0.2	282.9 ± 16.3	0.9372
K388-2	480.00 W	25.9 ± 9.1	249.2 ± 87.0	0.9981
K388-3	553.00 W	370.4 ± 101.2	2229.6 ± 608.7	0.9992
K388-4	600.00 W	436.0 ± 134.7	2518.9 ± 777.7	0.9994
K388-5	640.00 W	156.0 ± 68.2	992.2 ± 433.3	0.9996
K388-6	999.00 W	560.8 ± 222.4	3193.1 ± 1266.0	0.9995

Results	40(a)/36(a) ± 1σ	40(r)/39(k) ± 1σ	Age ± 1σ (Ma)	MSWD
Normal Isochron No Convergence	178.2177 ± 94.6390 ± 53.10%	5.3964 ± 0.2371 ± 4.39%	176.71 ± 7.44 ± 4.21%	0.43
		Minimal External Error ± 7.45		
		Analytical Error ± 7.40		

Statistics				
	Statistical F ratio	1.05	Convergence	0.0002198610
	Error Magnification	1.0000	Number of Iterations	100
	Number of Data Points	4	Calculated Line	Weighted York-2

Inverse Isochron		39(k)/40(a+r) ± 1σ	36(a)/40(a+r) ± 1σ	r.i.
K388-1A	400.00 W	0.013209 ± 0.000283	0.003535 ± 0.000204	0.0029
K388-2	480.00 W	0.104050 ± 0.002260	0.004013 ± 0.001402	0.0070
K388-3	553.00 W	0.166135 ± 0.001764	0.000449 ± 0.000122	0.0002
K388-4	600.00 W	0.173075 ± 0.001840	0.000397 ± 0.000123	0.0004
K388-5	640.00 W	0.157219 ± 0.001930	0.001008 ± 0.000440	0.0021
K388-6	999.00 W	0.175614 ± 0.002283	0.000313 ± 0.000124	0.0048

Results	40(a)/36(a) ± 1σ	40(r)/39(k) ± 1σ	Age ± 1σ (Ma)	MSWD
Inverse Isochron	249.0776 ± 170.6585 ± 68.52%	5.2544 ± 0.3525 ± 6.71%	172.27 ± 11.05 ± 6.42%	0.39
			Minimal External Error ± 11.06	
			Analytical Error ± 11.02	

Statistics				
	Statistical F ratio	1.05	Convergence	0.0002272471
	Error Magnification	1.0000	Number of Iterations	6
	Number of Data Points	4	Calculated Line	Weighted York-2

Relative Abundances		36Ar	%1σ	37Ar	%1σ	38Ar	%1σ	39Ar	%1σ	40Ar	%1σ	Age ± 1σ (Ma)	40Ar(r) (%)	39Ar(k) (%)	K/Ca ± 1σ
K388-1A	400.00 W	0.0003209	4.475	0.2423647	3.055	0.0030262	2.080	0.0011194	1.612	0.0713746	0.188	0.00 ± 0.00	0.00	1.75	0.00063 ######
K388-2	480.00 W	0.0000291	23.647	0.0317782	3.104	0.0017034	2.395	0.0005342	1.945	0.0049264	0.727	0.00 ± 0.00	0.00	0.95	0.00260 ######
K388-3	553.00 W	0.0002542	5.322	0.6413817	3.035	0.0745419	2.017	0.0205251	1.028	0.1213221	0.080	170.99 ± 7.10	86.18	37.16	0.00505 ######
K388-4	600.00 W	0.0001462	5.461	0.3780750	3.035	0.0440751	2.016	0.0125920	1.027	0.0715259	0.119	167.22 ± 6.85	87.70	22.82	0.00526 ######
K388-5	640.00 W	0.0000357	16.486	0.0716176	3.071	0.0075495	2.035	0.0021678	1.146	0.0135191	0.334	146.84 ± 26.57	69.59	3.92	0.00477 ######
K388-6	999.00 W	0.0002264	5.002	0.6320805	3.049	0.0626098	2.040	0.0184966	1.164	0.1032335	0.496	169.38 ± 6.95	90.18	33.41	0.00461 ######
	Σ	0.0010126	2.543	1.9972977	1.537	0.1935059	1.122	0.0554351	0.595	0.3859014	0.142				

Information on Analysis and Constants Used in Calculations

Sample = K386
Material = Amphibole (105 MC 54)
Location = Caucase
Analyst = YR-MH
Project = ROLLAND_HASSIG
Mass Discrimination Law = LIN
Irradiation = MC54
J = 0.01906980 ± 0.00009535
Hb3gr = 1074.000 ± 5.370 Ma
IGSN = Undefined
Preferred Age = Undefined
Classification = Undefined
Experiment Type = Undefined
Extraction Method = Undefined
Heating = 60 sec
Isolation = 2.00 min
Instrument = VG3600
Lithology = Undefined
Lat-Lon = Undefined - Undefined

Age Equations = Conventional
Negative Intensities = Forced Zero
Decay Constant 40K = 5.543 ± 0.010 E-10 1/a
Decay Constant 39Ar = 2.940 ± 0.029 E-07 1/h
Decay Constant 37Ar = 8.220 ± 0.010 E-04 1/h
Decay Constant 36Cl = 2.310 ± 0.016 E-06 1/a
Production Ratio 36/38 in Cl = 316.0 ± 15.8

Results	40(r)/39(k) ± 1σ	Age ± 1σ (Ma)	MSWD	39Ar(k) (%,n)	K/Ca ± 1σ
Age Plateau	5.1383 ± 0.1268 ± 2.47%	168.64 ± 4.06 ± 2.40%	0.28	97.31 4	0.00490 ######
	Minimal External Error ± 4.07		1.10	Statistical T Ratio	
	Analytical Error ± 3.97		1.0000	Error Magnification	
Total Fusion Age	4.9982 ± 0.1269 ± 2.54%	164.25 ± 4.06 ± 2.47%		6	0.00437 ######
	Minimal External Error ± 4.07				
	Analytical Error ± 3.99				
Normal Isochron No Convergence	5.3964 ± 0.2371 ± 4.39%	176.71 ± 7.44 ± 4.21%	0.43	97.31 4	
	Minimal External Error ± 7.45		1.05	Statistical F ratio	
	Analytical Error ± 7.40		1.0000	Error Magnification	
Inverse Isochron	5.2544 ± 0.3525 ± 6.71%	172.27 ± 11.05 ± 6.42%	0.39	97.31 4	
	Minimal External Error ± 11.06		1.05	Statistical F ratio	
	Analytical Error ± 11.02		1.0000	Error Magnification	

Degassing Patterns		36Ar(a)	%1σ	36Ar(c)	%1σ	36Ar(ca)	%1σ	36Ar(cl)	%1σ	37Ar(ca)	%1σ	38Ar(a)	%1σ	38Ar(c)	%1σ	38Ar(k)	%1σ
K388-1A	400.00 W	0.000252	5.76	0.000000	0.00	0.000068	3.21	0.000000	86.79	0.242365	3.06	0.000048	5.77	0.000000	0.00	0.000011	2.93
K388-2	480.00 W	0.000020	34.92	0.000000	0.00	0.000009	3.26	0.000000	12.79	0.031778	3.10	0.000004	34.92	0.000000	0.00	0.000006	2.86
K388-3	553.00 W	0.000054	27.30	0.000000	0.00	0.000181	3.20	0.000019	7.37	0.641382	3.04	0.000010	27.30	0.000000	0.00	0.000241	2.26
K388-4	600.00 W	0.000028	30.88	0.000000	0.00	0.000107	3.20	0.000011	7.36	0.378075	3.04	0.000005	30.88	0.000000	0.00	0.000148	2.26
K388-5	640.00 W	0.000014	43.67	0.000000	0.00	0.000020	3.23	0.000002	7.75	0.071618	3.07	0.000003	43.67	0.000000	0.00	0.000025	2.32
K388-6	999.00 W	0.000032	39.65	0.000000	0.00	0.000178	3.21	0.000016	8.02	0.632080	3.05	0.000006	39.65	0.000000	0.00	0.000216	2.33
	Σ	0.000400	6.85	0.000000	0.00	0.000563	1.62	0.000049	4.30	1.997298	1.54	0.000075	6.85	0.000000	0.00	0.000648	1.26
	Σ							0.001013	2.86	1.997298	1.54						

38Ar(ca)	%1σ	38Ar(cl)	%1σ	39Ar(k)	%1σ	39Ar(ca)	%1σ	40Ar(r)	%1σ	40Ar(a)	%1σ	40Ar(c)	%1σ	40Ar(k)	%1σ
0.001454	90.05	0.001513	86.94	0.000942	2.14	0.000177	5.03	0.000000	0.00	0.075294	5.76	0.000000	0.00	0.000028	2.93
0.000191	90.05	0.001503	13.75	0.000511	2.05	0.000023	5.06	0.000000	0.00	0.005885	34.92	0.000000	0.00	0.000015	2.86
0.003848	90.05	0.070443	8.93	0.020057	1.06	0.000468	5.02	0.104560	4.22	0.016166	27.30	0.000000	0.00	0.000596	2.26
0.002268	90.05	0.041653	8.92	0.012316	1.06	0.000276	5.02	0.062726	4.15	0.008434	30.88	0.000000	0.00	0.000366	2.26
0.000430	90.05	0.007092	9.25	0.002116	1.18	0.000052	5.04	0.009407	18.80	0.004049	43.67	0.000000	0.00	0.000063	2.32
0.003792	90.05	0.058595	9.47	0.018035	1.20	0.000461	5.03	0.093095	4.13	0.009602	39.65	0.000000	0.00	0.000536	2.33
0.011984	45.51	0.180799	5.14	0.053977	0.61	0.001458	2.54	0.269789	2.46	0.119430	6.85	0.000000	0.00	0.001603	1.26
		0.193506	5.57			0.055435	0.60							0.390822	2.70

Additional Parameters		40(r)/39(k)	1σ	40(r+a)	1σ	40Ar/39Ar	1σ	37Ar/39Ar	1σ	36Ar/39Ar	1σ	Time (days)	37Ar (decay)	39Ar (decay)	40Ar (moles)
K388-1A	400.00 W	0.000000	0.00000	0.071347	0.00013	63.764193	1.03476	216.522328	7.47974	0.286727	0.01364	136.500	15.28947317	1.00097596	1.427E-15
K388-2	480.00 W	0.000000	0.00000	0.004911	0.00004	9.221834	0.19147	59.486615	2.17879	0.054438	0.01292	136.515	15.29408211	1.00097607	9.853E-17
K388-3	553.00 W	5.213185	0.22691	0.120726	0.00010	5.910910	0.06095	31.248623	1.00133	0.012387	0.00067	136.531	15.29869244	1.00097618	2.426E-15
K388-4	600.00 W	5.093015	0.21829	0.071160	0.00009	5.680261	0.05873	30.025017	0.96215	0.011613	0.00065	136.565	15.30896590	1.00097642	1.431E-15
K388-5	640.00 W	4.446722	0.83773	0.013456	0.00005	6.236161	0.07443	33.036244	1.08301	0.016465	0.00272	136.583	15.31462974	1.00097655	2.704E-16
K388-6	999.00 W	5.161888	0.22182	0.102698	0.00051	5.581225	0.07061	34.172867	1.11536	0.012240	0.00063	136.598	15.31903639	1.00097665	2.065E-15

Procedure Blanks		36Ar	1σ	37Ar	1σ	38Ar	1σ	39Ar	1σ	40Ar	1σ
K388-1A	400.00 W	0.000021	0.000004	0.000054	0.000006	0.000022	0.000005	0.000024	0.000004	0.001057	0.000024
K388-2	480.00 W	0.000021	0.000004	0.000054	0.000006	0.000022	0.000005	0.000024	0.000004	0.001057	0.000024
K388-3	553.00 W	0.000021	0.000004	0.000054	0.000006	0.000022	0.000005	0.000024	0.000004	0.001057	0.000024
K388-4	600.00 W	0.000021	0.000004	0.000054	0.000006	0.000022	0.000005	0.000024	0.000004	0.001057	0.000024
K388-5	640.00 W	0.000021	0.000004	0.000054	0.000006	0.000022	0.000005	0.000024	0.000004	0.001057	0.000024
K388-6	999.00 W	0.000021	0.000004	0.000054	0.000006	0.000022	0.000005	0.000024	0.000004	0.001057	0.000024

Intercept Values		36Ar	1σ	r2		37Ar	1σ	r2		38Ar	1σ	r2		39Ar	1σ	r2		40Ar	1σ	r2	
K388-1A	400.00 W	0.000337	0.000004	0.9524	EXP #	0.015751	0.000060	0.9959	EXP #	0.003028	0.000016	0.9922	EXP #	0.001139	0.000014	0.9355	EXP #	0.072431	0.000132	0.9985	EXP #
K388-2	480.00 W	0.000049	0.000005	0.0288	EXP #	0.002112	0.000012	0.9900	EXP #	0.001714	0.000021	0.9567	EXP #	0.000556	0.000008	0.8507	EXP #	0.005983	0.000027	0.9943	EXP #
K388-3	553.00 W	0.000271	0.000008	0.4375	EXP #	0.041569	0.000063	0.9990	EXP #	0.074078	0.000152	0.9980	EXP #	0.020463	0.000050	0.9968	EXP #	0.122379	0.000094	0.9996	EXP #
K388-4	600.00 W	0.000165	0.000003	0.5539	LIN # 4	0.024509	0.000039	0.9993	EXP #	0.043810	0.000086	0.9988	EXP #	0.012563	0.000030	0.9981	EXP #	0.072583	0.000082	0.9994	EXP #
K388-5	640.00 W	0.000056	0.000004	0.0768	EXP #	0.004685	0.000022	0.9935	EXP #	0.007522	0.000025	0.9969	EXP #	0.002183	0.000011	0.9879	EXP #	0.014576	0.000038	0.9490	EXP #
K388-6	999.00 W	0.000244	0.000005	0.7440	EXP #	0.040913	0.000135	0.9959	EXP #	0.062224	0.000230	0.9946	EXP #	0.018443	0.000110	0.9861	EXP #	0.104290	0.000511	0.9876	EXP #

Sample Parameters		Sample	Material	Location	Analyst	Temp	Standard (in Ma)	%1σ	J	%1σ	MDF	%1σ
K388-1A	400.00 W	K386	Amphibole (105 MC 54)	Caucase	YR-MH	400	1074	0.5	0.0190698	0.5	0.996743	1
K388-2	480.00 W	K386	Amphibole (105 MC 54)	Caucase	YR-MH	480	1074	0.5	0.0190698	0.5	0.996743	1
K388-3	553.00 W	K386	Amphibole (105 MC 54)	Caucase	YR-MH	553	1074	0.5	0.0190698	0.5	0.996743	1
K388-4	600.00 W	K388	Amphibole (105 MC 54)	Caucase	YR-MH	600	1074	0.5	0.0190698	0.5	0.996743	1
K388-5	640.00 W	K388	Amphibole (105 MC 54)	Caucase	YR-MH	640	1074	0.5	0.0190698	0.5	0.996743	1
K388-6	999.00 W	K388	Amphibole (105 MC 54)	Caucase	YR-MH	999	1074	0.5	0.0190698	0.5	0.996743	1

Volume Ratio	Sensitivity (mol/volt)	Day	Month	Year	Hour	Min	Resist	Irradiation	Project	Experiment	Nmb	Standard Name
1	2.000E-14	23	FEB	2010	09	09	001	MC54	Rolland_Hassig	K388-1A	01	Hb3gr
1	2.000E-14	23	FEB	2010	09	31	001	MC54	Rolland_Hassig	K388-1A	01	Hb3gr
1	2.000E-14	23	FEB	2010	09	53	001	MC54	Rolland_Hassig	K388-1A	01	Hb3gr
1	2.000E-14	23	FEB	2010	10	42	001	MC54	Rolland_Hassig	K388-1A	01	Hb3gr
1	2.000E-14	23	FEB	2010	11	09	001	MC54	Rolland_Hassig	K388-1A	01	Hb3gr
1	2.000E-14	23	FEB	2010	11	30	001	MC54	Rolland_Hassig	K388-1A	01	Hb3gr

Irradiation Constants		40/36(a)	%1σ	40/36(c)	%1σ	38/36(a)	%1σ	38/36(c)	%1σ	39/37(ca)	%1σ	38/37(ca)	%1σ	36/37(ca)	%1σ
K388-1A	400.00 W	298.56	0.1	0.018	35	0.1885	0.16	1.7	3	0.00073	4	0.006	90	0.000282	1
K388-2	480.00 W	298.56	0.1	0.018	35	0.1885	0.16	1.7	3	0.00073	4	0.006	90	0.000282	1
K388-3	553.00 W	298.56	0.1	0.018	35	0.1885	0.16	1.7	3	0.00073	4	0.006	90	0.000282	1
K388-4	600.00 W	298.56	0.1	0.018	35	0.1885	0.16	1.7	3	0.00073	4	0.006	90	0.000282	1
K388-5	640.00 W	298.56	0.1	0.018	35	0.1885	0.16	1.7	3	0.00073	4	0.006	90	0.000282	1
K388-6	999.00 W	298.56	0.1	0.018	35	0.1885	0.16	1.7	3	0.00073	4	0.006	90	0.000282	1

40/39(k)	%1σ	38/39(k)	%1σ	36/38(cl)	%1σ	K/Ca	%1σ	K/Cl	%1σ	Ca/Cl	%1σ
0.0297	2	0.012	2	316	5	0.1616	4	5.4	33	33	33
0.0297	2	0.012	2	316	5	0.1616	4	5.4	33	33	33
0.0297	2	0.012	2	316	5	0.1616	4	5.4	33	33	33
0.0297	2	0.012	2	316	5	0.1616	4	5.4	33	33	33
0.0297	2	0.012	2	316	5	0.1616	4	5.4	33	33	33
0.0297	2	0.012	2	316	5	0.1616	4	5.4	33	33	33

Annexe 2 - Résultats de datation (1) sur Gabbro AR-08-29.

Incremental Heating		36Ar(a)	37Ar(ca)	38Ar(cl)	39Ar(k)	40Ar(r)	Age ± 1σ (Ma)	40Ar(r) (%)	39Ar(k) (%)	K/Ca ± 1σ
K423-1	500.00 W	0.000544	0.042459	0.001416	0.002847	0.018622	211.74 ± 75.26	10.29	1.91	0.0108 ± 0.0006
K423-2	550.00 W	0.000324	0.063131	0.000629	0.003736	0.017665	155.54 ± 40.49	15.41	2.50	0.0096 ± 0.0005
K423-3	600.00 W	0.000325	0.072127	0.000489	0.004511	0.022505	163.72 ± 33.96	18.79	3.02	0.0101 ± 0.0005
K423-4	620.00 W	0.000567	0.299009	0.000463	0.029743	0.153335	168.93 ± 9.39	47.39	19.94	0.0161 ± 0.0008
K423-5	655.00 W	0.000088	0.031311	0.001247	0.015870	0.088308	181.68 ± 5.20	76.77	10.64	0.0819 ± 0.0044
K423-6	#######	0.000996	2.038814	0.007589	0.092444	0.464233	164.74 ± 7.00	60.73	61.98	0.0073 ± 0.0004
	Σ	0.002845	2.546851	0.011833	0.149151	0.764669				

Information on Analysis
Sample = AMPHIBOLE AR-08-29
Material = Amphibole
Location = ???
Analyst = YR
Project = ROLLAND_HASSIG
Mass Discrimination Law = LIN
Irradiation = MC54
J = 0.01904040 ± 0.00009520
Hb3gr = 1074.000 ± 5.370 Ma

Results	40(r)/39(k) ± 1σ	Age ± 1σ (Ma)	MSWD	39Ar(k) (%,n)	K/Ca ± 1σ
Age Plateau	5.3241 ± 0.1287	174.20 ± 4.10	1.13	98.09	0.0095 ± 0.0024
Error Mean	± 2.42%	± 2.35%		5	
	Minimal External Error ± 4.11		1.06	Statistical T Ratio	
	Analytical Error ± 4.01		1.0638	Error Magnification	
Total Fusion Age	5.1268 ± 0.1655	168.03 ± 5.24		6	0.0095 ± 0.0004
	± 3.23%	± 3.12%			
	Minimal External Error ± 5.25				
	Analytical Error ± 5.18				

Normal Isochron		39(k)/36(a) ± 1σ	40(a+r)/36(a) ± 1σ	r.i.
K423-1	500.00 W	5.2 ± 0.2	332.8 ± 14.4	0.9676
K423-2	550.00 W	11.5 ± 0.6	353.0 ± 17.5	0.9735
K423-3	600.00 W	13.9 ± 0.7	367.7 ± 18.5	0.9781
K423-4	620.00 W	52.4 ± 2.8	568.9 ± 29.5	0.9812
K423-5	655.00 W	180.5 ± 17.1	1302.8 ± 122.9	0.9935
K423-6	#######	92.8 ± 6.3	764.5 ± 51.6	0.9885

Results	40(a)/36(a) ± 1σ	40(r)/39(k) ± 1σ	Age ± 1σ (Ma)	MSWD
Normal Isochron	288.8004 ± 11.4916	5.3721 ± 0.1848	175.69 ± 5.82	1.14
Error Chron	± 3.98%	± 3.44%	± 3.31%	
			Minimal External Error ± 5.83	
			Analytical Error ± 5.76	

Statistics				
	Statistical F ratio	1.09	Convergence	0.0000476297
	Error Magnification	1.0668	Number of Iterations	53
	Number of Data Points	5	Calculated Line	Weighted York-2

Inverse Isochron		39(k)/40(a+r) ± 1σ	36(a)/40(a+r) ± 1σ	r.i.
K423-1	500.00 W	0.015738 ± 0.000177	0.003005 ± 0.000130	0.0006
K423-2	550.00 W	0.032617 ± 0.000379	0.002833 ± 0.000140	0.0013
K423-3	600.00 W	0.037702 ± 0.000403	0.002719 ± 0.000136	0.0016
K423-4	620.00 W	0.092172 ± 0.000941	0.001758 ± 0.000091	0.0009
K423-5	655.00 W	0.138524 ± 0.001498	0.000768 ± 0.000072	0.0011
K423-6	#######	0.121369 ± 0.001254	0.001308 ± 0.000088	0.0003

Results	40(a)/36(a) ± 1σ	40(r)/39(k) ± 1σ	Age ± 1σ (Ma)	MSWD
Inverse Isochron	287.2467 ± 11.2375	5.4483 ± 0.1739	178.07 ± 5.48	1.15
Error Chron	± 3.91%	± 3.19%	± 3.08%	
			Minimal External Error ± 5.49	
			Analytical Error ± 5.41	

Statistics				
	Statistical F ratio	1.09	Convergence	0.0000784363
	Error Magnification	1.0719	Number of Iterations	3
	Number of Data Points	5	Calculated Line	Weighted York-2

Relative Abundances		36Ar	%1σ	37Ar	%1σ	38Ar	%1σ	39Ar	%1σ	40Ar	%1σ	Age ± 1σ (Ma)	40Ar(r) (%)	39Ar(k) (%)	K/Ca ± 1σ
K423-1	500.00 W	0.0005561	4.221	0.0424590	3.179	0.0018069	2.062	0.0028782	1.112	0.1810007	0.052	211.74 ± 75.26	10.29	1.91	0.0108 ± 0.0006
K423-2	550.00 W	0.0003425	4.684	0.0631311	3.123	0.0011140	2.079	0.0037817	1.144	0.1146397	0.085	155.54 ± 40.49	15.41	2.50	0.0096 ± 0.0005
K423-3	600.00 W	0.0003459	4.716	0.0721269	3.213	0.0010371	2.180	0.0045637	1.051	0.1197845	0.092	163.72 ± 33.96	18.79	3.02	0.0101 ± 0.0005
K423-4	620.00 W	0.0006517	4.493	0.2990086	3.048	0.0027207	2.161	0.0299612	1.010	0.3235713	0.067	168.93 ± 9.39	47.39	19.94	0.0161 ± 0.0008
K423-5	655.00 W	0.0000972	8.524	0.0313109	3.335	0.0016416	2.105	0.0158925	1.075	0.1150343	0.106	181.68 ± 5.20	76.77	10.64	0.0819 ± 0.0044
K423-6	#######	0.0015741	4.101	2.0388141	3.015	0.0211194	2.027	0.0939327	1.013	0.7644244	0.047	164.74 ± 7.00	60.73	61.98	0.0073 ± 0.0004
	Σ	0.0035676	2.201	2.5468506	2.444	0.0294397	1.482	0.1510100	0.672	1.6184550	0.029				

Information on Analysis and Constants Used in Calculations

Sample = AMPHIBOLE AR-08-29
Material = Amphibole
Location = ???
Analyst = YR
Project = ROLLAND_HASSIG
Mass Discrimination Law = LIN
Irradiation = MC54
J = 0.01904040 ± 0.00009520
Hb3gr = 1074.000 ± 5.370 Ma
IGSN = Undefined
Preferred Age = Undefined
Classification = Undefined
Experiment Type = Undefined
Extraction Method = Undefined
Heating = 60 sec
Isolation = 2.00 min
Instrument = VG3600
Lithology = Undefined
Lat-Lon = Undefined - Undefined

Age Equations = Conventional
Negative Intensities = Forced Zero
Decay Constant 40K = 5.543 ± 0.010 E-10 1/a
Decay Constant 39Ar = 2.940 ± 0.029 E-07 1/h
Decay Constant 37Ar = 8.220 ± 0.010 E-04 1/h
Decay Constant 36Cl = 2.310 ± 0.016 E-06 1/a
Production Ratio 36/38 in Cl = 316.0 ± 15.8

Results	40(r)/39(k) ± 1σ	Age ± 1σ (Ma)	MSWD	39Ar(k) (%,n)	K/Ca ± 1σ
Age Plateau	5.3241 ± 0.1287	174.20 ± 4.10	1.13	98.09	0.0095 ± 0.0024
Error Mean	± 2.42%	± 2.35%		5	
	Minimal External Error ± 4.11		1.06	Statistical T Ratio	
	Analytical Error ± 4.01		1.0638	Error Magnification	
Total Fusion Age	5.1268 ± 0.1655	168.03 ± 5.24		6	0.0095 ± 0.0004
	± 3.23%	± 3.12%			
	Minimal External Error ± 5.25				
	Analytical Error ± 5.18				
Normal Isochron	5.3721 ± 0.1848	175.69 ± 5.82	1.14	98.09	
Error Chron	± 3.44%	± 3.31%		5	
	Minimal External Error ± 5.83		1.09	Statistical F ratio	
	Analytical Error ± 5.76		1.0668	Error Magnification	
Inverse Isochron	5.4483 ± 0.1739	178.07 ± 5.48	1.15	98.09	
Error Chron	± 3.19%	± 3.08%		5	
	Minimal External Error ± 5.49		1.09	Statistical F ratio	
	Analytical Error ± 5.41		1.0719	Error Magnification	

Degassing Patterns		36Ar(a)	%1σ	36Ar(c)	%1σ	36Ar(ca)	%1σ	36Ar(cl)	%1σ	37Ar(ca)	%1σ	38Ar(a)	%1σ	38Ar(c)	%1σ	38Ar(k)	%1σ
K423-1	500.00 W	0.000544	4.32	0.000000	0.00	0.000012	3.33	0.000001	17.18	0.042459	3.18	0.000102	4.32	0.000000	0.00	0.000034	2.29
K423-2	550.00 W	0.000324	4.95	0.000000	0.00	0.000018	3.28	0.000000	54.58	0.063131	3.12	0.000061	4.95	0.000000	0.00	0.000045	2.31
K423-3	600.00 W	0.000325	5.02	0.000000	0.00	0.000020	3.36	0.000000	80.02	0.072127	3.21	0.000061	5.02	0.000000	0.00	0.000054	2.27
K423-4	620.00 W	0.000567	5.19	0.000000	0.00	0.000084	3.21	0.000000	349.36	0.299009	3.05	0.000107	5.19	0.000000	0.00	0.000357	2.24
K423-5	655.00 W	0.000088	9.43	0.000000	0.00	0.000009	3.48	0.000000	14.75	0.031311	3.33	0.000017	9.43	0.000000	0.00	0.000190	2.27
K423-6	#######	0.000996	6.75	0.000000	0.00	0.000575	3.18	0.000003	145.36	2.038814	3.01	0.000188	6.75	0.000000	0.00	0.001109	2.25
	Σ	0.002845	2.84	0.000000	0.00	0.000718	2.57	0.000005	94.37	2.546851	2.44	0.000536	2.84	0.000000	0.00	0.001790	1.49
	Σ							0.003568	2.33	2.546851	2.44						

38Ar(ca)	%1σ	38Ar(cl)	%1σ	39Ar(k)	%1σ	39Ar(ca)	%1σ	40Ar(r)	%1σ	40Ar(a)	%1σ	40Ar(c)	%1σ	40Ar(k)	%1σ
0.000255	90.06	0.001416	17.91	0.002847	1.13	0.000031	5.11	0.018622	37.65	0.162294	4.32	0.000000	0.00	0.000085	2.29
0.000379	90.05	0.000629	54.81	0.003736	1.16	0.000046	5.07	0.017665	27.14	0.096863	4.95	0.000000	0.00	0.000111	2.31
0.000433	90.06	0.000489	80.18	0.004511	1.06	0.000053	5.13	0.022505	21.67	0.097145	5.02	0.000000	0.00	0.000134	2.27
0.001794	90.05	0.000463	349.39	0.029743	1.02	0.000218	5.03	0.153335	5.73	0.169353	5.19	0.000000	0.00	0.000883	2.24
0.000188	90.06	0.001247	15.59	0.015870	1.08	0.000023	5.21	0.088308	2.81	0.026254	9.43	0.000000	0.00	0.000471	2.27
0.012233	90.05	0.007589	145.44	0.092444	1.03	0.001488	5.01	0.464233	4.32	0.297446	6.75	0.000000	0.00	0.002746	2.25
0.015281	72.96	0.011833	94.42	0.149151	0.68	0.001859	4.06	0.764669	3.16	0.849356	2.84	0.000000	0.00	0.004430	1.49
		0.029440	53.62			0.151010	0.68							1.618455	2.11

Additional Parameters		40(r)/39(k)	1σ	40(r+a)	1σ	40Ar/39Ar	1σ	37Ar/39Ar	1σ	36Ar/39Ar	1σ	Time (days)	37Ar (decay)	39Ar (decay)	40Ar (moles)
K423-1	500.00 W	6.540480	2.46383	0.180916	0.00009	62.885710	0.69992	14.751684	0.49678	0.193209	0.00843	191.474	45.22715422	1.00136431	3.620E-15
K423-2	550.00 W	4.728965	1.28472	0.114529	0.00010	30.314723	0.34768	16.694047	0.55527	0.090563	0.00437	191.491	45.24202735	1.00136443	2.293E-15
K423-3	600.00 W	4.989004	1.08243	0.119651	0.00011	26.247431	0.27686	15.804592	0.53422	0.075796	0.00366	191.505	45.25442536	1.00136453	2.396E-15
K423-4	620.00 W	5.155336	0.30004	0.322688	0.00022	10.799681	0.10936	9.979866	0.32046	0.021753	0.00100	191.533	45.27923158	1.00136472	6.471E-15
K423-5	655.00 W	5.564600	0.16734	0.114563	0.00012	7.238255	0.07816	1.970161	0.06903	0.006119	0.00053	191.546	45.29101930	1.00136482	2.301E-15
K423-6	#######	5.021752	0.22324	0.761679	0.00037	8.137998	0.08252	21.705044	0.69033	0.016758	0.00071	191.560	45.30405140	1.00136492	1.529E-14

Procedure Blanks		36Ar	1σ	37Ar	1σ	38Ar	1σ	39Ar	1σ	40Ar	1σ
K423-1	500.00 W	0.000026	0.000003	0.000041	0.000004	0.000007	0.000003	0.000012	0.000003	0.001262	0.000022
K423-2	550.00 W	0.000026	0.000003	0.000041	0.000004	0.000007	0.000003	0.000012	0.000003	0.001262	0.000022
K423-3	600.00 W	0.000026	0.000003	0.000041	0.000004	0.000007	0.000003	0.000012	0.000003	0.001262	0.000022
K423-4	620.00 W	0.000024	0.000007	0.000041	0.000007	0.000004	0.000006	0.000018	0.000004	0.001436	0.000013
K423-5	655.00 W	0.000024	0.000007	0.000041	0.000007	0.000004	0.000006	0.000018	0.000004	0.001436	0.000013
K423-6	1111.00 W	0.000024	0.000007	0.000041	0.000007	0.000004	0.000006	0.000018	0.000004	0.001436	0.000013

Intercept Values		36Ar	1σ	r2		37Ar	1σ	r2		38Ar	1σ	r2		39Ar	1σ	r2		40Ar	1σ	r2	
K423-1	500.00 W	0.000587	0.000007	0.9147	LIN # 6	0.000987	0.000009	0.9649	EXP # 7	0.001823	0.000009	0.9863	EXP #	0.002893	0.000014	0.9854	EXP #	0.182263	0.000092	0.9998	EXP #
K423-2	550.00 W	0.000371	0.000008	0.7902	EXP #	0.001447	0.000011	0.9771	EXP #	0.001127	0.000006	0.9869	EXP #	0.003797	0.000021	0.9862	EXP #	0.115902	0.000095	0.9996	EXP #
K423-3	600.00 W	0.000375	0.000008	0.7909	EXP #	0.001647	0.000017	0.9539	EXP #	0.001050	0.000009	0.9726	EXP #	0.004580	0.000015	0.9962	EXP #	0.121047	0.000107	0.9996	EXP #
K423-4	620.00 W	0.000681	0.000012	0.8822	EXP #	0.006692	0.000030	0.9919	EXP #	0.002737	0.000022	0.9702	EXP #	0.030010	0.000047	0.9988	EXP #	0.325007	0.000216	0.9998	EXP #
K423-5	655.00 W	0.000122	0.000003	0.0007	EXP #	0.000738	0.000007	0.9552	EXP #	0.001653	0.000010	0.9889	EXP #	0.015927	0.000063	0.9935	EXP #	0.116470	0.000121	0.9994	EXP #
K423-6	1111.00 W	0.001613	0.000015	0.9622	EXP #	0.045366	0.000048	0.9994	EXP #	0.021224	0.000076	0.9932	EXP #	0.094046	0.000162	0.9983	EXP #	0.765860	0.000362	0.9999	EXP #

Sample Parameters		Sample	Material	Location	Analyst	Temp	Standard (in Ma)	%1σ	J	%1σ	MDF	%1σ
K423-1	500.00 W	Amphibole AR-08-29	Amphibole	???	YR	500	1074	0.5	0.0190404	0.5	1.002391	1
K423-2	550.00 W	Amphibole AR-08-30	Amphibole	???	YR	550	1074	0.5	0.0190404	0.5	1.002391	1
K423-3	600.00 W	Amphibole AR-08-31	Amphibole	???	YR	600	1074	0.5	0.0190404	0.5	1.002391	1
K423-4	620.00 W	Amphibole AR-08-32	Amphibole	???	YR	620	1074	0.5	0.0190404	0.5	1.002391	1
K423-5	655.00 W	Amphibole AR-08-33	Amphibole	???	YR	655	1074	0.5	0.0190404	0.5	1.002391	1
K423-6	1111.00 W	Amphibole AR-08-34	Amphibole	???	YR	1111	1074	0.5	0.0190404	0.5	1.002391	1

Volume Ratio	Sensitivity (mol/volt)	Day	Month	Year	Hour	Min	Resist	Irradiation	Project	Experiment	Nmb	Standard Name
1	2.000E-14	19	APR	2010	08	32	001	MC54	Rolland_Hassig	K423-1	01	Hb3gr
1	2.000E-14	19	APR	2010	08	56	001	MC54	Rolland_Hassig	K423-1	01	Hb3gr
1	2.000E-14	19	APR	2010	09	16	001	MC54	Rolland_Hassig	K423-1	01	Hb3gr
1	2.000E-14	19	APR	2010	09	56	001	MC54	Rolland_Hassig	K423-1	01	Hb3gr
1	2.000E-14	19	APR	2010	10	15	001	MC54	Rolland_Hassig	K423-1	01	Hb3gr
1	2.000E-14	19	APR	2010	10	36	001	MC54	Rolland_Hassig	K423-1	01	Hb3gr

Irradiation Constants		40/36(a)	%1σ	40/36(c)	%1σ	38/36(a)	%1σ	38/36(c)	%1σ	39/37(ca)	%1σ	38/37(ca)	%1σ	36/37(ca)	%1σ
K423-1	500.00 W	298.56	0.1	0.018	35	0.1885	0.16	1.7	3	0.00073	4	0.006	90	0.000282	1
K423-2	550.00 W	298.56	0.1	0.018	35	0.1885	0.16	1.7	3	0.00073	4	0.006	90	0.000282	1
K423-3	600.00 W	298.56	0.1	0.018	35	0.1885	0.16	1.7	3	0.00073	4	0.006	90	0.000282	1
K423-4	620.00 W	298.56	0.1	0.018	35	0.1885	0.16	1.7	3	0.00073	4	0.006	90	0.000282	1
K423-5	655.00 W	298.56	0.1	0.018	35	0.1885	0.16	1.7	3	0.00073	4	0.006	90	0.000282	1
K423-6	1111.00 W	298.56	0.1	0.018	35	0.1885	0.16	1.7	3	0.00073	4	0.006	90	0.000282	1

40/39(k)	%1σ	38/39(k)	%1σ	36/38(cl)	%1σ	K/Ca	%1σ	K/Cl	%1σ	Ca/Cl	%1σ
0.0297	2	0.012	2	316	5	0.1616	4	5.4	33	33	33
0.0297	2	0.012	2	316	5	0.1616	4	5.4	33	33	33
0.0297	2	0.012	2	316	5	0.1616	4	5.4	33	33	33
0.0297	2	0.012	2	316	5	0.1616	4	5.4	33	33	33
0.0297	2	0.012	2	316	5	0.1616	4	5.4	33	33	33
0.0297	2	0.012	2	316	5	0.1616	4	5.4	33	33	33

Annexe 3 - Résultats de datation (1) sur Amphibole AR-09-08.

Incremental Heating		36Ar(a)	37Ar(ca)	38Ar(cl)	39Ar(k)	40Ar(r)	Age ± 1σ (Ma)	40Ar(r) (%)	39Ar(k) (%)	K/Ca ± 1σ
K390-1	400.00 W	0.000181	0.005240	0.000032	0.000520	0.002912	182.99 ± 195.05	5.12	0.40	0.0160 ± 0.0018
K390-2	500.00 W	0.000222	0.004529	0.000000	0.001264	0.004207	110.98 ± 100.70	5.97	0.98	0.0451 ± 0.0030
K390-3	551.00 W	0.000070	0.019876	0.000000	0.002286	0.012264	175.59 ± 27.34	36.83	1.78	0.0186 ± 0.0010
K390-4	601.00 W	0.000063	0.054423	0.000000	0.002816	0.009983	117.94 ± 22.31	34.43	2.19	0.0084 ± 0.0004
K390-5	659.00 W	0.000066	1.017743	0.000000	0.041821	0.110792	88.85 ± 4.69	84.11	32.48	0.0066 ± 0.0003
K390-6	712.00 W	0.000037	1.589338	0.000000	0.066204	0.170944	86.66 ± 4.20	92.94	51.42	0.0067 ± 0.0004
K390-7	999.00 W	0.000008	0.318296	0.000000	0.013853	0.036316	87.95 ± 5.91	92.84	10.76	0.0070 ± 0.0004
	Σ	0.000647	3.009443	0.000032	0.128763	0.347417				

Information on Analysis
Sample = AR09-08 (108 MC54 TR
Material = Amphibole
Location = ???
Analyst = YR
Project = ROLLAND_HASSIG
Mass Discrimination Law = LIN
Irradiation = MC54
J = 0.01905650 ± 0.00009528
Hb3gr = 1073.600 ± 5.368 Ma

Results	40(r)/39(k) ± 1σ	Age ± 1σ (Ma)	MSWD	39Ar(k) (%,n)	K/Ca ± 1σ
Age Plateau	2.6141 ± 0.0844 ± 3.23%	87.70 ± 2.80 ± 3.19%	0.06	94.65 3	0.0068 ± 0.0002
		Minimal External Error ± 2.80	1.21	Statistical T Ratio	
		Analytical Error ± 2.77	1.0000	Error Magnification	
Total Fusion Age	2.6981 ± 0.0947 ± 3.51%	90.45 ± 3.13 ± 3.46%		7	0.0069 ± 0.0003
		Minimal External Error ± 3.13			
		Analytical Error ± 3.10			

Normal Isochron		39(k)/36(a) ± 1σ	40(a+r)/36(a) ± 1σ	r.i.
K390-1	400.00 W	2.9 ± 0.2	314.7 ± 19.0	0.9613
K390-2	500.00 W	5.7 ± 0.4	317.5 ± 18.9	0.9661
K390-3	551.00 W	32.5 ± 3.1	473.2 ± 45.1	0.9899
K390-4	601.00 W	44.4 ± 4.6	456.0 ± 46.9	0.9909
K390-5	659.00 W	634.4 ± 187.9	1979.1 ± 585.8	0.9991
K390-6	712.00 W	1793.4 ± 1337.7	4929.3 ± 3676.3	0.9999
K390-7	999.00 W	1729.9 ± 1777.1	4833.7 ± 4965.0	0.9999

Results	40(a)/36(a) ± 1σ	40(r)/39(k) ± 1σ	Age ± 1σ (Ma)	MSWD
Normal Isochron No Convergence	351.5360 ± 204.0298 ± 58.04%	2.5645 ± 0.2104 ± 8.20%	86.08 ± 6.91 ± 8.03%	0.02
		Minimal External Error ± 6.91		
		Analytical Error ± 6.90		

Statistics				
	Statistical F ratio	0.87	Convergence	0.0000536789
	Error Magnification	1.0000	Number of Iterations	100
	Number of Data Points	3	Calculated Line	Weighted York-2

Inverse Isochron		39(k)/40(a+r) ± 1σ	36(a)/40(a+r) ± 1σ	r.i.
K390-1	400.00 W	0.009133 ± 0.000158	0.003178 ± 0.000192	0.0008
K390-2	500.00 W	0.017940 ± 0.000285	0.003149 ± 0.000187	0.0010
K390-3	551.00 W	0.068790 ± 0.000936	0.002113 ± 0.000201	0.0022
K390-4	601.00 W	0.097404 ± 0.001359	0.002193 ± 0.000225	0.0032
K390-5	659.00 W	0.320527 ± 0.004009	0.000505 ± 0.000150	0.0003
K390-6	712.00 W	0.363824 ± 0.004557	0.000203 ± 0.000151	0.0001
K390-7	999.00 W	0.357891 ± 0.004600	0.000207 ± 0.000213	0.0003

Results	40(a)/36(a) ± 1σ	40(r)/39(k) ± 1σ	Age ± 1σ (Ma)	MSWD
Inverse Isochron	354.8707 ± 207.1126 ± 58.36%	2.5624 ± 0.2136 ± 8.33%	86.01 ± 7.01 ± 8.15%	0.02
			Minimal External Error ± 7.02	
			Analytical Error ± 7.00	

Statistics				
	Statistical F ratio	0.87	Convergence	0.0000150390
	Error Magnification	1.0000	Number of Iterations	3
	Number of Data Points	3	Calculated Line	Weighted York-2

Relative Abundances		36Ar	%1σ	37Ar	%1σ	38Ar	%1σ	39Ar	%1σ	40Ar	%1σ	Age ± 1σ (Ma)	40Ar(r) (%)	39Ar(k) (%)	K/Ca ± 1σ
K390-1	400.00 W	0.0001823	5.992	0.0052398	10.659	0.0001036	16.143	0.0005236	1.715	0.0569241	0.094	182.99 ± 195.05	5.12	0.40	0.0160 ± 0.0018
K390-2	500.00 W	0.0002231	5.906	0.0045310	5.043	0.0000813	7.650	0.0012676	1.414	0.0704721	0.098	110.98 ± 100.70	5.97	0.98	0.0451 ± 0.0030
K390-3	551.00 W	0.0000758	8.813	0.0198861	3.238	0.0001593	5.722	0.0023020	1.143	0.0333032	0.168	175.59 ± 27.34	36.83	1.78	0.0186 ± 0.0010
K390-4	601.00 W	0.0000787	8.248	0.0544513	3.065	0.0003322	3.059	0.0028571	1.165	0.0289926	0.212	117.94 ± 22.31	34.43	2.19	0.0084 ± 0.0004
K390-5	659.00 W	0.0003531	4.888	1.0182771	3.008	0.0049208	2.043	0.0425862	1.004	0.1317176	0.108	88.85 ± 4.69	84.11	32.48	0.0066 ± 0.0003
K390-6	712.00 W	0.0004853	4.858	1.5901716	3.008	0.0078650	2.020	0.0673992	1.010	0.1839322	0.067	86.66 ± 4.20	92.94	51.42	0.0067 ± 0.0004
K390-7	999.00 W	0.0000978	7.887	0.3184631	3.014	0.0018204	2.140	0.0140927	1.035	0.0391186	0.188	87.95 ± 5.91	92.84	10.76	0.0070 ± 0.0004
	Σ	0.0014963	2.403	3.0110198	1.914	0.0152825	1.265	0.1310283	0.624	0.5444604	0.043				

Information on Analysis and Constants Used In Calculations

Sample = AR09-08 (108 MC54 TR B1)
Material = Amphibole
Location = ???
Analyst = YR
Project = ROLLAND_HASSIG
Mass Discrimination Law = LIN
Irradiation = MC54
J = 0.01905650 ± 0.00009528
Hb3gr = 1073.600 ± 5.368 Ma
IGSN = Undefined
Preferred Age = Undefined
Classification = Undefined
Experiment Type = Undefined
Extraction Method = Undefined
Heating = 60 sec
Isolation = 2.00 min
Instrument = VG3600
Lithology = Undefined
Lat-Lon = Undefined - Undefined

Age Equations = Conventional
Negative Intensities = Forced Zero
Decay Constant 40K = 5.543 ± 0.010 E-10 1/a
Decay Constant 39Ar = 2.940 ± 0.029 E-07 1/h
Decay Constant 37Ar = 8.220 ± 0.010 E-04 1/h
Decay Constant 36Cl = 2.310 ± 0.016 E-06 1/a
Production Ratio 36/38 in Cl = 316.0 ± 15.8

Results	40(r)/39(k) ± 1σ	Age ± 1σ (Ma)	MSWD	39Ar(k) (%,n)	K/Ca ± 1σ
Age Plateau	2.6141 ± 0.0844 ± 3.23%	87.70 ± 2.80 ± 3.19%	0.06	94.65 3	0.0068 ± 0.0002
		Minimal External Error ± 2.80	1.21	Statistical T Ratio	
		Analytical Error ± 2.77	1.0000	Error Magnification	
Total Fusion Age	2.6981 ± 0.0947 ± 3.51%	90.45 ± 3.13 ± 3.46%		7	0.0069 ± 0.0003
		Minimal External Error ± 3.13			
		Analytical Error ± 3.10			
Normal Isochron No Convergence	2.5645 ± 0.2104 ± 8.20%	86.08 ± 6.91 ± 8.03%	0.02	94.65 3	
		Minimal External Error ± 6.91	0.87	Statistical F ratio	
		Analytical Error ± 6.90	1.0000	Error Magnification	
Inverse Isochron	2.5624 ± 0.2136 ± 8.33%	86.01 ± 7.01 ± 8.15%	0.02	94.65 3	
		Minimal External Error ± 7.02	0.87	Statistical F ratio	
		Analytical Error ± 7.00	1.0000	Error Magnification	

Degassing Patterns	36Ar(a)	%1σ	36Ar(c)	%1σ	36Ar(ca)	%1σ	36Ar(cl)	%1σ	37Ar(ca)	%1σ	38Ar(a)	%1σ	38Ar(c)	%1σ	38Ar(k)	%1σ
K390-1 400.00 W	0.000181	6.04	0.000000	0.00	0.000001	10.71	0.000000	104.17	0.005240	10.66	0.000034	6.04	0.000000	0.00	0.000006	2.64
K390-2 500.00 W	0.000222	5.94	0.000000	0.00	0.000001	5.19	0.000000	0.00	0.004529	5.09	0.000042	5.94	0.000000	0.00	0.000015	2.55
K390-3 551.00 W	0.000070	9.52	0.000000	0.00	0.000006	3.46	0.000000	0.00	0.019876	3.31	0.000013	9.52	0.000000	0.00	0.000027	2.41
K390-4 601.00 W	0.000063	10.28	0.000000	0.00	0.000015	3.30	0.000000	0.00	0.054423	3.15	0.000012	10.28	0.000000	0.00	0.000034	2.43
K390-5 659.00 W	0.000066	29.60	0.000000	0.00	0.000287	3.25	0.000000	0.00	1.017743	3.09	0.000012	29.60	0.000000	0.00	0.000502	2.36
K390-6 712.00 W	0.000037	74.58	0.000000	0.00	0.000448	3.25	0.000000	0.00	1.589338	3.09	0.000007	74.58	0.000000	0.00	0.000794	2.36
K390-7 999.00 W	0.000008	102.72	0.000000	0.00	0.000090	3.25	0.000000	0.00	0.318296	3.10	0.000002	102.72	0.000000	0.00	0.000166	2.37
Σ	0.000647	6.15	0.000000	0.00	0.000849	2.07	0.000000	104.17	3.009443	1.97	0.000122	6.16	0.000000	0.00	0.001545	1.46
Σ							0.001496	2.91	3.009443	1.97						

38Ar(ca)	%1σ	38Ar(cl)	%1σ	39Ar(k)	%1σ	39Ar(ca)	%1σ	40Ar(r)	%1σ	40Ar(a)	%1σ	40Ar(c)	%1σ	40Ar(k)	%1σ
0.000031	90.63	0.000032	104.29	0.000520	1.73	0.000004	11.39	0.002912	112.07	0.053997	6.04	0.000000	0.00	0.000015	2.64
0.000027	90.14	0.000000	0.00	0.001264	1.58	0.000003	6.48	0.004207	93.55	0.066228	5.94	0.000000	0.00	0.000038	2.55
0.000119	90.06	0.000000	0.00	0.002286	1.35	0.000015	5.19	0.012264	16.29	0.020971	9.52	0.000000	0.00	0.000068	2.41
0.000327	90.05	0.000000	0.00	0.002816	1.38	0.000040	5.09	0.009983	19.49	0.018926	10.28	0.000000	0.00	0.000084	2.43
0.006106	90.05	0.000000	0.00	0.041821	1.25	0.000743	5.05	0.110792	5.26	0.019683	29.60	0.000000	0.00	0.001242	2.36
0.009536	90.05	0.000000	0.00	0.066204	1.25	0.001160	5.05	0.170944	4.81	0.011021	74.58	0.000000	0.00	0.001966	2.36
0.001910	90.05	0.000000	0.00	0.013853	1.27	0.000232	5.06	0.036316	6.77	0.002391	102.72	0.000000	0.00	0.000411	2.37
0.018057	57.30	0.000032	104.29	0.128763	0.77	0.002197	3.22	0.347417	3.42	0.193217	6.15	0.000000	0.00	0.003824	1.46
		0.019756	52.37			0.130960	0.76							0.544458	3.09

Additional Parameters	40(r)/39(k)	1σ	40(r+a)	1σ	40Ar/39Ar	1σ	37Ar/39Ar	1σ	36Ar/39Ar	1σ	Time (days)	37Ar (decay)	39Ar (decay)	40Ar (moles)
K390-1 400.00 W	5.602108	6.27924	0.056909	0.00005	108.721046	1.86685	10.007608	1.08045	0.348265	0.02171	136.763	15.36885661	1.00097781	1.138E-15
K390-2 500.00 W	3.329300	3.11494	0.070435	0.00007	55.596495	0.78780	3.574563	0.18722	0.176008	0.01069	136.794	15.37854511	1.00097804	1.409E-15
K390-3 551.00 W	5.364234	0.87670	0.033235	0.00006	14.467314	0.16718	8.638762	0.29667	0.032950	0.00293	136.810	15.38318090	1.00097815	6.661E-16
K390-4 601.00 W	3.545162	0.69274	0.028909	0.00006	10.147686	0.12021	19.058475	0.62486	0.027562	0.00230	136.825	15.38781809	1.00097826	5.799E-16
K390-5 659.00 W	2.649206	0.14320	0.130476	0.00014	3.092965	0.03123	23.910957	0.75821	0.008291	0.00041	136.856	15.39730761	1.00097848	2.634E-15
K390-6 712.00 W	2.582087	0.12830	0.181966	0.00013	2.728997	0.02762	23.593327	0.74855	0.007201	0.00036	136.874	15.40258209	1.00097860	3.679E-15
K390-7 999.00 W	2.621548	0.18046	0.038707	0.00007	2.775809	0.02921	22.597752	0.72022	0.006941	0.00055	136.888	15.40680297	1.00097870	7.824E-16

Procedure Blanks	36Ar	1σ	37Ar	1σ	38Ar	1σ	39Ar	1σ	40Ar	1σ
K390-1 400.00 W	0.000032	0.000003	0.000067	0.000007	0.000012	0.000004	0.000025	0.000004	0.001162	0.000016
K390-2 500.00 W	0.000040	0.000004	0.000126	0.000008	0.000022	0.000005	0.000035	0.000006	0.001186	0.000018
K390-3 551.00 W	0.000040	0.000004	0.000126	0.000008	0.000022	0.000005	0.000035	0.000006	0.001186	0.000018
K390-4 601.00 W	0.000040	0.000004	0.000126	0.000008	0.000022	0.000005	0.000035	0.000006	0.001186	0.000018
K390-5 659.00 W	0.000025	0.000006	0.000075	0.000016	0.000000	0.000005	0.000010	0.000009	0.001164	0.000015
K390-6 712.00 W	0.000025	0.000006	0.000075	0.000016	0.000000	0.000005	0.000010	0.000009	0.001164	0.000015
K390-7 999.00 W	0.000025	0.000006	0.000075	0.000016	0.000000	0.000005	0.000010	0.000009	0.001164	0.000015

Intercept Values	36Ar	1σ	r2		37Ar	1σ	r2		38Ar	1σ	r2		39Ar	1σ	r2		40Ar	1σ	r2	
K390-1 400.00 W	0.000216	0.000008	0.6500	LIN # 5	0.000411	0.000035	0.9291	EXP #	0.000116	0.000016	0.5313	EXP #	0.000550	0.000006	0.0253	LIN # 5	0.058086	0.000051	0.9997	EXP # 5
K390-2 500.00 W	0.000264	0.000009	0.7103	EXP #	0.000421	0.000009	0.9617	EXP #	0.000103	0.000003	0.8806	EXP #	0.001303	0.000011	0.9243	EXP #	0.071658	0.000067	0.9995	EXP #
K390-3 551.00 W	0.000116	0.000005	0.0032	EXP #	0.001422	0.000013	0.7614	EXP #	0.000181	0.000007	0.3270	EXP #	0.002337	0.000012	0.9861	EXP #	0.034489	0.000053	0.9961	EXP #
K390-4 601.00 W	0.000119	0.000005	0.3121	EXP #	0.003674	0.000019	0.9897	EXP #	0.000354	0.000006	0.8498	EXP #	0.002892	0.000016	0.9891	EXP #	0.030178	0.000059	0.9969	EXP #
K390-5 659.00 W	0.000379	0.000008	0.8791	EXP #	0.066376	0.000054	0.9999	EXP #	0.004929	0.000020	0.9963	EXP #	0.042590	0.000045	0.9997	EXP #	0.132882	0.000141	0.9997	EXP #
K390-6 712.00 W	0.000512	0.000012	0.8522	EXP #	0.103578	0.000081	0.9999	EXP #	0.007878	0.000023	0.9978	EXP #	0.067400	0.000103	0.9994	EXP #	0.185097	0.000123	0.9999	EXP #
K390-7 999.00 W	0.000123	0.000003	0.1429	EXP #	0.020798	0.000041	0.9988	EXP #	0.001824	0.000013	0.9824	EXP #	0.014101	0.000038	0.9976	EXP #	0.040283	0.000072	0.9972	EXP #

Sample Parameters	Sample	Material	Location	Analyst	Temp	Standard (in Ma)	%1σ	J	%1σ	MDF	%1σ
K390-1 400.00 W	AR09-08 (108 MC54 tr B1)	Amphibole	???	YR	400	1073.6	0.5	0.0190565	0.5	1.002391	1
K390-2 500.00 W	AR09-08 (108 MC54 tr B1)	Amphibole	???	YR	500	1073.6	0.5	0.0190665	0.5	1.000848	1
K390-3 551.00 W	AR09-08 (108 MC54 tr B1)	Amphibole	???	YR	551	1073.6	0.5	0.0190665	0.5	1.000848	1
K390-4 601.00 W	AR09-08 (108 MC54 tr B1)	Amphibole	???	YR	601	1073.6	0.5	0.0190665	0.5	1.000848	1
K390-5 659.00 W	AR09-08 (108 MC54 tr B1)	Amphibole	???	YR	659	1073.6	0.5	0.0190665	0.5	1.000848	1
K390-6 712.00 W	AR09-08 (108 MC54 tr B1)	Amphibole	???	YR	712	1073.6	0.5	0.0190665	0.5	1.000848	1
K390-7 999.00 W	AR09-08 (108 MC54 tr B1)	Amphibole	???	YR	999	1073.6	0.5	0.0190665	0.5	1.000848	1

Volume Ratio	Sensitivity (mol/volt)	Day	Month	Year	Hour	Min	Resist	Irradiation	Project	Experiment	Nmb	Standard Name
1	2.000E-14	23	FEB	2010	15	27	001	MC54	Rolland_Hassig	K390-1	01	Hb3gr
1	2.000E-14	23	FEB	2010	16	13	001	MC54	Rolland_Hassig	K390-1	01	Hb3gr
1	2.000E-14	23	FEB	2010	16	35	001	MC54	Rolland_Hassig	K390-1	01	Hb3gr
1	2.000E-14	23	FEB	2010	16	57	001	MC54	Rolland_Hassig	K390-1	01	Hb3gr
1	2.000E-14	23	FEB	2010	17	42	001	MC54	Rolland_Hassig	K390-1	01	Hb3gr
1	2.000E-14	23	FEB	2010	18	07	001	MC54	Rolland_Hassig	K390-1	01	Hb3gr
1	2.000E-14	23	FEB	2010	18	27	001	MC54	Rolland_Hassig	K390-1	01	Hb3gr

Irradiation Constants	40/36(a)	%1σ	40/36(c)	%1σ	38/36(a)	%1σ	38/36(c)	%1σ	39/37(ca)	%1σ	38/37(ca)	%1σ	36/37(ca)	%1σ
K390-1 400.00 W	298.56	0.1	0.018	35	0.1885	0.16	1.7	3	0.00073	4	0.006	90	0.000282	1
K390-2 500.00 W	298.56	0.1	0.018	35	0.1885	0.16	1.7	3	0.00073	4	0.006	90	0.000282	1
K390-3 551.00 W	298.56	0.1	0.018	35	0.1885	0.16	1.7	3	0.00073	4	0.006	90	0.000282	1
K390-4 601.00 W	298.56	0.1	0.018	35	0.1885	0.16	1.7	3	0.00073	4	0.006	90	0.000282	1
K390-5 659.00 W	298.56	0.1	0.018	35	0.1885	0.16	1.7	3	0.00073	4	0.006	90	0.000282	1
K390-6 712.00 W	298.56	0.1	0.018	35	0.1885	0.16	1.7	3	0.00073	4	0.006	90	0.000282	1
K390-7 999.00 W	298.56	0.1	0.018	35	0.1885	0.16	1.7	3	0.00073	4	0.006	90	0.000282	1

40/39(k)	%1σ	38/39(k)	%1σ	36/38(cl)	%1σ	K/Ca	%1σ	K/Cl	%1σ	Ca/Cl	%1σ
0.0297	2	0.012	2	316	5	0.1616	4	5.4	33	33	33
0.0297	2	0.012	2	316	5	0.1616	4	5.4	33	33	33
0.0297	2	0.012	2	316	5	0.1616	4	5.4	33	33	33
0.0297	2	0.012	2	316	5	0.1616	4	5.4	33	33	33
0.0297	2	0.012	2	316	5	0.1616	4	5.4	33	33	33
0.0297	2	0.012	2	316	5	0.1616	4	5.4	33	33	33
0.0297	2	0.012	2	316	5	0.1616	4	5.4	33	33	33

Annexe 4 - Résultats de datation (1) sur Amphibole AR-09-15.

Incremental Heating		36Ar(a)	37Ar(ca)	38Ar(cl)	39Ar(k)	40Ar(r)	Age ± 1σ (Ma)	40Ar(r) (%)	39Ar(k) (%)	K/Ca ± 1σ
K402-1	400.00 W	0.000021	0.000337	0.000073	0.000204	0.002469	374.16 ± 212.99	28.42	0.05	0.0980 ± 0.0511
K402-2	600.00 W	0.000039	0.011189	0.000022	0.000954	0.000708	25.34 ± 58.34	5.71	0.25	0.0138 ± 0.0008
K402-3	661.00 W	0.000008	0.061419	0.000000	0.004189	0.011381	91.08 ± 14.82	81.14	1.08	0.0110 ± 0.0006
K402-4	720.00 W	0.000000	0.381808	0.000000	0.026165	0.074227	95.01 ± 3.41	98.79	6.76	0.0111 ± 0.0006
K402-5	770.00 W	0.000059	3.540617	0.000000	0.272923	0.739798	90.89 ± 2.20	96.63	70.55	0.0125 ± 0.0006
K402-6	820.00 W	0.000025	0.912205	0.000000	0.075888	0.202241	89.39 ± 2.53	95.37	19.62	0.0134 ± 0.0007
K402-7	#######	0.000000	0.081556	0.000000	0.006531	0.018797	96.36 ± 1.10	98.98	1.69	0.0129 ± 0.0007
	Σ	0.000153	4.989131	0.000096	0.386855	1.049620				

Information on Analysis
Sample = AMPHIBOLE AR-09-15
Material = Amphibole
Location = ???
Analyst = JL
Project = ROLLAND_HASSIG
Mass Discrimination Law = LIN
Irradiation = MC54
J = 0.01906130 ± 0.00009531
Hb3gr = 1073.600 ± 5.368 Ma

Results	40(r)/39(k) ± 1σ	Age ± 1σ (Ma)	MSWD	39Ar(k) (%,n)	K/Ca ± 1σ
Age Plateau	2.7187 ± 0.0454 ± 1.67%	91.15 ± 1.55 ± 1.70%	0.59	98.01 4	0.0118 ± 0.0006
		Minimal External Error ± 1.56	1.10	Statistical T Ratio	
		Analytical Error ± 1.49	1.0000	Error Magnification	
Total Fusion Age	2.7132 ± 0.0509 ± 1.88%	90.97 ± 1.72 ± 1.90%		7	0.0125 ± 0.0006
		Minimal External Error ± 1.73			
		Analytical Error ± 1.67			

Normal Isochron		39(k)/36(a) ± 1σ	40(a+r)/36(a) ± 1σ	r.i.
K402-1	400.00 W	9.8 ± 2.5	417.2 ± 104.4	0.9896
K402-2	600.00 W	24.4 ± 3.5	316.7 ± 44.6	0.9944
K402-3	661.00 W	496.2 ± 372.8	1646.6 ± 1236.8	0.9999
K402-4	720.00 W	59897.4 ± 1204168.1	170220.0 ± 3422077.8	1.0000
K402-5	770.00 W	4601.3 ± 4358.3	12771.0 ± 12095.8	0.9999
K402-6	820.00 W	2994.7 ± 2172.4	8279.4 ± 6005.3	0.9999
K402-7	#######			

Results	40(a)/36(a) ± 1σ	40(r)/39(k) ± 1σ	Age ± 1σ (Ma)	MSWD
Normal Isochron	28.6634 ± 208.3896 ± 727.02%	2.8431 ± 0.0520 ± 1.83%	95.21 ± 1.76 ± 1.85%	2.07
Error Chron			Minimal External Error ± 1.77	
			Analytical Error ± 1.70	

Statistics				
	Statistical F ratio	1.05	Convergence	0.0000000070
	Error Magnification	1.4379	Number of Iterations	1
	Number of Data Points	4	Calculated Line	Weighted York-2

Inverse Isochron		39(k)/40(a+r) ± 1σ	36(a)/40(a+r) ± 1σ	r.i.
K402-1	400.00 W	0.023526 ± 0.000854	0.002397 ± 0.000599	0.0021
K402-2	600.00 W	0.077141 ± 0.001158	0.003158 ± 0.000444	0.0070
K402-3	661.00 W	0.301367 ± 0.003705	0.000607 ± 0.000456	0.0010
K402-4	720.00 W	0.351882 ± 0.003708	0.000006 ± 0.000118	0.0000
K402-5	770.00 W	0.360291 ± 0.003655	0.000078 ± 0.000074	0.0000
K402-6	820.00 W	0.361705 ± 0.003693	0.000121 ± 0.000088	0.0001
K402-7	#######			

Results	40(a)/36(a) ± 1σ	40(r)/39(k) ± 1σ	Age ± 1σ (Ma)	MSWD
Inverse Isochron	540.3732 ± 730.0913 ± 135.11%	2.6607 ± 0.1162 ± 4.37%	89.25 ± 3.83 ± 4.29%	0.74
			Minimal External Error ± 3.83	
			Analytical Error ± 3.80	

Statistics				
	Statistical F ratio	1.05	Convergence	0.0007833839
	Error Magnification	1.0000	Number of Iterations	7
	Number of Data Points	4	Calculated Line	Weighted York-2

Relative Abundances		36Ar	%1σ	37Ar	%1σ	38Ar	%1σ	39Ar	%1σ	40Ar	%1σ	Age ± 1σ (Ma)	40Ar(r) (%)	39Ar(k) (%)	K/Ca ± 1σ
K402-1	400.00 W	0.0000209	24.867	0.0003365	51.824	0.0000818	8.951	0.0002044	3.598	0.0086846	0.437	374.16 ± 212.99	28.42	0.05	0.0980 ± 0.0511
K402-2	600.00 W	0.0000422	13.014	0.0111891	3.770	0.0001083	5.485	0.0009624	1.438	0.0123979	0.384	25.34 ± 58.34	5.71	0.25	0.0138 ± 0.0008
K402-3	661.00 W	0.0000258	24.519	0.0614192	3.054	0.0003309	2.666	0.0042342	1.178	0.0140256	0.298	91.08 ± 14.82	81.14	1.08	0.0110 ± 0.0006
K402-4	720.00 W	0.0001081	7.481	0.3818082	3.018	0.0022274	2.103	0.0264436	1.031	0.0751341	0.144	95.01 ± 3.41	98.79	6.76	0.0111 ± 0.0006
K402-5	770.00 W	0.0010578	4.394	3.5406168	2.997	0.0226077	2.001	0.2755077	1.003	0.7656125	0.042	90.89 ± 2.20	96.63	70.55	0.0125 ± 0.0006
K402-6	820.00 W	0.0002826	5.833	0.9122054	3.000	0.0051907	2.109	0.0765540	1.008	0.2120603	0.074	89.39 ± 2.53	95.37	19.62	0.0134 ± 0.0007
K402-7	#######	0.0000223	20.105	0.0815562	3.093	0.0004806	2.454	0.0065904	1.119	0.0189913	0.325	96.36 ± 1.10	98.98	1.69	0.0129 ± 0.0007
	Σ	0.0015596	3.279	4.9891314	2.210	0.0310274	1.509	0.3904966	0.738	1.1069063	0.035				

Information on Analysis and Constants Used in Calculations

Sample = AMPHIBOLE AR-09-X
Material = Amphibole
Location = ???
Analyst = JL
Project = ROLLAND_HASSIG
Mass Discrimination Law = LIN
Irradiation = MC54
J = 0.01906130 ± 0.00009531
Hb3gr = 1073.600 ± 5.368 Ma
IGSN = Undefined
Preferred Age = Undefined
Classification = Undefined
Experiment Type = Undefined
Extraction Method = Undefined
Heating = 60 sec
Isolation = 2.00 min
Instrument = VG3600
Lithology = Undefined
Lat-Lon = Undefined - Undefined

Age Equations = Conventional
Negative Intensities = Forced Zero
Decay Constant 40K = 5.543 ± 0.010 E-10 1/a
Decay Constant 39Ar = 2.940 ± 0.029 E-07 1/h
Decay Constant 37Ar = 8.220 ± 0.010 E-04 1/h
Decay Constant 36Cl = 2.310 ± 0.016 E-06 1/a
Production Ratio 36/38 in Cl = 316.0 ± 15.8

Results	40(r)/39(k) ± 1σ	Age ± 1σ (Ma)	MSWD	39Ar(k) (%,n)	K/Ca ± 1σ
Age Plateau	2.7187 ± 0.0454 ± 1.67%	91.15 ± 1.55 ± 1.70%	0.59	98.01 4	0.0118 ± 0.0006
		Minimal External Error ± 1.56	1.10	Statistical T Ratio	
		Analytical Error ± 1.49	1.0000	Error Magnification	
Total Fusion Age	2.7132 ± 0.0509 ± 1.88%	90.97 ± 1.72 ± 1.90%		7	0.0125 ± 0.0006
		Minimal External Error ± 1.73			
		Analytical Error ± 1.67			
Normal Isochron (Error Chron)	2.8431 ± 0.0520 ± 1.83%	95.21 ± 1.76 ± 1.85%	2.07	98.01 4	
		Minimal External Error ± 1.77	1.05	Statistical F ratio	
		Analytical Error ± 1.70	1.4379	Error Magnification	
Inverse Isochron	2.6607 ± 0.1162 ± 4.37%	89.25 ± 3.83 ± 4.29%	0.74	98.01 4	
		Minimal External Error ± 3.83	1.05	Statistical F ratio	
		Analytical Error ± 3.80	1.0000	Error Magnification	

Degassing Patterns		36Ar(a)	%1σ	36Ar(c)	%1σ	36Ar(ca)	%1σ	36Ar(cl)	%1σ	37Ar(ca)	%1σ	38Ar(a)	%1σ	38Ar(c)	%1σ	38Ar(k)	%1σ
K402-1	400.00 W	0.000021	25.01	0.000000	0.00	0.000000	51.83	0.000000	11.62	0.000337	51.82	0.000004	25.01	0.000000	0.00	0.000002	4.12
K402-2	600.00 W	0.000039	14.07	0.000000	0.00	0.000003	3.90	0.000000	271.73	0.011189	3.77	0.000007	14.07	0.000000	0.00	0.000011	2.47
K402-3	661.00 W	0.000008	75.11	0.000000	0.00	0.000017	3.21	0.000000	0.00	0.061419	3.05	0.000002	75.11	0.000000	0.00	0.000050	2.33
K402-4	720.00 W	0.000000	2010.38	0.000000	0.00	0.000108	3.18	0.000000	0.00	0.381808	3.02	0.000000	2010.38	0.000000	0.00	0.000314	2.26
K402-5	770.00 W	0.000059	94.71	0.000000	0.00	0.000998	3.16	0.000000	0.00	3.540617	3.00	0.000011	94.71	0.000000	0.00	0.003275	2.24
K402-6	820.00 W	0.000025	72.53	0.000000	0.00	0.000257	3.16	0.000000	0.00	0.912205	3.00	0.000005	72.53	0.000000	0.00	0.000911	2.24
K402-7	1111.00 W	0.000000	0.00	0.000000	0.00	0.000022	20.11	0.000000	0.00	0.081556	3.09	0.000000	0.00	0.000000	0.00	0.000078	2.30
	Σ	0.000153	39.49	0.000000	0.00	0.001406	2.35	0.000000	64.08	4.989131	2.21	0.000029	39.49	0.000000	0.00	0.004642	1.65
	Σ							0.001560	4.42	4.989131	2.21						

38Ar(ca)	%1σ	38Ar(cl)	%1σ	39Ar(k)	%1σ	39Ar(ca)	%1σ	40Ar(r)	%1σ	40Ar(a)	%1σ	40Ar(c)	%1σ	40Ar(k)	%1σ
0.000002	103.85	0.000073	12.67	0.000204	3.60	0.000000	51.98	0.002469	62.93	0.006210	25.01	0.000000	0.00	0.000006	4.12
0.000067	90.08	0.000022	271.78	0.000954	1.45	0.000008	5.50	0.000708	231.83	0.011661	14.07	0.000000	0.00	0.000028	2.47
0.000369	90.05	0.000000	0.00	0.004189	1.19	0.000045	5.03	0.011381	16.64	0.002521	75.11	0.000000	0.00	0.000124	2.33
0.002291	90.05	0.000000	0.00	0.026165	1.04	0.000279	5.01	0.074227	3.54	0.000130	2010.38	0.000000	0.00	0.000777	2.26
0.021244	90.05	0.000000	0.00	0.272923	1.01	0.002585	5.00	0.739798	2.27	0.017709	94.71	0.000000	0.00	0.008106	2.24
0.005473	90.05	0.000000	0.00	0.075888	1.02	0.000666	5.00	0.202241	2.71	0.007566	72.53	0.000000	0.00	0.002254	2.24
0.000489	90.05	0.000000	0.00	0.006531	1.13	0.000060	5.06	0.018797	0.33	0.000000	0.00	0.000000	0.00	0.000194	2.30
0.029935	66.38	0.000096	64.20	0.386855	0.75	0.003642	3.68	1.049620	1.72	0.045797	39.49	0.000000	0.00	0.011490	1.65
		0.034702	57.26			0.390497	0.74							1.106906	2.31

Additional Parameters		40(r)/39(k)	1σ	40(r+a)	1σ	40Ar/39Ar	1σ	37Ar/39Ar	1σ	36Ar/39Ar	1σ	Time (days)	37Ar (decay)	39Ar (decay)	40Ar (moles)
K402-1	400.00 W	12.090860	7.62106	0.008679	0.00004	42.485286	1.54004	1.646397	0.85528	0.102325	0.02571	150.496	20.15141206	1.00107482	1.737E-16
K402-2	600.00 W	0.742092	1.72045	0.012370	0.00005	12.882676	0.19170	11.626611	0.46909	0.043872	0.00574	150.518	20.16024838	1.00107497	2.480E-16
K402-3	661.00 W	2.716556	0.45318	0.013901	0.00004	3.312457	0.04025	14.505529	0.47479	0.006084	0.00149	150.537	20.16770703	1.00107511	2.805E-16
K402-4	720.00 W	2.836876	0.10457	0.074357	0.00011	2.841294	0.02958	14.438582	0.46052	0.004088	0.00031	150.570	20.18097368	1.00107534	1.503E-15
K402-5	770.00 W	2.710646	0.06733	0.757507	0.00037	2.778915	0.02789	12.851244	0.40618	0.003839	0.00017	150.585	20.18705714	1.00107545	1.531E-14
K402-6	820.00 W	2.664986	0.07726	0.209806	0.00017	2.770075	0.02800	11.915842	0.37717	0.003691	0.00022	150.601	20.19314244	1.00107556	4.241E-15
K402-7	1111.00 W	2.878253	0.03388	0.018797	0.00006	2.881683	0.03358	12.375077	0.40699	0.003379	0.00068	150.616	20.19922957	1.00107566	3.798E-16

Procedure Blanks		36Ar	1σ	37Ar	1σ	38Ar	1σ	39Ar	1σ	40Ar	1σ
K402-1	400.00 W	0.000024	0.000004	0.000047	0.000008	0.000009	0.000004	0.000012	0.000003	0.001023	0.000021
K402-2	600.00 W	0.000024	0.000004	0.000047	0.000008	0.000009	0.000004	0.000012	0.000003	0.001023	0.000021
K402-3	661.00 W	0.000024	0.000004	0.000047	0.000008	0.000009	0.000004	0.000012	0.000003	0.001023	0.000021
K402-4	720.00 W	0.000035	0.000003	0.000057	0.000004	0.000010	0.000003	0.000029	0.000004	0.001052	0.000022
K402-5	770.00 W	0.000035	0.000003	0.000057	0.000004	0.000010	0.000003	0.000029	0.000004	0.001052	0.000022
K402-6	820.00 W	0.000035	0.000003	0.000057	0.000004	0.000010	0.000003	0.000029	0.000004	0.001052	0.000022
K402-7	1111.00 W	0.000035	0.000003	0.000057	0.000004	0.000010	0.000003	0.000029	0.000004	0.001052	0.000022

Intercept Values		36Ar	1σ	r2		37Ar	1σ	r2		38Ar	1σ	r2		39Ar	1σ	r2		40Ar	1σ	r2	
K402-1	400.00 W	0.000045	0.000003	0.2533	EXP #	0.000064	0.000004	0.3974	EXP #	0.000092	0.000006	0.3474	EXP #	0.000216	0.000006	0.3590	LIN #	0.009707	0.000031	0.0499	LIN #
K402-2	600.00 W	0.000067	0.000003	0.4621	EXP #	0.000608	0.000010	0.8997	EXP #	0.000118	0.000004	0.6374	EXP #	0.000976	0.000009	0.9347	EXP #	0.013421	0.000043	0.5452	EXP #
K402-3	661.00 W	0.000050	0.000005	0.0039	LIN # 12	0.003123	0.000017	0.9960	EXP # 12	0.000342	0.000005	0.9734	LIN # 12	0.004255	0.000026	0.9940	EXP # 12	0.015048	0.000036	0.9957	EXP # 12
K402-4	720.00 W	0.000144	0.000006	0.1950	EXP #	0.019161	0.000070	0.9966	EXP #	0.002251	0.000015	0.9888	EXP #	0.026531	0.000068	0.9981	EXP #	0.076186	0.000106	0.9992	EXP #
K402-5	770.00 W	0.001106	0.000020	0.9407	EXP #	0.177158	0.000165	0.9998	EXP #	0.022764	0.000040	0.9994	EXP #	0.276136	0.000264	0.9998	EXP #	0.766664	0.000320	1.0000	EXP #
K402-6	820.00 W	0.000321	0.000012	0.6091	EXP #	0.045672	0.000075	0.9988	EXP #	0.005234	0.000036	0.9785	EXP #	0.076750	0.000109	0.9991	EXP #	0.213112	0.000155	0.9997	EXP #
K402-7	1111.00 W	0.000057	0.000003	0.0204	EXP #	0.004134	0.000031	0.9623	EXP #	0.000493	0.000006	0.8447	EXP #	0.006634	0.000033	0.9778	EXP #	0.020043	0.000057	0.3438	EXP #

Sample Parameters		Sample	Material	Location	Analyst	Temp	Standard (in Ma)	%1σ	J	%1σ	MDF	%1σ
K402-1	400.00 W	Amphibole AR-09-X	Amphibole	???	JL	400	1073.6	0.5	0.0190613	0.5	1.003256	1
K402-2	600.00 W	Amphibole AR-09-X	Amphibole	???	JL	600	1073.6	0.5	0.0190613	0.5	1.003256	1
K402-3	661.00 W	Amphibole AR-09-X	Amphibole	???	JL	661	1073.6	0.5	0.0190613	0.5	1.003256	1
K402-4	720.00 W	Amphibole AR-09-X	Amphibole	???	JL	720	1073.6	0.5	0.0190613	0.5	1.003256	1
K402-5	770.00 W	Amphibole AR-09-X	Amphibole	???	JL	770	1073.6	0.5	0.0190613	0.5	1.003256	1
K402-6	820.00 W	Amphibole AR-09-X	Amphibole	???	JL	820	1073.6	0.5	0.0190613	0.5	1.003256	1
K402-7	1111.00 W	Amphibole AR-09-X	Amphibole	???	JL	1111	1073.6	0.5	0.0190613	0.5	1.003256	1

Volume Ratio	Sensitivity (mol/volt)	Day	Month	Year	Hour	Min	Resist	Irradiation	Project	Experiment	Nmb	Standard Name
1	2.000E-14	09	MAR	2010	09	03	001	MC54	Rolland_Hassig	K402-1	01	Hb3gr
1	2.000E-14	09	MAR	2010	09	35	001	MC54	Rolland_Hassig	K402-1	01	Hb3gr
1	2.000E-14	09	MAR	2010	10	02	001	MC54	Rolland_Hassig	K402-1	01	Hb3gr
1	2.000E-14	09	MAR	2010	10	50	001	MC54	Rolland_Hassig	K402-1	01	Hb3gr
1	2.000E-14	09	MAR	2010	11	12	001	MC54	Rolland_Hassig	K402-1	01	Hb3gr
1	2.000E-14	09	MAR	2010	11	34	001	MC54	Rolland_Hassig	K402-1	01	Hb3gr
1	2.000E-14	09	MAR	2010	11	56	001	MC54	Rolland_Hassig	K402-1	01	Hb3gr

Irradiation Constants		40/36(a)	%1σ	40/36(c)	%1σ	38/36(a)	%1σ	38/36(c)	%1σ	39/37(ca)	%1σ	38/37(ca)	%1σ	36/37(ca)	%1σ
K402-1	400.00 W	298.56	0.1	0.018	35	0.1885	0.16	1.7	3	0.00073	4	0.006	90	0.000282	1
K402-2	600.00 W	298.56	0.1	0.018	35	0.1885	0.16	1.7	3	0.00073	4	0.006	90	0.000282	1
K402-3	661.00 W	298.56	0.1	0.018	35	0.1885	0.16	1.7	3	0.00073	4	0.006	90	0.000282	1
K402-4	720.00 W	298.56	0.1	0.018	35	0.1885	0.16	1.7	3	0.00073	4	0.006	90	0.000282	1
K402-5	770.00 W	298.56	0.1	0.018	35	0.1885	0.16	1.7	3	0.00073	4	0.006	90	0.000282	1
K402-6	820.00 W	298.56	0.1	0.018	35	0.1885	0.16	1.7	3	0.00073	4	0.006	90	0.000282	1
K402-7	1111.00 W	298.56	0.1	0.018	35	0.1885	0.16	1.7	3	0.00073	4	0.006	90	0.000282	1

40/39(k)	%1σ	38/39(k)	%1σ	36/38(cl)	%1σ	K/Ca	%1σ	K/Cl	%1σ	Ca/Cl	%1σ
0.0297	2	0.012	2	316	5	0.1616	4	5.4	33	33	33
0.0297	2	0.012	2	316	5	0.1616	4	5.4	33	33	33
0.0297	2	0.012	2	316	5	0.1616	4	5.4	33	33	33
0.0297	2	0.012	2	316	5	0.1616	4	5.4	33	33	33
0.0297	2	0.012	2	316	5	0.1616	4	5.4	33	33	33
0.0297	2	0.012	2	316	5	0.1616	4	5.4	33	33	33
0.0297	2	0.012	2	316	5	0.1616	4	5.4	33	33	33

Annexe 5 - Résultats de datation (1) sur Amphibole AR-08-09c.

Incremental Heating		36Ar(a)	37Ar(ca)	38Ar(cl)	39Ar(k)	40Ar(r)	Age ± 1σ (Ma)	40Ar(r) (%)	39Ar(k) (%)	K/Ca ± 1σ
K427-1	450.00 W	0.001092	0.052262	0.000156	0.011236	0.002836	8.65 ± 40.97	0.86	3.49	0.0347 ± 0.0018
K427-2	500.00 W	0.000629	0.022170	0.000000	0.005863	0.004475	26.04 ± 46.22	2.32	1.82	0.0427 ± 0.0023
K427-3	552.00 W	0.000309	0.028006	0.000000	0.006086	0.009260	51.53 ± 22.67	9.10	1.89	0.0351 ± 0.0019
K427-4	600.00 W	0.000140	0.049605	0.000000	0.007619	0.020676	90.92 ± 12.03	33.02	2.37	0.0248 ± 0.0013
K427-5	651.00 W	0.000183	0.227194	0.000000	0.025468	0.068993	90.76 ± 5.48	55.40	7.92	0.0181 ± 0.0009
K427-6	694.00 W	0.000282	0.752815	0.000000	0.079264	0.213659	90.32 ± 3.00	71.19	24.63	0.0170 ± 0.0009
K427-7	726.00 W	0.000022	0.079078	0.000000	0.009050	0.023930	88.64 ± 8.70	77.70	2.81	0.0185 ± 0.0010
K427-8	#######	0.000119	1.570672	0.000335	0.177173	0.477149	90.24 ± 1.80	92.13	55.06	0.0182 ± 0.0009
	Σ	0.002777	2.781802	0.000491	0.321760	0.820979				

Information on Analysis
Sample = AMPHIBOLE
Material = Amphibole AR0809c (11
Location = ???
Analyst = YR
Project = ROLLAND_HASSIG
Mass Discrimination Law = LIN
Irradiation = MC54
J = 0.01904610 ± 0.00009523
Hb3gr = 1073.600 ± 5.368 Ma

Results	40(r)/39(k) ± 1σ	Age ± 1σ (Ma)	MSWD	39Ar(k) (%,n)	K/Ca ± 1σ
Age Plateau	2.6937 ± 0.0445 ± 1.65%	90.26 ± 1.52 ± 1.68%	0.01	92.79 5	0.0187 ± 0.0011
	Minimal External Error	± 1.53	1.06	Statistical T Ratio	
	Analytical Error	± 1.45	1.0000	Error Magnification	
Total Fusion Age	2.5515 ± 0.0652 ± 2.55%	85.61 ± 2.18 ± 2.54%		8	0.0187 ± 0.0008
	Minimal External Error	± 2.18			
	Analytical Error	± 2.14			

Normal Isochron		39(k)/36(a) ± 1σ	40(a+r)/36(a) ± 1σ	r.i.
K427-1	450.00 W	10.3 ± 0.4	301.2 ± 12.4	0.9692
K427-2	500.00 W	9.3 ± 0.4	305.7 ± 13.0	0.9692
K427-3	552.00 W	19.7 ± 0.9	328.5 ± 14.7	0.9744
K427-4	600.00 W	54.5 ± 3.7	446.6 ± 29.9	0.9876
K427-5	651.00 W	138.8 ± 10.7	674.6 ± 51.6	0.9894
K427-6	694.00 W	281.3 ± 23.4	1056.8 ± 87.3	0.9926
K427-7	726.00 W	409.5 ± 148.4	1381.3 ± 500.6	0.9995
K427-8	#######	1489.7 ± 352.1	4310.5 ± 1018.0	0.9990

Results	40(a)/36(a) ± 1σ	40(r)/39(k) ± 1σ	Age ± 1σ (Ma)	MSWD
Normal Isochron	299.5443 ± 16.2880 ± 5.44%	2.6931 ± 0.0562 ± 2.09%	90.24 ± 1.89 ± 2.09%	0.02
		Minimal External Error	± 1.90	
		Analytical Error	± 1.84	

Statistics				
	Statistical F ratio	1.09	Convergence	0.0000240470
	Error Magnification	1.0000	Number of Iterations	1
	Number of Data Points	5	Calculated Line	Weighted York-2

Inverse Isochron		39(k)/40(a+r) ± 1σ	36(a)/40(a+r) ± 1σ	r.i.
K427-1	450.00 W	0.034157 ± 0.000358	0.003321 ± 0.000137	0.0005
K427-2	500.00 W	0.030468 ± 0.000329	0.003272 ± 0.000139	0.0005
K427-3	552.00 W	0.059892 ± 0.000618	0.003044 ± 0.000136	0.0017
K427-4	600.00 W	0.122119 ± 0.001298	0.002239 ± 0.000150	0.0026
K427-5	651.00 W	0.205760 ± 0.002313	0.001482 ± 0.000113	0.0103
K427-6	694.00 W	0.266179 ± 0.002697	0.000946 ± 0.000078	0.0007
K427-7	726.00 W	0.296439 ± 0.003282	0.000724 ± 0.000262	0.0025
K427-8	#######	0.345598 ± 0.003611	0.000232 ± 0.000055	0.0009

Results	40(a)/36(a) ± 1σ	40(r)/39(k) ± 1σ	Age ± 1σ (Ma)	MSWD
Inverse Isochron	300.0551 ± 16.3024 ± 5.43%	2.6906 ± 0.0564 ± 2.10%	90.16 ± 1.90 ± 2.10%	0.01
			Minimal External Error ± 1.90	
			Analytical Error ± 1.84	

Statistics				
	Statistical F ratio	1.09	Convergence	0.0000015084
	Error Magnification	1.0000	Number of Iterations	3
	Number of Data Points	5	Calculated Line	Weighted York-2

Relative Abundances		36Ar	%1σ	37Ar	%1σ	38Ar	%1σ	39Ar	%1σ	40Ar	%1σ	Age ± 1σ (Ma)	40Ar(r) (%)	39Ar(k) (%)	K/Ca ± 1σ
K427-1	450.00 W	0.0011071	4.071	0.0522623	3.209	0.0008105	2.233	0.0112746	1.044	0.3292947	0.048	8.65 ± 40.97	0.86	3.49	0.0347 ± 0.0018
K427-2	500.00 W	0.0006357	4.214	0.0221699	3.317	0.0002790	3.212	0.0058788	1.077	0.1925896	0.047	26.04 ± 46.22	2.32	1.82	0.0427 ± 0.0023
K427-3	552.00 W	0.0003173	4.359	0.0280058	3.280	0.0002189	3.001	0.0061068	1.024	0.1018043	0.089	51.53 ± 22.67	9.10	1.89	0.0351 ± 0.0019
K427-4	600.00 W	0.0001537	6.082	0.0496051	3.183	0.0003277	3.872	0.0076548	1.049	0.0626135	0.135	90.92 ± 12.03	33.02	2.37	0.0248 ± 0.0013
K427-5	651.00 W	0.0002476	5.604	0.2271936	3.137	0.0015231	2.227	0.0256338	1.077	0.1245316	0.295	90.76 ± 5.48	55.40	7.92	0.0181 ± 0.0009
K427-6	694.00 W	0.0004941	4.508	0.7528147	3.043	0.0051914	2.077	0.0798138	1.003	0.3001397	0.073	90.32 ± 3.00	71.19	24.63	0.0170 ± 0.0009
K427-7	726.00 W	0.0000444	17.957	0.0790780	3.225	0.0005673	2.663	0.0091076	1.054	0.0307975	0.312	88.64 ± 8.70	77.70	2.81	0.0185 ± 0.0010
K427-8	#######	0.0005620	4.236	1.5706725	3.125	0.0119076	2.020	0.1783200	1.026	0.5179196	0.150	90.24 ± 1.80	92.13	55.06	0.0182 ± 0.0009
	Σ	0.0035618	1.851	2.7818020	1.968	0.0208255	1.284	0.3237904	0.626	1.6596905	0.055				

Information on Analysis and Constants Used in Calculations

Sample = AMPHIBOLE
Material = Amphibole AR0809c (110 MC
Location = ???
Analyst = YR
Project = ROLLAND_HASSIG
Mass Discrimination Law = LIN
Irradiation = MC54
J = 0.01904610 ± 0.00009523
Hb3gr = 1073.600 ± 5.368 Ma
IGSN = Undefined
Preferred Age = Undefined
Classification = Undefined
Experiment Type = Undefined
Extraction Method = Undefined
Heating = 60 sec
Isolation = 2.00 min
Instrument = VG3600
Lithology = Undefined
Lat-Lon = Undefined - Undefined

Age Equations = Conventional
Negative Intensities = Forced Zero
Decay Constant 40K = 5.543 ± 0.010 E-10 1/a
Decay Constant 39Ar = 2.940 ± 0.029 E-07 1/h
Decay Constant 37Ar = 8.220 ± 0.010 E-04 1/h
Decay Constant 36Cl = 2.310 ± 0.016 E-06 1/a
Production Ratio 36/38 in Cl = 316.0 ± 15.8

Results	40(r)/39(k) ± 1σ	Age ± 1σ (Ma)	MSWD	39Ar(k) (%,n)	K/Ca ± 1σ
Age Plateau	2.6937 ± 0.0445 ± 1.65%	90.26 ± 1.52 ± 1.68%	0.01	92.79 5	0.0187 ± 0.0011
	Minimal External Error ± 1.53		1.06	Statistical T Ratio	
	Analytical Error ± 1.45		1.0000	Error Magnification	
Total Fusion Age	2.5515 ± 0.0652 ± 2.55%	85.61 ± 2.18 ± 2.54%		8	0.0187 ± 0.0008
	Minimal External Error ± 2.18				
	Analytical Error ± 2.14				
Normal Isochron	2.6931 ± 0.0562 ± 2.09%	90.24 ± 1.89 ± 2.09%	0.02	92.79 5	
	Minimal External Error ± 1.90		1.09	Statistical F ratio	
	Analytical Error ± 1.84		1.0000	Error Magnification	
Inverse Isochron	2.6906 ± 0.0564 ± 2.10%	90.16 ± 1.90 ± 2.10%	0.01	92.79 5	
	Minimal External Error ± 1.90		1.09	Statistical F ratio	
	Analytical Error ± 1.84		1.0000	Error Magnification	

Degassing Patterns		36Ar(a)	%1σ	36Ar(c)	%1σ	36Ar(ca)	%1σ	36Ar(cl)	%1σ	37Ar(ca)	%1σ	38Ar(a)	%1σ	38Ar(c)	%1σ	38Ar(k)	%1σ
K427-1	450.00 W	0.001092	4.13	0.000000	0.00	0.000015	3.36	0.000000	181.32	0.052262	3.21	0.000206	4.13	0.000000	0.00	0.000135	2.26
K427-2	500.00 W	0.000629	4.26	0.000000	0.00	0.000006	3.46	0.000000	0.00	0.022170	3.32	0.000119	4.26	0.000000	0.00	0.000070	2.27
K427-3	552.00 W	0.000309	4.47	0.000000	0.00	0.000008	3.43	0.000000	0.00	0.028006	3.28	0.000058	4.47	0.000000	0.00	0.000073	2.25
K427-4	600.00 W	0.000140	6.70	0.000000	0.00	0.000014	3.34	0.000000	0.00	0.049605	3.18	0.000026	6.70	0.000000	0.00	0.000091	2.26
K427-5	651.00 W	0.000183	7.65	0.000000	0.00	0.000064	3.29	0.000000	0.00	0.227194	3.14	0.000035	7.65	0.000000	0.00	0.000306	2.27
K427-6	694.00 W	0.000282	8.26	0.000000	0.00	0.000212	3.20	0.000000	0.00	0.752815	3.04	0.000053	8.27	0.000000	0.00	0.000951	2.24
K427-7	726.00 W	0.000022	36.24	0.000000	0.00	0.000022	3.38	0.000000	0.00	0.079078	3.22	0.000004	36.24	0.000000	0.00	0.000109	2.26
K427-8	1111.00 W	0.000119	23.62	0.000000	0.00	0.000443	3.28	0.000000	2534.44	1.570672	3.13	0.000022	23.62	0.000000	0.00	0.002126	2.25
	Σ	0.002777	2.45	0.000000	0.00	0.000784	2.07	0.000000	1729.97	2.781802	1.97	0.000523	2.45	0.000000	0.00	0.003861	1.37
	Σ							0.003562	1.96	2.781802	1.97						

38Ar(ca)	%1σ	38Ar(cl)	%1σ	39Ar(k)	%1σ	39Ar(ca)	%1σ	40Ar(r)	%1σ	40Ar(a)	%1σ	40Ar(c)	%1σ	40Ar(k)	%1σ
0.000314	90.06	0.000156	181.39	0.011236	1.05	0.000038	5.13	0.002836	474.73	0.326125	4.13	0.000000	0.00	0.000334	2.26
0.000133	90.06	0.000000	0.00	0.005863	1.08	0.000016	5.20	0.004475	178.78	0.187940	4.26	0.000000	0.00	0.000174	2.27
0.000168	90.06	0.000000	0.00	0.006086	1.03	0.000020	5.17	0.009260	44.62	0.092363	4.47	0.000000	0.00	0.000181	2.25
0.000298	90.06	0.000000	0.00	0.007619	1.05	0.000036	5.11	0.020676	13.52	0.041711	6.70	0.000000	0.00	0.000226	2.26
0.001363	90.05	0.000000	0.00	0.025468	1.08	0.000166	5.08	0.068993	6.10	0.054782	7.65	0.000000	0.00	0.000756	2.27
0.004517	90.05	0.000000	0.00	0.079264	1.01	0.000550	5.03	0.213659	3.26	0.084126	8.27	0.000000	0.00	0.002354	2.24
0.000474	90.06	0.000000	0.00	0.009050	1.06	0.000058	5.14	0.023930	10.00	0.006598	36.24	0.000000	0.00	0.000269	2.26
0.009424	90.05	0.000335	2534.44	0.177173	1.03	0.001147	5.08	0.477149	1.77	0.035509	23.62	0.000000	0.00	0.005262	2.25
0.016691	56.98	0.000491	1729.42	0.321760	0.63	0.002031	3.21	0.820979	2.48	0.829155	2.45	0.000000	0.00	0.009556	1.37
		0.021567	59.13			0.323790	0.63							1.659690	1.73

Additional Parameters		40(r)/39(k)	1σ	40(r+a)	1σ	40Ar/39Ar	1σ	37Ar/39Ar	1σ	36Ar/39Ar	1σ	Time (days)	37Ar (decay)	39Ar (decay)	40Ar (moles)
K427-1	450.00 W	0.252397	1.19820	0.328961	0.00016	29.206767	0.30514	4.635397	0.15643	0.098196	0.00413	193.458	47.03184208	1.00137833	6.586E-15
K427-2	500.00 W	0.763320	1.36470	0.192415	0.00009	32.760074	0.35314	3.771166	0.13152	0.108142	0.00470	193.472	47.04473057	1.00137842	3.852E-15
K427-3	552.00 W	1.521446	0.67899	0.101624	0.00009	16.670522	0.17129	4.585970	0.15757	0.051952	0.00233	193.491	47.06278039	1.00137856	2.036E-15
K427-4	600.00 W	2.713921	0.36810	0.062387	0.00008	8.179588	0.08652	6.480220	0.21719	0.020078	0.00124	193.518	47.08793276	1.00137875	1.252E-15
K427-5	651.00 W	2.709019	0.16775	0.123775	0.00037	4.858094	0.05424	8.863039	0.29394	0.009657	0.00055	193.533	47.10148190	1.00137886	2.491E-15
K427-6	694.00 W	2.695534	0.09190	0.297786	0.00023	3.760499	0.03781	9.432140	0.30220	0.006190	0.00029	193.547	47.11503495	1.00137896	6.003E-15
K427-7	726.00 W	2.644250	0.26591	0.030529	0.00010	3.381500	0.03717	8.682612	0.29457	0.004875	0.00088	193.638	47.19902159	1.00137960	6.159E-16
K427-8	1111.00 W	2.693117	0.05509	0.512658	0.00078	2.904439	0.03012	8.808166	0.28974	0.003152	0.00014	193.652	47.21260271	1.00137970	1.036E-14

Procedure Blanks		36Ar	1σ	37Ar	1σ	38Ar	1σ	39Ar	1σ	40Ar	1σ
K427-1	450.00 W	0.000031	0.000004	0.000028	0.000003	0.000002	0.000003	0.000023	0.000002	0.001530	0.000019
K427-2	500.00 W	0.000031	0.000004	0.000028	0.000003	0.000002	0.000003	0.000023	0.000002	0.001530	0.000019
K427-3	552.00 W	0.000031	0.000004	0.000028	0.000003	0.000002	0.000003	0.000023	0.000002	0.001530	0.000019
K427-4	600.00 W	0.000031	0.000005	0.000048	0.000006	0.000007	0.000003	0.000021	0.000004	0.001753	0.000021
K427-5	651.00 W	0.000031	0.000005	0.000048	0.000006	0.000007	0.000003	0.000021	0.000004	0.001753	0.000021
K427-6	694.00 W	0.000031	0.000005	0.000048	0.000006	0.000007	0.000003	0.000021	0.000004	0.001753	0.000021
K427-7	726.00 W	0.000026	0.000004	0.000034	0.000011	0.000005	0.000005	0.000017	0.000009	0.001526	0.000079
K427-8	1111.00 W	0.000026	0.000004	0.000034	0.000011	0.000005	0.000005	0.000017	0.000009	0.001526	0.000079

Intercept Values		36Ar	1σ	r2		37Ar	1σ	r2		38Ar	1σ	r2		39Ar	1σ	r2		40Ar	1σ	r2	
K427-1	450.00 W	0.001148	0.000009	0.9678	EXP #	0.001147	0.000012	0.9526	EXP #	0.000817	0.000008	0.9472	EXP #	0.011309	0.000034	0.9944	EXP #	0.330825	0.000158	0.9999	EXP #
K427-2	500.00 W	0.000672	0.000008	0.9453	EXP #	0.000503	0.000006	0.9532	EXP #	0.000283	0.000007	0.7390	EXP #	0.005908	0.000024	0.9918	EXP #	0.194120	0.000089	0.9999	EXP #
K427-3	552.00 W	0.000351	0.000004	0.9467	EXP #	0.000627	0.000007	0.9431	EXP #	0.000222	0.000004	0.8393	EXP #	0.006136	0.000014	0.9976	EXP #	0.103335	0.000089	0.9996	EXP #
K427-4	600.00 W	0.000186	0.000005	0.5122	EXP #	0.001109	0.000009	0.9752	EXP #	0.000337	0.000010	0.6637	EXP #	0.007684	0.000024	0.9951	EXP #	0.064366	0.000082	0.9987	EXP #
K427-5	651.00 W	0.000281	0.000008	0.6253	EXP #	0.004906	0.000042	0.9670	EXP #	0.001538	0.000015	0.9553	EXP #	0.025681	0.000104	0.9918	EXP #	0.126284	0.000367	0.9942	EXP #
K427-6	694.00 W	0.000530	0.000009	0.9555	EXP #	0.016140	0.000068	0.9969	EXP #	0.005224	0.000030	0.9939	EXP #	0.079916	0.000079	0.9998	EXP #	0.301893	0.000218	0.9999	EXP #
K427-7	726.00 W	0.000071	0.000007	0.1831	EXP #	0.001722	0.000016	0.9890	EXP #	0.000575	0.000009	0.9684	EXP #	0.009134	0.000030	0.9986	EXP #	0.032323	0.000054	0.9994	EXP #
K427-8	1111.00 W	0.000593	0.000007	0.9738	LIN # 1 11	0.033541	0.000277	0.9921	EXP # 2	0.011970	0.000038	0.9986	EXP # 2	0.178516	0.000427	0.9992	EXP # 2	0.519446	0.000771	0.9997	EXP # 2

Sample Parameters		Sample	Material	Location	Analyst	Temp	Standard (in Ma)	%1σ	J	%1σ	MDF	%1σ
K427-1	450.00 W	Amphibole	Amphibole AR0809c (110 MC	???	YR	450	1073.6	0.5	0.0190461	0.5	1.002391	1
K427-2	500.00 W	Amphibole	Amphibole AR0809c (110 MC	???	YR	500	1073.6	0.5	0.0190461	0.5	1.002391	1
K427-3	552.00 W	Amphibole	Amphibole AR0809c (110 MC	???	YR	552	1073.6	0.5	0.0190461	0.5	1.002391	1
K427-4	600.00 W	Amphibole	Amphibole AR0809c (110 MC	???	YR	600	1073.6	0.5	0.0190461	0.5	1.002391	1
K427-5	651.00 W	Amphibole	Amphibole AR0809c (110 MC	???	YR	651	1073.6	0.5	0.0190461	0.5	1.002391	1
K427-6	694.00 W	Amphibole	Amphibole AR0809c (110 MC	???	YR	694	1073.6	0.5	0.0190461	0.5	1.002391	1
K427-7	726.00 W	Amphibole	Amphibole AR0809c (110 MC	???	YR	726	1073.6	0.5	0.0190461	0.5	1.002391	1
K427-8	1111.00 W	Amphibole	Amphibole AR0809c (110 MC	???	YR	1111	1073.6	0.5	0.0190461	0.5	1.002391	1

Volume Ratio	Sensitivity (mol/volt)	Day	Month	Year	Hour	Min	Resist	Irradiation	Project	Experiment	Nmb	Standard Name
1	2.000E-14	21	APR	2010	08	08	001	MC54	Rolland_Hassig	K427-1	01	Hb3gr
1	2.000E-14	21	APR	2010	08	28	001	MC54	Rolland_Hassig	K427-1	01	Hb3gr
1	2.000E-14	21	APR	2010	08	56	001	MC54	Rolland_Hassig	K427-1	01	Hb3gr
1	2.000E-14	21	APR	2010	09	35	001	MC54	Rolland_Hassig	K427-1	01	Hb3gr
1	2.000E-14	21	APR	2010	09	56	001	MC54	Rolland_Hassig	K427-1	01	Hb3gr
1	2.000E-14	21	APR	2010	10	17	001	MC54	Rolland_Hassig	K427-1	01	Hb3gr
1	2.000E-14	21	APR	2010	12	27	001	MC54	Rolland_Hassig	K427-1	01	Hb3gr
1	2.000E-14	21	APR	2010	12	48	001	MC54	Rolland_Hassig	K427-1	01	Hb3gr

Irradiation Constants		40/36(a)	%1σ	40/36(c)	%1σ	38/36(a)	%1σ	38/36(c)	%1σ	39/37(ca)	%1σ	38/37(ca)	%1σ	36/37(ca)	%1σ
K427-1	450.00 W	298.56	0.1	0.018	35	0.1885	0.16	1.7	3	0.00073	4	0.006	90	0.000282	1
K427-2	500.00 W	298.56	0.1	0.018	35	0.1885	0.16	1.7	3	0.00073	4	0.006	90	0.000282	1
K427-3	552.00 W	298.56	0.1	0.018	35	0.1885	0.16	1.7	3	0.00073	4	0.006	90	0.000282	1
K427-4	600.00 W	298.56	0.1	0.018	35	0.1885	0.16	1.7	3	0.00073	4	0.006	90	0.000282	1
K427-5	651.00 W	298.56	0.1	0.018	35	0.1885	0.16	1.7	3	0.00073	4	0.006	90	0.000282	1
K427-6	694.00 W	298.56	0.1	0.018	35	0.1885	0.16	1.7	3	0.00073	4	0.006	90	0.000282	1
K427-7	726.00 W	298.56	0.1	0.018	35	0.1885	0.16	1.7	3	0.00073	4	0.006	90	0.000282	1
K427-8	1111.00 W	298.56	0.1	0.018	35	0.1885	0.16	1.7	3	0.00073	4	0.006	90	0.000282	1

40/39(k)	%1σ	38/39(k)	%1σ	36/38(cl)	%1σ	K/Ca	%1σ	K/Cl	%1σ	Ca/Cl	%1σ
0.0297	2	0.012	2	316	5	0.1616	4	5.4	33	33	33
0.0297	2	0.012	2	316	5	0.1616	4	5.4	33	33	33
0.0297	2	0.012	2	316	5	0.1616	4	5.4	33	33	33
0.0297	2	0.012	2	316	5	0.1616	4	5.4	33	33	33
0.0297	2	0.012	2	316	5	0.1616	4	5.4	33	33	33
0.0297	2	0.012	2	316	5	0.1616	4	5.4	33	33	33
0.0297	2	0.012	2	316	5	0.1616	4	5.4	33	33	33
0.0297	2	0.012	2	316	5	0.1616	4	5.4	33	33	33

Annexe 6 - Résultats de datation (1) sur Mica AR-08-09c.

Incremental Heating		36Ar(a)	37Ar(ca)	38Ar(cl)	39Ar(k)	40Ar(r)	Age ± 1σ (Ma)	40Ar(r) (%)	39Ar(k) (%)	K/Ca ± 1σ
K428-1	400.00 W	0.000126	0.001717	0.000082	0.028695	0.084520	98.38 ± 3.74	68.74	3.01	2.70 ± 0.95
K428-2	460.00 W	0.000076	0.002876	0.000079	0.176270	0.477008	90.58 ± 1.00	94.45	18.48	9.90 ± 1.42
K428-3	493.00 W	0.000006	0.001770	0.000042	0.127781	0.342409	89.72 ± 1.20	98.41	13.40	11.67 ± 2.92
K428-4	523.00 W	0.000000	0.006737	0.000000	0.259309	0.689711	89.07 ± 0.87	98.90	27.19	6.22 ± 0.50
K428-5	544.00 W	0.000000	0.001887	0.000000	0.043423	0.116079	89.51 ± 0.91	98.90	4.55	3.72 ± 0.72
K428-6	616.00 W	0.000000	0.003828	0.000000	0.116762	0.309436	88.75 ± 0.88	98.89	12.24	4.93 ± 0.70
K428-7	695.00 W	0.000000	0.004404	0.000000	0.101934	0.272680	89.57 ± 0.89	98.90	10.69	3.74 ± 0.42
K428-8	#######	0.000000	0.011115	0.000000	0.099453	0.270540	91.04 ± 0.89	98.92	10.43	1.45 ± 0.09
	Σ	0.000208	0.034334	0.000202	0.953627	2.562382				

Information on Analysis
Sample = MUSCOVITE
Material = Muscovite
Location = ???
Analyst = YR
Project = ROLLAND_HASSIG
Mass Discrimination Law = LIN
Irradiation = MC54
J = 0.01902800 ± 0.00009514
Hb3gr = 1073.600 ± 5.368 Ma

Results	40(r)/39(k) ± 1σ	Age ± 1σ (Ma)	MSWD	39Ar(k) (%,n)	K/Ca ± 1σ
Age Plateau	2.6797 ± 0.0108 ± 0.40%	89.72 ± 0.56 ± 0.63%	0.80	96.99 7	1.84 ± 0.50
		Minimal External Error ± 0.59	1.01	Statistical T Ratio	
		Analytical Error ± 0.35	1.0000	Error Magnification	
Total Fusion Age	2.6870 ± 0.0123 ± 0.46%	89.96 ± 0.59 ± 0.66%		8	4.49 ± 0.25
		Minimal External Error ± 0.62			
		Analytical Error ± 0.40			

Normal Isochron		39(k)/36(a) ± 1σ	40(a+r)/36(a) ± 1σ	r.i.
K428-1	400.00 W	228.0 ± 19.4	970.1 ± 82.1	0.9927
K428-2	460.00 W	2306.5 ± 251.0	6540.1 ± 708.6	0.9957
K428-3	493.00 W	21925.6 ± 40190.4	59051.6 ± 108242.2	1.0000
K428-4	523.00 W			
K428-5	544.00 W			
K428-6	616.00 W			
K428-7	695.00 W			
K428-8	#######			

Inverse Isochron		39(k)/40(a+r) ± 1σ	36(a)/40(a+r) ± 1σ	r.i.
K428-1	400.00 W	0.235022 ± 0.002408	0.001031 ± 0.000087	0.0041
K428-2	460.00 W	0.352663 ± 0.003535	0.000153 ± 0.000017	0.0003
K428-3	493.00 W	0.371295 ± 0.003749	0.000017 ± 0.000031	0.0001
K428-4	523.00 W			
K428-5	544.00 W			
K428-6	616.00 W			
K428-7	695.00 W			
K428-8	#######			

Relative Abundances		36Ar	%1σ	37Ar	%1σ	38Ar	%1σ	39Ar	%1σ	40Ar	%1σ	Age ± 1σ (Ma)	40Ar(r) (%)	39Ar(k) (%)	K/Ca ± 1σ
K428-1	400.00 W	0.0001264	8.429	0.0017173	34.970	0.0004600	3.071	0.0286962	1.007	0.1229467	0.187	98.38 ± 3.74	68.74	3.01	2.70 ± 0.95
K428-2	460.00 W	0.0000773	10.716	0.0028760	13.755	0.0022256	2.173	0.1762719	1.001	0.5050602	0.055	90.58 ± 1.00	94.45	18.48	9.90 ± 1.42
K428-3	493.00 W	0.0000063	168.401	0.0017699	24.652	0.0015868	2.253	0.1277822	1.003	0.3479443	0.107	89.72 ± 1.20	98.41	13.40	11.67 ± 2.92
K428-4	523.00 W	0.0000097	82.852	0.0067368	6.824	0.0031885	2.055	0.2593139	1.004	0.6974123	0.046	89.07 ± 0.87	98.90	27.19	6.22 ± 0.50
K428-5	544.00 W	0.0000084	67.150	0.0018872	18.967	0.0005425	2.508	0.0434245	1.040	0.1173688	0.110	89.51 ± 0.91	98.90	4.55	3.72 ± 0.72
K428-6	616.00 W	0.0000117	62.746	0.0038280	13.609	0.0014521	2.161	0.1167650	1.013	0.3129037	0.085	88.75 ± 0.88	98.89	12.24	4.93 ± 0.70
K428-7	695.00 W	0.0000195	34.784	0.0044045	10.515	0.0013325	2.236	0.1019368	1.014	0.2757070	0.105	89.57 ± 0.89	98.90	10.69	3.74 ± 0.42
K428-8	#######	0.0000058	112.895	0.0111147	5.080	0.0014047	2.178	0.0994614	1.000	0.2734935	0.082	91.04 ± 0.89	98.92	10.43	1.45 ± 0.09
	Σ	0.0001548	14.952	0.0343344	3.963	0.0121927	0.864	0.9536519	0.410	2.6528366	0.029				

Information on Analysis and Constants Used in Calculations

Sample = MUSCOVITE
Material = Muscovite
Location = ???
Analyst = YR
Project = ROLLAND_HASSIG
Mass Discrimination Law = LIN
Irradiation = MC54
J = 0.01902800 ± 0.00009514
Hb3gr = 1073.600 ± 5.368 Ma
IGSN = Undefined
Preferred Age = Undefined
Classification = Undefined
Experiment Type = Undefined
Extraction Method = Undefined
Heating = 60 sec
Isolation = 2.00 min
Instrument = VG3600
Lithology = Undefined
Lat-Lon = Undefined - Undefined

Age Equations = Conventional
Negative Intensities = Forced Zero
Decay Constant 40K = 5.543 ± 0.010 E-10 1/a
Decay Constant 39Ar = 2.940 ± 0.029 E-07 1/h
Decay Constant 37Ar = 8.220 ± 0.010 E-04 1/h
Decay Constant 36Cl = 2.310 ± 0.016 E-06 1/a
Production Ratio 36/38 in Cl = 316.0 ± 15.8

Results	40(r)/39(k) ± 1σ	Age ± 1σ (Ma)	MSWD	39Ar(k) (%,n)	K/Ca ± 1σ
Age Plateau	2.6797 ± 0.0108 ± 0.40%	89.72 ± 0.56 ± 0.63%	0.80	96.99 7	1.84 ± 0.50
	Minimal External Error ± 0.59		1.01	Statistical T Ratio	
	Analytical Error ± 0.35		1.0000	Error Magnification	
Total Fusion Age	2.6870 ± 0.0123 ± 0.46%	89.96 ± 0.59 ± 0.66%		8	4.49 ± 0.25
	Minimal External Error ± 0.62				
	Analytical Error ± 0.40				
Normal Isochron	Cannot Calculate				
Inverse Isochron	Cannot Calculate				

Degassing Patterns		36Ar(a)	%1σ	36Ar(c)	%1σ	36Ar(ca)	%1σ	36Ar(cl)	%1σ	37Ar(ca)	%1σ	38Ar(a)	%1σ	38Ar(c)	%1σ	38Ar(k)	%1σ
K428-1	400.00 W	0.000126	8.46	0.000000	0.00	0.000000	34.98	0.000000	23.87	0.001717	34.97	0.000024	8.47	0.000000	0.00	0.000344	2.24
K428-2	460.00 W	0.000076	10.83	0.000000	0.00	0.000001	13.79	0.000000	88.67	0.002876	13.76	0.000014	10.84	0.000000	0.00	0.002115	2.24
K428-3	493.00 W	0.000006	183.30	0.000000	0.00	0.000000	24.67	0.000000	121.80	0.001770	24.65	0.000001	183.30	0.000000	0.00	0.001533	2.24
K428-4	523.00 W	0.000000	0.00	0.000000	0.00	0.000010	82.85	0.000000	0.00	0.006737	6.82	0.000000	0.00	0.000000	0.00	0.003112	2.24
K428-5	544.00 W	0.000000	0.00	0.000000	0.00	0.000008	67.15	0.000000	0.00	0.001887	18.97	0.000000	0.00	0.000000	0.00	0.000521	2.25
K428-6	616.00 W	0.000000	0.00	0.000000	0.00	0.000012	62.75	0.000000	0.00	0.003828	13.61	0.000000	0.00	0.000000	0.00	0.001401	2.24
K428-7	695.00 W	0.000000	0.00	0.000000	0.00	0.000020	34.78	0.000000	0.00	0.004404	10.51	0.000000	0.00	0.000000	0.00	0.001223	2.24
K428-8	1111.00 W	0.000000	0.00	0.000000	0.00	0.000006	112.89	0.000000	0.00	0.011115	5.08	0.000000	0.00	0.000000	0.00	0.001193	2.24
	Σ	0.000208	8.27	0.000000	0.00	0.000053	29.02	0.000000	43.78	0.034334	3.96	0.000039	8.27	0.000000	0.00	0.011444	0.91
	Σ							0.000155	14.95	0.034334	3.96						

38Ar(ca)	%1σ	38Ar(cl)	%1σ	39Ar(k)	%1σ	39Ar(ca)	%1σ	40Ar(r)	%1σ	40Ar(a)	%1σ	40Ar(c)	%1σ	40Ar(k)	%1σ
0.000010	96.56	0.000082	24.39	0.028695	1.01	0.000001	35.20	0.084520	3.77	0.037575	8.47	0.000000	0.00	0.000852	2.24
0.000017	91.05	0.000079	88.82	0.176270	1.00	0.000002	14.32	0.477008	0.52	0.022817	10.84	0.000000	0.00	0.005235	2.24
0.000011	93.32	0.000042	121.90	0.127781	1.00	0.000001	24.97	0.342409	0.94	0.001740	183.30	0.000000	0.00	0.003795	2.24
0.000040	90.26	0.000000	0.00	0.259309	1.00	0.000005	7.91	0.689711	0.05	0.000000	0.00	0.000000	0.00	0.007701	2.24
0.000011	91.98	0.000000	0.00	0.043423	1.04	0.000001	19.38	0.116079	0.11	0.000000	0.00	0.000000	0.00	0.001290	2.25
0.000023	91.02	0.000000	0.00	0.116762	1.01	0.000003	14.18	0.309436	0.09	0.000000	0.00	0.000000	0.00	0.003468	2.24
0.000026	90.61	0.000000	0.00	0.101934	1.01	0.000003	11.25	0.272680	0.11	0.000000	0.00	0.000000	0.00	0.003027	2.24
0.000067	90.14	0.000000	0.00	0.099453	1.00	0.000008	6.47	0.270540	0.09	0.000000	0.00	0.000000	0.00	0.002954	2.24
0.000206	39.16	0.000202	43.88	0.953627	0.41	0.000025	4.32	2.562382	0.20	0.062132	8.27	0.000000	0.00	0.028323	0.91
		0.011891	1.34			0.953652	0.41							2.652837	0.28

Additional Parameters		40(r)/39(k)	1σ	40(r+a)	1σ	40Ar/39Ar	1σ	37Ar/39Ar	1σ	36Ar/39Ar	1σ	Time (days)	37Ar (decay)	39Ar (decay)	40Ar (moles)
K428-1	400.00 W	2.945453	0.11503	0.122094	0.00023	4.284428	0.04388	0.059844	0.02094	0.004404	0.00037	193.669	47.22812876	1.00137982	2.459E-15
K428-2	460.00 W	2.706123	0.03054	0.499825	0.00030	2.865234	0.02871	0.016316	0.00225	0.000438	0.00005	193.698	47.25531165	1.00138002	1.010E-14
K428-3	493.00 W	2.679658	0.03681	0.344149	0.00038	2.722948	0.02748	0.013851	0.00342	0.000050	0.00008	193.713	47.26955655	1.00138013	6.959E-15
K428-4	523.00 W	2.659803	0.02675	0.689711	0.00037	2.689452	0.02704	0.025979	0.00179	0.000037	0.00003	193.728	47.28315795	1.00138023	1.395E-14
K428-5	544.00 W	2.673210	0.02797	0.116079	0.00013	2.702825	0.02827	0.043460	0.00826	0.000193	0.00013	193.756	47.30972436	1.00138044	2.347E-15
K428-6	616.00 W	2.650136	0.02695	0.309436	0.00028	2.679772	0.02724	0.032784	0.00447	0.000101	0.00006	193.772	47.32463401	1.00138055	6.258E-15
K428-7	695.00 W	2.675071	0.02727	0.272680	0.00030	2.704686	0.02756	0.043208	0.00456	0.000192	0.00007	193.787	47.33889980	1.00138066	5.514E-15
K428-8	1111.00 W	2.720270	0.02731	0.270540	0.00023	2.749746	0.02760	0.111749	0.00579	0.000058	0.00007	193.803	47.35316990	1.00138076	5.470E-15

Procedure Blanks		36Ar	1σ	37Ar	1σ	38Ar	1σ	39Ar	1σ	40Ar	1σ
K428-1	400.00 W	0.000026	0.000004	0.000034	0.000011	0.000005	0.000005	0.000017	0.000009	0.001526	0.000079
K428-2	460.00 W	0.000025	0.000005	0.000047	0.000003	0.000011	0.000003	0.000050	0.000005	0.001458	0.000019
K428-3	493.00 W	0.000025	0.000005	0.000047	0.000003	0.000011	0.000003	0.000050	0.000005	0.001458	0.000019
K428-4	523.00 W	0.000025	0.000005	0.000047	0.000003	0.000011	0.000003	0.000050	0.000005	0.001458	0.000019
K428-5	544.00 W	0.000031	0.000004	0.000042	0.000006	0.000010	0.000004	0.000123	0.000005	0.001656	0.000023
K428-6	616.00 W	0.000031	0.000004	0.000042	0.000006	0.000010	0.000004	0.000123	0.000005	0.001656	0.000023
K428-7	695.00 W	0.000031	0.000004	0.000042	0.000006	0.000010	0.000004	0.000123	0.000005	0.001656	0.000023
K428-8	#######	0.000031	0.000004	0.000042	0.000006	0.000010	0.000004	0.000123	0.000005	0.001656	0.000023

Intercept Values		36Ar	1σ	r2		37Ar	1σ	r2		38Ar	1σ	r2		39Ar	1σ	r2		40Ar	1σ	r2	
K428-1	400.00 W	0.000153	0.000009	0.0537	LIN # 5	0.000071	0.000007	0.7110	LIN # 3 5	0.000468	0.000010	0.8919	LIN # 5	0.028742	0.000037	0.9997	EXP # 3 5	0.124473	0.000216	0.9992	EXP # 5
K428-2	460.00 W	0.000103	0.000006	0.0341	EXP #	0.000109	0.000008	0.1509	EXP #	0.002247	0.000019	0.9737	EXP #	0.176499	0.000126	0.9998	EXP #	0.506519	0.000278	0.9999	EXP #
K428-3	493.00 W	0.000031	0.000010	0.0211	EXP #	0.000085	0.000009	0.0853	EXP #	0.001605	0.000016	0.9756	EXP #	0.127961	0.000133	0.9998	EXP #	0.349403	0.000373	0.9997	EXP #
K428-4	523.00 W	0.000015	0.000006	0.0863	EXP #	0.000191	0.000008	0.2443	EXP #	0.003215	0.000016	0.9921	EXP #	0.259625	0.000291	0.9996	EXP #	0.698871	0.000323	0.9999	EXP #
K428-5	544.00 W	0.000023	0.000004	0.2464	EXP #	0.000082	0.000005	0.0555	EXP #	0.000555	0.000007	0.8963	LIN #	0.043591	0.000127	0.9951	EXP #	0.119025	0.000127	0.9991	EXP #
K428-6	616.00 W	0.000019	0.000007	0.1028	EXP #	0.000123	0.000009	0.0031	LIN #	0.001469	0.000011	0.9787	LIN #	0.117005	0.000201	0.9989	EXP #	0.314560	0.000265	0.9997	EXP #
K428-7	695.00 W	0.000011	0.000006	0.5245	EXP #	0.000136	0.000007	0.2610	EXP #	0.001349	0.000013	0.9885	EXP #	0.102162	0.000181	0.9996	EXP #	0.277363	0.000288	0.9999	EXP #
K428-8	1111.00 W	0.000025	0.000006	0.2577	EXP #	0.000278	0.000008	0.8756	EXP #	0.001422	0.000012	0.9925	EXP #	0.099684	0.000066	1.0000	EXP #	0.275150	0.000222	0.9999	EXP #

Sample Parameters		Sample	Material	Location	Analyst	Temp	Standard (in Ma)	%1σ	J	%1σ	MDF	%1σ
K428-1	400.00 W	Muscovite	Muscovite	???	YR	400	1073.6	0.5	0.019028	0.5	1.002391	1
K428-2	460.00 W	Muscovite	Muscovite	???	YR	460	1073.6	0.5	0.019028	0.5	1.002391	1
K428-3	493.00 W	Muscovite	Muscovite	???	YR	493	1073.6	0.5	0.019028	0.5	1.002391	1
K428-4	523.00 W	Muscovite	Muscovite	???	YR	523	1073.6	0.5	0.019028	0.5	1.002391	1
K428-5	544.00 W	bl	Muscovite	???	YR	544	1073.6	0.5	0.019028	0.5	1.002391	1
K428-6	616.00 W	Muscovite	Muscovite	???	YR	616	1073.6	0.5	0.019028	0.5	1.002391	1
K428-7	695.00 W	Muscovite	Muscovite	???	YR	695	1073.6	0.5	0.019028	0.5	1.002391	1
K428-8	1111.00 W	Muscovite	Muscovite	???	YR	1111	1073.6	0.5	0.019028	0.5	1.002391	1

Volume Ratio	Sensitivity (mol/volt)	Day	Month	Year	Hour	Min	Resist	Irradiation	Project	Experiment	Nmb	Standard Name
1	2.000E-14	21	APR	2010	13	12	001	MC54	Rolland_Hassig	K428-1	01	Hb3gr
1	2.000E-14	21	APR	2010	13	54	001	MC54	Rolland_Hassig	K428-1	01	Hb3gr
1	2.000E-14	21	APR	2010	14	16	001	MC54	Rolland_Hassig	K428-1	01	Hb3gr
1	2.000E-14	21	APR	2010	14	37	001	MC54	Rolland_Hassig	K428-1	01	Hb3gr
1	2.000E-14	21	APR	2010	15	18	001	MC54	Rolland_Hassig	K428-1	01	Hb3gr
1	2.000E-14	21	APR	2010	15	41	001	MC54	Rolland_Hassig	K428-1	01	Hb3gr
1	2.000E-14	21	APR	2010	16	03	001	MC54	Rolland_Hassig	K428-1	01	Hb3gr
1	2.000E-14	21	APR	2010	16	25	001	MC54	Rolland_Hassig	K428-1	01	Hb3gr

Irradiation Constants		40/36(a)	%1σ	40/36(c)	%1σ	38/36(a)	%1σ	38/36(c)	%1σ	39/37(ca)	%1σ	38/37(ca)	%1σ	36/37(ca)	%1σ
K428-1	400.00 W	298.56	0.1	0.018	35	0.1885	0.16	1.7	3	0.00073	4	0.006	90	0.000282	1
K428-2	460.00 W	298.56	0.1	0.018	35	0.1885	0.16	1.7	3	0.00073	4	0.006	90	0.000282	1
K428-3	493.00 W	298.56	0.1	0.018	35	0.1885	0.16	1.7	3	0.00073	4	0.006	90	0.000282	1
K428-4	523.00 W	298.56	0.1	0.018	35	0.1885	0.16	1.7	3	0.00073	4	0.006	90	0.000282	1
K428-5	544.00 W	298.56	0.1	0.018	35	0.1885	0.16	1.7	3	0.00073	4	0.006	90	0.000282	1
K428-6	616.00 W	298.56	0.1	0.018	35	0.1885	0.16	1.7	3	0.00073	4	0.006	90	0.000282	1
K428-7	695.00 W	298.56	0.1	0.018	35	0.1885	0.16	1.7	3	0.00073	4	0.006	90	0.000282	1
K428-8	1111.00 W	298.56	0.1	0.018	35	0.1885	0.16	1.7	3	0.00073	4	0.006	90	0.000282	1

40/39(k)	%1σ	38/39(k)	%1σ	36/38(cl)	%1σ	K/Ca	%1σ	K/Cl	%1σ	Ca/Cl	%1σ
0.0297	2	0.012	2	316	5	0.1616	4	5.4	33	33	33
0.0297	2	0.012	2	316	5	0.1616	4	5.4	33	33	33
0.0297	2	0.012	2	316	5	0.1616	4	5.4	33	33	33
0.0297	2	0.012	2	316	5	0.1616	4	5.4	33	33	33
0.0297	2	0.012	2	316	5	0.1616	4	5.4	33	33	33
0.0297	2	0.012	2	316	5	0.1616	4	5.4	33	33	33
0.0297	2	0.012	2	316	5	0.1616	4	5.4	33	33	33
0.0297	2	0.012	2	316	5	0.1616	4	5.4	33	33	33

Annexe 7 – Données microsonde, transect Grenat de AR-03-62M.

Sample	AR-03-62M										
Analysis	1	2	3	4	5	6	7	8	9	10	11
SiO2	36.76	36.77	36.75	37.5	37.23	37.19	36.98	36.84	36.89	36.79	36.56
Al2O3	21.19	20.89	20.98	21.24	20.93	21.09	20.91	20.9	20.78	21.14	21.09
MgO	2.26	2.04	2.06	2	2.06	1.95	1.83	1.78	1.69	1.62	1.65
FeO	31.62	30.82	30.49	30.47	30.2	30	29.55	29.31	28.47	29.63	29.07
Fe2O3											
MnO	5.53	5.26	5.29	5.29	5.46	5.64	6.38	6.89	7.08	7.63	7.65
Cr2O3											
TiO2	0.11	0.04	0.07	0.1	0.14	0.15	0.2	0.07	0.1	0.09	0
NiO2											
CaO	3.16	4.1	4.83	4.45	4.04	4.85	4.67	4.6	4.66	4.27	4.01
Na2O	0.04	0.08	0.03	0.09	0.02	0.04	0	0.02	0.09	0.03	0.03
K2O	0	0	0	0	0	0	0.02	0	0	0	0
Total	100.67	100	100.5	101.14	100.08	100.91	100.54	100.41	99.76	101.2	100.06
Almandin	69.8	68.4	66.7	67.6	67.7	66.1	65.3	64.6	63.8	64.8	64.7
Grossulaire	8.9	11.7	13.5	12.6	11.6	13.7	13.2	13.0	13.4	12.0	11.4
Pyrope	8.9	8.1	8.0	7.9	8.2	7.7	7.2	7.0	6.8	6.3	6.6
Spessartine	12.4	11.8	11.7	11.9	12.4	12.6	14.3	15.4	16.1	16.9	17.3

Sample											
Analysis	12	13	14	15	16	17	18	19	20	21	22
SiO2	36.63	36.36	36.84	36.88	37.45	37.21	36.86	37.04	37.12	36.84	37.24
Al2O3	20.81	20.84	20.94	20.94	21.54	20.82	20.99	21.24	20.79	20.69	20.65
MgO	1.75	1.67	1.3	1.29	1.33	1.37	1.28	1.23	1.18	1.17	1.17
FeO	29.59	28.72	27.96	28.49	27.74	27.72	26.33	26.43	26.51	26.35	26.27
Fe2O3											
MnO	7.98	7.68	8.46	8.66	8.75	8.81	9.98	10.47	10.19	10.17	10.38
Cr2O3											
TiO2	0.09	0.14	0.13	0.1	0.1	0.12	0.1	0.03	0.13	0.19	0.2
NiO2											
CaO	4.23	4.6	4.89	4.65	4.88	4.79	4.94	4.61	4.88	5.08	5.12
Na2O	0.08	0.07	0.09	0.06	0.07	0.09	0.06	0.07	0.11	0.06	0.07
K2O	0	0.02	0.03	0.03	0	0	0.01	0.01	0	0	0
Total	101.16	100.1	100.64	101.1	101.86	100.93	100.55	101.13	100.91	100.55	101.1
Almandin	64.0	63.3	62.0	62.6	61.3	61.3	58.4	58.6	58.7	58.2	57.8
Grossulaire	11.7	13.0	13.9	13.1	13.8	13.6	14.0	13.1	13.8	14.4	14.4
Pyrope	6.8	6.6	5.1	5.1	5.2	5.4	5.1	4.9	4.7	4.6	4.6
Spessartine	17.5	17.1	19.0	19.3	19.6	19.7	22.4	23.5	22.8	22.8	23.1

Sample											
Analysis	23	24	25	26	27	28	29	30	31	32	33
SiO2	36.69	36.81	37.62	36.49	36.47	36.64	36.94	37.32	36.62	36.52	36.62
Al2O3	20.56	20.5	20.71	20.64	20.73	20.93	20.73	20.53	20.81	20.94	20.98
MgO	1.15	1.18	1.26	1.26	1.19	1.27	1.25	1.27	1.2	1.27	1.43
FeO	26.31	26.7	26.36	26.38	26.36	27.02	26.56	26.46	26.81	27.1	27.07
Fe2O3											
MnO	10.31	10.2	10.06	9.98	10.38	10.2	10.45	10.22	10.25	9.88	9.16
Cr2O3											
TiO2	0.18	0.1	0.11	0.08	0.11	0.06	0.13	0.15	0.1	0.07	0.12
NiO2											
CaO	4.84	5.12	4.89	4.82	4.65	4.7	4.82	4.81	4.93	4.86	4.79
Na2O	0.1	0.04	0.08	0.07	0.04	0.05	0.08	0.08	0.05	0.05	0.05
K2O	0.01	0	0	0	0.02	0.03	0.01	0.01	0	0	0
Total	100.15	100.65	101.09	99.72	99.95	100.9	100.97	100.85	100.77	100.69	100.22
Almandin	58.5	58.4	58.5	58.7	58.6	59.2	58.3	58.5	58.7	59.4	60.1
Grossulaire	13.8	14.4	13.9	13.8	13.3	13.2	13.6	13.6	13.8	13.7	13.6
Pyrope	4.6	4.6	5.0	5.0	4.7	5.0	4.9	5.0	4.7	5.0	5.7
Spessartine	23.2	22.6	22.6	22.5	23.4	22.6	23.2	22.9	22.7	21.9	20.6

Sample Analysis	34	35	36	37	38	39	40	41	42	43	44
SiO2	36.65	36.76	36.57	37.17	36.47	37.21	36.57	37.19	36.41	37.2	36.84
Al2O3	20.81	20.79	20.76	20.64	20.57	20.7	20.98	20.92	20.59	21.05	20.85
MgO	1.51	1.7	1.69	1.57	1.56	1.71	1.71	1.65	1.69	1.56	1.8
FeO	27.44	27.95	29.48	28.19	27.78	28.46	29.33	29.31	29.43	28.29	28.84
Fe2O3											
MnO	9.12	8.6	8.79	8.27	8.91	8.22	8.75	8.36	8.54	8.2	7.17
Cr2O3											
TiO2	0.15	1.37	0.15	0.12	0.1	0.1	0.07	0.08	0.11	0.13	0.15
NiO2											
CaO	4.78	4.25	3.38	4.86	4.8	4.32	3.09	3.36	3.62	4.75	4.51
Na2O	0.09	0.03	0.04	0.09	0.06	0.05	0.01	0.04	0.03	0.03	0.07
K2O	0	0	0.03	0	0.01	0.03	0.01	0	0	0.02	0.03
Total	100.55	101.45	100.89	100.91	100.26	100.8	100.52	100.91	100.42	101.23	100.26
Almandin	60.3	61.9	64.5	61.8	60.7	62.7	64.9	65.1	64.4	62.2	64.0
Grossulaire	13.5	12.1	9.5	13.7	13.4	12.2	8.8	9.6	10.1	13.4	12.8
Pyrope	5.9	6.7	6.6	6.1	6.1	6.7	6.7	6.5	6.6	6.1	7.1
Spessartine	20.3	19.3	19.5	18.4	19.7	18.4	19.6	18.8	18.9	18.3	16.1

Sample Analysis	45	46	47	48	49	50	51	52	53	54	55
SiO2	35.99	36.74	36.13	36.36	36.62	36.85	36.83	36.44	35.68	36.57	36.64
Al2O3	20.83	20.61	20.49	20.74	20.61	20.47	15.86	20.72	20.52	20.82	20.94
MgO	1.78	1.95	1.93	1.9	1.86	1.64	1.78	1.64	1.77	1.57	1.61
FeO	30.77	30.19	30.65	29.96	29.81	30.02	30.19	30.29	30.59	30.45	30.69
Fe2O3											
MnO	6.55	6.65	6.43	6.48	6.45	6.46	6.2	6.18	6.02	5.92	5.87
Cr2O3											
TiO2	0.1	0.1	0.07	0.11	0.19	0.07	0.17	0.11	0.11	0.18	0.08
NiO2											
CaO	3.37	4.34	3.43	4.18	4.6	4.71	4.52	4.8	4.76	4.74	4.88
Na2O	0.03	0.04	0.04	0.04	0.01	0.03	0.07	0.02	0.06	0.04	0.06
K2O	0.07	0	0	0.03	0	0	0	0	0	0	0
Total	99.49	100.62	99.17	99.8	100.15	100.25	95.62	100.2	99.51	100.29	100.77
Almandin	68.5	65.7	68.1	66.2	65.4	65.9	66.4	66.4	66.6	67.2	67.1
Grossulaire	9.6	12.1	9.8	11.8	12.9	13.3	12.7	13.5	13.3	13.4	13.7
Pyrope	7.1	7.6	7.6	7.5	7.3	6.4	7.0	6.4	6.9	6.2	6.3
Spessartine	14.8	14.7	14.5	14.5	14.3	14.4	13.8	13.7	13.3	13.2	13.0

Sample Analysis	56	57	58	59	60	61	62	63
SiO2	36.79	36.4	36.03	36.86	36.98	36.57	37.94	37.44
Al2O3	20.68	20.58	20.67	21.26	20.61	20.83	21.48	21.21
MgO	1.6	1.68	1.61	1.62	1.78	1.81	1.83	1.97
FeO	30.76	31.07	31.1	30.54	31.4	31.39	31.23	30.75
Fe2O3								
MnO	5.65	5.31	5.37	5.18	5.05	5	4.99	5.28
Cr2O3								
TiO2	0.33	0.18	0.21	0.22	0.02	0.09	0	0.06
NiO2								
CaO	4.82	4.54	4.8	4.62	4.74	4.89	4.78	4.56
Na2O	0.03	0	0.01	0.13	0.05	0.05	0	0.08
K2O	0	0	0	0.07	0	0.01	0	0
Total	100.66	99.76	99.8	100.5	100.63	100.64	102.25	101.35
Almandin	67.6	68.6	68.3	68.5	68.6	68.3	68.4	67.7
Grossulaire	13.6	12.9	13.5	13.3	13.3	13.6	13.4	12.9
Pyrope	6.3	6.6	6.3	6.5	6.9	7.0	7.1	7.7
Spessartine	12.6	11.9	11.9	11.8	11.2	11.0	11.1	11.8

Annexe 8 - Résultats de datation (2) sur Amphibole AR-03-64.

Incremental Heating		36Ar(a)	37Ar(ca)	38Ar(cl)	39Ar(k)	40Ar(r)	Age ± 2σ (Ma)	40Ar(r) (%)	39Ar(k) (%)	K/Ca ± 2σ
M1907-1	650 °C	0.000319	0.000215	0.005940	0.004460	0.007090	48.40 ± 57.32	6.92	0.20	3 ± 18
M1907-2	750 °C	0.000210	0.001270	0.000374	0.015699	0.047625	91.27 ± 11.54	43.00	0.70	2 ± 3
M1907-3	850 °C	0.000100	0.002105	0.000121	0.061914	0.263328	126.70 ± 3.10	89.23	2.77	5 ± 7
M1907-4	900 °C	0.000062	0.002051	0.000101	0.063995	0.284023	132.02 ± 2.86	93.28	2.86	5 ± 7
M1907-5	950 °C	0.000063	0.002643	0.000178	0.082391	0.380585	137.20 ± 2.95	94.73	3.68	5 ± 6
M1907-6	1000 °C	0.000110	0.000425	0.000510	0.313829	1.545068	145.88 ± 2.83	97.34	14.03	119 ± 408
M1907-7	1050 °C	0.000069	0.001467	0.000691	0.404585	1.928874	141.44 ± 2.73	98.34	18.08	45 ± 38
M1907-8	1100 °C	0.000060	0.000447	0.000366	0.208037	0.943910	134.85 ± 2.67	97.50	9.30	75 ± 186
M1907-9	1150 °C	0.000014	0.000633	0.000212	0.132829	0.614446	137.39 ± 2.77	98.70	5.94	34 ± 58
M1907-10	1200 °C	0.000015	0.000602	0.000326	0.171677	0.810801	140.16 ± 2.77	98.84	7.67	46 ± 94
M1907-11	1250 °C	0.000034	0.000180	0.000313	0.199202	0.958588	142.71 ± 2.83	98.34	8.90	179 ± 1095
M1907-12	1300 °C	0.000074	0.000775	0.001131	0.528662	2.663605	149.15 ± 2.87	98.60	23.63	110 ± 185
M1907-13	1400 °C	0.000021	0.000458	0.000112	0.034392	0.174547	150.19 ± 4.75	95.93	1.54	12 ± 22
M1907-14	1500 °C	0.000028	0.000754	0.000059	0.015718	0.079779	150.21 ± 4.75	89.95	0.70	3 ± 3
	Σ	0.001180	0.000839	0.010435	2.237389	10.702271				

Information on Analysis
Sample = AR-04-64
Material = Muscovite
Location = Arménie
Analyst = Yann ROLLAND
Project = ROLLAND_HASSIG
Mass Discrimination Law = LIN
Irradiation = MC45
J = 0.01710610 ± 0.00004277
Hb3gr = 1073.600 ± 5.368 Ma

Results	40(r)/39(k) ± 2σ	Age ± 2σ (Ma)	MSWD	39Ar(k) (%,n)	K/Ca ± 2σ
Age Plateau	4.7955 ± 0.1228	142.24 ± 3.57	12.21	89.79	4 ± 3
Error Mean	± 2.56%	± 2.51%		9	
	Minimal External Error ± 3.61		2.31	Statistical T Ratio	
	Analytical Error ± 3.50		3.4948	Error Magnification	
Total Fusion Age	4.7834 ± 0.0363	141.89 ± 1.24		14	431 ± 3434
	± 0.76%	± 0.87%			
	Minimal External Error ± 1.34				
	Analytical Error ± 1.03				

Normal Isochron		39(k)/36(a) ± 2σ	40(a+r)/36(a) ± 2σ	r.i.
M1907-1	650 °C	14.0 ± 1.3	320.8 ± 28.7	0.9690
M1907-2	750 °C	74.8 ± 7.4	525.4 ± 51.1	0.9785
M1907-3	850 °C	617.3 ± 84.5	2923.9 ± 396.2	0.9892
M1907-4	900 °C	1029.4 ± 159.6	4867.4 ± 748.2	0.9916
M1907-5	950 °C	1314.3 ± 264.1	6369.6 ± 1273.5	0.9950
M1907-6	1000 °C	2841.6 ± 361.0	14288.5 ± 1792.5	0.9875
M1907-7	1050 °C	5871.2 ± 922.2	28289.8 ± 4407.7	0.9919
M1907-8	1100 °C	3448.0 ± 874.3	15942.9 ± 4029.8	0.9969
M1907-9	1150 °C	9607.3 ± 8649.5	44740.5 ± 40270.2	0.9998
M1907-10	1200 °C	11573.0 ± 9825.8	54956.0 ± 46646.4	0.9997
M1907-11	1250 °C	5820.3 ± 2682.7	28306.7 ± 13034.8	0.9991
M1907-12	1300 °C	7159.0 ± 1448.8	36368.2 ± 7323.9	0.9951
M1907-13	1400 °C	1606.5 ± 1146.8	8451.9 ± 6031.0	0.9996
M1907-14	1500 °C	555.9 ± 137.0	3120.0 ± 766.3	0.9966

Results	40(a)/36(a) ± 2σ	40(r)/39(k) ± 2σ	Age ± 2σ (Ma)	MSWD
Normal Isochron Error Chron	541.0151 ± 431.5388 ± 79.76%	4.6961 ± 0.1551 ± 3.30%	139.40 ± 4.48 ± 3.22%	9.04
			Minimal External Error ± 4.51	
			Analytical Error ± 4.43	

Statistics				
	Statistical F ratio	2.01	Convergence	0.0000353476
	Error Magnification	3.0060	Number of Iterations	1
	Number of Data Points	9	Calculated Line	Weighted York-2

Inverse Isochron		39(k)/40(a+r) ± 2σ	36(a)/40(a+r) ± 2σ	r.i.
M1907-1	650 °C	0.043617 ± 0.000993	0.003117 ± 0.000279	0.0024
M1907-2	750 °C	0.142339 ± 0.002915	0.001903 ± 0.000185	0.0018
M1907-3	850 °C	0.211114 ± 0.004238	0.000342 ± 0.000046	0.0008
M1907-4	900 °C	0.211494 ± 0.004245	0.000205 ± 0.000032	0.0005
M1907-5	950 °C	0.206338 ± 0.004130	0.000157 ± 0.000031	0.0001
M1907-6	1000 °C	0.198872 ± 0.003975	0.000070 ± 0.000009	0.0001
M1907-7	1050 °C	0.207538 ± 0.004145	0.000035 ± 0.000006	0.0001
M1907-8	1100 °C	0.216272 ± 0.004326	0.000063 ± 0.000016	0.0001
M1907-9	1150 °C	0.214734 ± 0.004309	0.000022 ± 0.000020	0.0000
M1907-10	1200 °C	0.210587 ± 0.004213	0.000018 ± 0.000015	0.0000
M1907-11	1250 °C	0.205616 ± 0.004114	0.000035 ± 0.000016	0.0001
M1907-12	1300 °C	0.196847 ± 0.003933	0.000027 ± 0.000006	0.0001
M1907-13	1400 °C	0.190078 ± 0.003821	0.000118 ± 0.000084	0.0000
M1907-14	1500 °C	0.178167 ± 0.003605	0.000321 ± 0.000079	0.0007

Results	40(a)/36(a) ± 2σ	40(r)/39(k) ± 2σ	Age ± 2σ (Ma)	MSWD
Inverse Isochron Error Chron	578.3530 ± 176.5239 ± 30.52%	4.7371 ± 0.0829 ± 1.75%	140.57 ± 2.46 ± 1.75%	10.39
			Minimal External Error ± 2.51	
			Analytical Error ± 2.37	

Statistics				
	Statistical F ratio	2.01	Convergence	0.0005929558
	Error Magnification	3.2237	Number of Iterations	8
	Number of Data Points	9	Calculated Line	Weighted York-2

Relative Abundances			36Ar	%1σ	37Ar	%1σ	38Ar	%1σ	39Ar	%1σ	40Ar	%1σ	Age ± 2σ (Ma)	40Ar(r) (%)	39Ar(k) (%)	K/Ca ± 2σ
M1907-1	650 °C		0.0003215	4.429	0.0002151	272.916	0.0060554	2.029	0.0044606	1.133	0.1023963	0.111	48.40 ± 57.32	6.92	0.20	3 ± 18
M1907-2	750 °C		0.0002104	4.846	0.0012695	74.547	0.0006097	2.649	0.0157001	1.020	0.1107605	0.093	91.27 ± 11.54	43.00	0.70	2 ± 3
M1907-3	850 °C		0.0000998	6.796	0.0021048	76.597	0.0008699	2.382	0.0619128	1.001	0.2951133	0.072	126.70 ± 3.10	89.23	2.77	5 ± 7
M1907-4	900 °C		0.0000616	7.724	0.0020514	70.806	0.0008680	2.575	0.0639930	1.002	0.3044841	0.062	132.02 ± 2.86	93.28	2.86	5 ± 7
M1907-5	950 °C		0.0000620	10.080	0.0026428	57.844	0.0011629	2.226	0.0823891	1.000	0.4017480	0.034	137.20 ± 2.95	94.73	3.68	5 ± 6
M1907-6	1000 °C		0.0001108	6.250	0.0004249	170.907	0.0042993	2.039	0.3138289	0.999	1.5873620	0.017	145.88 ± 2.83	97.34	14.03	119 ± 408
M1907-7	1050 °C		0.0000696	7.704	0.0014672	42.774	0.0055681	2.014	0.4045859	0.998	1.9614640	0.017	141.44 ± 2.73	98.34	18.08	45 ± 38
M1907-8	1100 °C		0.0000606	12.575	0.0004468	123.678	0.0028765	2.051	0.2080374	1.000	0.9681029	0.028	134.85 ± 2.67	97.50	9.30	75 ± 186
M1907-9	1150 °C		0.0000137	45.260	0.0006332	85.972	0.0018050	2.199	0.1328282	1.003	0.6225187	0.036	137.39 ± 2.77	98.70	5.94	34 ± 58
M1907-10	1200 °C		0.0000152	41.534	0.0006020	102.347	0.0023928	2.016	0.1716770	1.000	0.8203284	0.021	140.16 ± 2.77	98.84	7.67	46 ± 94
M1907-11	1250 °C		0.0000344	22.891	0.0001798	305.949	0.0027110	2.058	0.1992017	1.000	0.9747223	0.032	142.71 ± 2.83	98.34	8.90	179 ± 1095
M1907-12	1300 °C		0.0000746	9.966	0.0007752	83.809	0.0074938	2.031	0.5286623	0.999	2.7013540	0.020	149.15 ± 2.87	98.60	23.63	110 ± 185
M1907-13	1400 °C		0.0000216	35.376	0.0004585	91.777	0.0005315	2.236	0.0343928	1.004	0.1819602	0.040	150.19 ± 4.75	95.93	1.54	12 ± 22
M1907-14	1500 °C		0.0000285	12.173	0.0007539	40.697	0.0002575	2.634	0.0157187	1.007	0.0886882	0.092	150.21 ± 4.75	89.95	0.70	3 ± 3
		Σ	0.0011844	2.411	0.0008392	398.525	0.0375014	0.711	2.2373886	0.370	11.1210027	0.008				

Information on Analysis and Constants Used in Calculations

Sample = AR-04-64
Material = Muscovite
Location = Arménie
Analyst = Yann ROLLAND
Project = ROLLAND_HASSIG
Mass Discrimination Law = LIN
Irradiation = MC45
J = 0.01710610 ± 0.00004277
Hb3gr = 1073.600 ± 5.368 Ma
IGSN = Undefined
Preferred Age = Undefined
Classification = Undefined
Experiment Type = Undefined
Extraction Method = Undefined
Heating = 600 sec
Isolation = 2.00 min
Instrument = FOUR
Lithology = Undefined
Lat-Lon = Undefined - Undefined

Age Equations = Conventional
Negative Intensities = Allowed
Decay Constant 40K = 5.543 ± 0.010 E-10 1/ a
Decay Constant 39Ar = 2.940 ± 0.029 E-07 1/ h
Decay Constant 37Ar = 8.220 ± 0.010 E-04 1/ h
Decay Constant 36Cl = 2.310 ± 0.016 E-06 1/ a
Production Ratio 36/ 38 in Cl = 316.0 ± 15.8

Results	40(r)/39(k) ± 2σ	Age ± 2σ (Ma)	MSWD	39Ar(k) (%,n)	K/Ca ± 2σ
Age Plateau	4.7955 ± 0.1228	142.24 ± 3.57	12.21	89.79	4 ± 3
Error Mean	± 2.56%	± 2.51%		9	
	Minimal External Error ± 3.61		2.31	Statistical T Ratio	
	Analytical Error ± 3.50		3.4948	Error Magnification	
Total Fusion Age	4.7834 ± 0.0363	141.89 ± 1.24		14	431 ± 3434
	± 0.76%	± 0.87%			
	Minimal External Error ± 1.34				
	Analytical Error ± 1.03				
Normal Isochron	4.6961 ± 0.1551	139.40 ± 4.48	9.04	89.79	
Error Chron	± 3.30%	± 3.22%		9	
	Minimal External Error ± 4.51		2.01	Statistical F ratio	
	Analytical Error ± 4.43		3.0060	Error Magnification	
Inverse Isochron	4.7371 ± 0.0829	140.57 ± 2.46	10.39	89.79	
Error Chron	± 1.75%	± 1.75%		9	
	Minimal External Error ± 2.51		2.01	Statistical F ratio	
	Analytical Error ± 2.37		3.2237	Error Magnification	

Degassing Patterns			36Ar(a)	%1σ	36Ar(c)	%1σ	36Ar(ca)	%1σ	36Ar(cl)	%1σ	37Ar(ca)	%1σ	38Ar(a)	%1σ	38Ar(c)	%1σ	38Ar(k)	%1σ
M1907-1	650 °C		0.000319	4.47	0.000000	0.00	0.000000	272.92	0.000003	5.46	0.000215	272.92	0.000060	4.47	0.000000	0.00	0.000054	2.30
M1907-2	750 °C		0.000210	4.86	0.000000	0.00	0.000000	74.55	0.000000	7.17	0.001270	74.55	0.000040	4.86	0.000000	0.00	0.000188	2.24
M1907-3	850 °C		0.000100	6.77	0.000000	0.00	0.000001	76.60	0.000000	25.82	0.002105	76.60	0.000019	6.78	0.000000	0.00	0.000743	2.24
M1907-4	900 °C		0.000062	7.69	0.000000	0.00	0.000001	70.81	0.000000	31.78	0.002051	70.81	0.000012	7.69	0.000000	0.00	0.000768	2.24
M1907-5	950 °C		0.000063	10.00	0.000000	0.00	0.000001	57.85	0.000000	21.99	0.002643	57.84	0.000012	10.00	0.000000	0.00	0.000989	2.24
M1907-6	1000 °C		0.000110	6.27	0.000000	0.00	0.000000	170.91	0.000000	24.45	0.000425	170.91	0.000021	6.27	0.000000	0.00	0.003766	2.24
M1907-7	1050 °C		0.000069	7.79	0.000000	0.00	0.000000	42.79	0.000000	23.23	0.001467	42.77	0.000013	7.79	0.000000	0.00	0.004855	2.24
M1907-8	1100 °C		0.000060	12.64	0.000000	0.00	0.000000	123.68	0.000000	22.85	0.000447	123.68	0.000011	12.64	0.000000	0.00	0.002496	2.24
M1907-9	1150 °C		0.000014	45.00	0.000000	0.00	0.000000	85.98	0.000000	25.82	0.000633	85.97	0.000003	45.00	0.000000	0.00	0.001594	2.24
M1907-10	1200 °C		0.000015	42.44	0.000000	0.00	0.000000	102.35	0.000000	21.17	0.000602	102.35	0.000003	42.44	0.000000	0.00	0.002060	2.24
M1907-11	1250 °C		0.000034	23.02	0.000000	0.00	0.000000	305.95	0.000000	25.29	0.000180	305.95	0.000006	23.02	0.000000	0.00	0.002390	2.24
M1907-12	1300 °C		0.000074	10.07	0.000000	0.00	0.000000	83.81	0.000001	19.13	0.000775	83.81	0.000014	10.07	0.000000	0.00	0.006344	2.24
M1907-13	1400 °C		0.000021	35.68	0.000000	0.00	0.000000	91.78	0.000000	14.79	0.000458	91.78	0.000004	35.68	0.000000	0.00	0.000413	2.24
M1907-14	1500 °C		0.000028	12.28	0.000000	0.00	0.000000	40.71	0.000000	16.36	0.000754	40.70	0.000005	12.28	0.000000	0.00	0.000189	2.24
		Σ	0.001180	2.42	0.000000	0.00	0.000000	398.56	0.000005	4.49	0.000839	398.53	0.000222	2.42	0.000000	0.00	0.026849	0.83
		Σ							0.001184	2.41	0.000839	398.53						

38Ar(ca)	%1σ	38Ar(cl)	%1σ	39Ar(k)	%1σ	39Ar(ca)	%1σ	40Ar(r)	%1σ	40Ar(a)	%1σ	40Ar(c)	%1σ	40Ar(k)	%1σ
0.000001	287.37	0.005940	7.44	0.004460	1.13	0.000000	272.95	0.007090	60.00	0.095173	4.47	0.000000	0.00	0.000132	2.30
0.000008	116.86	0.000374	8.77	0.015699	1.02	0.000001	74.65	0.047625	6.40	0.062669	4.86	0.000000	0.00	0.000466	2.24
0.000013	118.18	0.000121	26.31	0.061914	1.00	0.000002	76.70	0.263328	0.77	0.029946	6.78	0.000000	0.00	0.001839	2.24
0.000012	114.51	0.000101	32.17	0.063995	1.00	0.000001	70.92	0.284023	0.51	0.018560	7.69	0.000000	0.00	0.001901	2.24
0.000016	106.99	0.000178	22.56	0.082391	1.00	0.000002	57.98	0.380585	0.49	0.018716	10.00	0.000000	0.00	0.002447	2.24
0.000003	193.16	0.000510	24.97	0.313829	1.00	0.000000	170.95	1.545068	0.14	0.032973	6.27	0.000000	0.00	0.009321	2.24
0.000009	99.65	0.000691	23.78	0.404585	1.00	0.000001	42.96	1.928874	0.09	0.020574	7.79	0.000000	0.00	0.012016	2.24
0.000003	152.96	0.000366	23.40	0.208037	1.00	0.000000	123.74	0.943910	0.24	0.018014	12.64	0.000000	0.00	0.006179	2.24
0.000004	124.46	0.000212	26.30	0.132829	1.00	0.000000	86.07	0.614446	0.30	0.004128	45.00	0.000000	0.00	0.003945	2.24
0.000004	136.29	0.000326	21.77	0.171677	1.00	0.000000	102.42	0.810801	0.23	0.004429	42.44	0.000000	0.00	0.005099	2.24
0.000001	318.91	0.000313	25.79	0.199202	1.00	0.000000	305.98	0.958588	0.25	0.010218	23.02	0.000000	0.00	0.005916	2.24
0.000005	122.98	0.001131	19.78	0.528662	1.00	0.000001	83.90	2.663605	0.09	0.022048	10.07	0.000000	0.00	0.015701	2.24
0.000003	128.54	0.000112	15.63	0.034392	1.00	0.000000	91.86	0.174547	1.31	0.006392	35.68	0.000000	0.00	0.001021	2.24
0.000005	98.77	0.000059	17.12	0.015718	1.01	0.000001	40.89	0.079779	1.30	0.008442	12.28	0.000000	0.00	0.000467	2.24
0.000005	641.67	0.010435	5.38	2.237389	0.37	0.000001	399.15	10.702271	0.08	0.352282	2.42	0.000000	0.00	0.066450	0.83
		0.037501	1.61			2.237389	0.37							11.121003	0.11

Additional Parameters			40(r)/39(k)	1σ	40(r+a)	1σ	40Ar/39Ar	1σ	37Ar/39Ar	1σ	36Ar/39Ar	1σ	Time (days)	37Ar (decay)	39Ar (decay)	40Ar (moles)
M1907-1	650 °C		1.589629	0.95393	0.102264	0.00011	22.955575	0.26128	0.048221	0.13160	0.072080	0.00329	226.347	90.86509867	1.00161427	2.048E-15
M1907-2	750 °C		3.033599	0.19659	0.110294	0.00010	7.054758	0.07223	0.080861	0.06029	0.013403	0.00066	226.363	90.89248954	1.00161437	2.215E-15
M1907-3	850 °C		4.253107	0.05384	0.293274	0.00022	4.766592	0.04784	0.033996	0.02604	0.001611	0.00011	226.380	90.92362555	1.00161450	5.902E-15
M1907-4	900 °C		4.438245	0.04982	0.302583	0.00019	4.758081	0.04775	0.032056	0.02270	0.000963	0.00008	226.396	90.95228009	1.00161461	6.090E-15
M1907-5	950 °C		4.619247	0.05151	0.399301	0.00015	4.876225	0.04879	0.032077	0.01856	0.000753	0.00008	226.412	90.98219012	1.00161473	8.035E-15
M1907-6	1000 °C		4.923287	0.04965	1.578041	0.00034	5.058049	0.05055	0.001354	0.00231	0.000353	0.00002	226.429	91.01210998	1.00161484	3.175E-14
M1907-7	1050 °C		4.767539	0.04777	1.949448	0.00043	4.848078	0.04840	0.003626	0.00155	0.000172	0.00001	226.447	91.04328697	1.00161497	3.923E-14
M1907-8	1100 °C		4.537222	0.04668	0.961924	0.00030	4.653504	0.04654	0.002148	0.00266	0.000291	0.00004	226.463	91.07197923	1.00161508	1.936E-14
M1907-9	1150 °C		4.625855	0.04848	0.618574	0.00024	4.686647	0.04702	0.004767	0.00410	0.000103	0.00005	226.482	91.10692114	1.00161522	1.245E-14
M1907-10	1200 °C		4.722838	0.04849	0.815230	0.00020	4.778323	0.04779	0.003507	0.00359	0.000088	0.00004	226.495	91.13063936	1.00161531	1.641E-14
M1907-11	1250 °C		4.812149	0.04956	0.968806	0.00034	4.893142	0.04894	0.000903	0.00276	0.000173	0.00004	226.512	91.16060804	1.00161543	1.949E-14
M1907-12	1300 °C		5.038392	0.05050	2.685653	0.00064	5.109791	0.05104	0.001466	0.00123	0.000141	0.00001	226.528	91.19058658	1.00161555	5.403E-14
M1907-13	1400 °C		5.075160	0.08366	0.180939	0.00008	5.290651	0.05317	0.013330	0.01223	0.000628	0.00022	226.544	91.21932526	1.00161566	3.639E-15
M1907-14	1500 °C		5.075622	0.08362	0.088221	0.00008	5.642223	0.05707	0.047965	0.01953	0.001814	0.00022	226.563	91.25307353	1.00161579	1.774E-15

Procedure Blanks		36Ar	1σ	37Ar	1σ	38Ar	1σ	39Ar	1σ	40Ar	1σ
M1907-1	650 °C	0.000056	0.000005	0.000161	0.000003	0.000022	0.000003	0.000028	0.000003	0.008388	0.000016
M1907-2	750 °C	0.000046	0.000005	0.000165	0.000008	0.000016	0.000005	0.000030	0.000004	0.005026	0.000018
M1907-3	850 °C	0.000056	0.000004	0.000190	0.000016	0.000027	0.000005	0.000038	0.000005	0.006494	0.000063
M1907-4	900 °C	0.000056	0.000004	0.000190	0.000016	0.000027	0.000005	0.000038	0.000005	0.006494	0.000063
M1907-5	950 °C	0.000056	0.000004	0.000190	0.000016	0.000027	0.000005	0.000038	0.000005	0.006494	0.000063
M1907-6	1000 °C	0.000065	0.000003	0.000160	0.000005	0.000027	0.000005	0.000030	0.000003	0.009657	0.000021
M1907-7	1050 °C	0.000065	0.000003	0.000160	0.000005	0.000027	0.000005	0.000030	0.000003	0.009657	0.000021
M1907-8	1100 °C	0.000065	0.000003	0.000160	0.000005	0.000027	0.000005	0.000030	0.000003	0.009657	0.000021
M1907-9	1150 °C	0.000075	0.000004	0.000162	0.000005	0.000028	0.000004	0.000310	0.000007	0.015500	0.000021
M1907-10	1200 °C	0.000075	0.000004	0.000162	0.000005	0.000028	0.000004	0.000310	0.000007	0.015500	0.000021
M1907-11	1250 °C	0.000053	0.000005	0.000159	0.000003	0.000027	0.000002	0.000043	0.000004	0.007736	0.000014
M1907-12	1300 °C	0.000053	0.000005	0.000159	0.000003	0.000027	0.000002	0.000043	0.000004	0.007736	0.000014
M1907-13	1400 °C	0.000053	0.000006	0.000153	0.000003	0.000019	0.000003	0.000049	0.000004	0.007325	0.000017
M1907-14	1500 °C	0.000054	0.000002	0.000147	0.000003	0.000020	0.000003	0.000136	0.000007	0.009297	0.000030

Intercept Values		36Ar	1σ	r2		37Ar	1σ	r2		38Ar	1σ	r2		39Ar	1σ	r2		40Ar	1σ	r2	
M1907-1	650 °C	0.000390	0.000005	0.6962	LIN 11 of 11	0.000163	0.000006		AVE 11 of 11	0.006197	0.000027	0.9402	EXP 11 of 11	0.004526	0.000024	0.9115	EXP 11 of 11	0.110784	0.000112	0.9962	EXP 11 of 11
M1907-2	750 °C	0.000265	0.000004	0.4569	LIN 11 of 11	0.000179	0.000007	0.1199	LIN 11 of 11	0.000638	0.000010	0.5487	LIN 11 of 11	0.015860	0.000033	0.9852	EXP 11 of 11	0.115786	0.000101	0.9970	EXP 11 of 11
M1907-3	850 °C	0.000160	0.000004	0.3132	LIN 11 of 11	0.000166	0.000009		AVE 11 of 11	0.000914	0.000011	0.3460	LIN 11 of 11	0.062463	0.000048	0.9980	EXP 11 of 11	0.301607	0.000202	0.9983	EXP 11 of 11
M1907-4	900 °C	0.000120	0.000002	0.6861	LIN 11 of 11	0.000167	0.000004	0.3167	LIN 11 of 11	0.000912	0.000014	0.4809	LIN 11 of 11	0.064560	0.000054	0.9976	EXP 11 of 11	0.310978	0.000178	0.9988	EXP 11 of 11
M1907-5	950 °C	0.000120	0.000004		AVE 11 of 11	0.000160	0.000007		AVE 11 of 11	0.001213	0.000011	0.8616	EXP 11 of 11	0.083108	0.000052	0.9988	EXP 11 of 11	0.408242	0.000120	0.9997	EXP 11 of 11
M1907-6	1000 °C	0.000180	0.000005	0.3952	LIN 11 of 11	0.000165	0.000007		AVE 11 of 11	0.004412	0.000021	0.9215	EXP 11 of 11	0.316454	0.000151	0.9992	EXP 11 of 11	1.597019	0.000267	0.9999	EXP 11 of 11
M1907-7	1050 °C	0.000137	0.000004	0.2521	LIN 11 of 11	0.000177	0.000005	0.1555	LIN 11 of 11	0.005706	0.000020	0.9503	EXP 11 of 11	0.407962	0.000076	0.9999	EXP 11 of 11	1.971121	0.000330	0.9999	EXP 11 of 11
M1907-8	1100 °C	0.000128	0.000007		AVE 11 of 11	0.000165	0.000004		AVE 11 of 11	0.002961	0.000015	0.9160	EXP 11 of 11	0.209788	0.000118	0.9989	EXP 11 of 11	0.977760	0.000266	0.9997	EXP 11 of 11
M1907-9	1150 °C	0.000089	0.000005		AVE 11 of 11	0.000155	0.000004	0.3445	LIN 11 of 11	0.001869	0.000017	0.8069	EXP 11 of 11	0.134237	0.000128	0.9969	EXP 11 of 11	0.638019	0.000225	0.9996	EXP 11 of 11
M1907-10	1200 °C	0.000091	0.000005		AVE 11 of 11	0.000169	0.000005	0.2027	LIN 11 of 11	0.002468	0.000008	0.9696	EXP 11 of 11	0.173407	0.000104	0.9988	EXP 11 of 11	0.835828	0.000168	0.9999	EXP 11 of 11
M1907-11	1250 °C	0.000089	0.000006		AVE 11 of 11	0.000161	0.000005		AVE 11 of 11	0.002792	0.000015	0.8965	EXP 11 of 11	0.200892	0.000113	0.9990	EXP 11 of 11	0.982458	0.000313	0.9997	EXP 11 of 11
M1907-12	1300 °C	0.000131	0.000005		AVE 11 of 11	0.000168	0.000007		AVE 11 of 11	0.007669	0.000034	0.9295	EXP 11 of 11	0.533077	0.000173	0.9996	EXP 11 of 11	2.709090	0.000534	0.9999	EXP 11 of 11
M1907-13	1400 °C	0.000075	0.000005		AVE 11 of 11	0.000158	0.000004		AVE 11 of 11	0.000561	0.000005	0.4300	EXP 11 of 11	0.034726	0.000038	0.9957	EXP 11 of 11	0.189285	0.000071	0.9994	EXP 11 of 11
M1907-14	1500 °C	0.000084	0.000003	0.1261	LIN 11 of 11	0.000156	0.000002	0.4210	LIN 11 of 11	0.000283	0.000003	0.0887	LIN 11 of 11	0.015985	0.000020	0.9931	EXP 11 of 11	0.097985	0.000076	0.9973	EXP 11 of 11

Sample Parameters		Sample	Material	Location	Analyst	Temp	Standard (in Ma)	%1σ	J	%1σ	MDF	%1σ
M1907-1	650 °C	AR-04-64	Muscovite	Arménie	Yann ROLLAND	650	1073.6	0.5	0.0171061	0.25	1.009917	1
M1907-2	750 °C	AR-04-70	Muscovite	Arménie	Yann ROLLAND	750	1073.6	0.5	0.0171061	0.25	1.009917	1
M1907-3	850 °C	AR-04-71	Muscovite	Arménie	Yann ROLLAND	850	1073.6	0.5	0.0171061	0.25	1.009917	1
M1907-4	900 °C	AR-04-72	Muscovite	Arménie	Yann ROLLAND	900	1073.6	0.5	0.0171061	0.25	1.009917	1
M1907-5	950 °C	AR-04-73	Muscovite	Arménie	Yann ROLLAND	950	1073.6	0.5	0.0171061	0.25	1.009917	1
M1907-6	1000 °C	AR-04-74	Muscovite	Arménie	Yann ROLLAND	1000	1073.6	0.5	0.0171061	0.25	1.009917	1
M1907-7	1050 °C	AR-04-75	Muscovite	Arménie	Yann ROLLAND	1050	1073.6	0.5	0.0171061	0.25	1.009917	1
M1907-8	1100 °C	AR-04-76	Muscovite	Arménie	Yann ROLLAND	1100	1073.6	0.5	0.0171061	0.25	1.009917	1
M1907-9	1150 °C	AR-04-77	Muscovite	Arménie	Yann ROLLAND	1150	1073.6	0.5	0.0171061	0.25	1.009917	1
M1907-10	1200 °C	AR-04-65	Muscovite	Arménie	Yann ROLLAND	1200	1073.6	0.5	0.0171061	0.25	1.009917	1
M1907-11	1250 °C	AR-04-66	Muscovite	Arménie	Yann ROLLAND	1250	1073.6	0.5	0.0171061	0.25	1.009917	1
M1907-12	1300 °C	AR-04-67	Muscovite	Arménie	Yann ROLLAND	1300	1073.6	0.5	0.0171061	0.25	1.009917	1
M1907-13	1400 °C	AR-04-68	Muscovite	Arménie	Yann ROLLAND	1400	1073.6	0.5	0.0171061	0.25	1.009917	1
M1907-14	1500 °C	AR-04-69	Muscovite	Arménie	Yann ROLLAND	1500	1073.6	0.5	0.0171061	0.25	1.009917	1

Volume Ratio	Sensitivity (mol/volt)	Day	Month	Year	Hour	Min	Resist	Irradiation	Project	Experiment	Nmb	Standard Name
1	2.000E-14	14	NOV	2005	07	02	001	MC45	Rolland_Hassig	M1907	01	Hb3gr
1	2.000E-14	14	NOV	2005	07	24	001	MC45	Rolland_Hassig	M1907	01	Hb3gr
1	2.000E-14	14	NOV	2005	07	49	001	MC45	Rolland_Hassig	M1907	01	Hb3gr
1	2.000E-14	14	NOV	2005	08	12	001	MC45	Rolland_Hassig	M1907	01	Hb3gr
1	2.000E-14	14	NOV	2005	08	36	001	MC45	Rolland_Hassig	M1907	01	Hb3gr
1	2.000E-14	14	NOV	2005	09	00	001	MC45	Rolland_Hassig	M1907	01	Hb3gr
1	2.000E-14	14	NOV	2005	09	25	001	MC45	Rolland_Hassig	M1907	01	Hb3gr
1	2.000E-14	14	NOV	2005	09	48	001	MC45	Rolland_Hassig	M1907	01	Hb3gr
1	2.000E-14	14	NOV	2005	10	16	001	MC45	Rolland_Hassig	M1907	01	Hb3gr
1	2.000E-14	14	NOV	2005	10	35	001	MC45	Rolland_Hassig	M1907	01	Hb3gr
1	2.000E-14	14	NOV	2005	10	59	001	MC45	Rolland_Hassig	M1907	01	Hb3gr
1	2.000E-14	14	NOV	2005	11	23	001	MC45	Rolland_Hassig	M1907	01	Hb3gr
1	2.000E-14	14	NOV	2005	11	46	001	MC45	Rolland_Hassig	M1907	01	Hb3gr
1	2.000E-14	14	NOV	2005	12	13	001	MC45	Rolland_Hassig	M1907	01	Hb3gr

Irradiation Constants		40/36(a)	%1σ	40/36(c)	%1σ	38/36(a)	%1σ	38/36(c)	%1σ	39/37(ca)	%1σ	38/37(ca)	%1σ	36/37(ca)	%1σ
M1907-1	650 °C	298.56	0.1	0.018	35	0.1885	0.16	1.7	3	0.00073	4	0.006	90	0.000282	1
M1907-2	750 °C	298.56	0.1	0.018	35	0.1885	0.16	1.7	3	0.00073	4	0.006	90	0.000282	1
M1907-3	850 °C	298.56	0.1	0.018	35	0.1885	0.16	1.7	3	0.00073	4	0.006	90	0.000282	1
M1907-4	900 °C	298.56	0.1	0.018	35	0.1885	0.16	1.7	3	0.00073	4	0.006	90	0.000282	1
M1907-5	950 °C	298.56	0.1	0.018	35	0.1885	0.16	1.7	3	0.00073	4	0.006	90	0.000282	1
M1907-6	1000 °C	298.56	0.1	0.018	35	0.1885	0.16	1.7	3	0.00073	4	0.006	90	0.000282	1
M1907-7	1050 °C	298.56	0.1	0.018	35	0.1885	0.16	1.7	3	0.00073	4	0.006	90	0.000282	1
M1907-8	1100 °C	298.56	0.1	0.018	35	0.1885	0.16	1.7	3	0.00073	4	0.006	90	0.000282	1
M1907-9	1150 °C	298.56	0.1	0.018	35	0.1885	0.16	1.7	3	0.00073	4	0.006	90	0.000282	1
M1907-10	1200 °C	298.56	0.1	0.018	35	0.1885	0.16	1.7	3	0.00073	4	0.006	90	0.000282	1
M1907-11	1250 °C	298.56	0.1	0.018	35	0.1885	0.16	1.7	3	0.00073	4	0.006	90	0.000282	1
M1907-12	1300 °C	298.56	0.1	0.018	35	0.1885	0.16	1.7	3	0.00073	4	0.006	90	0.000282	1
M1907-13	1400 °C	298.56	0.1	0.018	35	0.1885	0.16	1.7	3	0.00073	4	0.006	90	0.000282	1
M1907-14	1500 °C	298.56	0.1	0.018	35	0.1885	0.16	1.7	3	0.00073	4	0.006	90	0.000282	1

40/39(k)	%1σ	38/39(k)	%1σ	36/38(cl)	%1σ	K/Ca	%1σ	K/Cl	%1σ	Ca/Cl	%1σ
0.0297	2	0.012	2	316	5	0.1616	4	5.4	33	33.3	33
0.0297	2	0.012	2	316	5	0.1616	4	5.4	33	33.3	33
0.0297	2	0.012	2	316	5	0.1616	4	5.4	33	33.3	33
0.0297	2	0.012	2	316	5	0.1616	4	5.4	33	33.3	33
0.0297	2	0.012	2	316	5	0.1616	4	5.4	33	33.3	33
0.0297	2	0.012	2	316	5	0.1616	4	5.4	33	33.3	33
0.0297	2	0.012	2	316	5	0.1616	4	5.4	33	33.3	33
0.0297	2	0.012	2	316	5	0.1616	4	5.4	33	33.3	33
0.0297	2	0.012	2	316	5	0.1616	4	5.4	33	33.3	33
0.0297	2	0.012	2	316	5	0.1616	4	5.4	33	33.3	33
0.0297	2	0.012	2	316	5	0.1616	4	5.4	33	33.3	33
0.0297	2	0.012	2	316	5	0.1616	4	5.4	33	33.3	33
0.0297	2	0.012	2	316	5	0.1616	4	5.4	33	33.3	33

Annexe 9 - Résultats de datation (2) sur Muscovite AR-03-62M.

Incremental Heating		36Ar(a)	37Ar(ca)	38Ar(cl)	39Ar(k)	40Ar(r)	Age ± 2σ (Ma)	40Ar(r) (%)	39Ar(k) (%)	K/Ca ± 2σ
H409-1	355.00 W	0.000462	0.000008	0.000000	0.168062	0.604200	104.72 ± 2.85	80.89	4.96	3284 ± 41511
H409-2	365.00 W	0.000218	0.000029	0.000000	0.337375	1.547168	132.54 ± 2.62	95.36	9.95	1866 ± 6482
H409-3	373.00 W	0.000062	0.000012	0.000000	0.264496	1.252341	136.68 ± 2.66	97.94	7.80	3676 ± 21064
H409-4	379.00 W	0.000065	0.000014	0.000000	0.406773	1.971187	139.77 ± 2.73	98.43	12.00	4584 ± 22364
H409-5	384.00 W	0.000072	0.000049	0.000000	0.425181	2.017713	136.98 ± 2.67	98.33	12.54	1408 ± 2612
H409-6	387.00 W	0.000025	0.000046	0.000000	0.157214	0.725169	133.28 ± 2.82	98.34	4.64	548 ± 1069
H409-7	398.00 W	0.000073	0.000017	0.000000	0.221367	1.003557	131.08 ± 2.59	97.25	6.53	2106 ± 11171
H409-8	416.00 W	0.000044	0.000030	0.000000	0.112155	0.509439	131.32 ± 2.85	96.88	3.31	608 ± 2351
H409-9	450.00 W	0.000123	0.000029	0.000000	0.275118	1.276800	134.07 ± 2.69	96.61	8.11	1516 ± 4209
H409-10	510.00 W	0.000052	0.000047	0.000000	0.421655	2.100328	143.52 ± 2.83	98.68	12.43	1452 ± 2864
H409-11	572.00 W	0.000001	0.000052	0.000000	0.214500	1.096436	147.13 ± 2.95	99.41	6.33	663 ± 1024
H409-12	800.00 W	0.000007	0.000096	0.000000	0.387055	1.987776	147.79 ± 2.90	99.32	11.41	653 ± 740
	Σ	0.001203	0.000187	0.000000	3.390953	16.092113				

Information on Analysis
Sample = AR-03-62M
Material = Muscovite
Location = Arménie
Analyst = Yann ROLLAND
Project = ROLLAND_HASSIG
Mass Discrimination Law = LIN
Irradiation = MC40
J = 0.01662300 ± 0.00001662
Hb3gr = 1073.600 ± 5.368 Ma

Results	40(r)/39(k) ± 2σ	Age ± 2σ (Ma)	MSWD	39Ar(k) (%,n)	K/Ca ± 2σ
Age Plateau	4.7443 ± 0.1321	136.95 ± 3.68	16.11	78.77	492 ± 557
Error Mean	± 2.78%	± 2.69%		9	
	Minimal External Error ± 3.71		2.31	Statistical T Ratio	
	Analytical Error ± 3.67		4.0139	Error Magnification	
Total Fusion Age	4.7456 ± 0.0302	136.98 ± 0.88		12	2937 ± 5023
	± 0.64%	± 0.64%			
	Minimal External Error ± 1.01				
	Analytical Error ± 0.84				

Normal Isochron		39(k)/36(a) ± 2σ	40(a+r)/36(a) ± 2σ	r.i.
H409-1	355.00 W	364.2 ± 31.6	1607.8 ± 135.7	0.9724
H409-2	365.00 W	1544.4 ± 171.5	7381.2 ± 806.1	0.9837
H409-3	373.00 W	4275.7 ± 857.8	20543.4 ± 4101.0	0.9950
H409-4	379.00 W	6269.0 ± 2232.3	30677.6 ± 10906.6	0.9984
H409-5	384.00 W	5882.3 ± 1843.0	28213.2 ± 8821.8	0.9980
H409-6	387.00 W	6194.3 ± 5325.9	28870.4 ± 24816.3	0.9997
H409-7	398.00 W	3036.3 ± 633.9	14063.3 ± 2922.7	0.9954
H409-8	416.00 W	2559.4 ± 1017.6	11924.2 ± 4735.1	0.9987
H409-9	450.00 W	2244.0 ± 450.4	10712.6 ± 2139.7	0.9950
H409-10	510.00 W	8080.3 ± 5244.2	40547.7 ± 26303.2	0.9995
H409-11	572.00 W	379363.0 ± 15034541.4	1939442.5 ± 76862056.7	1.0000
H409-12	800.00 W	57321.8 ± 241771.8	294682.7 ± 1242897.5	1.0000

Results	40(a)/36(a) ± 2σ	40(r)/39(k) ± 2σ	Age ± 2σ (Ma)	MSWD
Normal Isochron Error Chron	1276.4164 ± 620.8908 ± 48.64%	5.1691 ± 0.1652 ± 3.20%	148.72 ± 4.57 ± 3.07%	2.49
			Minimal External Error ± 4.60	
			Analytical Error ± 4.56	

Statistics				
	Statistical F ratio	2.01	Convergence	0.0000068624
	Error Magnification	1.5787	Number of Iterations	1
	Number of Data Points	9	Calculated Line	Weighted York-2

Inverse Isochron		39(k)/40(a+r) ± 2σ	36(a)/40(a+r) ± 2σ	r.i.
H409-1	355.00 W	0.226502 ± 0.004587	0.000622 ± 0.000052	0.0022
H409-2	365.00 W	0.209240 ± 0.004183	0.000135 ± 0.000015	0.0001
H409-3	373.00 W	0.208132 ± 0.004162	0.000049 ± 0.000010	0.0002
H409-4	379.00 W	0.204351 ± 0.004082	0.000033 ± 0.000012	0.0000
H409-5	384.00 W	0.208494 ± 0.004167	0.000035 ± 0.000011	0.0000
H409-6	387.00 W	0.214555 ± 0.004291	0.000035 ± 0.000030	0.0000
H409-7	398.00 W	0.215900 ± 0.004320	0.000071 ± 0.000015	0.0001
H409-8	416.00 W	0.214641 ± 0.004302	0.000084 ± 0.000033	0.0001
H409-9	450.00 W	0.209469 ± 0.004190	0.000093 ± 0.000019	0.0001
H409-10	510.00 W	0.199279 ± 0.003980	0.000025 ± 0.000016	0.0000
H409-11	572.00 W	0.195604 ± 0.003908	0.000001 ± 0.000020	0.0000
H409-12	800.00 W	0.194521 ± 0.003889	0.000003 ± 0.000014	0.0000

Results	40(a)/36(a) ± 2σ	40(r)/39(k) ± 2σ	Age ± 2σ (Ma)	MSWD
Inverse Isochron Error Chron	1356.7968 ± 360.6946 ± 26.58%	5.1279 ± 0.0842 ± 1.64%	147.58 ± 2.34 ± 1.59%	2.81
		Minimal External Error	± 2.40	
		Analytical Error	± 2.33	

Statistics				
Statistical F ratio	2.01	Convergence	0.0015705583
Error Magnification	1.6776	Number of Iterations	6
Number of Data Points	9	Calculated Line	Weighted York-2

Relative Abundances		36Ar	%1σ	37Ar	%1σ	38Ar	%1σ	39Ar	%1σ	40Ar	%1σ	Age ± 2σ (Ma)	40Ar(r) (%)	39Ar(k) (%)	K/Ca ± 2σ
H409-1	355.00 W	0.0004615	4.218	0.0000083	631.924	0.0050291	2.034	0.1680617	1.008	0.7469783	0.095	104.72 ± 2.85	80.89	4.96	3284 ± 41511
H409-2	365.00 W	0.0002184	5.460	0.0000292	173.591	0.0064769	2.054	0.3373754	0.999	1.6224074	0.025	132.54 ± 2.62	95.36	9.95	1866 ± 6482
H409-3	373.00 W	0.0000619	9.981	0.0000116	286.461	0.0036713	2.062	0.2644959	0.999	1.2786653	0.038	136.68 ± 2.66	97.94	7.80	3676 ± 21064
H409-4	379.00 W	0.0000649	17.775	0.0000143	243.908	0.0054584	1.995	0.4067733	0.999	2.0026406	0.023	139.77 ± 2.73	98.43	12.00	4584 ± 22364
H409-5	384.00 W	0.0000723	15.631	0.0000488	92.645	0.0057854	2.018	0.4251811	0.999	2.0519213	0.018	136.98 ± 2.67	98.33	12.54	1408 ± 2612
H409-6	387.00 W	0.0000254	43.001	0.0000463	97.401	0.0022297	2.145	0.1572144	0.999	0.7374157	0.038	133.28 ± 2.82	98.34	4.64	548 ± 1069
H409-7	398.00 W	0.0000729	10.391	0.0000170	265.200	0.0034314	2.041	0.2213674	1.000	1.0318987	0.024	131.08 ± 2.59	97.25	6.53	2106 ± 11171
H409-8	416.00 W	0.0000438	19.851	0.0000298	193.253	0.0017634	2.345	0.1121547	1.001	0.5258525	0.034	131.32 ± 2.85	96.88	3.31	608 ± 2351
H409-9	450.00 W	0.0001226	9.987	0.0000293	138.771	0.0050611	2.019	0.2751180	1.000	1.3215758	0.024	134.07 ± 2.69	96.61	8.11	1516 ± 4209
H409-10	510.00 W	0.0000522	32.443	0.0000469	98.494	0.0058517	2.027	0.4216550	0.998	2.1284306	0.023	143.52 ± 2.83	98.68	12.43	1452 ± 2864
H409-11	572.00 W	0.0000006	2034.615	0.0000523	77.151	0.0027586	2.182	0.2145004	0.999	1.1029753	0.011	147.13 ± 2.95	99.41	6.33	663 ± 1024
H409-12	800.00 W	0.0000067	211.734	0.0000958	56.496	0.0051061	2.043	0.3870553	0.999	2.0012874	0.016	147.79 ± 2.90	99.32	11.41	653 ± 740
	Σ	0.0012031	3.562	0.0001866	85.429	0.0526230	0.622	3.3909526	0.308	16.5520490	0.008				

Information on Analysis and Constants Used in Calculations

Sample = AR-03-62M
Material = Muscovite
Location = Arménie
Analyst = Yann ROLLAND
Project = ROLLAND_HASSIG
Mass Discrimination Law = LIN
Irradiation = MC40
J = 0.01662300 ± 0.00001662
Hb3gr = 1073.600 ± 5.368 Ma
IGSN = Undefined
Preferred Age = Undefined
Classification = Undefined
Experiment Type = Undefined
Extraction Method = Undefined
Heating = 60 sec
Isolation = 2.00 min
Instrument = VG3600
Lithology = Undefined
Lat-Lon = Undefined - Undefined

Age Equations = Conventional
Negative Intensities = Allowed
Decay Constant 40K = 5.543 ± 0.010 E-10 1/a
Decay Constant 39Ar = 2.940 ± 0.029 E-07 1/h
Decay Constant 37Ar = 8.220 ± 0.010 E-04 1/h
Decay Constant 36Cl = 2.310 ± 0.016 E-06 1/a
Production Ratio 36/38 in Cl = 316.0 ± 15.8

Results	40(r)/39(k) ± 2σ	Age ± 2σ (Ma)	MSWD	39Ar(k) (%,n)	K/Ca ± 2σ
Age Plateau Error Mean	4.7443 ± 0.1321 ± 2.78%	136.95 ± 3.68 ± 2.69%	16.11	78.77 9	492 ± 557
	Minimal External Error	± 3.71	2.31	Statistical T Ratio	
	Analytical Error	± 3.67	4.0139	Error Magnification	
Total Fusion Age	4.7456 ± 0.0302 ± 0.64%	136.98 ± 0.88 ± 0.64%		12	2937 ± 5023
	Minimal External Error	± 1.01			
	Analytical Error	± 0.84			
Normal Isochron Error Chron	5.1691 ± 0.1652 ± 3.20%	148.72 ± 4.57 ± 3.07%	2.49	78.77 9	
	Minimal External Error	± 4.60	2.01	Statistical F ratio	
	Analytical Error	± 4.56	1.5787	Error Magnification	
Inverse Isochron Error Chron	5.1279 ± 0.0842 ± 1.64%	147.58 ± 2.34 ± 1.59%	2.81	78.77 9	
	Minimal External Error	± 2.40	2.01	Statistical F ratio	
	Analytical Error	± 2.33	1.6776	Error Magnification	

Degassing Patterns		36Ar(a)	%1σ	36Ar(c)	%1σ	36Ar(ca)	%1σ	36Ar(cl)	%1σ	37Ar(ca)	%1σ	38Ar(a)	%1σ	38Ar(c)	%1σ	38Ar(k)	%1σ
H409-1	355.00 W	0.000462	4.22	0.000000	0.00	0.000000	631.92	0.000000	0.00	0.000008	631.92	0.000087	4.22	0.000000	0.00	0.002017	2.24
H409-2	365.00 W	0.000218	5.46	0.000000	0.00	0.000000	173.59	0.000000	0.00	0.000029	173.59	0.000041	5.46	0.000000	0.00	0.004049	2.24
H409-3	373.00 W	0.000062	9.98	0.000000	0.00	0.000000	286.46	0.000000	0.00	0.000012	286.46	0.000012	9.98	0.000000	0.00	0.003174	2.24
H409-4	379.00 W	0.000065	17.78	0.000000	0.00	0.000000	243.91	0.000000	0.00	0.000014	243.91	0.000012	17.78	0.000000	0.00	0.004881	2.24
H409-5	384.00 W	0.000072	15.63	0.000000	0.00	0.000000	92.65	0.000000	0.00	0.000049	92.64	0.000014	15.63	0.000000	0.00	0.005102	2.24
H409-6	387.00 W	0.000025	42.98	0.000000	0.00	0.000000	97.41	0.000000	0.00	0.000046	97.40	0.000005	42.98	0.000000	0.00	0.001887	2.24
H409-7	398.00 W	0.000073	10.39	0.000000	0.00	0.000000	265.20	0.000000	0.00	0.000017	265.20	0.000014	10.39	0.000000	0.00	0.002656	2.24
H409-8	416.00 W	0.000044	19.85	0.000000	0.00	0.000000	193.26	0.000000	0.00	0.000030	193.25	0.000008	19.86	0.000000	0.00	0.001346	2.24
H409-9	450.00 W	0.000123	9.99	0.000000	0.00	0.000000	138.77	0.000000	0.00	0.000029	138.77	0.000023	9.99	0.000000	0.00	0.003301	2.24
H409-10	510.00 W	0.000052	32.43	0.000000	0.00	0.000000	98.50	0.000000	0.00	0.000047	98.49	0.000010	32.44	0.000000	0.00	0.005060	2.24
H409-11	572.00 W	0.000001	1981.55	0.000000	0.00	0.000000	77.16	0.000000	0.00	0.000052	77.15	0.000000	1981.55	0.000000	0.00	0.002574	2.24
H409-12	800.00 W	0.000007	210.89	0.000000	0.00	0.000000	56.50	0.000000	0.00	0.000096	56.50	0.000001	210.89	0.000000	0.00	0.004645	2.24
	Σ	0.001203	3.56	0.000000	0.00	0.000000	85.43	0.000000	0.00	0.000187	85.43	0.000227	3.56	0.000000	0.00	0.040691	0.69
	Σ							0.001203	3.56	0.000187	85.43						

38Ar(ca)	%1σ	38Ar(cl)	%1σ	39Ar(k)	%1σ	39Ar(ca)	%1σ	40Ar(r)	%1σ	40Ar(a)	%1σ	40Ar(c)	%1σ	40Ar(k)	%1σ
0.000000	638.30	0.000000	0.00	0.168062	1.01	0.000000	631.94	0.604200	0.97	0.137787	4.22	0.000000	0.00	0.004991	2.24
0.000000	195.53	0.000000	0.00	0.337375	1.00	0.000000	173.64	1.547168	0.23	0.065219	5.46	0.000000	0.00	0.010020	2.24
0.000000	300.27	0.000000	0.00	0.264496	1.00	0.000000	286.49	1.252341	0.15	0.018469	9.98	0.000000	0.00	0.007856	2.24
0.000000	259.98	0.000000	0.00	0.406773	1.00	0.000000	243.94	1.971187	0.18	0.019372	17.78	0.000000	0.00	0.012081	2.24
0.000000	129.16	0.000000	0.00	0.425181	1.00	0.000000	92.73	2.017713	0.17	0.021580	15.63	0.000000	0.00	0.012628	2.24
0.000000	132.62	0.000000	0.00	0.157214	1.00	0.000000	97.48	0.725169	0.45	0.007578	42.98	0.000000	0.00	0.004669	2.24
0.000000	280.05	0.000000	0.00	0.221367	1.00	0.000000	265.23	1.003557	0.23	0.021767	10.39	0.000000	0.00	0.006575	2.24
0.000000	213.18	0.000000	0.00	0.112155	1.00	0.000000	193.29	0.509439	0.51	0.013083	19.86	0.000000	0.00	0.003331	2.24
0.000000	165.40	0.000000	0.00	0.275118	1.00	0.000000	138.83	1.276800	0.29	0.036605	9.99	0.000000	0.00	0.008171	2.24
0.000000	133.42	0.000000	0.00	0.421655	1.00	0.000000	98.58	2.100328	0.24	0.015580	32.44	0.000000	0.00	0.012523	2.24
0.000000	118.54	0.000000	0.00	0.214500	1.00	0.000000	77.25	1.096436	0.31	0.000169	1981.55	0.000000	0.00	0.006371	2.24
0.000001	106.26	0.000000	0.00	0.387055	1.00	0.000000	56.64	1.987776	0.21	0.002016	210.89	0.000000	0.00	0.011496	2.24
0.000001	111.36	0.000000	0.00	3.390953	0.31	0.000000	85.49	16.092113	0.08	0.359225	3.56	0.000000	0.00	0.100711	0.69
		0.040917	0.69			3.390953	0.31							16.552049	0.11

Additional Parameters		40(r)/39(k)	1σ	40(r+a)	1σ	40Ar/39Ar	1σ	37Ar/39Ar	1σ	36Ar/39Ar	1σ	Time (days)	37Ar (decay)	39Ar (decay)	40Ar (moles)
H409-1	355.00 W	3.595109	0.05028	0.741987	0.00072	4.444667	0.04500	0.000049	0.00031	0.002746	0.00012	- 22.938	2.97382930	1.00188440	1.494E-14
H409-2	365.00 W	4.585894	0.04704	1.612387	0.00046	4.808908	0.04806	0.000087	0.00015	0.000647	0.00004	- 22.922	2.97472574	1.00188451	3.245E-14
H409-3	373.00 W	4.734822	0.04785	1.270810	0.00051	4.834348	0.04833	0.000044	0.00013	0.000234	0.00002	- 22.907	2.97562246	1.00188462	2.557E-14
H409-4	379.00 W	4.845910	0.04914	1.990559	0.00054	4.923235	0.04917	0.000035	0.00009	0.000160	0.00003	- 22.878	2.97729434	1.00188482	4.005E-14
H409-5	384.00 W	4.745538	0.04809	2.039293	0.00047	4.825993	0.04823	0.000115	0.00011	0.000170	0.00003	- 22.862	2.97827343	1.00188494	4.104E-14
H409-6	387.00 W	4.612609	0.05057	0.732746	0.00030	4.690509	0.04690	0.000295	0.00029	0.000161	0.00007	- 22.847	2.97917122	1.00188505	1.475E-14
H409-7	398.00 W	4.533444	0.04649	1.025324	0.00029	4.661475	0.04663	0.000077	0.00020	0.000329	0.00003	- 22.813	2.98113097	1.00188528	2.064E-14
H409-8	416.00 W	4.542287	0.05107	0.522522	0.00020	4.688637	0.04698	0.000266	0.00051	0.000391	0.00008	- 22.798	2.98202962	1.00188539	1.052E-14
H409-9	450.00 W	4.640919	0.04828	1.313405	0.00037	4.803670	0.04803	0.000107	0.00015	0.000446	0.00004	- 22.782	2.98296940	1.00188550	2.643E-14
H409-10	510.00 W	4.981152	0.05117	2.115907	0.00057	5.047802	0.05041	0.000111	0.00011	0.000124	0.00004	- 22.753	2.98464541	1.00188570	4.257E-14
H409-11	572.00 W	5.111578	0.05339	1.096605	0.00019	5.142066	0.05136	0.000244	0.00019	0.000003	0.00005	- 22.738	2.98554511	1.00188581	2.206E-14
H409-12	800.00 W	5.135637	0.05250	1.989792	0.00041	5.170547	0.05168	0.000247	0.00014	0.000017	0.00004	- 22.720	2.98660875	1.00188594	4.003E-14

Procedure Blanks		36Ar	1σ	37Ar	1σ	38Ar	1σ	39Ar	1σ	40Ar	1σ
H409-1	355.00 W	0.000250	0.000004	0.000534	0.000010	0.000122	0.000011	0.000059	0.000006	0.002294	0.000015
H409-2	365.00 W	0.000250	0.000004	0.000534	0.000010	0.000122	0.000011	0.000059	0.000006	0.002294	0.000015
H409-3	373.00 W	0.000250	0.000004	0.000534	0.000010	0.000122	0.000011	0.000059	0.000006	0.002294	0.000015
H409-4	379.00 W	0.000249	0.000008	0.000543	0.000010	0.000121	0.000006	0.000264	0.000008	0.003730	0.000035
H409-5	384.00 W	0.000249	0.000008	0.000543	0.000010	0.000121	0.000006	0.000264	0.000008	0.003730	0.000035
H409-6	387.00 W	0.000249	0.000008	0.000543	0.000010	0.000121	0.000006	0.000264	0.000008	0.003730	0.000035
H409-7	398.00 W	0.000253	0.000005	0.000538	0.000010	0.000128	0.000004	0.000194	0.000004	0.005150	0.000028
H409-8	416.00 W	0.000253	0.000005	0.000538	0.000010	0.000128	0.000004	0.000194	0.000004	0.005150	0.000028
H409-9	450.00 W	0.000253	0.000005	0.000538	0.000010	0.000128	0.000004	0.000194	0.000004	0.005150	0.000028
H409-10	510.00 W	0.000266	0.000011	0.000567	0.000009	0.000168	0.000008	0.000422	0.000008	0.003911	0.000039
H409-11	572.00 W	0.000266	0.000011	0.000567	0.000009	0.000168	0.000008	0.000422	0.000008	0.003911	0.000039
H409-12	800.00 W	0.000266	0.000011	0.000567	0.000009	0.000168	0.000008	0.000422	0.000008	0.003911	0.000039

Intercept Values		36Ar	1σ	r2		37Ar	1σ	r2		38Ar	1σ	r2		39Ar	1σ	r2		40Ar	1σ	r2	
H409-1	355.00 W	0.000729	0.000007	0.4922	LIN 11 of 11	0.000531	0.000015		AVE 11 of 11	0.005247	0.000021	0.9854	EXP 9 of 11	0.169399	0.000238	0.9973	EXP 11 of 11	0.749272	0.000707	0.9984	EXP 11 of 11
H409-2	365.00 W	0.000477	0.000008		AVE 11 of 11	0.000524	0.000015		AVE 11 of 11	0.006722	0.000034	0.9681	EXP 11 of 11	0.340002	0.000159	0.9997	EXP 11 of 11	1.624701	0.000401	0.9999	EXP 11 of 11
H409-3	373.00 W	0.000315	0.000005	0.6800	LIN 11 of 11	0.000538	0.000006	0.4844	LIN 11 of 11	0.003863	0.000019	0.9563	EXP 11 of 11	0.266567	0.000115	0.9998	EXP 11 of 11	1.280959	0.000480	0.9998	EXP 11 of 11
H409-4	379.00 W	0.000316	0.000009	0.4078	LIN 11 of 11	0.000548	0.000006	0.2713	LIN 11 of 11	0.005683	0.000012	0.9936	EXP 11 of 11	0.410133	0.000118	0.9999	EXP 11 of 11	2.006370	0.000464	0.9999	EXP 11 of 11
H409-5	384.00 W	0.000324	0.000008	0.0968	LIN 11 of 11	0.000560	0.000012	0.1334	LIN 11 of 11	0.006016	0.000022	0.9822	EXP 11 of 11	0.428681	0.000197	0.9997	EXP 11 of 11	2.055651	0.000370	1.0000	EXP 11 of 11
H409-6	387.00 W	0.000275	0.000008	0.5214	LIN 11 of 11	0.000527	0.000012	0.1327	LIN 11 of 11	0.002393	0.000018	0.9530	EXP 10 of 11	0.158675	0.000074	0.9997	EXP 11 of 11	0.741145	0.000279	0.9998	EXP 11 of 11
H409-7	398.00 W	0.000329	0.000006	0.4787	LIN 11 of 11	0.000544	0.000012		AVE 11 of 11	0.003624	0.000017	0.9654	EXP 11 of 11	0.223245	0.000138	0.9995	EXP 11 of 11	1.037049	0.000248	0.9999	EXP 11 of 11
H409-8	416.00 W	0.000299	0.000008	0.1246	LIN 11 of 11	0.000549	0.000017		AVE 11 of 11	0.001924	0.000022	0.8301	LIN 11 of 11	0.113202	0.000092	0.9992	EXP 11 of 11	0.531002	0.000178	0.9998	EXP 11 of 11
H409-9	450.00 W	0.000381	0.000011		AVE 11 of 11	0.000528	0.000010		AVE 11 of 11	0.005285	0.000020	0.9851	EXP 11 of 11	0.277405	0.000155	0.9996	EXP 11 of 11	1.326726	0.000316	0.9999	EXP 11 of 11
H409-10	510.00 W	0.000320	0.000014		AVE 11 of 11	0.000551	0.000013		AVE 11 of 11	0.006131	0.000024	0.9818	EXP 11 of 11	0.425285	0.000096	0.9999	EXP 11 of 11	2.132341	0.000489	0.9999	EXP 11 of 11
H409-11	572.00 W	0.000266	0.000004	0.6968	LIN 11 of 11	0.000549	0.000010		AVE 11 of 11	0.002979	0.000024	0.9211	EXP 11 of 11	0.216554	0.000076	0.9999	EXP 11 of 11	1.106886	0.000112	1.0000	EXP 11 of 11
H409-12	800.00 W	0.000273	0.000010	0.2894	LIN 11 of 11	0.000534	0.000016		AVE 11 of 11	0.005371	0.000025	0.9647	EXP 11 of 11	0.390422	0.000199	0.9997	EXP 11 of 11	2.005198	0.000311	1.0000	EXP 11 of 11

Sample Parameters	Sample	Material	Location	Analyst	Temp	Standard (in Ma)	%1σ	J	%1σ	MDF	%1σ
H409-1	355.00 W	AR-03-62M	Muscovite	Arménie	Yann ROLLAND	355	1073.6	0.5	0.016623	0.1	1.009527	1
H409-2	365.00 W	AR-03-62M	Muscovite	Arménie	Yann ROLLAND	365	1073.6	0.5	0.016623	0.1	1.009527	1
H409-3	373.00 W	AR-03-62M	Muscovite	Arménie	Yann ROLLAND	373	1073.6	0.5	0.016623	0.1	1.009527	1
H409-4	379.00 W	AR-03-62M	Muscovite	Arménie	Yann ROLLAND	379	1073.6	0.5	0.016623	0.1	1.009527	1
H409-5	384.00 W	AR-03-62M	Muscovite	Arménie	Yann ROLLAND	384	1073.6	0.5	0.016623	0.1	1.009527	1
H409-6	387.00 W	AR-03-62M	Muscovite	Arménie	Yann ROLLAND	387	1073.6	0.5	0.016623	0.1	1.009527	1
H409-7	398.00 W	AR-03-62M	Muscovite	Arménie	Yann ROLLAND	398	1073.6	0.5	0.016623	0.1	1.009527	1
H409-8	416.00 W	AR-03-62M	Muscovite	Arménie	Yann ROLLAND	416	1073.6	0.5	0.016623	0.1	1.009527	1
H409-9	450.00 W	AR-03-62M	Muscovite	Arménie	Yann ROLLAND	450	1073.6	0.5	0.016623	0.1	1.009527	1
H409-10	510.00 W	AR-03-62M	Muscovite	Arménie	Yann ROLLAND	510	1073.6	0.5	0.016623	0.1	1.009527	1
H409-11	572.00 W	AR-03-62M	Muscovite	Arménie	Yann ROLLAND	572	1073.6	0.5	0.016623	0.1	1.009527	1
H409-12	800.00 W	AR-03-62M	Muscovite	Arménie	Yann ROLLAND	800	1073.6	0.5	0.016623	0.1	1.009527	1

Volume Ratio	Sensitivity (mol/volt)	Day	Month	Year	Hour	Min	Resist	Irradiation	Project	Experiment	Nmb	Standard Name
1	2.000E-14	07	APR	2005	05	00	001	MC40	Rolland_Hassig	H409	01	Hb3gr
1	2.000E-14	07	APR	2005	05	22	001	MC40	Rolland_Hassig	H409	01	Hb3gr
1	2.000E-14	07	APR	2005	05	44	001	MC40	Rolland_Hassig	H409	01	Hb3gr
1	2.000E-14	07	APR	2005	06	25	001	MC40	Rolland_Hassig	H409	01	Hb3gr
1	2.000E-14	07	APR	2005	06	49	001	MC40	Rolland_Hassig	H409	01	Hb3gr
1	2.000E-14	07	APR	2005	07	11	001	MC40	Rolland_Hassig	H409	01	Hb3gr
1	2.000E-14	07	APR	2005	07	59	001	MC40	Rolland_Hassig	H409	01	Hb3gr
1	2.000E-14	07	APR	2005	08	21	001	MC40	Rolland_Hassig	H409	01	Hb3gr
1	2.000E-14	07	APR	2005	08	44	001	MC40	Rolland_Hassig	H409	01	Hb3gr
1	2.000E-14	07	APR	2005	09	25	001	MC40	Rolland_Hassig	H409	01	Hb3gr
1	2.000E-14	07	APR	2005	09	47	001	MC40	Rolland_Hassig	H409	01	Hb3gr
1	2.000E-14	07	APR	2005	10	13	001	MC40	Rolland_Hassig	H409	01	Hb3gr

Irradiation Constants		40/36(a)	%1σ	40/36(c)	%1σ	38/36(a)	%1σ	38/36(c)	%1σ	39/37(ca)	%1σ	38/37(ca)	%1σ	36/37(ca)	%1σ
H409-1	355.00 W	298.56	0.1	0.018	35	0.1885	0.16	1.7	3	0.00073	4	0.006	90	0.000282	1
H409-2	365.00 W	298.56	0.1	0.018	35	0.1885	0.16	1.7	3	0.00073	4	0.006	90	0.000282	1
H409-3	373.00 W	298.56	0.1	0.018	35	0.1885	0.16	1.7	3	0.00073	4	0.006	90	0.000282	1
H409-4	379.00 W	298.56	0.1	0.018	35	0.1885	0.16	1.7	3	0.00073	4	0.006	90	0.000282	1
H409-5	384.00 W	298.56	0.1	0.018	35	0.1885	0.16	1.7	3	0.00073	4	0.006	90	0.000282	1
H409-6	387.00 W	298.56	0.1	0.018	35	0.1885	0.16	1.7	3	0.00073	4	0.006	90	0.000282	1
H409-7	398.00 W	298.56	0.1	0.018	35	0.1885	0.16	1.7	3	0.00073	4	0.006	90	0.000282	1
H409-8	416.00 W	298.56	0.1	0.018	35	0.1885	0.16	1.7	3	0.00073	4	0.006	90	0.000282	1
H409-9	450.00 W	298.56	0.1	0.018	35	0.1885	0.16	1.7	3	0.00073	4	0.006	90	0.000282	1
H409-10	510.00 W	298.56	0.1	0.018	35	0.1885	0.16	1.7	3	0.00073	4	0.006	90	0.000282	1
H409-11	572.00 W	298.56	0.1	0.018	35	0.1885	0.16	1.7	3	0.00073	4	0.006	90	0.000282	1
H409-12	800.00 W	298.56	0.1	0.018	35	0.1885	0.16	1.7	3	0.00073	4	0.006	90	0.000282	1

40/39(k)	%1σ	38/39(k)	%1σ	36/38(cl)	%1σ	K/Ca	%1σ	K/Cl	%1σ	Ca/Cl	%1σ
0.0297	2	0.012	2	316	5	0.1616	4	5.4	33	33.3	33
0.0297	2	0.012	2	316	5	0.1616	4	5.4	33	33.3	33
0.0297	2	0.012	2	316	5	0.1616	4	5.4	33	33.3	33
0.0297	2	0.012	2	316	5	0.1616	4	5.4	33	33.3	33
0.0297	2	0.012	2	316	5	0.1616	4	5.4	33	33.3	33
0.0297	2	0.012	2	316	5	0.1616	4	5.4	33	33.3	33
0.0297	2	0.012	2	316	5	0.1616	4	5.4	33	33.3	33
0.0297	2	0.012	2	316	5	0.1616	4	5.4	33	33.3	33
0.0297	2	0.012	2	316	5	0.1616	4	5.4	33	33.3	33
0.0297	2	0.012	2	316	5	0.1616	4	5.4	33	33.3	33
0.0297	2	0.012	2	316	5	0.1616	4	5.4	33	33.3	33
0.0297	2	0.012	2	316	5	0.1616	4	5.4	33	33.3	33

Annexe 10 - Résultats de datation (2) sur Muscovite AR-04-64.

Incremental Heating		36Ar(a)	37Ar(ca)	38Ar(cl)	39Ar(k)	40Ar(r)	Age ± 2σ (Ma)	40Ar(r) (%)	39Ar(k) (%)	K/Ca ± 2σ
H446-1	351.00 W	0.000804	0.000167	0.000278	0.193392	0.975933	149.25 ± 4.07	79.88	3.84	188 ± 82
H446-2	358.00 W	0.000235	0.000002	0.002237	1.129311	5.968824	156.02 ± 3.01	98.29	22.44	84237 ######
H446-3	362.00 W	0.000027	0.000004	0.000917	0.471625	2.484983	155.56 ± 3.00	99.12	9.37	19981 ######
H446-4	365.00 W	0.000031	0.000068	0.000491	0.288518	1.504205	153.99 ± 3.02	98.83	5.73	688 ± 765
H446-5	373.00 W	0.000140	0.000176	0.001048	0.581958	2.958373	150.31 ± 2.90	98.04	11.56	534 ± 253
H446-6	381.00 W	0.000061	0.000186	0.001896	1.206781	6.227024	152.48 ± 2.93	99.14	23.98	1051 ± 511
H446-7	385.00 W	0.000015	0.000056	0.000255	0.134098	0.685988	151.22 ± 3.22	98.79	2.66	386 ± 459
H446-8	390.00 W	0.000002	0.000032	0.000116	0.058248	0.298480	151.46 ± 3.90	99.25	1.16	296 ± 443
H446-9	402.00 W	0.000016	0.000049	0.000126	0.074419	0.369374	146.90 ± 3.42	98.15	1.48	246 ± 321
H446-10	422.00 W	0.000003	0.000009	0.000343	0.174811	0.877770	148.54 ± 2.95	99.52	3.47	3023 ± 22691
H446-11	459.00 W	0.000012	0.000011	0.000377	0.218512	1.132627	153.14 ± 3.00	99.13	4.34	3251 ± 16712
H446-12	512.00 W	0.000011	0.000042	0.000628	0.288210	1.544827	158.14 ± 3.10	99.24	5.73	1119 ± 2062
H446-13	580.00 W	0.000010	0.000000	0.000249	0.118598	0.634180	157.78 ± 3.36	99.00	2.36	56745 ######
H446-14	800.00 W	0.000004	0.000088	0.000237	0.094134	0.504083	157.99 ± 3.69	99.69	1.87	173 ± 200
	Σ	0.001355	0.000779	0.009196	5.032613	26.166670				

Information on Analysis

Sample = AR-04-64
Material = Muscovite
Location = Arménie
Analyst = Yann ROLLAND
Project = ROLLAND_HASSIG
Mass Discrimination Law = LIN
Irradiation = MC45
J = 0.01709140 ± 0.00004273
Hb3gr = 1073.600 ± 5.368 Ma

Results	40(r)/39(k) ± 2σ	Age ± 2σ (Ma)	MSWD	39Ar(k) (%,n)	K/Ca ± 2σ
Age Plateau	5.1820 ± 0.0672	153.10 ± 2.04	4.95	100.00	239 ± 88
Error Mean	± 1.30%	± 1.33%		14	
	Minimal External Error ± 2.11		2.16	Statistical T Ratio	
	Analytical Error ± 1.90		2.2252	Error Magnification	
Total Fusion Age	5.1994 ± 0.0398	153.59 ± 1.35		14	1043 ± 396
	± 0.77%	± 0.88%			
	Minimal External Error ± 1.46				
	Analytical Error ± 1.13				

Normal Isochron		39(k)/36(a) ± 2σ	40(a+r)/36(a) ± 2σ	r.i.
H446-1	351.00 W	240.4 ± 20.2	1512.0 ± 123.6	0.9711
H446-2	358.00 W	4812.8 ± 983.0	25736.0 ± 5231.1	0.9952
H446-3	362.00 W	17759.5 ± 12979.4	93873.2 ± 68580.5	0.9996
H446-4	365.00 W	9275.4 ± 6650.5	48656.7 ± 34873.4	0.9996
H446-5	373.00 W	4145.6 ± 745.7	21372.8 ± 3820.4	0.9938
H446-6	381.00 W	19899.7 ± 8853.9	102981.4 ± 45773.1	0.9990
H446-7	385.00 W	9055.0 ± 13629.2	46620.1 ± 70164.3	0.9999
H446-8	390.00 W	32380.6 ± 318836.4	166227.5 ± 1636758.4	1.0000
H446-9	402.00 W	4691.1 ± 4984.7	23582.4 ± 25054.4	0.9998
H446-10	422.00 W	54251.6 ± 232200.9	272113.1 ± 1164652.0	1.0000
H446-11	459.00 W	18713.4 ± 23837.2	97296.9 ± 123921.8	0.9999
H446-12	512.00 W	26819.6 ± 58707.6	144053.7 ± 315318.1	1.0000
H446-13	580.00 W	12233.1 ± 25296.1	65712.9 ± 135877.6	1.0000
H446-14	800.00 W	23045.2 ± 131876.4	123108.0 ± 704481.3	1.0000

Results	40(a)/36(a) ± 2σ	40(r)/39(k) ± 2σ	Age ± 2σ (Ma)	MSWD
Normal Isochron	253.6166 ± 46.9911 ± 18.53%	5.2200 ± 0.0564 ± 1.08%	154.18 ± 1.76 ± 1.14%	1.78
			Minimal External Error ± 1.85	
			Analytical Error ± 1.60	

Statistics				
	Statistical F ratio	1.83	Convergence	0.0000124957
	Error Magnification	1.3346	Number of Iterations	1
	Number of Data Points	12	Calculated Line	Weighted York-2

Inverse Isochron		39(k)/40(a+r) ± 2σ	36(a)/40(a+r) ± 2σ	r.i.
H446-1	351.00 W	0.159031 ± 0.003193	0.000661 ± 0.000054	0.0006
H446-2	358.00 W	0.187007 ± 0.003737	0.000039 ± 0.000008	0.0001
H446-3	362.00 W	0.189187 ± 0.003783	0.000011 ± 0.000008	0.0000
H446-4	365.00 W	0.190631 ± 0.003813	0.000021 ± 0.000015	0.0000
H446-5	373.00 W	0.193968 ± 0.003876	0.000047 ± 0.000008	0.0001
H446-6	381.00 W	0.193236 ± 0.003859	0.000010 ± 0.000004	0.0000
H446-7	385.00 W	0.194230 ± 0.003885	0.000021 ± 0.000032	0.0000
H446-8	390.00 W	0.194797 ± 0.003934	0.000006 ± 0.000059	0.0000
H446-9	402.00 W	0.198922 ± 0.003988	0.000042 ± 0.000045	0.0001
H446-10	422.00 W	0.199371 ± 0.004013	0.000004 ± 0.000016	0.0000
H446-11	459.00 W	0.192333 ± 0.003853	0.000010 ± 0.000013	0.0000
H446-12	512.00 W	0.186178 ± 0.003721	0.000007 ± 0.000015	0.0000
H446-13	580.00 W	0.186160 ± 0.003753	0.000015 ± 0.000031	0.0000
H446-14	800.00 W	0.187195 ± 0.003763	0.000008 ± 0.000046	0.0000

Results	40(a)/36(a) ± 2σ	40(r)/39(k) ± 2σ	Age ± 2σ (Ma)	MSWD
Inverse Isochron	263.5761 ± 34.1749	5.2027 ± 0.0358	153.68 ± 1.25	4.40
Error Chron	± 12.97%	± 0.69%	± 0.82%	
		Minimal External Error	± 1.37	
		Analytical Error	± 1.01	

Statistics				
	Statistical F ratio	1.83	Convergence	0.0000558446
	Error Magnification	2.0985	Number of Iterations	3
	Number of Data Points	12	Calculated Line	Weighted York-2

Relative Abundances		36Ar	%1σ	37Ar	%1σ	38Ar	%1σ	39Ar	%1σ	40Ar	%1σ	Age ± 2σ (Ma)	40Ar(r) (%)	39Ar(k) (%)	K/Ca ± 2σ
H446-1	351.00 W	0.0008044	4.087	0.0001665	21.585	0.0027514	2.115	0.1933923	1.003	1.2218068	0.050	149.25 ± 4.07	79.88	3.84	188 ± 82
H446-2	358.00 W	0.0002348	10.156	0.0000022	1558.713	0.0158328	2.008	1.1293110	0.999	6.0724205	0.023	156.02 ± 3.01	98.29	22.44	84237 ######
H446-3	362.00 W	0.0000266	36.443	0.0000038	933.231	0.0065815	2.028	0.4716255	0.999	2.5069186	0.020	155.56 ± 3.00	99.12	9.37	19981 ######
H446-4	365.00 W	0.0000312	35.775	0.0000678	55.477	0.0039591	2.075	0.2885178	1.000	1.5220611	0.021	153.99 ± 3.02	98.83	5.73	688 ± 765
H446-5	373.00 W	0.0001405	8.930	0.0001762	23.371	0.0080588	2.016	0.5819578	0.999	3.0175681	0.024	150.31 ± 2.90	98.04	11.56	534 ± 253
H446-6	381.00 W	0.0000608	22.157	0.0001856	23.965	0.0163902	2.011	1.2067810	0.998	6.2809709	0.011	152.48 ± 2.93	99.14	23.98	1051 ± 511
H446-7	385.00 W	0.0000148	75.082	0.0000562	59.352	0.0018670	2.090	0.1340985	0.999	0.6943926	0.041	151.22 ± 3.22	98.79	2.66	386 ± 459
H446-8	390.00 W	0.0000018	487.716	0.0000318	74.837	0.0008159	2.711	0.0582476	1.004	0.3007466	0.104	151.46 ± 3.90	99.25	1.16	296 ± 443
H446-9	402.00 W	0.0000159	53.046	0.0000489	65.171	0.0010219	2.465	0.0744188	1.000	0.3763204	0.068	146.90 ± 3.42	98.15	1.48	246 ± 321
H446-10	422.00 W	0.0000032	215.406	0.0000093	375.323	0.0024396	2.110	0.1748105	1.004	0.8820001	0.071	148.54 ± 2.95	99.52	3.47	3023 ± 22691
H446-11	459.00 W	0.0000117	63.524	0.0000109	256.958	0.0030012	2.306	0.2185122	1.001	1.1426028	0.032	153.14 ± 3.00	99.13	4.34	3251 ± 16712
H446-12	512.00 W	0.0000108	109.123	0.0000416	92.068	0.0040880	2.134	0.2882095	0.999	1.5565957	0.010	158.14 ± 3.10	99.24	5.73	1119 ± 2062
H446-13	580.00 W	0.0000097	103.203	0.0000003	#######	0.0016740	2.263	0.1185976	1.007	0.6405966	0.048	157.78 ± 3.36	99.00	2.36	56745 ######
H446-14	800.00 W	0.0000040	289.036	0.0000879	57.560	0.0013661	2.537	0.0941337	1.004	0.5056588	0.044	157.99 ± 3.69	99.69	1.87	173 ± 200
	Σ	0.0013558	4.012	0.0007794	18.552	0.0698475	0.763	5.0326138	0.378	26.7206596	0.008				

Information on Analysis and Constants Used in Calculations

Sample = AR-04-64
Material = Muscovite
Location = Arménie
Analyst = Yann ROLLAND
Project = ROLLAND_HASSIG
Mass Discrimination Law = LIN
Irradiation = MC45
J = 0.01709140 ± 0.00004273
Hb3gr = 1073.600 ± 5.368 Ma
IGSN = Undefined
Preferred Age = Undefined
Classification = Undefined
Experiment Type = Undefined
Extraction Method = Undefined
Heating = 600 sec
Isolation = 2.00 min
Instrument = VG3600
Lithology = Undefined
Lat-Lon = Undefined - Undefined

Age Equations = Conventional
Negative Intensities = Allowed
Decay Constant 40K = 5.543 ± 0.010 E-10 1/ a
Decay Constant 39Ar = 2.940 ± 0.029 E-07 1/ h
Decay Constant 37Ar = 8.220 ± 0.010 E-04 1/ h
Decay Constant 36Cl = 2.310 ± 0.016 E-06 1/ a
Production Ratio 36/ 38 in Cl = 316.0 ± 15.8

Results	40(r)/39(k) ± 2σ	Age ± 2σ (Ma)	MSWD	39Ar(k) (%,n)	K/Ca ± 2σ
Age Plateau	5.1820 ± 0.0672 ± 1.30%	153.10 ± 2.04 ± 1.33%	4.95	100.00 14	239 ± 88
Error Mean	Minimal External Error ± 2.11		2.16	Statistical T Ratio	
	Analytical Error ± 1.90		2.2252	Error Magnification	
Total Fusion Age	5.1994 ± 0.0398 ± 0.77%	153.59 ± 1.35 ± 0.88%		14	1043 ± 396
	Minimal External Error ± 1.46				
	Analytical Error ± 1.13				
Normal Isochron	5.2200 ± 0.0564 ± 1.08%	154.18 ± 1.76 ± 1.14%	1.78	94.66 12	
	Minimal External Error ± 1.85		1.83	Statistical F ratio	
	Analytical Error ± 1.60		1.3346	Error Magnification	
Inverse Isochron	5.2027 ± 0.0358 ± 0.69%	153.68 ± 1.25 ± 0.82%	4.40	94.66 12	
Error Chron	Minimal External Error ± 1.37		1.83	Statistical F ratio	
	Analytical Error ± 1.01		2.0985	Error Magnification	

Degassing Patterns		36Ar(a)	%1σ	36Ar(c)	%1σ	36Ar(ca)	%1σ	36Ar(cl)	%1σ	37Ar(ca)	%1σ	38Ar(a)	%1σ	38Ar(c)	%1σ	38Ar(k)	%1σ
H446-1	351.00 W	0.000804	4.09	0.000000	0.00	0.000000	21.61	0.000000	28.66	0.000167	21.59	0.000152	4.09	0.000000	0.00	0.002321	2.24
H446-2	358.00 W	0.000235	10.16	0.000000	0.00	0.000000	1558.71	0.000000	20.33	0.000002	1558.71	0.000044	10.16	0.000000	0.00	0.013552	2.24
H446-3	362.00 W	0.000027	36.53	0.000000	0.00	0.000000	933.23	0.000000	20.74	0.000004	933.23	0.000005	36.53	0.000000	0.00	0.005660	2.24
H446-4	365.00 W	0.000031	35.84	0.000000	0.00	0.000000	55.49	0.000000	23.62	0.000068	55.48	0.000006	35.84	0.000000	0.00	0.003462	2.24
H446-5	373.00 W	0.000140	8.94	0.000000	0.00	0.000000	23.39	0.000000	22.15	0.000176	23.37	0.000026	8.94	0.000000	0.00	0.006983	2.24
H446-6	381.00 W	0.000061	22.22	0.000000	0.00	0.000000	23.99	0.000000	24.95	0.000186	23.97	0.000011	22.22	0.000000	0.00	0.014481	2.24
H446-7	385.00 W	0.000015	75.25	0.000000	0.00	0.000000	59.36	0.000000	21.52	0.000056	59.35	0.000003	75.25	0.000000	0.00	0.001609	2.24
H446-8	390.00 W	0.000002	492.32	0.000000	0.00	0.000000	74.84	0.000000	23.91	0.000032	74.84	0.000000	492.32	0.000000	0.00	0.000699	2.24
H446-9	402.00 W	0.000016	53.12	0.000000	0.00	0.000000	65.18	0.000000	26.17	0.000049	65.17	0.000003	53.12	0.000000	0.00	0.000893	2.24
H446-10	422.00 W	0.000003	214.00	0.000000	0.00	0.000000	375.32	0.000000	21.02	0.000009	375.32	0.000001	214.00	0.000000	0.00	0.002098	2.24
H446-11	459.00 W	0.000012	63.68	0.000000	0.00	0.000000	256.96	0.000000	24.66	0.000011	256.96	0.000002	63.68	0.000000	0.00	0.002622	2.24
H446-12	512.00 W	0.000011	109.44	0.000000	0.00	0.000000	92.07	0.000000	19.30	0.000042	92.07	0.000002	109.44	0.000000	0.00	0.003459	2.24
H446-13	580.00 W	0.000010	103.39	0.000000	0.00	0.000000	17237.80	0.000000	20.58	0.000000	17237.80	0.000002	103.39	0.000000	0.00	0.001423	2.24
H446-14	800.00 W	0.000004	286.12	0.000000	0.00	0.000000	57.57	0.000000	18.88	0.000088	57.56	0.000001	286.12	0.000000	0.00	0.001130	2.24
	Σ	0.001355	4.01	0.000000	0.00	0.000000	18.56	0.000001	8.26	0.000779	18.55	0.000255	4.02	0.000000	0.00	0.060391	0.85
	Σ							0.001356	4.01	0.000779	18.55						

38Ar(ca)	%1σ	38Ar(cl)	%1σ	39Ar(k)	%1σ	39Ar(ca)	%1σ	40Ar(r)	%1σ	40Ar(a)	%1σ	40Ar(c)	%1σ	40Ar(k)	%1σ
0.000001	92.55	0.000278	29.10	0.193392	1.00	0.000000	21.95	0.975933	1.01	0.240130	4.09	0.000000	0.00	0.005744	2.24
0.000000	1561.31	0.002237	20.94	1.129311	1.00	0.000000	1558.72	5.968824	0.12	0.070056	10.16	0.000000	0.00	0.033541	2.24
0.000000	937.56	0.000917	21.34	0.471625	1.00	0.000000	933.24	2.484983	0.12	0.007929	36.53	0.000000	0.00	0.014007	2.24
0.000000	105.72	0.000491	24.15	0.288518	1.00	0.000000	55.62	1.504205	0.22	0.009287	35.84	0.000000	0.00	0.008569	2.24
0.000001	92.98	0.001048	22.72	0.581958	1.00	0.000000	23.71	2.958373	0.13	0.041911	8.94	0.000000	0.00	0.017284	2.24
0.000001	93.14	0.001896	25.45	1.206781	1.00	0.000000	24.30	6.227024	0.07	0.018106	22.22	0.000000	0.00	0.035841	2.24
0.000000	107.81	0.000255	22.10	0.134098	1.00	0.000000	59.49	0.685988	0.49	0.004421	75.25	0.000000	0.00	0.003983	2.24
0.000000	117.05	0.000116	24.44	0.058248	1.00	0.000000	74.94	0.298480	0.89	0.000537	492.32	0.000000	0.00	0.001730	2.24
0.000000	111.12	0.000126	26.65	0.074419	1.00	0.000000	65.29	0.369374	0.68	0.004736	53.12	0.000000	0.00	0.002210	2.24
0.000000	385.96	0.000343	21.61	0.174811	1.00	0.000000	375.34	0.877770	0.25	0.000962	214.00	0.000000	0.00	0.005192	2.24
0.000000	272.26	0.000377	25.17	0.218512	1.00	0.000000	256.99	1.132627	0.20	0.003486	63.68	0.000000	0.00	0.006490	2.24
0.000000	128.75	0.000628	19.95	0.288210	1.00	0.000000	92.15	1.544827	0.23	0.003208	109.44	0.000000	0.00	0.008560	2.24
0.000000	17238.03	0.000249	21.19	0.118598	1.01	0.000000	17237.80	0.634180	0.47	0.002894	103.39	0.000000	0.00	0.003522	2.24
0.000001	106.83	0.000237	19.54	0.094134	1.00	0.000000	57.70	0.504083	0.69	0.001220	286.12	0.000000	0.00	0.002796	2.24
0.000005	43.18	0.009196	8.48	5.032613	0.38	0.000001	18.63	26.166670	0.06	0.404521	4.01	0.000000	0.00	0.149469	0.85
		0.069847	1.33			5.032614	0.38							26.720660	0.09

Additional Parameters		40(r)/39(k)	1σ	40(r+a)	1σ	40Ar/39Ar	1σ	37Ar/39Ar	1σ	36Ar/39Ar	1σ	Time (days)	37Ar (decay)	39Ar (decay)	40Ar (moles)
H446-1	351.00 W	5.046394	0.07175	1.216063	0.00063	6.317764	0.06343	0.000861	0.00019	0.004159	0.00018	34.357	2.05811759	1.00025831	2.444E-14
H446-2	358.00 W	5.285367	0.05318	6.038880	0.00159	5.377102	0.05371	0.000002	0.00003	0.000208	0.00002	34.375	2.05885082	1.00025844	1.214E-13
H446-3	362.00 W	5.268975	0.05303	2.492911	0.00059	5.315486	0.05313	0.000008	0.00008	0.000056	0.00002	34.392	2.05952788	1.00025856	5.014E-14
H446-4	365.00 W	5.213561	0.05340	1.513492	0.00037	5.275449	0.05276	0.000235	0.00013	0.000108	0.00004	34.420	2.06068505	1.00025876	3.044E-14
H446-5	373.00 W	5.083484	0.05119	3.000284	0.00082	5.185201	0.05180	0.000303	0.00007	0.000241	0.00002	34.435	2.06130623	1.00025887	6.035E-14
H446-6	381.00 W	5.160029	0.05163	6.245129	0.00104	5.204731	0.05196	0.000154	0.00004	0.000050	0.00001	34.451	2.06192760	1.00025898	1.256E-13
H446-7	385.00 W	5.115557	0.05687	0.690410	0.00030	5.178227	0.05179	0.000419	0.00025	0.000111	0.00008	34.488	2.06345358	1.00025924	1.389E-14
H446-8	390.00 W	5.124327	0.06884	0.299017	0.00032	5.163245	0.05213	0.000546	0.00041	0.000031	0.00015	34.505	2.06413216	1.00025936	6.015E-15
H446-9	402.00 W	4.963453	0.06015	0.374110	0.00026	5.056795	0.05068	0.000658	0.00043	0.000213	0.00011	34.522	2.06481095	1.00025948	7.526E-15
H446-10	422.00 W	5.021266	0.05188	0.876808	0.00064	5.045463	0.05077	0.000053	0.00020	0.000018	0.00004	34.550	2.06597108	1.00025968	1.764E-14
H446-11	459.00 W	5.183358	0.05291	1.136113	0.00040	5.229012	0.05237	0.000050	0.00013	0.000054	0.00003	34.565	2.06659386	1.00025978	2.285E-14
H446-12	512.00 W	5.360084	0.05494	1.548036	0.00025	5.400917	0.05397	0.000144	0.00013	0.000037	0.00004	34.584	2.06735844	1.00025992	3.113E-14
H446-13	580.00 W	5.347326	0.05951	0.637074	0.00032	5.401432	0.05444	0.000003	0.00049	0.000082	0.00008	34.612	2.06849166	1.00026011	1.281E-14
H446-14	800.00 W	5.354969	0.06535	0.502863	0.00023	5.371710	0.05399	0.000933	0.00054	0.000043	0.00012	34.625	2.06903016	1.00026021	1.011E-14

Procedure Blanks		36Ar	1σ	37Ar	1σ	38Ar	1σ	39Ar	1σ	40Ar	1σ
H446-1	351.00 W	0.000207	0.000007	0.000536	0.000011	0.000134	0.000009	0.000125	0.000005	0.002181	0.000041
H446-2	358.00 W	0.000207	0.000007	0.000536	0.000011	0.000134	0.000009	0.000125	0.000005	0.002181	0.000041
H446-3	362.00 W	0.000207	0.000007	0.000536	0.000011	0.000134	0.000009	0.000125	0.000005	0.002181	0.000041
H446-4	365.00 W	0.000208	0.000009	0.000507	0.000017	0.000133	0.000009	0.000580	0.000008	0.004857	0.000024
H446-5	373.00 W	0.000208	0.000009	0.000507	0.000017	0.000133	0.000009	0.000580	0.000008	0.004857	0.000024
H446-6	381.00 W	0.000208	0.000009	0.000507	0.000017	0.000133	0.000009	0.000580	0.000008	0.004857	0.000024
H446-7	385.00 W	0.000219	0.000007	0.000521	0.000008	0.000114	0.000007	0.000469	0.000008	0.004147	0.000020
H446-8	390.00 W	0.000219	0.000007	0.000521	0.000008	0.000114	0.000007	0.000469	0.000008	0.004147	0.000020
H446-9	402.00 W	0.000219	0.000007	0.000521	0.000008	0.000114	0.000007	0.000469	0.000008	0.004147	0.000020
H446-10	422.00 W	0.000221	0.000004	0.000526	0.000011	0.000116	0.000007	0.000208	0.000012	0.002902	0.000031
H446-11	459.00 W	0.000221	0.000004	0.000526	0.000011	0.000116	0.000007	0.000208	0.000012	0.002902	0.000031
H446-12	512.00 W	0.000221	0.000004	0.000526	0.000011	0.000116	0.000007	0.000208	0.000012	0.002902	0.000031
H446-13	580.00 W	0.000219	0.000009	0.000516	0.000021	0.000074	0.000011	0.000175	0.000010	0.003017	0.000026
H446-14	800.00 W	0.000219	0.000009	0.000516	0.000021	0.000074	0.000011	0.000175	0.000010	0.003017	0.000026

Intercept Values		36Ar	1σ	r2		37Ar	1σ	r2		38Ar	1σ	r2		39Ar	1σ	r2		40Ar	1σ	r2	
H446-1	351.00 W	0.001042	0.000008	0.8576	LIN 11 of 11	0.000619	0.000014	0.0937	LIN 11 of 11	0.002938	0.000019	0.9180	LIN 11 of 11	0.195306	0.000187	0.9990	EXP 11 of 11	1.223988	0.000612	0.9997	EXP 11 of 11
H446-2	358.00 W	0.000450	0.000022	0.2132	LIN 11 of 11	0.000537	0.000013	0.9039	LIN 8 of 11	0.016269	0.000052	0.9929	EXP 11 of 11	1.139879	0.000394	0.9999	EXP 11 of 11	6.074602	0.001403	1.0000	EXP 11 of 11
H446-3	362.00 W	0.000234	0.000007	0.6902	LIN 11 of 11	0.000534	0.000014	0.4290	LIN 11 of 11	0.006841	0.000028	0.9773	EXP 11 of 11	0.476112	0.000244	0.9997	EXP 11 of 11	2.509100	0.000492	0.9999	EXP 11 of 11
H446-4	365.00 W	0.000240	0.000007	0.6715	LIN 11 of 11	0.000541	0.000008	0.8024	LIN 11 of 11	0.004168	0.000023	0.9584	EXP 11 of 11	0.291766	0.000172	0.9996	EXP 11 of 11	1.526918	0.000314	0.9999	EXP 11 of 11
H446-5	373.00 W	0.000354	0.000007	0.1912	LIN 11 of 11	0.000595	0.000011	0.3217	EXP 11 of 11	0.008346	0.000030	0.9797	EXP 11 of 11	0.587920	0.000200	0.9999	EXP 11 of 11	3.022425	0.000724	0.9999	EXP 11 of 11
H446-6	381.00 W	0.000271	0.000010	0.5343	LIN 11 of 11	0.000599	0.000014	0.5646	EXP 11 of 11	0.016836	0.000057	0.9815	EXP 11 of 11	1.218521	0.000239	0.9999	EXP 11 of 11	6.285828	0.000670	1.0000	EXP 11 of 11
H446-7	385.00 W	0.000235	0.000009	0.2113	LIN 11 of 11	0.000549	0.000014	0.2024	LIN 11 of 11	0.002016	0.000010	0.9688	EXP 11 of 11	0.135808	0.000066	0.9997	EXP 11 of 11	0.698539	0.000282	0.9997	EXP 11 of 11
H446-8	390.00 W	0.000221	0.000006	0.6135	LIN 11 of 11	0.000537	0.000009	0.0767	LIN 11 of 11	0.000945	0.000014	0.7467	EXP 11 of 11	0.059256	0.000065	0.9984	EXP 11 of 11	0.304893	0.000313	0.9978	EXP 11 of 11
H446-9	402.00 W	0.000236	0.000005	0.3915	LIN 11 of 11	0.000546	0.000014		AVE 11 of 11	0.001155	0.000013	0.8510	EXP 11 of 11	0.075576	0.000044	0.9996	EXP 11 of 11	0.380467	0.000255	0.9992	EXP 11 of 11
H446-10	422.00 W	0.000217	0.000006	0.7891	LIN 11 of 11	0.000522	0.000014	0.4585	LIN 11 of 11	0.002602	0.000016	0.9721	EXP 10 of 11	0.176635	0.000186	0.9987	EXP 11 of 11	0.884902	0.000627	0.9993	EXP 11 of 11
H446-11	459.00 W	0.000233	0.000006	0.4861	LIN 11 of 11	0.000532	0.000009	0.1802	LIN 11 of 11	0.003174	0.000035	0.8639	EXP 11 of 11	0.220741	0.000170	0.9993	EXP 11 of 11	1.145505	0.000368	0.9999	EXP 11 of 11
H446-12	512.00 W	0.000232	0.000011	0.1186	LIN 11 of 11	0.000506	0.000016	0.1950	LIN 11 of 11	0.004281	0.000032	0.9445	EXP 11 of 11	0.291083	0.000141	0.9997	EXP 11 of 11	1.559498	0.000159	1.0000	EXP 11 of 11
H446-13	580.00 W	0.000229	0.000005	0.5781	LIN 11 of 11	0.000516	0.000020	0.0704	LIN 11 of 11	0.001779	0.000015	0.8917	EXP 11 of 11	0.119869	0.000157	0.9980	EXP 11 of 11	0.643613	0.000305	0.9996	EXP 11 of 11
H446-14	800.00 W	0.000215	0.000008	0.5585	LIN 11 of 11	0.000560	0.000014	0.4637	LIN 11 of 11	0.001466	0.000019	0.8812	LIN 11 of 11	0.095179	0.000104	0.9986	EXP 11 of 11	0.508675	0.000220	0.9997	EXP 11 of 11

Sample Parameters		Sample	Material	Location	Analyst	Temp	Standard (in Ma)	%1σ	J	%1σ	MDF	%1σ
H446-1	351.00 W	AR-04-64	Muscovite	Arménie	Yann ROLLAND	351	1073.6	0.5	0.0170914	0.25	1.009527	1
H446-2	358.00 W	AR-04-64	Muscovite	Arménie	Yann ROLLAND	358	1073.6	0.5	0.0170914	0.25	1.009527	1
H446-3	362.00 W	AR-04-64	Muscovite	Arménie	Yann ROLLAND	362	1073.6	0.5	0.0170914	0.25	1.009527	1
H446-4	365.00 W	AR-04-64	Muscovite	Arménie	Yann ROLLAND	365	1073.6	0.5	0.0170914	0.25	1.009527	1
H446-5	373.00 W	AR-04-64	Muscovite	Arménie	Yann ROLLAND	373	1073.6	0.5	0.0170914	0.25	1.009527	1
H446-6	381.00 W	AR-04-64	Muscovite	Arménie	Yann ROLLAND	381	1073.6	0.5	0.0170914	0.25	1.009527	1
H446-7	385.00 W	AR-04-64	Muscovite	Arménie	Yann ROLLAND	385	1073.6	0.5	0.0170914	0.25	1.009527	1
H446-8	390.00 W	AR-04-64	Muscovite	Arménie	Yann ROLLAND	390	1073.6	0.5	0.0170914	0.25	1.009527	1
H446-9	402.00 W	AR-04-64	Muscovite	Arménie	Yann ROLLAND	402	1073.6	0.5	0.0170914	0.25	1.009527	1
H446-10	422.00 W	AR-04-64	Muscovite	Arménie	Yann ROLLAND	422	1073.6	0.5	0.0170914	0.25	1.009527	1
H446-11	459.00 W	AR-04-64	Muscovite	Arménie	Yann ROLLAND	459	1073.6	0.5	0.0170914	0.25	1.009527	1
H446-12	512.00 W	AR-04-64	Muscovite	Arménie	Yann ROLLAND	512	1073.6	0.5	0.0170914	0.25	1.009527	1
H446-13	580.00 W	AR-04-64	Muscovite	Arménie	Yann ROLLAND	580	1073.6	0.5	0.0170914	0.25	1.009527	1
H446-14	800.00 W	AR-04-64	Muscovite	Arménie	Yann ROLLAND	800	1073.6	0.5	0.0170914	0.25	1.009527	1

Volume Ratio	Sensitivity (mol/volt)	Day	Month	Year	Hour	Min	Resist	Irradiation	Project	Experiment	Nmb	Standard Name
1	2.000E-14	06	MAY	2005	07	16	001	MC45	Rolland_Hassig	H446	01	Hb3gr
1	2.000E-14	06	MAY	2005	07	42	001	MC45	Rolland_Hassig	H446	01	Hb3gr
1	2.000E-14	06	MAY	2005	08	06	001	MC45	Rolland_Hassig	H446	01	Hb3gr
1	2.000E-14	06	MAY	2005	08	47	001	MC45	Rolland_Hassig	H446	01	Hb3gr
1	2.000E-14	06	MAY	2005	09	09	001	MC45	Rolland_Hassig	H446	01	Hb3gr
1	2.000E-14	06	MAY	2005	09	31	001	MC45	Rolland_Hassig	H446	01	Hb3gr
1	2.000E-14	06	MAY	2005	10	25	001	MC45	Rolland_Hassig	H446	01	Hb3gr
1	2.000E-14	06	MAY	2005	10	49	001	MC45	Rolland_Hassig	H446	01	Hb3gr
1	2.000E-14	06	MAY	2005	11	13	001	MC45	Rolland_Hassig	H446	01	Hb3gr
1	2.000E-14	06	MAY	2005	11	54	001	MC45	Rolland_Hassig	H446	01	Hb3gr
1	2.000E-14	06	MAY	2005	12	16	001	MC45	Rolland_Hassig	H446	01	Hb3gr
1	2.000E-14	06	MAY	2005	12	43	001	MC45	Rolland_Hassig	H446	01	Hb3gr
1	2.000E-14	06	MAY	2005	13	23	001	MC45	Rolland_Hassig	H446	01	Hb3gr
1	2.000E-14	06	MAY	2005	13	42	001	MC45	Rolland_Hassig	H446	01	Hb3gr

Irradiation Constants		40/36(a)	%1σ	40/36(c)	%1σ	38/36(a)	%1σ	38/36(c)	%1σ	39/37(ca)	%1σ	38/37(ca)	%1σ	36/37(ca)	%1σ
H446-1	351.00 W	298.56	0.1	0.018	35	0.1885	0.16	1.7	3	0.00073	4	0.006	90	0.000282	1
H446-2	358.00 W	298.56	0.1	0.018	35	0.1885	0.16	1.7	3	0.00073	4	0.006	90	0.000282	1
H446-3	362.00 W	298.56	0.1	0.018	35	0.1885	0.16	1.7	3	0.00073	4	0.006	90	0.000282	1
H446-4	365.00 W	298.56	0.1	0.018	35	0.1885	0.16	1.7	3	0.00073	4	0.006	90	0.000282	1
H446-5	373.00 W	298.56	0.1	0.018	35	0.1885	0.16	1.7	3	0.00073	4	0.006	90	0.000282	1
H446-6	381.00 W	298.56	0.1	0.018	35	0.1885	0.16	1.7	3	0.00073	4	0.006	90	0.000282	1
H446-7	385.00 W	298.56	0.1	0.018	35	0.1885	0.16	1.7	3	0.00073	4	0.006	90	0.000282	1
H446-8	390.00 W	298.56	0.1	0.018	35	0.1885	0.16	1.7	3	0.00073	4	0.006	90	0.000282	1
H446-9	402.00 W	298.56	0.1	0.018	35	0.1885	0.16	1.7	3	0.00073	4	0.006	90	0.000282	1
H446-10	422.00 W	298.56	0.1	0.018	35	0.1885	0.16	1.7	3	0.00073	4	0.006	90	0.000282	1
H446-11	459.00 W	298.56	0.1	0.018	35	0.1885	0.16	1.7	3	0.00073	4	0.006	90	0.000282	1
H446-12	512.00 W	298.56	0.1	0.018	35	0.1885	0.16	1.7	3	0.00073	4	0.006	90	0.000282	1
H446-13	580.00 W	298.56	0.1	0.018	35	0.1885	0.16	1.7	3	0.00073	4	0.006	90	0.000282	1
H446-14	800.00 W	298.56	0.1	0.018	35	0.1885	0.16	1.7	3	0.00073	4	0.006	90	0.000282	1

40/39(k)	%1σ	38/39(k)	%1σ	36/38(cl)	%1σ	K/Ca	%1σ	K/Cl	%1σ	Ca/Cl	%1σ
0.0297	2	0.012	2	316	5	0.1616	4	5.4	33	33.3	33
0.0297	2	0.012	2	316	5	0.1616	4	5.4	33	33.3	33
0.0297	2	0.012	2	316	5	0.1616	4	5.4	33	33.3	33
0.0297	2	0.012	2	316	5	0.1616	4	5.4	33	33.3	33
0.0297	2	0.012	2	316	5	0.1616	4	5.4	33	33.3	33
0.0297	2	0.012	2	316	5	0.1616	4	5.4	33	33.3	33
0.0297	2	0.012	2	316	5	0.1616	4	5.4	33	33.3	33
0.0297	2	0.012	2	316	5	0.1616	4	5.4	33	33.3	33
0.0297	2	0.012	2	316	5	0.1616	4	5.4	33	33.3	33
0.0297	2	0.012	2	316	5	0.1616	4	5.4	33	33.3	33
0.0297	2	0.012	2	316	5	0.1616	4	5.4	33	33.3	33
0.0297	2	0.012	2	316	5	0.1616	4	5.4	33	33.3	33
0.0297	2	0.012	2	316	5	0.1616	4	5.4	33	33.3	33
0.0297	2	0.012	2	316	5	0.1616	4	5.4	33	33.3	33

Annexe 11 - Résultats de datation (2) sur Muscovite AR-04-64.

Incremental Heating		36Ar(a)	37Ar(ca)	38Ar(cl)	39Ar(k)	40Ar(r)	Age ± 2σ (Ma)	40Ar(r) (%)	39Ar(k) (%)	K/Ca ± 2σ
M1907-1	650 °C	0.000319	0.000215	0.005940	0.004460	0.007090	48.40 ± 57.32	6.92	0.20	3 ± 18
M1907-2	750 °C	0.000210	0.001270	0.000374	0.015699	0.047625	91.27 ± 11.54	43.00	0.70	2 ± 3
M1907-3	850 °C	0.000100	0.002105	0.000121	0.061914	0.263328	126.70 ± 3.10	89.23	2.77	5 ± 7
M1907-4	900 °C	0.000062	0.002051	0.000101	0.063995	0.284023	132.02 ± 2.86	93.28	2.86	5 ± 7
M1907-5	950 °C	0.000063	0.002643	0.000178	0.082391	0.380585	137.20 ± 2.95	94.73	3.68	5 ± 6
M1907-6	1000 °C	0.000110	0.000425	0.000510	0.313829	1.545068	145.88 ± 2.83	97.34	14.03	119 ± 408
M1907-7	1050 °C	0.000069	0.001467	0.000691	0.404585	1.928874	141.44 ± 2.73	98.34	18.08	45 ± 38
M1907-8	1100 °C	0.000060	0.000447	0.000366	0.208037	0.943910	134.85 ± 2.67	97.50	9.30	75 ± 186
M1907-9	1150 °C	0.000014	0.000633	0.000212	0.132829	0.614446	137.39 ± 2.77	98.70	5.94	34 ± 58
M1907-10	1200 °C	0.000015	0.000602	0.000326	0.171677	0.810801	140.16 ± 2.77	98.84	7.67	46 ± 94
M1907-11	1250 °C	0.000034	0.000180	0.000313	0.199202	0.958588	142.71 ± 2.83	98.34	8.90	179 ± 1095
M1907-12	1300 °C	0.000074	0.000775	0.001131	0.528662	2.663605	149.15 ± 2.87	98.60	23.63	110 ± 185
M1907-13	1400 °C	0.000021	0.000458	0.000112	0.034392	0.174547	150.19 ± 4.75	95.93	1.54	12 ± 22
M1907-14	1500 °C	0.000028	0.000754	0.000059	0.015718	0.079779	150.21 ± 4.75	89.95	0.70	3 ± 3
	Σ	0.001180	0.000839	0.010435	2.237389	10.702271				

Information on Analysis

Sample = AR-04-64
Material = Muscovite
Location = Arménie
Analyst = Yann ROLLAND
Project = ROLLAND_HASSIG
Mass Discrimination Law = LIN
Irradiation = MC45
J = 0.01710610 ± 0.00004277
Hb3gr = 1073.600 ± 5.368 Ma

Results	40(r)/39(k) ± 2σ	Age ± 2σ (Ma)	MSWD	39Ar(k) (%,n)	K/Ca ± 2σ
Age Plateau	4.7955 ± 0.1228	142.24 ± 3.57	12.21	89.79	4 ± 3
Error Mean	± 2.56%	± 2.51%		9	
	Minimal External Error ± 3.61		2.31	Statistical T Ratio	
	Analytical Error ± 3.50		3.4948	Error Magnification	
Total Fusion Age	4.7834 ± 0.0363	141.89 ± 1.24		14	431 ± 3434
	± 0.76%	± 0.87%			
	Minimal External Error ± 1.34				
	Analytical Error ± 1.03				

Normal Isochron		39(k)/36(a) ± 2σ	40(a+r)/36(a) ± 2σ	r.i.
M1907-1	650 °C	14.0 ± 1.3	320.8 ± 28.7	0.9690
M1907-2	750 °C	74.8 ± 7.4	525.4 ± 51.1	0.9785
M1907-3	850 °C	617.3 ± 84.5	2923.9 ± 396.2	0.9892
M1907-4	900 °C	1029.4 ± 159.6	4867.4 ± 748.2	0.9916
M1907-5	950 °C	1314.3 ± 264.1	6369.6 ± 1273.5	0.9950
M1907-6	1000 °C	2841.6 ± 361.0	14288.5 ± 1792.5	0.9875
M1907-7	1050 °C	5871.2 ± 922.2	28289.8 ± 4407.7	0.9919
M1907-8	1100 °C	3448.0 ± 874.3	15942.9 ± 4029.8	0.9969
M1907-9	1150 °C	9607.3 ± 8649.5	44740.5 ± 40270.2	0.9998
M1907-10	1200 °C	11573.0 ± 9825.8	54956.0 ± 46646.4	0.9997
M1907-11	1250 °C	5820.3 ± 2682.7	28306.7 ± 13034.8	0.9991
M1907-12	1300 °C	7159.0 ± 1448.8	36368.2 ± 7323.9	0.9951
M1907-13	1400 °C	1606.5 ± 1146.8	8451.9 ± 6031.0	0.9996
M1907-14	1500 °C	555.9 ± 137.0	3120.0 ± 766.3	0.9966

Results	40(a)/36(a) ± 2σ	40(r)/39(k) ± 2σ	Age ± 2σ (Ma)	MSWD
Normal Isochron Error Chron	541.0151 ± 431.5388 ± 79.76%	4.6961 ± 0.1551 ± 3.30%	139.40 ± 4.48 ± 3.22%	9.04
			Minimal External Error ± 4.51	
			Analytical Error ± 4.43	

Statistics				
	Statistical F ratio	2.01	Convergence	0.0000353476
	Error Magnification	3.0060	Number of Iterations	1
	Number of Data Points	9	Calculated Line	Weighted York-2

Inverse Isochron		39(k)/40(a+r) ± 2σ	36(a)/40(a+r) ± 2σ	r.i.
M1907-1	650 °C	0.043617 ± 0.000993	0.003117 ± 0.000279	0.0024
M1907-2	750 °C	0.142339 ± 0.002915	0.001903 ± 0.000185	0.0018
M1907-3	850 °C	0.211114 ± 0.004238	0.000342 ± 0.000046	0.0008
M1907-4	900 °C	0.211494 ± 0.004245	0.000205 ± 0.000032	0.0005
M1907-5	950 °C	0.206338 ± 0.004130	0.000157 ± 0.000031	0.0001
M1907-6	1000 °C	0.198872 ± 0.003975	0.000070 ± 0.000009	0.0001
M1907-7	1050 °C	0.207538 ± 0.004145	0.000035 ± 0.000006	0.0001
M1907-8	1100 °C	0.216272 ± 0.004326	0.000063 ± 0.000016	0.0001
M1907-9	1150 °C	0.214734 ± 0.004309	0.000022 ± 0.000020	0.0000
M1907-10	1200 °C	0.210587 ± 0.004213	0.000018 ± 0.000015	0.0000
M1907-11	1250 °C	0.205616 ± 0.004114	0.000035 ± 0.000016	0.0001
M1907-12	1300 °C	0.196847 ± 0.003933	0.000027 ± 0.000006	0.0001
M1907-13	1400 °C	0.190078 ± 0.003821	0.000118 ± 0.000084	0.0000
M1907-14	1500 °C	0.178167 ± 0.003605	0.000321 ± 0.000079	0.0007

Results	40(a)/36(a) ± 2σ	40(r)/39(k) ± 2σ	Age ± 2σ (Ma)	MSWD
Inverse Isochron	578.3530 ± 176.5239 ± 30.52%	4.7371 ± 0.0829 ± 1.75%	140.57 ± 2.46 ± 1.75%	10.39
Error Chron			Minimal External Error ± 2.51	
			Analytical Error ± 2.37	

Statistics				
	Statistical F ratio	2.01	Convergence	0.0005929558
	Error Magnification	3.2237	Number of Iterations	8
	Number of Data Points	9	Calculated Line	Weighted York-2

Relative Abundances			36Ar	%1σ	37Ar	%1σ	38Ar	%1σ	39Ar	%1σ	40Ar	%1σ	Age ± 2σ (Ma)	40Ar(r) (%)	39Ar(k) (%)	K/Ca ± 2σ
M1907-1	650 °C		0.0003215	4.429	0.0002151	272.916	0.0060554	2.029	0.0044606	1.133	0.1023963	0.111	48.40 ± 57.32	6.92	0.20	3 ± 18
M1907-2	750 °C		0.0002104	4.846	0.0012695	74.547	0.0006097	2.649	0.0157001	1.020	0.1107605	0.093	91.27 ± 11.54	43.00	0.70	2 ± 3
M1907-3	850 °C		0.0000998	6.796	0.0021048	76.597	0.0008699	2.382	0.0619128	1.001	0.2951133	0.072	126.70 ± 3.10	89.23	2.77	5 ± 7
M1907-4	900 °C		0.0000616	7.724	0.0020514	70.806	0.0008680	2.575	0.0639930	1.002	0.3044841	0.062	132.02 ± 2.86	93.28	2.86	5 ± 7
M1907-5	950 °C		0.0000620	10.080	0.0026428	57.844	0.0011629	2.226	0.0823891	1.000	0.4017480	0.034	137.20 ± 2.95	94.73	3.68	5 ± 6
M1907-6	1000 °C		0.0001108	6.250	0.0004249	170.907	0.0042993	2.039	0.3138289	0.999	1.5873620	0.017	145.88 ± 2.83	97.34	14.03	119 ± 408
M1907-7	1050 °C		0.0000696	7.704	0.0014672	42.774	0.0055681	2.014	0.4045859	0.998	1.9614640	0.017	141.44 ± 2.73	98.34	18.08	45 ± 38
M1907-8	1100 °C		0.0000606	12.575	0.0004468	123.678	0.0028765	2.051	0.2080374	1.000	0.9681029	0.028	134.85 ± 2.67	97.50	9.30	75 ± 186
M1907-9	1150 °C		0.0000137	45.260	0.0006332	85.972	0.0018050	2.199	0.1328282	1.003	0.6225187	0.036	137.39 ± 2.77	98.70	5.94	34 ± 58
M1907-10	1200 °C		0.0000152	41.534	0.0006020	102.347	0.0023928	2.016	0.1716770	1.000	0.8203284	0.021	140.16 ± 2.77	98.84	7.67	46 ± 94
M1907-11	1250 °C		0.0000344	22.891	0.0001798	305.949	0.0027110	2.058	0.1992017	1.000	0.9747223	0.032	142.71 ± 2.83	98.34	8.90	179 ± 1095
M1907-12	1300 °C		0.0000746	9.966	0.0007752	83.809	0.0074938	2.031	0.5286623	0.999	2.7013540	0.020	149.15 ± 2.87	98.60	23.63	110 ± 185
M1907-13	1400 °C		0.0000216	35.376	0.0004585	91.777	0.0005315	2.236	0.0343928	1.004	0.1819602	0.040	150.19 ± 4.75	95.93	1.54	12 ± 22
M1907-14	1500 °C		0.0000285	12.173	0.0007539	40.697	0.0002575	2.634	0.0157187	1.007	0.0886882	0.092	150.21 ± 4.75	89.95	0.70	3 ± 3
		Σ	0.0011844	2.411	0.0008392	398.525	0.0375014	0.711	2.2373886	0.370	11.1210027	0.008				

Information on Analysis and Constants Used in Calculations

Sample = AR-04-64
Material = Muscovite
Location = Arménie
Analyst = Yann ROLLAND
Project = ROLLAND_HASSIG
Mass Discrimination Law = LIN
Irradiation = MC45
J = 0.01710610 ± 0.00004277
Hb3gr = 1073.600 ± 5.368 Ma
IGSN = Undefined
Preferred Age = Undefined
Classification = Undefined
Experiment Type = Undefined
Extraction Method = Undefined
Heating = 600 sec
Isolation = 2.00 min
Instrument = FOUR
Lithology = Undefined
Lat-Lon = Undefined - Undefined

Age Equations = Conventional
Negative Intensities = Allowed
Decay Constant 40K = 5.543 ± 0.010 E-10 1/ a
Decay Constant 39Ar = 2.940 ± 0.029 E-07 1/ h
Decay Constant 37Ar = 8.220 ± 0.010 E-04 1/ h
Decay Constant 36Cl = 2.310 ± 0.016 E-06 1/ a
Production Ratio 36/ 38 in Cl = 316.0 ± 15.8

Results	40(r)/39(k) ± 2σ	Age ± 2σ (Ma)	MSWD	39Ar(k) (%,n)	K/Ca ± 2σ
Age Plateau	4.7955 ± 0.1228	142.24 ± 3.57	12.21	89.79	4 ± 3
Error Mean	± 2.56%	± 2.51%		9	
	Minimal External Error ± 3.61		2.31	Statistical T Ratio	
	Analytical Error ± 3.50		3.4948	Error Magnification	
Total Fusion Age	4.7834 ± 0.0363	141.89 ± 1.24		14	431 ± 3434
	± 0.76%	± 0.87%			
	Minimal External Error ± 1.34				
	Analytical Error ± 1.03				
Normal Isochron	4.6961 ± 0.1551	139.40 ± 4.48	9.04	89.79	
Error Chron	± 3.30%	± 3.22%		9	
	Minimal External Error ± 4.51		2.01	Statistical F ratio	
	Analytical Error ± 4.43		3.0060	Error Magnification	
Inverse Isochron	4.7371 ± 0.0829	140.57 ± 2.46	10.39	89.79	
Error Chron	± 1.75%	± 1.75%		9	
	Minimal External Error ± 2.51		2.01	Statistical F ratio	
	Analytical Error ± 2.37		3.2237	Error Magnification	

Degassing Patterns			36Ar(a)	%1σ	36Ar(c)	%1σ	36Ar(ca)	%1σ	36Ar(cl)	%1σ	37Ar(ca)	%1σ	38Ar(a)	%1σ	38Ar(c)	%1σ	38Ar(k)	%1σ
M1907-1	650 °C		0.000319	4.47	0.000000	0.00	0.000000	272.92	0.000003	5.46	0.000215	272.92	0.000060	4.47	0.000000	0.00	0.000054	2.30
M1907-2	750 °C		0.000210	4.86	0.000000	0.00	0.000000	74.55	0.000000	7.17	0.001270	74.55	0.000040	4.86	0.000000	0.00	0.000188	2.24
M1907-3	850 °C		0.000100	6.77	0.000000	0.00	0.000001	76.60	0.000000	25.82	0.002105	76.60	0.000019	6.78	0.000000	0.00	0.000743	2.24
M1907-4	900 °C		0.000062	7.69	0.000000	0.00	0.000001	70.81	0.000000	31.78	0.002051	70.81	0.000012	7.69	0.000000	0.00	0.000768	2.24
M1907-5	950 °C		0.000063	10.00	0.000000	0.00	0.000001	57.85	0.000000	21.99	0.002643	57.84	0.000012	10.00	0.000000	0.00	0.000989	2.24
M1907-6	1000 °C		0.000110	6.27	0.000000	0.00	0.000000	170.91	0.000000	24.45	0.000425	170.91	0.000021	6.27	0.000000	0.00	0.003766	2.24
M1907-7	1050 °C		0.000069	7.79	0.000000	0.00	0.000000	42.79	0.000000	23.23	0.001467	42.77	0.000013	7.79	0.000000	0.00	0.004855	2.24
M1907-8	1100 °C		0.000060	12.64	0.000000	0.00	0.000000	123.68	0.000000	22.85	0.000447	123.68	0.000011	12.64	0.000000	0.00	0.002496	2.24
M1907-9	1150 °C		0.000014	45.00	0.000000	0.00	0.000000	85.98	0.000000	25.82	0.000633	85.97	0.000003	45.00	0.000000	0.00	0.001594	2.24
M1907-10	1200 °C		0.000015	42.44	0.000000	0.00	0.000000	102.35	0.000000	21.17	0.000602	102.35	0.000003	42.44	0.000000	0.00	0.002060	2.24
M1907-11	1250 °C		0.000034	23.02	0.000000	0.00	0.000000	305.95	0.000000	25.29	0.000180	305.95	0.000006	23.02	0.000000	0.00	0.002390	2.24
M1907-12	1300 °C		0.000074	10.07	0.000000	0.00	0.000000	83.81	0.000001	19.13	0.000775	83.81	0.000014	10.07	0.000000	0.00	0.006344	2.24
M1907-13	1400 °C		0.000021	35.68	0.000000	0.00	0.000000	91.78	0.000000	14.79	0.000458	91.78	0.000004	35.68	0.000000	0.00	0.000413	2.24
M1907-14	1500 °C		0.000028	12.28	0.000000	0.00	0.000000	40.71	0.000000	16.36	0.000754	40.70	0.000005	12.28	0.000000	0.00	0.000189	2.24
		Σ	0.001180	2.42	0.000000	0.00	0.000000	398.56	0.000005	4.49	0.000839	398.53	0.000222	2.42	0.000000	0.00	0.026849	0.83
		Σ							0.001184	2.41	0.000839	398.53						

38Ar(ca)	%1σ	38Ar(cl)	%1σ	39Ar(k)	%1σ	39Ar(ca)	%1σ	40Ar(r)	%1σ	40Ar(a)	%1σ	40Ar(c)	%1σ	40Ar(k)	%1σ
0.000001	287.37	0.005940	7.44	0.004460	1.13	0.000000	272.95	0.007090	60.00	0.095173	4.47	0.000000	0.00	0.000132	2.30
0.000008	116.86	0.000374	8.77	0.015699	1.02	0.000001	74.65	0.047625	6.40	0.062669	4.86	0.000000	0.00	0.000466	2.24
0.000013	118.18	0.000121	26.31	0.061914	1.00	0.000002	76.70	0.263328	0.77	0.029946	6.78	0.000000	0.00	0.001839	2.24
0.000012	114.51	0.000101	32.17	0.063995	1.00	0.000001	70.92	0.284023	0.51	0.018560	7.69	0.000000	0.00	0.001901	2.24
0.000016	106.99	0.000178	22.56	0.082391	1.00	0.000002	57.98	0.380585	0.49	0.018716	10.00	0.000000	0.00	0.002447	2.24
0.000003	193.16	0.000510	24.97	0.313829	1.00	0.000000	170.95	1.545068	0.14	0.032973	6.27	0.000000	0.00	0.009321	2.24
0.000009	99.65	0.000691	23.78	0.404585	1.00	0.000001	42.96	1.928874	0.09	0.020574	7.79	0.000000	0.00	0.012016	2.24
0.000003	152.96	0.000366	23.40	0.208037	1.00	0.000000	123.74	0.943910	0.24	0.018014	12.64	0.000000	0.00	0.006179	2.24
0.000004	124.46	0.000212	26.30	0.132829	1.00	0.000000	86.07	0.614446	0.30	0.004128	45.00	0.000000	0.00	0.003945	2.24
0.000004	136.29	0.000326	21.77	0.171677	1.00	0.000000	102.42	0.810801	0.23	0.004429	42.44	0.000000	0.00	0.005099	2.24
0.000001	318.91	0.000313	25.79	0.199202	1.00	0.000000	305.98	0.958588	0.25	0.010218	23.02	0.000000	0.00	0.005916	2.24
0.000005	122.98	0.001131	19.78	0.528662	1.00	0.000001	83.90	2.663605	0.09	0.022048	10.07	0.000000	0.00	0.015701	2.24
0.000003	128.54	0.000112	15.63	0.034392	1.00	0.000000	91.86	0.174547	1.31	0.006392	35.68	0.000000	0.00	0.001021	2.24
0.000005	98.77	0.000059	17.12	0.015718	1.01	0.000001	40.89	0.079779	1.30	0.008442	12.28	0.000000	0.00	0.000467	2.24
0.000005	641.67	0.010435	5.38	2.237389	0.37	0.000001	399.15	10.702271	0.08	0.352282	2.42	0.000000	0.00	0.066450	0.83
		0.037501	1.61			2.237389	0.37							11.121003	0.11

Additional Parameters		40(r)/39(k)	1σ	40(r+a)	1σ	40Ar/39Ar	1σ	37Ar/39Ar	1σ	36Ar/39Ar	1σ	Time (days)	37Ar (decay)	39Ar (decay)	40Ar (moles)
M1907-1	650 °C	1.589629	0.95393	0.102264	0.00011	22.955575	0.26128	0.048221	0.13160	0.072080	0.00329	226.347	90.86509867	1.00161427	2.048E-15
M1907-2	750 °C	3.033599	0.19659	0.110294	0.00010	7.054758	0.07223	0.080861	0.06029	0.013403	0.00066	226.363	90.89248954	1.00161437	2.215E-15
M1907-3	850 °C	4.253107	0.05384	0.293274	0.00022	4.766592	0.04784	0.033996	0.02604	0.001611	0.00011	226.380	90.92362555	1.00161450	5.902E-15
M1907-4	900 °C	4.438245	0.04982	0.302583	0.00019	4.758081	0.04775	0.032056	0.02270	0.000963	0.00008	226.396	90.95228009	1.00161461	6.090E-15
M1907-5	950 °C	4.619247	0.05151	0.399301	0.00015	4.876225	0.04879	0.032077	0.01856	0.000753	0.00008	226.412	90.98219012	1.00161473	8.035E-15
M1907-6	1000 °C	4.923287	0.04965	1.578041	0.00034	5.058049	0.05055	0.001354	0.00231	0.000353	0.00002	226.429	91.01210998	1.00161484	3.175E-14
M1907-7	1050 °C	4.767539	0.04777	1.949448	0.00043	4.848078	0.04840	0.003626	0.00155	0.000172	0.00001	226.447	91.04328697	1.00161497	3.923E-14
M1907-8	1100 °C	4.537222	0.04668	0.961924	0.00030	4.653504	0.04654	0.002148	0.00266	0.000291	0.00004	226.463	91.07197923	1.00161508	1.936E-14
M1907-9	1150 °C	4.625855	0.04848	0.618574	0.00024	4.686647	0.04702	0.004767	0.00410	0.000103	0.00005	226.482	91.10692114	1.00161522	1.245E-14
M1907-10	1200 °C	4.722838	0.04849	0.815230	0.00020	4.778323	0.04779	0.003507	0.00359	0.000088	0.00004	226.495	91.13063936	1.00161531	1.641E-14
M1907-11	1250 °C	4.812149	0.04956	0.968806	0.00034	4.893142	0.04894	0.000903	0.00276	0.000173	0.00004	226.512	91.16060804	1.00161543	1.949E-14
M1907-12	1300 °C	5.038392	0.05050	2.685653	0.00064	5.109791	0.05104	0.001466	0.00123	0.000141	0.00001	226.528	91.19058658	1.00161555	5.403E-14
M1907-13	1400 °C	5.075160	0.08366	0.180939	0.00008	5.290651	0.05317	0.013330	0.01223	0.000628	0.00022	226.544	91.21932526	1.00161566	3.639E-15
M1907-14	1500 °C	5.075622	0.08362	0.088221	0.00008	5.642223	0.05707	0.047965	0.01953	0.001814	0.00022	226.563	91.25307353	1.00161579	1.774E-15

Procedure Blanks		36Ar	1σ	37Ar	1σ	38Ar	1σ	39Ar	1σ	40Ar	1σ
M1907-1	650 °C	0.000056	0.000005	0.000161	0.000003	0.000022	0.000003	0.000028	0.000003	0.008388	0.000016
M1907-2	750 °C	0.000046	0.000005	0.000165	0.000008	0.000016	0.000005	0.000030	0.000004	0.005026	0.000018
M1907-3	850 °C	0.000056	0.000004	0.000190	0.000016	0.000027	0.000005	0.000038	0.000005	0.006494	0.000063
M1907-4	900 °C	0.000056	0.000004	0.000190	0.000016	0.000027	0.000005	0.000038	0.000005	0.006494	0.000063
M1907-5	950 °C	0.000056	0.000004	0.000190	0.000016	0.000027	0.000005	0.000038	0.000005	0.006494	0.000063
M1907-6	1000 °C	0.000065	0.000003	0.000160	0.000005	0.000027	0.000005	0.000030	0.000003	0.009657	0.000021
M1907-7	1050 °C	0.000065	0.000003	0.000160	0.000005	0.000027	0.000005	0.000030	0.000003	0.009657	0.000021
M1907-8	1100 °C	0.000065	0.000003	0.000160	0.000005	0.000027	0.000005	0.000030	0.000003	0.009657	0.000021
M1907-9	1150 °C	0.000075	0.000004	0.000162	0.000005	0.000028	0.000004	0.000310	0.000007	0.015500	0.000021
M1907-10	1200 °C	0.000075	0.000004	0.000162	0.000005	0.000028	0.000004	0.000310	0.000007	0.015500	0.000021
M1907-11	1250 °C	0.000053	0.000005	0.000159	0.000003	0.000027	0.000002	0.000043	0.000004	0.007736	0.000014
M1907-12	1300 °C	0.000053	0.000005	0.000159	0.000003	0.000027	0.000002	0.000043	0.000004	0.007736	0.000014
M1907-13	1400 °C	0.000053	0.000006	0.000153	0.000003	0.000019	0.000003	0.000049	0.000004	0.007325	0.000017
M1907-14	1500 °C	0.000054	0.000002	0.000147	0.000003	0.000020	0.000003	0.000136	0.000007	0.009297	0.000030

Intercept Values		36Ar	1σ	r2		37Ar	1σ	r2		38Ar	1σ	r2		39Ar	1σ	r2		40Ar	1σ	r2	
M1907-1	650 °C	0.000390	0.000005	0.6962	LIN 11 of 11	0.000163	0.000006		AVE 11 of 11	0.006197	0.000027	0.9402	EXP 11 of 11	0.004526	0.000024	0.9115	EXP 11 of 11	0.110784	0.000112	0.9962	EXP 11 of 11
M1907-2	750 °C	0.000265	0.000004	0.4569	LIN 11 of 11	0.000179	0.000007	0.1199	LIN 11 of 11	0.000638	0.000010	0.5487	LIN 11 of 11	0.015860	0.000033	0.9852	EXP 11 of 11	0.115786	0.000101	0.9970	EXP 11 of 11
M1907-3	850 °C	0.000160	0.000004	0.3132	LIN 11 of 11	0.000166	0.000009		AVE 11 of 11	0.000914	0.000011	0.3460	LIN 11 of 11	0.062463	0.000048	0.9980	EXP 11 of 11	0.301607	0.000202	0.9983	EXP 11 of 11
M1907-4	900 °C	0.000120	0.000002	0.6861	LIN 11 of 11	0.000167	0.000004	0.3167	LIN 11 of 11	0.000912	0.000014	0.4809	LIN 11 of 11	0.064560	0.000054	0.9976	EXP 11 of 11	0.310978	0.000178	0.9988	EXP 11 of 11
M1907-5	950 °C	0.000120	0.000004		AVE 11 of 11	0.000160	0.000007		AVE 11 of 11	0.001213	0.000011	0.8616	EXP 11 of 11	0.083108	0.000052	0.9988	EXP 11 of 11	0.408242	0.000120	0.9997	EXP 11 of 11
M1907-6	1000 °C	0.000180	0.000005	0.3952	LIN 11 of 11	0.000165	0.000007		AVE 11 of 11	0.004412	0.000021	0.9215	EXP 11 of 11	0.316454	0.000151	0.9992	EXP 11 of 11	1.597019	0.000267	0.9999	EXP 11 of 11
M1907-7	1050 °C	0.000137	0.000004	0.2521	LIN 11 of 11	0.000177	0.000005	0.1555	LIN 11 of 11	0.005706	0.000020	0.9503	EXP 11 of 11	0.407962	0.000076	0.9999	EXP 11 of 11	1.971121	0.000330	0.9999	EXP 11 of 11
M1907-8	1100 °C	0.000128	0.000007		AVE 11 of 11	0.000165	0.000004		AVE 11 of 11	0.002961	0.000015	0.9160	EXP 11 of 11	0.209788	0.000118	0.9989	EXP 11 of 11	0.977760	0.000266	0.9997	EXP 11 of 11
M1907-9	1150 °C	0.000089	0.000005		AVE 11 of 11	0.000155	0.000004	0.3445	LIN 11 of 11	0.001869	0.000017	0.8069	EXP 11 of 11	0.134237	0.000128	0.9969	EXP 11 of 11	0.638019	0.000225	0.9996	EXP 11 of 11
M1907-10	1200 °C	0.000091	0.000005		AVE 11 of 11	0.000169	0.000005	0.2027	LIN 11 of 11	0.002468	0.000008	0.9696	EXP 11 of 11	0.173407	0.000104	0.9988	EXP 11 of 11	0.835828	0.000168	0.9999	EXP 11 of 11
M1907-11	1250 °C	0.000089	0.000006		AVE 11 of 11	0.000161	0.000005		AVE 11 of 11	0.002792	0.000015	0.8965	EXP 11 of 11	0.200892	0.000113	0.9990	EXP 11 of 11	0.982458	0.000313	0.9997	EXP 11 of 11
M1907-12	1300 °C	0.000131	0.000005		AVE 11 of 11	0.000168	0.000007		AVE 11 of 11	0.007669	0.000034	0.9295	EXP 11 of 11	0.533077	0.000173	0.9996	EXP 11 of 11	2.709090	0.000534	0.9999	EXP 11 of 11
M1907-13	1400 °C	0.000075	0.000005		AVE 11 of 11	0.000158	0.000004		AVE 11 of 11	0.000561	0.000005	0.4300	EXP 11 of 11	0.034726	0.000038	0.9957	EXP 11 of 11	0.189285	0.000071	0.9994	EXP 11 of 11
M1907-14	1500 °C	0.000084	0.000003	0.1261	LIN 11 of 11	0.000156	0.000002	0.4210	LIN 11 of 11	0.000283	0.000003	0.0887	LIN 11 of 11	0.015985	0.000020	0.9931	EXP 11 of 11	0.097985	0.000076	0.9973	EXP 11 of 11

Sample Parameters		Sample	Material	Location	Analyst	Temp	Standard (in Ma)	%1σ	J	%1σ	MDF	%1σ
M1907-1	650 °C	AR-04-64	Muscovite	Arménie	Yann ROLLAND	650	1073.6	0.5	0.0171061	0.25	1.009917	1
M1907-2	750 °C	AR-04-70	Muscovite	Arménie	Yann ROLLAND	750	1073.6	0.5	0.0171061	0.25	1.009917	1
M1907-3	850 °C	AR-04-71	Muscovite	Arménie	Yann ROLLAND	850	1073.6	0.5	0.0171061	0.25	1.009917	1
M1907-4	900 °C	AR-04-72	Muscovite	Arménie	Yann ROLLAND	900	1073.6	0.5	0.0171061	0.25	1.009917	1
M1907-5	950 °C	AR-04-73	Muscovite	Arménie	Yann ROLLAND	950	1073.6	0.5	0.0171061	0.25	1.009917	1
M1907-6	1000 °C	AR-04-74	Muscovite	Arménie	Yann ROLLAND	1000	1073.6	0.5	0.0171061	0.25	1.009917	1
M1907-7	1050 °C	AR-04-75	Muscovite	Arménie	Yann ROLLAND	1050	1073.6	0.5	0.0171061	0.25	1.009917	1
M1907-8	1100 °C	AR-04-76	Muscovite	Arménie	Yann ROLLAND	1100	1073.6	0.5	0.0171061	0.25	1.009917	1
M1907-9	1150 °C	AR-04-77	Muscovite	Arménie	Yann ROLLAND	1150	1073.6	0.5	0.0171061	0.25	1.009917	1
M1907-10	1200 °C	AR-04-65	Muscovite	Arménie	Yann ROLLAND	1200	1073.6	0.5	0.0171061	0.25	1.009917	1
M1907-11	1250 °C	AR-04-66	Muscovite	Arménie	Yann ROLLAND	1250	1073.6	0.5	0.0171061	0.25	1.009917	1
M1907-12	1300 °C	AR-04-67	Muscovite	Arménie	Yann ROLLAND	1300	1073.6	0.5	0.0171061	0.25	1.009917	1
M1907-13	1400 °C	AR-04-68	Muscovite	Arménie	Yann ROLLAND	1400	1073.6	0.5	0.0171061	0.25	1.009917	1
M1907-14	1500 °C	AR-04-69	Muscovite	Arménie	Yann ROLLAND	1500	1073.6	0.5	0.0171061	0.25	1.009917	1

Volume Ratio	Sensitivity (mol/volt)	Day	Month	Year	Hour	Min	Resist	Irradiation	Project	Experiment	Nmb	Standard Name
1	2.000E-14	14	NOV	2005	07	02	001	MC45	Rolland_Hassig	M1907	01	Hb3gr
1	2.000E-14	14	NOV	2005	07	24	001	MC45	Rolland_Hassig	M1907	01	Hb3gr
1	2.000E-14	14	NOV	2005	07	49	001	MC45	Rolland_Hassig	M1907	01	Hb3gr
1	2.000E-14	14	NOV	2005	08	12	001	MC45	Rolland_Hassig	M1907	01	Hb3gr
1	2.000E-14	14	NOV	2005	08	36	001	MC45	Rolland_Hassig	M1907	01	Hb3gr
1	2.000E-14	14	NOV	2005	09	00	001	MC45	Rolland_Hassig	M1907	01	Hb3gr
1	2.000E-14	14	NOV	2005	09	25	001	MC45	Rolland_Hassig	M1907	01	Hb3gr
1	2.000E-14	14	NOV	2005	09	48	001	MC45	Rolland_Hassig	M1907	01	Hb3gr
1	2.000E-14	14	NOV	2005	10	16	001	MC45	Rolland_Hassig	M1907	01	Hb3gr
1	2.000E-14	14	NOV	2005	10	35	001	MC45	Rolland_Hassig	M1907	01	Hb3gr
1	2.000E-14	14	NOV	2005	10	59	001	MC45	Rolland_Hassig	M1907	01	Hb3gr
1	2.000E-14	14	NOV	2005	11	23	001	MC45	Rolland_Hassig	M1907	01	Hb3gr
1	2.000E-14	14	NOV	2005	11	46	001	MC45	Rolland_Hassig	M1907	01	Hb3gr
1	2.000E-14	14	NOV	2005	12	13	001	MC45	Rolland_Hassig	M1907	01	Hb3gr

Irradiation Constants		40/36(a)	%1σ	40/36(c)	%1σ	38/36(a)	%1σ	38/36(c)	%1σ	39/37(ca)	%1σ	38/37(ca)	%1σ	36/37(ca)	%1σ
M1907-1	650 °C	298.56	0.1	0.018	35	0.1885	0.16	1.7	3	0.00073	4	0.006	90	0.000282	1
M1907-2	750 °C	298.56	0.1	0.018	35	0.1885	0.16	1.7	3	0.00073	4	0.006	90	0.000282	1
M1907-3	850 °C	298.56	0.1	0.018	35	0.1885	0.16	1.7	3	0.00073	4	0.006	90	0.000282	1
M1907-4	900 °C	298.56	0.1	0.018	35	0.1885	0.16	1.7	3	0.00073	4	0.006	90	0.000282	1
M1907-5	950 °C	298.56	0.1	0.018	35	0.1885	0.16	1.7	3	0.00073	4	0.006	90	0.000282	1
M1907-6	1000 °C	298.56	0.1	0.018	35	0.1885	0.16	1.7	3	0.00073	4	0.006	90	0.000282	1
M1907-7	1050 °C	298.56	0.1	0.018	35	0.1885	0.16	1.7	3	0.00073	4	0.006	90	0.000282	1
M1907-8	1100 °C	298.56	0.1	0.018	35	0.1885	0.16	1.7	3	0.00073	4	0.006	90	0.000282	1
M1907-9	1150 °C	298.56	0.1	0.018	35	0.1885	0.16	1.7	3	0.00073	4	0.006	90	0.000282	1
M1907-10	1200 °C	298.56	0.1	0.018	35	0.1885	0.16	1.7	3	0.00073	4	0.006	90	0.000282	1
M1907-11	1250 °C	298.56	0.1	0.018	35	0.1885	0.16	1.7	3	0.00073	4	0.006	90	0.000282	1
M1907-12	1300 °C	298.56	0.1	0.018	35	0.1885	0.16	1.7	3	0.00073	4	0.006	90	0.000282	1
M1907-13	1400 °C	298.56	0.1	0.018	35	0.1885	0.16	1.7	3	0.00073	4	0.006	90	0.000282	1
M1907-14	1500 °C	298.56	0.1	0.018	35	0.1885	0.16	1.7	3	0.00073	4	0.006	90	0.000282	1

40/39(k)	%1σ	38/39(k)	%1σ	36/38(cl)	%1σ	K/Ca	%1σ	K/Cl	%1σ	Ca/Cl	%1σ
0.0297	2	0.012	2	316	5	0.1616	4	5.4	33	33.3	33
0.0297	2	0.012	2	316	5	0.1616	4	5.4	33	33.3	33
0.0297	2	0.012	2	316	5	0.1616	4	5.4	33	33.3	33
0.0297	2	0.012	2	316	5	0.1616	4	5.4	33	33.3	33
0.0297	2	0.012	2	316	5	0.1616	4	5.4	33	33.3	33
0.0297	2	0.012	2	316	5	0.1616	4	5.4	33	33.3	33
0.0297	2	0.012	2	316	5	0.1616	4	5.4	33	33.3	33
0.0297	2	0.012	2	316	5	0.1616	4	5.4	33	33.3	33
0.0297	2	0.012	2	316	5	0.1616	4	5.4	33	33.3	33
0.0297	2	0.012	2	316	5	0.1616	4	5.4	33	33.3	33
0.0297	2	0.012	2	316	5	0.1616	4	5.4	33	33.3	33
0.0297	2	0.012	2	316	5	0.1616	4	5.4	33	33.3	33
0.0297	2	0.012	2	316	5	0.1616	4	5.4	33	33.3	33

Annexe 12 - Résultats de datation (2) sur Muscovite AR-04-62B.

Incremental Heating		36Ar(a)	37Ar(ca)	38Ar(cl)	39Ar(k)	40Ar(r)	Age ± 2σ (Ma)	40Ar(r) (%)	39Ar(k) (%)	K/Ca ± 2σ
M1905-1	650 °C	0.000462	0.002387	0.009344	0.005985	0.010686	54.27 ± 57.66	7.18	0.19	0.4 ± 0.3
M1905-2	750 °C	0.000309	0.005139	0.000545	0.023735	0.080449	101.67 ± 10.18	46.40	0.74	0.7 ± 0.3
M1905-3	850 °C	0.000201	0.002586	0.000771	0.079983	0.362860	134.83 ± 3.47	85.35	2.49	5.0 ± 2.6
M1905-4	900 °C	0.000173	0.002100	0.000422	0.145327	0.745054	151.64 ± 3.12	93.01	4.53	11.2 ± 8.0
M1905-5	950 °C	0.000116	0.002855	0.001147	0.552643	2.892190	154.67 ± 2.97	98.26	17.23	31.3 ± 17.9
M1905-6	1000 °C	0.000071	0.002607	0.001065	0.576185	2.947935	151.35 ± 2.91	98.72	17.97	35.7 ± 15.5
M1905-7	1025 °C	0.000022	0.002129	0.000543	0.267826	1.331580	147.24 ± 2.85	98.91	8.35	20.3 ± 11.7
M1905-8	1050 °C	0.000033	0.002332	0.000357	0.190230	0.909768	141.85 ± 2.77	98.32	5.93	13.2 ± 7.9
M1905-9	1075 °C	0.000024	0.000754	0.000301	0.140682	0.671341	141.55 ± 2.89	98.34	4.39	30.1 ± 40.4
M1905-10	1115 °C	0.000029	0.001071	0.000383	0.161274	0.782770	143.88 ± 2.86	98.31	5.03	24.3 ± 30.0
M1905-11	1225 °C	0.000099	0.003746	0.001163	0.404458	1.997440	146.30 ± 2.84	97.96	12.61	17.4 ± 8.1
M1905-12	1325 °C	0.000046	0.007577	0.001434	0.558374	2.854513	151.23 ± 2.90	98.95	17.41	11.9 ± 2.4
M1905-13	1450 °C	0.000007	0.001298	0.000227	0.060878	0.316185	153.54 ± 3.48	98.74	1.90	7.6 ± 5.8
M1905-14	1550 °C	0.000008	0.001404	0.000088	0.039442	0.202769	152.05 ± 3.88	98.29	1.23	4.5 ± 3.7
	Σ	0.001600	0.037986	0.017790	3.207022	16.105540				

Information on Analysis

Sample = AR-04-62B
Material = Muscovite
Location = Arménie
Analyst = Yann ROLLAND
Project = ROLLAND_HASSIG
Mass Discrimination Law = LIN
Irradiation = MC45
J = 0.01710430 ± 0.00004276
Hb3gr = 1073.600 ± 5.368 Ma

Results	40(r)/39(k) ± 2σ	Age ± 2σ (Ma)	MSWD	39Ar(k) (%,n)	K/Ca ± 2σ
Age Plateau	5.0052 ± 0.1006	148.19 ± 2.95	9.98	96.58	10.9 ± 3.3
Error Mean	± 2.01%	± 1.99%		11	
	Minimal External Error ± 2.99		2.23	Statistical T Ratio	
	Analytical Error ± 2.86		3.1587	Error Magnification	
Total Fusion Age	5.0220 ± 0.0363	148.67 ± 1.25		14	13.6 ± 2.1
	± 0.72%	± 0.84%			
	Minimal External Error ± 1.36				
	Analytical Error ± 1.03				

Normal Isochron		39(k)/36(a) ± 2σ	40(a+r)/36(a) ± 2σ	r.i.
M1905-1	650 °C	13.0 ± 1.1	321.7 ± 26.9	0.9714
M1905-2	750 °C	76.8 ± 6.9	559.0 ± 49.2	0.9742
M1905-3	850 °C	398.6 ± 43.3	2106.9 ± 224.8	0.9828
M1905-4	900 °C	840.1 ± 95.3	4605.4 ± 514.4	0.9843
M1905-5	950 °C	4744.8 ± 694.2	25129.9 ± 3642.5	0.9906
M1905-6	1000 °C	8148.9 ± 2151.0	41990.9 ± 11052.0	0.9971
M1905-7	1025 °C	12005.4 ± 6209.7	59987.2 ± 31005.0	0.9993
M1905-8	1050 °C	5730.5 ± 1876.5	27704.6 ± 9055.4	0.9981
M1905-9	1075 °C	5854.4 ± 3943.4	28236.1 ± 19010.9	0.9996
M1905-10	1115 °C	5559.2 ± 2623.7	27281.0 ± 12863.7	0.9991
M1905-11	1225 °C	4084.6 ± 834.5	20470.8 ± 4162.4	0.9952
M1905-12	1325 °C	12188.8 ± 2017.5	62610.1 ± 10287.5	0.9927
M1905-13	1450 °C	8201.4 ± 14619.7	42895.1 ± 76458.9	0.9999
M1905-14	1550 °C	5016.5 ± 7492.7	26088.4 ± 38962.0	0.9999

Results	40(a)/36(a) ± 2σ	40(r)/39(k) ± 2σ	Age ± 2σ (Ma)	MSWD
Normal Isochron No Convergence	284.0727 ± 301.9643 ± 106.30%	5.0771 ± 0.1297 ± 2.55%	150.23 ± 3.75 ± 2.50%	7.19
			Minimal External Error ± 3.79	
			Analytical Error ± 3.68	

Statistics				
	Statistical F ratio	1.88	Convergence	0.0000747344
	Error Magnification	2.6810	Number of Iterations	100
	Number of Data Points	11	Calculated Line	Weighted York-2

Inverse Isochron		39(k)/40(a+r) ± 2σ	36(a)/40(a+r) ± 2σ	r.i.
M1905-1	650 °C	0.040274 ± 0.000822	0.003109 ± 0.000260	0.0008
M1905-2	750 °C	0.137463 ± 0.002801	0.001789 ± 0.000157	0.0006
M1905-3	850 °C	0.189189 ± 0.003798	0.000475 ± 0.000051	0.0001
M1905-4	900 °C	0.182410 ± 0.003650	0.000217 ± 0.000024	0.0002
M1905-5	950 °C	0.188811 ± 0.003771	0.000040 ± 0.000006	0.0000
M1905-6	1000 °C	0.194064 ± 0.003877	0.000024 ± 0.000006	0.0000
M1905-7	1025 °C	0.200133 ± 0.003998	0.000017 ± 0.000009	0.0000
M1905-8	1050 °C	0.206843 ± 0.004136	0.000036 ± 0.000012	0.0000
M1905-9	1075 °C	0.207339 ± 0.004146	0.000035 ± 0.000024	0.0000
M1905-10	1115 °C	0.203775 ± 0.004080	0.000037 ± 0.000017	0.0000
M1905-11	1225 °C	0.199535 ± 0.003987	0.000049 ± 0.000010	0.0000
M1905-12	1325 °C	0.194678 ± 0.003889	0.000016 ± 0.000003	0.0000
M1905-13	1450 °C	0.191198 ± 0.003834	0.000023 ± 0.000042	0.0000
M1905-14	1550 °C	0.192290 ± 0.003887	0.000038 ± 0.000057	0.0000

Results	40(a)/36(a) ± 2σ	40(r)/39(k) ± 2σ	Age ± 2σ (Ma)	MSWD
Inverse Isochron Error Chron	477.7413 ± 129.9030 ± 27.19%	4.9721 ± 0.0678 ± 1.36%	147.25 ± 2.05 ± 1.39%	9.80
			Minimal External Error ± 2.12	
			Analytical Error ± 1.93	

Statistics				
	Statistical F ratio	1.88	Convergence	0.0004586691
	Error Magnification	3.1312	Number of Iterations	5
	Number of Data Points	11	Calculated Line	Weighted York-2

Relative Abundances			36Ar	%1σ	37Ar	%1σ	38Ar	%1σ	39Ar	%1σ	40Ar	%1σ	Age ± 2σ (Ma)	40Ar(r) (%)	39Ar(k) (%)	K/Ca ± 2σ
M1905-1	650 °C		0.0004668	4.132	0.0023870	31.241	0.0095170	2.000	0.0059869	1.018	0.1487898	0.060	54.27 ± 57.66	7.18	0.19	0.4 ± 0.3
M1905-2	750 °C		0.0003106	4.377	0.0051394	17.119	0.0009190	2.385	0.0237384	1.017	0.1733673	0.052	101.67 ± 10.18	46.40	0.74	0.7 ± 0.3
M1905-3	850 °C		0.0002017	5.305	0.0025859	25.427	0.0017845	2.121	0.0799849	1.003	0.4251432	0.024	134.83 ± 3.47	85.35	2.49	5.0 ± 2.6
M1905-4	900 °C		0.0001738	5.558	0.0021003	35.312	0.0022106	2.122	0.1453282	1.000	0.8010192	0.031	151.64 ± 3.12	93.01	4.53	11.2 ± 8.0
M1905-5	950 °C		0.0001178	7.163	0.0028546	28.371	0.0078181	2.013	0.5526449	0.998	2.9433776	0.011	154.67 ± 2.97	98.26	17.23	31.3 ± 17.9
M1905-6	1000 °C		0.0000719	12.936	0.0026074	21.346	0.0080077	2.014	0.5761874	0.999	2.9861580	0.014	151.35 ± 2.91	98.72	17.97	35.7 ± 15.5
M1905-7	1025 °C		0.0000232	24.890	0.0021291	28.391	0.0037743	2.095	0.2678279	0.998	1.3461946	0.026	147.24 ± 2.85	98.91	8.35	20.3 ± 11.7
M1905-8	1050 °C		0.0000340	15.939	0.0023323	29.802	0.0026599	2.014	0.1902312	1.000	0.9253285	0.023	141.85 ± 2.77	98.32	5.93	13.2 ± 7.9
M1905-9	1075 °C		0.0000244	33.179	0.0007544	66.944	0.0019983	2.115	0.1406830	0.999	0.6826937	0.029	141.55 ± 2.89	98.34	4.39	30.1 ± 40.4
M1905-10	1115 °C		0.0000295	23.189	0.0010710	61.604	0.0023303	2.069	0.1612750	1.001	0.7962217	0.030	143.88 ± 2.86	98.31	5.03	24.3 ± 30.0
M1905-11	1225 °C		0.0001006	10.004	0.0037463	22.861	0.0060579	2.046	0.4044606	0.999	2.0390157	0.018	146.30 ± 2.84	97.96	12.61	17.4 ± 8.1
M1905-12	1325 °C		0.0000486	7.732	0.0075771	9.139	0.0081884	2.004	0.5583795	0.999	2.8847737	0.014	151.23 ± 2.90	98.95	17.41	11.9 ± 2.4
M1905-13	1450 °C		0.0000079	83.824	0.0012975	38.349	0.0009670	2.191	0.0608785	1.002	0.3202093	0.040	153.54 ± 3.48	98.74	1.90	7.6 ± 5.8
M1905-14	1550 °C		0.0000083	70.730	0.0014040	40.496	0.0005712	2.344	0.0394429	1.010	0.2062875	0.041	152.05 ± 3.88	98.29	1.23	4.5 ± 3.7
		Σ	0.0016190	2.219	0.0379863	6.764	0.0568041	0.676	3.2070493	0.355	16.6785800	0.006				

Information on Analysis and Constants Used in Calculations

Sample = AR-04-62B
Material = Muscovite
Location = Arménie
Analyst = Yann ROLLAND
Project = ROLLAND_HASSIG
Mass Discrimination Law = LIN
Irradiation = MC45
J = 0.01710430 ± 0.00004276
Hb3gr = 1073.600 ± 5.368 Ma
IGSN = Undefined
Preferred Age = Undefined
Classification = Undefined
Experiment Type = Undefined
Extraction Method = Undefined
Heating = 600 sec
Isolation = 2.00 min
Instrument = FOUR
Lithology = Undefined
Lat-Lon = Undefined - Undefined

Age Equations = Conventional
Negative Intensities = Allowed
Decay Constant 40K = 5.543 ± 0.010 E-10 1/ a
Decay Constant 39Ar = 2.940 ± 0.029 E-07 1/ h
Decay Constant 37Ar = 8.220 ± 0.010 E-04 1/ h
Decay Constant 36Cl = 2.310 ± 0.016 E-06 1/ a
Production Ratio 36/ 38 in Cl = 316.0 ± 15.8

Results	40(r)/39(k) ± 2σ	Age ± 2σ (Ma)	MSWD	39Ar(k) (%,n)	K/Ca ± 2σ
Age Plateau Error Mean	5.0052 ± 0.1006 ± 2.01%	148.19 ± 2.95 ± 1.99%	9.98	96.58 11	10.9 ± 3.3
	Minimal External Error ± 2.99		2.23	Statistical T Ratio	
	Analytical Error ± 2.86		3.1587	Error Magnification	
Total Fusion Age	5.0220 ± 0.0363 ± 0.72%	148.67 ± 1.25 ± 0.84%		14	13.6 ± 2.1
	Minimal External Error ± 1.36				
	Analytical Error ± 1.03				
Normal Isochron No Convergence	5.0771 ± 0.1297 ± 2.55%	150.23 ± 3.75 ± 2.50%	7.19	96.58 11	
	Minimal External Error ± 3.79		1.88	Statistical F ratio	
	Analytical Error ± 3.68		2.6810	Error Magnification	
Inverse Isochron Error Chron	4.9721 ± 0.0678 ± 1.36%	147.25 ± 2.05 ± 1.39%	9.80	96.58 11	
	Minimal External Error ± 2.12		1.88	Statistical F ratio	
	Analytical Error ± 1.93		3.1312	Error Magnification	

Degassing Patterns			36Ar(a)	%1σ	36Ar(c)	%1σ	36Ar(ca)	%1σ	36Ar(cl)	%1σ	37Ar(ca)	%1σ	38Ar(a)	%1σ	38Ar(c)	%1σ	38Ar(k)	%1σ
M1905-1	650 °C		0.000462	4.18	0.000000	0.00	0.000001	31.26	0.000004	5.45	0.002387	31.24	0.000087	4.18	0.000000	0.00	0.000072	2.24
M1905-2	750 °C		0.000309	4.40	0.000000	0.00	0.000001	17.15	0.000000	8.38	0.005139	17.12	0.000058	4.40	0.000000	0.00	0.000285	2.24
M1905-3	850 °C		0.000201	5.33	0.000000	0.00	0.000001	25.45	0.000000	7.82	0.002586	25.43	0.000038	5.34	0.000000	0.00	0.000960	2.24
M1905-4	900 °C		0.000173	5.58	0.000000	0.00	0.000001	35.33	0.000000	15.64	0.002100	35.31	0.000033	5.59	0.000000	0.00	0.001744	2.24
M1905-5	950 °C		0.000116	7.25	0.000000	0.00	0.000001	28.39	0.000001	19.62	0.002855	28.37	0.000022	7.25	0.000000	0.00	0.006632	2.24
M1905-6	1000 °C		0.000071	13.16	0.000000	0.00	0.000001	21.37	0.000000	21.69	0.002607	21.35	0.000013	13.16	0.000000	0.00	0.006914	2.24
M1905-7	1025 °C		0.000022	25.84	0.000000	0.00	0.000001	28.41	0.000000	20.47	0.002129	28.39	0.000004	25.84	0.000000	0.00	0.003214	2.24
M1905-8	1050 °C		0.000033	16.34	0.000000	0.00	0.000001	29.82	0.000000	21.72	0.002332	29.80	0.000006	16.34	0.000000	0.00	0.002283	2.24
M1905-9	1075 °C		0.000024	33.66	0.000000	0.00	0.000000	66.95	0.000000	19.62	0.000754	66.94	0.000005	33.66	0.000000	0.00	0.001688	2.24
M1905-10	1115 °C		0.000029	23.58	0.000000	0.00	0.000000	61.61	0.000000	17.79	0.001071	61.60	0.000005	23.58	0.000000	0.00	0.001935	2.24
M1905-11	1225 °C		0.000099	10.17	0.000000	0.00	0.000001	22.88	0.000001	15.18	0.003746	22.86	0.000019	10.17	0.000000	0.00	0.004853	2.24
M1905-12	1325 °C		0.000046	8.22	0.000000	0.00	0.000002	9.19	0.000001	16.59	0.007577	9.14	0.000009	8.22	0.000000	0.00	0.006700	2.24
M1905-13	1450 °C		0.000007	89.12	0.000000	0.00	0.000000	38.36	0.000000	13.28	0.001298	38.35	0.000001	89.12	0.000000	0.00	0.000731	2.24
M1905-14	1550 °C		0.000008	74.67	0.000000	0.00	0.000000	40.51	0.000000	22.25	0.001404	40.50	0.000001	74.67	0.000000	0.00	0.000473	2.24
		Σ	0.001600	2.25	0.000000	0.00	0.000011	6.77	0.000008	3.93	0.037986	6.76	0.000302	2.25	0.000000	0.00	0.038484	0.79
		Σ							0.001619	2.22	0.037986	6.76						

38Ar(ca)	%1σ	38Ar(cl)	%1σ	39Ar(k)	%1σ	39Ar(ca)	%1σ	40Ar(r)	%1σ	40Ar(a)	%1σ	40Ar(c)	%1σ	40Ar(k)	%1σ
0.000014	95.27	0.009344	7.43	0.005985	1.02	0.000002	31.50	0.010686	53.91	0.137926	4.18	0.000000	0.00	0.000178	2.24
0.000031	91.61	0.000545	9.78	0.023735	1.02	0.000004	17.58	0.080449	5.05	0.092214	4.40	0.000000	0.00	0.000705	2.24
0.000016	93.52	0.000771	9.31	0.079983	1.00	0.000002	25.74	0.362860	0.88	0.059908	5.34	0.000000	0.00	0.002375	2.24
0.000013	96.68	0.000422	16.44	0.145327	1.00	0.000002	35.54	0.745054	0.39	0.051649	5.59	0.000000	0.00	0.004316	2.24
0.000017	94.37	0.001147	20.26	0.552643	1.00	0.000002	28.65	2.892190	0.09	0.034774	7.25	0.000000	0.00	0.016413	2.24
0.000016	92.50	0.001065	22.27	0.576185	1.00	0.000002	21.72	2.947935	0.10	0.021110	13.16	0.000000	0.00	0.017113	2.24
0.000013	94.37	0.000543	21.09	0.267826	1.00	0.000002	28.67	1.331580	0.13	0.006661	25.84	0.000000	0.00	0.007954	2.24
0.000014	94.81	0.000357	22.30	0.190230	1.00	0.000002	30.07	0.909768	0.18	0.009911	16.34	0.000000	0.00	0.005650	2.24
0.000005	112.17	0.000301	20.26	0.140682	1.00	0.000001	67.06	0.671341	0.36	0.007174	33.66	0.000000	0.00	0.004178	2.24
0.000006	109.06	0.000383	18.50	0.161274	1.00	0.000001	61.73	0.782770	0.26	0.008661	23.58	0.000000	0.00	0.004790	2.24
0.000022	92.86	0.001163	16.00	0.404458	1.00	0.000003	23.21	1.997440	0.15	0.029563	10.17	0.000000	0.00	0.012012	2.24
0.000045	90.46	0.001434	17.34	0.558374	1.00	0.000006	9.98	2.854513	0.04	0.013677	8.22	0.000000	0.00	0.016584	2.24
0.000008	97.83	0.000227	14.21	0.060878	1.00	0.000001	38.56	0.316185	0.63	0.002216	89.12	0.000000	0.00	0.001808	2.24
0.000008	98.69	0.000088	22.82	0.039442	1.01	0.000001	40.69	0.202769	0.87	0.002347	74.67	0.000000	0.00	0.001171	2.24
0.000228	29.32	0.017790	4.81	3.207022	0.36	0.000028	6.88	16.105540	0.07	0.477792	2.25	0.000000	0.00	0.095249	0.79
		0.056804	1.60			3.207049	0.36							16.678580	0.09

Additional Parameters		40(r)/39(k)	1σ	40(r+a)	1σ	40Ar/39Ar	1σ	37Ar/39Ar	1σ	36Ar/39Ar	1σ	Time (days)	37Ar (decay)	39Ar (decay)	40Ar (moles)
M1905-1	650 °C	1.785427	0.96277	0.148612	0.00009	24.852376	0.25340	0.398695	0.12462	0.077972	0.00332	223.317	85.59294610	1.00159285	2.976E-15
M1905-2	750 °C	3.389493	0.17454	0.172662	0.00009	7.303228	0.07440	0.216500	0.03713	0.013082	0.00059	223.333	85.61992069	1.00159297	3.467E-15
M1905-3	850 °C	4.536715	0.06059	0.422768	0.00011	5.315296	0.05334	0.032330	0.00823	0.002522	0.00014	223.350	85.64807715	1.00159308	8.503E-15
M1905-4	900 °C	5.126757	0.05500	0.796703	0.00026	5.511795	0.05514	0.014452	0.00511	0.001196	0.00007	223.366	85.67506911	1.00159320	1.602E-14
M1905-5	950 °C	5.233380	0.05246	2.926964	0.00049	5.325984	0.05318	0.005165	0.00147	0.000213	0.00002	223.383	85.70324370	1.00159331	5.887E-14
M1905-6	1000 °C	5.116295	0.05133	2.969045	0.00056	5.182616	0.05176	0.004525	0.00097	0.000125	0.00002	223.400	85.73260209	1.00159344	5.972E-14
M1905-7	1025 °C	4.971802	0.05008	1.338240	0.00039	5.026342	0.05020	0.007949	0.00226	0.000086	0.00002	223.417	85.76197054	1.00159356	2.692E-14
M1905-8	1050 °C	4.782473	0.04857	0.919679	0.00025	4.864230	0.04863	0.012261	0.00366	0.000179	0.00003	223.434	85.79017371	1.00159368	1.851E-14
M1905-9	1075 °C	4.772032	0.05070	0.678515	0.00022	4.852710	0.04851	0.005362	0.00359	0.000173	0.00006	223.451	85.81956188	1.00159380	1.365E-14
M1905-10	1115 °C	4.853663	0.05021	0.791432	0.00026	4.937044	0.04942	0.006641	0.00409	0.000183	0.00004	223.467	85.84660788	1.00159391	1.592E-14
M1905-11	1225 °C	4.938562	0.04990	2.027003	0.00045	5.041321	0.05036	0.009262	0.00212	0.000249	0.00003	223.484	85.87483889	1.00159403	4.078E-14
M1905-12	1325 °C	5.112189	0.05111	2.868190	0.00055	5.166332	0.05160	0.013570	0.00125	0.000087	0.00001	223.503	85.90660987	1.00159416	5.770E-14
M1905-13	1450 °C	5.193788	0.06135	0.318401	0.00013	5.259809	0.05273	0.021313	0.00818	0.000130	0.00011	223.519	85.93486060	1.00159428	6.404E-15
M1905-14	1550 °C	5.140951	0.06837	0.205116	0.00009	5.230030	0.05285	0.035595	0.01442	0.000210	0.00015	223.537	85.96429833	1.00159440	4.126E-15

Procedure Blanks		36Ar	1σ	37Ar	1σ	38Ar	1σ	39Ar	1σ	40Ar	1σ
M1905-1	650 °C	0.000045	0.000005	0.000149	0.000008	0.000021	0.000004	0.000024	0.000003	0.005552	0.000016
M1905-2	750 °C	0.000043	0.000004	0.000151	0.000008	0.000018	0.000003	0.000025	0.000002	0.005073	0.000014
M1905-3	850 °C	0.000052	0.000006	0.000151	0.000006	0.000020	0.000005	0.000023	0.000004	0.007434	0.000024
M1905-4	900 °C	0.000052	0.000006	0.000151	0.000006	0.000020	0.000005	0.000023	0.000004	0.007434	0.000024
M1905-5	950 °C	0.000052	0.000006	0.000151	0.000006	0.000020	0.000005	0.000023	0.000004	0.007434	0.000024
M1905-6	1000 °C	0.000067	0.000005	0.000152	0.000005	0.000022	0.000003	0.000028	0.000004	0.011870	0.000036
M1905-7	1025 °C	0.000067	0.000005	0.000152	0.000005	0.000022	0.000003	0.000028	0.000004	0.011870	0.000036
M1905-8	1050 °C	0.000067	0.000005	0.000152	0.000005	0.000022	0.000003	0.000028	0.000004	0.011870	0.000036
M1905-9	1075 °C	0.000067	0.000005	0.000152	0.000005	0.000022	0.000003	0.000028	0.000004	0.011870	0.000036
M1905-10	1115 °C	0.000067	0.000005	0.000152	0.000005	0.000022	0.000003	0.000028	0.000004	0.011870	0.000036
M1905-11	1225 °C	0.000067	0.000005	0.000152	0.000005	0.000022	0.000003	0.000028	0.000004	0.011870	0.000036
M1905-12	1325 °C	0.000079	0.000002	0.000155	0.000005	0.000022	0.000008	0.000037	0.000008	0.014360	0.000050
M1905-13	1450 °C	0.000058	0.000006	0.000161	0.000004	0.000025	0.000001	0.000022	0.000003	0.009249	0.000023
M1905-14	1550 °C	0.000075	0.000003	0.000144	0.000004	0.000021	0.000005	0.000022	0.000005	0.012883	0.000025

Intercept Values		36Ar	1σ	r2		37Ar	1σ	r2		38Ar	1σ	r2		39Ar	1σ	r2		40Ar	1σ	r2	
M1905-1	650 °C	0.000529	0.000005	0.8022	LIN 11 of 11	0.000178	0.000004	0.1772	LIN 11 of 11	0.009712	0.000026	0.9788	EXP 11 of 11	0.006056	0.000012	0.9835	EXP 11 of 11	0.154342	0.000087	0.9986	EXP 11 of 11
M1905-2	750 °C	0.000365	0.000005	0.5694	LIN 11 of 11	0.000213	0.000007	0.0072	LIN 10 of 11	0.000954	0.000012	0.7099	LIN 11 of 11	0.023943	0.000047	0.9862	EXP 11 of 11	0.178440	0.000089	0.9990	EXP 11 of 11
M1905-3	850 °C	0.000261	0.000005	0.3962	LIN 11 of 11	0.000182	0.000005	0.1091	LIN 11 of 11	0.001837	0.000013	0.8645	EXP 11 of 11	0.080611	0.000082	0.9966	EXP 11 of 11	0.432577	0.000098	0.9998	EXP 11 of 11
M1905-4	900 °C	0.000232	0.000004	0.4631	LIN 11 of 11	0.000176	0.000007		AVE 11 of 11	0.002271	0.000016	0.8393	EXP 11 of 11	0.146448	0.000089	0.9987	EXP 11 of 11	0.808453	0.000244	0.9997	EXP 11 of 11
M1905-5	950 °C	0.000174	0.000004	0.3826	LIN 11 of 11	0.000185	0.000008		AVE 11 of 11	0.007981	0.000028	0.9458	EXP 11 of 11	0.556837	0.000144	0.9998	EXP 11 of 11	2.950812	0.000321	1.0000	EXP 11 of 11
M1905-6	1000 °C	0.000142	0.000008		AVE 11 of 11	0.000183	0.000004	0.3274	LIN 11 of 11	0.008177	0.000029	0.9536	EXP 11 of 11	0.580562	0.000187	0.9997	EXP 11 of 11	2.998028	0.000403	0.9999	EXP 11 of 11
M1905-7	1025 °C	0.000091	0.000003	0.4441	LIN 11 of 11	0.000178	0.000005	0.2554	LIN 11 of 11	0.003866	0.000026	0.8589	EXP 11 of 11	0.269876	0.000076	0.9997	EXP 11 of 11	1.358065	0.000344	0.9998	EXP 11 of 11
M1905-8	1050 °C	0.000102	0.000002	0.0882	LIN 11 of 11	0.000180	0.000007		AVE 11 of 11	0.002731	0.000009	0.9412	EXP 11 of 11	0.191694	0.000103	0.9990	EXP 11 of 11	0.937198	0.000210	0.9998	EXP 11 of 11
M1905-9	1075 °C	0.000092	0.000007		AVE 11 of 11	0.000161	0.000003	0.5467	LIN 11 of 11	0.002057	0.000015	0.8661	EXP 11 of 11	0.141772	0.000065	0.9993	EXP 11 of 11	0.694564	0.000198	0.9997	EXP 11 of 11
M1905-10	1115 °C	0.000098	0.000005		AVE 11 of 11	0.000165	0.000006	0.0888	LIN 11 of 11	0.002395	0.000014	0.9241	EXP 11 of 11	0.162520	0.000114	0.9984	EXP 11 of 11	0.808092	0.000233	0.9997	EXP 11 of 11
M1905-11	1225 °C	0.000171	0.000008		AVE 11 of 11	0.000197	0.000009		AVE 11 of 11	0.006191	0.000031	0.9008	EXP 11 of 11	0.407540	0.000154	0.9996	EXP 11 of 11	2.050886	0.000360	0.9999	EXP 11 of 11
M1905-12	1325 °C	0.000129	0.000003	0.3737	LIN 11 of 11	0.000246	0.000006		AVE 11 of 11	0.008360	0.000023	0.9649	EXP 11 of 11	0.562628	0.000200	0.9996	EXP 11 of 11	2.899134	0.000401	0.9999	EXP 11 of 11
M1905-13	1450 °C	0.000066	0.000003	0.2192	LIN 11 of 11	0.000177	0.000004		AVE 11 of 11	0.001010	0.000009	0.7717	EXP 11 of 11	0.061360	0.000052	0.9975	EXP 11 of 11	0.329458	0.000125	0.9994	EXP 11 of 11
M1905-14	1550 °C	0.000084	0.000005		AVE 11 of 11	0.000161	0.000005		AVE 11 of 11	0.000603	0.000005	0.8084	EXP 11 of 11	0.039762	0.000061	0.9911	EXP 11 of 11	0.219171	0.000081	0.9994	EXP 11 of 11

Sample Parameters		Sample	Material	Location	Analyst	Temp	Standard (in Ma)	%1σ	J	%1σ	MDF	%1σ
M1905-1	650 °C	AR-04-62B	Muscovite	Arménie	Yann ROLLAND	650	1073.6	0.5	0.0171043	0.25	1.009167	1
M1905-2	750 °C	AR-04-62B	Muscovite	Arménie	Yann ROLLAND	750	1073.6	0.5	0.0171043	0.25	1.009167	1
M1905-3	850 °C	AR-04-62B	Muscovite	Arménie	Yann ROLLAND	850	1073.6	0.5	0.0171043	0.25	1.009167	1
M1905-4	900 °C	AR-04-62B	Muscovite	Arménie	Yann ROLLAND	900	1073.6	0.5	0.0171043	0.25	1.009167	1
M1905-5	950 °C	AR-04-62B	Muscovite	Arménie	Yann ROLLAND	950	1073.6	0.5	0.0171043	0.25	1.009167	1
M1905-6	1000 °C	AR-04-62B	Muscovite	Arménie	Yann ROLLAND	1000	1073.6	0.5	0.0171043	0.25	1.009167	1
M1905-7	1025 °C	AR-04-62B	Muscovite	Arménie	Yann ROLLAND	1025	1073.6	0.5	0.0171043	0.25	1.009167	1
M1905-8	1050 °C	AR-04-62B	Muscovite	Arménie	Yann ROLLAND	1050	1073.6	0.5	0.0171043	0.25	1.009167	1
M1905-9	1075 °C	AR-04-62B	Muscovite	Arménie	Yann ROLLAND	1075	1073.6	0.5	0.0171043	0.25	1.009167	1
M1905-10	1115 °C	AR-04-62B	Muscovite	Arménie	Yann ROLLAND	1115	1073.6	0.5	0.0171043	0.25	1.009167	1
M1905-11	1225 °C	AR-04-62B	Muscovite	Arménie	Yann ROLLAND	1225	1073.6	0.5	0.0171043	0.25	1.009167	1
M1905-12	1325 °C	AR-04-62B	Muscovite	Arménie	Yann ROLLAND	1325	1073.6	0.5	0.0171043	0.25	1.009167	1
M1905-13	1450 °C	AR-04-62B	Muscovite	Arménie	Yann ROLLAND	1450	1073.6	0.5	0.0171043	0.25	1.009167	1
M1905-14	1550 °C	AR-04-62B	Muscovite	Arménie	Yann ROLLAND	1550	1073.6	0.5	0.0171043	0.25	1.009167	1

Volume Ratio	Sensitivity (mol/volt)	Day	Month	Year	Hour	Min	Resist	Irradiation	Project	Experiment	Nmb	Standard Name
1	2.000E-14	11	NOV	2005	06	19	001	MC45	Rolland_Hassig	M1905	01	Hb3gr
1	2.000E-14	11	NOV	2005	06	42	001	MC45	Rolland_Hassig	M1905	01	Hb3gr
1	2.000E-14	11	NOV	2005	07	06	001	MC45	Rolland_Hassig	M1905	01	Hb3gr
1	2.000E-14	11	NOV	2005	07	29	001	MC45	Rolland_Hassig	M1905	01	Hb3gr
1	2.000E-14	11	NOV	2005	07	53	001	MC45	Rolland_Hassig	M1905	01	Hb3gr
1	2.000E-14	11	NOV	2005	08	18	001	MC45	Rolland_Hassig	M1905	01	Hb3gr
1	2.000E-14	11	NOV	2005	08	43	001	MC45	Rolland_Hassig	M1905	01	Hb3gr
1	2.000E-14	11	NOV	2005	09	07	001	MC45	Rolland_Hassig	M1905	01	Hb3gr
1	2.000E-14	11	NOV	2005	09	32	001	MC45	Rolland_Hassig	M1905	01	Hb3gr
1	2.000E-14	11	NOV	2005	09	55	001	MC45	Rolland_Hassig	M1905	01	Hb3gr
1	2.000E-14	11	NOV	2005	10	19	001	MC45	Rolland_Hassig	M1905	01	Hb3gr
1	2.000E-14	11	NOV	2005	10	46	001	MC45	Rolland_Hassig	M1905	01	Hb3gr
1	2.000E-14	11	NOV	2005	11	10	001	MC45	Rolland_Hassig	M1905	01	Hb3gr
1	2.000E-14	11	NOV	2005	11	35	001	MC45	Rolland_Hassig	M1905	01	Hb3gr

Irradiation Constants		40/36(a)	%1σ	40/36(c)	%1σ	38/36(a)	%1σ	38/36(c)	%1σ	39/37(ca)	%1σ	38/37(ca)	%1σ	36/37(ca)	%1σ
M1905-1	650 °C	298.56	0.1	0.018	35	0.1885	0.16	1.7	3	0.00073	4	0.006	90	0.000282	1
M1905-2	750 °C	298.56	0.1	0.018	35	0.1885	0.16	1.7	3	0.00073	4	0.006	90	0.000282	1
M1905-3	850 °C	298.56	0.1	0.018	35	0.1885	0.16	1.7	3	0.00073	4	0.006	90	0.000282	1
M1905-4	900 °C	298.56	0.1	0.018	35	0.1885	0.16	1.7	3	0.00073	4	0.006	90	0.000282	1
M1905-5	950 °C	298.56	0.1	0.018	35	0.1885	0.16	1.7	3	0.00073	4	0.006	90	0.000282	1
M1905-6	1000 °C	298.56	0.1	0.018	35	0.1885	0.16	1.7	3	0.00073	4	0.006	90	0.000282	1
M1905-7	1025 °C	298.56	0.1	0.018	35	0.1885	0.16	1.7	3	0.00073	4	0.006	90	0.000282	1
M1905-8	1050 °C	298.56	0.1	0.018	35	0.1885	0.16	1.7	3	0.00073	4	0.006	90	0.000282	1
M1905-9	1075 °C	298.56	0.1	0.018	35	0.1885	0.16	1.7	3	0.00073	4	0.006	90	0.000282	1
M1905-10	1115 °C	298.56	0.1	0.018	35	0.1885	0.16	1.7	3	0.00073	4	0.006	90	0.000282	1
M1905-11	1225 °C	298.56	0.1	0.018	35	0.1885	0.16	1.7	3	0.00073	4	0.006	90	0.000282	1
M1905-12	1325 °C	298.56	0.1	0.018	35	0.1885	0.16	1.7	3	0.00073	4	0.006	90	0.000282	1
M1905-13	1450 °C	298.56	0.1	0.018	35	0.1885	0.16	1.7	3	0.00073	4	0.006	90	0.000282	1
M1905-14	1550 °C	298.56	0.1	0.018	35	0.1885	0.16	1.7	3	0.00073	4	0.006	90	0.000282	1

40/39(k)	%1σ	38/39(k)	%1σ	36/38(cl)	%1σ	K/Ca	%1σ	K/Cl	%1σ	Ca/Cl	%1σ
0.0297	2	0.012	2	316	5	0.1616	4	5.4	33	33.3	33
0.0297	2	0.012	2	316	5	0.1616	4	5.4	33	33.3	33
0.0297	2	0.012	2	316	5	0.1616	4	5.4	33	33.3	33
0.0297	2	0.012	2	316	5	0.1616	4	5.4	33	33.3	33
0.0297	2	0.012	2	316	5	0.1616	4	5.4	33	33.3	33
0.0297	2	0.012	2	316	5	0.1616	4	5.4	33	33.3	33
0.0297	2	0.012	2	316	5	0.1616	4	5.4	33	33.3	33
0.0297	2	0.012	2	316	5	0.1616	4	5.4	33	33.3	33
0.0297	2	0.012	2	316	5	0.1616	4	5.4	33	33.3	33
0.0297	2	0.012	2	316	5	0.1616	4	5.4	33	33.3	33
0.0297	2	0.012	2	316	5	0.1616	4	5.4	33	33.3	33
0.0297	2	0.012	2	316	5	0.1616	4	5.4	33	33.3	33
0.0297	2	0.012	2	316	5	0.1616	4	5.4	33	33.3	33

Annexe 13 - Résultats de datation (2) sur Biotite AR-04-62M.

Incremental Heating		36Ar(a)	37Ar(ca)	38Ar(cl)	39Ar(k)	40Ar(r)	Age ± 2σ (Ma)	40Ar(r) (%)	39Ar(k) (%)	K/Ca ± 2σ
M1908-1	650 °C	0.004860	0.000428	0.003920	0.005003	0.012974	81.84 ± 733.48	0.90	0.23	1.9 ± 4.5
M1908-2	750 °C	0.026371	0.004633	0.004513	0.096105	0.397558	123.32 ± 184.81	4.81	4.36	3.4 ± 1.1
M1908-3	850 °C	0.009181	0.003833	0.033570	0.750346	3.125050	124.13 ± 8.60	53.07	34.01	31.6 ± 25.1
M1908-4	900 °C	0.001492	0.000033	0.013321	0.298012	1.258230	125.78 ± 4.18	73.47	13.51	1479.7 ######
M1908-5	950 °C	0.000546	0.000915	0.006075	0.135505	0.576958	126.81 ± 3.76	77.55	6.14	23.9 ± 78.9
M1908-6	1000 °C	0.000406	0.002049	0.004832	0.108386	0.452041	124.30 ± 3.61	78.40	4.91	8.5 ± 4.9
M1908-7	1050 °C	0.000491	0.001787	0.005289	0.122149	0.504072	123.03 ± 3.66	77.05	5.54	11.0 ± 10.6
M1908-8	1100 °C	0.000417	0.001385	0.005422	0.120542	0.495507	122.57 ± 3.55	79.44	5.46	14.1 ± 14.9
M1908-9	1150 °C	0.000378	0.000544	0.006265	0.137599	0.563396	122.10 ± 3.14	82.82	6.24	40.9 ± 94.7
M1908-10	1200 °C	0.000335	0.000519	0.004617	0.103719	0.413845	119.09 ± 3.45	80.06	4.70	32.3 ± 63.8
M1908-11	1300 °C	0.001399	0.003438	0.013042	0.291395	1.194147	122.21 ± 4.05	73.69	13.21	13.7 ± 4.8
M1908-12	1400 °C	0.000109	0.001560	0.001472	0.032755	0.139155	126.54 ± 5.13	80.58	1.48	3.4 ± 2.1
M1908-13	1550 °C	0.000020	0.000118	0.000253	0.004692	0.019760	125.46 ± 18.46	76.40	0.21	6.4 ± 71.4
	Σ	0.046005	0.019346	0.102591	2.206208	9.126744				

Information on Analysis
Sample = AR-04-62B
Material = Biotite
Location = Arménie
Analyst = Yann ROLLAND
Project = ROLLAND_HASSIG
Mass Discrimination Law = LIN
Irradiation = MC45
J = 0.01710240 ± 0.00004276
Hb3gr = 1073.600 ± 5.368 Ma

Results	40(r)/39(k) ± 2σ	Age ± 2σ (Ma)	MSWD	39Ar(k) (%,n)	K/Ca ± 2σ
Age Plateau	4.1352 ± 0.0504 ± 1.22%	123.28 ± 1.57 ± 1.27%	1.39	95.42 11	6.0 ± 2.8
		Minimal External Error ± 1.63	2.23	Statistical T Ratio	
		Analytical Error ± 1.45	1.1793	Error Magnification	
Total Fusion Age	4.1368 ± 0.3033 ± 7.33%	123.33 ± 8.76 ± 7.10%		13	18.4 ± 6.5
		Minimal External Error ± 8.77			
		Analytical Error ± 8.74			

Normal Isochron		39(k)/36(a) ± 2σ	40(a+r)/36(a) ± 2σ	r.i.
M1908-1	650 °C	1.0 ± 0.1	295.9 ± 23.2	0.9609
M1908-2	750 °C	3.6 ± 0.3	313.6 ± 24.5	0.9687
M1908-3	850 °C	81.7 ± 6.6	639.0 ± 50.1	0.9691
M1908-4	900 °C	199.7 ± 16.3	1141.7 ± 90.3	0.9695
M1908-5	950 °C	248.2 ± 21.0	1355.5 ± 111.4	0.9716
M1908-6	1000 °C	266.8 ± 22.9	1411.1 ± 117.6	0.9722
M1908-7	1050 °C	248.9 ± 20.6	1325.5 ± 106.5	0.9703
M1908-8	1100 °C	288.8 ± 26.2	1485.6 ± 131.4	0.9753
M1908-9	1150 °C	364.3 ± 32.8	1790.2 ± 157.2	0.9750
M1908-10	1200 °C	309.7 ± 29.2	1534.2 ± 141.3	0.9772
M1908-11	1300 °C	208.3 ± 17.1	1152.3 ± 91.6	0.9698
M1908-12	1400 °C	300.4 ± 47.5	1574.8 ± 247.1	0.9918
M1908-13	1550 °C	234.9 ± 117.3	1287.5 ± 642.5	0.9990

Results	40(a)/36(a) ± 2σ	40(r)/39(k) ± 2σ	Age ± 2σ (Ma)	MSWD
Normal Isochron	319.4232 ± 36.7938 ± 11.52%	4.0455 ± 0.1524 ± 3.77%	120.69 ± 4.44 ± 3.68%	1.34
			Minimal External Error ± 4.46	
			Analytical Error ± 4.40	

Statistics				
	Statistical F ratio	1.88	Convergence	0.0000359632
	Error Magnification	1.1596	Number of Iterations	27
	Number of Data Points	11	Calculated Line	Weighted York-2

Inverse Isochron		39(k)/40(a+r) ± 2σ	36(a)/40(a+r) ± 2σ	r.i.
M1908-1	650 °C	0.003479 ± 0.000078	0.003380 ± 0.000265	0.0000
M1908-2	750 °C	0.011620 ± 0.000233	0.003188 ± 0.000250	0.0004
M1908-3	850 °C	0.127914 ± 0.002555	0.001565 ± 0.000123	0.0001
M1908-4	900 °C	0.174910 ± 0.003497	0.000876 ± 0.000069	0.0002
M1908-5	950 °C	0.183129 ± 0.003665	0.000738 ± 0.000061	0.0003
M1908-6	1000 °C	0.189039 ± 0.003794	0.000709 ± 0.000059	0.0003
M1908-7	1050 °C	0.187743 ± 0.003758	0.000754 ± 0.000061	0.0005
M1908-8	1100 °C	0.194379 ± 0.003894	0.000673 ± 0.000060	0.0004
M1908-9	1150 °C	0.203501 ± 0.004068	0.000559 ± 0.000049	0.0002
M1908-10	1200 °C	0.201852 ± 0.004042	0.000652 ± 0.000060	0.0002
M1908-11	1300 °C	0.180794 ± 0.003616	0.000868 ± 0.000069	0.0002
M1908-12	1400 °C	0.190758 ± 0.003868	0.000635 ± 0.000100	0.0003
M1908-13	1550 °C	0.182405 ± 0.004011	0.000777 ± 0.000388	0.0015

Results	40(a)/36(a) ± 2σ	40(r)/39(k) ± 2σ	Age ± 2σ (Ma)	MSWD
Inverse Isochron	319.6099 ± 18.9642 ± 5.93%	4.0542 ± 0.0776 ± 1.92%	120.94 ± 2.32 ± 1.91%	1.35
			Minimal External Error ± 2.36	
			Analytical Error ± 2.24	

Statistics				
	Statistical F ratio	1.88	Convergence	0.0001141468
	Error Magnification	1.1622	Number of Iterations	5
	Number of Data Points	11	Calculated Line	Weighted York-2

Relative Abundances		36Ar	%1σ	37Ar	%1σ	38Ar	%1σ	39Ar	%1σ	40Ar	%1σ	Age ± 2σ (Ma)	40Ar(r) (%)	39Ar(k) (%)	K/Ca ± 2σ
M1908-1	650 °C	0.0048620	3.914	0.0004283	119.789	0.0048989	2.006	0.0050034	1.128	1.4382101	0.014	81.84 ± 733.48	0.90	0.23	1.9 ± 4.5
M1908-2	750 °C	0.0263741	3.912	0.0046331	16.490	0.0106651	2.007	0.0961082	1.001	8.2736519	0.039	123.32 ± 184.81	4.81	4.36	3.4 ± 1.1
M1908-3	850 °C	0.0091969	3.914	0.0038327	39.463	0.0443273	1.987	0.7503490	0.998	5.8882887	0.019	124.13 ± 8.60	53.07	34.01	31.6 ± 25.1
M1908-4	900 °C	0.0014984	3.939	0.0000325	4699.532	0.0171779	2.004	0.2980117	0.999	1.7126491	0.026	125.78 ± 4.18	73.47	13.51	1479.7 ######
M1908-5	950 °C	0.0005484	4.091	0.0009153	164.839	0.0077986	2.003	0.1355039	1.000	0.7439656	0.034	126.81 ± 3.76	77.55	6.14	23.9 ± 78.9
M1908-6	1000 °C	0.0004091	4.137	0.0020489	28.526	0.0062215	2.015	0.1083872	1.003	0.5765689	0.032	124.30 ± 3.61	78.40	4.91	8.5 ± 4.9
M1908-7	1050 °C	0.0004937	3.991	0.0017874	47.832	0.0068579	2.022	0.1221503	1.000	0.6542442	0.042	123.03 ± 3.66	77.05	5.54	11.0 ± 10.6
M1908-8	1100 °C	0.0004203	4.393	0.0013845	52.666	0.0069556	2.014	0.1205430	1.001	0.6237182	0.039	122.57 ± 3.55	79.44	5.46	14.1 ± 14.9
M1908-9	1150 °C	0.0003807	4.354	0.0005442	115.781	0.0079908	2.007	0.1375996	0.999	0.6802478	0.023	122.10 ± 3.14	82.82	6.24	40.9 ± 94.7
M1908-10	1200 °C	0.0003372	4.574	0.0005186	98.672	0.0059278	2.001	0.1037197	1.001	0.5169192	0.026	119.09 ± 3.45	80.06	4.70	32.3 ± 63.8
M1908-11	1300 °C	0.0014056	3.955	0.0034382	16.876	0.0168232	2.000	0.2913973	1.000	1.6204088	0.025	122.21 ± 4.05	73.69	13.21	13.7 ± 4.8
M1908-12	1400 °C	0.0001101	7.766	0.0015597	30.837	0.0018953	2.099	0.0327560	1.012	0.1726818	0.050	126.54 ± 5.13	80.58	1.48	3.4 ± 2.1
M1908-13	1550 °C	0.0000201	24.751	0.0001184	557.063	0.0003138	2.904	0.0046925	1.080	0.0258647	0.203	125.46 ± 18.46	76.40	0.21	6.4 ± 71.4
	Σ	0.0460567	2.417	0.0193463	17.156	0.1378536	0.789	2.2062218	0.414	22.9274190	0.015				

Information on Analysis and Constants Used In Calculations

Sample = AR-04-62B
Material = Biotite
Location = Arménie
Analyst = Yann ROLLAND
Project = ROLLAND_HASSIG
Mass Discrimination Law = LIN
Irradiation = MC45
J = 0.01710240 ± 0.00004276
Hb3gr = 1073.600 ± 5.368 Ma
IGSN = Undefined
Preferred Age = Undefined
Classification = Undefined
Experiment Type = Undefined
Extraction Method = Undefined
Heating = 600 sec
Isolation = 2.00 min
Instrument = FOUR
Lithology = Undefined
Lat-Lon = Undefined - Undefined

Age Equations = Conventional
Negative Intensities = Allowed
Decay Constant 40K = 5.543 ± 0.010 E-10 1/ a
Decay Constant 39Ar = 2.940 ± 0.029 E-07 1/ h
Decay Constant 37Ar = 8.220 ± 0.010 E-04 1/ h
Decay Constant 36Cl = 2.310 ± 0.016 E-06 1/ a
Production Ratio 36/ 38 in Cl = 316.0 ± 15.8

Results	40(r)/39(k) ± 2σ	Age ± 2σ (Ma)	MSWD	39Ar(k) (%,n)	K/Ca ± 2σ
Age Plateau	4.1352 ± 0.0504 ± 1.22%	123.28 ± 1.57 ± 1.27%	1.39	95.42 11	6.0 ± 2.8
	Minimal External Error	± 1.63	2.23	Statistical T Ratio	
	Analytical Error	± 1.45	1.1793	Error Magnification	
Total Fusion Age	4.1368 ± 0.3033 ± 7.33%	123.33 ± 8.76 ± 7.10%		13	18.4 ± 6.5
	Minimal External Error	± 8.77			
	Analytical Error	± 8.74			
Normal Isochron	4.0455 ± 0.1524 ± 3.77%	120.69 ± 4.44 ± 3.68%	1.34	95.42 11	
	Minimal External Error	± 4.46	1.88	Statistical F ratio	
	Analytical Error	± 4.40	1.1596	Error Magnification	
Inverse Isochron	4.0542 ± 0.0776 ± 1.92%	120.94 ± 2.32 ± 1.91%	1.35	95.42 11	
	Minimal External Error	± 2.36	1.88	Statistical F ratio	
	Analytical Error	± 2.24	1.1622	Error Magnification	

Degassing Patterns		36Ar(a)	%1σ	36Ar(c)	%1σ	36Ar(ca)	%1σ	36Ar(cl)	%1σ	37Ar(ca)	%1σ	38Ar(a)	%1σ	38Ar(c)	%1σ	38Ar(k)	%1σ
M1908-1	650 °C	0.004860	3.92	0.000000	0.00	0.000000	119.79	0.000002	5.72	0.000428	119.79	0.000916	3.92	0.000000	0.00	0.000060	2.30
M1908-2	750 °C	0.026371	3.91	0.000000	0.00	0.000001	16.52	0.000002	8.21	0.004633	16.49	0.004971	3.92	0.000000	0.00	0.001153	2.24
M1908-3	850 °C	0.009181	3.92	0.000000	0.00	0.000001	39.48	0.000015	5.73	0.003833	39.46	0.001731	3.92	0.000000	0.00	0.009004	2.24
M1908-4	900 °C	0.001492	3.96	0.000000	0.00	0.000000	4699.53	0.000006	5.71	0.000033	4699.53	0.000281	3.96	0.000000	0.00	0.003576	2.24
M1908-5	950 °C	0.000546	4.11	0.000000	0.00	0.000000	164.84	0.000003	5.71	0.000915	164.84	0.000103	4.11	0.000000	0.00	0.001626	2.24
M1908-6	1000 °C	0.000406	4.17	0.000000	0.00	0.000001	28.54	0.000002	5.72	0.002049	28.53	0.000077	4.17	0.000000	0.00	0.001301	2.24
M1908-7	1050 °C	0.000491	4.02	0.000000	0.00	0.000001	47.84	0.000002	5.73	0.001787	47.83	0.000093	4.02	0.000000	0.00	0.001466	2.24
M1908-8	1100 °C	0.000417	4.42	0.000000	0.00	0.000000	52.68	0.000002	5.71	0.001385	52.67	0.000079	4.43	0.000000	0.00	0.001447	2.24
M1908-9	1150 °C	0.000378	4.39	0.000000	0.00	0.000000	115.79	0.000003	5.70	0.000544	115.78	0.000071	4.39	0.000000	0.00	0.001651	2.24
M1908-10	1200 °C	0.000335	4.60	0.000000	0.00	0.000000	98.68	0.000002	5.70	0.000519	98.67	0.000063	4.61	0.000000	0.00	0.001245	2.24
M1908-11	1300 °C	0.001399	3.97	0.000000	0.00	0.000001	16.91	0.000006	5.71	0.003438	16.88	0.000264	3.98	0.000000	0.00	0.003497	2.24
M1908-12	1400 °C	0.000109	7.85	0.000000	0.00	0.000000	30.85	0.000001	5.80	0.001560	30.84	0.000021	7.85	0.000000	0.00	0.000393	2.24
M1908-13	1550 °C	0.000020	24.95	0.000000	0.00	0.000000	557.06	0.000000	6.44	0.000118	557.06	0.000004	24.95	0.000000	0.00	0.000056	2.27
	Σ	0.046005	2.42	0.000000	0.00	0.000005	17.16	0.000047	2.31	0.019346	17.16	0.008672	2.42	0.000000	0.00	0.026474	0.93
	Σ							0.046057	2.42	0.019346	17.16						

38Ar(ca)	%1σ	38Ar(cl)	%1σ	39Ar(k)	%1σ	39Ar(ca)	%1σ	40Ar(r)	%1σ	40Ar(a)	%1σ	40Ar(c)	%1σ	40Ar(k)	%1σ
0.000003	149.83	0.003920	7.63	0.005003	1.13	0.000000	119.86	0.012974	438.04	1.451035	3.92	0.000000	0.00	0.000149	2.30
0.000028	91.50	0.004513	9.64	0.096105	1.00	0.000003	16.97	0.397558	77.51	7.873240	3.91	0.000000	0.00	0.002854	2.24
0.000023	98.27	0.033570	7.64	0.750346	1.00	0.000003	39.66	3.125050	3.44	2.740954	3.92	0.000000	0.00	0.022285	2.24
0.000000	4700.39	0.013321	7.62	0.298012	1.00	0.000000	4699.53	1.258230	1.40	0.445569	3.96	0.000000	0.00	0.008851	2.24
0.000005	187.81	0.006075	7.62	0.135505	1.00	0.000001	164.89	0.576958	1.16	0.162983	4.11	0.000000	0.00	0.004024	2.24
0.000012	94.41	0.004832	7.63	0.108386	1.00	0.000001	28.81	0.452041	1.12	0.121309	4.17	0.000000	0.00	0.003219	2.24
0.000011	101.92	0.005289	7.64	0.122149	1.00	0.000001	48.00	0.504072	1.17	0.146544	4.02	0.000000	0.00	0.003628	2.24
0.000008	104.28	0.005422	7.62	0.120542	1.00	0.000001	52.82	0.495507	1.11	0.124631	4.43	0.000000	0.00	0.003580	2.24
0.000003	146.65	0.006265	7.61	0.137599	1.00	0.000000	115.85	0.563396	0.88	0.112765	4.39	0.000000	0.00	0.004087	2.24
0.000003	133.55	0.004617	7.62	0.103719	1.00	0.000000	98.75	0.413845	1.11	0.099994	4.61	0.000000	0.00	0.003080	2.24
0.000021	91.57	0.013042	7.62	0.291395	1.00	0.000003	17.34	1.194147	1.39	0.417607	3.98	0.000000	0.00	0.008654	2.24
0.000009	95.14	0.001472	7.69	0.032755	1.01	0.000001	31.10	0.139155	1.84	0.032554	7.85	0.000000	0.00	0.000973	2.24
0.000001	564.29	0.000253	8.18	0.004692	1.08	0.000000	557.08	0.019760	7.54	0.005965	24.95	0.000000	0.00	0.000139	2.27
0.000116	40.27	0.102591	3.07	2.206208	0.41	0.000014	17.23	9.126744	3.64	13.735151	2.42	0.000000	0.00	0.065524	0.93
		0.137854	2.30			2.206222	0.41							22.927419	2.05

Additional Parameters		40(r)/39(k)	1σ	40(r+a)	1σ	40Ar/39Ar	1σ	37Ar/39Ar	1σ	36Ar/39Ar	1σ	Time (days)	37Ar (decay)	39Ar (decay)	40Ar (moles)
M1908-1	650 °C	2.593183	11.35918	1.438062	0.00020	287.446825	3.24204	0.085606	0.10255	0.971743	0.03958	227.340	92.66151912	1.00162128	2.876E-14
M1908-2	750 °C	4.136709	3.20680	8.270798	0.00323	86.086805	0.86245	0.048207	0.00796	0.274420	0.01108	227.357	92.69326113	1.00162140	1.655E-13
M1908-3	850 °C	4.164810	0.14921	5.866003	0.00122	7.847400	0.07836	0.005108	0.00202	0.012257	0.00050	227.373	92.72247337	1.00162151	1.178E-13
M1908-4	900 °C	4.222082	0.07267	1.703798	0.00049	5.746920	0.05744	0.000109	0.00513	0.005028	0.00020	227.389	92.75169483	1.00162163	3.425E-14
M1908-5	950 °C	4.257850	0.06529	0.739941	0.00027	5.490363	0.05494	0.006755	0.01113	0.004047	0.00017	227.406	92.78219660	1.00162174	1.488E-14
M1908-6	1000 °C	4.170671	0.06267	0.573350	0.00020	5.319529	0.05337	0.018903	0.00540	0.003774	0.00016	227.422	92.81270840	1.00162186	1.153E-14
M1908-7	1050 °C	4.126697	0.06348	0.650616	0.00028	5.356059	0.05359	0.014633	0.00700	0.004042	0.00017	227.438	92.84195830	1.00162198	1.308E-14
M1908-8	1100 °C	4.110659	0.06157	0.620138	0.00026	5.174238	0.05182	0.011486	0.00605	0.003487	0.00016	227.455	92.87248975	1.00162209	1.247E-14
M1908-9	1150 °C	4.094472	0.05449	0.676161	0.00018	4.943677	0.04940	0.003955	0.00458	0.002767	0.00012	227.472	92.90303125	1.00162221	1.360E-14
M1908-10	1200 °C	3.990046	0.05974	0.513839	0.00015	4.983811	0.04990	0.005000	0.00493	0.003251	0.00015	227.488	92.93230960	1.00162232	1.034E-14
M1908-11	1300 °C	4.098039	0.07020	1.611754	0.00045	5.560823	0.05561	0.011799	0.00199	0.004824	0.00020	227.504	92.96287077	1.00162244	3.241E-14
M1908-12	1400 °C	4.248361	0.08910	0.171709	0.00009	5.271757	0.05344	0.047615	0.01469	0.003363	0.00026	227.522	92.99599004	1.00162257	3.454E-15
M1908-13	1550 °C	4.211041	0.32065	0.025725	0.00005	5.511903	0.06058	0.025223	0.14051	0.004290	0.00106	227.537	93.02274884	1.00162267	5.173E-16

Procedure Blanks		36Ar	1σ	37Ar	1σ	38Ar	1σ	39Ar	1σ	40Ar	1σ
M1908-1	650 °C	0.000056	0.000005	0.000161	0.000003	0.000022	0.000003	0.000028	0.000003	0.008388	0.000016
M1908-2	750 °C	0.000046	0.000005	0.000165	0.000008	0.000016	0.000005	0.000030	0.000004	0.005026	0.000018
M1908-3	850 °C	0.000056	0.000004	0.000190	0.000016	0.000027	0.000005	0.000038	0.000005	0.006494	0.000063
M1908-4	900 °C	0.000056	0.000004	0.000190	0.000016	0.000027	0.000005	0.000038	0.000005	0.006494	0.000063
M1908-5	950 °C	0.000056	0.000004	0.000190	0.000016	0.000027	0.000005	0.000038	0.000005	0.006494	0.000063
M1908-6	1000 °C	0.000065	0.000003	0.000160	0.000005	0.000027	0.000005	0.000030	0.000003	0.009657	0.000021
M1908-7	1050 °C	0.000065	0.000003	0.000160	0.000005	0.000027	0.000005	0.000030	0.000003	0.009657	0.000021
M1908-8	1100 °C	0.000065	0.000003	0.000160	0.000005	0.000027	0.000005	0.000030	0.000003	0.009657	0.000021
M1908-9	1150 °C	0.000075	0.000004	0.000162	0.000005	0.000028	0.000004	0.000310	0.000007	0.015500	0.000021
M1908-10	1200 °C	0.000075	0.000004	0.000162	0.000005	0.000028	0.000004	0.000310	0.000007	0.015500	0.000021
M1908-11	1300 °C	0.000053	0.000005	0.000159	0.000003	0.000027	0.000002	0.000043	0.000004	0.007736	0.000014
M1908-12	1400 °C	0.000053	0.000006	0.000153	0.000003	0.000019	0.000003	0.000049	0.000004	0.007325	0.000017
M1908-13	1550 °C	0.000071	0.000003	0.000147	0.000004	0.000033	0.000005	0.000761	0.000007	0.015925	0.000038

Intercept Values		36Ar	1σ	r2		37Ar	1σ	r2		38Ar	1σ	r2		39Ar	1σ	r2		40Ar	1σ	r2	
M1908-1	650 °C	0.005061	0.000008	0.9923	EXP 11 of 11	0.000166	0.000005		AVE 11 of 11	0.004993	0.000014	0.9769	EXP 11 of 11	0.005060	0.000026	0.8704	EXP 11 of 11	1.446598	0.000202	0.9999	EXP 11 of 11
M1908-2	750 °C	0.027198	0.000041	0.9925	LIN 11 of 11	0.000216	0.000002	0.1521	LIN 11 of 11	0.010838	0.000031	0.9698	EXP 11 of 11	0.096689	0.000075	0.9977	EXP 11 of 11	8.278678	0.003226	0.9995	EXP 11 of 11
M1908-3	850 °C	0.009524	0.000019	0.9860	EXP 11 of 11	0.000232	0.000005	0.0783	LIN 11 of 11	0.045008	0.000033	0.9984	EXP 11 of 11	0.754689	0.000181	0.9998	EXP 11 of 11	5.894783	0.001109	0.9999	EXP 11 of 11
M1908-4	900 °C	0.001599	0.000006	0.9750	EXP 10 of 11	0.000190	0.000005		AVE 11 of 11	0.017458	0.000048	0.9777	LIN 11 of 11	0.299758	0.000138	0.9994	EXP 11 of 11	1.719143	0.000449	0.9998	EXP 11 of 11
M1908-5	950 °C	0.000621	0.000006	0.7653	LIN 11 of 11	0.000180	0.000004		AVE 11 of 11	0.007941	0.000021	0.9841	EXP 11 of 11	0.136319	0.000085	0.9988	EXP 11 of 11	0.750460	0.000247	0.9996	EXP 11 of 11
M1908-6	1000 °C	0.000486	0.000005	0.6873	EXP 11 of 11	0.000183	0.000004	0.0467	LIN 11 of 11	0.006340	0.000021	0.9641	EXP 11 of 11	0.109039	0.000106	0.9970	EXP 11 of 11	0.586226	0.000184	0.9997	EXP 11 of 11
M1908-7	1050 °C	0.000573	0.000003	0.9005	LIN 10 of 11	0.000180	0.000008		AVE 11 of 11	0.006986	0.000026	0.9566	EXP 11 of 11	0.122881	0.000071	0.9991	EXP 11 of 11	0.663901	0.000272	0.9995	EXP 11 of 11
M1908-8	1100 °C	0.000498	0.000008	0.5945	LIN 11 of 11	0.000175	0.000006		AVE 11 of 11	0.007085	0.000024	0.9777	EXP 11 of 11	0.121264	0.000089	0.9989	EXP 11 of 11	0.633375	0.000245	0.9997	EXP 11 of 11
M1908-9	1150 °C	0.000467	0.000006	0.3860	LIN 11 of 11	0.000168	0.000005	0.1094	LIN 11 of 11	0.008137	0.000023	0.9795	EXP 11 of 11	0.138698	0.000060	0.9995	EXP 11 of 11	0.695748	0.000152	0.9999	EXP 11 of 11
M1908-10	1200 °C	0.000422	0.000007	0.4085	LIN 11 of 11	0.000168	0.000003	0.0649	LIN 11 of 11	0.006043	0.000014	0.9854	EXP 11 of 11	0.104624	0.000077	0.9986	EXP 11 of 11	0.532419	0.000135	0.9998	EXP 11 of 11
M1908-11	1300 °C	0.001500	0.000007	0.9861	EXP 11 of 11	0.000197	0.000006	0.1234	LIN 11 of 11	0.017098	0.000042	0.9959	EXP 11 of 11	0.293111	0.000167	0.9998	EXP 11 of 11	1.628145	0.000407	1.0000	EXP 11 of 11
M1908-12	1400 °C	0.000166	0.000005	0.1763	LIN 11 of 11	0.000170	0.000004	0.0950	LIN 11 of 11	0.001942	0.000013	0.8749	EXP 11 of 11	0.032993	0.000056	0.9921	EXP 11 of 11	0.180007	0.000085	0.9993	EXP 11 of 11
M1908-13	1550 °C	0.000092	0.000004	0.1428	LIN 11 of 11	0.000148	0.000006	0.1282	LIN 11 of 11	0.000351	0.000005	0.3511	LIN 11 of 11	0.005480	0.000018	0.9314	EXP 11 of 11	0.041790	0.000036	0.9919	EXP 11 of 11

Sample Parameters		Sample	Material	Location	Analyst	Temp	Standard (in Ma)	%1σ	J	%1σ	MDF	%1σ
M1908-1	650 °C	AR-04-62B	Biotite	Arménie	Yann ROLLAND	650	1073.6	0.5	0.0171024	0.25	1.007379	1
M1908-2	750 °C	AR-04-62B	Biotite	Arménie	Yann ROLLAND	750	1073.6	0.5	0.0171024	0.25	1.007379	1
M1908-3	850 °C	AR-04-62B	Biotite	Arménie	Yann ROLLAND	850	1073.6	0.5	0.0171024	0.25	1.007379	1
M1908-4	900 °C	AR-04-62B	Biotite	Arménie	Yann ROLLAND	900	1073.6	0.5	0.0171024	0.25	1.007379	1
M1908-5	950 °C	AR-04-62B	Biotite	Arménie	Yann ROLLAND	950	1073.6	0.5	0.0171024	0.25	1.007379	1
M1908-6	1000 °C	AR-04-62B	Biotite	Arménie	Yann ROLLAND	1000	1073.6	0.5	0.0171024	0.25	1.007379	1
M1908-7	1050 °C	AR-04-62B	Biotite	Arménie	Yann ROLLAND	1050	1073.6	0.5	0.0171024	0.25	1.007379	1
M1908-8	1100 °C	AR-04-62B	Biotite	Arménie	Yann ROLLAND	1100	1073.6	0.5	0.0171024	0.25	1.007379	1
M1908-9	1150 °C	AR-04-62B	Biotite	Arménie	Yann ROLLAND	1150	1073.6	0.5	0.0171024	0.25	1.007379	1
M1908-10	1200 °C	AR-04-62B	Biotite	Arménie	Yann ROLLAND	1200	1073.6	0.5	0.0171024	0.25	1.007379	1
M1908-11	1300 °C	AR-04-62B	Biotite	Arménie	Yann ROLLAND	1300	1073.6	0.5	0.0171024	0.25	1.007379	1
M1908-12	1400 °C	AR-04-62B	Biotite	Arménie	Yann ROLLAND	1400	1073.6	0.5	0.0171024	0.25	1.007379	1
M1908-13	1550 °C	AR-04-62B	Biotite	Arménie	Yann ROLLAND	1550	1073.6	0.5	0.0171024	0.25	1.007379	1

Volume Ratio	Sensitivity (mol/volt)	Day	Month	Year	Hour	Min	Resist	Irradiation	Project	Experiment	Nmb	Standard Name
1	2.000E-14	15	NOV	2005	06	51	001	MC45	Rolland_Hassig	M1908	01	Hb3gr
1	2.000E-14	15	NOV	2005	07	16	001	MC45	Rolland_Hassig	M1908	01	Hb3gr
1	2.000E-14	15	NOV	2005	07	39	001	MC45	Rolland_Hassig	M1908	01	Hb3gr
1	2.000E-14	15	NOV	2005	08	02	001	MC45	Rolland_Hassig	M1908	01	Hb3gr
1	2.000E-14	15	NOV	2005	08	26	001	MC45	Rolland_Hassig	M1908	01	Hb3gr
1	2.000E-14	15	NOV	2005	08	50	001	MC45	Rolland_Hassig	M1908	01	Hb3gr
1	2.000E-14	15	NOV	2005	09	13	001	MC45	Rolland_Hassig	M1908	01	Hb3gr
1	2.000E-14	15	NOV	2005	09	37	001	MC45	Rolland_Hassig	M1908	01	Hb3gr
1	2.000E-14	15	NOV	2005	10	01	001	MC45	Rolland_Hassig	M1908	01	Hb3gr
1	2.000E-14	15	NOV	2005	10	24	001	MC45	Rolland_Hassig	M1908	01	Hb3gr
1	2.000E-14	15	NOV	2005	10	48	001	MC45	Rolland_Hassig	M1908	01	Hb3gr
1	2.000E-14	15	NOV	2005	11	14	001	MC45	Rolland_Hassig	M1908	01	Hb3gr
1	2.000E-14	15	NOV	2005	11	35	001	MC45	Rolland_Hassig	M1908	01	Hb3gr

Irradiation Constants		40/36(a)	%1σ	40/36(c)	%1σ	38/36(a)	%1σ	38/36(c)	%1σ	39/37(ca)	%1σ	38/37(ca)	%1σ	36/37(ca)	%1σ
M1908-1	650 °C	298.56	0.1	0.018	35	0.1885	0.16	1.7	3	0.00073	4	0.006	90	0.000282	1
M1908-2	750 °C	298.56	0.1	0.018	35	0.1885	0.16	1.7	3	0.00073	4	0.006	90	0.000282	1
M1908-3	850 °C	298.56	0.1	0.018	35	0.1885	0.16	1.7	3	0.00073	4	0.006	90	0.000282	1
M1908-4	900 °C	298.56	0.1	0.018	35	0.1885	0.16	1.7	3	0.00073	4	0.006	90	0.000282	1
M1908-5	950 °C	298.56	0.1	0.018	35	0.1885	0.16	1.7	3	0.00073	4	0.006	90	0.000282	1
M1908-6	1000 °C	298.56	0.1	0.018	35	0.1885	0.16	1.7	3	0.00073	4	0.006	90	0.000282	1
M1908-7	1050 °C	298.56	0.1	0.018	35	0.1885	0.16	1.7	3	0.00073	4	0.006	90	0.000282	1
M1908-8	1100 °C	298.56	0.1	0.018	35	0.1885	0.16	1.7	3	0.00073	4	0.006	90	0.000282	1
M1908-9	1150 °C	298.56	0.1	0.018	35	0.1885	0.16	1.7	3	0.00073	4	0.006	90	0.000282	1
M1908-10	1200 °C	298.56	0.1	0.018	35	0.1885	0.16	1.7	3	0.00073	4	0.006	90	0.000282	1
M1908-11	1300 °C	298.56	0.1	0.018	35	0.1885	0.16	1.7	3	0.00073	4	0.006	90	0.000282	1
M1908-12	1400 °C	298.56	0.1	0.018	35	0.1885	0.16	1.7	3	0.00073	4	0.006	90	0.000282	1
M1908-13	1550 °C	298.56	0.1	0.018	35	0.1885	0.16	1.7	3	0.00073	4	0.006	90	0.000282	1

40/39(k)	%1σ	38/39(k)	%1σ	36/38(cl)	%1σ	K/Ca	%1σ	K/Cl	%1σ	Ca/Cl	%1σ
0.0297	2	0.012	2	316	5	0.1616	4	5.4	33	33.3	33
0.0297	2	0.012	2	316	5	0.1616	4	5.4	33	33.3	33
0.0297	2	0.012	2	316	5	0.1616	4	5.4	33	33.3	33
0.0297	2	0.012	2	316	5	0.1616	4	5.4	33	33.3	33
0.0297	2	0.012	2	316	5	0.1616	4	5.4	33	33.3	33
0.0297	2	0.012	2	316	5	0.1616	4	5.4	33	33.3	33
0.0297	2	0.012	2	316	5	0.1616	4	5.4	33	33.3	33
0.0297	2	0.012	2	316	5	0.1616	4	5.4	33	33.3	33
0.0297	2	0.012	2	316	5	0.1616	4	5.4	33	33.3	33
0.0297	2	0.012	2	316	5	0.1616	4	5.4	33	33.3	33
0.0297	2	0.012	2	316	5	0.1616	4	5.4	33	33.3	33
0.0297	2	0.012	2	316	5	0.1616	4	5.4	33	33.3	33